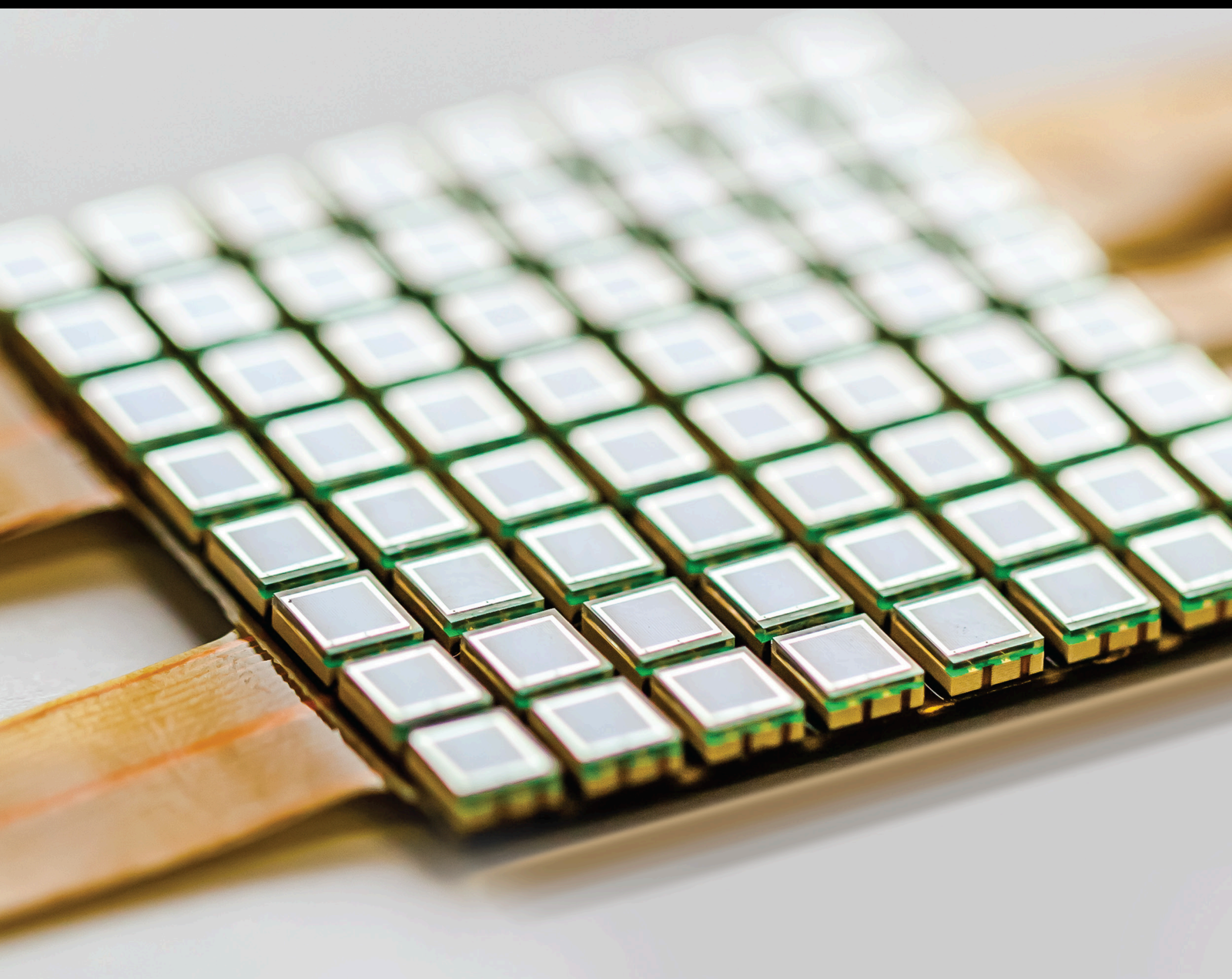


Sensors and Applications in Agricultural and Environmental Monitoring

Lead Guest Editor: Yuan Li

Guest Editors: Ajit Ghosh, Zhenxing Zhang, Zhifeng Yu, and Jingwei Wang





Sensors and Applications in Agricultural and Environmental Monitoring

Sensors and Applications in Agricultural and Environmental Monitoring

Lead Guest Editor: Yuan Li

Guest Editors: Ajit Ghosh, Zhenxing Zhang,
Zhifeng Yu, and Jingwei Wang

Chief Editor

Harith Ahmad, Malaysia

Editorial Board

Ghufran Ahmed, Pakistan
Manuel Aleixandre, Spain
Bruno Andò, Italy
Constantin Apetrei, Romania
Fernando Benito-Lopez, Spain
Romeo Bernini, Italy
Shekhar Bhansali, USA
Matthew Brodie, Australia
Paolo Bruschi, Italy
Belén Calvo, Spain
Stefania Campopiano, Italy
Binghua Cao, China
Domenico Caputo, Italy
Sara Casciati, Italy
Gabriele Cazzulani, Italy
Chi Chiu Chan, Singapore
Edmon Chehura, United Kingdom
Marvin H Cheng, USA
Mario Collotta, Italy
Marco Consales, Italy
Jesus Corres, Spain
Andrea Cusano, Italy
Dzung Dao, Australia
Egidio De Benedetto, Italy
Luca De Stefano, Italy
Manel del Valle, Spain
Francesco Dell'Olio, Italy
Franz L. Dickert, Austria
Giovanni Diraco, Italy
Nicola Donato, Italy
Mauro Epifani, Italy
Congbin Fan, China
Vittorio Ferrari, Italy
Luca Francioso, Italy
Bin Gao, China
Manel Gasulla, Spain
Carmine Granata, Italy
Banshi D. Gupta, India
Mohammad Haider, USA
María del Carmen Horrillo, Spain
Evangelos Hristoforou, Greece
Shahid Hussain, China
Syed K. Islam, USA
Stephen James, United Kingdom



Bruno C. Janegitz, Brazil
Hai-Feng Ji, USA
Sang Sub Kim, Republic of Korea
Antonio Lazaro, Spain
Chengkuo Lee, Singapore
Yuan Li, China
Chenzong Li, USA
Rosalba Liguori, Italy
Duo Lin, China
Xinyu Liu, Canada
Eduard Llobet, Spain
Jaime Lloret, Spain
Yu-Lung Lo, Taiwan
Jesús Lozano, Spain
Oleg Lupan, Moldova
Frederick Mailly, France
Pawel Malinowski, Poland
Vincenzo Marletta, Italy
Carlos Marques, Portugal
Eugenio Martinelli, Italy
Antonio Martinez-Olmos, Spain
Giuseppe Maruccio, Italy
Yasuko Y. Maruo, Japan
Fanli Meng, China
Carlos Michel, Mexico
Stephen. J. Mihailov, Canada
Heinz C. Neitzert, Italy
Sing Kiong Nguang, New Zealand
Calogero M. Oddo, Italy
Marimuthu Palaniswami, Australia
Alberto J. Palma, Spain
Davide Palumbo, Italy
Roberto Paolesse, Italy
Giovanni Pau, Italy
Giorgio Pennazza, Italy
Michele Penza, Italy
Salvatore Pirozzi, Italy
Antonina Pirrotta, Italy
Stelios M. Potirakis, Greece
Biswajeet Pradhan, Malaysia
Giuseppe Quero, Italy
Valerie Renaudin, France
Armando Ricciardi, Italy
Christos Riziotis, Greece



Maria Luz Rodriguez-Mendez, Spain
Jerome Rossignol, France
Carlos Ruiz, Spain
Ylias Sabri, Australia
José P. Santos, Spain
Sina Sareh, United Kingdom
Isabel Sayago, Spain
Andreas Schütze, Germany
Praveen K. Sekhar, USA
Sandra Sendra, Spain
Pietro Siciliano, Italy
Vincenzo Spagnolo, Italy
Sachin K. Srivastava, India
Grigore Stamatescu, Romania
Stefano Stassi, Italy
Vincenzo Stornelli, Italy
Salvatore Surdo, Italy
Roshan Thotagamuge, Brunei Darussalam
Guiyun Tian, United Kingdom
Vijay Tomer, USA
Abdellah Touhafi, Belgium
Hoang Vinh Tran, Vietnam
Aitor Urrutia, Spain
Hana Vaisocherova - Lisalova, Czech
Republic
Everardo Vargas-Rodriguez, Mexico
Xavier Vilanova, Spain
Luca Vollero, Italy
Tomasz Wandowski, Poland
He Wen, China
Qihao Weng, USA
Qiang Wu, United Kingdom
Penghai Wu, China
Chen Yang, China
Aijun Yin, China
Chouki Zerrouki, France

Contents



Sensors and Applications in Agricultural and Environmental Monitoring

Yuan Li , Ajit Ghosh, Zhenxing Zhang , Zhifeng Yu, and Jingwei Wang
Editorial (3 pages), Article ID 9841470, Volume 2021 (2021)




Anonymous and Efficient Certificateless Multirecipient Signcryption Scheme for Ecological Data Sharing

Pengfei Su, Yong Xie, and Ping Liu 
Research Article (16 pages), Article ID 5132861, Volume 2020 (2020)


A Novel Biofloculant from *Raoultella planticola* Enhances Removal of Copper Ions from Water

Fancheng Zeng, Liang Xu , Caiyun Sun , Hong Liu, and Libo Chen
Research Article (10 pages), Article ID 2581205, Volume 2020 (2020)



Electronic Nose Technologies in Monitoring Black Tea Manufacturing Process

Tharaga Sharmilan , Iresha Premarathne, Indika Wanniarachchi , Sandya Kumari, and Dakshika Wanniarachchi 
Review Article (8 pages), Article ID 3073104, Volume 2020 (2020)



A Model with Leaf Area Index and Trunk Diameter for LoRaWAN Radio Propagation in Eastern China Mixed Forest

Yin Wu , Genwei Guo, Guiyun Tian, and Wenbo Liu
Research Article (16 pages), Article ID 2687148, Volume 2020 (2020)


Response Mechanism of Cotton Growth to Water and Nutrients under Drip Irrigation with Plastic Mulch in Southern Xinjiang

Meng Li, Jun Xiao , Yungang Bai , Yingji Du, Fucang Zhang, Houliang Cheng, and Haoran Wang
Research Article (16 pages), Article ID 2575162, Volume 2020 (2020)

Application of Low-Cost Sensors for the Development of a Methodology to Design Front-End Loaders for Tractors

H. Malon , A. Ayuda, F. J. Garcia-Ramos , M. Vidal, and J. Cuartero 
Research Article (13 pages), Article ID 3504389, Volume 2020 (2020)





Change Analysis of Spring Vegetation Green-Up Date in Qinba Mountains under the Support of Spatiotemporal Data Cube

Jiyuan Li , Xiao Feng , Jiangbin Yin, and Fang Chen
Research Article (12 pages), Article ID 6413654, Volume 2020 (2020)

Variation Characteristics of Stem Water Content in *Lagerstroemia indica* and Its Response to Environmental Factors

Hao Liang , Meng Zhang, Hailan Wang , Chao Gao, and Yandong Zhao 
Research Article (10 pages), Article ID 8689272, Volume 2020 (2020)

Sensors Applied for the Detection of Pesticides and Heavy Metals in Freshwaters


Hongyong Xiang , Qinghua Cai, Yuan Li , Zhenxing Zhang , Lina Cao, Kun Li, and Haijun Yang 
Review Article (22 pages), Article ID 8503491, Volume 2020 (2020)

Stem Water Content for Crape Myrtle in Response to Drought, Cold, and Disease Stress

Chao Gao , Yue Zhao , and Yandong Zhao 

Research Article (10 pages), Article ID 2893069, Volume 2020 (2020)

Leymus chinensis Tolerates Mowing Disturbance by Maintaining Photosynthesis in Saline-Alkali Heterogeneous Habitats

Nan Lu, Luhao Qu, Jun Liu , Jiyun Yang, Long Bai, Yue Huang, and Yanchun Zhou



Research Article (10 pages), Article ID 4510275, Volume 2020 (2020)

Effects on Local Temperature and Energy of Oasis City Expansion in Arid Area of Northwest China

Miao Zhang , Geping Luo , Peng Cai, and Rafiq Hamdi

Research Article (12 pages), Article ID 3282475, Volume 2020 (2020)

Optimized Cluster-Based Dynamic Energy-Aware Routing Protocol for Wireless Sensor Networks in Agriculture Precision

Kashif Naseer Qureshi , Muhammad Umair Bashir, Jaime Lloret , and Antonio Leon





Research Article (19 pages), Article ID 9040395, Volume 2020 (2020)

Elite Immune Ant Colony Optimization-Based Task Allocation for Maximizing Task Execution Efficiency in Agricultural Wireless Sensor Networks

Mengying Xu  and Jie Zhou 

Research Article (9 pages), Article ID 3231864, Volume 2020 (2020)

Colloidal Influence Factor of Biofloculant in Coagulation of Chromium and Nitrobenzene

Renshi Ma , Guang Chen , Kai Liu , and Shihuan Cheng 




Research Article (10 pages), Article ID 9702147, Volume 2020 (2020)

Evaluation of the Spatial Pattern of the Resolution-Enhanced Thermal Data for Urban Area

Xiao Feng  and Jiyuan Li 





Research Article (15 pages), Article ID 3427321, Volume 2020 (2020)

Development of an IoT-Based Indoor Air Quality Monitoring Platform

JunHo Jo , ByungWan Jo , JungHoon Kim , SungJun Kim, and WoonYong Han




Research Article (14 pages), Article ID 8749764, Volume 2020 (2020)

A Novel Method for Broiler Abnormal Sound Detection Using WMFCC and HMM

Longshen Liu , Bo Li , Ruqian Zhao, Wen Yao, Mingxia Shen , and Ji Yang 

Research Article (7 pages), Article ID 2985478, Volume 2020 (2020)

A Review of Underwater Localization Techniques, Algorithms, and Challenges

Xin Su , Inam Ullah , Xiaofeng Liu, and Dongmin Choi 



Review Article (24 pages), Article ID 6403161, Volume 2020 (2020)

Contents


Online Measuring and Size Sorting for Perillae Based on Machine Vision

Bo Zhao, Ye Wang, Jun Fu , Rongqiang Zhao , Yashuo Li, Xin Dong, Chengxu Lv, and Hanlu Jiang
Research Article (8 pages), Article ID 3125708, Volume 2020 (2020)

Accurate Variable Control System for Boom Sprayer Based on Auxiliary Antidrift System

Jun Fu , Chao Chen, Rongqiang Zhao , and Luquan Ren
Research Article (8 pages), Article ID 8037046, Volume 2020 (2020)

Variation in Morphological and Physiological Characteristics of Wild *Elymus nutans* Ecotypes from Different Altitudes in the Northeastern Tibetan Plateau

Juan Qi , Wenhui Liu, Ting Jiao, and Ann Hamblin
Research Article (11 pages), Article ID 2869030, Volume 2020 (2020)

Editorial

Sensors and Applications in Agricultural and Environmental Monitoring

Yuan Li¹, Ajit Ghosh², Zhenxing Zhang^{3,4}, Zhifeng Yu⁵, and Jingwei Wang⁶

¹Northwest Land and Resources Research Center, Shaanxi Normal University, Xi'an, China

²Max Planck Institute for Plant Breeding, Köln, Germany

³Key Laboratory of Vegetation Ecology, Ministry of Education, Northeast Normal University, Changchun, China

⁴State Environmental Protection Key Laboratory of Wetland Ecology and Vegetation Restoration, School of Environment, Northeast Normal University, Changchun, China

⁵The Ohio State University, Columbus, USA

⁶Shanxi University of Finance and Economics, Taiyuan, China

Correspondence should be addressed to Yuan Li; liy681@nenu.edu.cn

Received 28 July 2021; Accepted 28 July 2021; Published 13 August 2021

Copyright © 2021 Yuan Li et al. This is an open access article distributed under the Creative Commons Attribution License, which permits unrestricted use, distribution, and reproduction in any medium, provided the original work is properly cited.

Sensors and applications in agricultural and environmental monitoring have become more essential to (1) farming practices, (2) crop growth estimation, (3) environmental changes, (4) global and regional observations on the earth's environment, and (5) monitoring/environmental analysis. Among the 31 papers submitted to this special issue, 22 original research articles, which address the sensors and applications in agricultural and environmental monitoring, have been published. The published papers can be summarized as follows.

J. Qi et al. in their paper entitled "Variation in Morphological and Physiological Characteristics of Wild *Elymus nutans* Ecotypes from Different Altitudes in the Northeastern Tibetan Plateau" identify the alteration in morphological and physiological characteristics by measuring photosynthetic physiology, nutrient content, and growth associated with adaptation of plants to conditions at different altitudes 2450, 2950, 3100, and 3300 m above sea level on the plateau. The authors conclude that the increased thermal regime experienced by plants introduced from high altitude to low altitude may facilitate the increased growth of *Elymus nutans* subtypes.

J. Fu et al. in their paper entitled "Accurate Variable Control System for Boom Sprayer Based on Auxiliary Antidrift System" utilize the auxiliary antidrift system of wind-

curtain type air flow and the variable spraying control system for adaptive fertilizing and online measuring of working conditions. Their results showed that benefitting from the auxiliary air flow, the average utility of pesticide is improved from 26.76% to 37.98%.

L. Liu et al. in their paper entitled "A Novel Method for Broiler Abnormal Sound Detection Using WMFCC and HMM" develop a method for broiler abnormal sound detection. Results showed that the developed recognition algorithm, using wavelet transform, Mel frequency, cepstrum coefficients (WMFCCs), correlation distance, Fisher criterion (CDF), and hidden Markov model (HMM), provided an average accuracy, precision, recall, and *F1* of 93.8%, 94.4%, 94.1%, and 94.2%, respectively, for broiler sound samples.

X. Su et al. in their paper entitled "A Review of Underwater Localization Techniques, Algorithms, and Challenges" unveil the existing challenges in the underwater environment.

B. Zhao et al. in their paper entitled "Online Measuring and Size Sorting for Perillae Based on Machine Vision" develop an approach based on the machine vision (MV) technique for online measuring and size sorting. Experimental results demonstrate that the average time consumption for a captured image, the average measuring error, the variance of measuring error, and the overall sorting accuracy

are 204.175 ms, 1.48 mm, 0.07 mm, and 93%, respectively, implying the feasibility and satisfied accuracy of the proposed approach.

In the paper entitled “Development of an IoT-Based Indoor Air Quality Monitoring Platform” authored by J. Jo et al., an IoT-based indoor air quality monitoring platform, consisting of an air quality sensing device called “Smart-Air” and a web server, is demonstrated. An application was developed to help in monitoring the air quality. Thus, approved personnel can monitor the air quality at any time and from anywhere, via either the web server or the application.

M. Li et al. in their paper entitled “Response Mechanism of Cotton Growth to Water and Nutrients under Drip Irrigation with Plastic Mulch in Southern Xinjiang” studied the effects of water and nutrient control measures on cotton plant height, stem diameter, biomass, seed yield, and soil moisture under an irrigated plastic mulch production system. It is suggested that deficit irrigation at 60–80% of the potential evapotranspiration at the flowering stage and 16–5.6–2.4 (N-P₂O₅-K₂O) fertilizer can be applied as an optimal water and nutrient management strategy to maximize the seed cotton yield, irrigation water efficiency, and overall growth and development of cotton.

X. Feng and J. Li in their paper entitled “Evaluation of the Spatial Pattern of the Resolution-Enhanced Thermal Data for Urban Area” chose three typical methods from the limited number of thermal sharpening methods designed for the urban area and made a comparison between them, together with a newly proposed thermal sharpening method, superresolution-based thermal sharpener. It is found that all methods obtained lower accuracy for data in winter than for data in other seasons. Linear water features and areas along it are difficult to be detected correctly using most methods.

R. Ma et al. in their paper entitled “Colloidal Influence Factor of Biofloculant in Coagulation of Chromium and Nitrobenzene” investigate the flocculation capacity of activated sludge flocculants in chromium ion and nitrobenzene solutions. It is found that compared with activated carbon, the activated sludge flocculant showed a good flocculation capacity for nitrobenzene, but poor flocculation for chromium following the initial concentration increase. The flocculation of nitrobenzene or chromium increased at the initial stage and decreased gradually following the primary dosage of flocculant increase. The flocculation for nitrobenzene increased at the primary stage and decreased after the peak, while the flocculation for chromium increased following the pH increase of both solutions.

K. N. Qureshi et al. in their paper entitled “Optimized Cluster-Based Dynamic Energy-Aware Routing Protocol for Wireless Sensor Networks in Agriculture Precision” propose a Gateway Clustering Energy-Efficient Centroid-(GCEEC-) based routing protocol where a cluster head is selected from the centroid position and gateway nodes are selected from each cluster.

M. Xu and J. Zhou in their paper entitled “Elite Immune Ant Colony Optimization-Based Task Allocation for Maximizing Task Execution Efficiency in Agricultural Wireless Sensor Networks” propose an elite immune ant colony opti-

mization (EIACO) to deal with the problem of task allocation optimization, which is motivated by immune theory and elite optimization theory. Simulation results show that the proposed elite immune ant colony optimization has a better task execution efficiency and higher convergence speed than genetic algorithm and simulated annealing.

M. Zhang et al. in their paper entitled “Effects on Local Temperature and Energy of Oasis City Expansion in Arid Area of Northwest China” study the climate effect of urban expansion located in oases in arid area of Northwest China by surface and 2 m urban heat island (UHI) intensity and available energy ratio. The results show that 2 m UHI always displays positive twin peaks during the whole day, while surface UHI only displays a positive single peak for several hours during daytime at four seasons in the four years.

N. Lu et al. in their paper entitled “*Leymus chinensis* Tolerates Mowing Disturbance by Maintaining Photosynthesis in Saline-Alkali Heterogeneous Habitats” tested the effects of mowing intensity on plant photosynthesis under different heterogeneous patches with different saline-alkali soils. The results imply that moderate grazing or mowing can be used to maintain the productivity and economic benefits of grassland when soil heterogeneous patches with moderate saline-alkali conditions.

G. Gao et al. in their paper entitled “Stem Water Content for Crape Myrtle in Response to Drought, Cold, and Disease Stress” selected Crape myrtle as an experimental subject and its stresses on stem water content were observed in four experiments including no stress, drought, cold, and disease stress. The authors conclude that the stresses on stem water content can be used as a qualitative evaluation index of the degree of the three types of stress.

H. Xiang et al. in their paper entitled “Sensors Applied for the Detection of Pesticides and Heavy Metals in Freshwaters” briefly introduce the pollution status of two major pollutants, i.e., pesticides and heavy metals, in freshwaters worldwide. The results imply that future development of pesticides and heavy metal sensors should (1) enhance the sensitivity to meet the requirements for the protection of aquatic ecosystems and human health and (2) cover more diverse pesticides and heavy metals especially those toxic pollutants that are widely used and frequently are detected in freshwaters (e.g., glyphosate, fungicides, zinc, chromium, and arsenic).

H. Liang et al. in their paper entitled “Variation Characteristics of Stem Water Content in *Lagerstroemia indica* and Its Response to Environmental Factors” studied the change characteristics of stem water content (StWC) in the plant and its response to environmental factors. The results showed that the StWC of *Lagerstroemia indica* varies regularly day and night during the growth cycle. Meanwhile, the rising time, valley time, and falling time of StWC were various at the different growth stages of *Lagerstroemia indica*.

J. Li et al. in their paper entitled “Change Analysis of Spring Vegetation Green-Up Date in Qinba Mountains under the Support of Spatiotemporal Data Cube” propose a new data model based on data cube technologies to efficiently organize remote sensing phenology and related reanalysis data in different scales. This research provided a new approach for analyzing phenology phenomena and its

changes in Qinba Mountains that had the same reference value for other regional phenology studies.

H. Malon et al. in their paper entitled “Application of Low-Cost Sensors for the Development of a Methodology to Design Front-End Loaders for Tractors” developed a methodology to design tractor front-end loaders with a view of obtaining their accurate design during the bucket loading process. The experimental results obtained by means of low-cost sensors fitted to the front-end loader allow analyzing the existing strains at the points measured as well as validating the numerical model developed.

F. Zeng et al. in their paper entitled “A Novel Biofloculant from *Raoultella planticola* Enhances Removal of Copper Ions from Water” studied copper ions in the water of Songhua River flowing through the chemical and living areas of Jilin City. The results showed that copper ions in the water of Songhua River flowing through the chemical and living areas of Jilin City show that the copper concentration in this area is between 0.066 ppb and 0.159 ppb. The copper content index of the three water samples did not exceed the Class III standard of the Surface Water Quality Standard.

P. Su et al. in their paper entitled “Anonymous and Efficient Certificateless Multirecipient Signcryption Scheme for Ecological Data Sharing” propose a solution to the key escrow problem and aim to improve efficiency on the basis of ensuring security by adopting elliptic curve cryptography. A rigorous security analysis proves that the scheme can resist various security attacks and ensure privacy protection based on random oracle model. Performance analysis also shows that this scheme has the advantage of computational overhead compared to the same type of scheme.

T. Sharmilan et al. in their paper entitled “Electronic Nose Technologies in Monitoring Black Tea Manufacturing Process” introduce an electronic nose to find the optimum level of fermentation detecting the variation in aroma level. It is found that the systems developed are capable of detecting the variation of aroma level using an array of metal oxide semiconductor gas sensors using different statistical and neural network techniques successfully.

Y. Wu et al. in their paper entitled “A Model with Leaf Area Index and Trunk Diameter for LoRaWAN Radio Propagation in Eastern China Mixed Forest” developed a model for leaf area index and trunk diameter. The results show that the 433 MHz LoRa path loss in the mingled forest could be precisely predicted by our proposed model.

Acknowledgments

We wish to thank all the researchers who have contributed in their great work to the success of this special issue. Also, we would like to thank the reviewers that have been involved in the reviewing process. We would like to acknowledge the editorial board members for approving the publication of this special issue.

*Yuan Li
Ajit Ghosh
Zhenxing Zhang
Jingwei Wang
Zhifeng Yu*

Conflicts of Interest

The editors declare that they have no conflicts of interest regarding the publication of this special issue.

Research Article

Anonymous and Efficient Certificateless Multirecipient Signcryption Scheme for Ecological Data Sharing

Pengfei Su, Yong Xie, and Ping Liu 

Department of Computer Technology and Application, Qinghai University, Xining 810016, China

Correspondence should be addressed to Ping Liu; 247750940@qq.com

Received 22 November 2019; Revised 22 June 2020; Accepted 29 July 2020; Published 19 August 2020

Academic Editor: Yuan Li

Copyright © 2020 Pengfei Su et al. This is an open access article distributed under the Creative Commons Attribution License, which permits unrestricted use, distribution, and reproduction in any medium, provided the original work is properly cited.

Air pollution, water pollution, soil erosion, land desertification, and other environmental issues are becoming more and more serious. And ecological security has become a key issue for the sustainable development of the world, so research on ecology has received more and more attention. At present, ecological data is collected and stored separately by various departments or agencies. In order to conduct better research, various institutions or individuals begin to share their own data. However, data sharing between different organizations is affected by many factors, especially data security issues. At the moment, there is no scheme that has been commonly recognized to solve the problem of ecological data sharing. To provide a secure data sharing way for ecological research, a certificateless multireceiver signcryption scheme is proposed. In this paper, the proposed scheme can solve the key escrow problem, and it can improve efficiency on the basis of ensuring security by adopting elliptic curve cryptography (ECC). A rigorous security analysis proves that the scheme can resist various security attacks and ensure privacy protection based on a random oracle model. Performance analysis also shows that this scheme has the advantage of computational overhead compared to the same type of scheme. Therefore, the scheme is very suitable for the safe sharing of ecological data.

1. Introduction

Ecological data is receiving more and more attentions nowadays. It plays an important role in global climate change prediction, ecological network observation and simulation, regional air pollution control, and so on. However, the scope, degree, quality, and usability of data sets mastered by different research institutions vary greatly, which is not conducive to the research in related fields. In order to solve this problem, relevant organizations begin to share their own data, which enables researchers to find and reuse relevant data. Combining data from multiple sources can better raise new questions and accelerate the pace of science. Sharing of relevant data can also make the related scientific research more transparent, which helps boost public trust.

In the process of information sharing, on the one hand, the sender of the information only wants the authorized receiver to receive the correct information in order to prevent the information from being maliciously revealed. On the other hand, the recipient of the message wants to verify the

sender of the message to prevent the message from being tampered with and the sender from being forged.

In view of all the requirements above, the information sent needs to be confidential and verifiable. The confidentiality needs to be implemented by encryption, and the verification needs to be implemented by signature. Traditionally, the method of first signing and then encrypting is adopted, but it is too computationally intensive resulted in the low efficiency. In order to improve the efficiency on the basis of ensuring confidentiality and verification of messages, Zheng [1] proposed the concept of signcryption, which enables encryption and signature to be performed simultaneously; therefore, encryption and signature functions can be realized by one signcryption.

With the development of communication, the identity-based multireceiver encryption (IMRE) proposal was presented by Baek et al. [2]; this proposal can encrypt multiple recipients' messages by one calculation. And then, the IMRE schemes [3–5] were proposed successively. Subsequently, on the basis of the scheme in [2], the identity-based multireceiver

signcryption (IMRS) proposal was presented by Duan and Cao [6]. According to this scheme, the sender only needs to perform a signcryption operation to simultaneously send messages to multiple authorized recipients, and each authorized recipient can perform corresponding decryption and verification. The ciphertext received by the receiver does not contain a list of receiver identity information, and the receiver cannot find the relevant information in the ciphertext. It is more effective than one-to-one scheme and is an ideal choice for information sharing. Then, many IMRS schemes [7–14] were proposed. What is more, communicators are paying more and more attentions to personal privacy issues. Usually, people intend to conceal their identities when they use multi-receiver signcryption-related devices. In order to realize anonymity, Fan et al. [15] proposed the first anonymous IMRE scheme. However, Wang et al. [16] proposed that the scheme in [15] does not truly achieve that goal. Also, Wang et al. [16] proposed a new anonymity scheme, but Li and Pang [17] proposed that the scheme in [16] still could not completely realize anonymity either. Later, Fan and Tseng [18] proposed an anonymous IMRE scheme and the receiver of the scheme has the capability of identity verification, but the efficiency is not high because of the excessive bilinear pairings operations in the scheme. Then, Pang et al. [19] put forward an absolutely cryptonymous IMRS proposal which can realize the anonymity of the receiver and sender. Gradually, people have found a serious problem that these multireceiver schemes have key escrow problems because they cannot block malicious key generation center (KGC) attacks. If nothing is done to solve this problem, the KGC can view all users' communications and can pretend to be any user, which is insecure.

Given the above requirements, Al-Riyami and Paterson [20] proposed a certificateless public key cryptosystem. For the user in this system, he and KGC jointly generate his private key, and the system parameters and his private key jointly determine his public key. The scheme in [20] can solve the problem of certificate management in traditional public key cryptography and key escrow in identity-based cryptosystems, so the certificateless multirecipient scheme has become a research hotspot. Influenced by the scheme in [20], the proposals [21–24] were successively put forward. Selvi et al. [25] came up with the earliest certificateless multireceiver signcryption (CMRS) scheme, but it does not have the confidentiality of messages under external attacks and is inefficient due to the use of a large number of bilinear pairing operations (BPO).

Gradually, people began to pursue efficiency on the basis of satisfying the safety function. A cryptonymous certificateless multireceiver encryption (CMRE) proposal was presented by Islam et al. [26]. In order to improve efficiency, the scheme in [26] uses scalar point multiplication operations on elliptic curve cryptography (SPMOOECC), which does not use BPO. Since schemes in [26] can still further improve efficiency, schemes in [27–30] have been proposed successively. The scheme in [27] used the BPO and map-to-point hash function (MTPHF), scheme in [28] and scheme in [30] used lots of SPMOOECC, and scheme in [29] used BPO in the decryption step, all of which greatly limit the efficiency of the scheme. Among them, schemes in [26–30] have no signature function and cannot resist forgery attacks, and

schemes in [25, 27–29] did not successfully achieve fair decryption, nor did they implement the verification of part of the private key.

Through the analysis of the schemes, we found that the multirecipient signcryption scheme is required to solve the main problems as below during the communication process:

- (1) Key escrow problem: malicious KGC can forge encrypted ciphertext and decrypt ciphertext, which dramatically reduces the confidentiality of the message. In order to prevent malicious KGC attacks, we need to solve the key escrow problem
- (2) The calculation efficiency is not ideal: in the process of encryption or decryption, BPO or a large number of SPMOOECC will result in inefficiency

In view of the requirements of ecological data sharing communication and taking into account the shortcomings of existing communication mechanisms, we propose a CMRS scheme for ecological data sharing. Relevant institutions or researchers can send data to other researchers or related institutions through our program. The communication process is shown in Figures 1 and 2. When multiple researchers or related organizations share relevant ecological data (such as forest ecological data, grassland ecological data, and desert ecological data), they first exchange key with KGC to obtain their own public key and private key; then, they signcrypt the data and send the signcrypted message to the cloud space; finally, the signcrypted data in the cloud space will be forwarded to the authorized recipient and the receiver performs verification and decryption after receiving the message.

The specific features of the scheme are as follows:

- (1) The scheme realizes the anonymity of the receiver. Not only the attacker cannot obtain the information of the receiver, but also the receiver does not know the information of other receivers
- (2) The scheme uses a certificateless method and can perform partial private key verification. It not only solves the key escrow problem but also ensures the correctness of some private keys received from KGC
- (3) The scheme is of high efficiency. Instead of using BPO and exponential operations in the signcryption and decryption phases, the scheme uses the SPMOOECC during encryption and decryption processes and minimizes the number of SPMOOECC, which greatly increases efficiency

Finally, in using the stochastic prediction model, we prove the confidentiality, unforgeability, and recipient anonymity of our CMRS scheme based on the difficult problems.

The rest of the paper is as follows: in the second part, the initial knowledge is described. In the third part, the proposed scheme is described. In addition, in the fourth part, the correctness and security of the scheme were analyzed. Next, in the fifth part, the proposed scheme and the existing scheme are compared in terms of efficiency and functionality. Finally, the sixth section summarizes this paper.

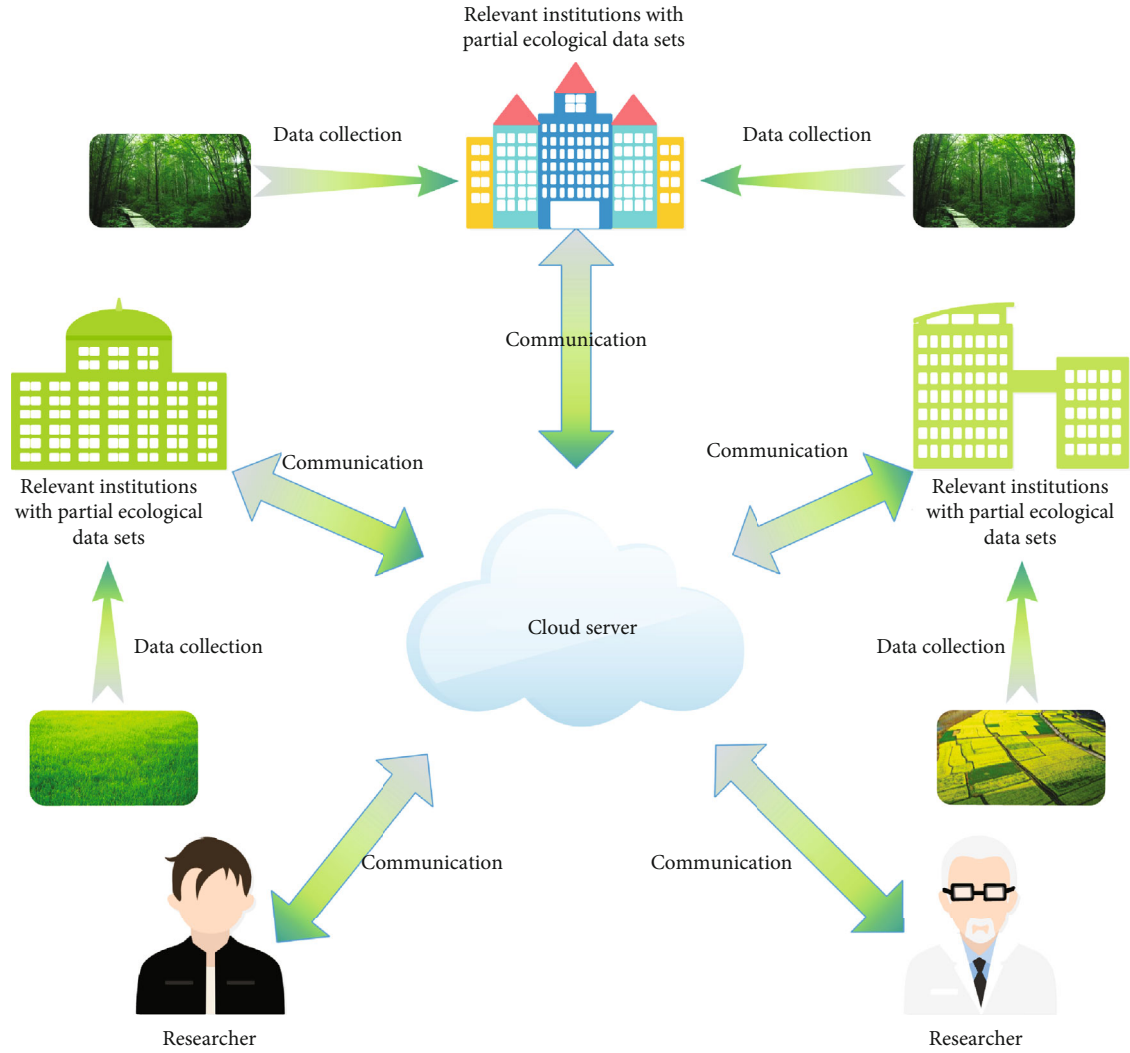


FIGURE 1: Ecological data sharing application framework.

For ease of understanding, the symbols used are listed in Table 1.

2. Preliminaries

We will make an introduction of difficult problems, algorithm model, and security models.

2.1. Difficult Problems. It is specified that G_p is a cyclic group on ECC, the generator of G_p is the P , and Z_p^* is the nonzero multiplication group, which depend on the big prime number p . The elliptic curve discrete logarithm problem (ECDLP) and Diffie-Hellman problem (CDHP) are described below:

(1) **CDHP.** Known $(P, xP, yP) \in G_p$, $x, y \in Z_p^*$, calculating $xyP \in G_p$ is CDHP

Definition 1. If the probabilistic polynomial time (PPT) algorithm A can solve CDHP, the probability advantage is specified as

$$Adv_A^{CDHP} = \Pr [A(P, xP, yP) = xyP]. \quad (1)$$

CDHP hypothesis: we believe that Adv_A^{CDHP} can be ignored for any PPT algorithm A. (2) **ECDLP.** Known $(P, xP) \in G_p$, $x \in Z_p^*$, calculating x is ECDLP

Definition 2. If the PPT algorithm B can solve CDHP, the probability advantage is specified as

$$Adv_B^{ECDLP} = \Pr [B(P, xP) = x]. \quad (2)$$

ECDLP hypothesis: we believe that Adv_B^{ECDLP} can be ignored for any PPT algorithm B.

2.2. Algorithm Model

Definition 3. The algorithm model of this proposal consists of *SetUpAlgorithm*, *SetSecretValueAlgorithm*, *ExtractPartialPrivateKeyAlgorithm*, *SetPublicAndPrivateKeysAlgorithm*, *Sign-cryptionAlgorithm*, and *Design-cryptionAlgorithm*:

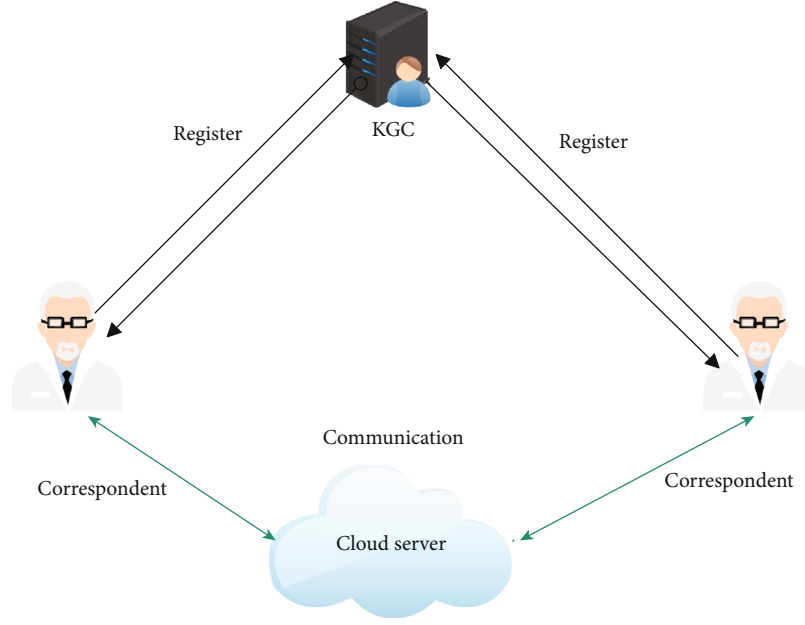


FIGURE 2: Ecological data sharing network framework.

TABLE 1: Notations.

Name	Meaning
BPO	Bilinear pairing operations
MTPHF	Map-to-point hash function
ECC	Elliptic curve cryptography
KGC	Key generation center
SPMOOECC	Scalar point multiplication operations on elliptic curve cryptography
CDHP	Computational Diffie-Hellman problem
ECDLP	Elliptic curve discrete logarithm problem
G_p	A cycle group of points on ECC
PK_i	Public key of user i , i represents the user's identity
P	Generator of G_p
p	Large prime integer
Pr	The probability of an event
SK_i	Private key of user i , i represents the user's identity
Z_p^*	Nonzero multiplicative group with large prime p
IME	Identity-based multireceiver encryption
IMS	Identity-based multireceiver signcryption
CME	Certificateless multireceiver encryption
CMS	Certificateless multireceiver signcryption

SetUpAlgorithm: input λ , λ is the security parameter; KGC executes the algorithm; the system's master key s and the public parameter $params$ are generated by KGC; and KGC exposes $params$ and secretly saves s .

SetSecretValueAlgorithm: enter ID_i , ID_i is the user's information; the user executes the algorithm; and the user gets the secret value x_i and the secret value parameter X_i .

ExtractPartialPrivateKeyAlgorithm: enter the user's information ID_i , the master key s , the secret value parameter X_i , and the public key parameter $params$. For the user, KGC uses this algorithm to obtain the partial private key z_i and key generation parameter W_i .

SetPublicAndPrivateKeysAlgorithm: input the parameter $params$ of the system, the information ID_i of the user, the partial private key z_i of the user, the secret value x_i , and the key generation parameter W_i and the user uses the algorithm to obtain public key pair PK_i and the private key pair SK_i .

SigncryptionAlgorithm: input the system's public parameter $params$, receiver information $L = \{ID_1, ID_2 \dots ID_n\}$, plaintext M , the recipient's public key PK_i ($1 \leq i \leq n$), the private key SK_c of THE transmitter, and the information ID_c of the transmitter. The transmitter initiates the algorithm to obtain the ciphertext $C = \text{Signcryption}(params, M, L, PK_i, SK_c, ID_c)$.

DesigncryptionAlgorithm: enter the public parameter $params$, the recipient's private key SK_i , the recipient's information ID_i , and ciphertext C . The receiver uses the algorithm to gain the plaintext $M = \text{Designcryption}(params, C, SK_i, ID_i)$ and verifies M using the sender's public key PK_c .

2.3. Security Models. The security model required for our scheme consists of information confidentiality, unforgeability, and recipient anonymity. In each security model, there are two types of opponents, called \mathcal{A}_1 and \mathcal{A}_2 [20]. \mathcal{A}_1 does not know the system master key but \mathcal{A}_2 does, and \mathcal{A}_1 can replace the user's public key but \mathcal{A}_2 cannot. Specific descriptions are as follows:

2.3.1. Information Confidentiality. Information confidentiality means that an attacker cannot successfully decrypt a plaintext message in his or her own attack. In this scheme, information confidentiality is the indistinguishability of certificateless signcryption in the context of selecting ciphertext

attack and selective multiple ID (IN-CMRS-CA) [25]. We defined *Game1* for \mathcal{A}_1 's IN-CMRS-CA and *Game2* for \mathcal{A}_2 's IN-CMRS-CA.

Game1: this game is the interaction of opponent \mathcal{A}_1 and challenger \mathcal{C} in the context of IN-CMRS-CA.

Setup. \mathcal{C} performs the corresponding steps for obtaining the public parameter $pars$ and the master key s , then sends the $pars$ to the \mathcal{A}_1 and secretly saves s . After \mathcal{A}_1 receives the $pars$, the \mathcal{A}_1 outputs a group of target identities $L = \{ID_1, ID_2, \dots, ID_n\}$, where n is a positive integer.

Phase 4. \mathcal{A}_1 requires \mathcal{C} to perform flexible queries, and \mathcal{C} performs feedback. The details are the following:

SetSecretValueQuery: \mathcal{A}_1 requires \mathcal{C} to run the *SetSecretValueQuery* on the ID . After the request is received, \mathcal{C} uses the *SetSecretValueAlgorithm* to get the user's secret value, and \mathcal{C} transmits the result to \mathcal{A}_1 .

ExtractPartialPrivateKeyQuery: \mathcal{A}_1 lets \mathcal{C} run the *ExtractPartialPrivateKeyQuery* against the ID . After the request is received, \mathcal{C} executes the *ExtractPartialPrivateKeyAlgorithm* to gain the partial private key of the user and sends result to \mathcal{A}_1 .

SetPublicAndPrivateKeysQuery: \mathcal{A}_1 requires \mathcal{C} to run the *SetPublicAndPrivateKeysQuery* on the ID . After receiving the request, \mathcal{C} executes the *SetPublicAndPrivateKeysAlgorithm* to get the public and private keys of user and returns them to \mathcal{A}_1 .

PublicKeyReplacementQuery: \mathcal{A}_1 requires \mathcal{C} to use the PK_{ID} to run the *PublicKeyReplacementQuery* on the ID . Upon receipt, \mathcal{C} will retain the PK_{ID} as the new public key.

SigncryptionQuery: \mathcal{A}_1 lets \mathcal{C} perform the *SigncryptionQuery* with a series of information and plaintext M . After the request is received, \mathcal{C} randomly selects the information ID_s to execute the *SigncryptionAlgorithm* to obtain the ciphertext C and transmits C to \mathcal{A}_1 .

DesigncryptionQuery: \mathcal{A}_1 requires \mathcal{C} to perform the *DesigncryptionQuery* for ciphertext C . After the request is received, \mathcal{C} executes the *DesigncryptionAlgorithm* to obtain the plaintext M , after that, verify that M is compliant, and returns M to \mathcal{A}_1 .

Challenge: \mathcal{A}_1 chooses a pair of plaintext (M_0, M_1) , the length of the plaintext is the same, and transmits (M_0, M_1) to \mathcal{C} . \mathcal{C} selects $\varphi \in \{0, 1\}$; then, \mathcal{C} uses the selected plaintext M_φ to obtain C^* and \mathcal{C} transmits C^* to \mathcal{A}_1 .

Phase 5. \mathcal{A}_1 wants \mathcal{C} to provide the same query as Phase 4, but \mathcal{A}_1 cannot perform the private key portion of *SetPublicAndPrivateKeysQuery* and *ExtractPartialPrivateKeyQuery* on the user who has replaced the public key. \mathcal{A}_1 cannot perform *DesigncryptionQuery* on ciphertext C^* .

Guess: \mathcal{A}_1 gives φ^* , and if $\varphi^* = \varphi$ can be determined, \mathcal{A}_1 wins, otherwise, \mathcal{A}_1 fails. The probability advantage of \mathcal{A}_1 winning is defined as follows:

$$\text{Adv}^{\text{IN-CMRS-CA}}(\mathcal{A}_1) = |2 \Pr[\varphi^* = \varphi] - 1|. \quad (3)$$

Definition 6. The probability that any \mathcal{A}_1 in the case of IN-CMRS-CA can obtain the *Game1* victory in time τ can satisfy $\text{Adv}^{\text{IN-CMRS-CA}}(\mathcal{A}_1) \leq \epsilon$, indicating that the scheme conforms to (τ, ϵ) -IN-CMRS-CA security, ϵ represents a nonnegligible probability advantage and τ represents the time of a polynomial operation.

Game2: this game is the interaction of opponent \mathcal{A}_2 and challenger \mathcal{C} in the context of IN-CMRS-CA. The details are the following:

Setup. \mathcal{C} performs the corresponding steps for obtaining the public parameter $pars$ and the master key s , then transmits the result to the \mathcal{A}_2 . After successful reception, \mathcal{A}_2 gives a set of target identifiers $L = \{ID_1, ID_2, ID_3, \dots, ID_n\}$, n is a positive integer.

Phase 7. \mathcal{A}_2 makes a series of queries to \mathcal{C} like Phase 4 of *Game1*, but \mathcal{A}_2 cannot carry out *PublicKeyReplacementQuery*. \mathcal{C} responds accordingly.

Challenge: \mathcal{A}_2 selects a pair of plaintext (M_0, M_1) ; the length of the plaintext is the same and transmits (M_0, M_1) to \mathcal{C} . \mathcal{C} selects $\varphi \in \{0, 1\}$; then, \mathcal{C} uses the selected plaintext M_φ to obtain C^* , \mathcal{C} transmits C^* to \mathcal{A}_2 .

Phase 8. \mathcal{A}_2 needs \mathcal{C} to perform the same query as Phase 4, but \mathcal{A}_2 cannot execute the *SetSecretValueQuery* for the target identity L , and \mathcal{A}_2 cannot run the *DesigncryptionQuery* against the ciphertext C^* .

Guess: \mathcal{A}_2 gives φ^* , and if $\varphi^* = \varphi$ can be determined, \mathcal{A}_2 wins, otherwise, \mathcal{A}_2 fails. The probability advantage of \mathcal{A}_2 winning is defined as follows:

$$\text{Adv}^{\text{IN-CMRS-CA}}(\mathcal{A}_2) = |2 \Pr[\varphi^* = \varphi] - 1|. \quad (4)$$

Definition 9. The probability that any \mathcal{A}_2 in the case of IN-CMRS-CA can obtain the *Game2* victory in time τ can satisfy $\text{Adv}^{\text{IN-CMRS-CA}}(\mathcal{A}_2) \leq \epsilon$, indicating that the scheme conforms to (τ, ϵ) -IN-CMRS-CA security, ϵ represents a nonnegligible probability advantage and τ represents a time of a polynomial operation.

2.3.2. Unforgeability. The unforgeability of the proposal in this paper is prescribed as the strong unforgeability of certificateless signcryption in the context of selecting ciphertext attacks and optional multiple ID (SU-CMRS-PA) [25]. *Game3* and *Game4* are used to describe the SU-CMRS-PA of the opponent \mathcal{A}_1 and \mathcal{A}_2 , respectively.

Game3: this section is the mutual response between \mathcal{C} and \mathcal{A}_2 under SU-CMRS-PA. The details are the following:

Setup. This procedure is similar to Setup in *Game1*.

Attack: \mathcal{A}_1 requires \mathcal{C} to perform flexible queries. The queries are similar to Phase 4 in *Game1*, after which \mathcal{C} responds.

Forgery: \mathcal{A}_1 uses $L = \{ID_1, ID_2, \dots, ID_n\}$ and plaintext M to forge ciphertext C^* . If any recipient in L can correctly decrypt C^* , then \mathcal{A}_1 wins, otherwise \mathcal{A}_1 fails. In this process, *SigncryptionQuery* cannot get C^* , other restrictions are similar to Phase 5 in *Game1*.

Definition 10. The probability that any \mathcal{A}_1 in the case of SU-CMRS-PA can obtain the *Game3* victory in time τ can satisfy $\text{Adv}^{\text{SU-CMRS-PA}}_{(A_1)} \leq \epsilon$, indicating that the scheme conforms to (τ, ϵ) -SU-CMRS-PA security, ϵ represents a nonnegligible probability advantage and τ represents the time of a polynomial operation.

Game4: this process is the interaction between \mathcal{C} and \mathcal{A}_2 under SU-CMRS-PA. The details are the following:

Setup. This procedure is similar to *Setup* in *Game2*.

Attack: \mathcal{A}_2 performs flexible queries for \mathcal{C} . The queries are similar to Phase 4 in *Game2*, after which \mathcal{C} responds.

Forgery: \mathcal{A}_2 uses $L = \{ID_1, ID_2, \dots, ID_n\}$ and plaintext M to forge ciphertext C^* . If any recipient in L can correctly decrypt C^* , then \mathcal{A}_2 wins, otherwise \mathcal{A}_2 fails. In this process, *SigncryptionQuery* cannot get C^* , and the other restrictions are similar to Phase 5 in *Game2*.

Definition 11. The probability that any \mathcal{A}_2 in the case of SU-CMRS-PA can obtain the *Game4* victory in time τ can satisfy $\text{Adv}^{\text{SU-CMRS-PA}}_{(A_2)} \leq \epsilon$, indicating that the scheme conforms to (τ, ϵ) -SU-CMRS-PA security, ϵ represents a probabilistic advantage that is not negligible. τ represents the time of a polynomial operation.

2.3.3. Receiver Anonymity. In this scheme, receiver anonymity is prescribed as the anonymous indistinguishability of certificateless signcryption in the context of selecting ciphertext attacks and selective multiple ID (ANO-CMRS-CA) [26]. *Game5* and *Game6* each implement ANO-CMRS-CA for \mathcal{A}_1 and \mathcal{A}_2 .

Game5: this process is the interaction between \mathcal{C} and \mathcal{A}_1 under ANO-CMRS-CA. The details are the following:

Setup. \mathcal{C} performs the corresponding steps for obtaining the public parameter $pars$ and the master key s , then transmits $pars$ to \mathcal{A}_1 and secretly saves s . After receiving, \mathcal{A}_1 selects $L = \{ID_0, ID_1\}$ and sends L to \mathcal{C} .

Phase 12. This procedure is similar to Phase 4 in *Game1*.

Challenge: \mathcal{A}_1 picks identity list $L^* = \{ID_2, ID_3, \dots, ID_n\}$ and plaintext M , \mathcal{A}_1 transmits them to \mathcal{C} . \mathcal{C} selects $e \in \{0, 1\}$ and forms the ciphertext C^* with a new set of identity list $L^{**} = \{ID_e, ID_2, ID_3, \dots, ID_n\}$, and \mathcal{C} transmits C^* to \mathcal{A}_1 .

Phase 13. This procedure is similar to Phase 5 in *Game1*.

Guess: \mathcal{A}_1 gives e^* , and If $e^* = e$ can be determined, \mathcal{A}_1 wins, otherwise, \mathcal{A}_1 fails. The probability advantage of \mathcal{A}_1

winning is defined as follows:

$$\text{Adv}^{\text{ANO-CMRS-CA}}_{(A_1)} = |2 \Pr[e^* = e] - 1|. \quad (5)$$

Definition 14. The probability that any \mathcal{A}_1 in the case of I ANO-CMRS-CA can obtain the *Game5* victory in time τ can satisfy $\text{Adv}^{\text{ANO-CMRS-CA}}_{(A_1)} \leq \epsilon$, indicating that the scheme conforms to (τ, ϵ) -ANO-CMRS-CA security, ϵ represents a nonnegligible probability advantage and τ represents the time of a polynomial operation.

Game6: this process is the interaction between \mathcal{C} and \mathcal{A}_2 under ANO-CMRS-CA. The details are the following:

Setup. \mathcal{C} performs the corresponding steps for obtaining the public parameter $pars$ and the master key s , then transmits the result to \mathcal{A}_2 , \mathcal{A}_2 selects $L = \{ID_0, ID_1\}$ and output L .

Phase 15. This procedure is similar to Phase 4 in *Game2*.

Challenge: \mathcal{A}_2 picks identity list $L^* = \{ID_2, ID_3, \dots, ID_n\}$ and a plaintext M , \mathcal{A}_2 transmits L^* and M to \mathcal{C} . \mathcal{C} selects $e \in \{0, 1\}$ and forms a ciphertext with a new set of identity list $L^{**} = \{ID_e, ID_2, ID_3, \dots, ID_n\}$, and \mathcal{C} sends C^* to \mathcal{A}_2 .

Phase 16. This procedure is similar to Phase 5 in *Game2*.

Guess: \mathcal{A}_2 gives e^* , and if $e^* = e$ can be determined, \mathcal{A}_2 wins, otherwise, \mathcal{A}_2 fails. The probability advantage of \mathcal{A}_2 winning is defined as follows:

$$\text{Adv}^{\text{ANO-CMRS-CA}}_{(A_2)} = |2 \Pr[e^* = e] - 1|. \quad (6)$$

Definition 17. The probability that any \mathcal{A}_2 in the case of ANO-CMRS-CA can obtain the *Game6* victory in time τ can satisfy $\text{Adv}^{\text{ANO-CMRS-CA}}_{(A_2)} \leq \epsilon$, indicating that the scheme conforms to (τ, ϵ) -ANO-CMRS-CA security, ϵ represents a nonnegligible probability advantage and τ represents the time of a polynomial operation.

3. The Proposed Scheme

Our scheme includes *SetUpAlgorithm*, *KeyExtractAlgorithm*, *SigncryptionAlgorithm*, and *DesigncryptionAlgorithm*. The *KeyExtractAlgorithm* includes *SetSecretValueAlgorithm*, *ExtractPartialPrivateKeyAlgorithm*, and *SetPublicAndPrivateKeysAlgorithm*.

3.1. Setup Algorithm. KGC performs the corresponding steps for obtaining the public parameter and master keys. The details are the following:

- (1) Input λ , λ is the security parameter and KGC selects a large prime number p on the finite field at random and generates a finite field F_p with p order. Next, a suitable elliptic curve E_p is generated on the domain F_p , and an addition cycle group G_p is determined on the elliptic curve E_p , and the generator of G_p is P

- (2) Select a positive whole number $s \in Z_p^*$ at random, s is the system master key and secretly save and calculate the system public key $P_{\text{pub}}, P_{\text{pub}} = sP$

- (3) Select five safe and reliable hash function as follows:

$$\begin{aligned} H_1 &= \{0, 1\}^* \times G_p \times G_p \longrightarrow Z_p^*, \\ H_2 &= G_p \times \{0, 1\}^* \longrightarrow Z_p^*, \\ H_3 &= G_p \times \{0, 1\}^* \longrightarrow Z_p^*, \\ H_4 &= Z_p^* \longrightarrow \{0, 1\}^*, \\ H_5 &= \{0, 1\}^* \times \{0, 1\}^* \times G_p \times G_p \times \{0, 1\}^* \\ &\quad \times G_p \times Z_p^* \times Z_p^* \times Z_p^* \times \cdots \times Z_p^* \times Z_p^* \longrightarrow Z_p^* \end{aligned} \quad (7)$$

- (4) The appropriate symmetric encryption algorithm E_k and decryption algorithm D_k are selected at random. k as a symmetric key
- (5) Output the public parameters $\text{pars} = \{Ep, G_p, E_k, D_k, p, P, P_{\text{pub}}, H_1, H_2, H_3, H_4, H_5\}$.

3.2. Key Extract Algorithm. The user and KGC perform the corresponding steps for obtaining the user's private and public keys.

- (1) *SetSecretValueAlgorithm*: user ID_i randomly selects $x_i \in Z_p^*$ as a secret value and keeps it in secret, calculates $X_i = x_i P$, and sends ID_i and X_i to KGC via a secure channel
- (2) *ExtractPartialPrivateKeyAlgorithm*: after receiving, KGC randomly selects the integer $w_i \in Z_p^*$, then calculates $W_i = w_i P$ and $h_i = H_1(ID_i, X_i, W_i)$, and then calculates $y_i = w_i + h_i s \mod q$ and $z_i = y_i + H_2(sX_i, ID_i) \mod q$, finally sending z_i and W_i to the user ID_i via a secure channel
- (3) *SetPublicAndPrivateKeysAlgorithm*: after the user ID_i receives z_i and W_i , it calculates $y_i = z_i - H_2(x_i P_{\text{pub}}, ID_i)$ and $Y_i = y_i P$. Then, check if the equation $y_i P = W_i + h_i P_{\text{pub}}$ is established, and if so, the user receives successfully. Otherwise, the reception fails

The user ID_i public key pair is $PK_i = (X_i, Y_i)$, private key pair is $SK_i = (x_i, y_i)$. PK_i is published by KGC.

3.3. Signcryption Algorithm. The sender uses the public parameter pars , its own private key SK_c , plaintext M , a set of recipient information $L = \{ID_1, ID_2, \dots, ID_n\}$, the recipient's public key PK_i ($1 \leq i \leq n$), and the information ID_c of a transmitter for signcryption:

- (1) Select the integer $r \in Z_p^*$ at random and then calculate $R = rP$
- (2) Calculate $\alpha_i = H_3(rX_i, ID_i)$, $i = 1, 2, 3, \dots, n$

- (3) Select the whole number ξ at random, $\xi \in Z_p^*$, then calculate the formula:

$$\begin{aligned} f(x) &= \prod_{j=1}^n (x - \alpha_j) + f(x) = \prod_{j=1}^n (x - \alpha_j) + \xi \pmod{p} \\ &= a_0 + a_1 x + \dots + a_{n-1} x_{n-1} + x_n, a_i \in Z_p^* \end{aligned} \quad (8)$$

- (4) Calculate $k = H_4(\xi)$, $J = E_k(M \| ID_c)$.
- (5) Calculate $h_c = H_5(M, ID_c, X_c, PK_c, J, R, a_0, a_1, \dots, a_n)$, where $\sigma = x_c + y_c + h_c r \mod q$
- (6) Generate ciphertext $C = \{J, R, a_0, a_1, \dots, a_n, \sigma\}$ and send the ciphertext to all recipients

3.4. Designcryption Algorithm. The receiver ID_i decrypts after receiving the ciphertext $C = \{J, R, a_0, a_1, \dots, a_n, \sigma\}$. Proceed as follows:

- (1) Calculate $\alpha_i^* = H_3(x_i, R, ID_i)$
- (2) Calculate $f(\alpha_i^*) \longrightarrow \xi$
- (3) Calculate $k = H_4(\xi)$ and $M \| ID_c = D_k(J)$
- (4) Search and obtain PK_c , calculate $h_c = H_5(M, ID_c, X_c, PK_c, J, R, a_0, a_1, \dots, a_n)$.

And judge whether $\sigma P = X_c + Y_c + h_c R$ is established, If successful, the recipient receives the plaintext M and then exits. Otherwise, the recipient rejects and quits.

4. Correctness Analysis and Security Proofs

4.1. Correctness Analysis

Theorem 18. Confirm that the part private key of the user in *KeyExtractAlgorithm* is right.

Proof. In order for the user's partial private key to be verified correctly, $y_i P = W_i + h_i P_{\text{pub}}$ needs to be established. The specific inference of this equation is as follows:

$$y_i P = (w_i + h_i s)P = w_i P + h_i s P = W_i + h_i P_{\text{pub}}. \quad (9)$$

The establishment of the formula $y_i P = W_i + h_i P_{\text{pub}}$ determines that the verification of the part private key is right in the *KeyExtractAlgorithm*.

Theorem 19. The *DesigncryptionAlgorithm* is right.

Proof. The formula $\sigma P = X_c + Y_c + h_c R$ guarantees the correctness of the *DesigncryptionAlgorithm*. The specific inference of the formula is as follows:

$$\sigma P = (x_i + y_i + h_c r)P = x_i P + y_i P + h_c r P = X_c + Y_c + h_c R. \quad (10)$$

The formula $\sigma P = X_c + Y_c + h_c R$ holds, so it is determined that the *DesigncryptonAlgorithm* is correct.

4.2. Security Proofs. We have security proofs of the proposal based on the safety model outlined in section 2. Theorem 20 and Theorem 23 guarantee confidentiality of the message, Theorem 26 and Theorem 27 ensure unforgeability, and recipient anonymity is ensured by Theorem 28 and Theorem 31.

Theorem 20. *There is an opponent \mathcal{A}_1 under the IN-CMRS-CA, in the polynomial time τ , if \mathcal{A}_1 wins the Game1 victory with a probability advantage ϵ that cannot be ignored, (\mathcal{A}_1 can request up to q_i hash queries $H_i (i = 1, 2, 3, 4, 5)$, q_c KeyQuery, SetSecretValueQuery, q_b ExtractPrivateKeyQuery, q_{pk} SetPublicAndPrivateKeysQuery, q_r PublicKeyReplacementQuery, q_a SigncryptonQuery, and q_d DesigncryptonQuery), then within time $\tau' \leq \tau + (2q_c + 3q_d)O(\tau_s)$, challenger \mathcal{C} 's interaction with opponent \mathcal{A}_1 makes \mathcal{C} overcome CDHP with a probability advantage of $\epsilon' \geq 2(\epsilon - q_d q_5 / 2^k) / nq_3$, τ_s is the time of SPMOOECC.*

Proof. Under a nonnegligible probability, it is assumed that opponent \mathcal{A}_1 can attack the IN-CMRS-CA security, the probability advantage is ϵ , and under the stochastic prediction model, \mathcal{A}_1 requires challenger \mathcal{C} to perform queries. Given (P, xP, yP) , in the time-limited polynomial, \mathcal{C} obtains xyP through the opponent \mathcal{A}_1 interaction to overcome CDHP. \mathcal{C} and opponent \mathcal{A}_1 will interact with the followings:

Setup. \mathcal{C} performs the corresponding steps for obtaining the public parameter $params = (E_p, G_p, E_k, D_k, P, P_{pub} = aP, H_1, H_2, H_3, H_4, H_5)$ and master key $= a \in Z_p^*$, and then transmits $params$ to \mathcal{A}_1 and save s . After the recipient receives it, \mathcal{A}_1 selects the target identity $L = \{ID_1, ID_2, \dots, ID_n\}$ and transmits L to \mathcal{C} , n denotes a positive whole number. H_1, H_2, H_3, H_4 , and H_5 are all random oracles; they are controlled by \mathcal{C} . The details are the following:

- (1) H_1 HashQuery: the tuple (ID_j, X_j, W_j) is taken as input, and \mathcal{A}_1 requires \mathcal{C} to execute H_1 HashQuery. After receiving, \mathcal{C} checks whether the tuple (ID_j, X_j, W_j, d_j) exists in list L_1 . If it exists, \mathcal{C} will send d_j to \mathcal{A}_1 . Otherwise, \mathcal{C} selects $d_j \in Z_p^*$ at random and sends d_j to \mathcal{A}_1 and restores the tuple (ID_j, X_j, W_j, d_j) into list L_1
- (2) H_2 HashQuery: the tuple (sX_j, ID_j) and $(X_j P_{pub}, ID_j)$ are taken as input, and \mathcal{A}_1 requires \mathcal{C} to execute H_2 HashQuery. After receiving, \mathcal{C} checks whether the tuple (sX_j, ID_j, θ_j) and $(X_j P_{pub}, ID_j, \delta_j)$ exist in the list L_2 . If yes, \mathcal{C} will send θ_j and δ_j to \mathcal{A}_1 . Otherwise, \mathcal{C} selects two integer θ_j and $\delta_j \in Z_p^*$ at random and transmits them to \mathcal{A}_1 and restores the tuple (sX_j, ID_j, θ_j) and $(X_j P_{pub}, ID_j, \delta_j)$ into list L_2

- (3) H_3 HashQuery: the tuple (rX_j, ID_j) is taken as input, and \mathcal{A}_1 requires \mathcal{C} to execute H_3 HashQuery. After receiving, \mathcal{C} judges whether or not the tuple (rX_j, ID_j, α_j) exists in the list L_3 . If it exists, \mathcal{C} will send α_j to \mathcal{A}_1 . Otherwise, \mathcal{C} selects $\alpha_j \in Z_p^*$ at random and sends α_j to \mathcal{A}_1 and restores the tuple (rX_j, ID_j, α_j) into list L_3
- (4) H_4 HashQuery: the tuple (ξ) is taken as input, and \mathcal{A}_1 requires \mathcal{C} to execute H_4 HashQuery. After receiving, \mathcal{C} judges whether or not the tuple (ξ, k) exists in the list L_4 . If it exists, \mathcal{C} will send k to \mathcal{A}_1 . Otherwise, \mathcal{C} selects $k \in Z_p^*$ at random, and sends k to \mathcal{A}_1 , and restores the tuple (ξ, k) into list L_4
- (5) H_5 HashQuery: The tuple $(M, ID_j, X_j, PK_j, J, R, a_0, a_1, \dots, a_n)$ is taken as input, and \mathcal{A}_1 requires \mathcal{C} to execute H_5 HashQuery. After receiving, \mathcal{C} judges whether or not the tuple $(M, ID_j, X_j, PK_j, J, R, a_0, a_1, \dots, a_n, h_j)$ exists in list L_5 . If it exists, \mathcal{C} will send h_j to \mathcal{A}_1 . Otherwise, \mathcal{C} selects $h_j \in Z_p^*$ at random, and sends h_j to \mathcal{A}_1 and restores the tuple $(M, ID_j, X_j, PK_j, J, R, a_0, a_1, \dots, a_n, h_j)$ into list L_5

Phase 21. \mathcal{A}_1 requires \mathcal{C} to perform flexible queries and \mathcal{C} performs feedback. The details are the following:

- (1) KeyQuery: \mathcal{C} checks if the tuple $(ID_j, SK_j, PK_j, x_j, z_j)$ exists in the list L_C . If it exists, \mathcal{C} reserves the tuple $(ID_j, SK_j, PK_j, x_j, z_j)$. Otherwise, \mathcal{C} does the following:
 - (a) If $ID_j = ID_i, i = 1, 2, 3, \dots, n$, \mathcal{C} selects two integers $x_j, w_j \in Z_p^*$ at random, sets $X_j = x_j P$ and $SK_j \leftarrow \perp$, computes $W_j = w_j P, y_j = w_j + H_1(ID_i, X_j, W_j) \text{ mod } q, Y_j = y_j P, PK_j = (X_j, Y_j)$ and then updates tuples $(ID_j, SK_j, PK_j, x_j, z_j)$ in list L_C and (ID_j, X_j, W_j, d_j) in list L_1 , respectively
 - (b) If $ID_j \neq ID_i, i = 1, 2, 3, \dots, n$, \mathcal{C} selects two integers $x_j, z_j \in Z_p^*$ at random, sets $X_j = x_j P$, computes $y_i = z_i - H_2(x_i P_{pub}, ID_i), Y_j = y_j P, PK_j = (X_j, Y_j), SK_j = (x_j, y_j)$ and then updates tuples $(ID_j, SK_j, PK_j, x_j, z_j)$ in list L_C and (ID_j, X_j, W_j, d_j) in list L_1 , respectively
- (2) SetSecretValueQuery: \mathcal{A}_1 requires \mathcal{C} to execute the SetSecretValueQuery on ID_j . After receiving the request, \mathcal{C} checks whether there are tuples $(ID_j, SK_j, PK_j, x_j, z_j)$ in list L_C . if it exists, \mathcal{C} sends x_j to \mathcal{A}_1 , otherwise, \mathcal{C} performs the KeyQuery to generate a tuple $(ID_j, SK_j, PK_j, x_j, z_j)$ and then sends x_j to \mathcal{A}_1
- (3) ExtractPartialPrivateKeyQuery: \mathcal{A}_1 requires \mathcal{C} to perform the ExtractPartialPrivateKeyQuery on ID_j .

After receiving the request, the details are the followings:

- (a) If $ID_j = ID_i$, $i = 1, 2, 3, \dots, n$, \mathcal{E} sends “failure” to \mathcal{A}_1
- (b) If $ID_j \neq ID_i$, $i = 1, 2, 3, \dots, n$, \mathcal{E} judges whether or not the tuple $(ID_j, SK_j, PK_j, w_j, x_j, z_j)$ exists in the list L_C , and if so, \mathcal{E} sends z_j to \mathcal{A}_1 , otherwise, \mathcal{E} performs the *KeyQuery* to generate tuple $(ID_j, SK_j, PK_j, x_j, z_j)$ and sends z_j to \mathcal{A}_1
- (4) *SetPublicAndPrivateKeysQuery*: \mathcal{A}_1 requires \mathcal{E} to execute the public key portion of *SetPublicAndPrivateKeysQuery* on the ID_j . After the recipient receives it, \mathcal{E} judges whether or not the tuple $(ID_j, SK_j, PK_j, x_j, z_j)$ exists in list L_C . If it exists, \mathcal{E} sends PK_j to \mathcal{A}_1 , otherwise \mathcal{E} performs *KeyQuery* to generate a tuple $(ID_j, SK_j, PK_j, x_j, z_j)$ and then send PK_j to \mathcal{A}_1

\mathcal{A}_1 requires \mathcal{E} to execute the private key portion of *SetPublicAndPrivateKeysQuery* on the ID_j . After the recipient receives it, \mathcal{E} responds:

- (a) If $ID_j = ID_i$, for $i = 1, 2, 3, \dots, n$, \mathcal{E} sends “failure” to \mathcal{A}_1
- (b) If $ID_j \neq ID_i$, for $i = 1, 2, 3, \dots, n$, \mathcal{E} judges whether or not the tuple $(ID_j, SK_j, PK_j, w_j, x_j, z_j)$ exists in list L_C , and if so, \mathcal{E} sends SK_j to \mathcal{A}_1 , otherwise, \mathcal{E} uses *KeyQuery* to generate tuple $(ID_j, SK_j, PK_j, x_j, z_j)$ and sends SK_j to \mathcal{A}_1
- (5) *PublicKeyReplacementQuery*: \mathcal{A}_1 requires \mathcal{E} to perform a *PublicKeyReplacementQuery* on ID_j with PK'_j . After the recipient receives it, \mathcal{E} queries the tuple $(ID_j, SK_j, PK_j, w_j, x_j, z_j)$ in list L_C , and uses PK'_j instead of PK_j . Next, \mathcal{E} restores the tuple $(ID_j, SK_j, PK_j, x_j, z_j)$ in list L_C
- (6) *SigncryptionQuery*: \mathcal{A}_1 requires \mathcal{E} to perform the *SigncryptionQuery* for plaintext \mathbf{M} and information ID_s . After receiving the request, \mathcal{E} determines if $ID_s \neq ID_i$ is correct, $i = 1, 2, 3, \dots, n$. If the expression is correct, \mathcal{E} executes the *SetPublicAndPrivateKeysQuery* to generate the private key SK_s and ciphertext \mathbf{C} , and then sends \mathbf{C} to \mathcal{A}_1 if not, \mathcal{E} implements the corresponding operation

- (a) Select $r \in Z_p^*$ at random and calculate Select

$$\begin{aligned}
 R &= rP, \\
 rX_j &= rx_jP, \\
 \alpha_j &= H_3(rX_j, ID_j), j = 1, 2, 3, \dots, n; \\
 \xi &\in Z_p^*
 \end{aligned} \tag{11}$$

at random and define the formula:

$$\begin{aligned}
 f(x) &= \prod_{j=1}^n (x - \alpha_j) + \xi(\text{mod } p) = a_0 + a_1x + \dots \\
 &\quad + a_{n-1}x^{n-1} + x^n, a_j \in Z_p^*.
 \end{aligned} \tag{12}$$

- (b) Calculate $k = H_4(\xi)$, $J = E_k(M \| ID_s)$, $h = H_5(M, ID_s, X_s, PK_s, J, R, a_0, a_1, \dots, a_{n-1})$, $\sigma = x_s + y_s + h \text{ mod } q$;
- (c) Select $z \in Z_p^*$ at random
- (d) Output the ciphertext $C = (J, R, a_0, a_1, \dots, a_{n-1}, \sigma)$ to \mathcal{A}_1
- (7) *DesigncryptionQuery*: \mathcal{A}_1 requires \mathcal{E} to perform a *DesigncryptionQuery* for ciphertext \mathbf{C} . After receiving the request, \mathcal{E} selects ID_j at random and verifies whether $ID_j = ID_i$ is true, $i = 1, 2, 3, \dots, n$. If the formula is true, \mathcal{E} sends “failure” to \mathcal{A}_1 . Otherwise, \mathcal{E} will perform the corresponding operation:

- (a) Search for the tuple $(ID_j, SK_j, PK_j, x_j, z_j)$ in list L_C to obtain SK_j and compute $\alpha_j = H_3(x_jR, ID_j)$
- (b) Calculate $f(x) = a_0 + a_1x + \dots + a_{n-1}x^{n-1} + x^n$, generate ξ with α_j and $f(x)$.
- (c) Calculate $k = H_4(\xi)$, $\mathbf{M} \| ID_s = D_k(J)$
- (d) Consider whether the equation $\sigma P = X_s + Y_s + h_s R$ can be established. If it is established, \mathcal{E} sends \mathbf{M} to \mathcal{A}_1 . If not, \mathcal{E} sends “failure” to \mathcal{A}_1

Challenge: \mathcal{A}_1 selects the plaintext (M_0, M_1) at random, they are equal in length, and they are transmitted to \mathcal{E} . After receiving, \mathcal{E} selects a bit $\varphi \in \{0, 1\}$ at random, \mathcal{E} uses M_φ to get the ciphertext C^* , and M_φ is the selected plaintext. The details are the following:

- (a) Stipulate $R = yPK_i$, $rX_i = y(PK_i + P_{\text{pub}})$ and $\alpha_i = H_3(rX_i)$, $i = 1, 2, 3, \dots, n$
- (b) Select $\xi \in Z_p^*$ at random and define the formula:

$$\begin{aligned}
 f(x) &= \prod_{j=1}^n (x - \alpha_j) + \xi(\text{mod } p) = a_0 + a_1x + \dots \\
 &\quad + a_{n-1}x^{n-1} + x^n, a_j \in Z_p^*
 \end{aligned} \tag{13}$$

- (c) Calculate $k = H_4(\xi)$, $J^* = E_k(\|ID_s)$ and $h = (M, ID_s, X_s, PK_s, J, R, a_0, a_1, \dots, a_n)$
- (d) Select $z \in Z_p^*$ at random

- (e) Output the $C * = (J^*, W_j, z, h, a_0, a_1, \dots, a_{n-1})$ to \mathcal{A}_1

Phase 22. \mathcal{A}_1 requires \mathcal{C} to perform the same queries as Phase 4, but \mathcal{A}_1 cannot run the *DesigncryptonQuery* against $C *$.

Guess: \mathcal{A}_1 gives a φ^* at random. If $\varphi^* = \varphi$, then \mathcal{A}_1 wins, \mathcal{C} outputs CDHP's solution $xyP = rX_i - R$. Otherwise, \mathcal{C} outputs "failure."

From the above discussion, it can be concluded that the H_5 hash provides a valid ciphertext during the *DesigncryptonQuery*; therefore, the probability of ciphertext being denied is no more than $q_5/2^k$. During the attack process, since \mathcal{A}_1 requires \mathcal{C} to execute the q_d *DesigncryptonQuery*, the probability of \mathcal{C} decryption success is $\varepsilon_d \geq \varepsilon - q_5q_d/2^k$. The H_3 hash satisfies CDHP during the guessing process, so the probability that xyP is correctly calculated by \mathcal{C} is at least $\varepsilon_g = 2/nq_3$. in the running time $\tau' \leq \tau + (2q_c + 3q_d)O(\tau_s)$, \mathcal{C} 's interaction with opponent \mathcal{A}_1 makes \mathcal{C} overcome CDHP, and the probability advantage is $\varepsilon' \geq \varepsilon_d\varepsilon_g \geq 2(\varepsilon - q_dq_5/2^k)/nq_3$, τ_s is the time of the SPMOOECC.

Theorem 23. *There is an opponent \mathcal{A}_2 under the IN-CLMS-CA. In the polynomial time τ , if the \mathcal{A}_2 wins the Game2 victory with a probability advantage ε that cannot be ignored, (\mathcal{A}_2 can request up to q_i hash queries $H_i(i = 1, 2, 3, 4, 5)$, q_c KeyQuery, q_e SetSecretValueQuery, q_b ExtractPrivateKeyQuery, q_{pk} SetPublicAndPrivateKeysQuery, q_a SigncryptonQuery, and q_d DesigncryptonQuery.), then within time $\tau' \leq \tau + (3q_c + 3q_d)O(\tau_s)$, challenger \mathcal{C} 's interaction with opponent \mathcal{A}_2 makes \mathcal{C} overcome CDHP with a probability advantage of $\varepsilon' \geq 2(\varepsilon - q_dq_5/2^k)/nq_3$, τ_s is the time of SPMOOECC.*

Proof. Under a nonnegligible probability, it is assumed that the opponent \mathcal{A}_2 can attack the IN-CMRS-CA security, the probability advantage is ε , and under the stochastic prediction model, \mathcal{A}_2 requires challenger \mathcal{C} to perform a series of queries. Given (P, xP, yP) , in the time-limited polynomial, \mathcal{C} obtains xyP through the opponent \mathcal{A}_2 interaction to overcome CDHP. \mathcal{C} and opponent \mathcal{A}_2 will interact with the following:

Setup. \mathcal{C} performs the corresponding steps for obtaining the public parameter $\text{pars} = (E_p, G_p, E_k, D_k, p, P, K = xP, P_{\text{pub}}, H_1, H_2, H_3, H_4, H_5)$ and master key $s \in Z_p^*$, and then returns the result to \mathcal{A}_2 , where $x \in Z_p^*$. After receiving the result, \mathcal{A}_2 outputs $L = \{ID_1, ID_2, ID_3, \dots, ID_n\}$, where n is a positive integer. H_1, H_2, H_3, H_4 , and H_5 are random predictions controlled by \mathcal{C} , the interactions between \mathcal{A}_2 and \mathcal{C} is similar to Setup in Theorem 20.

Phase 24. \mathcal{A}_2 requires \mathcal{C} to perform flexible queries and \mathcal{C} performs feedback. The details are the following:

- (1) *KeyQuery:* \mathcal{C} checks if there is a tuple $(ID_j, SK_j, PK_j, x_j, z_j)$ in the list L_C . If it exists, \mathcal{C} reserves the tuple. Otherwise, \mathcal{C} will perform related operations as follows:

- (a) If $ID_j = ID_i, i = 1, 2, 3, \dots, n$, \mathcal{C} selects two integers $x_j, w_j \in Z_p^*$ at random and computes $W_j = w_jP, y_j = w_j + H_1(ID_j, X_j, W_j)s \bmod q, Y_j = y_jP, PK_j = (X_j, Y_j)$, and then updates tuples $(ID_j, SK_j, PK_j, x_j, z_j)$ in list L_C and (ID_j, X_j, W_j, h_j) in list L_1 , respectively, where $X_j = x_jP$ and $SK_j \leftarrow \perp$.
- (b) If $ID_j \neq ID_i, i = 1, 2, 3, \dots, n$, \mathcal{C} selects two integers $x_j, z_j \in Z_p^*$ at random, and sets $X_j = x_jP$, computes $y_j = z_j - H_2(x_jP_{\text{pub}}, ID_j), Y_j = y_jP, PK_j = (X_j, Y_j), SK_j = (x_j, y_j)$, and then updates tuples $(ID_j, SK_j, PK_j, x_j, z_j)$ in list L_C and (ID_j, X_j, W_j, h_j) in list L_1 , respectively.
- (2) *SetSecretValueQuery:* \mathcal{A}_2 requires \mathcal{C} to execute *SetSecretValueQuery* for c . Upon receipt of the request, \mathcal{C} executes as follows:
 - (a) If $ID_j = ID_i, i = 1, 2, 3, \dots, n$, \mathcal{C} sends "failure" to \mathcal{A}_2 .
 - (b) If $ID_j \neq ID_i, i = 1, 2, 3, \dots, n$, \mathcal{C} judges whether or not the tuple $(ID_j, SK_j, PK_j, x_j, z_j)$ exists in list L_C . If yes, \mathcal{C} returns x_j to \mathcal{A}_2 . Otherwise, \mathcal{C} uses *KeyQuery* to generate the tuple $(ID_j, SK_j, PK_j, x_j, z_j)$ and sends x_j to \mathcal{A}_2 .
- (3) *ExtractPartialPrivateKeyQuery:* \mathcal{A}_2 requires \mathcal{C} to perform *ExtractPartialPrivateKeyQuery* against ID_j . After the recipient receives it, \mathcal{C} checks whether there is a tuple $(ID_j, SK_j, PK_j, x_j, z_j)$ in list L_C . If it exists, \mathcal{C} sends z_j to \mathcal{A}_2 . Otherwise, \mathcal{C} runs *KeyQuery* to generate tuple $(ID_j, SK_j, PK_j, x_j, z_j)$ and sends z_j to \mathcal{A}_2 .
- (4) *SetPublicAndPrivateKeysQuery:* \mathcal{A}_2 requires \mathcal{C} to perform the public key portion of *SetPublicAndPrivateKeysQuery* against ID_j . After receiving the request, \mathcal{C} checks whether there is a tuple $(ID_j, SK_j, PK_j, x_j, z_j)$ in list L_C . If it exists, \mathcal{C} sends PK_j to \mathcal{A}_2 . Otherwise, \mathcal{C} runs *KeyQuery* to generate tuple $(ID_j, SK_j, PK_j, x_j, z_j)$ and sends PK_j to \mathcal{A}_2 .

\mathcal{A}_2 requires \mathcal{C} to perform the private key portion of *SetPublicAndPrivateKeysQuery* against ID_j . After the recipient receives it, \mathcal{C} responded with the following response:

- (a) If $ID_j = ID_i, i = 1, 2, 3, \dots, n$, \mathcal{C} sends "failure" to \mathcal{A}_2 .
- (b) If $ID_j \neq ID_i, i = 1, 2, 3, \dots, n$, \mathcal{C} judges whether or not the tuple $(ID_j, SK_j, PK_j, x_j, z_j)$ exists in list L_C . If yes, \mathcal{C} returns SK_j to \mathcal{A}_2 . Otherwise, \mathcal{C} run the *KeyQuery* to generate the tuple $(ID_j, SK_j, PK_j, x_j, z_j)$ and sends SK_j to \mathcal{A}_2 .

- (5) *SigncryptonQuery:* this section is similar to the *SigncryptonQuery* in Theorem 20

- (6) *DesigncryptonQuery*: this section is similar to the *DesigncryptonQuery* in Theorem 20

Challenge: \mathcal{A}_2 selects plaintext (M_0, M_1) at random, they are equal in length, and transmits the result to \mathcal{C} . After receiving the result, \mathcal{C} selects $\varphi \in \{0, 1\}$ at random and obtains the ciphertext C^* generated by M_φ :

- (a) Stipulate $R = y(PK_i + Y)$, $rX_i = y(PK_i + P_{\text{pub}})$ and $\alpha_i = H_3(rX_i, ID_i)$, $i = 1, 2, 3, \dots, n$, $Y = K + P_{\text{pub}}$
 (b) Select $\xi \in Z_p^*$ at random and define the formula:

$$f(x) = \prod_{j=1}^n (x - \alpha_j) + \xi \pmod{p} = a_0 + a_1 x + \dots + a_{n-1} x_{n-1} + x_n, a_i \in Z_p^* \quad (14)$$

- (c) Calculate $k = H_3(\xi)$, $J^* = E_k(M_\varphi \| ID_s)$ and

$$h = H_5(m, ID_s, X_s, Y_s, J, R, a_0, a_1, \dots, a_n); \quad (15)$$

- (d) Select $z \in Z_p^*$ at random
 (e) Output the ciphertext $C^* = (J^*, R, z, h, a_0, a_1, \dots, a_{n-1})$ to \mathcal{A}_2

Phase 25. \mathcal{A}_2 requires \mathcal{C} to perform the same queries as Phase 4, but \mathcal{A}_2 cannot run the *DesigncryptonQuery* against C^* .

Guess: \mathcal{A}_2 gives a φ^* at random. If $\varphi^* = \varphi$, then \mathcal{A}_2 wins, \mathcal{C} outputs CDHP's solution $xyP = R - rX_i$. If not \mathcal{C} outputs "failure."

From the above discussion, it can be concluded that the H_5 hash provides a valid ciphertext during the *DesigncryptonQuery*, therefore, the probability of ciphertext being denied is no more than $q_5/2^k$. During the attack process, since \mathcal{A}_2 requires \mathcal{C} to execute the q_d *DesigncryptonQuery*, the probability of \mathcal{C} decryption success is $\varepsilon_d \geq \varepsilon - q_5 q_d / 2^k$. The H_3 hash satisfies CDHP during the guessing process, so the probability that xyP is correctly calculated by \mathcal{C} is at least $\varepsilon_g = 2/nq_3$. In the running time $\tau' \leq \tau + (3q_c + 3q_d)O(\tau_s)$, \mathcal{C} 's interaction with opponent \mathcal{A}_2 makes \mathcal{C} overcome CDHP, and the probability advantage is $\tau_s(\tau_s)\varepsilon' \geq 2(\varepsilon - q_d q_5 / 2^k) / nq_3$, τ_s is the time of the SPMOOECC.

Theorem 26. *There is an opponent \mathcal{A}_1 under the SU-CMRS-PA. In the polynomial time τ , if the \mathcal{A}_1 wins the Game3 victory with a probability advantage that cannot be ignored (\mathcal{A}_1 can obtain queries similar to that obtained by \mathcal{A}_1 in Theorem 20), then within time $\tau' \leq \tau + (2q_c + 2q_d)O(\tau_s)$, challenger \mathcal{C} can overcome CDHP by interacting with opponent \mathcal{A}_1 with a probability advantage of $\varepsilon' \geq (\varepsilon - q_d / 2^k) / 2$, τ_s is the time of SPMOOECC.*

Proof. Under a nonnegligible probability, it is assumed that the opponent \mathcal{A}_1 can attack the SU-CMRS-PA security, the probability advantage is ε , under the stochastic prediction model, \mathcal{A}_1 requires challenger \mathcal{C} to perform a series of queries. Given (P, xP, yP) , in the time-limited polynomial, \mathcal{C} obtains xyP through the opponent \mathcal{A}_1 interaction to overcome CDHP. \mathcal{C} and opponent \mathcal{A}_1 will interact with the following:

Setup. The process is similar to *Setup* in Theorem 20.

Attack: \mathcal{A}_1 requires \mathcal{C} to perform flexible queries similar to Phase 4 in Theorem 20.

Forgery: \mathcal{A}_2 falsifies ciphertext $C^* = (J, R, z, h, a_0, a_1, \dots, a_{n-1})$ using $L = \{ID_1, ID_2, \dots, ID_n\}$ and a plaintext M . If the formula $\sigma P = X_s + Y_s + h_s R$ can be established, C^* faked successfully, defining $PK'_i = y^{-1} PK_i$ and $rX_i = y(PK_i + P_{\text{pub}})$, \mathcal{C} calculates $rX_i = PK'_i + xyP$, and outputs $xyP = rX_i - PK_i$, xyP is the CDHP's solution. Otherwise \mathcal{C} returns "failure".

From the above discussion, it is concluded that the probability of success of the q_a *SigncryptonQuery* is at least $\varepsilon_a = \varepsilon - q_a / 2^k$. calculates xyP in the forgery process, and the probability of xP correct is at least $\varepsilon_g = 1/2$. Therefore, \mathcal{C} can overcome CDHP by interacting with opponent \mathcal{A}_1 within the running time $\tau' \leq \tau + (2q_c + 2q_d)O(\tau_s)$, and the probability advantage is $\varepsilon' \geq \varepsilon_a \varepsilon_g = (\varepsilon - q_a / 2^k) / 2$. τ_s is the time of the SPMOOECC.

Theorem 27. *There is an opponent \mathcal{A}_2 under the SU-CMRS-PA. In the polynomial time τ , if the \mathcal{A}_2 wins the Game4 victory with a probability advantage ε that cannot be ignored (\mathcal{A}_2 can obtain queries similar to that obtained by \mathcal{A}_2 in Theorem 23), then within time $\tau' \leq \tau + (3q_c + 2q_d)O(\tau_s)$, challenger \mathcal{C} can overcome CDHP by interacting with opponent \mathcal{A}_2 with a probability advantage of $\varepsilon' \geq (\varepsilon - q_a / 2^k) / 2$, τ_s is the time of SPMOOECC.*

Proof. Under a non-negligible probability, it is assumed that the opponent \mathcal{A}_2 can attack the SU-CMRS-PA security, the probability advantage is ε , under the stochastic prediction model, \mathcal{A}_2 requires challenger \mathcal{C} to perform a series of queries. Given (P, xP, yP) , in the time-limited polynomial, Challenger \mathcal{C} obtains xyP through the opponent \mathcal{A}_2 interaction to overcome CDHP. The details are the followings:

Setup. The process is similar to *Setup* in Theorem 23.

Attack: \mathcal{A}_1 requires \mathcal{C} to perform flexible queries similar to Phase 4 in Theorem 23.

Forgery: \mathcal{A}_2 falsifies ciphertext $C^* = (J, R, z, h, a_0, a_1, \dots, a_{n-1})$ using $L = \{ID_1, ID_2, \dots, ID_n\}$ and a plaintext M . If the formula $\sigma P = X_s + Y_s + h_s R$ can be established, C^* faked successfully, defining $PK'_i = y^{-1} PK_i$ and $rX_i = y(PK_i + P_{\text{pub}})$, \mathcal{C} calculates $rX_i = PK'_i + xyP$ and outputs $xyP = rX_i - PK_i$, xyP is the CDHP's solution. Otherwise \mathcal{C} returns "failure."

From the above discussion, it is concluded that the probability of success of the q_a *SigncryptonQuery* is at least $\varepsilon_a = \varepsilon - q_a / 2^k$ calculates xyP in the forgery process, and the

probability of xyP correct is at least $\varepsilon_g = 1/2$. Therefore, in the running time $\tau' \leq \tau + (3q_c + 2q_d)O(\tau_s)$, \mathcal{C} 's interaction with opponent \mathcal{A}_2 makes \mathcal{C} overcome CDHP, and the probability advantage is $\varepsilon' \geq \varepsilon_a \varepsilon_g (\varepsilon - q_d/2^k)/2$. τ_s is the time of the SPMOOECC.

Theorem 28. *There is an opponent \mathcal{A}_1 under the ANO-CMRS-CA. In the polynomial time τ , if the \mathcal{A}_1 wins the Game5 victory with a probability advantage ε that cannot be ignored (\mathcal{A}_1 can obtain queries similar to that obtained by \mathcal{A}_1 in Theorem 20), within time $\tau' \leq \tau + (2q_c + 3q_d)O(\tau_s)$, challenger \mathcal{C} can overcome CDHP by interacting with opponent \mathcal{A}_1 with a probability advantage of $\varepsilon' \geq (\varepsilon - q_d q_5/2^k)/nq_3$, τ_s is the time of SPMOOECC.*

Proof. Under a non-negligible probability, it is assumed that the opponent \mathcal{A}_1 can attack the ANO-CMRS-CA security, the probability advantage is ε , under the stochastic prediction model, \mathcal{A}_1 requires challenger \mathcal{C} to perform a series of queries. Given (P, xP, yP) , in the time-limited polynomial, \mathcal{C} obtains xyP through the opponent \mathcal{A}_1 interaction to overcome CDHP. The details are the followings:

Setup. \mathcal{C} execution of this algorithm is used to generate the public parameter $\text{pars} = (E_p, G_p, E_k, D_k, p, P, P_{\text{pub}} = xP, H_1, H_2, H_3, H_4, H_5)$ and the master key $s = a \in Z_p^*$, then sends the pars to the \mathcal{A}_1 and secretly saves s . After the \mathcal{A}_1 receives the pars , the \mathcal{A}_1 outputs $L = \{\text{ID}_0, \text{ID}_1\}$, where n is a positive integer. H_1, H_2, H_3, H_4 , and H_5 are all random oracles, they are controlled by \mathcal{C} . The interaction is similar to *Setup* in Theorem 20, and the two sides of the interaction are \mathcal{A}_1 and \mathcal{C} .

Phase 29. \mathcal{A}_1 makes a series of queries to \mathcal{C} like Phase 4 in Theorem 20.

Challenge: \mathcal{A}_1 selects the target identifier $L^* = \{\text{ID}_2, \text{ID}_3, \dots, \text{ID}_n\}$ and plaintext \mathbf{M} , and sends L^* and \mathbf{M} to \mathcal{C} . After receiving, \mathcal{C} selects a bit $e \in \{0, 1\}$ and uses the new target identifier $L^{**} = \{\text{ID}_e, \text{ID}_2, \text{ID}_3, \dots, \text{ID}_n\}$ to obtain the ciphertext C^* :

- (a) Calculate $R = y(\text{PK}_i)$, $rX_i = y(\text{PK}_i + P_{\text{pub}})$ and $\alpha_j = H_3(rX_i, \text{ID}_i)$
- (b) Select $\xi \in Z_p^*$ at random and define the formula:

$$f(x) = \prod_{j=1}^n (x - \alpha_j) + \xi(\text{mod } p) = a_0 + a_1 x \dots + a_{n-1} x_{n-1} + x_n, a_i \in Z_p^* \quad (16)$$

- (c) Calculate $k = H_3(\xi)$, $J^* = E_k(\mathbf{M}_\phi \| \text{ID}_s)$ and $h^* = H_4(\mathbf{M}, \text{ID}_s, X_s, Y_s, J, R, a_0, a_1, \dots, a_n)$
- (d) Select $z \in Z_p^*$ at random
- (e) Output the ciphertext $C^* = (J^*R, z, h, a_0, a_1, \dots, a_{n-1})$ to \mathcal{A}_1

Phase 30. \mathcal{A}_1 requires \mathcal{C} to execute the queries, and the contents are similar to Phase 5, but \mathcal{A}_1 cannot run the *Design-cryptionQuery* against C^* .

Guess: \mathcal{A}_1 gives a e^* at random. If $e^* = e$, then \mathcal{A}_1 wins, \mathcal{C} outputs CDHP's solution $xyP = rX_i - R$. If not, \mathcal{C} outputs "failure."

From the above discussion, it can be concluded that the H_5 hash provides a valid ciphertext during the *Design-cryptionQuery*, therefore, the probability of ciphertext being denied is no more than $q_5/2^k$. During the attack process, since \mathcal{A}_1 requires \mathcal{C} to execute the q_d *Design-cryptionQuery*, the probability of \mathcal{C} decryption success is $\varepsilon_d \geq \varepsilon - q_5 q_d/2^k$. The H_3 hash satisfies CDHP during the guessing process, so the probability that xyP is correctly calculated by \mathcal{C} is at least $\varepsilon_g = 1/nq_3$. \mathcal{C} can solve CDHP by interacting with opponent \mathcal{A}_1 in the running time $\tau' \leq \tau + (2q_c + 3q_d)O(\tau_s)$, and the probability advantage is $\varepsilon' \geq \varepsilon_a \varepsilon_g (\varepsilon - q_d q_5/2^k)/nq_3$, τ_s is the time of the SPMOOECC.

Theorem 31. *There is an opponent \mathcal{A}_2 under the ANO-CMRS-CA. In the polynomial time τ , if the \mathcal{A}_2 wins the Game6 victory with a probability advantage ε that cannot be ignored (\mathcal{A}_2 can obtain queries similar to that obtained by \mathcal{A}_2 in Theorem 23.), then within time $\tau' \leq \tau + (3q_c + 3q_d)O(\tau_s)$, challenger \mathcal{C} can overcome CDHP by interacting with opponent \mathcal{A}_2 with a probability advantage of $\varepsilon' \geq \varepsilon - q_d q_5/2^k/nq_3$, τ_s is the time of SPMOOECC.*

Proof. Under a nonnegligible probability, it is assumed that the opponent \mathcal{A}_2 can attack the ANO-CMRS-CA security, the probability advantage is ε , under the stochastic prediction model, \mathcal{A}_2 requires challenger \mathcal{C} to perform a series of queries. Given (P, xP, yP) , in the time-limited polynomial, \mathcal{C} obtains xyP through the opponent \mathcal{A}_2 interaction to overcome CDHP. The details are the followings:

Setup. \mathcal{C} performs the corresponding steps for obtaining the public parameter $\text{pars} = (E_p, G_p, E_k, D_k, p, P, K = xP, P_{\text{pub}}, H_1, H_2, H_3, H_4, H_5)$ and master key $s \in Z_p^*$ and then returns the result to \mathcal{A}_2 , where $x \in Z_p^*$. After receiving the result, \mathcal{A}_2 outputs $L = \{\text{ID}_0, \text{ID}_1\}$. H_1, H_2, H_3, H_4 , and H_5 are random predictions controlled by \mathcal{C} . The interaction is similar to *Setup* in Theorem 20, and the two sides of the interaction are \mathcal{A}_2 and \mathcal{C} .

Phase 32. \mathcal{A}_2 makes a series of queries to \mathcal{C} like Phase 4 in Theorem 23.

Challenge: \mathcal{A}_2 selects the target identifier $L^* = \{\text{ID}_2, \text{ID}_3, \dots, \text{ID}_n\}$ and plaintext \mathbf{M} and sends L^* and \mathbf{M} to \mathcal{C} . After receiving, \mathcal{C} selects a bit $e \in \{0, 1\}$ and uses the new target identifier $L^{**} = \{\text{ID}_e, \text{ID}_2, \text{ID}_3, \dots, \text{ID}_n\}$ to obtain the ciphertext C^* :

- (a) Calculate $R = y(\text{PK}_i + Y)$, $rX_i = y(\text{PK}_i + P_{\text{pub}})$ and $\alpha_j = H_3(rX_i, \text{ID}_i)$, $Y = K + P_{\text{pub}}$, $i = e, 2, 3, \dots, n$

TABLE 2: Comparison of functions.

Schemes	Decryption fairness	Receiver anonymity	Partial private key verifiability	Signature
Selvi et al. [25]	N	N	N	Y
Hung et al. [27]	N	Y	N	N
Zhu et al. [29]	N	N	N	N
Win et al. [30]	N	N	Y	N
Our program	Y	Y	Y	Y

TABLE 3: Symbols' definition.

Symbols	Symbols' definition
T_m	Time of a modular multiplication
T_{pm}	Time of a scalar point multiplication on ECC operation, $T_{pm} \approx 29T_m$.
T_{pa}	Time of a point addition on ECC operation, $T_{pa} \approx 0.12T_m$.
T_b	Time of a bilinear pairing operation, $T_b \approx 87T_m$.
T_t	Time of modular inversion operation, $T_t \approx 11.6T_m$.
T_{be}	Time of a bilinear pairing exponentiation operation, $T_{be} \approx 43.5T_m$.
T_h	Time of a map-to-point hash function operation, $T_h \approx 29T_m$.

(b) Select $\xi \in Z_p^*$ at random and define the formula:

$$f(x) = \prod_{i=1}^n (x - \alpha_i) + \xi \pmod{p} = a_0 + a_1x \cdots + a_{n-1}x_{n-1} + x_n, a_i \in Z_p^* \quad (17)$$

(c) Calculate $k = H_3(\xi)$, $J^* = E_k(\mathbf{M}_\varphi \| ID_s)$ and $h^* = H_4(\mathbf{M}, ID_s, X_s, Y_s, J, R, a_0, a_1, \dots, a_n)$

(d) Select $z \in Z_p^*$ at random

(e) Output the ciphertext $C^* = (J^*, R, z, h, a_0, a_1, \dots, a_{n-1})$ to \mathcal{A}_2

Phase 33. \mathcal{A}_2 requires \mathcal{C} to perform the same queries as Phase 5, but \mathcal{A}_2 cannot run the *DesigncryptonQuery* against C^* .

Guess: \mathcal{A}_2 gives a e^* at random. If $e^* = e$, then \mathcal{A}_2 wins, \mathcal{C} outputs CDHP's solution $xyP = R - rX_i$. If not \mathcal{C} outputs "failure."

From the above discussion, it can be concluded that the H_5 hash provides a valid ciphertext during the *DesigncryptonQuery*; therefore, the probability of ciphertext being denied is no more than $q_5/2^k$. During the attack process, since \mathcal{A}_2 requires \mathcal{C} to execute the q_d *DesigncryptonQuery* process, the probability of \mathcal{C} decryption success is $\varepsilon_d \geq \varepsilon - q_5q_d/2^k$. The H_3 hash satisfies CDHP during the guessing process, so the probability that xyP is correctly calculated by \mathcal{C} is at least $\varepsilon_g = 1/nq_3$. In the running time $\tau' \leq \tau + (3q_c + 3q_d)O(\tau_s)$, \mathcal{C} 's interaction with opponent \mathcal{A}_2 makes \mathcal{C}

overcome CDHP, and the probability advantage is $\varepsilon' \geq \varepsilon_d \varepsilon_g \geq (\varepsilon - q_dq_5/2^k)/nq_3$, τ_s is the time of the SPMOOECC.

5. Efficiency Analysis and Functional Comparison

Schemes in [25, 27, 29, 30] and our scheme are based on certificateless signcryptions. To reflect the superiority of our scheme, we will compare our scheme with them in terms of functions and efficiency.

5.1. Functional Comparison. We have compared the functions of our scheme and the functions of schemes in [25, 27, 29, 30], as shown in Table 2.

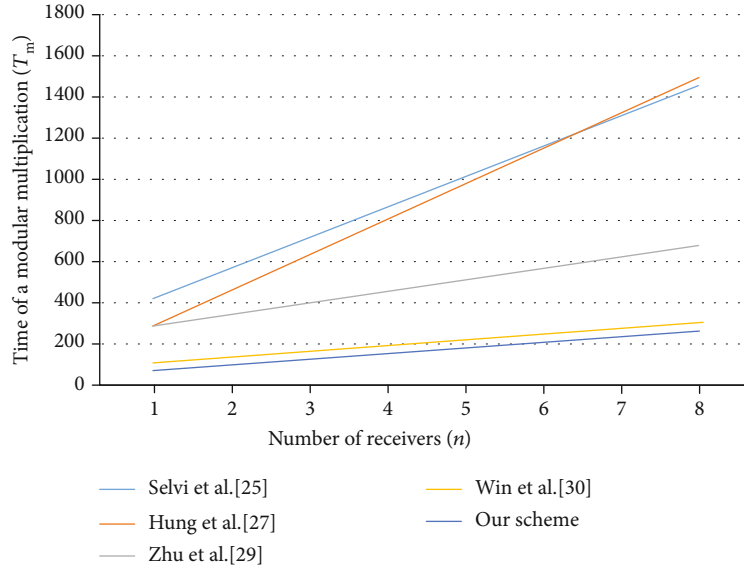
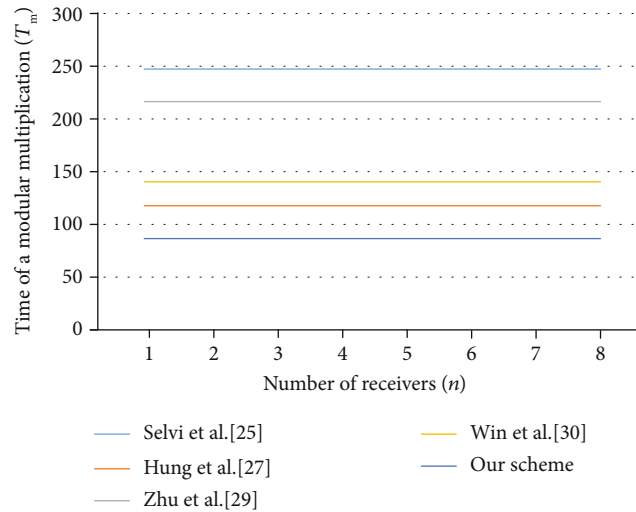
From the graph, we can get the following results, schemes in [25, 27, 29, 30] do not satisfy decryption fairness and do not guarantee that each recipient has the same chance of decryption. Schemes in [25, 29, 30] are not anonymous to the recipient, which may result in the disclosure of the recipient information, greatly reducing the encryption effect. Schemes in [25, 27, 29] cannot implement the verifiability of partial private key, which means they can be attacked by malicious KGC. Schemes in [27, 29, 30] have no signature function and cannot prevent an attacker from sending an unreliable messages.

5.2. Efficiency Analysis. For the sake of comparison, we have defined some symbols to represent the calculation of different operations in the encryption process and the decryption process, and the corresponding data is taken from [26]. We only consider the calculations defined in Table 3, because what is shown in Table 3 is the key to computational performance.

With the integration of encryption and decryption processes, as shown in Table 4, Figures 3 and 4, our scheme is

TABLE 4: Comparison of efficiency.

Schemes	Signcryption/encryption	Decryption/designcryption
Selvi et al. [25]	$(n+1)T_{pm} + T_i + (n+1)T_b + (n+1)T_{be} \approx (159.5n + 171.1)T_m$	$T_{pm} + T_{pa} + 2T_b + T_{be} \approx 246.62T_m$
Hung et al. [27]	$(n+1)T_{pm} + nT_{be} + nT_b + nT_h \approx (188.5n + 29)T_m$	$T_{pm} + T_b \approx 116T_m$
Zhu et al. [29]	$(2n+3)T_{pm} + nT_{pa} + T_b \approx (58.12n + 174)T_m$	$2T_b + T_{pm} + T_i \approx 214.6T_m$
Win et al. [30]	$(n+2)T_{pm} + nT_{pa} \approx (29.12n + 58)T_m$	$4T_{pm} + 4T_{pa} + 2T_i \approx 139.68T_m$
Our scheme	$(n+1)T_{pm} \approx (29n + 29)T_m$	$3T_{pm} + 2T_{pa} \approx 87.24T_m$

FIGURE 3: Efficiency in signcryption/encryption. The unit is T_m .FIGURE 4: Efficiency in decryption/designcryption. The unit is T_m .

better than the schemes in [25, 27, 29, 30], because the scheme in [25] and scheme in [29] use the BPO, scheme in [27] uses the BPO and MTPHF, and scheme in [30] uses lots of SPMOOECC. In this way, these operations all cause a lot

of overheads, making the scheme less efficient. Our scheme also uses SPMOOECC, but we attempt to reduce the number of SPMOOECC. Therefore, the performance of our scheme is superior to the scheme in [25, 27, 29, 30].

6. Conclusion

In this paper, we propose a CMRS scheme of high efficiency for ecological data sharing. After functional analysis, our scheme satisfies the security requirements, and it solves the problems of decryption fairness, recipient anonymity, and so on. After efficiency analysis, our scheme has high efficiency. It does not use BPO, but uses SPMOOECC for encryption and decryption, and ensures that SPMOOECC is used as little as possible, which greatly improves the efficiency of our scheme. After analysis, we can conclude that our scheme can be well applied to ecological data sharing.

Data Availability

The data used to support the findings of this study are available from the corresponding author upon request.

Disclosure

The authors disclosed receipt of the following financial support for the research, authorship, and/or publication of this article.

Conflicts of Interest

The authors declared no potential conflicts of interest with respect to the research, authorship, and/or publication of this article.

Acknowledgments

The work was supported in part by the National Natural Science Foundation of China (61862052) and the Natural Science Function of Qinghai Province (2019-ZJ-7065).

References

- [1] Y. L. Zheng, "Digital signcryption or how to achieve cost (signature & encryption) cost (signature) + cost (encryption)," in *Advances in Cryptology—CRYPTO*, vol. 1294, pp. 165–179, Springer, Berlin, Germany, 1997.
- [2] J. Baek, R. Safavi-Naini, and W. Susilo, "Efficient multi-receiver identity-based encryption and its application to broadcast encryption," in *Public Key Cryptography—PKC (Lecture Notes in Computer Science)*, vol. 3386, pp. 380–397, Springer, Berlin, Germany, 2005.
- [3] X. Du, Y. Wang, J. Ge, and Y. Wang, "An ID-based broadcast encryption scheme for key distribution," *IEEE Transactions on Broadcasting*, vol. 51, no. 2, pp. 264–266, 2005.
- [4] C. Delerablée, "Identity-based broadcast encryption with constant size ciphertexts and private keys," in *Advances in Cryptology—ASIACRYPT (Lecture Notes in Computer Science)*, vol. 4833, pp. 200–215, Springer, Berlin, Germany, 2007.
- [5] Y. M. Tseng, T. T. Tsai, and Y. T. Wu, "Efficient revocable multi-receiver ID-based encryption," *Information Technology And Control*, vol. 42, no. 2, pp. 159–169, 2013.
- [6] S. Duan and Z. Cao, "Efficient and provably secure multi-receiver identity-based signcryption," in *Information Security and Privacy*, vol. 4058, pp. 195–206, Springer, Berlin, Germany, 2006.
- [7] S. Lal and P. Kushwah, *Anonymous ID based signcryption scheme for multiple receivers*, IACR Cryptology ePrint Archive, Las Vegas, NV, USA, 2009.
- [8] L. Pang, L. Gao, H. Li, and Y. Wang, "Anonymous multi-receiver ID-based signcryption scheme," *IET Information Security*, vol. 9, no. 3, pp. 194–201, 2015.
- [9] X. Zhang, C. Xu, and J. Xue, "Efficient multi-receiver identity-based signcryption from lattice assumption," *International Journal of Electronic Security and Digital Forensics*, vol. 10, no. 1, pp. 20–28, 2018.
- [10] Z. Yu, Z. Jing, H. Yang, and C. Gu, "ID-based multi-receiver signcryption scheme in the standard model," *International Journal of Internet Protocol Technology*, vol. 10, no. 1, pp. 4–12, 2017.
- [11] S. S. D. Selvi, S. S. Vivek, R. Srinivasan, and C. P. Rangan, "An efficient identity-based signcryption scheme for multiple receivers," in *Advances in Information and Computer Security (Lecture Notes in Computer Science)*, vol. 5824, pp. 71–88, Springer, Berlin, Germany, 2009.
- [12] S. Khullar, V. Richhariya, and V. Richhariya, "An efficient identity based multi-receiver signcryption scheme using ECC," *International Journal of Advancements in Technology*, vol. 2, no. 4, pp. 189–193, 2013.
- [13] L. Pang, H. Li, L. Gao, and Y. Wang, "Completely anonymous multirecipient signcryption scheme with public verification," *PLoS One*, vol. 8, no. 5, article e63562, 2013.
- [14] Y.-M. Tseng, T.-T. Tsai, S.-S. Huang, and H.-Y. Chien, "Efficient anonymous multi-receiver ID-based encryption with constant decryption cost," in *2014 International Conference on Information Science, Electronics and Electrical Engineering*, pp. 131–137, Sapporo, Japan, April 2014.
- [15] C.-I. Fan, L.-Y. Huang, and P.-H. Ho, "Anonymous multireceiver identity-based encryption," *IEEE Transactions on Computers*, vol. 59, no. 9, pp. 1239–1249, 2010.
- [16] H. Wang, Y. Zhang, H. Xiong, and B. Qin, "Cryptanalysis and improvements of an anonymous multi-receiver identity-based encryption scheme," *IET Information Security*, vol. 6, no. 1, pp. 20–27, 2012.
- [17] H. Li and L. Pang, "Cryptanalysis of Wang et al.'s improved anonymous multi-receiver identity-based encryption scheme," *IET Information Security*, vol. 8, no. 1, pp. 8–11, 2014.
- [18] C.-I. Fan and Y.-F. Tseng, "Anonymous multi-receiver identity-based authenticated encryption with CCA security," *Symmetry*, vol. 7, no. 4, pp. 1856–1881, 2015.
- [19] L. Pang, X. Yan, H. Zhao, Y. Hu, and H. Li, "A novel multi-receiver signcryption scheme with complete anonymity," *PLoS One*, vol. 11, no. 11, article e0166173, 2016.
- [20] S. S. Al-Riyami and K. G. Paterson, "Certificateless public key cryptography," in *Advances in Cryptology—ASIACRYPT (LNCS)*, vol. 2894, pp. 452–473, Springer, Berlin, Germany, 2003.
- [21] X. Huang, W. Susilo, Y. Mu, and F. Zhang, "On the security of certificateless signature schemes from asiacrypt 2003," in *Proc. Int. Conf. Crypto. Netw. Secur., in Lecture Notes in Computer Science*, vol. 3810, pp. 13–25, Berlin, Germany: Springer, 2005.
- [22] Z. F. Zhang, D. S. Wong, J. Xu, and D. G. Feng, "Certificateless public-key signature: Security model and efficient construction," in *Proc. Int. Conf. Appl. Crypto. Netw. Secur., in Lecture Notes in Computer Science*, vol. 3989, pp. 293–308, Berlin, Germany: Springer, 2006.

- [23] X. Y. Huang, Y. Mu, W. Susilo, D. S. Wong, and W. Wu, "Certificateless signature revisited," in *Information Security and Privacy, in Lecture Notes in Computer Science*, vol. 4586, pp. 308–322, Springer, Berlin, Germany, 2007.
- [24] M. Barbosa and P. Farshim, "Certificateless signcryption," in *Proceedings of the 2008 ACM symposium on Information, computer and communications security - ASIACCS '08*, pp. 369–372, Tokyo, Japan, 2008.
- [25] S. S. D. Selvi, S. S. Vivek, D. Shukla, and P. R. Chandrasekaran, "Efficient and provably secure CMS," in *Provable Security (Lecture Notes in Computer Science)*, vol. 5324, pp. 52–67, Springer, Berlin, Germany, 2008.
- [26] S. H. Islam, M. K. Khan, and A. M. Al-Khouri, "Anonymous and provably secure certificateless multireceiver encryption without bilinear pairing," *Security and Communication Networks*, vol. 8, no. 13, 2231 pages, 2015.
- [27] Y.-H. Hung, S.-S. Huang, Y.-M. Tseng, and T.-T. Tsai, "Efficient anonymous multireceiver certificateless encryption," *IEEE Systems Journal*, vol. 11, no. 4, pp. 2602–2613, 2017.
- [28] D. He, H. Wang, L. Wang, J. Shen, and X. Yang, "Efficient certificateless anonymous multi-receiver encryption scheme for mobile devices," *Soft Computing*, vol. 21, no. 22, pp. 6801–6810, 2017.
- [29] J. Zhu, L.-L. Chen, X. Zhu, and L. Xie, "A new efficient certificateless multi-receiver public key encryption scheme," *International Journal of Computer Science Issues*, vol. 13, no. 6, pp. 1–7, 2016.
- [30] E. K. Win, T. Yoshihisa, Y. Ishi, T. Kawakami, Y. Teranishi, and S. Shimojo, "A lightweight multi-receiver encryption scheme with mutual authentication," in *2017 IEEE 41st Annual Computer Software and Applications Conference (COMPSAC)*, pp. 491–497, Turin, Italy, July 2017.

Research Article

A Novel Biofloculant from *Raoultella planticola* Enhances Removal of Copper Ions from Water

Fancheng Zeng,¹ Liang Xu ,^{1,2} Caiyun Sun ,^{1,2} Hong Liu,¹ and Libo Chen¹

¹Jilin Institute of Chemical Technology, Jilin, China

²School of Chemical Engineering, University of Birmingham, Birmingham, UK

Correspondence should be addressed to Liang Xu; xlsdydnl@126.com and Caiyun Sun; suncaiyun1985@126.com

Received 7 November 2019; Accepted 6 February 2020; Published 23 July 2020

Guest Editor: Yuan Li

Copyright © 2020 Fancheng Zeng et al. This is an open access article distributed under the Creative Commons Attribution License, which permits unrestricted use, distribution, and reproduction in any medium, provided the original work is properly cited.

Copper is one of the most toxic heavy metals. In this work, a sampling survey of copper ions in the water of Songhua River flowing through the chemical and living areas of Jilin City was studied. A new biofloculant from *Raoultella planticola* was obtained. The investigation of Songhua River flowing through Jilin City shows that the copper concentration is between 0.07 ppb and 0.16 ppb. The biofloculant supporting graphite oxide (GO) as a biofloculant inducer used in this study has been utilized in treatment of copper ions in water. GO and biofloculant infrared radiation (IR) spectrum and zeta potential were studied. Flocculational conditions of copper ion (0.2 ppm) were modeled and optimized using RSM (response surface methodology). Our data showed that flocculation efficiency was over 80%. Significant influencing factors and variables were pH, flocculation time, biofloculant dosage, and GO inducer which had major impact effects on flocculation efficiency. The highest flocculation efficiency which is 86.01% was achieved at pH = 5, at 1.62 h and 13.11 mg biofloculant with 13.11 mg GO as an inducer. However, temperature (A) and GO inducer were significant impact factors on the flocculation efficiency.

1. Introduction

Copper is widely used in metallurgy, machine manufacturing, electroplating, chemistry, and other industries. In agriculture and forestry, copper sulfate can prevent diseases and insect pests and inhibit the proliferation of algae in water. Copper chloride, copper sulfate, and copper nitrate are easy to dissolve in water. The total content of copper in a normal human body is about 100-150 mg [1]. However, excessive intake will stimulate the digestive system, causing abdominal pain and vomiting. The oral lethal dose of humans is about 10 g [2]. The toxicity of copper to lower organisms and crops is relatively high. When the concentration of copper reaches 0.1-0.2 mg/L [3], fish will die. When it coexists with zinc, the toxicity will increase, and the toxicity to shellfish water will be greater [4]. Generally, the concentration of copper in water for aquaculture is required to be below 0.01 mg/L [5]. For crops, copper is the most toxic heavy metal, which is fixed in the root cortex after absorbing copper ions, affecting nutrient absorption. When the copper

content in irrigation water is high, it accumulates in soil and crops, which can make crops wither [6].

Biofloculant is a kind of polymer compound. It must be secreted by specific microbial groups under specific growth conditions. The complexity of the molecular components of biofloculant, such as protein, polysaccharide, and glycoprotein, determines its good electrochemical properties. Therefore, it is endowed with good flocculation characteristics [7, 8]. At present, it is widely explored and studied as a new flocculant. Many publications have reported on biofloculants to replace traditional industrial flocculants in drinking and wastewater treatment process and fermentation processes because of its high removal efficiency, low dosage, and less secondary pollution in the environment [9, 10]. Graphene oxide (GO) is a new material which has attracted wide attention in recent years. Because of its excellent electrochemical properties, it has been widely used in electronic technology, biosensors, nanotubes, semiconductors, and other fields. Graphite oxide, as a novel material with a unique structure and excellent properties, has attracted extensive attention

[11, 12]. GO is a two-dimensional nanomaterial with a honeycomb-like monolayer structure and has a large number of its surface's active groups, such as epoxy groups, hydroxyl, and carboxyl. GO has an aromatic structure and can adsorb aromatic compounds through the interaction between the active groups and the electron cloud [13].

Therefore, due to graphite oxide's unique structure, there are excellent physical and chemical properties and good biocompatibility. Though graphene oxide has been used as a flocculant in water treatment, the main research is still at the laboratory level, and there are few reports on the actual application of wastewater treatment. The bioflocculant supporting graphite oxide as a bioflocculant inducer used in this study has been studied in the treatment of copper ions in surface water. Accordingly, the objectives of this work are to (1) study a sample survey of copper ions in the water of Songhua River flowing through the chemical and living areas of Jilin City; (2) screen bioflocculant-producing strains for flocculation of copper ions; (3) optimize temperature, pH, bioflocculant dosage, GO inducer, and flocculation time on the flocculation process by response surface methodology (RSM); and (4) analyze the end group properties of bioflocculant and the potential changes in the process of flocculation.

2. Material and Methods

2.1. Identification of Bioflocculant-Producing Strains. Approximately 200 isolates (N-1 to N-200) were screened from the activated sludge of the Secondary Wastewater Treatment Plant in Jilin, China. The 16s rDNA was amplified by PCR in Shanghai Sangon Biotechnology Co., Ltd. Primers (27F: AGAGTTTGTATCCTGGCTCAG and 1492R: GGTTACCTTGTTACGACTT) were used in 16s rDNA amplification and identification of strains. Sequence similarity was over 97.1%. The comparison of sequencing data showed that the species of the strain was *Raoultella planticola* by which ncbi access No. is KC456530.1. The Nikon-e100 microscope was used to observe the morphological characteristics of the strain, and the Bergey system bacteriology manual was used to identify the physiological and biochemical characteristics of the strain. *Raoultella planticola* is a gram-negative, aerobic, rod bacterium.

2.2. Culture Medium for *Raoultella planticola* Bioflocculant Production. *Raoultella planticola* was cultivated using beef extract-peptone medium containing 5 g/L of peptone, 1.5 g/L of beef extract, 1.5 g/L of yeast extract, and 5 g/L of NaCl. Bioflocculant production culture medium was different from PT-1 which we used in former work [14, 15]. Composition of the bioflocculant medium in this study was as follows: glucose, 20 g/L; yeast extract, 0.5 g/L; urea, 0.5 g/L; $(\text{NH}_4)_2\text{SO}_4$, 0.2 g/L; KH_2PO_4 , 7 g/L; MgSO_4 , 0.2 g/L; and NaCl, 0.1 g/L. The initial pH of the medium was adjusted to 7.0 ± 0.5 . After sterilization, the strain was put into the flask containing the medium, the culture temperature was 30°C , the vibration frequency was 150 rpm, and the best time for bacteria to secrete flocculant was 72 hours.

2.3. Preparation of the *Raoultella planticola* Bioflocculant (MBF-51). *Raoultella planticola* was inoculated into a 150 mL flask containing 50 mL PT-1 medium. The bioflocculant was termed MBF-51 and was produced by shaking the flask at 30°C at 150 rpm for 72 h. Cell-free supernatants were obtained by centrifugation at 7000 rpm for 30 min. Bioflocculant purification methods were conducted according to previous methods. Briefly, two volumes of cold ethanol (at 4°C) were added to 1 L culture broth. Following centrifugation at 8000 rpm for 30 min, the precipitate was washed with ethanol, dissolved in 5 mL of deionized water, and vacuum-dried resulting in approximately 12.50 ± 0.5 g of MBF-51 per 1 L of culture broth.

2.4. Preparation of Nanoscale Graphene Oxide. Graphene oxide was prepared by the modified Hummers method [16]. The preparation steps were as follows: 2.0 g graphite powder was added into 50 mL concentrated H_2SO_4 solution with 2.0 g NaNO_3 dissolved. After stirring for 15 minutes, 6.0 g KMnO_4 was added slowly (keeping system temperature below 15°C), reaction at 35°C for 1 h, heating up to 90°C for 15 min, distilled water at 200 mL was added. Graphite powder was heated with boiling reaction for 15 min. As the graphite dropped to room temperature, it is added with 12 mL H_2O_2 for 8 hours. Then, the mixture is filtered and collected after centrifugation. SO_4 ion was removed by washing with distilled water. The powder was vacuum-dried until constant weight. Then, GO powder was obtained. 0.2 g GO powder is dispersed in 400 mL distilled water to make the concentration to 0.5 mg/mL.

2.5. Batch Experiment of Microbial Flocculation of Copper. By adding distilled water, the microbial flocculant MBF-51 was diluted to 60 mg/L for copper flocculation. The impacts of flocculation conditions (temperature ($^\circ\text{C}$), pH value, flocculation time (hour), dosage of bioflocculant (mg/L), and dosage of GO inducer (mg/L)) on flocculation effect were analyzed. The pH was adjusted from 0.1 M HCl and 0.1 M NaOH to about 3.0-1.0. Similarly, the effect of temperature is cultivated at the desired temperature.

After the setting of fixed variable factors, the mixture containing MBF-51 solution, GO inducer, and copper ion (CuCl_2) was shaken in the track vibrating screen (mode-hzq-x100, HDL Equipment Co., Ltd., China) and stirred at a constant speed of 250 rpm. The initial copper concentration was selected as 0.2 ppm (area No. 4). The optical density of supernatant was measured at the middle height of clarified liquid. The culture medium without flocculant and GO was used as the control. Flocculation efficiency of copper was calculated by

$$\text{Flocculation Efficiency (\%)} = \frac{A - B}{A} \times 100, \quad (1)$$

where A is the value of the atomic absorption spectrum determined by the sample and B is the value of the reference sample determined by atomic absorption spectrometry.

2.6. The Establishment of Mathematical Model for the Influence of Different Factors. The Design-Expert software

TABLE 1: Independent variables and their levels in the experimental design.

Independent factors	Symbols	Code levels				
		-2	-1	0	+1	+2
Temperature (°C)	A	5	10	20	30	35
pH	B	4	5	7	9	10
Flocculation time (hour)	C	0	0.5	1.5	2.5	3
Bioflocculant dosage (mg/L)	D	2.5	5	10	15	17.5
GO inducer (mg/L)	E	1.5	3	6	9	10.5

(8.3 edition) adopts the experimental statistical design and data analysis, and the experimental design is referred to our previous research papers [17]. The narrow temperature, pH value, flocculation time, the dosage of bioflocculant, and the range of GO inducer were determined before central composite design (CCD) and response surface method (RSM) were used for modeling. The narrower ranges of temperature, pH, flocculation time, bioflocculant dosage, and GO inducer were chosen as 5–35°C, 4–10, 0–3 hours, 2.5–17.5 mg/L, and 1.5–10.5 mg/L, respectively. Five independent factors at different levels (-2, -1, 0, +1, and +2) were studied. The experimental design is shown in Table 1.

The relationship between the response variable (y) of flocculation efficiency and each factor variable is fitted by the second-order model, and the following quadratic polynomial equation (2) is finally obtained for calculation:

$$\begin{aligned}
 \text{Flocculation Efficiency} = & +80.09 + 2.79 * A - 10.14 * B \\
 & + 5.65 * C + 21.39 * D + 4.76 * E \\
 & + 1.55 * A * B - 0.84 * A * C \\
 & + 2.93 * A * D - 6.35 * A * E \\
 & + 0.13 * B * C + 1.10 * B * D \\
 & + 1.95 * B * E + 1.06 * C * D \\
 & - 1.15 * C * E + 1.63 * D * E \\
 & - 1.07 * A^2 - 4.31 * B^2 \\
 & - 16.17 * C^2 - 15.88 * D^2 \\
 & + 1.64 * E^2.
 \end{aligned} \tag{2}$$

All analyses are in triplicate. The data in the response surface was fitted with the average of three groups of repeated data, and variance analysis was carried out.

2.7. Analytical Methods. Zeta potential measurement was conducted by a zeta potential analyzer (Malvern Nano ZS, Malvern, England). A Fourier-transform infrared spectrometer (Nicolet 6700, ThermoFisher, USA) was used for space atmospheric component detection. A scanning electron microscope (XL30-ESEM, FEI, USA) was used for studies. An atomic absorption spectrometer (180-Series, HITACHI, Japan) was used to determine the total copper concentration in water. The positions and longitude and latitude of the required logging stations are shown in Table 2.

3. Results and Discussion

3.1. Investigation on Copper Content in Water in Songhua River Section Flowing through Jilin City. Jilin City is located in the east of the central part of Jilin Province, the northeast hinterland of Changbai Mountains, the junction of Songnen Plain and Changbai Mountains. It is the secondary economic and cultural center of northeast Jilin Province as is shown in Figure 1(a). Its geographical coordinates are between 42 degrees north latitude 31' to 44 degrees 40' and 125 degrees 40' to 127 degrees east longitude 56'. The north and south are about 91 kilometers long and 44 kilometers wide. The total area under the jurisdiction of Jilin City is 27700 square kilometers, of which the urban area is 3774.35 square kilometers; by the end of 2016, the urban area of Jilin City is 498.75 square kilometers, and the built-up area is 189.04 square kilometers. The positions and longitude and latitude of the required logging stations are shown in Table 2. The investigation in Figure 1(a) shows that the copper concentration in this area is the lowest 0.066 ppb (area No. 10) and the highest is 0.159 ppb (area No. 4). From data in Figure 1(b), it can be seen that the copper content index of the three water samples did not exceed the Class III standard of the Surface Water Quality Standard [18].

3.2. Zeta Potential and Fourier-Transform Infrared Spectrometer Analysis of GO and Bioflocculant. GO and bioflocculant infrared radiation (IR) spectrum was investigated. The IR spectrum of GO exhibited a carboxyl band at 1620, 1582, and 1384 cm^{-1} as presented in Figure 2(a). The absorption peaks at 1620 cm^{-1} and 1582 cm^{-1} are caused by C=O carbonyl expansion and C=C expansion in the GO skeleton, respectively. The absorption peaks at 1384 cm^{-1} and 587 cm^{-1} are related to the deformation vibration of C-O-H and the bending vibration of -O, respectively [19], as shown in Figure 2(a). The adsorption peak at 587 cm^{-1} indicated the C-O-H stretching vibration [20] as shown in Figures 2(a) and 2(b). Further FTIR characterization of bioflocculant is shown in Figure 1(b). It is found that the peaks of GO and bioflocculant at 2920 cm^{-1} and 2850 cm^{-1} correspond to the characteristic absorption peaks of -OH and -C-H, respectively [21]. The enhancement of absorption peaks at 3420 cm^{-1} and 1620 cm^{-1} is attributed to the O-H and N-H vibrations in C-OH and N-OH groups which form hydrogen bonds. Oxygen-containing groups above, especially the strong polar groups such as -OH, are abundant on the surface of the materials, which makes the materials in water-soluble solvents. The dispersion is good, and the polarity is enhanced, and

TABLE 2: Existing monitoring wells (residential wells, drilling wells, farmland irrigation wells, and centralized water supply wells).

No.	Name of water source area	Longitude (east longitude)	Latitude (north latitude)	Remarks
1	Longtan District	126°29'29"	43°55'59"	Surface water
2	Songhua River	126°30'33"	43°55'56"	Surface water
3	Songhua River	126°31'52"	43°55'36"	Surface water
4	Songhua River	126°32'22"	43°54'51"	Surface water
5	Songhua River	126°32'39"	43°54'05"	Surface water
6	Songhua River	126°33'45"	43°53'36"	Surface water
7	Songhua River	126°34'39"	43°53'37"	Surface water
8	Songhua River	126°35'23"	43°53'32"	Surface water
9	Sewage outfall of Changyi District, Songhua River	126°36'00"	43°53'09"	Surface water
10	Sewage outfall of Longtan District, Songhua River	126°36'12"	43°52'42"	Surface water
11	Water supply well in Changyi Township	126°36'07"	43°52'17"	Village-owned wells
12	Residents in Tiedong Township	126°35'60"	43°51'45"	Village-owned wells
13	Songhua River	126°36'04"	43°51'19"	Surface water
14	Songhua River	126°36'08"	43°50'27"	Surface water
15	Songhua River	126°35'32"	43°49'56"	Surface water

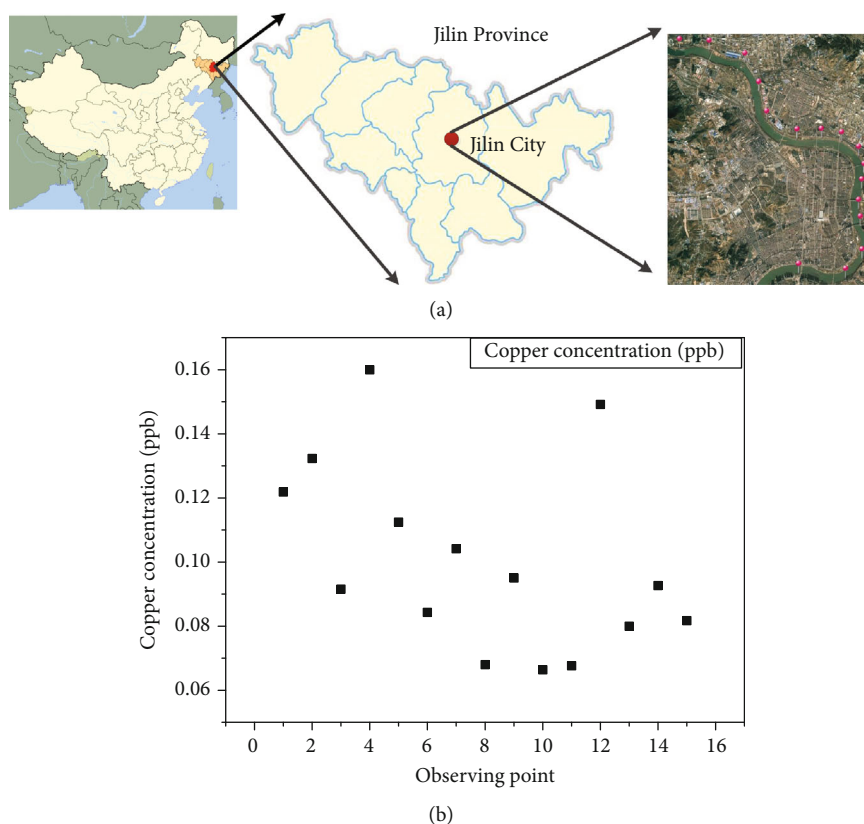


FIGURE 1: Copper content in surface water of Songhua River in Jilin City of Jilin Province: (a) sketch map of sampling area; (b) concentration of copper in surface water at 16 sampling sites.

the adsorption of copper by adsorbents is promoted. Zeta potential measurement of biofloculant with GO inducer solution (Figure 1(c)), indicated that the solution before flocculation

of copper was negatively charged in both alkaline solution and acidic solution; however, zeta potential of the solution after flocculation with copper (Figure 1(d)) was

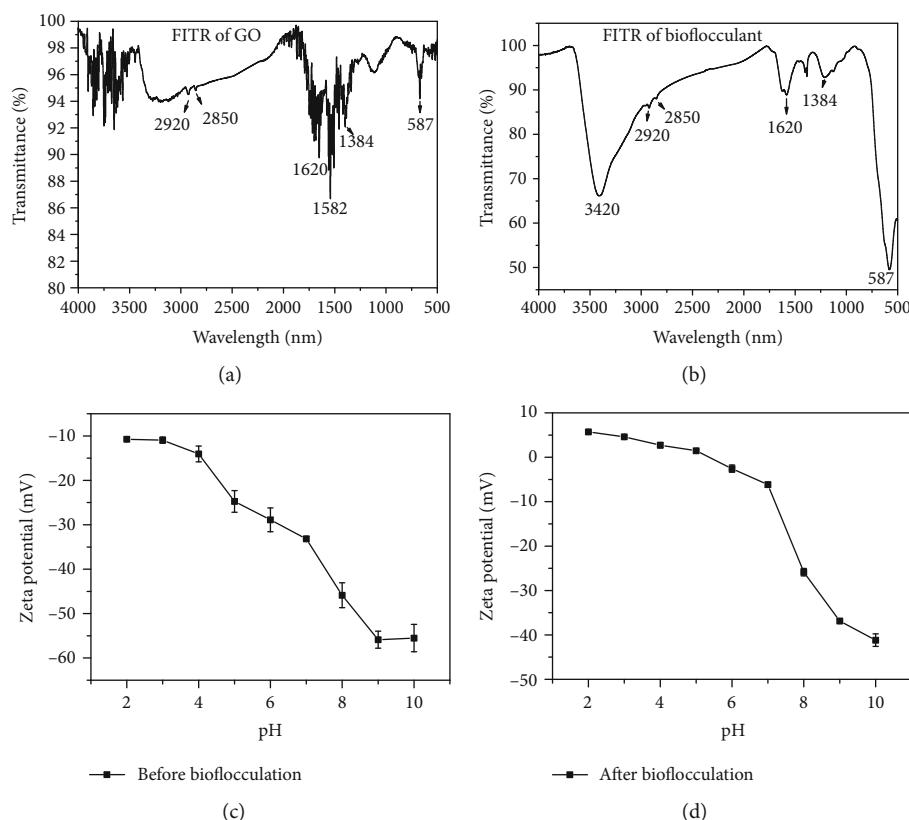


FIGURE 2: Zeta potential of bioflocculant with GO inducer solution before and after flocculation and Fourier-transform infrared spectrometer analysis of GO and bioflocculant: (a) infrared radiation of GO; (b) infrared radiation of bioflocculant; (c) zeta potential of bioflocculant with GO inducer solution; (d) zeta potential of solution after flocculation.

electrically neutral ($2 < \text{pH} < 6$) and was increased by $\text{Cu}(\text{OH})_2$ in alkaline ($10 < \text{pH} < 6$).

3.3. RSM Optimization of Copper Flocculation Process

3.3.1. Analysis of the Effect of Single Factor on Flocculation Efficiency. The experimental tasks and the collected response data are shown in Table 1. As shown in Table 3, the linear terms of pH (B), flocculation time (C), dosage of bioflocculant (D), and GO inducer (E) have a significant impact on flocculation efficiency (F value < 0.05), while temperature (A) has no significant impact on flocculation efficiency. Figure 3(a) shows the highest flocculation efficiency achieved at $\text{pH} = 5$. With the increase of pH value from 4 to 5, the flocculation efficiency increased from 85.65% to 86.01%, and with the increase of pH value to 9, the flocculation efficiency decreased to 65.66%. If the pH value is changed, the flocculation will be completely different; for example, copper ion will precipitate in alkaline condition. Figure 3(b) shows that the flocculation efficiency reaches the maximum at 1.62 h and increases from 51.21% to 80.55% as the flocculation time increases from 0.05 to 1.62 h and decreases to 60.16% as the flocculation time increases to 3 h. Figure 3(c) shows that the flocculation efficiency reaches the maximum at 13.11 mg. With the increase of bioflocculant dosage from 2.5 mg to 13.11 mg, the flocculation efficiency increased from 12.77% to 87.26%. With the increase of bioflocculant dosage to

17.5, the flocculation efficiency decreased to 76.60%. Figure 3(d) shows the highest flocculation efficiency achieved at 10.5 mg. With the increase of the GO inducer from 1.5 to 10.5, the flocculation efficiency increased from 76.59% to 90.88%. Table 3 and Figure 4 show that temperature has no significant effect on flocculation, the flocculation efficiency only increases by 8.39%, and the temperature rises from 5°C to 35°C .

3.3.2. Analysis of the Effect of Two Factors on Flocculation Efficiency. Table 3 shows that temperature (A) and GO inducer (E) are important factors affecting flocculation efficiency. RSM provides a response surface and contour map to study the interaction between parameters and flocculation efficiency in Figure 5 by changing the other two variables in the experimental range and keeping the values of other variables at a medium level. As shown in Figure 3, under the fixed pH value, flocculation time, and bioflocculant dosage, the flocculation efficiency increases from 48.91% to 84.46% as the dosage increases from 5 mg/L to 15 mg/L; when the dosage of MBF-51 is 10 mg/L, the flocculation efficiency increases from 67.48% to 75.15%, and the time increases from 0.5 hours to 2.5 hours.

The large surface of GO is rich in oxygen-containing functional groups, such as hydroxyl and carboxyl, which makes it extremely hydrophilic in the water environment (Figure 4(a)), but at the same time, as a lamellar organic

TABLE 3: Experimental design and results using central composite design.

Run	^d T	pH	Variables ^b FT	^c FD	^c GI	^a FE(%)
1	20	7	1.5	10	6	81.76
2	30	5	0.5	15	9	76.65
3	10	5	2.5	15	9	75.65
4	20	7	1.5	10	6	81.94
5	20	7	1.5	10	1.51	81.30
6	10	5	2.5	5	9	66.41
7	10	9	2.5	15	9	71.87
8	10	9	0.5	5	9	11.98
9	20	7	1.5	2.52	6	0.75
10	10	5	0.5	15	9	69.82
11	30	9	2.5	5	9	14.10
12	20	7	0	10	6	0.15
13	20	7	1.5	10	6	82.86
14	20	7	1.5	17.48	6	82.77
15	10	5	2.5	15	3	73.80
16	10	9	2.5	5	9	12.47
17	20	7	1.5	10	6	82.17
18	30	9	0.5	15	9	66.76
19	30	9	0.5	5	9	11.75
20	30	5	0.5	5	9	28.80
21	10	5	0.5	5	9	56.45
22	30	5	2.5	5	3	46.12
23	10	5	2.5	5	3	19.39
24	30	9	2.5	5	3	12.64
25	30	9	2.5	15	9	73.16
26	30	5	2.5	15	3	84.07
27	20	7	3	10	6	82.06
28	30	5	2.5	5	9	21.78
29	20	9.99	1.5	10	6	60.78
30	30	5	2.5	15	9	77.39
31	20	7	1.5	10	6	82.06
32	10	9	0.5	15	9	67.29
33	10	9	2.5	5	3	12.55
34	30	5	0.5	5	3	42.53
35	20	7	1.5	10	6	81.76
36	10	5	0.5	15	3	67.91
37	10	5	0.5	5	3	7.78
38	30	9	0.5	5	3	11.93
39	10	9	0.5	5	3	9.50
40	30	9	2.5	15	3	62.35
41	20	4.01	1.5	10	6	74.48
42	10	9	0.5	15	3	19.10
43	20	7	1.5	10	10.49	80.57
44	30	5	0.5	15	3	75.08
45	10	9	2.5	15	3	32.85
46	20	7	1.5	10	6	81.61
47	20	7	1.5	10	6	82.09

TABLE 3: Continued.

Run	^d T	pH	Variables ^b FT	^c FD	^c GI	^a FE(%)
48	34.95	7	1.5	10	6	82.06
49	5.05	7	1.5	10	6	67.67
50	30	9	0.5	15	3	49.85

^aFlocculation efficiency. ^bFlocculation time. ^cFlocculant dosage.
^dTemperature. ^eGO inducer.

matter, its ionic properties are also very good, which is the main reason why we use it as coagulant aids. In the research and experiment, such characteristics play a key role in the removal of copper ions [22]. In the process of flocculation, net catching is the main factor of flocculation mechanism, as shown in Figure 4(b), but at the same time, our experiment shows that due to the function of the GO coagulant aid, electric neutralization and compression double electric layers also play a key role in flocculation. Although we only have data results of zeta potential, it is obvious that such a conclusion is [23]. The induction efficiency of a low dose of 12 mg/L was over 80%. As a long-chain biopolymer, MBF-51 bridges between GO particles and copper, as shown in Figure 4(b). When MBF-51 is insufficient, a bridging phenomenon will not form effectively. At the same time, even if GO plays the role of compressing the double electric layer to make copper ions adhere to its surface for a short time, because there is not enough bioflocculant, such removal effect cannot be played for a long time, so the dosage of bioflocculant is the guarantee of the removal rate. These oxygen functional groups make GO have good dispersibility in water. As shown in Figure 2, the zeta potential measurement of MBF-51 shows that MBF-51 is mainly negatively charged under alkaline and acidic conditions. It is reported that GO has different electric states at different pH values. It is a positive charge under acidic conditions (pH value lower than 4) and a negative charge under neutral and alkaline conditions (pH value higher than 4). This result just proves that the copper ion, as a cation, can fully connect with GO and bioflocculant to attach and adsorb and finally be removed ([24, 25]).

3.3.3. ANOVA Analysis of Quadratic Model. As shown in Table 4, the experimental data of flocculation efficiency were analyzed by ANOVA. All factors are consistent with the quadratic equation model fitted in the above material method, and our quadratic equation model has significant statistical significance and value, because the results show that our equation p value is far less than 0.05. The results show that temperature (A) has little effect on flocculation. Its p value is greater than 0.05 (data not shown in Table 3 and Table 4). At the same time, the variance analysis of the response surface quadratic model also proves that temperature is not a key factor in the flocculation process [26]. The p value less than 0.05 indicates that the model term is important, and the insignificant terms (p value > 0.05) are removed from the final expression of the model [27]. We assume that the most ideal flocculation efficiency is 100%, and the logit equation is used to fit, and the determined upper limit of the

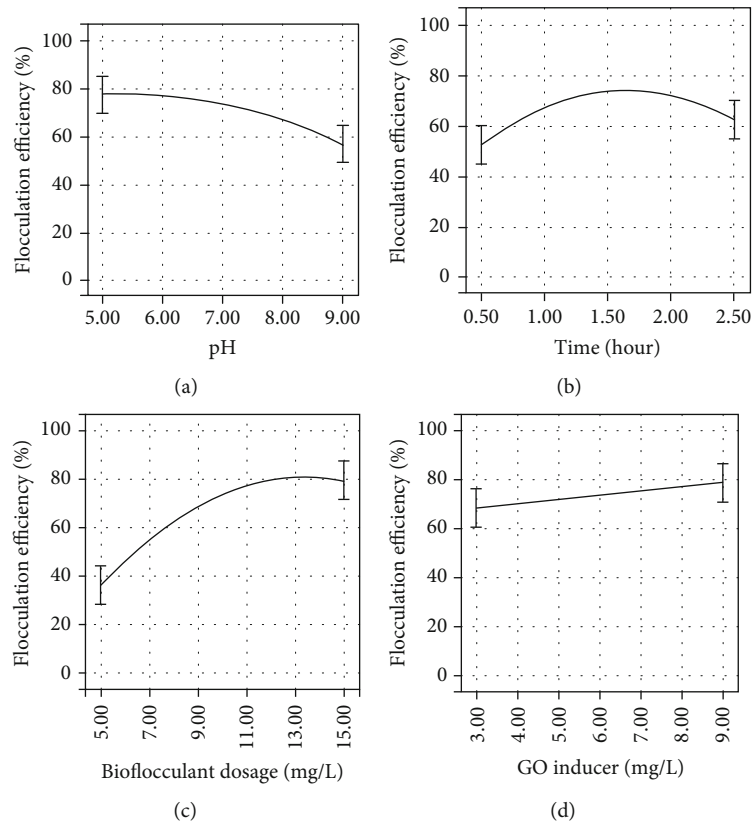


FIGURE 3: Effect of four linear variable factors on flocculation efficiency, including pH, time, biofloculant dosage, and GO inducer.

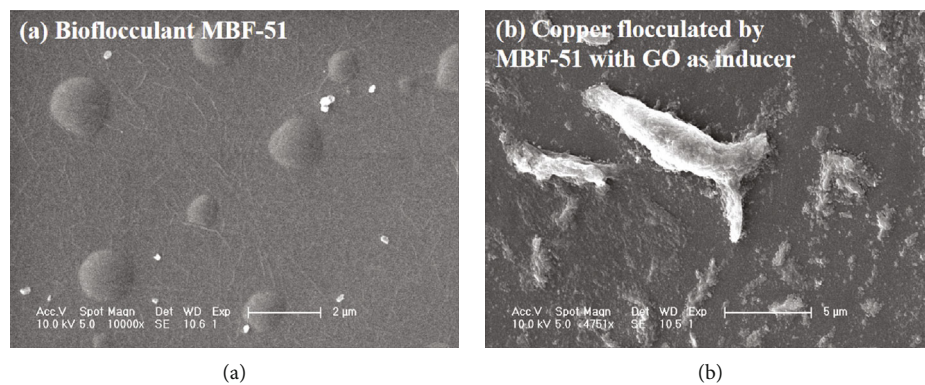


FIGURE 4: Scanning electron microscopy: (a) biofloculant MBF-51; (b) copper flocculated by MBF-51 with GO inducer.

dependent variable of flocculation rate is 100. According to the factor change of the flocculation process and the experiment of five factors without levels, the quadratic equation (2) is finally obtained. As shown in Table 4, the p value of the equation is less than 0.0001 (far less than 0.05). Using the SNR parameter to evaluate the equation, it is found that the SNR is less than 4, which also has statistical value [28]. The missing of fitting value is not significant compared with the pure error. The correlation coefficient (R^2) obtained in this study is 0.87, close to R^2 adj (0.78), indicating that the predicted value of the experiment is in good agreement with the observed value [29].

4. Conclusions

The results showed that *Raoultella planticola* produced flocculant which had never been reported before. The biofloculant supporting graphite oxide as a biofloculant inducer used in this study has been studied in the treatment of copper ions in surface water. *Raoultella planticola* was inoculated in PT-1 medium and resulted in approximately 12.50 ± 0.5 g of MBF-51 per 1 L of culture broth. The investigation of copper ions in the water of Songhua River flowing through the chemical and living areas of Jilin City shows that the copper concentration in this area is between 0.066 ppb and

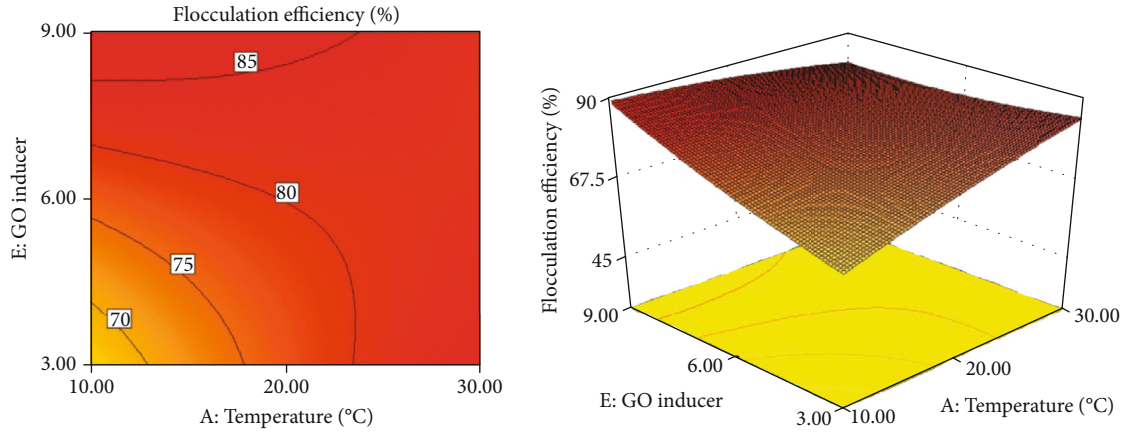


FIGURE 5: Surface responses and contour plots showing two factors affecting flocculation efficiency simultaneously.

TABLE 4: ANOVA analysis for quadratic model.

Source	Sum of squares	DF	Mean square	F value	p value
Model	36978.58	20	1848.93	9.84	<0.0001
B: pH	3752.76	1	3752.76	19.97	0.0001
C: time	1162.27	1	1162.27	6.18	0.0189
D: biofloculant	16684.25	1	16684.25	88.78	<0.0001
E: GO inducer	827.94	1	827.94	4.41	0.0446
AE	1291.13	1	1291.13	6.87	0.0138
Residual	5450.09	29	187.93		
Lack of fit	5449.06	22	247.68	1682.20	<0.0001
Pure error	1.03	7	0.15		
R-squared	0.87				
Adj R-squared	0.78				
Adeq precision	11.12				

0.159 ppb. Our sampling time is in the dry season, during which the pollutant concentration is the highest. We did not test it at other times. The copper content index of the three water samples did not exceed the Class III standard of the Surface Water Quality Standard. GO and biofloculant infrared radiation (IR) spectrum were investigated. It is found that the peaks of GO and biofloculant at 2920 cm^{-1} and 2850 cm^{-1} correspond to the characteristic absorption peaks of -OH and -C-H, respectively. The enhancement of absorption peaks at 3420 cm^{-1} and 1620 cm^{-1} is attributed to the O-H and N-H vibrations in C-OH and N-OH groups which form hydrogen bonds. Oxygen-containing groups above, especially the strong polar groups such as -OH, are abundant on the surface of the materials, which promoted the adsorption of copper. Zeta potential measurement of biofloculant with GO inducer solution indicated that the solution before flocculation of copper was negatively charged in both alkaline solution and acidic solution. Flocculation conditions of copper ion (0.2 ppm) were optimized using response surface methodology. The results showed that the highest flocculation efficiency over 80% occurred under optimistic conditions. We determined the influencing factors and the corresponding value range through the preexperiment.

At the same time, in the preexperiment, we also found that the biofloculant aid GO also has a certain adsorption effect on copper ions. We use the adsorption here because we found the phenomenon of saturation and desorption in the experiment. The linear terms for pH (B), flocculation time (C), biofloculant dosage (D), and GO inducer (E) had significant effects on flocculation efficiency (F value < 0.05), but temperature (A) had no significant effects on the flocculation efficiency. The highest flocculation efficiency which is 86.01% was achieved at pH = 5, at 1.62 h and 13.11 mg biofloculant with 13.11 mg GO as an inducer. The influence of temperature on flocculation was not significant, and the flocculation efficiency just increased by 8.39%, with temperature rising from 5 to 35°C ; however, the temperature (A) and GO inducer (E) were significant impact factors on the flocculation efficiency. As for the mechanism of flocculation, our SEM results do not fully explain the mechanism. However, we speculate that the flocculation removal of copper ions is mainly due to the adsorption and compression of double electric layers. This research has some special significance and value compared with the previous research in our laboratory, although it seems that the research methods and article structure are similar [14]. First of all, this article found a new

strain. According to our research results, the flocculant production of this strain is very competitive, and the flocculant secretion ability of this strain is much higher than that of the strain mentioned in the previous article [14, 17]. Second, another difference is that graphene oxide is no longer regarded as a pollutant in this work but developed by us as a coagulant aid. This is also because of the use of graphene oxide itself, which has produced new and different flocculation mechanisms and effects. I think this is the greatest value of this article. At the same time, the nanosized GO plays a key role in this process, which may include both adsorption and ion balance change. But we still lack further research and data.

Data Availability

The data used to support the findings of this study are included within the article.

Conflicts of Interest

The authors declare that they have no conflicts of interest.

Acknowledgments

This work was supported by the National Natural Science Foundation of China (Nos. 51708248, 51708094, and 51908241) and funded by the China Scholarship Council (No.201808220182), Doctoral Fund of Jilin Institute of Chemical Technology (No. 2018001), and Program of Science and Technology of Jilin Institute of Chemical Technology (No. 2018044). I also want to thank the support of the China Scholarship Council.

References

- [1] T. Lech and J. Sadlik, "Copper concentration in body tissues and fluids in normal subjects of southern Poland," *Biological Trace Element Research*, vol. 118, no. 1, pp. 10–15, 2007.
- [2] G. Arakeri, S. Patil, D. Ramesh, S. Hunasgi, and P. Brennan, "Evaluation of the possible role of copper ions in drinking water in the pathogenesis of oral submucous fibrosis: a pilot study," *British Journal of Oral and Maxillofacial Surgery*, vol. 52, no. 1, pp. 24–28, 2014.
- [3] Y. Li, Z. Gu, H. Liu, H. Shen, and J. Yang, "Biochemical response of the mussel *Mytilus coruscus* (Mytiloida: Mytilidae) exposed to in vivo sub-lethal copper concentrations," *Chinese Journal of Oceanology and Limnology*, vol. 30, no. 5, pp. 738–745, 2012.
- [4] A. A. Filippov and I. L. Golovanova, "Separate and joint effects of copper and zinc on the intestine carboxylase activity in vitro in freshwater teleosts," *Inland Water Biology*, vol. 3, no. 1, pp. 96–101, 2010.
- [5] L. Song, M. G. Vijver, W. J. G. M. Peijnenburg, T. S. Galloway, and C. R. Tyler, "A comparative analysis on the in vivo toxicity of copper nanoparticles in three species of freshwater fish," *Chemosphere*, vol. 139, pp. 181–189, 2015.
- [6] A. Bhatia, S. D. Singh, and A. Kumar, "Heavy metal contamination of soil, irrigation water and vegetables in peri-urban agricultural areas and markets of Delhi," *Water Environment Research*, vol. 87, no. 11, pp. 2027–2034, 2015.
- [7] Q. Liu, C. Zhao, D. Zhao, and Y. Zhang, "Screening of Bioflocculant-Producing Strains and Study on the Production and Oily Wastewater Flocculation Characteristics," in *2012 2nd International Conference on Remote Sensing, Environment and Transportation Engineering*, Nanjing, China, 2012.
- [8] P. Sun, C. Hui, N. Bai et al., "Revealing the characteristics of a novel bioflocculant and its flocculation performance in *Microcystis aeruginosa* removal," *Scientific Reports*, vol. 5, p. 17465, 2015.
- [9] L. Peng, C. Yang, G. Zeng et al., "Characterization and application of bioflocculant prepared by *Rhodococcus erythropolis* using sludge and livestock wastewater as cheap culture media," *Applied Microbiology and Biotechnology*, vol. 98, no. 15, pp. 6847–6858, 2014.
- [10] S. Zaki, M. Elkady, S. Farag, and D. Abd-El-Haleem, "Characterization and flocculation properties of a carbohydrate bio-flocculant from a newly isolated *Bacillus velezensis* 40B," *Journal of Environmental Biology*, vol. 34, no. 1, pp. 51–58, 2012.
- [11] X. Hu, Y. Yu, J. Zhou, and L. Song, "Effect of graphite precursor on oxidation degree, hydrophilicity and microstructure of graphene oxide," *Nano*, vol. 9, no. 3, p. 1450037, 2014.
- [12] X. Ji, Y. Xu, W. Zhang, L. Cui, and J. Liu, "Review of functionalization, structure and properties of graphene/polymer composite fibers," *Composites Part A: Applied Science and Manufacturing*, vol. 87, pp. 29–45, 2016.
- [13] Q.-J. Wang, H.-J. Sun, T.-J. Peng, and M.-Z. Feng, "Structure development during the cation exchange processes of graphite oxide," *Acta Physico-Chimica Sinica*, vol. 33, no. 2, pp. 413–418, 2017.
- [14] L. Xu, R. S. Ma, C. Y. Sun, and D. Z. Sun, "Enterococcus faecalis bioflocculant enhances recovery of graphene oxide from water," *Polish Journal of Environmental Studies*, vol. 27, no. 6, pp. 2811–2820, 2018.
- [15] Z. H. Yang, Y. Tao, G. M. Zeng, Y. Xiao, and E. J. Deng, "Culture medium and grading culture technics for bioflocculant production by *Paenibacillus polymyxa* GA1," *Environmental Science*, vol. 27, pp. 1444–1449, 2006.
- [16] H. Yu, B. Zhang, C. Bulin, R. Li, and R. Xing, "High-efficient synthesis of graphene oxide based on improved hummers method," *Scientific Reports*, vol. 6, no. 1, 2016.
- [17] L. Xu, M. Huo, W. Yang, D. Zhou, and H. Huo, "Klebsiella pneumoniae metabolites enhance *Microcystis aeruginosa* biomass flocculation," *Chemistry and Ecology*, vol. 32, no. 9, pp. 858–871, 2016.
- [18] Y. Wang, K. Tang, J. Weng, and R. Wang, "Research on water quality standards of drinking water sources," *China Standardization*, vol. 3, pp. 70–74, 2014.
- [19] Y. L. Pei, Z. S. Wu, X. Y. Shi, X. N. Pan, and Y. J. Qiao, "Nir assignment of magnolol by 2d-cos technology and model application huoxiangzhengqi oral liquid," *Guang pu xue yu guang pu fen xi = Guang pu*, vol. 35, no. 8, pp. 2119–2123, 2015.
- [20] G. A. Pitsevich, A. E. Malevich, E. N. Kozlovskaya et al., "Theoretical study of the C-H/O-H stretching vibrations in malonaldehyde," *Spectrochimica Acta Part A: Molecular and Biomolecular Spectroscopy*, vol. 145, pp. 384–393, 2015.
- [21] Y. Li, et al. H. A. Ma, X. Jia et al., "Electrical properties of diamond single crystals co-doped with hydrogen and boron," *CrystEngComm*, vol. 16, no. 32, p. 7547, 2014.

- [22] J. Vlček, L. Lapčík, M. Havrdová et al., "Flow induced HeLa cell detachment kinetics show that oxygen-containing functional groups in graphene oxide are potent cell adhesion enhancers," *Nanoscale*, vol. 11, no. 7, pp. 3222–3228, 2019.
- [23] Y. Li, Y. Xu, T. Zheng, and H. Wang, "Flocculation mechanism of the actinomycete *Streptomyces* sp. hsn06 on *Chlorella vulgaris*," *Bioresource Technology*, vol. 239, pp. 137–143, 2017.
- [24] O. Bajjou, A. Bakour, M. Khenfouch et al., "Charge carrier dynamics and ph effect on optical properties of anionic and cationic porphyrin–graphene oxide composites," *Journal of Electronic Materials*, vol. 47, no. 5, pp. 2897–2904, 2018.
- [25] Y. Q. He, H. B. Chen, H. Sun, X. D. Wang, and J. P. Gao, "A pH and electric responsive graphene oxide based composite hydrogel," *Advanced Materials Research*, vol. 430–432, pp. 327–330, 2012.
- [26] H. Ding, P.-M. Feng, W. Chen, and H. Lin, "Identification of bacteriophage virion proteins by the ANOVA feature selection and analysis," *Molecular BioSystems*, vol. 10, no. 8, pp. 2229–2235, 2014.
- [27] J. Dick and M. Gnewuch, "Optimal randomized changing dimension algorithms for infinite-dimensional integration on function spaces with anova-type decomposition," *Journal of Approximation Theory*, vol. 184, pp. 111–145, 2014.
- [28] A. O. J. Cramer, D. van Ravenzwaaij, D. Matzke et al., "Hidden multiplicity in exploratory multiway anova: prevalence and remedies," *Psychonomic Bulletin & Review*, vol. 23, no. 2, pp. 640–647, 2016.
- [29] A. Cuevas, M. Febrero, and R. Fraiman, "An anova test for functional data," *Computational Statistics & Data Analysis*, vol. 47, no. 1, pp. 111–122, 2004.

Review Article

Electronic Nose Technologies in Monitoring Black Tea Manufacturing Process

Tharaga Sharmilan ^{1,2} **Iresha Premarathne**² **Indika Wanniarachchi** ³ **Sandya Kumari**⁴
and Dakshika Wanniarachchi ²

¹Department of Engineering Technology, Faculty of Technology, University of Sri Jayewardenepura, Sri Lanka

²Instrument Center, Faculty of Applied Sciences, University of Sri Jayewardenepura, Sri Lanka

³Department of Physics, Faculty of Applied Sciences, University of Sri Jayewardenepura, Sri Lanka

⁴Department of Science & Technology, Uva Wellasa University, Sri Lanka

Correspondence should be addressed to Dakshika Wanniarachchi; dakshikacw@sjp.ac.lk

Received 22 November 2019; Revised 18 March 2020; Accepted 17 June 2020; Published 9 July 2020

Academic Editor: Yuan Li

Copyright © 2020 Tharaga Sharmilan et al. This is an open access article distributed under the Creative Commons Attribution License, which permits unrestricted use, distribution, and reproduction in any medium, provided the original work is properly cited.

“Tea” is a beverage which has a unique taste and aroma. The conventional method of tea manufacturing involves several stages. These are plucking, withering, rolling, fermentation, and finally firing. The quality parameters of tea (color, taste, and aroma) are developed during the fermentation stage where polyphenolic compounds are oxidized when exposed to air. Thus, controlling the fermentation stage will result in more consistent production of quality tea. The level of fermentation is often detected by humans as “first” and “second” noses as two distinct smell peaks appear during fermentation. The detection of the “second” aroma peak at the optimum fermentation is less consistent when decided by humans. Thus, an electronic nose is introduced to find the optimum level of fermentation detecting the variation in the aroma level. In this review, it is found that the systems developed are capable of detecting variation of the aroma level using an array of metal oxide semiconductor (MOS) gas sensors using different statistical and neural network techniques (SVD, 2-NM, MDM, PCA, SVM, RBF, SOM, PNN, and Recurrent Elman) successfully.

1. Introduction

Black tea is the most commonly consumed beverage in the world. The world production of black tea is about 3000 tons per year [1]. Quality parameters of tea such as liquor color, state, and mouth feel are evaluated by “tea tasters” when deciding market price for tea. A higher price for tea can only be guaranteed if the manufacturing process was conducted with the highest quality. This includes quality tea leaves plucked from plantations and proper factory conditions.

Stages in the black tea manufacturing process are plucking, withering, rolling, fermentation, firing, and packaging. The plucked tea leaves are dried to remove moisture content during the withering stage [2] and fed into the rollers. Tea particles after the rolling step are loaded to a rotorvane to

separate smaller tea particles from larger pieces. The first set of smaller tea particles is called the “first dhool” and directly sent for fermentation. Then, larger particles undergo the rolling step again and are loaded back to the rotorvane to separate. The second set of smaller particles is called the “second dhool,” and the tea particles from a third repeat of this cycle are called the “third dhool” [3]. Then, these classified leaves are laid on a tea bed to expose to oxygen during the fermentation process. In the presence of oxygen, chemical constituents in tea leaves react and produce polyphenol compounds and aromatic compounds [4]. Therefore, quality characteristics such as color, aroma, and taste of the tea are produced in this stage. Theaflavin (TF) and thearubigin (TR) are the main oxidized chemical compounds responsible for the brightness and briskness of the tea infusion while

increasing mouth feel, color, and body of the tea infusion [5]. After that, fermented tea leaves are sent to the dryers. Then, dried leaves are sorted and packaged.

The fermentation stage is the most important among other stages [6–8] because final tea quality characteristics are developed at this stage. Fermentation time directly relates to the chemical changes during the fermentation process. Therefore, fermentation time has a significant impact on the final tea quality [9]. Since over and low fermentation leads to lack of final tea quality, optimum fermentation time should be identified to maintain high quality of black tea.

The optimum fermentation time is found in almost all tea factories based on the decision of the human detecting aroma and color changes of tea leaves. These decisions are very subjective. In general, it is accepted that the best quality tea will have a TF/TR ratio 1 : 10 [10] measured using spectrometric methods, and it was used for many decades as the main quality controlling parameter [11, 12]. However, this method is not practical to analyze the fermentation level in real time due to time-consuming chemical analysis.

Therefore, development of a system which can detect the optimum fermentation level without use of chemicals and minimum human intervention is needed. Innovative technologies were developed by several research groups using an electronic eye method which analyzes images of tea leaves during fermentation to notice color changes [3, 12–17]. The second method involves an electronic nose system which detects aroma levels of tea particles during fermentation [18–32]. Recent studies focused on the combination of electronic eye and electronic nose methods [32–35] which are aimed at minimizing human intervention of observing color changes and smelling of tea particles. However, adopting these developed methods into the real factory condition is challenging as most of the studies are conducted in a laboratory scale [36]. There are very few studies conducted under factory conditions [26, 27].

Recently, the use of the e-nose technique for tea quality evaluation has increased. Therefore, a comparison of current systems and identification of drawbacks are important in developing novel technologies. Therefore, this paper will focus on the comparison of methods developed for analysis of tea aroma during the fermentation stage using “e-nose” systems under laboratory conditions and factory scale. In this paper, a brief discussion on chemical compounds detected in tea aroma followed by conventional methods used for detection is also discussed. Then, existing e-nose technologies and statistical algorithms which were used in data analysis will be discussed.

2. Tea Quality Evaluation

2.1. Aroma Compounds Released during Fermentation Process. When developing an e-nose system, it is important to identify different chemical compounds present in tea aroma. Enzymes catalyze oxidation of fatty acid, phenylalanine, terpenoids, and carotenoid compounds in tea leaves when exposed to air [37–39]. Oxidation of fatty acids results in grassy smelling compounds such as hexanol and hexanal (alcohols and aldehydes containing 6–9 carbon

atoms) [37, 38]. The extent of volatile compounds present depends on the climatic conditions as activity of lipoxygenase (LOX) and alcohol dehydrogenase enzymes is influenced by the temperature of the processing time. In fully oxidized tea and semioxidized tea, geraniol, linalool, and linalool oxides are major contributors to the overall aroma profile [37, 38]. These floral and sweet smelling compounds are derived by geranyl pyrophosphate (GPP) which is degraded by geraniol synthase and linalool oxidase enzymes. Phenylethanol (flowery), phenylacetaldehyde (honey), and benzyl alcohol (sweet, fruity) are another group of compounds derived from phenylalanine. These compounds also contribute to the floral smell in aroma profile. Oxidation of β -carotenoids results in woody smell compound β -ionone and damascone. These contribute to the aroma compounds with C9–C13 aroma. The variation of carotenoid content in tea leaves subject to climatic, clone variety, and processing conditions results in variations in aroma profile. It was reported that high carotene content yields enhanced volatile flavor compounds [40, 41]. There are some biochemical compounds mainly responsible for the tea aroma and flavor, such as linalool, geraniol, phenyl acetaldehyde, benzaldehyde, methyl salicylate, and hexanal [37, 38, 40, 42] which are mostly aldehydes, ketones, esters, hydrocarbons, and furans [15].

In most of the factories, fermentation is continued until appearance of two distinct smell peaks with time. These are commonly denoted as “first nose” and “second nose” which can be identified only by highly trained factory personnel [10]. The first nose corresponds to a rawer, grassy smell of tea leaves while a fruity smell of tea leaves is prominent when tea particles turned to a more copper color. Table 1 indicates that prominent compounds correspond to each smell peak and their biochemical origin.

Therefore, when developing the “e-nose” system, it is important to choose sensors which are responsive to aldehydes and ketones with excellent sensitivities to detect subtle changes such as “first nose” and “second nose” as practiced in the factory.

2.2. Conventional Methods Used to Analyze Tea Aroma. Identification of aroma compounds present in tea is done with gas chromatography mass spectrometry (GCMS) and their characteristics (floral, grassy, sweet, etc.) using Gas Chromatography-Olfactometry (GC-O) [37, 38, 40–42]. GCMS has high sensitivity, and over 70 different chemical compounds present in tea aroma were identified in different studies [10, 37, 38, 40–56]. However, GCMS instruments are not found in almost all tea factories due to high price of the instrument. Since oxidation will continue on the way from the factory to the lab, GCMS has limitations to adapt to regular quality checking in the production line. Nowadays, these conventional techniques are used to compare the results of electronic devices when calibration is required.

2.3. Electronic Nose Technologies. Humans can detect different odors by special receptors located in the nasal cavity. These are olfactory cells located in the epithelium. When a specific odor is dissolved in mucus, chemical compounds will

TABLE 1: Some prominent compounds present in tea aroma [37, 38, 40].

	Compound	Aroma type	Biosynthetic pathway
(1)	(Z)-3-Hexenol	Green	Lipids
(2)	Hexanal	Grassy, green	Lipid
(3)	(Z)-4-Heptanal	Hay-like	Lipid
(4)	(E)-2-Hexenal	Green	Lipid
(5)	Hexanoic acid	Sweaty, green	Lipid
(6)	β -Ionone	Woody, violet	Carotenoids
(7)	α -Ionone	Woody hay-like	Carotenoids
(8)	Geranylacetone	Floral, hay-like	Carotenoids
(9)	cis-Jasmone	Floral, jasmin-like	Lipids
(10)	Methyljasmonate	Floral	Lipids
(11)	(E)-Geraniol	Rose-like	Glycosides
(12)	Linalool	Floral	Carotenoids, glycosides
(13)	Linalool oxide I II III IV	Earthy, floral	Glycosides
(14)	Methyl salicylate	Mint	Glycosides
(15)	β -Damascenone	Fruity, apple-like	Carotenoids, glycosides
(16)	Benzyl alcohol	Burning taste, faint aromatic	Glycosides
(17)	2-Phenyl ethanol	Honey-like	Glycosides
(18)	4-Hydroxy-2,5-dimethyl-3(2H)-furanone	Caramel-like	Glycosides
(19)	2-Ethyl-3,5-dimethylpyrazine	Nutty	Maillard reaction
(20)	5-Ethyl-2,3-dimethylpyrazine	Nutty	Maillard reaction
(21)	2-Acetyl-2-thiazoline	Popcorn-like	Maillard reaction
(22)	Phenyl-acetaldehyde	Honey-like	Maillard reaction

bind with specific proteins in the receptor cells. The strength of binding differs from chemical to chemical thus creating a unique pattern of a signal which is sent to the brain as an electrical response. The brain identifies the particular order recalling memory of a similar smell [57].

Inspired by nature, electronic nose devices are fabricated to identify a particular aroma profile. Such a system consists of an array of gas sensors, where a combined response is evaluated as the aroma profile. There is a significant level of aroma produced during tea manufacturing which can be smelled even along the roadside of the factory. Therefore, as a quality controlling device, “e-nose” systems were developed by many research groups. The most comprehensive contribution for the study of the fermentation stage in black tea manufacturing is given by Ghosh et al. where they have developed e-nose, e-vision, and electronic tongue techniques to monitor the tea quality [19, 25, 58]. Then, research by Tozlu and coworkers has presented adapting e-nose technology to the factory level, real-time monitoring [26, 27]. Furthermore, use of e-nose systems to monitor the fermentation stage has also been conducted using commercially available e-nose systems recently [59].

A typical “e-nose” system contains an array of different gas sensors and vacuum pumps to collect aroma with programmable sequence control [27, 31]. The sensor array is placed in an airtight chamber which has inlets to introduce either the gas to be analyzed or the reference gas and an outlet. Most of the studies used metal oxide semiconductor (MOS) sensors for the multiple sensor arrays to classify the tea aroma. MOS are characterized by high sensitivity and

mechanical robustness and can be continuously operated over a long time period [60]. The sensing element is based on tin dioxide (SnO_2). It has low conductivity in clean air. In the presence of detectable vapor, the sensor conductivity increases, depending on the concentration of odor molecules in the vapor. The sensor output is processed by a signal conditioning circuit for signal amplification, buffering, and signal conversion [36]. Sensor signals are converted into electrical signals, and data are interpreted using a developed algorithm. Table 2 indicates the summary of different gas sensors used in “e-nose” systems which are used in monitoring black tea fermentation.

Most “e-nose” systems contained several gas sensors which detect alcohols, Volatile Organic Compounds (VOC), liquefied petroleum (LP) gas, carbon monoxide (CO), and ammonia. In these systems, the highest response towards tea aroma was indicated by TGS 832, 823, and 2620 sensors which are commonly used to detect organic solvent gases [19, 22, 25, 29, 31]. This result agrees well with the chemical composition of tea aroma as listed in Table 1. But other types of sensors are also responding to the tea aroma as well. Therefore, the responses from multiple sensors are analyzed using an appropriate statistical method for further evaluation. Apart from this, custom-made devices [19, 27, 61] are also used to monitor the fermentation process [59]. Furthermore, e-nose systems have been used for classification of tea varieties as well [62].

2.4. Sniffing Process. The e-nose systems operate similar to breathing where an automated set of internal operations are

TABLE 2: Summary of different gas sensors used in the e-nose system.

Sensor Id	Main compound	References
MQ 7	CO, H ₂ , LPG, CH ₄ , alcohol	[18]
MQ 3	Alcohol, benzene, hexane, LPG, CO, CH ₄	
MQ 4	LPG, CH ₄ , H ₂ , CO, alcohol, smoke	
MQ 6	LPG, H ₂ , CH ₄ , CO, alcohol	
MQ 9	LPG, CO, CH ₄	
MQ 8	H ₂ , alcohol, CO, CH ₄	
TGS 832	R-12, R-22, R-134 a	[22, 25, 29, 31, 63]
TGS 823	Methane, CO, isobutane, n-hexane, benzene, ethanol, acetone	[22, 25, 29, 63, 64]
TGS 831	R-21, R-22	[25, 31, 63]
TGS 816	CO, CH ₄ , ethanol, propane, iso-butane, H ₂	[25, 63, 64]
TGS 2600	Methane, CO, isobutane, ethanol, H ₂	[22, 25, 29, 31, 63]
TGS 2610	Ethanol, H ₂ , isobutane, methane, propane	[22, 25, 29, 31, 63]
TGS 2611	Ethanol, H ₂ , isobutane, methane	[22, 25, 29, 31, 63]
TGS 2620	CH ₄ , CO, isobutane, H ₂ , ethanol	[25, 28]

conducted during a test cycle, namely, (1) sensor warming up, (2) sampling, (3) purging, and (4) cleaning the sensor chamber before starting the next test cycle. At the first stage, sensors are warming up for some time. It optimizes the saturation of the sensor head space. Therefore, adequate sensor response can be obtained for the sampling process. The sampling process is conducted by exposing sensor array to a constant flow of volatile compounds through the pipe. During the cleaning operation, the sensor chamber is cleared with a blow of fresh air. Therefore, sensor heads go back to the baseline values. Typical sniffing cycle duration is 3-5 minutes in most of the e-nose systems developed so far. Figure 1 indicates the response of a typical sniffing cycle.

2.5. Validating E-Nose Response for Tea Fermentation. Quality checking using an e-nose system was done in using tea infusion preparation [30], sniffing aroma of fresh tea leaf particles placed in a container [64], or directly sniffing aroma from the production line as fermentation progresses [26, 27]. In these studies, e-nose response is validated or compared with the response obtained from human, or measuring TF/TR ratio, colorimetric methods, and good correlation to sensor response to pure aroma compounds were obtained in most studies [27, 36]. A recent study has introduced a new fermentation band system to function with the e-nose system [27]. A simple colorimetric method is frequently used in tea factories to observe the progress of fermentation. There two distinct bands are observed which later correspond to the “first” and “second nose” in aroma. The studies conducted by Bhattacharyya and coworkers have clearly recorded a similar trend with the e-nose systems they developed [31].

2.6. Sensitivity Evaluation of E-Nose Sensors. Metal oxide sensors are subjected to the different chemicals that are present in black tea to evaluate the sensitivity of the sensors. A particular amount of each chemical is taken during the sensor evaluation. Then, $\Delta R_s/R_s$ values of the sensors, where ΔR_s is the change in resistance of the sensor and R_s is the base resistance value of the respective sensor, are calculated

[36]. The base resistance value may interfere if aroma is not removed properly from the sensor chamber. Therefore, reference gas is introduced to the chamber before the next sniffing cycle. Common reference gases used are oxygen [27], nitrogen [65], and fresh air [31].

3. E-Nose Data Analysis

PC-based data acquisition and automated operation were controlled by specially designed software using LabVIEW [27, 30, 64]. In this case, minimum human intervention is needed to use a graphical user interface, yet basic computer knowledge is needed to handle the instrument.

3.1. Data Processing. In most of the e-nose devices, sensor raw response is recorded with time. There are many factors such as efficiency of the pumping system, noisy gas sensor recordings, and retention of sample aroma after the cleaning stage that influence the sensor response. Therefore, raw data are pretreated using single value decomposition (SVD) or using a difference model where change in sensor resistance with respect to a reference air is calculated and then entire dR data set is normalized by maximum value to set range to (0-1) [30]. In another study, standard normal variate (SNV) is used for data preprocessing with commercial devices [66]. Furthermore, feature extraction methods are also used in e-nose signal preprocessing [65].

3.2. Methodologies Used in Finding the Optimum Fermentation Time. Attempts to find the optimum fermentation time for black tea processing were conducted using unsupervised and supervised pattern recognition methods. Tea classification from e-nose data is complex as the emission of volatile compounds from tea leaves varies with time. Singular Value Decomposition (SVD) technique was used to analyze the peaks of sensor outputs [67]. In some studies, data were processed using Principal Component Analysis (PCA) and Fuzzy C Means (FCM) algorithm [61], and then, 2-Norm Method (2-NM) and Mahalanobis distance method

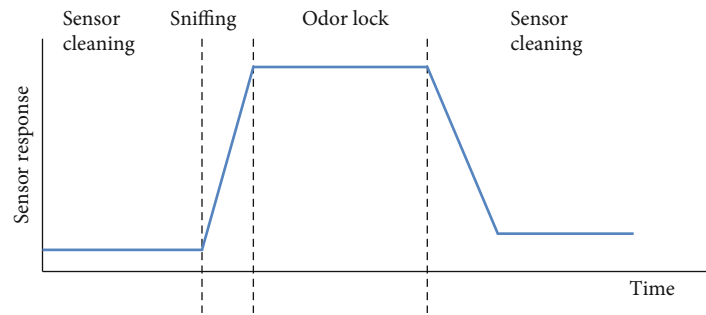


FIGURE 1: A sample sniffing cycle.

(MDM) have been used to analyze data [67]. Linear Discriminant Analysis (LDA), Back Propagation Multilayer Perceptron (BP-MLP), Bayes, and KNN-3 methods were used for the odor classification; the self-organizing map (SOM) method along with Radial Basis Function (RBF) network and Probabilistic Neural Network (PNN) classifier [27, 30, 67] were also used for the odor classification where PNN produced best results [67]. MATLAB software was used to perform these techniques. In [27], the KNN-3 method has given the best accuracy with 74.19% classification performance achieved in [28]. Using FCM and SOM feature extraction techniques along with the RBF neural network, it has achieved 100% correct classification for five different tea samples, each of which has different qualities [30].

When analyzing e-nose data, a scoring method based on 2-NM and MDM has shown similar behavior to the colorimetric variation of tea during fermentation [31]. However, when considering updating the tea fermentation data, the Radial Basis Function (RBF) neural network method was used to incorporate new data acquired while keeping the previous data [29]. The data analysis component was further developed by Battacharya and coworkers so that the optimum fermentation level can be predicted with the initial set of data collected while fermentation is ongoing. This prediction of optimum fermentation time is useful to maintain constant quality of tea during production.

However, there are many challenges when adopting an e-nose system to monitor the fermentation process in real time. The work of Tozlu and Okumus has developed an e-nose system so that fermentation can be monitored at the production line [27]. A different approach was introduced by Sharma and coworkers where eight quartz crystal microbalance (QCM) sensors were used in construction of the e-nose system. The sensors are coated with different glucose derivatives with polyethylene glycol (PEG) with varying molecular weights. A comparison of QCM results with traditional colorimetric methods indicated good agreement suggesting it as a promising method to detect the optimum fermentation level [68].

4. Conclusions

Aroma, color, and taste are the most common testing quality parameters of tea. These quality parameters are highly dependent on the fermentation stage in the black tea manufacturing process. Therefore, finding the optimum

fermentation time is crucial to maintain consistent high-quality tea. In this review, use of e-nose systems to monitor the fermentation stage in black tea manufacturing is discussed. The e-nose systems consist of an array of gas sensors which are commercially used to monitor alcohol, methane, hydrogen, LPG, VOC, ammonia, carbon monoxide, and smoke. The combined response of these sensors is used in classification, quantification, and prediction of the level of aroma during the fermentation stage. Here, both unsupervised and supervised classification techniques are used to distinguish aroma profile generated during different time intervals. The results obtained in e-nose systems developed so far are capable of identifying the “first” and “second” smell peaks with the aid of a statistical method. However, the current systems developed require insight into the following perspectives for further development.

- (i) In most systems, the sample is isolated from the production environment when aroma levels are detected. However, this is not practical when adapting to the real production line. Care should be taken to minimize the influence from the adjacent fermentation beds when adapting to factory conditions
- (ii) Most studies have not addressed which level of dhool is used. Depending on the dhool number, fermentation duration is set in such that dhool 1 has the longest fermentation period and big bulk or dhool 4 will have the shortest fermentation time. The future system should be able to distinguish the aroma level based on the dhool number as well
- (iii) All studies have been conducted under controlled weather conditions. However, in real factory conditions, weather and temperatures are dynamic and even show 10-15 degrees centigrade difference between morning batches to noon batches. Thus, statistical analysis should incorporate correlations with humidity and temperature data

Conflicts of Interest

The authors declare that there is no conflict of interest regarding the publication of this paper.

Acknowledgments

The authors would like to thank the National Research Council of Sri Lanka (NRC 17-038) and University of Sri Jayewardenepura, Sri Lanka (ASP/01/RE/SCI/2019/28), for their funding support.

References

- [1] K. Chang, *World tea economy: trends and opportunities*, pp. 1–14, 2016.
- [2] P. O. Owuor and M. Obanda, “Clonal variations in the response of hard physically withered leaf to rehydration following long chemical wither durations,” *International Journal of Tea Science*, vol. 13, no. 1-2, 2016.
- [3] S. Saranka, T. Kartheeswaran, D. D. C. Wanniarachchi, and W. Wanniarachchi, “Monitoring fermentation of black tea with image processing techniques,” *Proc. Tech. Sess.*, vol. 32, pp. 31–37, 2016.
- [4] L. P. Bhuyan, S. Sabhapondit, B. D. Baruah, C. Bordoloi, R. Gogoi, and P. Bhattacharyya, “Polyphenolic compounds and antioxidant activity of CTC black tea of North-East India,” *Food Chemistry*, vol. 141, no. 4, pp. 3744–3751, 2013.
- [5] M. Obanda, P. Okinda Owuor, and R. Mang’oka, “Changes in the chemical and sensory quality parameters of black tea due to variations of fermentation time and temperature,” *Food Chemistry*, vol. 75, no. 4, pp. 395–404, 2001.
- [6] W. A. J. M. De Costa, A. J. Mohotti, and M. A. Wijeratne, “Ecophysiology of tea,” *Brazilian Journal of Plant Physiology*, vol. 19, no. 4, pp. 299–332, 2007.
- [7] L. Emdadi, B. Nasernajad, and S. T. Shokrgozar, “Optimization of withering time and fermentation conditions during the manufacture of black tea using a response surface methodology,” *Scientia Iranica*, vol. 16, no. 1, 2009.
- [8] P. Tang, D.-Y. Shen, Y.-Q. Xu, X.-C. Zhang, J. Shi, and J.-F. Yin, “Effect of fermentation conditions and plucking standards of tea leaves on the chemical components and sensory quality of fermented juice,” *Journal of Chemistry*, vol. 2018, Article ID 4312875, 7 pages, 2018.
- [9] T. Muthumani and R. S. S. Kumar, “Influence of fermentation time on the development of compounds responsible for quality in black tea,” *Food Chemistry*, vol. 101, no. 1, pp. 98–102, 2007.
- [10] K. R. Jolvis Pou, “Fermentation: the key step in the processing of black tea,” *Journal of Biosystems Engineering*, vol. 41, no. 2, pp. 85–92, 2016.
- [11] E. A. H. Roberts and R. F. Smith, “Spectrophotometric measurements of theaflavins and thearubigins in black tea liquors in assessments of quality in teas,” *Analyst*, vol. 86, no. 1019, p. 94, 1961.
- [12] S. Borah and M. Bhuyan, “Quality indexing by machine vision during fermentation in black tea manufacturing,” in *Proceedings Volume 5132, Sixth International Conference on Quality Control by Artificial Vision*, Gatlinburg, TE, United States, 2003.
- [13] S. Borah, *Machine vision for tea quality monitoring with special emphasis on fermentation and grading emphasis on fermentation and grading*, p. 178, 2005.
- [14] G. Singh and N. Kamal, “Machine vision system for tea quality determination -tea quality index (TQI),” *IOSR Journal of Engineering*, vol. 3, no. 7, pp. 46–50, 2013.
- [15] Y.-Q. Yang, H.-X. Yin, H.-B. Yuan, Y.-W. Jiang, C.-W. Dong, and Y.-L. Deng, “Characterization of the volatile components in green tea by IRAE-HS-SPME/GC-MS combined with multivariate analysis,” *PLoS One*, vol. 13, no. 3, article e0193393, pp. 1–19, 2018.
- [16] G. S. Gill, A. Kumar, and R. Agarwal, “Monitoring and grading of tea by computer vision - a review,” *Journal of Food Engineering*, vol. 106, no. 1, pp. 13–19, 2011.
- [17] S. Borah, M. Bhuyan, and H. Saikia, *ANN based colour detection in tea fermentation*, 2002.
- [18] J. B. Lazaro, A. Ballado, F. P. F. Bautista, J. K. B. So, and J. M. J. Villegas, “Chemometric data analysis for black tea fermentation using principal component analysis,” in *AIP Conference Proceedings*, pp. 1–6, Location- Bandung, Indonesia, December 2018.
- [19] S. Ghosh, N. Bhattacharyya, B. Tudu, and R. Bandyopadhyay, “Electronic nose for on-line quality evaluation of black tea using incremental SOM techniques,” in *2015 2nd International Symposium on Physics and Technology of Sensors (ISPTS)*, Pune, India, March 2015.
- [20] Z. Qin, X. Pang, D. Chen, H. Cheng, X. Hu, and J. Wu, “Evaluation of Chinese tea by the electronic nose and gas chromatography-mass spectrometry: correlation with sensory properties and classification according to grade level,” *Food Research International*, vol. 53, no. 2, pp. 864–874, 2013.
- [21] H. Jiang and Q. Chen, “Development of electronic nose and near infrared spectroscopy analysis techniques to monitor the critical time in SSF process of feed protein,” *Sensors*, vol. 14, no. 10, pp. 19441–19456, 2014.
- [22] B. T. Ghosh, N. Bhattacharyya, and R. Bandyopadhyay, “A recurrent Elman network in conjunction with an electronic nose for fast prediction of optimum fermentation time of black tea,” *Neural Computing and Applications*, vol. 31, Supplement 2, pp. 1165–1171, 2019.
- [23] H. Li, B. Zhang, W. Hu, Y. Liu, C. Dong, and Q. Chen, “Monitoring black tea fermentation using a colorimetric sensor array-based artificial olfaction system,” *Journal of Food Processing and Preservation*, vol. 42, no. 1, article e13348, 2018.
- [24] H. Yu, Y. Wang, and J. Wang, “Identification of tea storage times by linear discrimination analysis and back-propagation neural network techniques based on the eigenvalues of principal components analysis of E-nose sensor signals,” *Sensors*, vol. 9, no. 10, pp. 8073–8082, 2009.
- [25] M. Sharma, D. Ghosh, and N. Bhattacharya, “Electronic nose – a new way for predicting the optimum point of fermentation of black tea,” *International Journal of Engineering and Science Invention*, vol. 2, no. 3, pp. 56–60, 2013.
- [26] B. Tozlu, H. İ. Okumuş, C. Şimşek, and Ö. Aydemir, “On-line monitoring of theaflavins and thearubigins ratio in Turkish black tea using electronic nose,” *International Journal of Scientific Engineering and Applied Science*, vol. 7, no. 5, pp. 2305–8269, 2015.
- [27] B. H. Tozlu and H. İ. Okumuş, “A new approach to automation of black tea fermentation process with electronic nose,” *Automatika*, vol. 59, no. 3-4, pp. 373–381, 2018.
- [28] B. Tozlu, H. I. Okumus, and C. Simsek, “Online quality classifying with electronic nose for black tea production,” *International Journal of Academic Research*, vol. 6, no. 4, 2014.
- [29] B. Tudu, A. Jana, A. Metla, D. Ghosh, N. Bhattacharyya, and R. Bandyopadhyay, “Electronic nose for black tea quality

- evaluation by an incremental RBF network,” *Sensors and Actuators B: Chemical*, vol. 138, no. 1, pp. 90–95, 2009.
- [30] R. Dutta, K. R. Kashwan, M. Bhuyan, E. L. Hines, and J. W. Gardner, “Electronic nose based tea quality standardization,” *Neural Networks*, vol. 16, no. 5–6, pp. 847–853, 2003.
- [31] N. Bhattacharyya, S. Seth, B. Tudu et al., “Monitoring of black tea fermentation process using electronic nose,” *Journal of Food Engineering*, vol. 80, no. 4, pp. 1146–1156, 2007.
- [32] S. Buratti, A. Casiraghi, P. Minghetti, and G. Giovanelli, “The joint use of electronic nose and electronic tongue for the evaluation of the sensorial properties of green and black tea infusions as related to their chemical composition,” *Food and Nutrition Sciences*, vol. 4, no. 6, pp. 605–615, 2013.
- [33] M. Xu, J. Wang, and S. Gu, “Rapid identification of tea quality by E-nose and computer vision combining with a synergetic data fusion strategy,” *Journal of Food Engineering*, vol. 241, pp. 10–17, 2019.
- [34] R. Banerjee, P. Chattopadhyay, R. Rani, B. Tudu, R. Bandyopadhyay, and N. Bhattacharyya, “Discrimination of black tea using electronic nose and electronic tongue: a Bayesian classifier approach,” in *2011 International Conference on Recent Trends in Information Systems*, Kolkata, India, December 2011.
- [35] R. Banerjee, B. Tudu, L. Shaw, A. Jana, N. Bhattacharyya, and R. Bandyopadhyay, “Instrumental testing of tea by combining the responses of electronic nose and tongue,” *Journal of Food Engineering*, vol. 110, no. 3, pp. 356–363, 2012.
- [36] N. Bhattacharyya, R. Bandyopadhyay, M. Bhuyan, B. Tudu, D. Ghosh, and A. Jana, “Electronic nose for black tea classification and correlation of measurements with “tea taster” marks,” *IEEE Transactions on Instrumentation and Measurement*, vol. 57, no. 7, pp. 1313–1321, 2008.
- [37] Z. Yang, S. Baldermann, and N. Watanabe, “Recent studies of the volatile compounds in tea,” *Food Research International*, vol. 53, no. 2, pp. 585–599, 2013.
- [38] X. Q. Zheng, Q. S. Li, L. P. Xiang, and Y. R. Liang, “Recent advances in volatiles of teas,” *Molecules*, vol. 21, no. 3, p. 338, 2016.
- [39] H. Co and G. W. Sanderson, “Biochemistry of tea fermentation: conversion of amino acids to black tea aroma constituents,” *Journal of Food Science*, vol. 35, no. 2, pp. 160–164, 1970.
- [40] C.-T. Ho, X. Zheng, and S. Li, “Tea aroma formation,” *Food Science and Human Wellness*, vol. 4, no. 1, pp. 9–27, 2015.
- [41] X. Chen, D. Chen, H. Jiang et al., “Aroma characterization of Hanzhong black tea (*Camellia sinensis*)_ using solid phase extraction coupled with gas chromatography -mass spectrometry and olfactometry and sensory analysis,” *Food Chemistry*, vol. 274, pp. 130–136, 2019.
- [42] V. Sai, P. Chaturvedula, and I. Prakash, “The aroma, taste, color and bioactive constituents of tea,” *Journal of Medicinal Plants Research*, vol. 5, no. 11, pp. 2110–2124, 2011.
- [43] P. V. S. Kumar, S. Basheer, R. Ravi, and M. S. Thakur, “Comparative assessment of tea quality by various analytical and sensory methods with emphasis on tea polyphenols,” *Journal of Food Science and Technology*, vol. 48, no. 4, pp. 440–446, 2011.
- [44] N. Togari, A. Kobayashi, and T. Aishima, “Pattern recognition applied to gas chromatographic profiles of volatile components in three tea categories,” *Food Research International*, vol. 28, no. 5, pp. 495–502, 1995.
- [45] L. Cao, X. Guo, G. Liu et al., “A comparative analysis for the volatile compounds of various Chinese dark teas using combinatory metabolomics and fungal solid-state fermentation,” *Journal of Food and Drug Analysis*, vol. 26, no. 1, pp. 112–123, 2018.
- [46] S. Baldermann, Z. Yang, T. Katsuno et al., “Discrimination of green, oolong, and black teas by GC-MS analysis of characteristic volatile flavor compounds,” *American Journal of Analytical Chemistry*, vol. 5, no. 9, pp. 620–632, 2014.
- [47] P. Pripdeevech, S. Moonggoot, S. Popluechai, and E. Chukeatirote, “Analysis of volatile constituents of fermented tea with *Bacillus subtilis* by SPME-GC-MS,” *Chiang Mai Journal of Science*, vol. 41, no. 2, pp. 395–402, 2014.
- [48] E. Sheibani, S. E. Duncan, D. D. Kuhn, A. M. Dietrich, J. J. Newkirk, and S. F. O’Keefe, “Changes in flavor volatile composition of oolong tea after panning during tea processing,” *Food Science & Nutrition*, vol. 4, no. 3, pp. 456–468, 2016.
- [49] S. K. Chandini, L. J. Rao, M. K. Gowthaman, D. J. Haware, and R. Subramanian, “Enzymatic treatment to improve the quality of black tea extracts,” *Food Chemistry*, vol. 127, no. 3, pp. 1039–1045, 2011.
- [50] A. Laddi, S. Sharma, A. Kumar, and N. R. Prakash, “Influence on color attributes of freshly brewed tea with time due to variations in temperature conditions,” *International Journal of Computer Applications*, vol. 34, no. 7, pp. 7–9, 2011.
- [51] A. E. Thea, M. A. Lloret, L. A. Brumovsky, and M. E. Schmalko, “Differences in quality parameters between types of commercial tea from Argentina,” *International Journal of Food Studies*, vol. 2, pp. 168–178, 2012.
- [52] D. L. Whitehead and C. M. Temple, “Rapid method for measuring thearubigins and theaflavins in black tea using C18 sorbent cartridges,” *Journal of the Science of Food and Agriculture*, vol. 58, no. 1, pp. 149–152, 1992.
- [53] T. Samanta, V. Cheeni, S. Das, A. B. Roy, B. C. Ghosh, and A. Mitra, “Assessing biochemical changes during standardization of fermentation time and temperature for manufacturing quality black tea,” *Journal of Food Science and Technology*, vol. 52, no. 4, pp. 2387–2393, 2015.
- [54] S.-D. Lv, Y. S. Wu, Y. Z. Song et al., “Multivariate analysis based on GC-MS fingerprint and volatile composition for the quality evaluation of Pu-Erh green tea,” *Food Analytical Methods*, vol. 8, no. 2, pp. 321–333, 2015.
- [55] A. Y. Yashin, B. V. Nemzer, E. Combet, and Y. I. Yashin, “Determination of the chemical composition of tea by chromatographic methods: a review,” *Journal of Food Research*, vol. 4, no. 3, p. 56, 2015.
- [56] H. Q. Tuan, N. D. Thinh, and N. T. Minh Tu, “Composition analysis of OTD and CTC black teas (*Camellia sinensis*) for the volatile profile differentiation by HS-SPME/GC-MS,” *Vietnam Journal of Science and Technology*, vol. 54, no. 4, p. 483, 2016.
- [57] W. Hu, L. Wan, Y. Jian et al., “Electronic noses: from advanced materials to sensors aided with data processing,” *Advanced Materials Technologies*, vol. 4, no. 2, article 1800488, 2018.
- [58] A. Akuli, A. Pal, G. Bej et al., “A machine vision system for estimation of theaflavins and thearubigins in orthodox black tea,” *International Journal of Smart Sensing and Intelligent Systems*, vol. 9, no. 2, pp. 709–731, 2016.
- [59] N. Manigandan, V. A. S. And, and P. Surendar, “Handheld electronic nose (HEN) for detection of optimum fermentation time during tea manufacture and assessment of tea quality,”

- International Journal of Advanced Research*, vol. 7, no. 7, pp. 697–702, 2019.
- [60] Z. Yunusa, *Sensors & transducers gas sensors: a review*, 2014.
- [61] R. Dutta, E. L. Hines, J. W. Gardner, K. R. Kashwan, and M. Bhuyan, “Tea quality prediction using a tin oxide-based electronic nose: an artificial intelligence approach,” *Sensors and Actuators B: Chemical*, vol. 94, no. 2, pp. 228–237, 2003.
- [62] S. N. Hidayat, K. Triyana, I. Fauzan et al., “The electronic nose coupled with chemometric tools for discriminating the quality of black tea samples in situ,” *Chemosensors*, vol. 7, no. 3, p. 29, 2019.
- [63] A. Ghosh, A. K. Bag, P. Sharma et al., “Monitoring the fermentation process and detection of optimum fermentation time of black tea using an electronic tongue,” *IEEE Sensors Journal*, vol. 15, no. 11, pp. 6255–6262, 2015.
- [64] N. Bhattacharyya, S. Seth, B. Tudu et al., “Detection of optimum fermentation time for black tea manufacturing using electronic nose,” *Sensors and Actuators B: Chemical*, vol. 122, no. 2, pp. 627–634, 2007.
- [65] R. Zhi, L. Zhao, and D. Zhang, “A framework for the multi-level fusion of electronic nose and electronic tongue for tea quality assessment,” *Sensors*, vol. 17, no. 5, p. 1007, 2017.
- [66] S. Kumar, P. C. Panchariya, P. B. Prasad, and A. L. Sharma, “Non-destructive classification of Assam black tea using ultra-fast gas chromatography (UFGC) coupled with soft independent modeling of class analogy (SIMCA),” *Sensors and Transducers*, vol. 186, no. 3, pp. 2014–2015, 2015.
- [67] N. Bhattacharya, B. Tudu, A. Jana, D. Ghosh, R. Bandhopadhyaya, and M. Bhuyan, “Preemptive identification of optimum fermentation time for black tea using electronic nose,” *Sensors and Actuators B: Chemical*, vol. 131, no. 1, pp. 110–116, 2008.
- [68] P. Sharma, A. Ghosh, B. Tudu et al., “Monitoring the fermentation process of black tea using QCM sensor based electronic nose,” *Sensors and Actuators B: Chemical*, vol. 219, pp. 146–157, 2015.

Research Article

A Model with Leaf Area Index and Trunk Diameter for LoRaWAN Radio Propagation in Eastern China Mixed Forest

Yin Wu¹, Genwei Guo¹, Guiyun Tian², and Wenbo Liu³

¹College of Information Science and Technology, Nanjing Forestry University, No. 159, LongPan Road, Nanjing 210037, China

²School of Engineering, Newcastle University, Newcastle upon Tyne NE1 7RU, UK

³College of Automation, Nanjing University of Aeronautics and Astronautics, No. 29, JiangJun Avenue, Nanjing 211106, China

Correspondence should be addressed to Yin Wu; wuyin@njfu.edu.cn

Received 18 September 2019; Revised 26 May 2020; Accepted 3 June 2020; Published 22 June 2020

Academic Editor: Yuan Li

Copyright © 2020 Yin Wu et al. This is an open access article distributed under the Creative Commons Attribution License, which permits unrestricted use, distribution, and reproduction in any medium, provided the original work is properly cited.

Internet of Things (IoT) is a very promising technology in forest engineering, especially for the environment and plant growth monitoring. LoRa Wide Area Network (LoRaWAN) is a prevailing choice for the Forestry IoT owing to its low-power and long-range ability. Real-world deployment and network optimization require accurate path-loss modeling, so the LoRaWAN radio channel in the forest is needed to be intensively studied. However, most of the subsistent propagation models do not involve specific forestry environmental parameters. In this paper, two parameters related with the trees are considered: the leaf area index and the tree trunk diameter. Due to the time-changing characteristics of these two items (from spring to winter), an empirical model has been developed through extensive measurement campaigns: Firstly, the channel measurement platform is designed based on a real scene of mixed forest. Secondly, the fading characteristics of the channel transmission for LoRa nodes are tested, and the corresponding model is presented and evaluated. Lastly, an energy harvesting LoRaWAN is deployed and operated in a sampled forest region of Eastern China for environment monitoring based on our propagation model. The results show that 433 MHz LoRa path loss in the mingled forest could be precisely predicted by our proposed model. Moreover, network coverage and energy consumption optimization of the LoRa nodes could be performed, which enables the perpetual development of reliable forestry evolution monitoring system.

1. Introduction

The multispecies forest is an important silvicultural regime for sustainable forest management. Due to its vertical stratification structure, canopy plasticity, and niche separation, the mixed forest could utilize canopy space more efficiently to improve forest productivity and nutrient cycle more effectively than the natural forest. Along with its increasing area, mixed forest management faces different challenges [1]: competitions for natural resources of different tree species, different tending measures of growth stages, and improving pest control technologies. So it is urgent to develop and exploit reasonable resource monitoring systems for the prediction and management of mixed forest [2, 3]. Low-power wide-area networks (LPWANs) are a promising technology because of their high applicability, low energy consumption,

and self-organizing mechanism. An overview and comparison of different emerging LPWAN technologies have been presented in [4–6] and listed in Table 1. In particular, LoRaWAN is one of the most prospective LPWAN technologies, gaining greater interest from the research and industrial communities. It has also been increasingly adopted in the Internet of Things (IoT) in the forest [7–10].

LoRaWAN links every node via wireless communication, just as Figure 1 shows. When they are deployed in the forest, the radio signal may experience attenuation as a result of diffraction, reflection, scattering, and absorption effects caused by various obstacles of trees and shrub. Mixed forests are challenging radio propagation environments, and there is a need to understand better the propagation characteristics in order to design efficient wireless systems that can operate inside them. However, the modeling of forest radio propaga-

TABLE 1: Comparison of LPWAN technologies.

	LoRa	NB-IoT	Sigfox	ZigBee	WiFi
Frequency	868 MHz (EU); 915 MHz (USA); 433 MHz (Asia)	Depends on the frequency licensed to LTE	868 MHz (EU); 915 MHz (USA); 433 MHz (Asia)	868 MHz (EU); 915 MHz (USA); 433 MHz (Asia); 2.4GHz	2.4 GHz and 5 GHz
Transmission distance	Long (1-2 km in urban, 20 km in rural)	Long (10 km in rural)	Long (40 km in rural)	Short (10-100 m)	Short (50 -100 m)
Data transfer rate	0.3-50 kbps	160 kbps-250 kbps	100 bps	250 kbps	2.4 Gbps
Theoretical battery life	10 years/AA battery	10 years/AA battery	10 years/AA battery	1 year/AA battery	1 year/AA battery
Network delay	1 sec-3 sec	6 sec-10 sec	20 sec-25 sec	Less than 1 sec	Less than 1 sec
Networking mode	Gateway-based	Telecommunication operator-based	Gateway-based	Gateway-based	Gateway-based

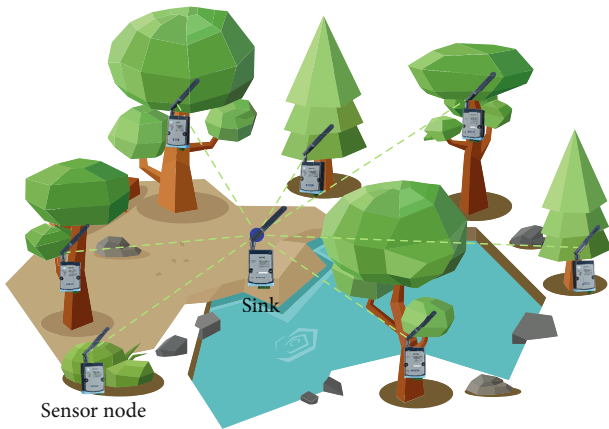


FIGURE 1: The diagram of LoRaWAN in a mixed forest.

tion is relatively complicated as different environmental parameters (such as type of vegetation, density, height of trees, and weather conditions) can have strong effects.

Researchers have developed several well-known empirical models to study the radio channel characteristics in the forest: Meng et al. performed experimental path loss modeling for a near ground radio wave propagation in a plantation at 240 and 700 MHz over a large forest depth [11], the proposed LITU-R mode mainly considers the lateral wave effect and shows better performance for the prediction of foliage loss over a large foliage depth (up to 5 km). Azevedo et al. found that the signal attenuation is dependent on the vegetation density, defined by the product of the tree density and the average diameter of the trunks [12]. Anderson et al. presented the results of a UWB measurement campaign and comprehensive parametric analysis for four different forest densities across multiple diverse locations in Maryland of Virginia. They demonstrated that UWB propagation in a forest environment heavily depends on the forest density, antenna type, and forest configuration [13]. Palaios et al. studied the near-ground propagation characteristics in a typical central European forest in UHF-bands around 485 MHz [14]; the result showed that the forest type has a significant effect to the propagation and thus mixed-type of forest requires its own model.

On the other hand, the characterization of the LoRa radio channel also got few achievements recently: Benaissa et al. studied LoRa path loss and temporal fading (868 MHz) for dairy cows in barns [15]. Hosseinzadeh et al. assessed the indoor propagation performance of LoRa technology and identified the model that best describes the process [16]. El Chall et al. investigated the LoRaWAN radio channel in both indoor and outdoor environments at urban and rural locations in Lebanon [17]. Sanchez-Iborra et al. presented a comprehensive performance evaluation of LoRaWAN under different environmental conditions [18]. A point-to-point LoRa path loss characterization has been researched in the urban, forest, and coastal environment [19]. Especially Sardar et al. analyzed some environmental factors in the forestry LoRa communication such as different antenna heights and packet lengths [20].

Based on the above literature, we find that most of the existing empirical models concentrated on single species of trees such as cedars and pines. Small *Acacia confusa* or *cryptomeria*, glass, and shrub wood were rarely taken into account, much less the mixed forest. Secondly, most models are based on the radio frequency and transmission distance, while the environmental parameters were scarcely considered. The prior models mainly divided the trees into in-leaf and out-of-leaf situations. However, the leaf area of trees changes with different seasons, and the cross-sectional area of tree trunk would also influence the radio propagation in its growth stage. Thirdly, the randomly distributed trees in a mixed forest are spatially different from the artificially planted trees that are arranged in rows and columns, whereas sub-GHz LoRa for this kind of forest has not yet been investigated up to now. Finally, since on-field measuring devices are always energy-constrained, it is likely that novel energy-harvesting (EH) IoT technologies will find their use in the forest monitoring [21–23]. So to combine the energy-efficient radio transmission power control mechanism with the accurate propagation model would be essential and inevitable for the EH-wireless sensor system in the forest.

In this work, practical LoRaWAN sensor nodes are used to characterize the path loss effect at 433 MHz band in the mangle forest environment at different heights from the ground. The measurement result which compared with the Okumura-Hata-Rural path loss model [24] and the LITU-R



FIGURE 2: The variation of the same tree at four different growth stages in the sample forest.

model [11] shows a significant difference. Hence, the Leaf Area Index (LAI) that can reflect the density of leaves at different growth stages is introduced as one characteristic parameter, and the trunk Diameter at Breast Height (DBH) that represents cross-section area of trees as the other. An empirical model comprising these two new parameters is then developed, and we compared it with the existing models to demonstrate its accuracy among the LoRaWAN nodes deployed in a mixed forest district in Nanjing city of Eastern China. The measured data, as well as the developed path loss models, can be used for efficient planning and deployment of EH-WSN in mixed forest environments. To the best of our knowledge, this is the first study on the analysis of propagation characteristics of LoRa in a mixed forest.

The rest of this paper is organized as follows: Section 2 describes the measurement campaign and presents the practical sensor nodes used and the investigated scenarios. Data analysis and model construction are discussed in Section 3. Section 4 tests the proposed model in a real field and compares it with existing models. Conclusions and future studies are given in Section 5.

2. Experimental Setup and Measurement Campaign

2.1. Mixed Forest Environment Description. We hold the modeling procedure at one typical mixed forest in Nanjing Forestry University, Jiangsu Province, Eastern China

($118^{\circ}48'55.98''\text{E}$, $32^{\circ}04'59.01''\text{N}$). This demonstration forest base was built in 1999 and has a length of 300 m and a width of 200 m. *Pinus massoniana*, *Ilex chinensis*, *Quercus variabilis*, *Lindera glauca*, *Photinia beauverdieana*, and *Rubus corchorifolius* were the dominant variety with an average crown of approximately 2.75 m. The plants were approximately 1.3–11.9 m high with trunk DBH of approximately 0.11–0.56 m.

The modeling measurement was mainly carried out at four growth stages including spring germination stage, summer leaf expanding stage, autumn leaf falling stage, and winter senescence stage in 2018. A variation of the same tree at the four growth stages is shown in Figure 2: In early March, the tree came up and had sparse leaves (Figure 2(a)); next, the leaves grew rapidly in late June (Figure 2(b)); and the LAI and DBH also reached the peak value; then the tree was in leaf falling stage by September (Figure 2(c)); finally, the leaves faded away and only branches existed in Winter (Figure 2(d)). These different morphological characteristics could definitely affect the wireless signal propagation that passed through and nearby.

2.2. Measurement Devices. The experimental platform used in our measurement campaigns is depicted in Figure 3. An Arduino UNO with Dragino LoRa shield expansion board was used as the sensor node, powered by a 3.7 V, 3000 mAH rechargeable lithium battery [25]. It has an integrated LoRa SX1278 transceiver and runs LoRaWAN protocol. One node without associated sensors that connected to a



FIGURE 3: The DBH and PAR sensor node mounted in trees.

laptop was used as the sink, and it was able to receive LoRa frames from -20 to -141 dBm depending on the LoRa BW and SF [26]. Both sink and sensor nodes used an omnidirectional dipole antenna of 3 dBi gain. Upon the reception of each frame, the sink provided the received signal strength indicator (RSSI), the signal-to-noise ratio (SNR), and the payload message. These received parameters were recorded on the server side on the laptop for further analysis and processing. The quality of reception can be monitored in real-time with an MQTT Web client application.

The LoRa nodes were configured to send a packet every interval. The packets also included a sequential number in order to identify the packet loss. The transmit power was set to 14 dBm, SF to 12 (to achieve the best receiver sensitivity), and the BW to 125 kHz, using the three default channels (433.175, 433.375, and 433.575 MHz). The packet payload was 37 bytes including 13 bytes MAC header. The measurement setup parameters are listed in Table 2. During all the measurements, the position of the sink was fixed, whereas the sensor nodes could be moved to different locations.

As can be seen from Figure 3, there were two particular designed forestry sensors: DBH and Photosynthetically Active Radiation (PAR). The DBH sensor mainly consisted of a high accuracy sliding film potentiometer, a circular flexible elastic wheel rim, a fixed position deck, and a signal processing bridge circuit. After tightened installation onto the tree trunk, the potentiometer's slider could point out the exact value of its resistance, with which we can deduce the DBH. The PAR sensor was designed for the measurement of LAI, which was based on the reference system [27, 28], it included two parts: the testing components and the reference component. The testing PAR sensors should be placed around the crown to measure the luminous flux which passed through, where the reference sensor could be set up in a clear field to provide contrast and evaluation. Both kinds of sen-

TABLE 2: Measurement setup parameters.

Parameter	Value
Sensor node	SX1278
Sink	LG01-P, Dragino IoT kit
TX power	14 dBm
Frequency	433 MHz
Bandwidth (BW)	125 KHz
Antenna	3 dBi omnidirectional
Spreading factor (SF)	12
Coding rate	4/5
Payload length	37 bytes
Time interval	10 sec
Sensor node antenna height	0.5 m, 1.3 m, 2.0 m, 2.5 m, 3.0 m
Sink antenna height	1.3 m

sors make up an effective and indispensable supply to the proposed radio propagation analysis of IoT in the forest.

2.3. Practical Measurement Setup. Throughout the experiments, the intention was to place the sink node at the center of designated deployment field and collect RSS readings at eleven different distances (i.e., 5, 10, 20, 30, 40, 50, 60, 70, 80, 90, and 100 meters) and along twelve different 30 degrees separated radials. Therefore, an area of 200 m x 200 m is ideally needed to carry out the real field deployment experiment.

The antenna of the sink node was placed 1.3 m above the ground, i.e., height of DBH. RSSIs were then measured by the transmitting node with 5 heights from bottom to top at heights of 0.5, 1.3, 2, 2.5, and 3 m. The transmitting and receiving antenna were maintained erect in all of the tests. The top and side views of the measurement site are shown

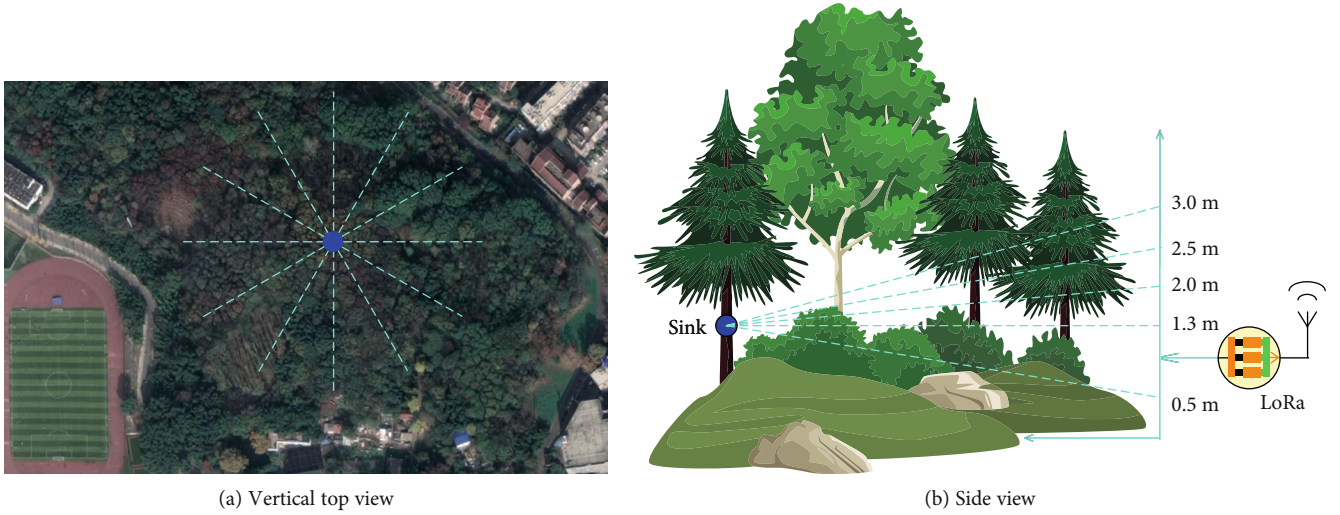


FIGURE 4: Measurement site: the dashed lines represent the testing points, while the center dot is the sink.

in Figure 4. Note that as a result of extensive randomly scattered leaves, branches and bushes, the signal strength may change considerably even when there is a little variation in the position of transmitting antenna. So for each measurement point, 100 samples were collected, providing a sufficiently large dataset for approximating important statistical properties of the signal, such as mean and variability. Hence, the RF measurement of every 660 measuring point is an average of each 100 RSSI samples.

Besides, DBH and LAI results have also been collected and stored in the laptop which is connected with the sink. These two kinds of dedicated sensor nodes sent their data once a day to the sink for subsequent data analysis. They were all mounted on some specific trees selected by forest cultivation criterion [29]. We have held up the whole measurement campaign in four growth stages of the mixed forest once each; the average LAI and DBH values of the selected trees were used as the exact novel parameters in the next path loss model analysis.

3. Measurement Results and Empirical Model

In this section, we present the results of measurements conducted in the sample Mixed Forest of Nanjing Forestry University as described in Section 2. Then, we derive Pass Loss (PL) models from four different environments (spring, summer, august, and winter). At last, the proposed PL model is analyzed and discussed.

The RSSI values collected in the mixed forest environment were all converted into PL values which represent the signal attenuation on the path between the transmitter and the receiver antennas. As for the PL, value is a unique property of the transmission environment. Generally, the relationship between PL, transmission power, and RSSI is given as:

$$PL[\text{dB}] = P_T[\text{dBm}] - P_R[\text{dBm}] + G_T[\text{dB}] + G_R[\text{dB}], \quad (1)$$

where PL refers to the path loss, P_T refers to the transmitting power, P_R is the receiving power ($P_R = \text{RSSI} + \text{SNR}$), G_T is the transmit antenna gain, and G_R is the receive antenna gain. Table 3 just presents the PL results in the spring stage measurement when transmitting node's height is 0.5 m.

Then, we calculate the average PL values related to each testing point including the very corresponding 5 heights. Figure 5 illustrates the average PL values versus the log of distance. Moreover, it illustrates the corresponding linear regression model lines.

It can be clearly pointed out that the variations among PL values which at the same distances are relatively large. In the mixed forest environment, such variations mainly occur as a result of the absence of Light of Sight communication between the transmitter and receiver, resulting in great signal fluctuation. In some instances, multiple waves of the transmitted signal may arrive at the sink, causing multipath fading. In other instances, only a small scattered portion of the transmitted signal may be received. Meanwhile, the season changes of mixed forest have a great influence on the PL values, the growth, and decay of branches and leaves directly transform the transmission routes of LoRaWAN.

Also, we can see that the average PL values closely follow the linear regression line, which indicates a dependency between the PL values and the log of distance. As a matter of fact, the linear regression provided in Figure 5 produces a reliable coefficient of determination (i.e., $0.8913 < R^2 < 0.985$), so the log-normal model is suitable for estimating the PL:

$$PL_{LN}(\text{dB}) = PL(d_0) + 10n \log_{10} \left(\frac{d}{d_0} \right) + X_{\sigma}, \quad (2)$$

where n is the path loss exponent that indicates the rate at which the signal attenuates with the distance, $PL(d_0)$ is the

TABLE 3: Path loss measurement result (dB) in the spring stage with transmitting height 0.5 m.

Radial no.	Degree	5 m	10 m	20 m	30 m	40 m	50 m	60 m	70 m	80 m	90 m	100 m
1	0	54.5	60.1	78.6	81.9	84.2	90.5	89.8	101.3	105.4	110.7	115.0
2	30	52.2	64.3	82.1	85.2	81.7	93.2	97.3	97.1	110.5	112.2	118.3
3	60	55.1	66.9	75.3	79.7	86.9	94.1	98.8	95.6	112.4	123.8	109.9
4	90	56.9	68.2	73.7	83.8	88.2	97.7	96.9	103.4	107.6	121.1	117.1
5	120	49.8	69.5	79.9	89.7	78.4	86.9	85.4	106.8	103.2	126.7	114.6
6	150	51.6	63.3	83.5	86.5	82.5	88.1	88.7	109.7	99.3	117.5	107.3
7	180	56.9	59.2	85.4	83.4	89.6	89.4	99.4	103.5	98.8	111.2	109.7
8	210	59.3	65.7	89.1	90.3	92.3	92.5	98.5	101.9	104.7	107.5	119.2
9	240	53.6	67.8	80.6	84.9	85.1	85.8	91.0	97.6	108.1	106.4	110.8
10	270	48.8	62.6	77.2	81.1	86.8	94.3	94.7	93.4	102.6	109.3	133.5
11	300	55.2	70.3	79.8	88.3	88.9	93.6	93.9	108.2	104.9	104.6	128.4
12	330	58.4	64.8	78.4	82.6	84.6	87.7	95.5	110.1	103.8	109.9	116.7

path loss at a known reference distance d_0 in the far-field, X_σ denotes a zero-mean Gaussian random variable with standard deviation σ , which reflects the variation of the received power around the average.

Figure 6 shows the variations of attenuation index n and PL (d_0) according to different heights. For the heights above 1.3 m, n increases along with the height, especially when in the summer time, it is very reasonable due to the lush branches and leaves. The communication path always passes through the crown when the height is over 2 m. However, the attenuation of 0.5 m is more or less larger than the 1.3 m except for the winter stage, we mainly attribute the phenomena to the bushes and thick undergrowth of the mixed forest. PL (d_0) shows the opposite trends as the testing nodes' height increase, the values decline mostly because of the obstructions between transmitter, and receiver increase simultaneously. Furthermore, according to the different seasons, these two curves show a similar variation tendency, which we should thoroughly analyze. In other words, we may try to combine specific forest parameters together.

Here, we record the average DBH and LAI values with respect to the distance between transmitting nodes and sink. These two particular sensor nodes were located half-randomly based on the forestry cultivation rules [29]. We can see that the average DBH values almost keep the same from spring to summer, then it has a rapid growth until winter in Figure 7(a). However, Figure 7(b) shows that the LAI values mainly change along with the seasons, while not with the distance. The two items could perfectly represent the characteristic of the sample mixed forest.

The last parameter of the log-normal model, represented by X_σ , can be defined by the standard deviation. Figure 5 reveals that a good approximation of the values can be obtained by using the mean. Here, we considered that $X_\sigma = 6.94$ dB.

So to precisely evaluate the parameters n and PL (d_0), we introduce joint polynomials to combine the DBH and LAI together. The formulae that are shown below elaborate the three constants of the linear fitting (x_{n1}, x_{n2}, x_{n3}) with distance (d_M , from sender to receiver) and height (h_G , nodes'

vertical position above the ground). These parameters were determined by curve fitting of the above Figures 6 and 7:

$$n = x_{n1} \cdot \Phi + x_{n2}, \quad (3)$$

$$\Phi = x_{n3} \cdot [10 \cdot \log_{10}(V_{DBH} - 8.63) + V_{LAI}], \quad (4)$$

$$x_{n3} = 0.036 \cdot (d_M - 24)^{0.61}, \quad (5)$$

$$x_{n2} = -0.5169 \cdot h_G^2 + 2.9773 \cdot h_G + 1.485, \quad (6)$$

$$x_{n1} = -0.0931 \cdot h_G^2 + 0.8575 \cdot h_G - 0.04392. \quad (7)$$

Similarly, we can have:

$$PL(d_0) = x_{PL1} \cdot \Psi + x_{PL2}, \quad (8)$$

$$\Psi = x_{PL3} \cdot [\log_{10}(V_{DBH} - V_{LAI})], \quad (9)$$

$$x_{PL3} = 0.045 \cdot d_M + 0.32, \quad (10)$$

$$x_{PL2} = 41.8, \quad (11)$$

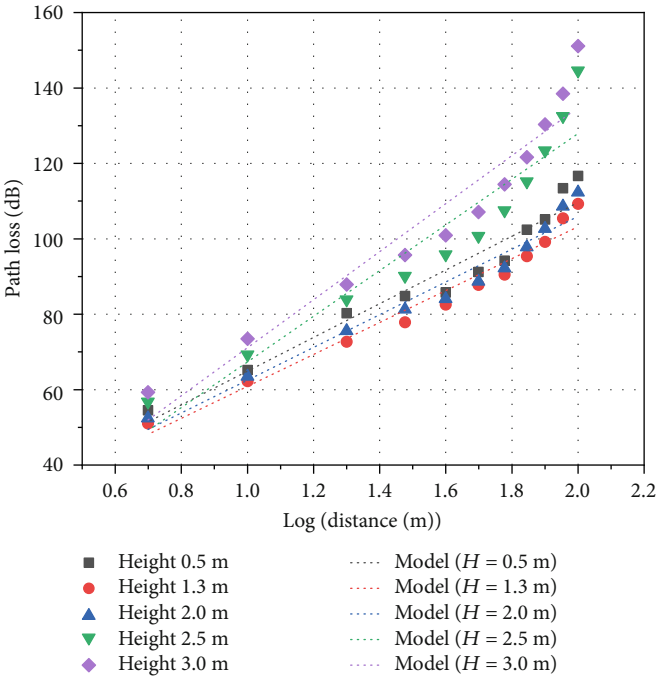
$$x_{PL1} = -5.1856 \cdot h_G. \quad (12)$$

V_{DBH} and V_{LAI} are just the values of DBH and LAI. Thus, a new empirical model could be created by using equations ((3)–(12)) to estimate the LoRaWAN path loss in a typical mixed forest.

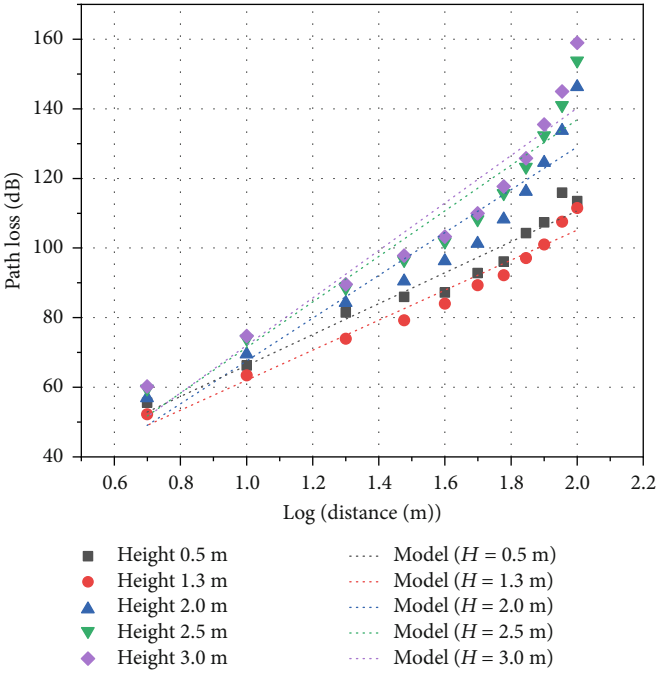
4. Evaluation and Discussion

4.1. Model Validation. We carried out the experimental evaluation at a different mixed forest in Eastern China's Nanjing city in 2019, it is located at the west side of Zi Jin Shan Mountain and has a length of 170 m and a width of 120 m. The tree species structure is similar with our modeling forest, except for the heavy brush approximate 0.6 m high. Also, the DBH and LAI values are higher due to the well-protected natural environment.

The testing method was similar to that in the modeling experiments. Here, the validation measurement was executed



(a) Spring stage



(b) Summer stage

FIGURE 5: Continued.

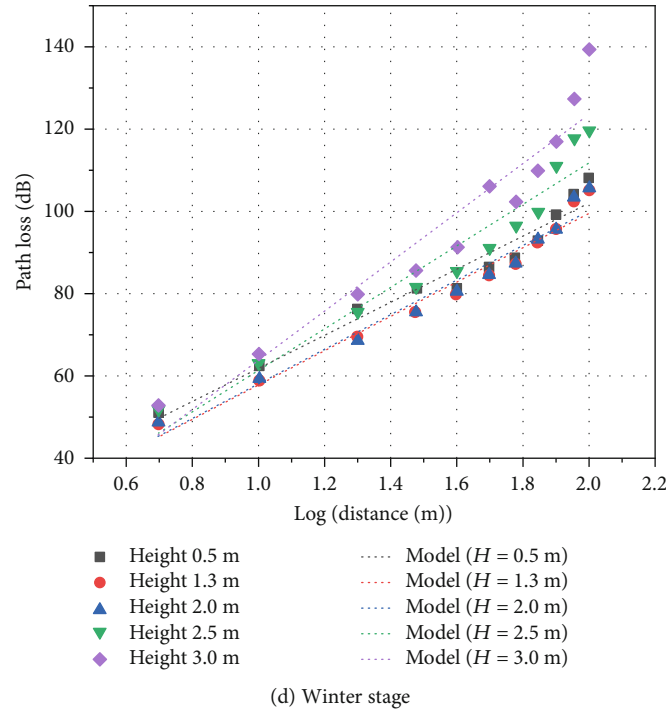
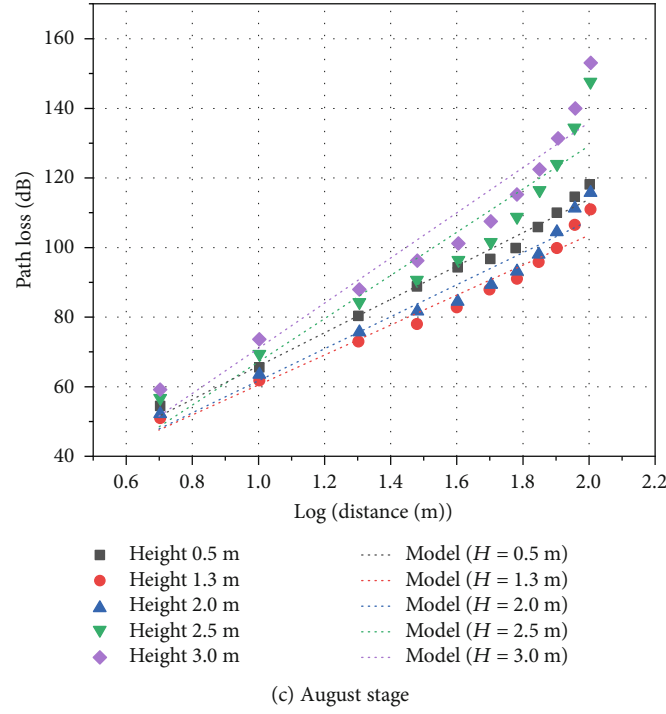


FIGURE 5: Average path loss and linear regression lines for the four-stage environments.

at 5 different heights (0.75 m, 1.3 m, 1.75 m, 2.25 m, and 2.75 m) along one straight line between the transmitter and receiver. On the same time, two forestry parameters (LAI and DBH) at each validation point could be collected conveniently. So we implemented the whole validation from March to July, and the testing positions were chosen with an extensive representativeness for different growth stages as much as possible.

The comparison of measurement results and the proposed new model is shown below in Figure 8. 95% of the R^2 values are larger than 0.85, the least value being 0.81. Most of the Root Mean Square Error (RMSE) values were between 2 and 4, as shown in Table 4.

We can see from the results that the proposed model matches the measurements quite well. In general, the presence of high density of trees can lead to a bad quality

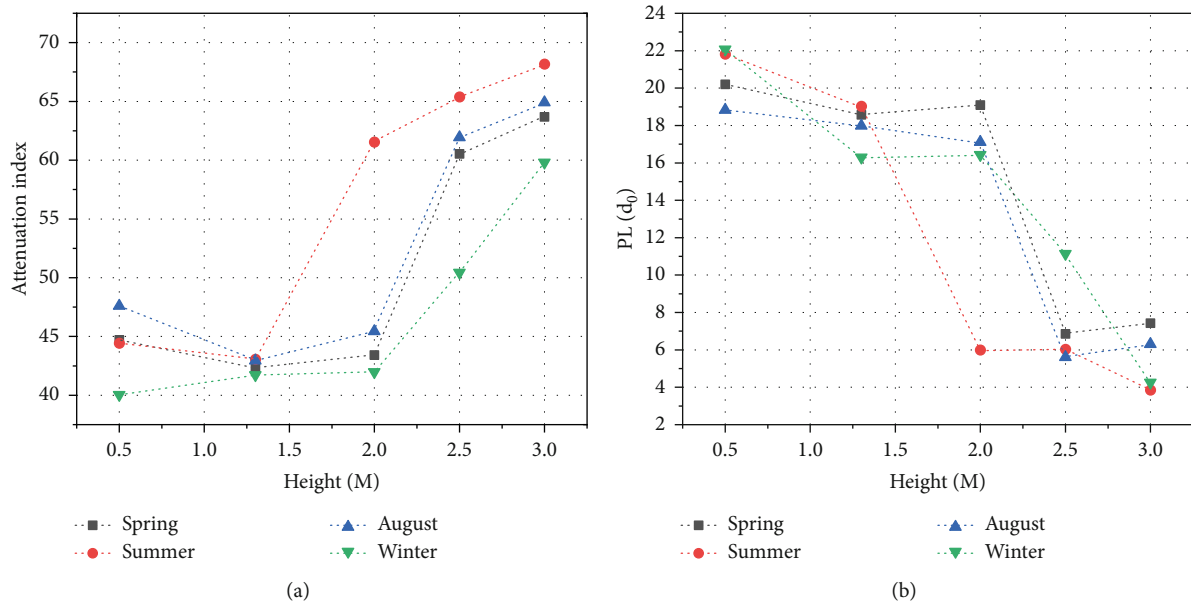
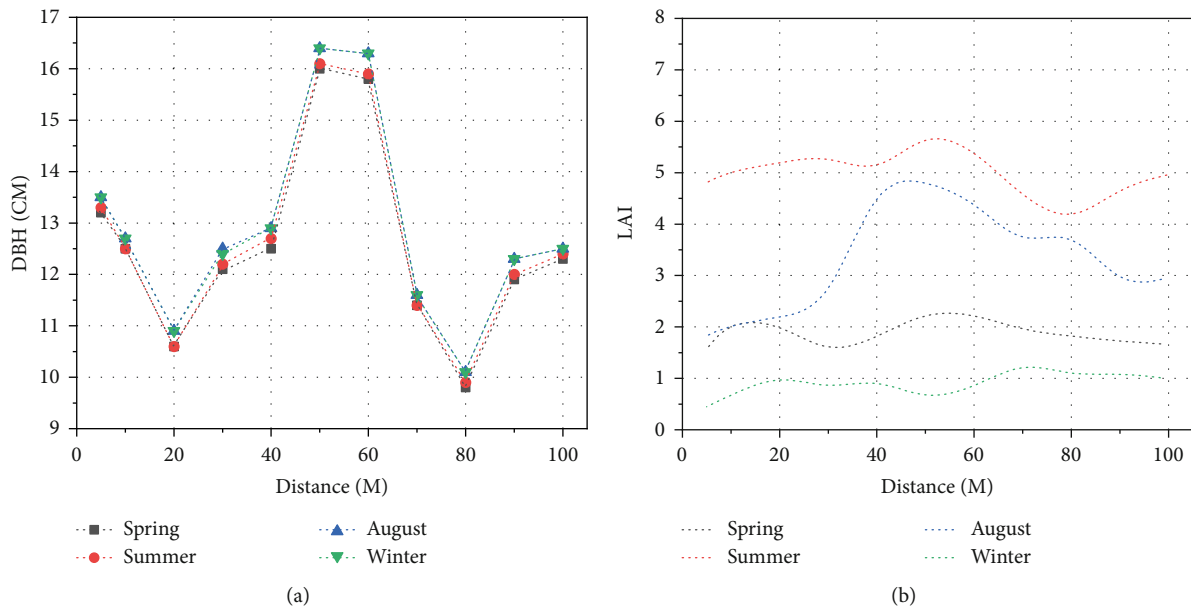
FIGURE 6: Average attenuation index n and $PL(d_0)$ of the four-stage environments.

FIGURE 7: Average DBH and LAI of the four-stage environments.

reception: the higher value of LAI and DBH always means that there are more obstructions of radio scattering, reflections, diffractions, and absorptions. Hence, this nonlinear of sight PL values increase sharply along with the transmission distance and antenna height.

Then, the proposed new model has also been compared with some existing models at testing point (d), as shown in Figure 9: The results for the empirical model Okumura-Hata-Rural are represented by a dash-dot line, it can be observed that Okumura-Hata model underestimates the PL values and presents a slower rising tendency; By contrast, the result of LITU-R model in dotted line shows smaller error

since it was developed to follow data for higher dissipation. However, they all show relatively large deviations compared with our proposed models. So to evaluate the different path loss models thoroughly, we use three parameters: the RMSE, the Mean Absolute Error (MAE), and the Mean Absolute Percentage Error (MAPE). From Table 5, we can observe that the best prediction is achieved by using the proposed path loss model.

The primary cause is that none of the existing models could estimate the path loss at any height without any LAI or DBH. Furthermore, the value of RMSE, MAE, and MAPE in Okumura-Hata-Rural and LITU-R highly vary

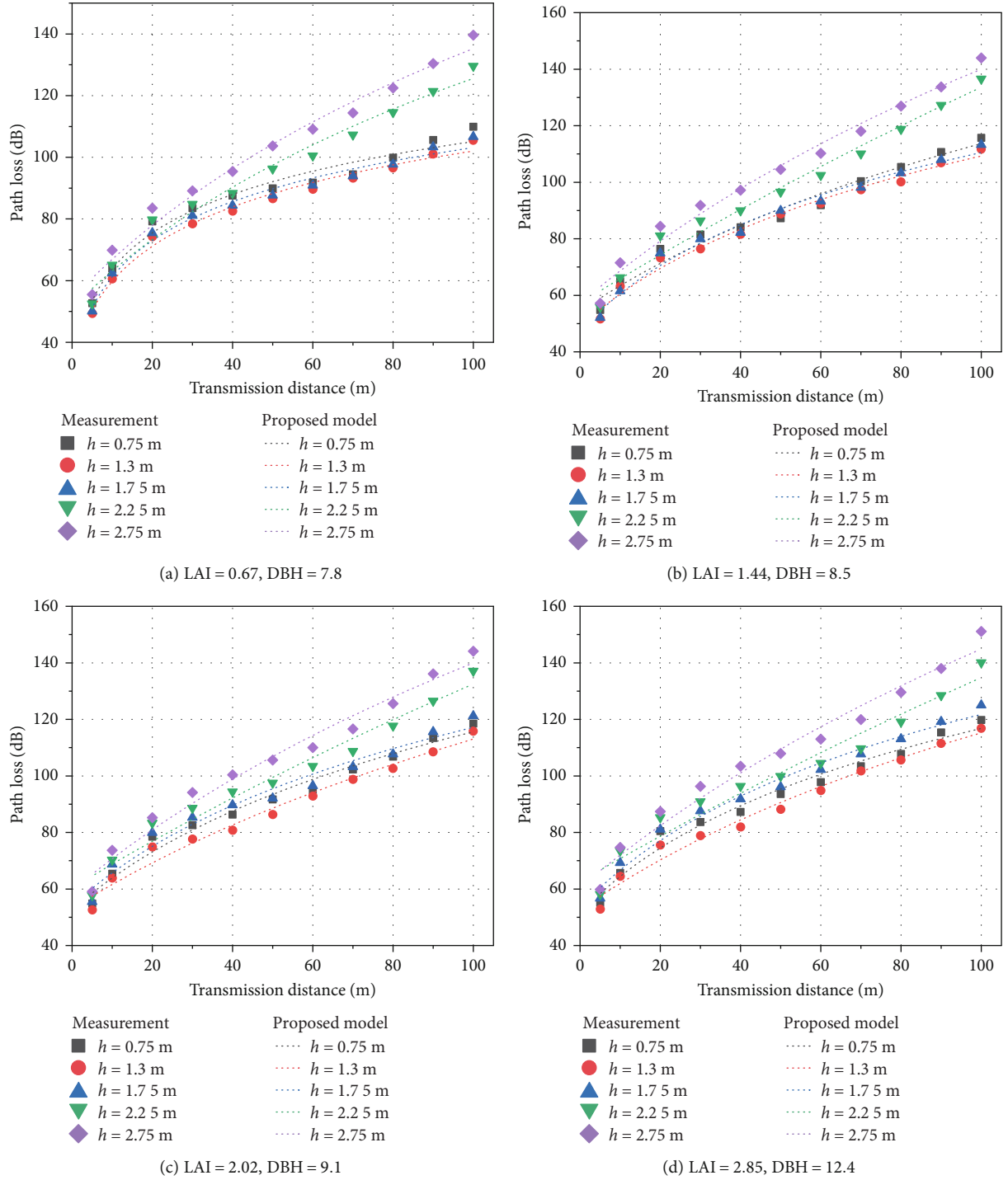


FIGURE 8: Continued.

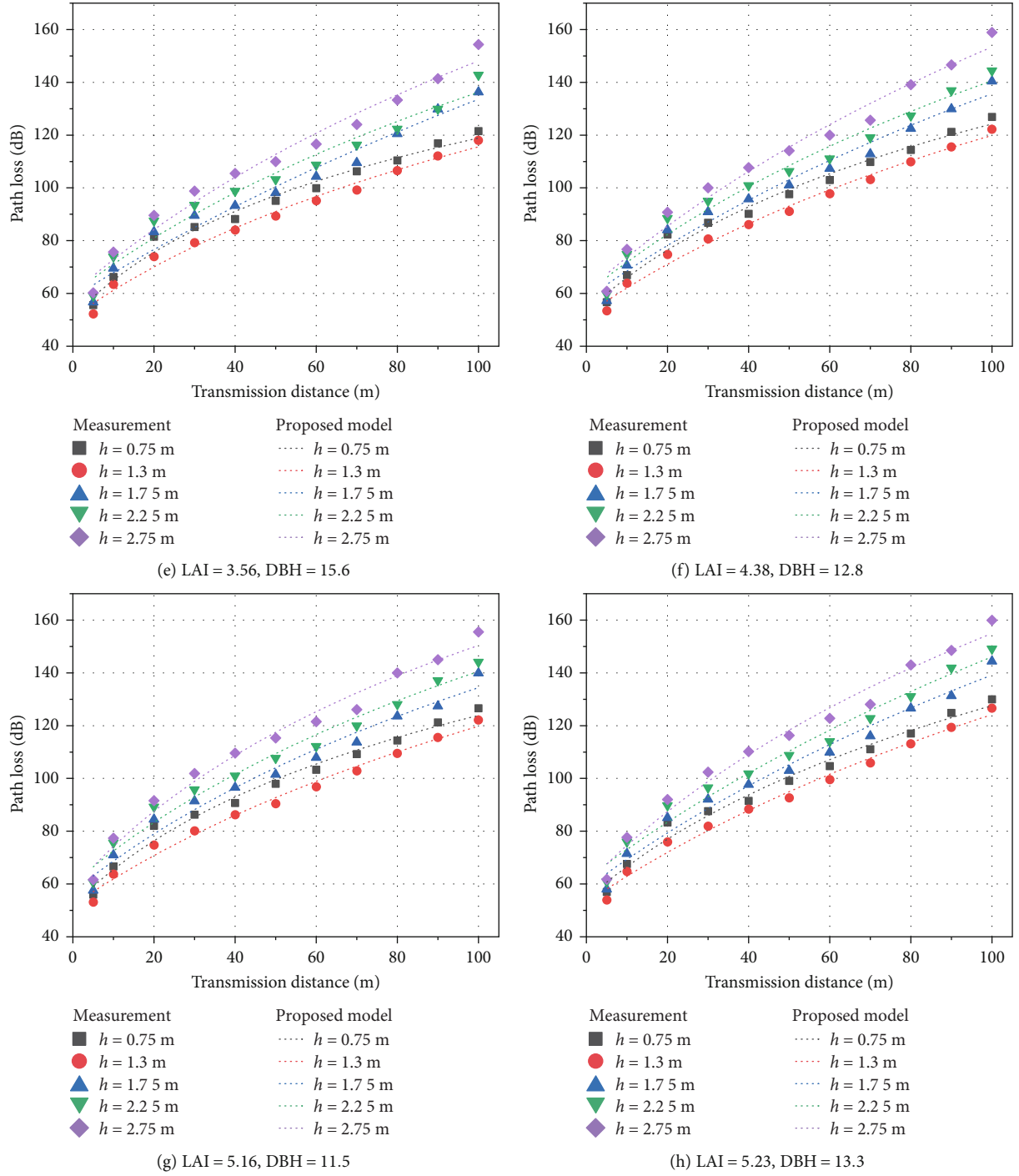


FIGURE 8: Comparisons between the measurements and the new model at 8 selected points.

from one height to another, therefore, a slight variation of antenna or forestry parameters would negatively affect the prediction of the path loss in these models. Our proposed new model outperforms the existing models with the lowest RMSE, MAE, and MAPE regardless of the height of the antenna. Thus, the predicted values of our model are closer to real observations than the existing models.

4.2. Field Measurement on Energy-Harvesting LoRa Nodes. In this section, we evaluate the performance of the proposed

radio propagation model based on the wind energy harvesting LoRaWAN which has been mounted in the sample mixed forest at Nanjing Forestry University [22]. We take the wind-powered sensor nodes serving as transmitters (Figure 10 shows the node's mainboard, while the sensors could be attached on when in practice). An unlimited power supply sink is responsible for receiving messages and returning the packet delivery ratio (PDR) every day. The transmitting rate is 250 bps, and the payload length is 50 bytes. The selected nodes are located at 3 different positions: (i) $\text{LAI}_i = 1.99$,

TABLE 4: Validation results at different heights for 8 testing points.

Antenna height (m)	(a)	(b)	(c)	(d)	(e)	(f)	(g)	(h)
0.75	0.93	0.91	0.88	0.95	0.93	0.90	0.94	0.96
	2.87	1.89	3.84	3.15	2.69	2.41	2.95	3.37
1.3	0.96	0.96	0.84	0.93	0.87	0.86	0.91	0.95
	3.91	2.16	2.96	2.37	2.19	3.58	3.40	1.77
1.75	0.94	0.93	0.95	0.96	0.90	0.92	0.88	0.99
	1.72	3.74	2.06	2.89	3.06	4.07	3.76	2.55
2.25	0.92	0.90	0.97	0.94	0.95	0.97	0.85	0.97
	2.49	3.81	3.41	3.86	3.34	2.61	2.79	2.72
2.75	0.88	0.89	0.85	0.87	0.91	0.93	0.82	0.84
	3.14	2.76	2.82	2.63	2.99	3.67	4.11	2.09

*The first line denotes the R^2 values, and the second line indicates the RMSE values at each height.

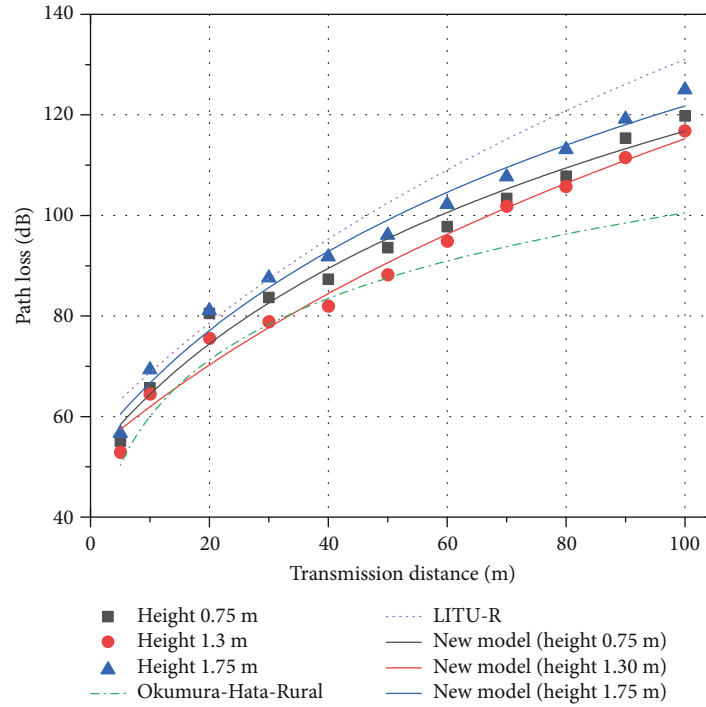


FIGURE 9: Comparisons between the new model and two existing models (LAI = 2.85, DBH = 12.4).

TABLE 5: The RMSE, MAE, and MAPE values between the proposed model and existing models.

Location	Okumura-Hata-rural			RMSE	LITU-R		RMSE	Proposed model	
	RMSE	MAE	MAPE (%)		MAE	MAPE (%)		MAE	MAPE (%)
Height 0.75 m	11.66	10.17	10.70	8.84	7.03	8.11	3.15	2.79	2.96
Height 1.30 m	9.78	8.56	9.44	6.93	5.49	5.87	2.37	1.96	2.17
Height 1.75 m	15.41	13.79	14.12	13.35	11.24	12.63	2.89	2.02	2.79

DBH_i = 13.82; (ii) LAI_{ii} = 3.01, DBH_{ii} = 10.78; (iii) LAI_{iii} = 2.63, DBH_{iii} = 15.84. The corresponding communication distances and antenna heights are (i) $d_i = 37\text{m}$, $h_i = 1.0\text{m}$; (ii) $d_{ii} = 55\text{m}$, $h_{ii} = 1.3\text{m}$; (iii) $d_{iii} = 64\text{m}$, $h_{iii} = 2.0\text{m}$.

We validate the effectiveness of our propagation loss calculation module by using two comparisons. The existing

fixed transmission power scheme is implemented as a reference, which is referred to as the Fixed-TX scheme. One of the wind-harvesting LoRaWAN nodes works under our proposed model at position (iii), while the other nodes located at positions (i) and (ii) be set with the fixed transmission power TX = 7 dBm and TX = 14 dBm, respectively. The node (iii)

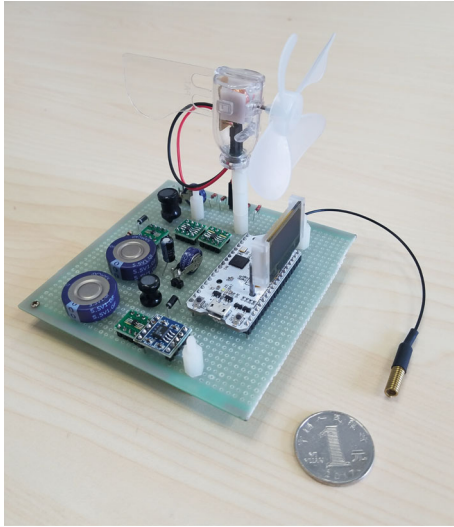


FIGURE 10: Wind energy harvesting LoRa node (mainboard).

could compute its transmitting power by equation (1) based on the RSSI value efficiently. All three nodes start with an initial energy of 1 Joule, and the average wind speed during the experiment is 4.4 m/s.

Table 6 presents the average PDR of total of 10,080 packets (ten packets per minute during 7 days) and the residual energy of three nodes in the final time. We can see that the proposed method achieves the lowest energy consumption compared with the other transmission power strategies no matter the distance. Compared with the Fixed-TX-14 dBm scheme, our proposed module achieves energy reduction around 30%. Compared with the Fixed-TX-7 dBm scheme, our proposed module improves the PDR around 5%. The wireless path loss and the background noise are always time-varying, the fixed transmission power definitely cannot guarantee the optimal transmission energy efficiency. The proposed PL model is effective in dynamically calculating the optimal transmission power along with the lowest energy cost.

4.3. Rain Attenuation of LoRaWAN in the Forest. Rain and fog is quite common in the forestry district. Many studies indicate that the propagation of the radio signal is affected by rain and there are some remarkable models deduced to analyze its influence [30, 31]. However, most existing researches focus on the rain attenuation by wireless signals with frequencies above 10 GHz. So in this part, we investigate the influence of rain attenuation within the proposed forestry LoRaWAN for the first time. The experiment setup is just the same as part 4.2 and we record the variations of RSSI in position (ii) every 10 seconds when rainfall comes. The measurement data presented in Figure 11 are filtered by a moving average window with 30 samples. It is noticeable that during rainfall periods there is an obvious attenuation of PL.

Figure 11(a) shows a significant impact on path loss of LoRa signal when it is rainy during a 7-day consecutive observation, every increasement of PL values corresponds to a rainfall event accurately. Although the rain rate which

has been recorded by a standard rain gauge [32] does not exceed the extremely heavy level, a nearly 8 dB variation of PL has occurred. Figure 11(b) shows a detailed changing process of rain attenuation, PL value increases sharply when the rain begins to fall, and it returns to the original state relatively slow after the rain stops. The main reason of fading may be the water molecular which is adhered on the antenna of LoRa nodes and pervaded in the transmission space, it would change the propagation characteristic and the antenna property drastically.

According to reference [33], the rain attenuation can be represented by aR_p^b , where R_p is the rain rate with a given period P while a and b are depending on the radio wave frequency and the rain temperature. Hence, we calculate this item with the collected rainy data and deduce the result as R_p is set to 3.86 mm/hr based on the conventional rain information from local weather station, a and b just are 2.11 and 0.55, respectively. So the updated general PL model would be:

$$PL_{LN}(\text{dB}) = PL(d_0) + 10n \log_{10} \left(\frac{d}{d_0} \right) + X_\sigma + aR_p^b. \quad (13)$$

Furthermore, we also apply the updated model on the wind-harvesting LoRaWAN node to verify its effectiveness. It is located in position (iii) as well and the average wind speed is 4.9 m/s during the rainy period. The other two nodes located at positions (i) and (ii) are set the same as part 4.2, and the corresponding results are shown in Table 7.

It can be seen that the residual energy of the updated model decreases slightly otherwise the two Fixed-TX nodes get higher due to the larger wind speed. However, PDR of the updated scheme keeps 100%, while the comparative two nodes drop significantly. This indicates that the updated PL model matches the real rain attenuation efficiently and works stably in energy neutral mechanism.

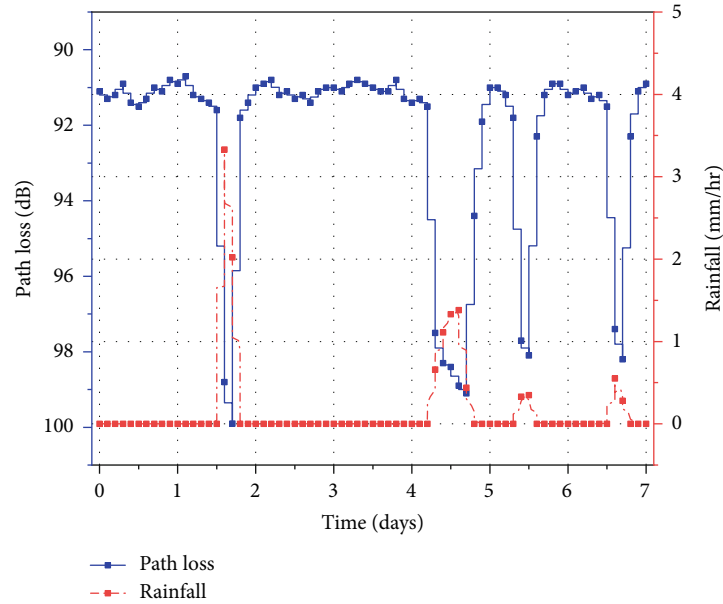
5. Conclusion

IoT in forest environments can support applications such as fire alarm, environment surveillance, pest diagnosis, and tree growth monitoring. Large-scale deployment of LoRaWAN in forest environments requires accurate characterization of the propagation channel utilizing practical sensor nodes. However, most of the existing studies in forest environments use signal generators instead of practical sensor nodes, which, in turn, may lead to inaccurate models and, as a result, poor decision making during large-scale deployment of LoRa nodes. Inaccurate models may also result in the poor energy efficiency of the network as well as inaccuracy in localization and coverage control applications.

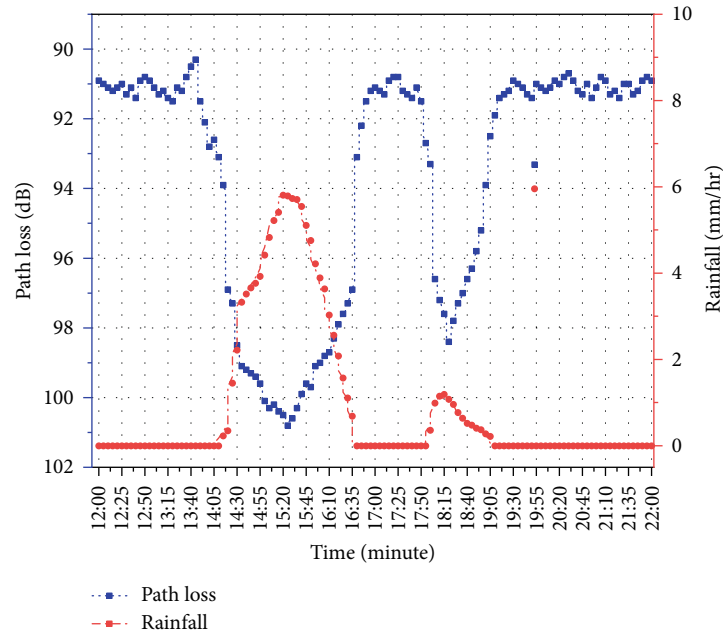
In this work, empirical path loss models for LoRaWAN in the mixed forest of Eastern China are researched using practical sensor node measurements at 433 MHz. New proposed model based on the DBH and LAI with different heights is developed and compared with the existing

TABLE 6: The residual energy and PDR of three nodes.

Average testing result	Proposed PL model	Fixed-TX-14 dBm	Fixed-TX-7 dBm
Supercapacitor voltage (volt, residual energy)	3.194	2.372	2.468
PDR (%)	100	97	95



(a)



(b)

FIGURE 11: Variation of RSSI vs. rainfall in position (ii) from 2019.05.01 to 2019.05.08.

Okumura-Hata-Rural model and LITU-R path loss models to demonstrate its accuracy. Moreover, the performance of wind energy harvesting based LoRa nodes equipped with our model has also been investigated. Results show that the

RMSE, MAE, and MAPE values of the new model were almost all smaller than the existing models, thus the proposed model best matches the real field application status of LoRaWAN in mixed forest.

TABLE 7: The residual energy and PDR of three nodes during rainy time.

Average testing result	Proposed PL model	Fixed-TX-14 dBm	Fixed-TX-7 dBm
Supercapacitor voltage (volt, residual energy)	3.031	2.447	2.584
PDR (%)	100	93	90

The measured data, as well as the proposed models, can be useful for efficient planning and deployment of LoRaWAN in forest environments, even during the rainy season. In addition, a future study will include using the same approach to investigate the behavior of other LPWAN protocols like LTE-M and NB-IoT in forest environments.

Data Availability

The data used to support the findings of this study are included within the article.

Conflicts of Interest

The authors declare that they have no conflicts of interest.

Acknowledgments

This study was financially supported by the National Natural Science Foundation of China under Grants 31700478 and 31670554.

References

- [1] H. Xiang, L. Zhang, and D. Wen, "Change of soil carbon fractions and water-stable aggregates in a Forest ecosystem succession in South China," *Forests*, vol. 6, no. 12, pp. 2703–2718, 2015.
- [2] J. Dempewolf, J. Nagol, S. Hein, C. Thiel, and R. Zimmermann, "Measurement of within-season tree height growth in a mixed Forest stand using UAV imagery," *Forests*, vol. 8, no. 7, p. 231, 2017.
- [3] P. Surový and K. Kuželka, "Acquisition of forest attributes for decision support at the forest enterprise level using remote-sensing techniques—a review," *Forests*, vol. 10, no. 3, p. 273, 2019.
- [4] W. Ayoub, A. E. Samhat, F. Nouvel, M. Mroue, and J.-C. Prevotet, "Internet of mobile things: overview of LoRaWAN, DASH7, and NB-IoT in LPWANs standards and supported mobility," *IEEE Communications Surveys & Tutorials*, vol. 21, no. 2, pp. 1561–1581, 2019.
- [5] M. Rady, M. Hafeez, and S. A. Raza Zaidi, "Computational methods for network-aware and network-agnostic IoT low power wide area networks (LPWANs)," *IEEE Internet of Things Journal*, vol. 6, no. 3, pp. 5732–5744, 2019.
- [6] M. Chen, Y. Miao, X. Jian, X. Wang, and I. Humar, "Cognitive-LPWAN: towards intelligent wireless services in hybrid low power wide area networks," *IEEE Transactions on Green Communications and Networking*, vol. 3, no. 2, pp. 409–417, 2019.
- [7] T. O. Olasupo and C. E. Otero, "The impacts of node orientation on radio propagation models for airborne-deployed sensor networks in large-scale tree vegetation terrains," *IEEE Transactions on Systems, Man, and Cybernetics: Systems*, vol. 50, no. 1, pp. 256–269, 2020.
- [8] S. Sendra, L. García, J. Lloret, I. Bosch, and R. Vega-Rodríguez, "LoRaWAN network for fire monitoring in rural environments," *Electronics*, vol. 9, no. 3, p. 531, 2020.
- [9] P. Avila-Campos, F. Astudillo-Salinas, A. Vazquez-Rodas, and A. Araujo, "Evaluation of LoRaWAN transmission range for wireless sensor networks in riparian forests," in *Proceedings of the 22nd International ACM Conference on Modeling, Analysis and Simulation of Wireless and Mobile Systems - MSWIM '19*, pp. 199–206, Miami Beach, FL, USA, November 2019.
- [10] O. Iova, A. L. Murphy, G. P. Picco et al., "LoRa from the city to the mountains: exploration of hardware and environmental factors," in *Proceedings of the 2017 International conference on embedded wireless systems and networks*, pp. 317–322, Uppsala, Sweden, February 2017.
- [11] Y. S. Meng, Y. H. Lee, and B. C. Ng, "Empirical near ground path loss modeling in a forest at VHF and UHF bands," *IEEE Transactions on Antennas and Propagation*, vol. 57, no. 5, pp. 1461–1468, 2009.
- [12] J. A. R. Azevedo and F. E. S. Santos, "An empirical propagation model for forest environments at tree trunk level," *IEEE Transactions on Antennas and Propagation*, vol. 59, no. 6, pp. 2357–2367, 2011.
- [13] C. R. Anderson, H. I. Volos, and R. M. Buehrer, "Characterization of low-antenna ultra-wideband propagation in a forest environment," *IEEE Transactions on Vehicular Technology*, vol. 62, no. 7, pp. 2878–2895, 2013.
- [14] A. Palaos, Y. Labou, and P. Mähönen, "A study on the forest radio propagation characteristics in European mixed forest environment," in *2014 IEEE Military Communications Conference*, pp. 376–381, Baltimore, MD, USA, October 2014.
- [15] S. Benaissa, D. Plets, E. Tanghe et al., "Internet of animals: characterisation of LoRa sub-GHz off-body wireless channel in dairy barns," *Electronics Letters*, vol. 53, no. 18, pp. 1281–1283, 2017.
- [16] S. Hosseinzadeh, H. Larijani, K. Curtis, A. Wixted, and A. Amini, "Empirical propagation performance evaluation of LoRa for indoor environment," in *2017 IEEE 15th International Conference on Industrial Informatics (INDIN)*, pp. 26–31, Emden, Germany, July 2017.
- [17] R. El Chall, S. Lahoud, and M. El Helou, "LoRaWAN network: radio propagation models and performance evaluation in various environments in Lebanon," *IEEE Internet of Things Journal*, vol. 6, no. 2, pp. 2366–2378, 2019.
- [18] R. Sanchez-Iborra, J. Sanchez-Gomez, J. Ballesta-Viñas, M.-D. Cano, and A. Skarmeta, "Performance evaluation of LoRa considering scenario conditions," *Sensors*, vol. 18, no. 3, p. 772, 2018.
- [19] G. Callebaut and L. Van der Perre, "Characterization of LoRa point-to-point path loss: measurement campaigns and modeling considering censored data," *IEEE Internet of Things Journal*, vol. 7, no. 3, pp. 1910–1918, 2020.
- [20] M. S. Sardar, Y. Yi, W. Xue-fen et al., "Experimental analysis of LoRa CSS wireless transmission characteristics for forestry monitoring and sensing," in *2018 International Symposium*

- in *Sensing and Instrumentation in IoT Era (ISSI)*, pp. 01249–01254, Shanghai, China, September 2018.
- [21] Y. Wu, B. Li, Y. Zhu, and W. Liu, “Energy-neutral communication protocol for living-tree bioenergy-powered wireless sensor network,” *Mobile Information Systems*, vol. 2018, Article ID 5294026, 15 pages, 2018.
 - [22] Y. Wu, B. Li, and F. Zhang, “Predictive power management for wind powered wireless sensor node,” *Future Internet*, vol. 10, no. 9, p. 85, 2018.
 - [23] D. Gao, S. Zhang, F. Zhang, T. He, and J. Zhang, “RowBee: a routing protocol based on cross-technology communication for energy-harvesting wireless sensor networks,” *IEEE Access*, vol. 7, pp. 40663–40673, 2019.
 - [24] Y. Okumura, E. Ohmori, T. Kawano, and K. Fukuda, “Field strength and its variability in VHF and UHF land mobile radio service,” *Review of the Electrical Communication Laboratory*, vol. 16, no. 9-10, pp. 825–873, 1968.
 - [25] T. O. Olasupo, “Wireless communication modeling for the deployment of tiny IoT devices in rocky and mountainous environments,” *IEEE Sensors Letters*, vol. 3, no. 7, pp. 1–4, 2019.
 - [26] S. Gao, X. Zhang, C. du, and Q. Ji, “A multichannel low-power wide-area network with high-accuracy synchronization ability for machine vibration monitoring,” *IEEE Internet of Things Journal*, vol. 6, no. 3, pp. 5040–5047, 2019.
 - [27] J. Bauer, B. Siegmann, T. Jarmer, and N. Aschenbruck, “On the potential of wireless sensor networks for the in-situ assessment of crop leaf area index,” *IEEE Sensors Letters*, vol. 128, pp. 149–159, 2016.
 - [28] Y. Qu, J. Meng, H. Wan, and Y. Li, “Preliminary study on integrated wireless smart terminals for leaf area index measurement,” *Computers and Electronics in Agriculture*, vol. 129, pp. 56–65, 2016.
 - [29] Y. Hong, N. Heerink, S. Jin, P. Berentsen, L. Zhang, and W. van der Werf, “Intercropping and agroforestry in China - Current state and trends,” *Agriculture, Ecosystems & Environment*, vol. 244, no. 15, pp. 52–61, 2017.
 - [30] S.-H. Fang, Y.-C. Cheng, and Y.-R. Chien, “Exploiting sensed radio strength and precipitation for improved distance estimation,” *IEEE Sensors Journal*, vol. 18, no. 16, pp. 6863–6873, 2018.
 - [31] M. Cheffena and M. Mohamed, “Empirical path loss models for wireless sensor network deployment in snowy environments,” *IEEE Antennas and Wireless Propagation Letters*, vol. 16, pp. 2877–2880, 2017.
 - [32] “TS RMS 1000Tsingsense Co., Beijing, ChinaMay 2020, http://www.tsingsense.com.cn/index.php?act=goods&op=index&goods_id=100076.
 - [33] R. Olsen, D. Rogers, and D. Hodge, “The aR^b relation in the calculation of rain attenuation,” *IEEE Transactions on Antennas and Propagation*, vol. 26, no. 2, pp. 318–329, 1978.

Research Article

Response Mechanism of Cotton Growth to Water and Nutrients under Drip Irrigation with Plastic Mulch in Southern Xinjiang

Meng Li,^{1,2} Jun Xiao ,³ Yungang Bai ,³ Yingji Du,⁴ Fucang Zhang,^{1,2} Houliang Cheng,^{1,2} and Haoran Wang⁴

¹Key Laboratory of Agricultural Soil and Water Engineering in Arid and Semiarid Areas of Ministry of Education, Northwest A&F University, Yangling 712100, China

²Institute of Water-Saving Agriculture in Arid Areas of China, Northwest A&F University, Yangling 712100, China

³Xinjiang Institute of Water Resources and Hydropower Research, Urumqi, 830049 Xinjiang, China

⁴College of Water Resources and Architectural Engineering, Northwest A&F University, Yangling, 712100 Shaanxi, China

Correspondence should be addressed to Jun Xiao; xiaojun100100157@163.com and Yungang Bai; xjbaiyg@sina.com

Received 8 November 2019; Revised 16 January 2020; Accepted 31 January 2020; Published 7 March 2020

Guest Editor: Zhifeng Yu

Copyright © 2020 Meng Li et al. This is an open access article distributed under the Creative Commons Attribution License, which permits unrestricted use, distribution, and reproduction in any medium, provided the original work is properly cited.

The effects of water and nutrient control measures on the cotton plant height, stem diameter, biomass, seed yield, and soil moisture under an irrigated plastic mulch production system were studied. Using field experiments in the 2018 cotton-growing season, 6 fertilization treatments (30-10.5-4.5 (N-P₂O₅-K₂O), 24-8.4-3.6 (N-P₂O₅-K₂O), 20-7-3 (N-P₂O₅-K₂O), 16-5.6-2.4 (N-P₂O₅-K₂O), 10-3.5-1.5 (N-P₂O₅-K₂O), and 0-0-0 (N-P₂O₅-K₂O) kg/mu) and 6 deficit irrigation treatments (40% PET, 60% PET, and 80% PET) were established at the cotton budding and flowering stages. Analysis of variance (ANOVA) ($P < 0.05$) was used to evaluate the significant differences among the treatments. The results showed that the effects of the water and nutrient control measures were obvious. The irrigation water use efficiency (IWUE) was the highest under the 80% deficit irrigation (T7) treatment at the flowering stage (2.62 kg/m³). Increases in cotton plant height and stem diameter were promoted by mild or moderate deficit irrigation at the flowering stage, but normal growth and development were affected by severe deficit irrigation at any growth stage. The growth indexes of cotton increased with increasing fertilization, but significant differences between each fertilization gradient were not obvious. At the same time, excessive fertilization not only had a positive effect on the LAI (leaf area index) and yield but also caused fertilizer waste and unnecessary cotton growth. The cotton seed yield and single boll yield reached their highest values (566 kg/mu) under the 1.2 times fertilizer treatment (T9), but the 0.8 times fertilizer treatment had the highest IWUE among the nutrient control treatments (1.91 kg/m³). Therefore, it is suggested that deficit irrigation at 60~80% of the potential evapotranspiration (PET) at the flowering stage and 16-5.6-2.4 (N-P₂O₅-K₂O) fertilizer be applied as an optimal water and nutrient management strategy to maximize the seed cotton yield, IWUE, and overall growth and development of cotton.

1. Introduction

Xinjiang is the most important high-quality commodity cotton production base in China. Cotton production is completely dependent on irrigation. At present, the shortage of irrigation water resources restricts the comprehensive improvement of cotton productivity [1]. Water-deficit irrigation practices are inevitable for the sustainable development

of Xinjiang's agricultural economy [2–4]. Saline-alkali land is widely distributed in Xinjiang, accounting for approximately 32% of the total area of cultivated land [5, 6]. Due to soil salinization and secondary salinization, the average annual loss of grain is $2-2.5 \times 10^9$ kg and of cotton is 5×10^8 kg [7]. In addition, due to irrational irrigation, the increase in the groundwater level and phreatic water evaporation intensify the occurrence of secondary salinization of

soil [8]. Therefore, it is urgent that saline-alkali land be managed appropriately to ensure the sustainable development of land resources. Second, there is scarce rainfall and a lack of water resources in Xinjiang, and rational utilization of water resources to increase crop water and fertilizer use efficiencies are necessary. Agriculture in Xinjiang requires irrigation. To solve water shortages, we must achieve agricultural water savings to promote the healthy development of the ecological environment.

Drip irrigation under plastic film mulch has been widely used in arid or semiarid regions, such as the Tarim River Basin in the Xinjiang Uygur Autonomous Region, over the past two decades [9–11], because it incorporates the advantages of plastic film mulch and drip irrigation. In this irrigation system, the soil is covered by a plastic film to decrease evaporation and eliminate the energy exchange between the atmosphere and the soil at the same time [12]. Additionally, this method prevents soil salinization to some degree [13, 14]. Drip irrigation under plastic mulch can supply enough heat for sowing in the frigid spring (sowing season), especially for summer crops such as cotton, which are among the most important in Xinjiang's agricultural production. In addition, crops can acquire adequate water during the whole growing season despite high evaporative demands under this pattern [15, 16]. On the other hand, by avoiding water vapor waste and decreasing needless evaporation, plastic mulch drip irrigation has proven to be an economical way to change the soil-microclimate thermal environment and improve water use efficiency [17]. In this context, crop evapotranspiration changes under plastic mulch compared to that under bare soil.

The effects of water on crop growth are mainly reflected in the root system, plant height, stem diameter, leaf area index, and yield. The effects of water on crop physiology are mainly related to leaf water potential, enzyme activity, photosynthetic rate, transpiration rate, and stomatal conductance. A large number of studies have been conducted, generally focusing on the response of crops to water deficit. In terms of crop growth, Kozłowski and Winget [18] and Goldhamer and Fereres [19] showed that water stress can cause stems to shrink. Molz and Klepper [20] noted that the distribution of roots under moderate drought treatment (50%–60% of field capacity) increased significantly in the lower layer, the root biomass under the sufficient water supply treatment (80%–90% of field capacity) was mainly concentrated in the upper layer, and the total biomass of the root system was higher. Other researchers studying different crops [21–25] (cotton, pea, maize, winter wheat, etc.) showed that water deficit inhibits plant height growth, leaf area expansion, and dry matter accumulation, especially during the crop seedling stage, and that crop yield and composition are also affected because of the inhibited crop growth. In crop physiology, when moisture is insufficient, stomata may close and stomatal conductance may be reduced. On the one hand, transpiration loss through the stomata decreases. On the other hand, CO_2 , which enters the blade through the stomata, decreases, resulting in a decrease in the photosynthetic rate. Generally, the transpiration rate decreases more than the photosynthesis rate. Under light-water stress, stomatal

closure may increase water use efficiency. Farquhar and Sharkey [26] showed that the effect of water stress on the photosynthesis of crops was also affected by nonstomatal factors; that is, the activities of the photosynthetic organs of crops were decreased under water stress, the diffusivity and RuBP carboxylase activity of mesophyll were decreased, and the transport of electrons and phosphorylation were inhibited. The chlorophyll content decreased, resulting in a decline in the photosynthesis rate.

Similar to crop responses to water, crop responses to nutrients are mainly reflected in crop morphology, physiology, and biochemistry. Li et al. [27] stated that nitrogen fertilization was the dominant factor affecting the leaf area index and plant height in the early growth stage of spring wheat, and the combination of nitrogen and phosphorus could promote increases in plant height and leaf area of spring wheat. Bezborodov et al. [28], through cotton field experiments with drip irrigation, found that the amount of nitrogen application significantly affected the dry matter weight, nitrogen accumulation, and yield of hybrid cotton. When the amount of applied nitrogen was 450 kg hm^{-2} , the frequency of nitrogen application had no significant effect on cotton growth. Cowell and Dawes [29] and Anderson and Nelson [30] studied the effects of nutrient stress on grain filling. The results showed that under nutrient stress, stress-related proteins increased significantly in the early and middle stages of grain filling, photosynthesis of grains decreased, respiration increased in the late stages, nitrogen metabolism of grains was significantly affected, and glutenin and embryo protein expression was delayed. Additionally, the synthesis of protein and fat decreased, resulting in insufficient grain filling and lower yield; the photosynthesis and respiration of rice leaves decreased significantly during grain filling; the expression of scavenging reactive oxygen species (ROS) proteins decreased; the expression of ROS-producing proteins and stress signal transduction proteins increased; the stress resistance of rice decreased; the accumulation of ROS in leaves increased; and the senescence of rice increased.

Therefore, the effects of different control measures (water and nutrient control measures) on soil-water movement and crop growth characteristics and the relationships between different control measures and soil-water availability, water consumption, crop yield, and composition were quantified. The objective of this study was to determine the optimal control measures under a drip irrigation-plastic mulch cotton production system. This study provides a reference for improving crop water and fertilizer utilization and crop yields. In addition, these findings also have important significance for guiding irrigation and fertilization, water conservation, and sustainable development of agriculture in arid saline-alkaline areas.

2. Materials and Methods

2.1. Experimental Site Description. The experiments were performed at the 31st Regiment of the Second Agricultural Division, which belongs to the Tarim Reclamation Area of the Second Agricultural Division of Xinjiang Production



FIGURE 1: The soil profile and experimental plot.

TABLE 1: Initial soil properties of experimental plots.

Layer (cm)	Clay (%)	Silt (%)	Bulk density (g·cm ⁻³)	Wilting point (cm ³ ·cm ⁻³)	Field capacity (cm ³ ·cm ⁻³)	Saturated water content (cm ³ ·cm ⁻³)	Initial water content (cm ³ ·cm ⁻³)
0-10	4.16	46.29	1.59	0.047	0.207	0.278	0.152
10-20	4.16	46.29	1.44	0.047	0.228	0.360	0.150
20-30	3.8	52.65	1.67	0.045	0.161	0.215	0.183
30-40	3.8	52.65	1.58	0.045	0.175	0.247	0.217
40-50	3.8	47.83	1.68	0.046	0.172	0.235	0.216
50-60	3.8	47.83	1.47	0.047	0.230	0.357	0.282
60-80	4.2	46.99	1.70	0.047	0.122	0.246	0.205
80-100	4.1	46.35	1.66	0.047	0.082	0.246	0.225

and Construction Corps. The field site (86°56'E, 40°53'N) is located in the suburbs of Korla in southern Xinjiang, an autonomous region in northwestern China, which is at the foot of the Tianshan Mountain and the northeast edge of the Taklamakan Desert. This region has a typical continental arid desert climate in the north temperate zone and belongs to the Kaidu-Peacock River Basin (a tributary of the Tarim River). Large temperature fluctuations occur between day and night, and the area is also characterized by many sunshine hours, hot winters and cold summers, drought, and abundant light and heat. These climate conditions are particularly conducive to the growth of cotton. The annual and average precipitations during the cotton-growing season are approximately 34.1 mm and 30.6 mm, respectively. The mean annual potential evaporation (measured using an evaporation pan with an inside diameter equal to 20 cm) reaches 2417 mm, with 2082 mm in the cotton-growing season. In the same period, the evaporation is 50-80 times the precipitation, the annual average sunshine hours are approximately 2941.8, the annual average temperature is 10.9°C, and the annual accumulated temperature is 4218.3°C, while the frost-free period is 180-220 days. Because of the high evaporation, agriculture and forestry in the region rely entirely on irrigation. The soil textures of the experimental fields were silty loam (41.4% sand, 54.4% silt, and 4.2% clay) and sandy loam (50.2% sand, 46.0% silt, and 3.8% clay) (Figure 1). The soil bulk density of the experimental field varied from 1.44 g·cm⁻³ to 1.68 g·cm⁻³ in the 0-1 m soil profile, and the saturated water content of the soil was nearly 0.27. Before the experiment, the 0-1.0 m soil depth was

divided into 5 layers, and the soil particle size distribution from each layer was analyzed by a laser particle size analyzer. The wilting point, field water capacity, and saturated water content were determined by high-speed centrifugation. The bulk density of each layer was measured by the ring knife method. The initial soil-water content was also determined before planting by the soil-drying method. The soil properties, including the saturated water content, field capacity, and wilting point in the experimental field, are listed in Table 1 [31–33]. The average depth of groundwater was approximately 1.5 m. The experimental cotton cultivar was Xinluzhong 78 (*Gossypium hirsutum* L.).

2.2. Experimental Design. The experiments were conducted during the 2018 cotton-growing seasons under drip irrigation with plastic film mulch. A planting setup of “one film, two pipes, and four rows of cotton” was used (Figure 2), that is, 10 cm + 10 cm + 10 cm + 46 cm + 10 cm + 10 cm + 10 cm, with row spacings of 10 cm, 10 cm, 10 cm, and 46 cm with the plastic film. The plant spacing with a row was 10 cm, and the planting density was 22 plants m⁻². A polyethylene resin-embedded thin-walled labyrinth drip tape with an inner diameter of 16 mm was used, with an emitter spacing of 30 cm and emitter discharge range of 2.4 L/h. In this pattern, two drip pipes were placed in the wide rows beneath the film mulch, so each basic planting unit was divided into three parts: a wide row, a narrow row, and bare soil (Figure 2). The plot size was 7 m × 7 m. To reduce experimental error, 1 m protection lines were arranged between each plot and two replicates were set up in each experiment.

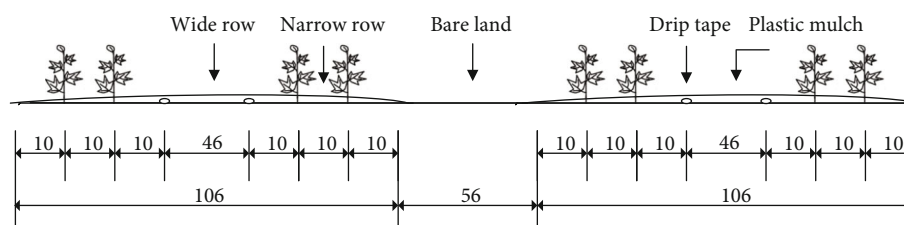


FIGURE 2: Drip irrigation pipe arrangement. Note: the arrows point to the soil moisture-monitoring points.

TABLE 2: Different irrigation treatments used in the experiment.

Treatment	Emergence	Budding	Flowering and boll development	Boll opening	Irrigation amount	Degree of deficit
T2	0	0.4 PET	PET	0	322.54	I
T3	0	0.6 PET	PET	0	298.21	II
T4	0	0.8 PET	PET	0	298.13	III
T5	0	PET	0.4 PET	0	338.28	I
T6	0	PET	0.6 PET	0	322.05	II
T7	0	PET	0.8 PET	0	321.99	III
T1	0	PET	PET	0	369.74	IV

Note: I: severe deficit; II: moderate deficit; III: mild deficit; IV: no deficit.

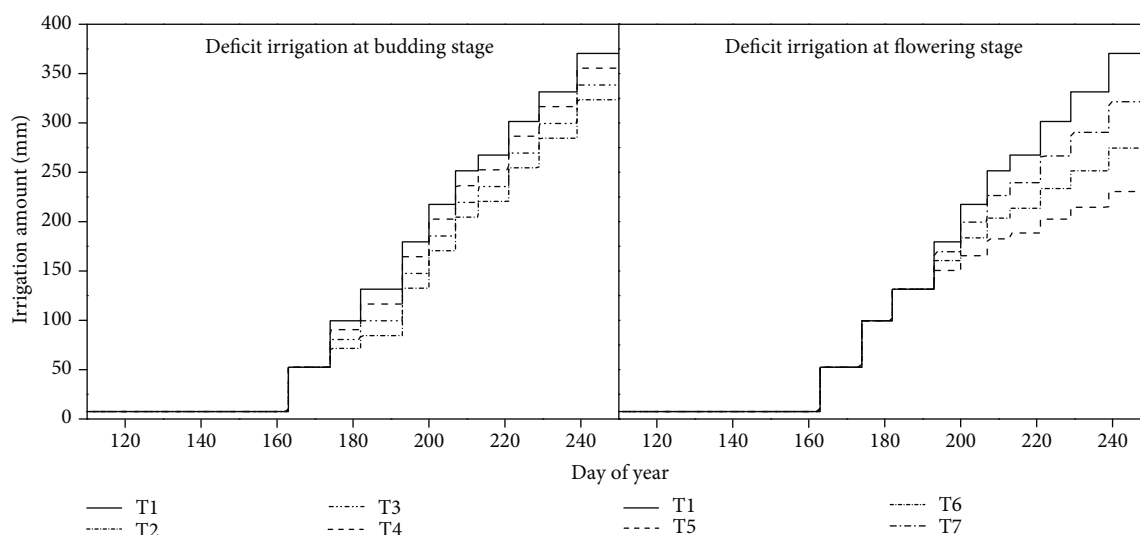


FIGURE 3: Irrigation during the cotton growth period.

The irrigation water mainly came from the Peacock River, with an average irrigation salinity of 0.8 g/L. To provide sufficient water and to leach salt from the soil, flood irrigation (irrigation amount of approximately 300 mm) was carried out every spring (early March). The experimental treatments were as follows.

2.2.1. Water Control Measures. When the cotton started to emerge, drip irrigation was conducted. The conventional irrigation amount in this region is approximately 500 mm based on the annual water requirement for cotton. The irrigation amounts in this experiment were calculated based on the potential evapotranspiration (PET) during the cotton growth season, which was calculated according to the meteorological data. The water control measures were mainly divided into 10 water treatments. Irrigation amounts corresponding to

0.4, 0.6, and 0.8 times the potential evapotranspiration (0.4 PET, 0.6 PET, and 0.8 PET) were applied in the budding, flowering, and boll development stages, respectively, and were designated as T2-T7. Full irrigation was designated T1 (PET). Irrigation water was from a local reservoir, and the planned irrigation period was 7~10 days in the growing season, with no irrigation during cotton emergence and boll-opening periods. A water flowmeter was used to control the water volume. Fertilization was carried out according to the local fertilization practices (20-7-3 kg/mu (N-P₂O₅-K₂O)) and adjusted according to actual local conditions. The treatment details and irrigation schedules are shown in Table 2 and Figure 3.

2.2.2. Nutrient Control Measures. Cotton was sown after plowing on 5 April. Basal fertilizers (700 kg ha⁻¹ diammonium

TABLE 3: Fertilization treatments at different cotton growth periods.

Date	Full fertilization	Urea (g)	Diammonium phosphate (g)	Crystal potassium (g)
June 23rd	F	320	127	36
July 1st	F	320	127	36
July 12th	F	320	127	36
July 19th	2F	640	254	72
July 26th	2F	640	254	72
August 1st	F	320	127	36
August 9th	F	320	127	36
August 17th	F	320	127	36
Total	10F	3200	1270	360

phosphate with 18% N and 46% P, 75 kg ha⁻¹ urea with 46% N, 75 kg ha⁻¹ potassium sulfate with 45% K₂O, and 600 kg ha⁻¹ compound fertilizer with 25% N, 25% K, and 25% P) were directly applied in the field before sowing, following local agronomic practices. Additional fertilizers were applied through the drip irrigation system during the cotton-growing season. Nutrient control measures were mainly aimed at the regulation of nitrogen, phosphorus, and potassium fertilizers. Urea, diammonium phosphate, and crystal potassium were used in the nitrogen, phosphorus, and potassium fertilizer treatments, respectively, mainly in the flowering and boll development stages. According to the recommended level of fertilization of 20-7-3 kg/mu (N-P₂O₅-K₂O), 6 fertilization treatments were set up on the basis of the annual growth requirements and were converted to nitrogen, phosphorus, and potassium gradients, specifically, 30-10.5-4.5 (N-P₂O₅-K₂O), 24-8.4-3.6 (N-P₂O₅-K₂O), 16-5.6-2.4 (N-P₂O₅-K₂O), 10-3.5-1.5 (N-P₂O₅-K₂O), and 0-0-0 (N-P₂O₅-K₂O) kg/mu (designated 1.5F, 1.2F, 0.8F, 0.5F, and 0F), recorded as T8, T9, T10, T11, and T12. Irrigation water also used local reservoir water, and the planned irrigation period was 7-10 days during the growth period. No irrigation was required for the cotton seedling and boll-opening periods. The irrigation amounts were based on the potential evapotranspiration (PET) and adjusted according to actual local conditions. The treatment details and fertilization schedules are shown in Table 3 and Figure 4.

2.2.3. Field Control Measures. To reflect the benefits of drip irrigation under mulch more directly (the plastic film was released on June 10th, after cotton seeding, ensuring cotton growth), an experimental plot was selected randomly for examination of the differences in soil moisture, soil temperature, and cotton growth indexes between plastic mulch and bare soil, and this was recorded as treatment 13 (T13). The irrigation and nutrient measures were the same as those of the control treatment (T1). To prevent the low temperature from affecting the emergence of cotton, the plastic film mulch was deployed on June 10th.

(1) Phenological Phases and Agronomic Measures. Phenological monitoring under the different treatments was not comprehensive, and the subtle differences between different

treatments were not fully considered. However, in the second year of the experiment, the time points of agronomic measures were adjusted according to the different treatments. Main phenological phases and agronomic measures applied during the cotton-growing season are shown in Tables 4 and 5.

2.3. Data Collection and Analysis

2.3.1. Meteorological Data. Daily meteorological data were used for calculating the PET. The minimum daily data included solar radiation, maximum temperature, minimum temperature, and rainfall. Daily meteorological data were collected from a HOBOWare 3.7 weather station (Onset Computer Corporation, Pocasset, USA). The daily meteorological data during the two cotton-growing seasons are shown in Figure 5.

The crop evapotranspiration (ET) was calculated by FAO56 Penman-Monteith models. According to the FAO56 Penman-Monteith method, the wind speed and relative humidity were considered in the calculation process. In Bayingolin of Xinjiang, the windy climate and sandy soils had a great impact on the cotton growth process.

FAO56 Penman-Monteith [34, 35]: solar radiation, maximum and minimum temperature, wind speed, and relative humidity

$$ET_0 = \frac{0.408\Delta(R_n - G) + r(900/(T + 273))u_2(e_s - e_a)}{\Delta + r(1 + 0.34u_2)}, \quad (1)$$

where ET_0 is the reference rate of evapotranspiration (mm day⁻¹), R_n is the net radiation on the crop surface (MJ m⁻² day⁻¹), G is the soil heat flux (MJ m⁻² day⁻¹), T is the daily mean temperature at a 2 m height (°C), u_2 is the wind speed at a 2 m height (m/s), e_s is the saturated vapor pressure (kpa), e_a is the actual vapor pressure (kpa), $e_s - e_a$ is the saturated vapor pressure difference (kpa), Δ is the slope of the saturated vapor pressure curve, and γ is a thermometer constant (kpa/°C).

2.3.2. Determination of Soil Physical and Chemical Indexes

(1) Measurement of Soil-Water Content. Because there were multiple irrigation events during the cotton-growing season, soil was collected only before sowing, before irrigation, at harvesting, and at key cotton growth periods, and the soil-water content was also measured in the flowering and boll development periods. Two sampling points were set up in each plot, and the soil-water content was measured by the drying method (105°C, 24 h) in the same section at the wide line (below the dripper), narrow line, and middle position between the bare soil. The sampled soil layers were 0-10, 10-20, 20-40, 40-60, 60-80, and 80-100 cm.

(2) Measurement of Soil-Salt Content. A DDS-307 conductivity meter was used to determine the conductivity of the soil in a soil-water ratio of 1:5. The salt content in the soil was determined according to the relationship between the conductivity and the total salt content.

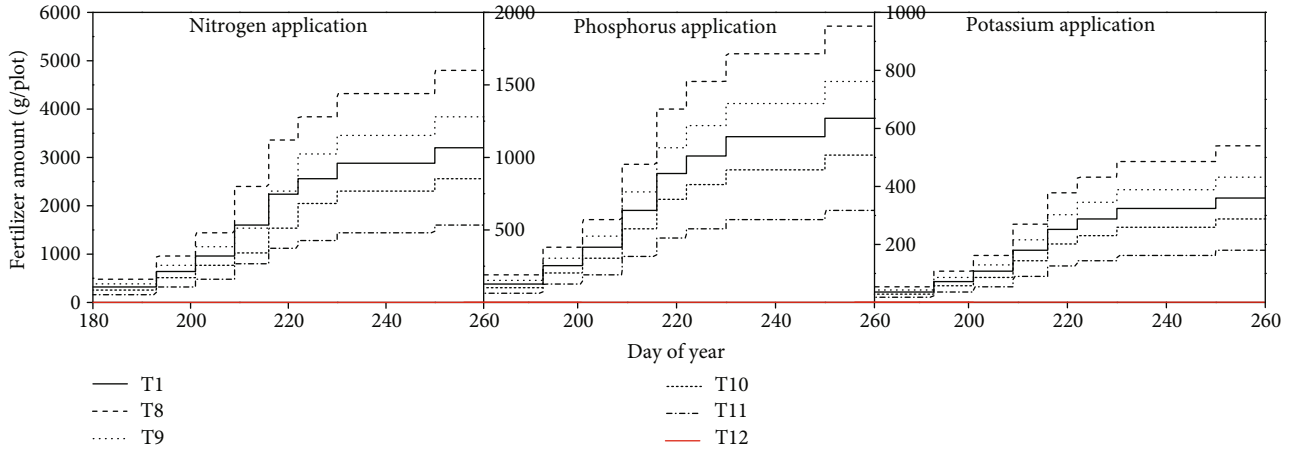


FIGURE 4: Fertilization during the cotton growth period.

TABLE 4: Main phenological phases of cotton.

	Sowing	Emergence	Trifoliolate	Budding	Flowering (closure)	Boll opening
Date	April 5th	April 16th	May 10th	June 2nd	July 4th	August 21st

TABLE 5: Main agronomic measures applied during the cotton-growing season.

	Pesticide	Pesticide	Pesticide	Pesticide	Film uncovering	Topping
Date	May 13th	June 17th	July 5th	July 10th	June 10th	July 1st
Measure	DPC	DPC Acetamiprid pyridaben Emamectin benzoate	Acetamiprid pyridaben	DPC Pyridaben Boron fertilizer		

Note: DPC: mepiquat chloride.

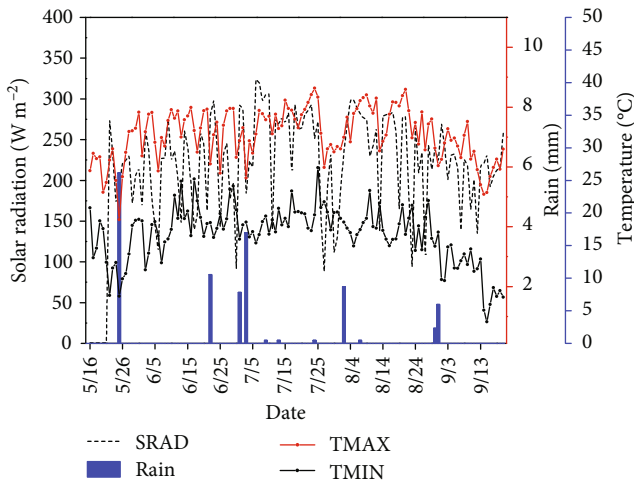


FIGURE 5: Daily maximum and minimum temperatures, rainfall, and solar radiation during two cotton-growing seasons of 2018.

(3) *Soil Evaporation*. Soil evaporation was measured at 20:00 each day using a homemade miniature evaporating dish (a PVC tube with an inner diameter of 12.5 cm and a height of 20 cm). Daily changes were measured at each growth stage from 8:00 to 20:00 once every 2 h.

2.3.3. Cotton Growth Measurements

(1) *Emergence Rate*. The emergence of cotton seedlings was observed every three days after sowing. At the end of the seedling stage, the survival rate was measured as emergence per unit area, and then the emergence rate of the whole area was estimated. The emergence rate was calculated as follows:

$$\text{Emergence rate} = \left(\frac{\text{seedling number}}{\text{number of seeds sown}} \right) * 100\%. \quad (2)$$

(2) *Cotton Growth Index*. Six representative cotton plants (three from the inside line and three from the outside line) with uniform growth were selected from each plot. The plant height, leaf area index, stem diameter, and effective boll number were measured at each stage of cotton growth, and additional tests were conducted at the flowering and boll development stages. The cotton yield was measured after the experiments.

Plant height: the distance between the cotyledon node and apical growing point was measured by a tape measure.

Stem diameter: the stem diameter of the cotyledon node was measured using a Vernier caliper.

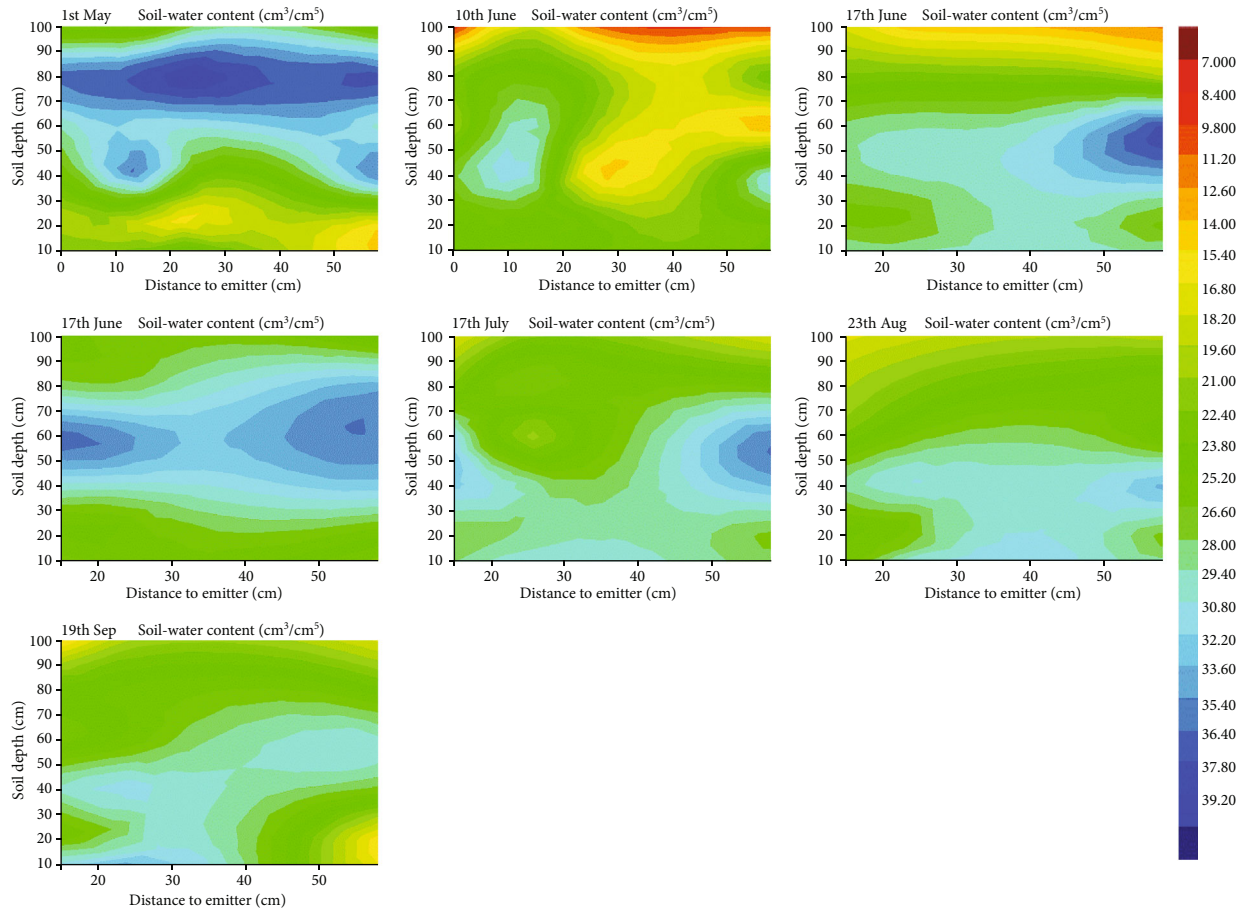


FIGURE 6: Soil-water distribution in the CK(T1) plots during different cotton growth periods (1st May, 10th June, 17th June, 27th June, 17th July, 23rd August, and 19th September).

Leaf area index: the length and width of each leaf were measured with a tape, the leaf area of the whole individual plant was then calculated, and the leaf area index was finally calculated as follows:

$$\text{LAI} = \frac{\text{leaf area}}{\text{ground area}}, \quad (3)$$

where LAI is the leaf area index, a dimensionless quantity that characterizes plant canopies.

Dry matter quality: the aboveground parts of cotton plants were separated from the stem base and underground parts, and the surface dust was removed. The aboveground parts were put into an oven at 105°C for 1 hour. The sample was dried to constant weight at 75°C and then weighed after cooling.

Yield and components: at harvest, uniform and robustly growing areas of 6.67 m² were randomly selected from three fields from each treatment. The number of bolls larger than 2 cm in diameter was recorded. A total of 30 bolls, 40 bolls, and 30 bolls were picked from the upper, middle, and lower layers of cotton plants in each plot, respectively, to calculate the 100-boll weight.

2.3.4. Data Analysis. The data were analyzed by the SPSS statistical program, and analysis of variance (ANOVA) was conducted to evaluate the effects of the treatments on plant height, stem diameter, LAI, and biomass. Duncan's multiple range test was used to compare and rank the treatment means. Differences were declared significant at $P < 0.05$ and $P < 0.01$.

3. Results and Discussion

3.1. Soil-Water Content. Because drip irrigation is a type of partial irrigation, the area under the dripper is humid during irrigation; after irrigation, soil moisture is changed by many factors, such as the crop root system, atmospheric evaporation, self-gravity, and the influence of film mulching, which makes the conditions in the surrounding soil more complex and causes soil moisture to have both temporal and spatial distribution patterns [36]. The spatial and temporal distribution of soil moisture is not homogeneous (Figure 6).

In the 0–30 cm soil layer, the soil-water content increased gradually with increasing soil depth; when the soil depth reached 40 cm, the high soil-water content decreased slightly. The soil-water content on May 1st (initial) showed a continuous increasing trend. Because the main roots of cotton are distributed in the 0–40 cm layer, the water absorption of roots

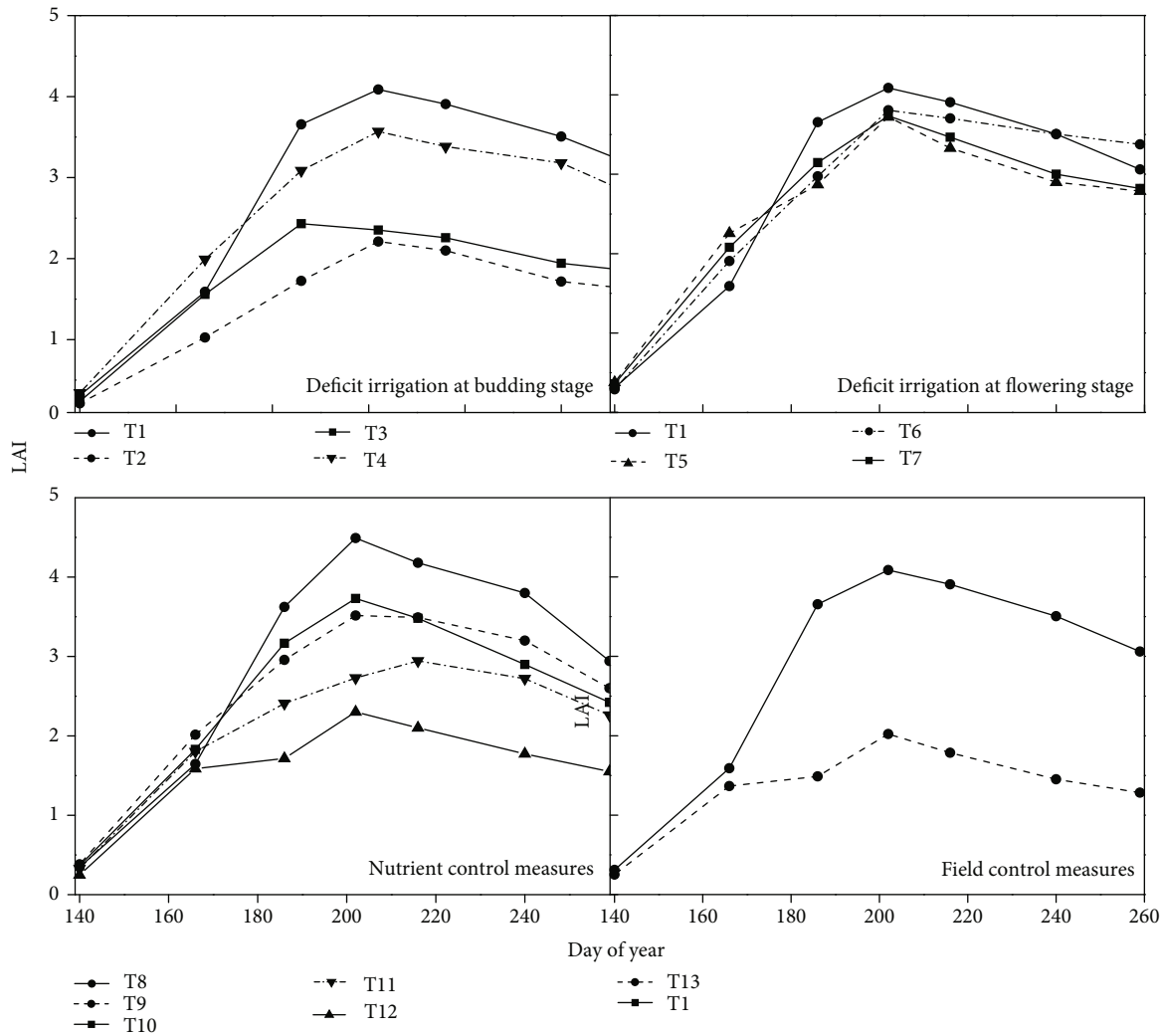


FIGURE 7: Changes in the LAI during the cotton growth period under different treatments.

mainly occurs in this layer. The water absorption of roots decreased gradually with increasing depth, from top to bottom. Therefore, the soil-water content increased gradually in the 0-30 cm layer, but the degree of change in this layer was not clear. In the 40-80 cm soil layer, the soil-water content was almost constant.

In addition, on May 1st, the soil-water content in the 80-100 cm soil layer was higher than that in the 60-80 cm soil layer, possibly because the average depth of the groundwater was shallow, and the groundwater recharged the upper soil. The soil-water content in other areas was higher than that at 80-100 cm, which indicates that seepage occurred at 80 cm. Root seepage should be estimated when calculating the water consumption of cotton.

The soil-water content in the wide rows was the highest in the 0-5 cm surface layer and was higher than that of the bare land and narrow rows. This is because the root distribution was more "sparse" in wide rows than narrow rows, and film mulching reduced the loss of soil moisture in the 0-5 cm surface layer. For the 5-40 cm soil layer, the soil-water content during the growth period showed the trend of bare land > wide row > narrow row. The root system was mainly

distributed in the wide and narrow rows during the growth period and occupied a large proportion of the narrow rows. During cotton growth, cotton roots absorb more water from the soil of narrow rows, while the root system was less distributed in the bare land. Additionally, the cotton canopy shields the bare land from direct sunlight, so the soil-water content in the bare land was the highest, and that in the narrow rows was the lowest. For the soil layer below 40 cm, the soil-water content between the bare land, narrow rows, and wide rows was almost equal. This was mainly because the soil below 40 cm was subjected to a smaller vertical effect of cotton root water absorption and soil evaporation, and after irrigation during the growth period, the soil moisture under 40 cm was redistributed mainly by its own gravity because the time of soil extraction was one day before irrigation or two or three days after irrigation, and the soil texture was sand. The soil-water content in the soil layer below 40 cm was uniform during the growth period, and the water potential gradient between the bare land, narrow rows, and wide rows was small, so the water content in the soil layer below 40 cm showed slight differences along a horizontal gradient.

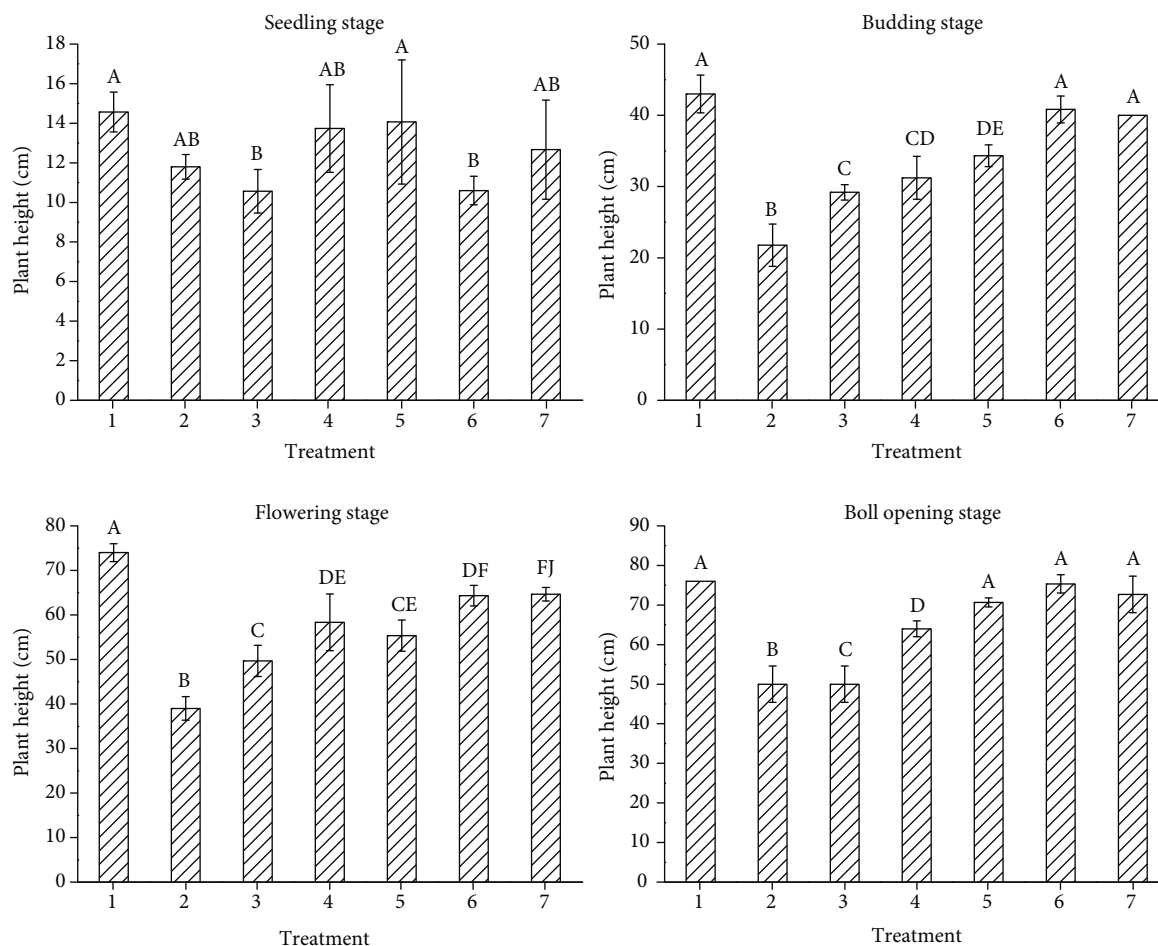


FIGURE 8: Changes in cotton plant height under different irrigation treatments.

3.2. Leaf Area Index (LAI). The changes in the LAI during cotton growth under each treatment are shown in Figure 7. During the cotton growth period, the LAI showed a trend of increasing at first and then decreasing with time.

In the early growth stages, the LAI increased as the fertilizer application increased under the same irrigation amount, which may be because in the early growth stage, cotton needs to absorb a large number of nutrients for vegetative growth and to increase the leaf area, thereby promoting photosynthesis and synthesis of organic compounds. Therefore, increasing the amount of fertilizer applied in the early stage can promote the growth of cotton. The LAI reached its maximum value at approximately 190–200 days in 2018, which was in the period of vigorous vegetative growth and sufficient photosynthesis of cotton. Then, with the passage of time, the growth of cotton changed from vegetative growth to reproductive growth. In this stage, the water and nutrients needed for cotton growth decreased, and those in the leaves were gradually transferred to the reproductive organs. The rate of the increase in the LAI declined, and the LAI began to decrease. At this time, the LAI increased with increasing fertilizer application, although excessive fertilizer application inhibited cotton growth to a certain extent, which led to the maximum LAI of cotton under the T9 treatment being lower than that under the T10 treatment. Since the test site had

saline-alkali soil, drip irrigation resulted in the leaching of salt, enabling the cotton root system to avoid salt stress and ensuring the growth of cotton. Therefore, the LAI increased with increasing irrigation amount with the same fertilizer application conditions. At the same time, the cumulative amount of leaf area was lower in the budding stage deficit treatments (T2, T3, and T4) than in the flowering stage deficit treatments (T5, T6, and T7). This was due to the lack of irrigation in the budding stage, which limits the vegetative growth of cotton and has a greater impact than deficits in the flowering and boll development stages.

3.3. Plant Height and Stem Diameter. The effects of different irrigation and fertilizer treatments on cotton height and stem diameter are shown in Figures 8 and 9, respectively. The topping date was July 1st, which was at the flowering stage, and thus, the increase in cotton height was influenced by the topping. Before topping, the cotton plant height increased rapidly by 24.23–47.54 cm, and after topping, the height only increased by 1.79–6.00 cm. The cotton height and stem diameter during the topping period and mature period were similar, mainly because topping can control the vegetative growth of cotton, and during the mature period, the cotton height and stem diameter basically no longer increased.

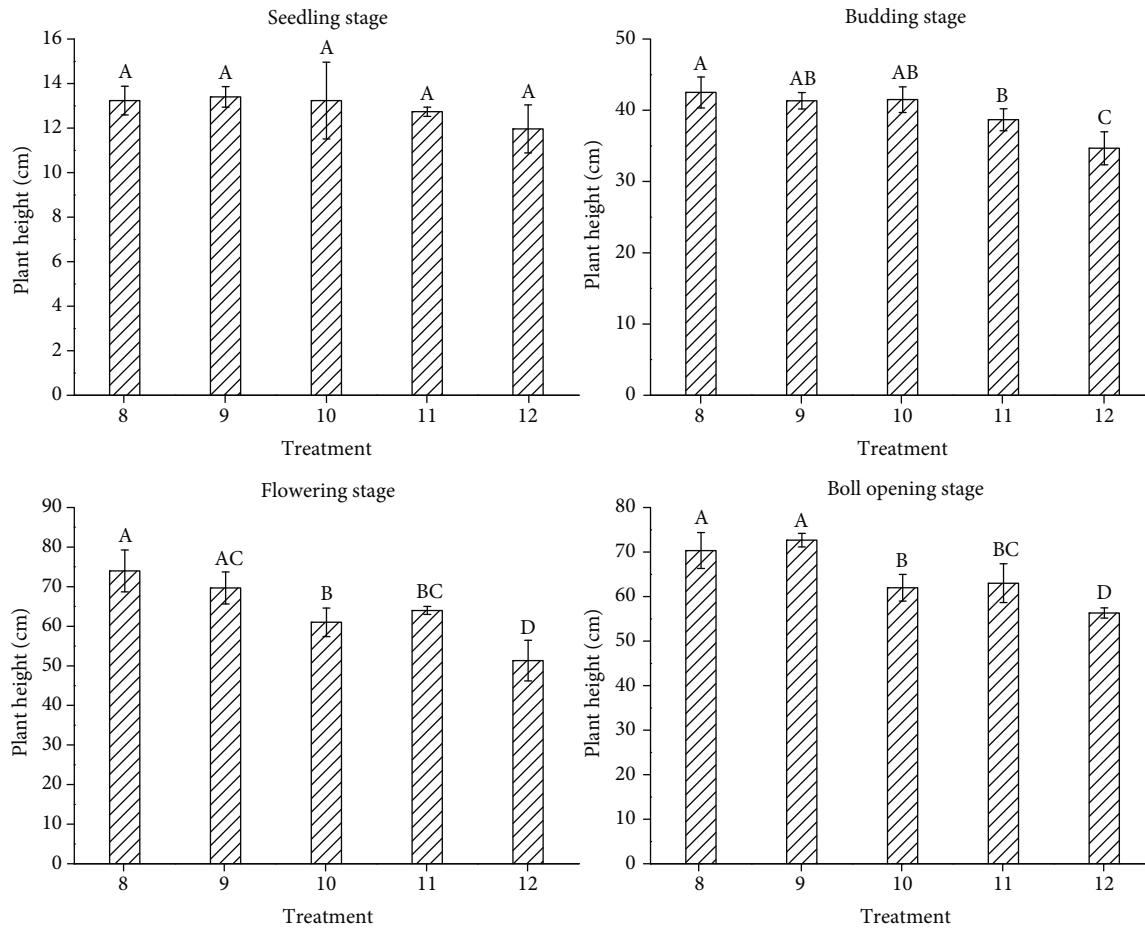


FIGURE 9: Changes in cotton plant height under different fertilization treatments.

With the increase in fertilizer application, the height increased at the early stage and then decreased at the later stage; specifically, the height of cotton plants increased with fertilizer application at all stages under the most severe deficit irrigation conditions (T2 and T5). Under saline soil conditions, the height of the cotton plants increased with the irrigation amount, and the average plant height under the flowering stage deficit irrigation treatments (T5, T6, and T7) was 72.92 cm, which was 36.63% and 3.03% higher than those of the budding stage deficit irrigation treatment (T2, T3, and T4) and full irrigation treatment (T1), respectively. In other words, deficit irrigation at the flowering stage has little effect on cotton height, and efficient water utilization can also be achieved by controlling the irrigation amount at this stage.

Figures 8 and 9 show that in each period of cotton growth, most of the plant heights under the different fertilization treatments were not significantly different. However, there were significant differences in plant height under different irrigation treatments. This indicated that the effect of water control measures was greater than that of nutrient control measures. Reasonable control of irrigation can ensure that the plant height of cotton is within the normal range. At the same time, we found that there were no significant differences between the moderate and mild deficit irrigation

treatments in the flowering stage (T6 and T7) and the full irrigation treatment (T1).

During the growth period, the stem diameter changes over time were basically the same, increasing first and then becoming stable. Since stem diameter variations reflect the combined effects of environmental variables and plant vegetative characteristics, the maximum stem diameter had a great response to water stress under different water conditions [37].

In terms of nutrient control measures, cotton height was positively correlated with the amount of fertilizer application, and stem diameter also increased with the increase in fertilizer. For the water control measures, cotton height was inversely correlated with the amount of irrigation applied. Deficit irrigation at the budding stage had the most obvious effect on cotton height, while stem diameter decreased with increasing irrigation amount. However, the nonhomogeneous soil qualities and proximity to the bare field hindered the growth of cotton and affected the experimental results to a certain extent.

Statistical analysis indicated that different amounts of irrigation and fertilization had little effect on stem diameter (Figures 10 and 11). The difference in stem diameter between the nutrient control treatments was no more than 2 mm and no more than 4 mm between the water control treatments. Except for the significant difference in stem diameter between

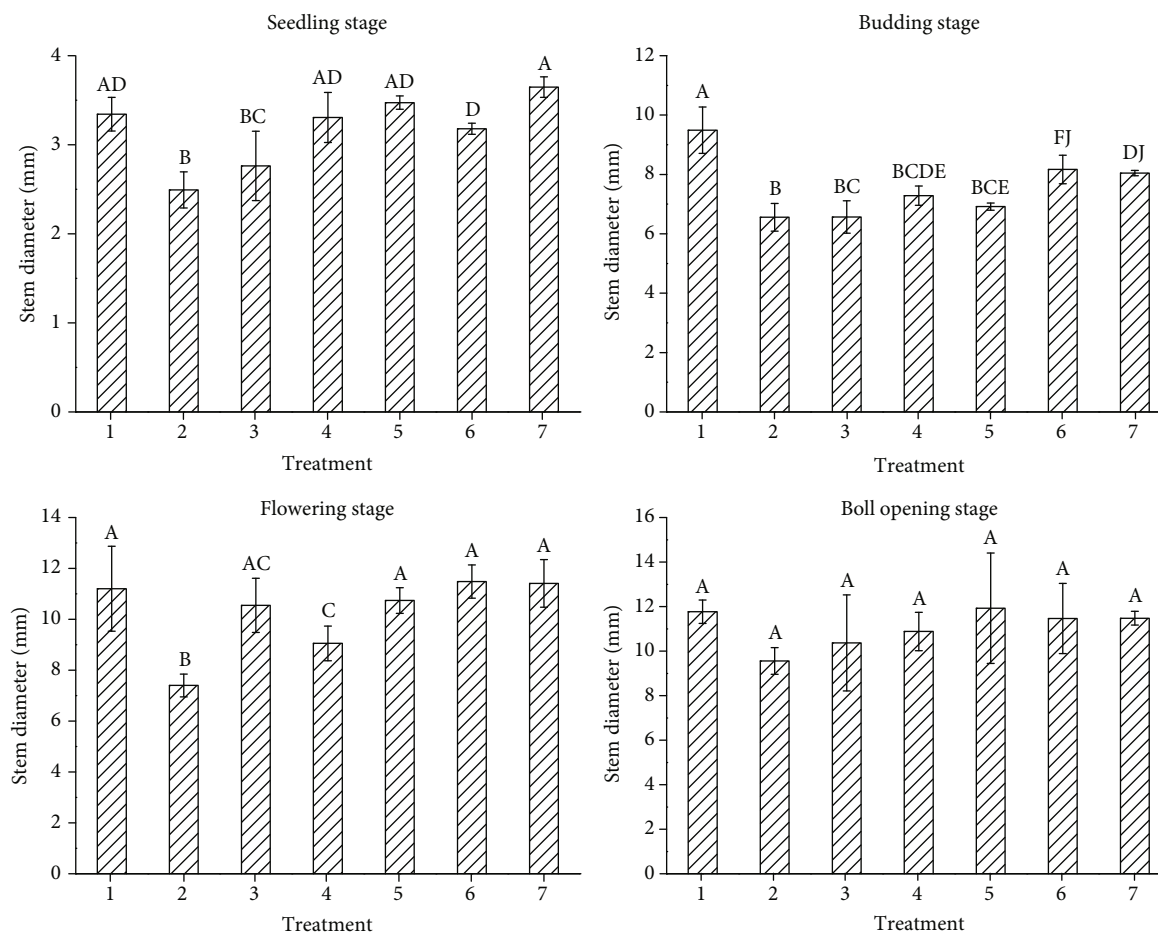


FIGURE 10: Changes in cotton stem diameter under different irrigation treatments.

the severe deficit irrigation in the budding stage (T2) and the full irrigation treatment (T1), the difference between treatments was not obvious. At the same time, because of errors in the measurement process, the changes in irrigation and fertilization amount had no significant effect on the stem diameter.

3.4. Biomass. Biomass is the basis for crop production. According to the local topping date, the biomass at the topping period was compared with that at the later stage. In the early stage of cotton growth, the main components of cotton biomass were stems, leaves, and other vegetative organs; in the late stage, the content of nutrients (water, nutrients, etc.) transferred from vegetative organs such as stems and leaves to reproductive organs was far lower than the change in biomass. The biomass of yield-related organs showed a trend of gradual increase with the progression of the growth period, and the most intense change was at the beginning of the boll development stage. This is because in the reproductive growth stage, roots, stems, leaves, and other vegetative organs transfer most of their nutrients to the reproductive organs, promoting the rapid development of the reproductive organs. In the later growth stage, the proportion of yield-related organs to the total biomass is considered the stem-leaf yield composition.

The proportion of biomass of cotton organs at different growth stages is shown in Figure 12. In the seedling stage, the dry matter was mainly concentrated on the leaves because of the thin stems, and leaf dry matter accounted for more than 70% of the total dry matter mass. After the seedling stage, the proportion of dry matter mass of reproductive organs among the total dry matter mass increased continuously, and the proportions at the budding, early flowering, late flowering, and boll-opening stages were 4.27~13.05%, 17.53~21.88%, 51.34~58.63%, and 51.92~59.48% under the different treatments, respectively. Under the experimental saline-alkaline soil, the dry matter of different organs of cotton increased with increasing fertilizer amount. In the boll development stage, the average total dry matter mass of T8 was 177.42 g, 41.66%, 40.64%, 14.19%, and 4.12% higher than those of T12, T11, T10, and T9, respectively.

3.5. Yield Components and Irrigation Water Use Efficiency (IWUE). It can be seen from Figure 13 that the cotton yield was different under the different fertilization treatments, showing a trend of $1.5F > 1.2F > F > 0.8F > 0.5F > 0F$, which shows that the yearly increase in N, P, and K can effectively guarantee cotton production.

The different irrigation and fertilization treatments had extremely significant effects on the boll number (Table 6),

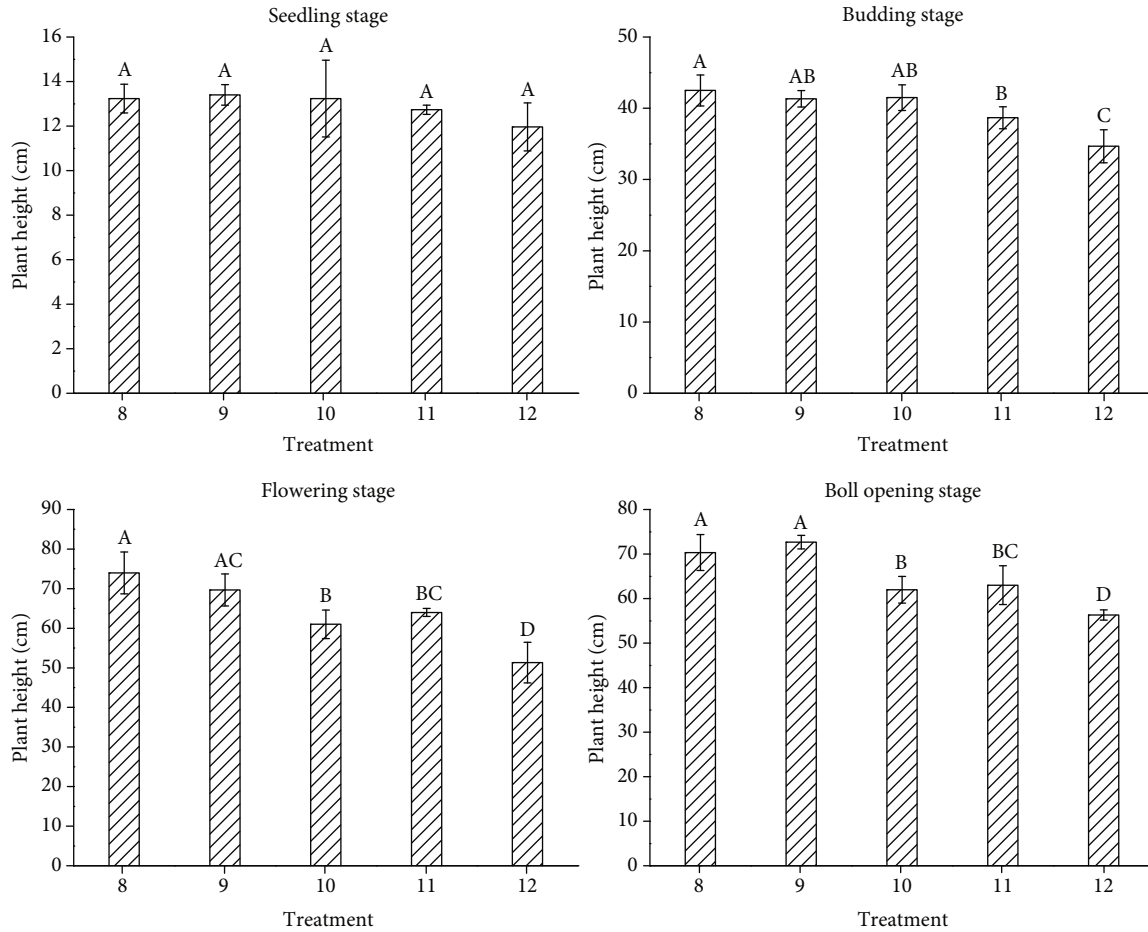
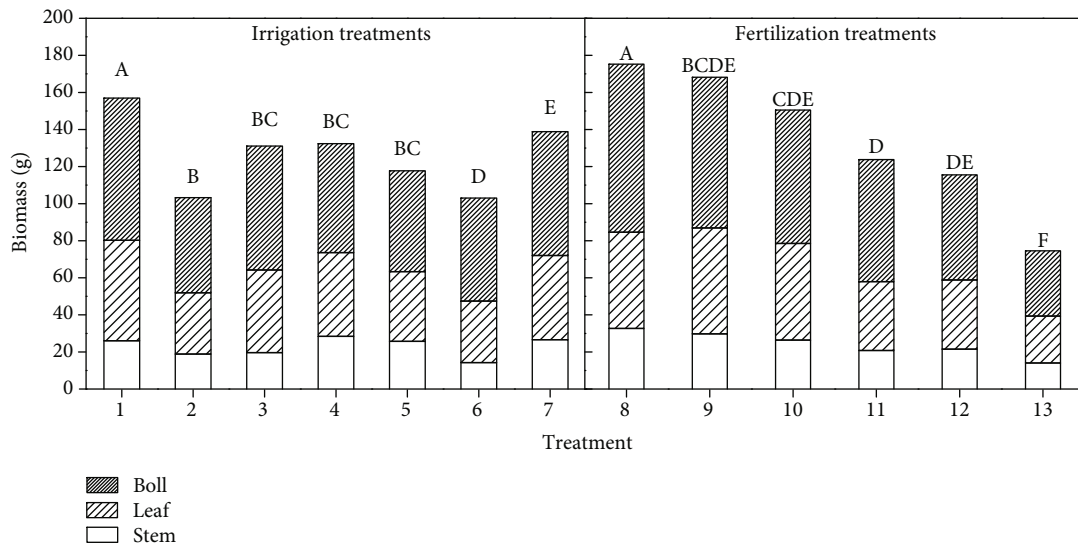


FIGURE 11: Changes in cotton stem diameter under different fertilization treatments.

FIGURE 12: Changes in cotton biomass on September 16th (late growth stage).

seed cotton yield, and IWUE ($P < 0.01$) and a significant effect on the boll weight ($P < 0.05$). Under the three deficit irrigation treatments (T2-T7), the number of bolls per plant and the weight of bolls per plant increased with increasing irrigation, and the effect of deficit irrigation on the yield

was less than that at the bud stage. This result shows that serious irrigation deficits have a great influence on cotton growth and yield components. Under T7, the boll number and boll weight were higher than those under T6, but the difference was not significant, which indicated that slight

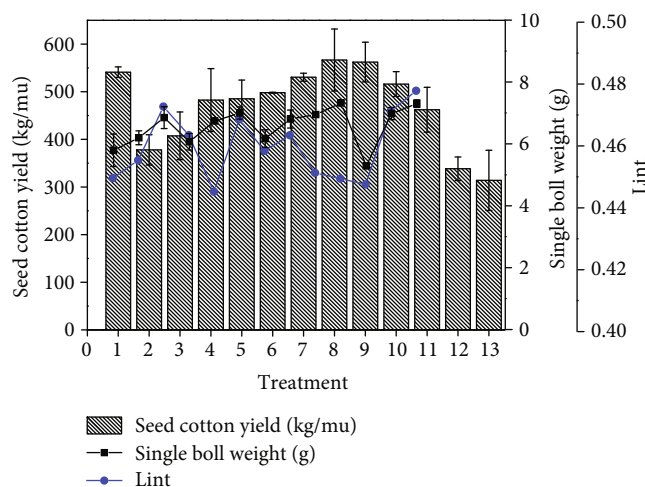


FIGURE 13: Seed cotton yield under different irrigation and fertilization treatments.

TABLE 6: Effect of irrigation and fertilization on yield and water use efficiency.

Treatment	Boll number/plant	Single boll weight (g)	Seed cotton yield (kg/mu)	IWUE (kg/m ³)
Irrigation				
T1	6.58cdef	7.32bcd	541.16g	1.77ef
T2	5.18h	6.19d	485.25k	2.18bc
T3	5.32h	6.85abcd	496.16j	2.35b
T4	6.11fg	6.07bcd	407.45h	2.29a
T5	5.91g	6.74bcd	497.15i	1.97d
T6	6.26efg	6.99cd	490.52h	2.03cd
T7	6.47abc	6.17abcd	482.53l ef	2.62b
Bare land				
T13	4.43ab	5.32abc	313.93b	2.04cd
Fertilization				
T8	6.76a	6.98abcd	563.66cd	1.64de
T9	6.98bcde	7.30abcd	566.29f	1.55g
T10	6.13cdefg	7.29abc	534.05de	1.91fg
T11	6.22abcd	6.74a	462.28a	1.78ef
T12	5.13cdef	4.72ab	338.32c	1.66fg
ANOVA				
W	**	*	**	**
F	**	*	**	**

Note: different small letters in the same column indicate significant differences among treatments at the 0.05 level. ** indicates a significant difference at 1%; * indicates a significant difference at 5%.

deficit irrigation could ensure the normal growth of cotton and achieve efficient water utilization at the same time. This conclusion was consistent with the study from Yazar et al. [38], who found that the boll number decreased under a decrease in the water supply.

Under the five different fertilization treatments (T8-T12) at the same irrigation level (full irrigation), the change in the boll weight formed a quadratic parabola with the increase in

fertilization. The maximum value appeared under T9, and the average boll weight of T9 was 7.30 g, which was 4.58%, 1.37%, 8.31%, and 54.6% higher than that under T8, T10, T11, and T12, respectively. This result indicates that under the same irrigation level, appropriate increases in fertilization are beneficial to the boll weight, but overfertilization reduces the boll weight.

The results indicated that under drip irrigation with plastic mulch, the effect of an increasing irrigation amount on cotton seed yield was more significant than that of increasing fertilization application, especially under saline soil conditions, and appropriate irrigation promotes cotton growth (vegetative and reproductive growth). Furthermore, with appropriate irrigation, the salt can be leached from the cotton root area, providing appropriate conditions for cotton growth.

For drip irrigation without plastic mulch (T13), under sufficient irrigation and fertilization, the yield, dry matter, plant height, and stem diameter of cotton were all at the lowest level in the bare land. This also shows that in areas with large temperature differences between day and night, plastic mulch can ensure that the accumulated temperature requirements of crops are met, reduce soil evaporation, increase soil temperature, and improve the soil and water microenvironment in the root area of the crops. In this experiment, mulch release that was too early also has some influence on the test results. In future comparative tests, further quantitative analysis is needed.

The experimental site was located in southern Xinjiang, an area with an extreme lack of water resources, so improving the water use efficiency has great significance for relieving the local water resource shortage. The IWUE values under the different treatments are shown in Table 6. At the same irrigation level, the IWUE had the same trend as the seed cotton yield. The results indicated that under the same irrigation conditions, fertilization application affected the IWUE by affecting cotton seed yield. The IWUE decreased gradually with increasing irrigation amount, and the same results were found by Dağdelen et al. [39], who found that the IWUE increased as the irrigation amount decreased. Hence, under drip irrigation with plastic mulch, increasing the irrigation

amount can increase the seed cotton yield; however, the IWUE decreases to a large extent at the same time.

The mechanisms by which drip irrigation under plastic mulch regulates field conditions and increases yields are unclear at present; methods to quantify the relationship between the regulatory measures and the soil-water and salt transport, water availability, water consumption, salt accumulation, and crop yield also need to be further understood. In addition, it is also worth exploring ways to modify the water and nutrient stress coefficients under the regulatory measures; moreover, methods for the prediction of field salt accumulation and crop growth should also be developed.

In summary, various water, nutrient, and field control measures under a drip irrigation-plastic mulch production system will inevitably have a certain impact on soil-salt accumulation and crop growth. Scholars have performed much research on the mechanism and model of soil-water, salt transport, and crop growth processes under various field control measures, which lay a theoretical and experimental foundation for later research in this field.

4. Conclusion

Soil moisture has a significant effect on cotton growth; when the water supply is excessive, vegetative growth is vigorous but can easily become excessive, thus increasing crop water consumption and reducing IWUE. However, if soil moisture is insufficient, vegetative growth is easily inhibited, and the distribution of water among underground and aboveground parts will further affect root growth and dry matter accumulation. Soil moisture also affects the accumulation of photosynthetic products and the yield of cotton.

In the early stage of cotton growth (vegetative growth stage), the plant height increases rapidly with the progression of the growth process; after entering the budding stage (vegetative and reproductive growth stages), this increase in plant height slows gradually; after entering the flowering stage, which is dominated by reproductive growth, and with the application of artificial topping, the rate of increase of cotton height further slows and tends to stop. Moderate water stress at the seedling stage is beneficial to cotton height, and the same degree of water deficit at the later growth stage has a less negative effect on cotton height than that at the earlier growth stage.

The cotton stem diameter trend was opposite to that of plant height in the early growth stage, but the increase in stem diameter gradually decreased and stopped in the later growth stage. Water deficit at the flowering stage resulted in a slow increase in stem diameter, while deficit irrigation at budding promoted the increase in stem diameter.

The effect of soil-water on the LAI was similar to that on plant height. The LAI decreased with the increase in the water deficit at the budding stage, but after restoring the water supply at the flowering stage, a water-deficit compensation effect appeared with this treatment. The negative effects of water stress on the LAI increased with an increasing degree of water deficit.

The effects of nutrient control measures on plant height and stem diameter were not significant, and excessive ferti-

zation had little effect on the LAI. However, the greater the amount of fertilizer applied, the greater the biomass accumulation. At the same time, because the biomass accumulated in the later growth stage, deficit irrigation at the flowering stage had a greater effect on biomass accumulation than the same treatment at other stages.

In general, cotton irrigation practices in the study area should include mild deficits at the flowering stage (60%~80% PET), while ensuring that the water demand is met in the budding stage (full irrigation during the early period). Fertilization at 0.8 times the standard local application amount can ensure normal yields and improve the IWUE of cotton.

Data Availability

1) the nature of the data is agricultural data, 2) the data can be accessed by contact with first or corresponding author, and 3) This study was financially supported by the National Key Research and Development Program of China (No. 2017YFC0403303), and the National Key Research and Development Program of China (No. 2017YFC0403305). so there are some restrictions on data access.

Conflicts of Interest

The authors declare that they have no conflicts of interest.

Acknowledgments

This study was financially supported by the National Key Research and Development Program of China (Nos. 2017YFC0403303 and 2017YFC0403305).

References

- [1] M. Liu, J. Yang, X. Li, G. Liu, M. Yu, and J. Wang, "Distribution and dynamics of soil water and salt under different drip irrigation regimes in Northwest China," *Irrigation Science*, vol. 31, no. 4, pp. 675–688, 2013.
- [2] C. Wang, A. Isoda, and P. Wang, "Growth and yield performance of some cotton cultivars in Xinjiang, China, an arid area with short growing period," *Journal of Agronomy and Crop Science*, vol. 190, no. 3, pp. 177–183, 2004.
- [3] R. Wang, Y. Kang, S. Wan, W. Hu, S. Liu, and S. Liu, "Salt distribution and the growth of cotton under different drip irrigation regimes in a saline area," *Agricultural Water Management*, vol. 100, no. 1, pp. 58–69, 2011.
- [4] R. Wang, Y. Kang, S. Wan et al., "Influence of different amounts of irrigation water on salt leaching and cotton growth under drip irrigation in an arid and saline area," *Agricultural Water Management*, vol. 110, pp. 109–117, 2012.
- [5] M. Deng and Q. Shi, "Management and regulation pattern of water resource in inland arid regions," *Advances in Earth Science*, vol. 29, no. 9, pp. 1046–1054, 2014.
- [6] C. Tian, "Some problems and their scientific and technological countermeasures for sustainable development of cotton production in Xinjiang," *Arid Zone Research*, vol. 18, no. 4, pp. 62–67, 2001.
- [7] X. Chen, J. Yang, C. Liu, and S. Hu, "Soil salinization under integrated agriculture and its countermeasures in Xinjiang," *The Soil*, vol. 39, no. 3, pp. 347–353, 2007.

- [8] X. Dong, M. Deng, J. Zhou, and J. Zhong, "On exploitation of water resources and soil salinization in irrigation area of Xinjiang plain," *Journal of Irrigation and Drainage*, vol. 24, no. 5, pp. 14–17, 2005.
- [9] J. E. Ayars, C. J. Phene, R. B. Hutmacher et al., "Subsurface drip irrigation of row crops: a review of 15 years of research at the Water Management Research Laboratory," *Agricultural Water Management*, vol. 42, no. 1, pp. 1–27, 1999.
- [10] R. Ding, S. Kang, F. Li, Y. Zhang, and L. Tong, "Evapotranspiration measurement and estimation using modified Priestley-Taylor model in an irrigated maize field with mulching," *Agricultural and Forest Meteorology*, vol. 168, pp. 140–148, 2013.
- [11] X. Feipeng, L. Yunkai, and R. Shumei, "Investigation and discussion of drip irrigation under mulch in Xinjiang Uygur Autonomous Region," *Transactions of The Chinese Society of Agricultural Engineering*, vol. 1, p. 5, 2003.
- [12] J. Zheng, J. Fan, F. Zhang et al., "Mulching mode and planting density affect canopy interception loss of rainfall and water use efficiency of dryland maize on the Loess Plateau of China," *Journal of Arid Land*, vol. 10, no. 5, pp. 794–808, 2018.
- [13] H. J. Cai, G. C. Shao, and Z. H. Zhang, "Water demand and irrigation scheduling of drip irrigation for cotton under plastic mulch," *Journal of Hydraulic Engineering*, vol. 11, pp. 119–123, 2002.
- [14] X. Dong, "Effects of plastic film covering on dropping ground temperature at the full-growing stages of cotton, maize and soybean," *Acta Ecologica Sinica*, vol. 23, no. 8, pp. 1667–1672, 2003.
- [15] F. M. Li, J. Wang, J. Z. Xu, and H. L. Xu, "Productivity and soil response to plastic film mulching durations for spring wheat on entisols in the semiarid Loess Plateau of China," *Soil and Tillage Research*, vol. 78, no. 1, pp. 9–20, 2004.
- [16] Y. Li, W. Y. Wang, Q. Men, X. C. Zhong, and X. W. Xie, "Field characters of soil temperature under the wide plastic mulch," *Transactions of the Chinese Society of Agricultural Engineering*, vol. 17, no. 3, pp. 32–36, 2001.
- [17] Z. Zhang, H. Hu, F. Tian, X. Yao, and M. Sivapalan, "Groundwater dynamics under water-saving irrigation and implications for sustainable water management in an oasis: Tarim River basin of western China," *Hydrology and Earth System Sciences*, vol. 18, no. 10, pp. 3951–3967, 2014.
- [18] T. T. Kozlowski and C. H. Winget, "Diurnal and seasonal variation in radii of tree stems," *Ecology*, vol. 45, no. 1, pp. 149–155, 1964.
- [19] D. A. Goldhamer and E. Fereres, "Irrigation scheduling of almond trees with trunk diameter sensors," *Irrigation Science*, vol. 23, no. 1, pp. 11–19, 2004.
- [20] F. J. Molz and B. Klepper, "On the mechanism of water-stress-induced stem deformation 1," *Agronomy Journal*, vol. 65, no. 2, pp. 304–306, 1973.
- [21] P. Liu, "Study on growth development, physiological characteristics and production of crop under soil water stress," Master's thesis, Northwest A&F University, 2010.
- [22] X. Shi, "Study on the physiological and biochemical response and compensation effect of maize under water deficit," Master's thesis, Northwest A&F University, 2009.
- [23] Z. Yan, *The Study on Response of Pea to Water Stress and Rewater Effect*, Doctoral dissertation, Gansu Agricultural University, 2009.
- [24] N. Yao, Y. Li, F. Xu et al., "Permanent wilting point plays an important role in simulating winter wheat growth under water deficit conditions," *Agricultural Water Management*, vol. 229, article 105954, 2020.
- [25] J. Zhang, A. Duan, Z. Meng, Z. Liu, J. Chen, and Z. Liu, "Stem diameter variations of cotton under different water conditions," *Transactions of The Chinese Society of Agricultural Engineering*, vol. 21, no. 5, pp. 7–11, 2005.
- [26] G. D. Farquhar and T. D. Sharkey, "Stomatal conductance and photosynthesis," *Annual Review of Plant Physiology*, vol. 33, no. 1, pp. 317–345, 1982.
- [27] J. Li, J. Zhang, and L. Ren, "Water and nitrogen distribution as affected by fertigation of ammonium nitrate from a point source," *Irrigation Science*, vol. 22, no. 1, pp. 19–30, 2003.
- [28] G. A. Bezborodov, D. K. Shadmanov, R. T. Mirhashimov et al., "Mulching and water quality effects on soil salinity and sodicity dynamics and cotton productivity in Central Asia," *Agriculture, Ecosystems & Environment*, vol. 138, no. 1–2, pp. 95–102, 2010.
- [29] B. C. Cowell and C. J. Dawes, "Growth and nitrate-nitrogen uptake by the cyanobacterium *Lyngbya wollei*," *Journal of Aquatic Plant Management*, vol. 42, pp. 69–71, 2004.
- [30] R. L. Anderson and L. A. Nelson, "A family of models involving intersecting straight lines and concomitant experimental designs useful in evaluating response to fertilizer nutrients," *Biometrics*, vol. 31, no. 2, pp. 303–318, 1975.
- [31] S. Tan, Q. Wang, J. Zhang, Y. Chen, Y. Shan, and D. Xu, "Performance of AquaCrop model for cotton growth simulation under film-mulched drip irrigation in southern Xinjiang, China," *Agricultural Water Management*, vol. 196, pp. 99–113, 2018.
- [32] P. Yang, H. Hu, F. Tian, Z. Zhang, and C. Dai, "Crop coefficient for cotton under plastic mulch and drip irrigation based on eddy covariance observation in an arid area of northwestern China," *Agricultural Water Management*, vol. 171, pp. 21–30, 2016.
- [33] Z. Zhang, H. Hu, F. Tian, H. Hu, X. Yao, and R. Zhong, "Soil salt distribution under mulched drip irrigation in an arid area of northwestern China," *Journal of Arid Environments*, vol. 104, pp. 23–33, 2014.
- [34] R. G. Allen and L. S. R. Pereira, *FAO irrigation and drainage paper. No. 56, crop evapotranspiration*, 1998.
- [35] M. Li, Y. Du, F. Zhang et al., "Simulation of cotton growth and soil water content under film-mulched drip irrigation using modified CSM-CROPGRO-cotton model," *Agricultural Water Management*, vol. 218, pp. 124–138, 2019.
- [36] H. Zhang, A. Khan, D. K. Y. Tan, and H. Luo, "Rational water and nitrogen management improves root growth, increases yield and maintains water use efficiency of cotton under mulch drip irrigation," *Frontiers in Plant Science*, vol. 8, p. 912, 2017.
- [37] Z. Jiyang, D. Aiwan, M. Zhaojiang, L. Zugui, C. Jinping, and L. Zhandong, "Stem diameter variations of cotton under different water conditions," *Transactions of The Chinese Society of Agricultural Engineering*, vol. 5, 2005.
- [38] A. Yazar, S. M. Sezen, and S. Sesveren, "LEPA and trickle irrigation of cotton in the Southeast Anatolia Project (GAP) area in Turkey," *Agricultural Water Management*, vol. 54, no. 3, pp. 189–203, 2002.
- [39] N. Dağdelen, E. Yılmaz, F. Sezgin, and T. Gürbüz, "Water-yield relation and water use efficiency of cotton (*Gossypium hirsutum* L.) and second crop corn (*Zea mays* L.) in western Turkey," *Agricultural Water Management*, vol. 82, no. 1–2, pp. 63–85, 2006.

- [40] L. Ahuja, Ed., *Response of crops to limited water: understanding and modeling water stress effects on plant growth processes* (vol. 1), ASA-CSSA-SSSA, 2008.
- [41] A. Guo and H. Wei, "The effect of soil water deficiency on the accumulation and allocation of root biomass of spring wheat," *Acta Ecologica Sinica*, vol. 19, no. 2, pp. 179–184, 1999.

Research Article

Application of Low-Cost Sensors for the Development of a Methodology to Design Front-End Loaders for Tractors

H. Malon ¹, A. Ayuda,¹ F. J. Garcia-Ramos ², M. Vidal,¹ and J. Cuartero ¹

¹Departamento de Ingeniería Mecánica, Escuela de Ingeniería y Arquitectura, University of Zaragoza, 50018, Spain

²Departamento de Ciencias Agrarias y del Medio Rural, Escuela Politécnica Superior, University of Zaragoza, C/Cuarte s/n, 22004 Huesca, Spain

Correspondence should be addressed to H. Malon; hml@unizar.es

Received 22 November 2019; Revised 27 January 2020; Accepted 5 February 2020; Published 28 February 2020

Guest Editor: Jingwei Wang

Copyright © 2020 H. Malon et al. This is an open access article distributed under the Creative Commons Attribution License, which permits unrestricted use, distribution, and reproduction in any medium, provided the original work is properly cited.

Tractor front-end loaders are an essential part of the equipment used on farms. At present, there are an important number of small- and medium-sized companies involved in the manufacturing of this equipment. These companies rely heavily on experience for innovative designs, as in the vast majority of cases they lack access to adequate methodology for the optimal design of new front-end loaders. The study conducted has developed a methodology to design tractor front-end loaders with a view of obtaining their accurate design during the bucket loading process. The methodology comprises two phases: the first phase involves a numerical analysis of the structural behaviour of the front-end loader components by means of the Finite Element Method; the second phase, the experimental phase, makes use of low-cost sensors, in particular, strain gauges, to analyse existing strains at selected points in the front-end loader structure. The experimental results obtained by means of low-cost sensors fitted onto the front-end loader allow analysing the existing strains at the points measured, as well as validate the numerical model developed. This methodology is validated by applying it to a commercial front-end loader, more specifically to model 430E2 of the company Maquinaria Agrícola El León S.A (Spain).

1. Introduction

Tractor front-end loaders are frequently used in the daily tasks carried out on agricultural holdings [1]. A loader is fitted to the front part of the tractor so as to carry or move loads around [2]. There are currently an important number of small- and medium-sized companies involved in the manufacturing of this equipment. These companies heavily rely on its experience for design, as in the vast majority of cases they lack access to adequate methodology for the optimal design of new front-end loaders. Current methodology used by these companies does not include traditional experimental testing. On the contrary, after the manufacture of a prototype, companies analyse its operation thanks to the help of reliable customers who detect faults in it which are used to improve its design. In this methodology, the manufacturer does not have an exhaustive control of the work carried out by the machine. For this reason, it is not possible to confirm

whether the failures indicated by the customer are really due to a design failure or to a misuse of the prototype.

While some studies deal with tractor loaders [3–5], no reference to the structural behaviour of the loader is made in them. Likewise, those studies analysing the structural safety of front-end loaders focus on the study of impact loads [2, 6].

Technical experts point out that most damage occurring to the structure of a front-end loader fitted to a tractor stems from the misuse of the equipment during the carrying out of daily tasks. More specifically, the majority of the defects detected are plastic strains or even breaking of welded joints in the resistant structure, which occur as a result of the misuse of these devices during the loading manoeuvres where the bucket is involved. The most frequent instances of misuse are the excessive speed of tractor in the bucket loading process or the use of the bucket to pull down walls or uproot trees. Both instances lead to the same outcome: there is a point in time

when the bucket is unable to move forward while the tractor keeps doing so. This fact results in a deformation of the resistant structure of the front-end loader, leading to plastic strains or even the breaking of some welded joints.

Thus, it is evident that there is a need for a methodology to develop the design of front-end loaders mounted on tractors during the bucket loading process. This methodology must allow obtaining the strains and stresses at the selected points of the front-end loader structure. The results should be obtained by means of low-cost sensors, specifically strain gauges. The use of these types of sensors is widespread as a technique for the structural analysis of components of metal structures in general [7–10]. In addition, this methodology must allow analysing the structural behaviour of each component of the front-end loader by means of numerical techniques based on the Finite Element Method (FEM). The structural analysis by means of the FEM is a technology with a proven track record frequently used for the analysis of vehicles [9, 11–16] and more recently in some agricultural implements [6, 17, 18]. Moreover, it is necessary to define two manoeuvres: static and dynamic. The static manoeuvre allows analysing the structural behaviour of the front-end loader in a load case in which load is known. On the other hand, the dynamic manoeuvre allows analysing the structural behaviour of the front-end loader in a load case in which load is unknown.

2. Objective

The main objective of this study is to develop and validate a methodology for the design and development of front-end loaders for agricultural tractors, which can be used by companies that do not have resources to apply expensive design methodologies. In order to achieve the comprehensive objective of this project, two technical objectives need to be met: the definition of an experimental test phase and a numerical analysis phase. The experimental test phase is aimed at obtaining, by means of low-cost sensors, more specifically strain gauges, the strains and stresses generated at the front-end loader structure during the bucket loading process, where most damage occurs. Likewise, the aim of the numerical analysis phase is to obtain the comprehensive structural behaviour of a front-end loader mounted on a tractor during the bucket loading process.

3. Materials and Methods

The methodology is made up of two phases. In the first phase (experimental), low-cost sensors—more specifically strain gauges—are used to measure strains and stresses at selected points of the front-end loader structure. In the second phase (numerical analysis), the structural behaviour of the front-end loader components are analysed by means of the FEM.

The methodology developed has been validated through its application to a commercial front-end loader, more specifically to a 430E2 model of Maquinaria Agrícola El León Company (Spain). The technical specifications have been obtained from its commercial brochure [19], as well as from information provided by the company itself.



FIGURE 1: Front loader 430E2 mounted on a FENDT 718 Vario tractor.

The method used during the experimental and numerical analysis phases is described below.

3.1. Experimental Phase. For the experimental test, a front-end loader 430E2 was mounted on a FENDT 718 Vario tractor, as shown in Figure 1.

Once the front-end loader was coupled, 11 low-cost sensors were fitted, more specifically 9 unidirectional strain gauges and 2 rosettes. A rosette is a sensor with multiple strain gauges on a common carrier. The rosettes used in the study are composed by three strain gauges [20]. In addition, a further unidirectional strain gauge (in a total series of ten strain gauges) was used, so as to perform due corrections arising from temperature effects. Table 1 describes the position where the strain gauges were placed. Figure 1 shows the position of sensors on the front-end loader. Figures 2 and 3 show in detail rosette 1 and strain gauges 8 and 10, respectively.

The strain gauge signals were recorded by a strain gauge measurement system (StrainBook/616, Measurement Computing, Norton, MA, USA). This equipment allows simultaneous measurements of twenty-four channels. The measurement system was connected to a laptop computer equipped with data acquisition software (Waveview 7.15, Measurement Computing).

During this phase, two types of tests were defined. The first involved a static load test, while the second one was a dynamic load test. These tests were conducted in the facilities of Virgen de la Oliva Cooperative, in Ejea de los Caballeros (Spain), while the Cooperative was open. The experimental tests had to be conducted with the tractor engine running for safety reasons. This fact implies the presence of vibrations in the front loader transmitted by the tractor engine.

The acquisition frequency used for the recording of data during the tests was 1 Hz for the static load case and 50 Hz for the dynamic load test.

3.1.1. Static Load Test. Strains and stresses were obtained for the case of a mass of 320 kg placed in the loader bucket. To

TABLE 1: Location of the strain gauges.

Strain gauge	Location
1	Rosette fitted onto the left longitudinal beam in front of the fastening blot for the hydraulic cylinder
2	Unidirectional strain gauge placed onto the front area of the left longitudinal beam, close to the crossbeam gap
3	Unidirectional strain gauge attached to the right longitudinal beam, in a symmetric position to strain gauge 2
4	Unidirectional strain gauge located at the upper fold of the left longitudinal beam
5	Unidirectional strain gauges placed at the top of the parallelogram beams of the left longitudinal beam
6	Unidirectional strain gauges placed at the top of the parallelogram beams of the right longitudinal beam, in a symmetric position to strain gauge 5
7	Unidirectional strain gauge located at the lower area of the outer surface of the front-end loader left support
8	Rosette was placed close to the support area of the front-end loader in the clamping pillar
9	Unidirectional strain gauge fitted onto the front face of the clamping pillar, at the same height where the clamping pillar is attached to the tractor chassis
10	Unidirectional strain gauge placed on the rear face of the clamping pillar
11	Unidirectional strain gauge placed onto the outer surface of the front loader left support, close to the loader's lock-in mechanism

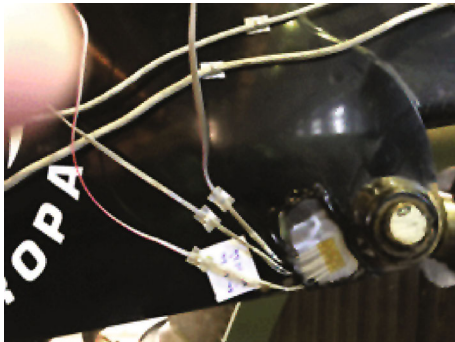


FIGURE 2: Gauge 1: rosette placed at the left longitudinal beam.



FIGURE 3: Strain gauges 8 and 10 placed at the left clamping pillar.

that aim, 8 bags of fertiliser, with a mass of 40 kg each, were located in the loader bucket. They were evenly distributed on the bucket surface. Once the mass was in place, the position of the front-end loader was maintained for at least 60 s, so as to obtain a steady record of stresses and strains. In the test conducted, the time of the loading process was 88 seconds and the time of maintaining the position was 86 seconds.

The front loader's bucket base was placed horizontally, 5 cm high from the ground. Figure 4 shows the position of the front-end loader and the even distribution of the bags for the static load case.

3.1.2. Dynamic Load Test. The dynamic load test seeks to analyse the behaviour of the structural components of a front-end loader during the loading process. The usual loading process with this type of equipment consists of placing the bucket in a horizontal position on the ground while the tractor drives forward. During this process, the bucket fitted to the front-end loader is shoved into the heap of the material to load, generally grain, fertiliser, or soil. The bucket is subsequently turned upwards, thus ending the bucket loading process. Figure 5 shows the front-end loader and its load, in this case, of fertiliser.

To define the test, the possibility of defining a dynamic essay with real-life loads was ruled out, owing to its low repeatability, given the high variability in the density of the materials used (grain, fertiliser, and soil) associated to changeable environmental conditions. Instead, a dynamic experimental test showing high repeatability was designed. Thus, the ensemble formed by the tractor and front loader was set to push against a concrete loading bay. To execute this action, the front loader was placed onto the ground, with its bucket placed in a horizontal position. The contact with the loading bay by the ensemble formed by the tractor and the front loader occurred at the front part of the front loader's bucket. Figure 6 shows how the tractor-front loader ensemble is positioned during the execution of the dynamic load test. The same manoeuvre was performed twice. Data from strain gauges was recorded at a frequency of 50 Hz.



FIGURE 4: Positioning of the front-end loader and distribution of bags for the static load test.



FIGURE 5: Fertiliser load in the front loader.

The execution of the dynamic test allows obtaining the strains and stresses undergone during the front loader load process for any material, with high repeatability regardless of environmental conditions, getting to the critical point where the tractor fails to move any further.

3.2. Numerical Analysis Phase. During the study conducted, the front-end loader was modelled. The numerical model (Figure 7) was formed by 71,039 nodes and 64,294 elements. For the discretization of the front loader structural components (shown in grey in Figure 7), shell-type elements were used. Shell-type elements were also used for the bucket model, shown in blue in Figure 7. The clamping pillar of the tractor (in green in Figure 7) was discretized by means of volumetric elements. The modelling of the hydraulic cylinders and bolts of the movable joints in the front-end loader was carried out by means of beam-type elements, as shown in red in Figure 7. Multipoint constraints (MPCs) were used to avoid completely rigid joints between bolts and bush and thus replicate their actual behaviour.

The material used in the numerical analysis in all components for the front loader, the bucket, and the clamping pillars has been Steel S355-JR. On the other hand, linear elastic steel has been applied for the hydraulic cylinders and bolts. The mechanical properties of the steels used are shown in Table 2.

Similar to the experimental phase, two load cases have been defined for the numerical analysis. The first one was a static load case, whereas the second was a dynamic load case. Both tests are described in detail below.

3.2.1. Static Load Case. The static load case is aimed at analysing the comprehensive structural behaviour of the front loader in terms of stiffness and strength when known loads are applied to it. The numerical analysis has been carried out by means of the software Abaqus 6.14-2, with a standard formulation for the analysis of a static load case.

To perform the numerical analysis, the ensemble bucket-front loader was positioned with the bucket base horizontal 5 cm high from the ground.

The load applied corresponds to a descending vertical force of 3,136 N, evenly distributed over the base of the bucket in the numerical model. This is shown in blue in Figure 8. The load applied corresponds to the weight used in the experimental phase (320 kg).

As for the boundary conditions defined in the numerical analysis, displacements were restricted in the bores for the attachment bolts of the clamping pillars to the tractor. These areas where displacements were restricted for the numerical analysis are shown in red in Figure 8.

3.2.2. Dynamic Load Case. The dynamic load case is aimed at analysing the structural behaviour of the front-end loader in terms of stiffness and strength during the loading process. The numerical analysis has been carried out by means of the commercial software Abaqus 6.14-2, with explicit formulation for the analysis of a dynamic load case.

In the numerical model, the loader-bucket set has been placed in the low position, with the base of the bucket in horizontal position.

For this load case, a forward displacement of the tractor rather than a force has been selected. More specifically, the load case under analysis consisted in a 50 mm forward movement in 1 second. This forward movement was defined taking into account the information provided by technical experts in the manufacturing of tractor front loaders. The forward movement was applied at the bores of the attachment bolts of the clamping pillars to the tractor. The clamping pillars convey displacement of the tractor's chassis to the front-end loader in real life. The zones where the forward movement was applied are shown in red in Figure 9.

The imposed boundary conditions restricted displacement in forward direction of the tractor at the frontal line nodes of the bucket base. These nodes are shown in blue in Figure 9.



FIGURE 6: Dynamic load test.

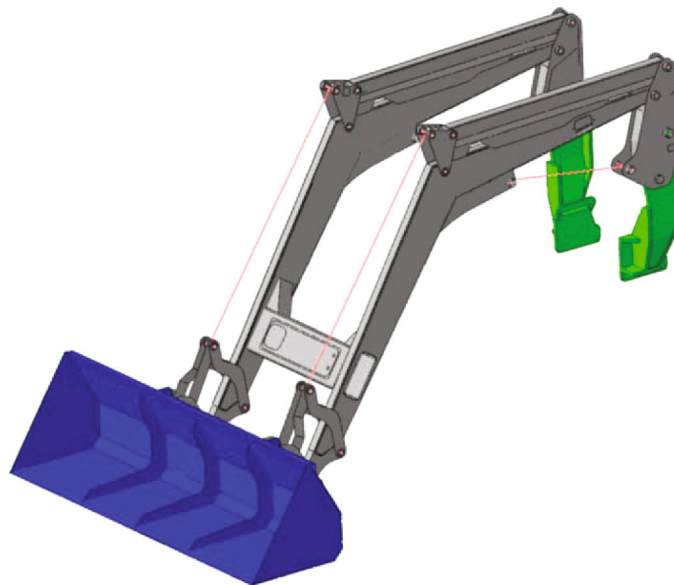


FIGURE 7: Numerical model of front-end loader 430E2.

TABLE 2: Mechanical properties of steels used in the numerical model.

Material	Density (kg/m ³)	Young's modulus (MPa)	Poisson's ratio	Yield strength (MPa)	Tensile strength (MPa)	Elongation (%)
Steel S355	7,800	210,000	0.3	355	470	17
Steel	7,800	210,000	0.3			

4. Results and Discussion

4.1. Experimental Phase

4.1.1. Static Load Test. In the static load test conducted, the time of the loading process was 88 seconds and the time of maintaining the load was 86 seconds. The results of the static load test obtained are shown in Figures 10 and 11. These figures show the values of microstrains ($\mu\epsilon$) from unidirectional strain gauges, as well as Von Mises stress values obtained from the rosettes. It must be pointed out that the metering

channels associated to unidirectional strain gauges 6 and 9 were damaged during the journey to the test area, and therefore, they recorded no strain variations over the entirety of the tests performed.

The mean values as well as standard deviation of recorded data from the 9 low-cost sensors during the test are shown in Table 3.

The results obtained provide evidence that the load level in the front loader was very low, with mean stress values for rosettes 1 and 8 of 11.7 and 7.3 MPa, respectively, and maximum mean strain values of $88 \mu\epsilon$ from unidirectional strain

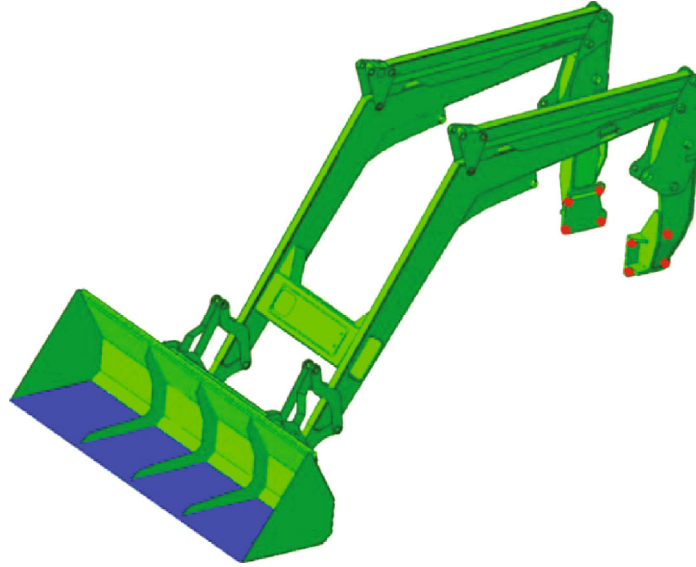


FIGURE 8: Areas where load (blue) and boundary conditions (red) were applied in the static load case.

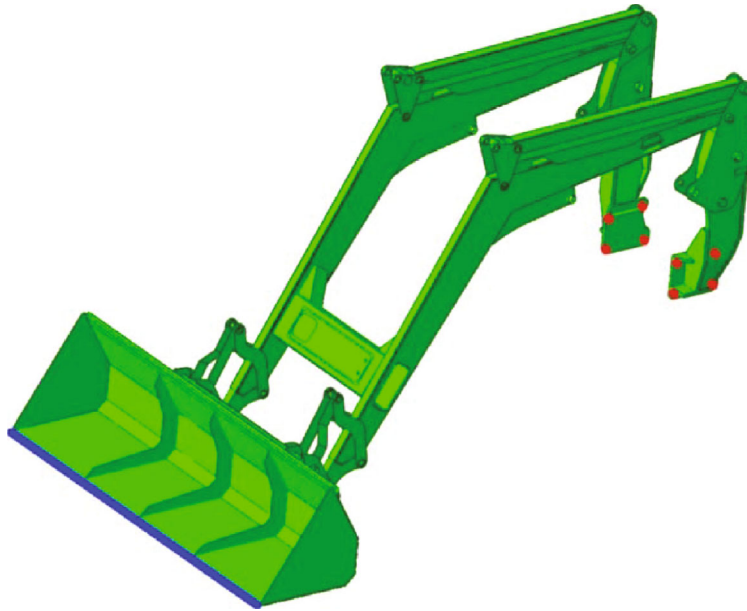


FIGURE 9: Areas where load (red) and boundary conditions (blue) were applied in the dynamic load case.

gauge 10. These results are consistent with the load applied during the experimental test (320 kg) with respect to the maximum admissible load for the bucket in the defined position (3,400 kg).

Standard deviations obtained from gauges 2 and 3 show high values with respect to the mean. However, two considerations must be taken into account when analysing these results. The first one concerns the location of these gauges. Gauges 2 and 3 were placed in the overhang of the loader, where the vibrations generated by the tractor engine in operation had greater effect. Secondly, the average value recorded by these gauges ($1 \mu\epsilon$ and $6 \mu\epsilon$, respectively) was very low. These values are equivalent to a unidirectional stress of 0.21 MPa and 1.26 MPa, respectively. In addition, the results

obtained from strain gauge 2 were in a range between $+5 \mu\epsilon$ and $-2 \mu\epsilon$, while for gauge 3 the range was between $9 \mu\epsilon$ and $2 \mu\epsilon$. These results show that the strain variations were less than $7 \mu\epsilon$ (equivalent to a unidirectional stress of 1.47 MPa) in both gauges. These minor variations generate that the standard deviations have a high value with respect to the mean, because the strain values recorded are very low.

On the other hand, the results obtained from the gauges placed in more stable areas of the front-end loader structure (gauge 10 placed in the clamping pillar or gauge 11 placed in the left support) had a minor standard deviation in relation to the mean. In addition, these areas were subject to greater efforts generated by the loading placed in the loader bucket.

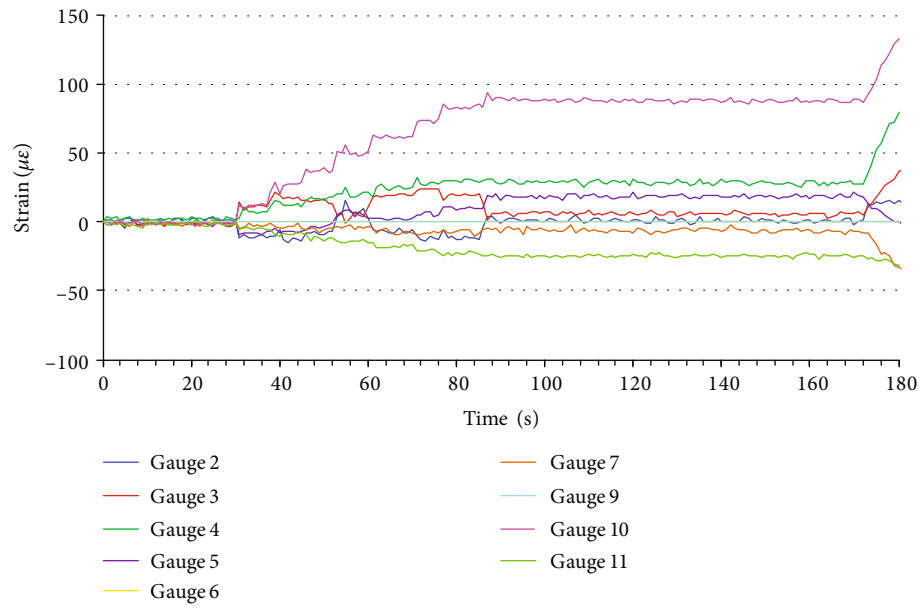


FIGURE 10: Results from unidirectional strain gauges from the static load test.

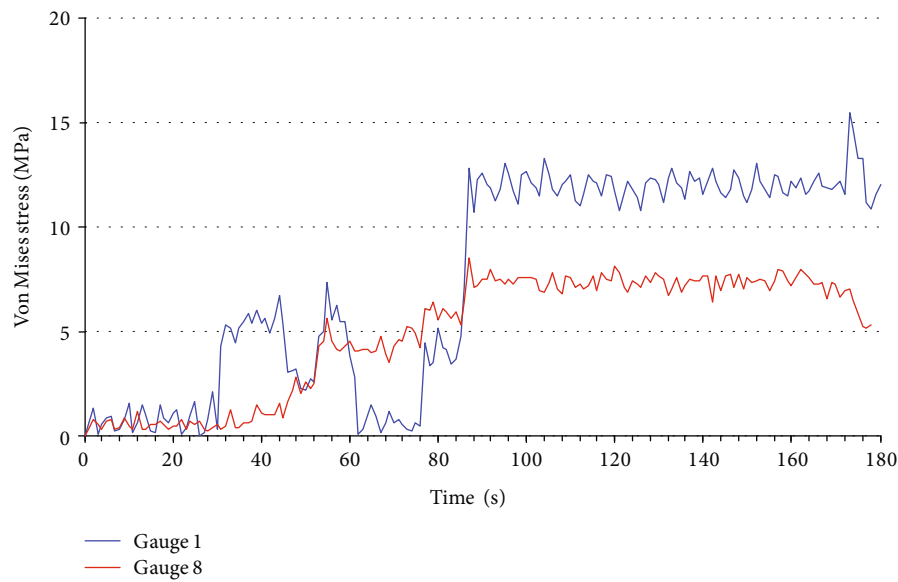


FIGURE 11: Results from the rosettes from the static load test.

TABLE 3: Mean and standard deviation values from the static load test.

	1 (MPa)	2 ($\mu\epsilon$)	3 ($\mu\epsilon$)	4 ($\mu\epsilon$)	Gauges		8 (MPa)	10 ($\mu\epsilon$)	11 ($\mu\epsilon$)
					5 ($\mu\epsilon$)	7 ($\mu\epsilon$)			
Mean	11.7	1	6	29	18	-6	7.3	88	-25
Standard deviation	1.4	2	2	1	2	1	0.4	1	1

4.1.2. Dynamic Load Test. Results obtained from the nine unidirectional strain gauges and the two rosettes are shown in Figures 12 and 13, respectively. As previously mentioned, the measurement channels corresponding to strain gauges 6 and 9 were damaged during the journey to the test area,

and therefore, no values from these gauges were obtained during the dynamic load test.

The first dynamic load test was conducted between seconds 55 and 57, as can be seen in Figures 12 and 13. The previous variations in strains and stresses corresponded to

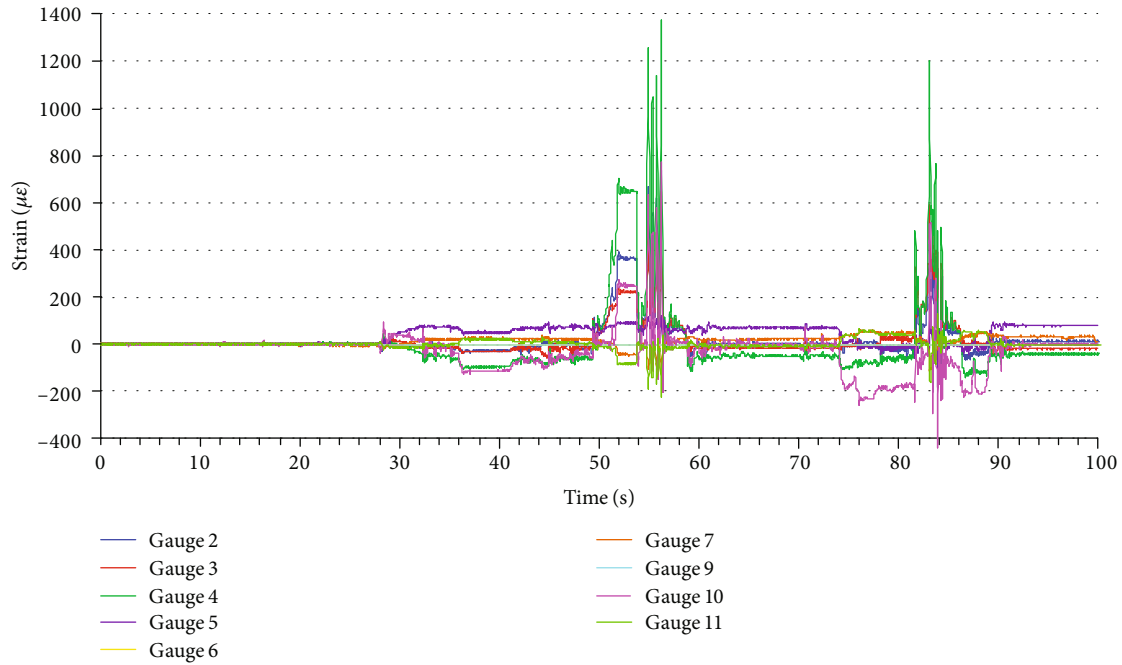


FIGURE 12: Results from unidirectional strain gauges from the dynamic load test.

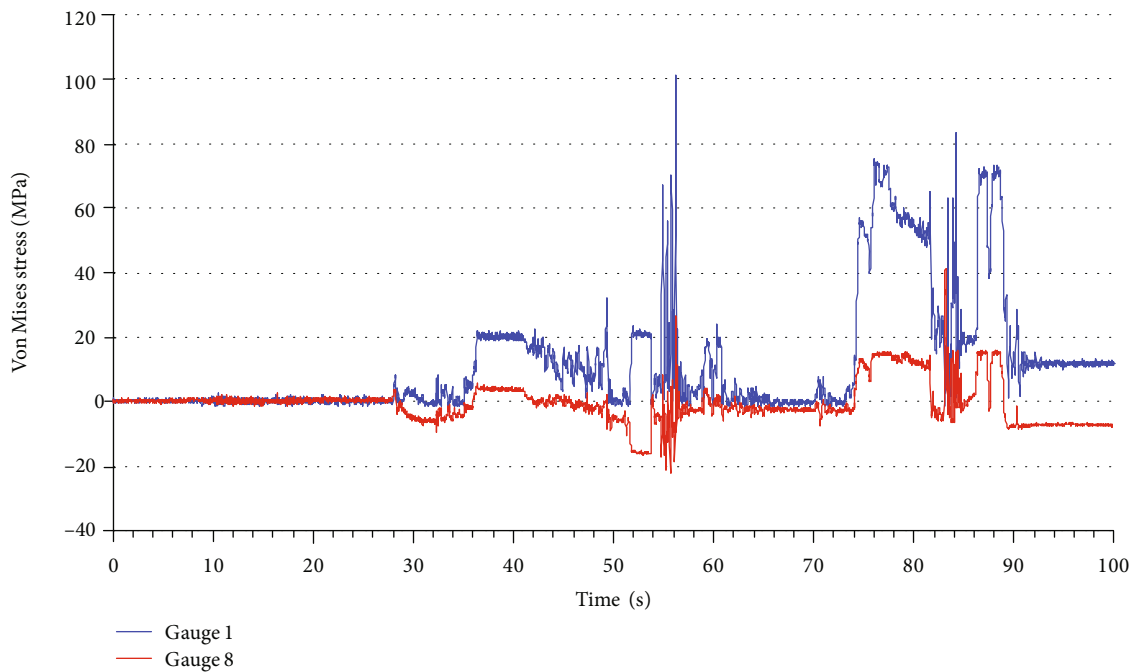


FIGURE 13: Results from rosettes from the dynamic load test.

different manoeuvres carried out to place the front loader bucket in a position that was perpendicular to the loading bay, so that both longitudinal beams of the front-end loader were balanced. Positioning and load application during the second test started at 73.6 seconds with the load application ending at 84.5 seconds.

Upon analysis of results obtained from dynamic load tests 1 and 2, a clear difference during the test execution

can be observed. The variation in the strains and stresses obtained shows differing structural behaviour of the front loader during both tests. This variation in the loader structural behaviour resulted from plastic strains generated in some components of the loader during the execution of the first test.

The maximum strain and stress values obtained during the first experimental dynamic load case are summarised in

TABLE 4: Maximum strain and stress values from the first dynamic load test.

	1	2	3	4	Gauges		7	8	10	11
Strain ($\mu\epsilon$)	—	734	647	1,369	5	121	41	—	770	31
Von Mises stress (MPa)	100.9	—	—	—	—	—	—	26.4	—	—

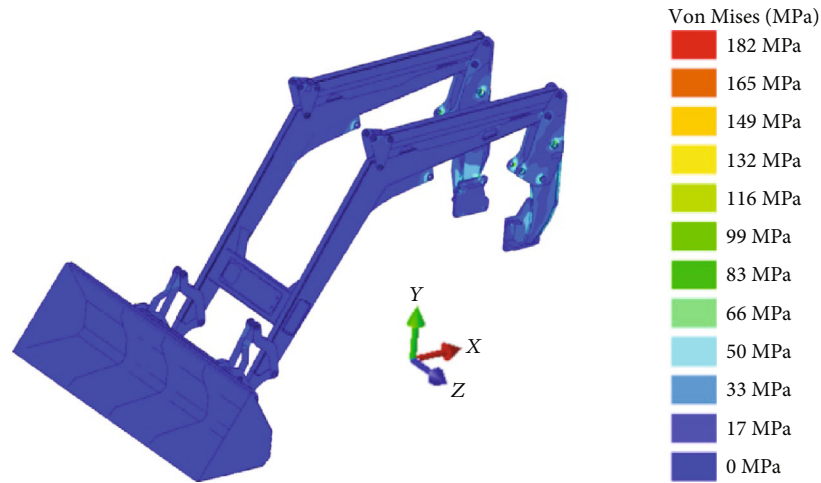


FIGURE 14: Von Mises stresses (MPa) from the analysis of static load case.

Table 4. The strains recorded by strain gauges 2, 3, 4, and 10 were $734 \mu\epsilon$, $647 \mu\epsilon$, $1369 \mu\epsilon$, and $770 \mu\epsilon$, respectively. These results prove that those points where the strain gauges were located recorded significant strains which may lead to plastic strain of the front loader.

The entire analysis of the results obtained at both qualitative level (with the different behaviour of the front loader during the first and second tests) and quantitative level (the strain values recorded mainly from strain gauges 2, 3, 4, and 10) proves the need to analyse the structural behaviour of the entire front loader. The results obtained seem to indicate that plastic strains were most likely generated in some structural components of the front-end loader during the execution of the first dynamic load test.

4.2. Numerical Analysis Phase

4.2.1. Static Load Case. Figure 14 shows the results for Von Mises stresses obtained from the numerical analysis. The maximum stress values (182 MPa) were located at the upper support bolt of the front loader on the clamping pillar. The higher tensions were located in the support components of the front-end loader in the clamping pillar, as well as in the clamping pillar itself. Nevertheless, the Von Mises stress values obtained, with the exception of the front loader support bolt, were no higher than 110 MPa for the rest of the components.

The maximum value of vertical displacement obtained was 9.99 mm at the front edge of the bucket, as shown in Figure 15.

The results obtained allow confirming that the design of the front-end loader analysed showed no stiffness or strength issues for the static load case.

Additionally, Table 5 shows strains and Von Mises stress values obtained from the static load case at those points where low-cost sensors were placed for the experimental test.

4.2.2. Dynamic Load Case. Figure 16 shows Von Mises stresses obtained from the numerical analysis. The stress map shows that the stress levels for the front loader in the dynamic load case were far higher than the results from the static load case. More specifically, in the dynamic load case analysed, the maximum stress value was 370 MPa which is higher than the yield strength of Steel S355-JR. This result shows that there are front loader components that get plastically deformed for the dynamic load case. In this instance, those components are the longitudinal beams of the front-end loader, as shown in Figure 16.

Displacement results are shown in Figure 17. The maximum horizontal displacement was 50 mm. These values were placed in the bores of the attachment bolts of the clamping pillars to the tractor. In contrast, displacements were nonexistent at the frontal line nodes of the bucket base. These results are consistent with the boundary conditions imposed in the numerical analysis.

Table 6 shows the strains and Von Mises stresses obtained from the numerical analysis of the front-end loader in the dynamic load case in those points where low-cost sensors were placed for the experimental test model.

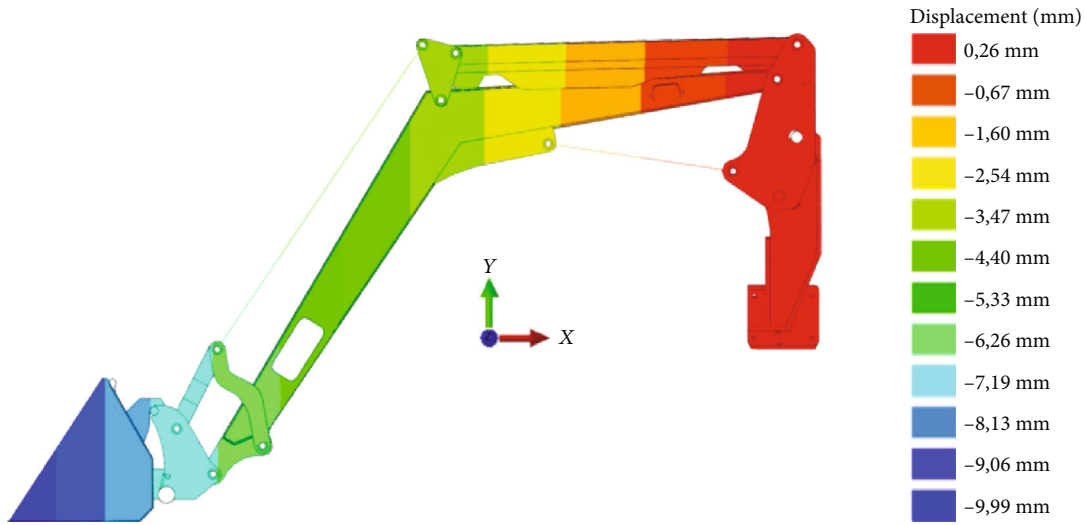


FIGURE 15: Vertical displacements (mm) from the analysis of static load case.

TABLE 5: Strain and stress values for the numerical analysis of static load case.

	Gauges								
	1	2	3	4	5	7	8	10	11
Strain ($\mu\epsilon$)	—	8	9	36	19	-7	—	79	-26
Von Mises stress (MPa)	12.1	—	—	—	—	—	7.6	—	—

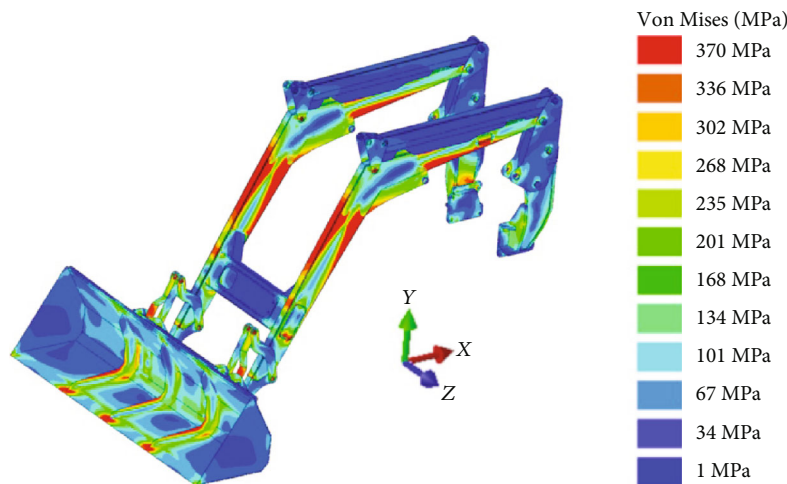


FIGURE 16: Von Mises stresses (MPa) from dynamic load case.

4.3. Correlation between Experimental and Numerical Results. In a study of this nature, correlation between numerical and experimental results is of paramount importance. On the one hand, correlation between numerical and experimental results allows validating the numerical models used in the study. In this study, this validation allows knowing the structural behaviour of the front-end loader analysed. On the other hand, the validation of the numerical model allows verifying the impressions created from the experimental results recorded by means of the strain gauges of the structural behaviour of the entire front-end loader analysed.

4.3.1. Analysis of the Static Load Case. Table 7 shows the results obtained for a static load case from each of the 9 strain gauges. It also shows the results obtained from the numerical analysis conducted by means of the FEM. Additionally, the error obtained when comparing the numerical results to the experimental results is provided.

Errors obtained from strain gauges 1, 5, 8, and 11 were less than 10%, a magnitude regarded as admissible for the correlation of results from the FEM. On the other hand, errors of the values from strain gauges 2 and 3 were -700% and -50%. Values of strains recorded by strain gauges 2 and 3 from the experimental test were $1 \mu\epsilon$ and $6 \mu\epsilon$, which were

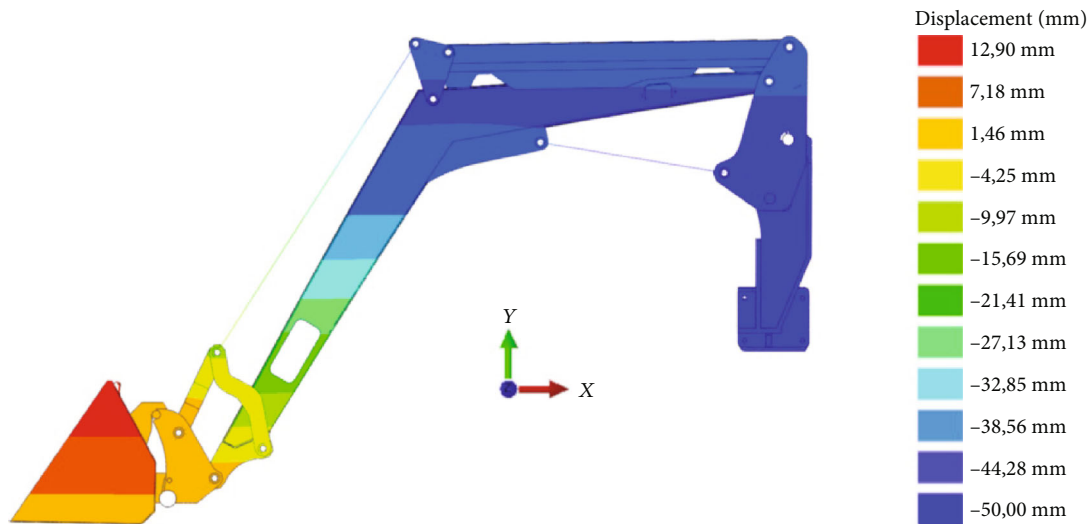


FIGURE 17: Vertical displacements (mm) from the dynamic load case.

TABLE 6: Strain and stress values for the numerical analysis of dynamic load case.

	1	2	3	4	Gauges					
					5	7	8	10	11	
Strain ($\mu\epsilon$)	—	726	711	1374	129	-100	—	631	-163	
Von Mises stress (MPa)	90.5	—	—	—	—	—	28.3	—	—	

TABLE 7: Correlation of numerical and experimental results from static load case.

Results		1	2	3	4	Gauges					
						5	7	8	10	11	
Test	$\mu\epsilon$	—	1	6	29	18	-6	—	88	-25	
	MPa	11.7	—	—	—	—	—	7.3	—	—	
Numerical analysis	$\mu\epsilon$	—	8	9	36	19	-7	—	79	-26	
	MPa	12.1	—	—	—	—	—	7.6	—	—	
Error	%	-3.42	-700	-50	-24.14	-5.56	-16.67	-4.11	10.23	-4.00	

very low strain values. Values of strain obtained from the numerical analysis for strain gauges 2 and 3 were $8 \mu\epsilon$ and $9 \mu\epsilon$, respectively. The numerical difference of the results from gauges 2 and 3 was $7 \mu\epsilon$ and $3 \mu\epsilon$, respectively, that is equivalent to a unidirectional stress of 1.47 MPa and 0.63 MPa for gauges 2 and 3, which is a minor difference for strain or stress results. Owing to the fact that the strains results were at such low level, the error generated in the correlation of numerical results with respect to experimental results was quite high. Due to the minor differences in numerical value between the experimental and numerical results, $7 \mu\epsilon$ and $3 \mu\epsilon$ at the positions for strain gauges 2 and 3, respectively, the numerical error obtained from gauges 2 and 3 is not significant in machinery design and thus allows validating the results obtained by means of numerical techniques in the measuring points of strain gauges 2 and 3. The relative error between experimental and numerical

results obtained from strain gauges 4 and 7 is 24.14% and 16.67%. Nonetheless, in both cases, the difference between numerical and experimental results is $7 \mu\epsilon$ for gauge 4 and $1 \mu\epsilon$ for gauge 7. This strain values are equivalent to a unidirectional stress of 1.47 MPa and 0.21 MPa, respectively. Therefore, and similar to gauges 2 and 3, the relative error obtained from gauges 4 and 7 is not significant in machinery design. The minor differences between experimental and numerical results allow validating the results obtained by means of numerical techniques in the measuring points of strain gauges 4 and 7. In the case of gauge 10, the error is 10.23%. This error is considered as admissible.

The results obtained allow concluding that there is good correlation between the numerical and experimental results obtained from the study of a front-end loader 430E2. The good correlation of results allows validating the numerical model of front-end loader, as well as the study of the static

TABLE 8: Correlation of numerical and experimental results from dynamic load case.

Results		Gauges								
		1	2	3	4	5	7	8	10	11
Test	$\mu\epsilon$	—	734	647	1,369	121	-104	—	609	-178
	MPa	93.4	—	—	—	—	—	26.4	—	—
Numerical analysis	$\mu\epsilon$	—	726	711	1,374	129	-100	—	631	-163
	MPa	90.5	—	—	—	—	—	28.3	—	—
Error	%	3.10	1.09	-9.89	-0.37	-6.61	3.85	-7.2	-3.61	8.43

load case defined during the development of the methodology for the design of front-end loaders.

4.3.2. Analysis of the Dynamic Load Case. Table 8 shows the strain and stress results obtained from the experimental test and the numerical analysis of the dynamic load case. These results correspond to the points in which the strain gauges were placed at the front-end loader. On the other hand, this table provides the error obtained when comparing the numerical results with the results obtained experimentally.

Unlike the static load case where the mass applied (320 kg) was known, for the dynamic load case, neither the force exerted by the tractor nor its displacement was known. Thus, in order to conduct the correlation of results, it is necessary to find a time period where the results obtained experimentally coincide with the results obtained from the numerical analysis for the dynamic load case.

The experimental results shown in Table 8 were obtained between seconds 56.18 and 56.24, thus involving a time interval of 0.06 seconds. As shown in Table 8, the error of the results obtained by means of the numerical analysis when compared to the experimental results was under 10% for the nine measuring points analysed. These errors less than 10% and a time interval in which they were obtained very small (0.06 seconds) allow confirming that the experimental and numerical results have a high correlation. This correlation allows validating the numerical model of front-end loader, as well as the study of the dynamic load case defined during the development of the methodology for the design of front-end loaders.

5. Conclusions

This study has shown the steps implemented for the development of a methodology which allows improving the current techniques for design and development of front-end loaders for agricultural tractors. In particular, this methodology analyses the manoeuvre that generates most instances of damage at the front-end loader, i.e., bucket loading.

The methodology developed consists of two phases: one experimental and the other involving numerical analysis. The experimental phase, by making use of low-cost sensors, more specifically 9 strain gauges, has allowed obtaining the strains and stresses generated at specific points of the front-end loader structure. On the other hand, the numerical analysis phase has allowed studying the structural behaviour of

the entire front-end loader by means of numerical techniques based on the Finite Element Method.

In the development of the methodology, two load cases, one static and the other dynamic, have been defined. The static case study allowed obtaining the strains and stresses generated in the front-end loader when a known mass was placed onto the bucket. The second load case, a dynamic case, allowed analysing the structural behaviour of the front-end loader during the bucket loading process. In order to ensure the repeatability of the study, the experimental test was defined in such a way that the front part of the bucket coupled to the front-end loader pushed to a concrete loading bay while the tractor moved forward. The numerical analysis for this test was defined in a similar way, limiting the forward movement of the tractor to 5 cm.

The experimental results obtained by means of the nine strain gauges and the results of the numerical analysis from the static load case show high correlation. The difference between the numerical results and the experimental results was lower than $9 \mu\epsilon$ for the unidirectional strain gauges and 0.4 MPa for the rosettes. This correlation of results allows validating the numerical model for the front-end loader, as well as the static load case defined during the development of the methodology for the design of the front-end loader.

On the other hand, the experimental results and the numerical results obtained from the dynamic load case show high correlation. Concretely, the error of the results obtained by means of the numerical analysis when compared to the experimental results was under 10% for the nine measuring points analysed. The experimental results were obtained in an interval of 0.06 seconds. This high correlation of results allows validating the numerical model for the front-end loader, as well as the study of the dynamic load case defined during the development of the methodology for the design of front-end loaders.

Data Availability

The data used to support the findings of this study are available from the corresponding author upon request.

Conflicts of Interest

The authors declare that there is no conflict of interest regarding the publication of this paper.

Acknowledgments

The authors express their gratitude to the cooperative “Virgen de la Oliva, Ejea de los Caballeros,” for their assistance with this research. This research was funded by VEHIVIAL Research Group (University of Zaragoza) and by the company Maquinaria Agrícola El León (Spain).

References

- [1] B. J. Cho, S. W. Ahn, C. J. Lee, Y. H. Yoon, S. S. Lee, and H. J. Kim, “Improved design of hydraulic circuit of front-end loader for bump shock reduction of an agricultural tractor,” *Journal of Drive and Control*, vol. 13, no. 2, pp. 10–18, 2016.
- [2] Y.-J. Park, S.-B. Shim, and J.-S. Nam, “Experimental study on the structural safety of the tractor front-end loader against impact load,” *Journal of Biosystems Engineering*, vol. 41, no. 3, pp. 153–160, 2016.
- [3] Y. J. Kim, S. O. Chung, S. J. Park, and C. H. Choi, “Analysis of power requirement of agricultural tractor by major field operation,” *Journal of Biosystems Engineering*, vol. 36, no. 2, pp. 79–88, 2011.
- [4] S. W. Ahn, H. J. Kim, S. S. Lee, and D. S. Choi, “Study on driving shock reduction of a front end loader by accumulator,” *Korean Society for Agricultural Machinery*, vol. 19, no. 1, pp. 91–92, 2014.
- [5] P. Simion and S. Nastase, “Contributions to the study of the dynamics of agricultural tractors equipped with front-end loader and rear forklift loader,” in *8th International Scientific Conference. Engineering for Rural Development*, Jelgava, Latvia, 2009.
- [6] G. S. Lim and B. Y. Lee, “Study on the impact analysis of front loader for tractor,” *Journal of the Korea Academia-Industrial cooperation Society*, vol. 16, no. 8, pp. 5051–5059, 2015.
- [7] Z. Yu, Z. Shan, J. Yuan, and X. Li, “Performance deterioration of heavy-haul railway bridges under fatigue loading monitored by a multisensor system,” *Journal of Sensors*, vol. 2018, Article ID 5465391, 14 pages, 2018.
- [8] A. Gregori, E. di Giampaolo, A. di Carlofelice, and C. Castoro, “Presenting a new wireless strain method for structural monitoring: experimental validation,” *Journal of Sensors*, vol. 2019, Article ID 5370838, 12 pages, 2019.
- [9] M. Carrera Alegre, L. Castejon Herrer, H. Malon Litago et al., “Fatigue life analysis of semitrailers. Fatigue testing bench and numerical simulation,” *DYNA*, vol. 91, no. 4, pp. 406–412, 2016.
- [10] H. Malon, L. Castejon, J. Cuartero, and P. Martin-Buro, “Numerical-Experimental analysis of two Floor Platform Designs for auxiliary Construction Truck,” *Experimental Techniques*, vol. 39, no. 6, pp. 53–60, 2015.
- [11] H. J. Beermann, “Static analysis of commercial vehicle frames: A hybrid-finite element and analytical-method,” *International Journal of Vehicle Design*, vol. 5, no. 1–2, pp. 26–52, 1984.
- [12] C. Karaoglu and N. S. Kuralay, “Stress analysis of a truck chassis with riveted joints,” *Finite Elements in Analysis and Design*, vol. 38, no. 12, pp. 1115–1130, 2002.
- [13] F. Cappello, T. Ingrassia, A. Mancuso, and V. Nigrelli, “Methodical redesign of a semitrailer,” in *9th International Conference on Computer Aided Optimum Design in Engineering. Computer Aided Optimum Design in Engineering IX Book Series: Wit Transactions on the Built Environment*, vol. 80, pp. 359–369, 2005.
- [14] R. M. Buil and L. C. Herrer, “Diseño Frente a Fatiga De Semi-remolques Cisterna. Fatigue design of tanker semi-trailers,” *Dyna Ingenieria E Industria*, vol. 85, no. 3, pp. 480–488, 2010.
- [15] Y. Q. Deng, J. G. Wang, Y. Wen, S. Zhao, and L. L. Dai, “The static and dynamic characteristics study of aluminum tank semitrailer,” *Advanced Materials Research*, vol. 189–193, pp. 2233–2237, 2011.
- [16] P. Luque, D. A. Mántaras, A. Rodríguez et al., “Low-cost monitoring system of sensors for evaluating dynamic solicitations of semitrailer structure,” *Journal of Sensors*, vol. 2016, Article ID 1740854, 15 pages, 2016.
- [17] H. Malon, F. J. Garcia-Ramos, M. Vidal, and A. Bone, “Design and optimization of a chassis for an air-assisted sprayer with two fans using the finite element method,” in *Project Management and Engineering Research, 2014*, pp. 103–115, Springer, Cham, 2016.
- [18] H. Malón, A. Aguirre, A. Boné, M. Vidal, and F. García-Ramos, “Design and testing of an agricultural implement for underground application of rodenticide bait,” *Sensors*, vol. 15, no. 1, pp. 2006–2020, 2015.
- [19] Data Sheet, “Front-end loader 430E2,” http://www.el-leon.es/productos/palas-cargadoras/productos/palas-cargadoras/copy5_of_serie-europa.
- [20] K. Hoffmann, “An Introduction to Measurement Using Strain Gauges,” Publisher by Hottinger Baldwin Messtechnik GmbH, Darmstadt (Germany), 1989.

Research Article

Change Analysis of Spring Vegetation Green-Up Date in Qinba Mountains under the Support of Spatiotemporal Data Cube

Jiyuan Li ¹, Xiao Feng ², Jiangbin Yin,¹ and Fang Chen³

¹Northwest Land and Resources Research Center, Shaanxi Normal University, No. 620 West Chang'an Street, Xi'an 710119, China

²School of Highway, Chang'an University, Middle of South Er'huan Road, Xi'an 710064, China

³State Key Laboratory of Information Engineering in Surveying, Mapping and Remote Sensing, Wuhan University, Wuhan 430079, China

Correspondence should be addressed to Xiao Feng; fengxiao0126@chd.edu.cn

Received 15 November 2019; Accepted 6 January 2020; Published 27 February 2020

Guest Editor: Zhifeng Yu

Copyright © 2020 Jiyuan Li et al. This is an open access article distributed under the Creative Commons Attribution License, which permits unrestricted use, distribution, and reproduction in any medium, provided the original work is properly cited.

In recent decades, global and local vegetation phenology has undergone significant changes due to the combination of climate change and human activities. Current researches have revealed the temporal and spatial distribution of vegetation phenology in large scale by using remote sensing data. However, researches on spatiotemporal differentiation of remote sensing phenology and its changes are limited which involves high-dimensional data processing and analysing. A new data model based on data cube technologies was proposed in the paper to efficiently organize remote sensing phenology and related reanalysis data in different scales. The multidimensional aggregation functions in the data cube promote the rapid discovery of the spatiotemporal differentiation of phenology. The exploratory analysis methods were extended to the data cube to mine the change characteristics of the long-term phenology and its influencing factors. Based on this method, the case study explored that the spring phenology of Qinba Mountains has a strong dependence on the topography, and the temperature plays a leading role in the vegetation green-up date distribution of the high-altitude areas while human activities dominate the low-altitude areas. The response of green-up trend slope seems to be the most sensitive at an altitude of about 2000 meters. This research provided a new approach for analysing phenology phenomena and its changes in Qinba Mountains that had the same reference value for other regional phenology studies.

1. Introduction

The phenology is an important indicator reflecting the status of vegetation growth as it responds to the ecological environment correspondingly [1]. Meanwhile, vegetation phenology has impact on the food supply, animal activities, and human health, further affecting the carbon budget and material recycling process at a global scale [2]. Therefore, the phenology observation and analysis are a critical way to understand the changes of the environment. In recent years, studies have found vegetation phenology changed significantly since the last century due to dual influence of global climate change and human activities. Several analyses have revealed the earlier green-up dates and delayed dormancy. Although the researches have shown no trends in spring and autumn phe-

nology during the global warming hiatus (1998-2012) [3], the green-up date of some climate-sensitive areas still had an obvious advancement, such as Qinba Mountains. As the transitional belt between the north and south climate zones of China, this area shows complex topography and spatiotemporal heterogeneity of climate. More than six cities are distributed in this area. It is essential to understand the spatiotemporal differentiation of the vegetation phenology and related influencing factors in Qinba Mountains.

Nowadays, the network of site-based phenology observation has been established in some regions/countries [4–6]. The long-term FLUXNET measurements were analysed to present no widespread advancement of vegetation green-up date within the warming hiatus [3]. The phenology modelling methods based on the in situ observation of specific

plants were also proposed to predict the trends with the climate changes [7]. The in situ observation data has high quality but limited site numbers. In Qinba Mountains, complex topography and rich biodiversity lead to great spatial heterogeneity of phenology distribution and its changes [8]. The observation data of limited monitoring sites cannot describe the spatial distribution of the phenology in the entire research area properly.

Remote sensing data provided long-term observations for large-scale land surface phenology research. The NDVI (normalized difference vegetation index)/EVI (enhanced vegetation index) dataset was used widely to find SOS (start of the growing season), EOS (end of the growing season), and LOS (length of the growing season) accordingly with the global climate change [9]. Various available remote sensing data source and related phenology parameter extraction methods established a good scientific foundation for the further analyses of the change characteristic [10–12]. The remote-sensed phenology map described the considerable spatial differentiations, especially between urban and rural areas, which suggested the potential influence of an urban heat island caused by human activities [13, 14]. Land cover change and vegetation type were also considered to examine the differences of phenology change rate in the northern high-latitude areas [11]. In Qinba Mountains, several studies showed the overall spatial distribution of the spring phenology has an advanced trend [15, 16]. The spatial pattern was consistent with the local hydrothermal conditions and has strong topographic dependence in the area [17, 18].

The complex topography and special geolocation of Qinba Mountains lead to various types of climatic conditions with differentiations on several aspects, such as longitude, latitude, altitude, and slope. Therefore, it is necessary to explore the pattern of the phenology distribution in the area from multiple aspects. Although phenology change in Qinba Mountains draws much attention, studies of comprehensive change analysis from multiple dimensions are limited. Current studies by using remote sensing data mainly focused on the parameter extraction, overall spatial patterns, and trends of phenology. Such an analysis involves spatial and temporal unified computing and high-dimensional data processing of remote sensing data. A traditional remote sensing data model is a layer-based stack that is not efficient for multidimensional map algebra. In addition, the inconsistency of multivariate data scales poses great challenges to this research. Currently, data cube technologies become more and more popular for remote sensing data processing [19, 20]. Data cube organizes gridded data through multidimensional arrays and is indexed by coordinates. Therefore, its dimensional independence and array operations help to achieve high-performance computing. The data cube can handle large-scale data efficiently if combined with an array database and parallel procedures [21, 22]. Based on this idea, the EO Data Cube provides comprehensive platform supports from data acquisition to analysis services [23, 24]. This paper built a tidy data model under the support of data cube technologies. Based on this model, the change analysis of vegetation green-up date along multiple dimensions has been investigated to discover more spatiotemporal differentiation.

The natural exploratory analysis method in the data cube has been used to understand climate-phenology-human interactions in the area. This research provided a new approach for analysing phenology phenomena and changes in Qinba Mountains that had the same reference value for other regional phenology studies.

The paper is organized as follows: Section 2 describes the data sources and methodology. Section 3 presents the results and analysis works based on the data cube. Section 4 and Section 5 finish with discussion and conclusions, respectively.

2. Data and Methodology

2.1. Study Area and Data Source. Qinba Mountains is located in central China and consists of Qinling Mountains in the north and Daba Mountains in the south (see Figure 1). Its western part is connected to Qinghai-Tibet Plateau, and the east reaches the North China Plain. The landscape of mountains is dominant in the area with several basins, such as Hanzhong, Ankang, and Shandan, distributed in the middle. Due to the diverse hydrothermal conditions and the significant vertical changes, there are three climate types from the south to the north in Qinba Mountains: north subtropical climate, subtropical-warm temperate transitional climate, and warm temperate climates. The research area within the black boundary as shown in Figure 1 is covered by geographical regions of 80 counties with a total area of 230,000 km² and a maximum elevation of over 4000 m.

We utilized the long-term vegetation green-up products in the period of 1981–2016 from NASA MEaSUREs Project which fused measurements from different satellite missions and sensors: AVHRR (Advanced Very High Resolution Radiometer), MODIS (Moderate Resolution Imaging Spectroradiometer), and VIIRS (Visible infrared Imaging Radiometer). The products had been validated with the ground observations from US national phenology network (US-NPN) at a climate modelling grid (CMG, 0.05 DEG) resolution (<https://vip.arizona.edu>).

SRTM (Shuttle Radar Topography Mission) digital elevation data (DEM) was resampled to 5 km resolution by the nearest-neighborhood methods that were then used to generate slope and aspect data with the same resolution. Land use data in the year 2015 was derived from 500 m land cover products provided by Climate Change Initiative (CCI) of the European Space Agency (<https://www.esa-landcover-cci.org>). All the land use types in raw data were reclassified into six groups: settlement place, cropland, forest cover, other natural vegetation, water body, and bare land. The meteorological data are provided by the Meteorological Science Data Sharing Service Network of China (<http://data.cma.cn>), including the daily average temperature and precipitation from 43 national meteorological stations within the 40 km buffer zone of the study area. Daily meteorological data were interpolated to raster data at 5 km resolution by Auspln4.2 tools using thin plate smoothing splines and DEM data. All the data were projected onto Albers equal-area conic projection along with a WGS 1984 coordinate system, which is

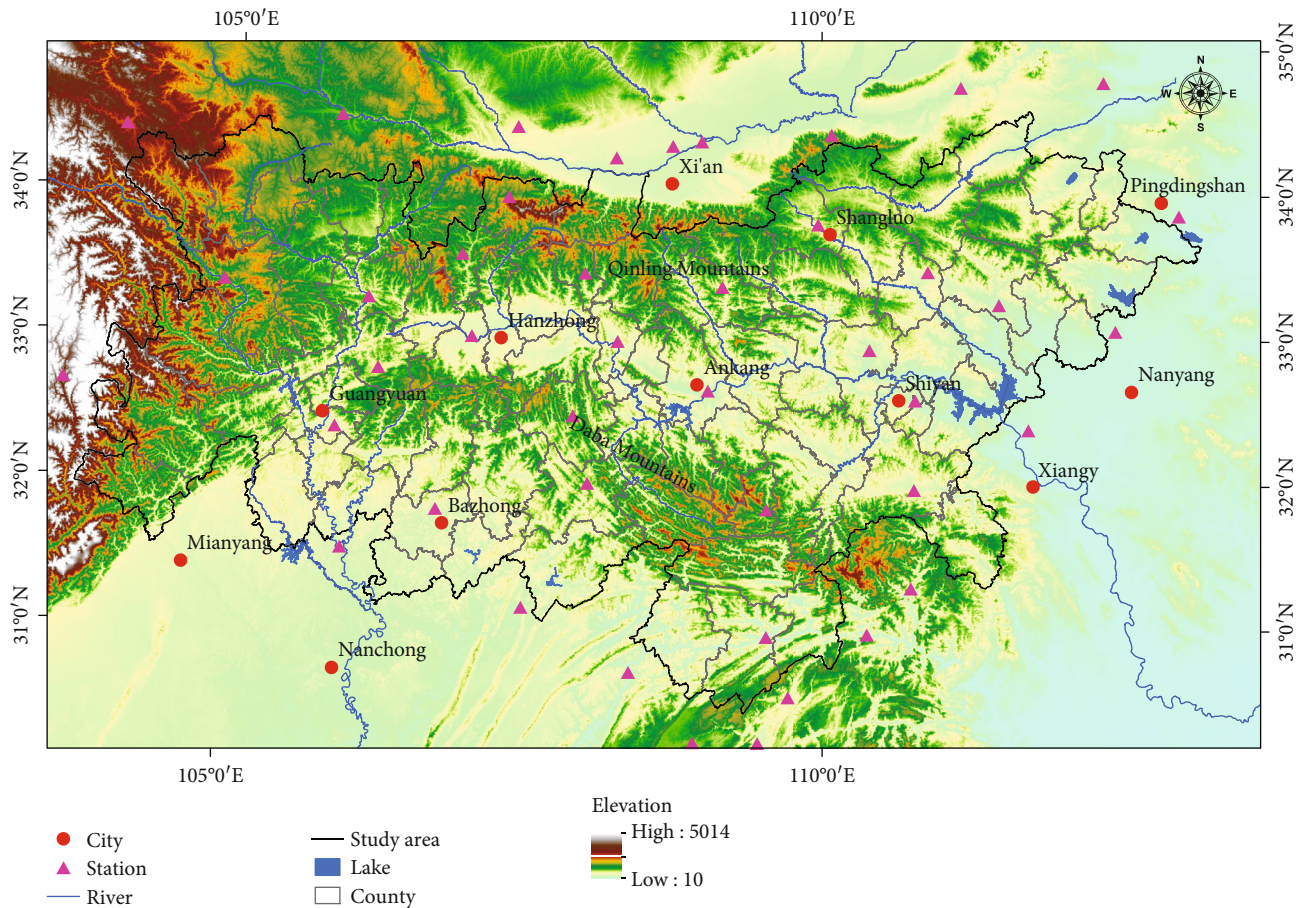


FIGURE 1: Study area covered by 80 counties in Qinba Mountains.

considered a standard projection and coordinate system throughout our study.

2.2. Methodology

2.2.1. Data Cube Model. A data cube has been applied in several domains for multidimensional data managing and processing [25]. Therefore, there are no standards for the model definition and operations. Normally, a data cube can be seen as the specified container of multidimensional arrays with spatial and temporal dimensions at least. Certainly, it is able to contain more numbers of arbitrary dimensions to be a hypercube. The data cube used in this paper can be defined as a tuple of three elements: $\langle D, C, A, M \rangle$, where D represents the dimension set including space and time, and the space can be expressed as one or two dimensions (see Figure 2). The combination of all the dimensions is used to locate a fixed point-named cell in the cube. A is the attribute associated with the cube, such as name or projection information.

One cell stores a series of measurements (M in the tuple) from various data sources, such as temperature, precipitation, and phenology data. There are three types of measurements in the cube: numeric, proportional, and typological metrics. The numeric metric means a single value, such as temperature. The proportional metric is structured as a dictionary recording the proportion of multiple categories in the

cell, such as land covers. If one cell is covered by one type of land use, we employ specified integer to code instead, namely, typological metric. In the tuple, C means the coordinate set, and each coordinate must keep the same size with some of the dimension members. A coordinate is used to describe the dimension from special perspective. For example, we define DEM as a coordinate to label every cell in the space by elevation. That means different labelling or indexing rules can be established by coordinates beyond dimensions. It is worth noting that the data of the coordinate can be converted to or from the dimension and measurement that facilitates realizing different kinds of operation, such as slice, aggregate, and pivot.

All of data modelling work is based on the Xarray which is a python library designed for multidimensional array computing [26]. The object-oriented cube implementation includes DimensionSet, CoordinateSet, MeasurementSet, and AttributeSet. Both Measurement and Dimension are the types of DataArray object that support 1D time series, 2D array, or array of arbitrary dimensions. The Coordinate object is inherited from Dimension objects; thus, it can be transformed to Dimension. The data cube inherits the mathematical capabilities of multidimensional arrays, and the spatial and temporal functions are able to execute simultaneously to generate new cubes. For instance, $\text{Cube}' = \alpha \text{Cube} + \beta$, where Cube is the input data and α/β is the linear

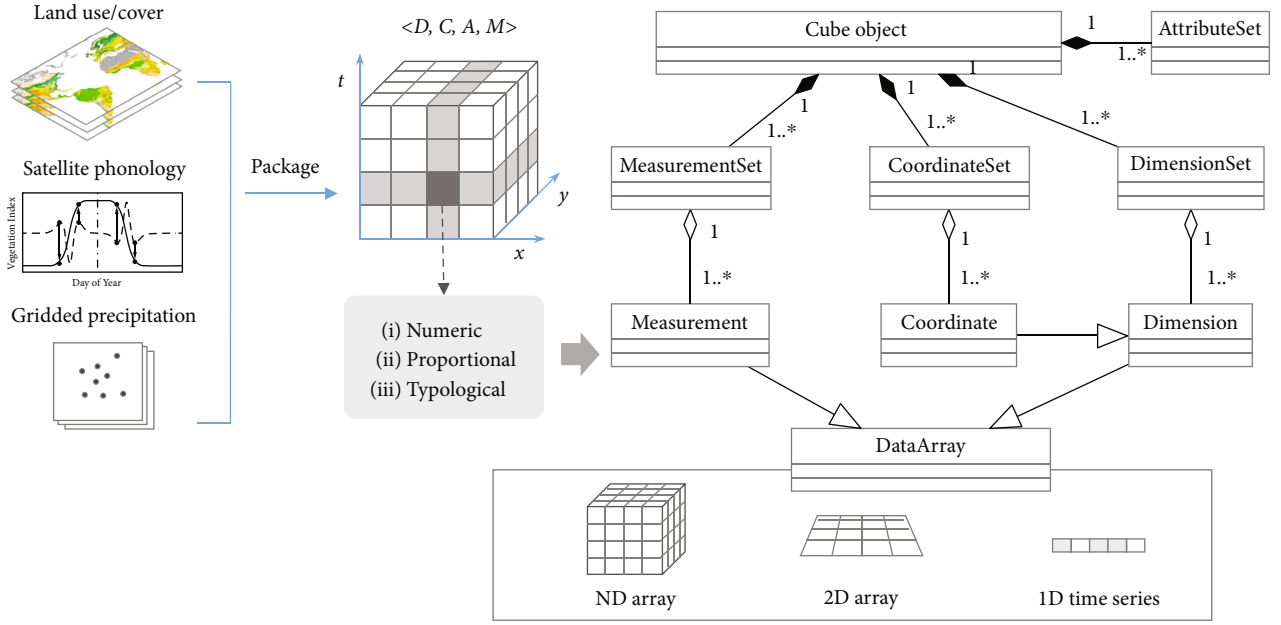


FIGURE 2: UML diagram of the data cube model.

parameter. The proposed cube model is cached in memory, and NetCDF (Network Common Data Form) file is supported to store the big cube data in the disk. The cube keeps the file handle open and lazily loads its contents from on-disk datasets to improve the efficiency of memory utilization.

2.2.2. Spatiotemporal Pattern Analysis by Cube Aggregation.

Due to the high dimensionality and large amount of data cube, the spatiotemporal pattern cannot be recognized visually. Therefore, the data cube needs to be aggregated according to a certain scale on one or several dimensions to reduce dimensionality. Then the summarized maps/charts that conform to the human visual cognition would help to visually analyse the spatiotemporal patterns of metrics along different perspective/dimensions.

There are only space and time dimension in the proposed data cube; thus, the cube aggregations can be categorized into three types: temporal aggregation, spatial aggregation, and spatiotemporal aggregation (see Figure 3). The temporal aggregation summarized the cube into time bins, such as monthly average precipitation. The spatial aggregation divides the space into several zones according to values or geographical boundaries and then aggregates the data within the zones. The spatiotemporal aggregation generates space-time zones for further statics, which is useful when analysing the impact of climate on phenology. For example, the corresponding cumulative rainfall on the cell, where each SOS is located, can be calculated since the time bins for cumulative rainfall on these cells are different. The cube aggregations can be described by Zonal function in multidimensional map algebra proposed by Mennis [27] as follows:

$$\text{Agg} = \text{Zonal}(\text{cube}, \text{zone}, f), \quad (1)$$

where zone is the aggregation zones of specific dimensions and f indicates the aggregate functions, such as the mean/sum/variance. Based on the data cube model, the Zonal function is realized through three steps: (1) convert the data of coordinate for aggregation to the members of cube dimension, (2) construct the bins of the resultant dimension for aggregation, and (3) group the data of cube by bins and then carry out aggregate functions for each bin.

2.2.3. Trend Analysis in the Cube. The Mann-Kendall method was widely used to examine the trend because it does not assume a specific distribution for the data and is not disturbed by outliers [28, 29]. We utilized the method to test the trend for the time-series values in each bin of the cube. The formulas are as follows:

$$S = \sum_{i=1}^{n-1} \sum_{j=i+1}^n \text{sgn}(x_j - x_i), \quad (2)$$

$$\text{sgn}(\theta) = \begin{cases} 1, & \theta > 0, \\ 0, & \theta = 0, \\ -1, & \theta < 0, \end{cases}$$

where x_j is the j th value in the current bin and n indicates the number of the bin's item. The trend for each bin time series is recorded as a z -score and a p value. The Theil-Sen method can be calculated for each bin to estimate the slope of the Mann-Kendall trend as follows [30]:

$$\text{Slope} = \text{Median} \left(\frac{x_i - x_j}{i - j} \right). \quad (3)$$

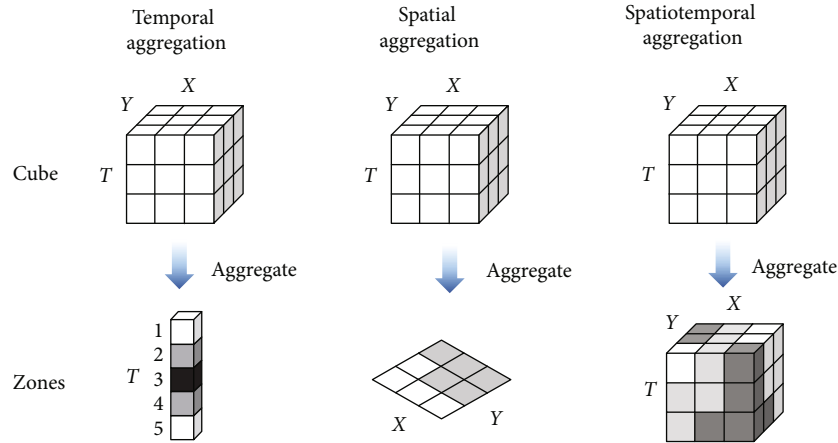


FIGURE 3: Zonal functions in multidimensional map algebra (Mennis, 2010).

Based on the result of the data trend analysis, the Getis-Ord G_i^* statistic was employed to identify trends (hot spot) in the cube that had passed the significance test [31]. The formulas are as follows:

$$G_i^* = \frac{\sum_{j=1}^n w_{i,j} x_j - \bar{X} \sum_{j=1}^n w_{i,j}}{S \sqrt{\left[n \sum_{j=1}^n w_{i,j}^2 - \left(\sum_{j=1}^n w_{i,j} \right)^2 \right] / (n-1)}},$$

$$\bar{X} = \frac{\sum_{j=1}^n x_j}{n}, \quad (4)$$

$$S = \sqrt{\frac{\sum_{j=1}^n x_j^2}{n} - (\bar{X})^2},$$

where x_j is the value of the cell in spatiotemporal bin j , $w_{i,j}$ is the spatiotemporal weight between bin i and bin j , and n indicates the numbers of bins with spatiotemporal proximity to bin i . Once Getis-Ord G_i^* statistic was completed for each bin, the hot spot trends were tested using the Mann-Kendall method. The results of the data trends and hot spot trends were combined to find new, intensifying, diminishing, and sporadic hot and cold spots in the cube. ArcGIS 10.5 is utilized to carry out hot spot analysis. The proposed data cube supports reading or writing NetCDF data that can be directly piped to ArcGIS hot spot analysis tool by using ArcPy (python library for ArcGIS).

3. Results and Analysis

3.1. Data Cube Building. Two data cubes were generated: the SOS data cube and climate data cube and the basic structures of them are shown (see Table 1).

There are two types of measures in the SOS data cube. One of them is SOS represented by days of year (DOY), and a 5 km grid is used as a spatial dimension. Another one is land use data that are aggregated into the same grid. Due to the use of map projection, the latitude information and longitude information are regarded as coordi-

nates in the cube to facilitate further analysis based on geographical locations.

Time series climate data in the period of 13149 days are packaged into the climate data cube where two types of aggregate rules are built to generate new measurements (temperature and precipitation) for the SOS data cube. The first one is yearly aggregation by aggregating data within year-length bins. The other one is aggregating data within the time bins, in the form of (SOS, SOS + N month], based on the SOS for each location. We denote the average value aggregated within one month before SOS as 1 m Lag and the summarized value aggregated within one month before SOS as $\Sigma 1$ m Lag. The aggregated climate data are injected into the SOS data cube as new measurements.

3.2. Spatiotemporal Pattern Analysis. The topography of Qinba Mountains is diverse with multidimensional characteristics, and the climate also varies in different dimensions, such as latitude, longitude, elevation, and slope. These differences may lead to a high degree of complexity, diversity, and heterogeneity in the phenology of Qinba Mountains. Figure 4 presents the spatial distribution of average SOS between year 1981 and 2016 that indicates obvious consistency with the distribution of the topography shown in Figure 1. The cities and residential areas are distributed in the valleys or basins which are located in the northern, southern, eastern, and central parts of the area. Therefore, the impact intensity of human activities on the environment should have a strong correlation with the topographical distribution. The spatiotemporal patterns of SOS were analysed separately according to the three topographic factors as follows.

The SOS varying with increased elevation was calculated by aggregation SOS into elevation bins as shown in Figure 5(a). It appears that SOS becomes earlier while elevation increases. In the range below the elevation of 700 m, SOS increases greatly at first, then decreases a little. The possible reason is that human activities are more frequent in this zone, and the SOS gradually returns to the natural level at around 700 m. Temperature becomes the major controlling factor in phenology at high altitudes. When it reaches 3500 m, the upward trend of SOS is gradually flattening. The time-

TABLE 1: Structures of the SOS data cube and climate data cube.

	SOS data cube	Climate data cube
Dimension	X (5 km), Y (5 km), T (yearly) Size: $200 \times 100 \times 36$	X (5 km), Y (5 km), T (daily) Size: $200 \times 100 \times 13149$
Coordinate	Latitude, longitude, elevation, slope, aspect	/
Measurement	SOS, land use	Temperature, precipitation

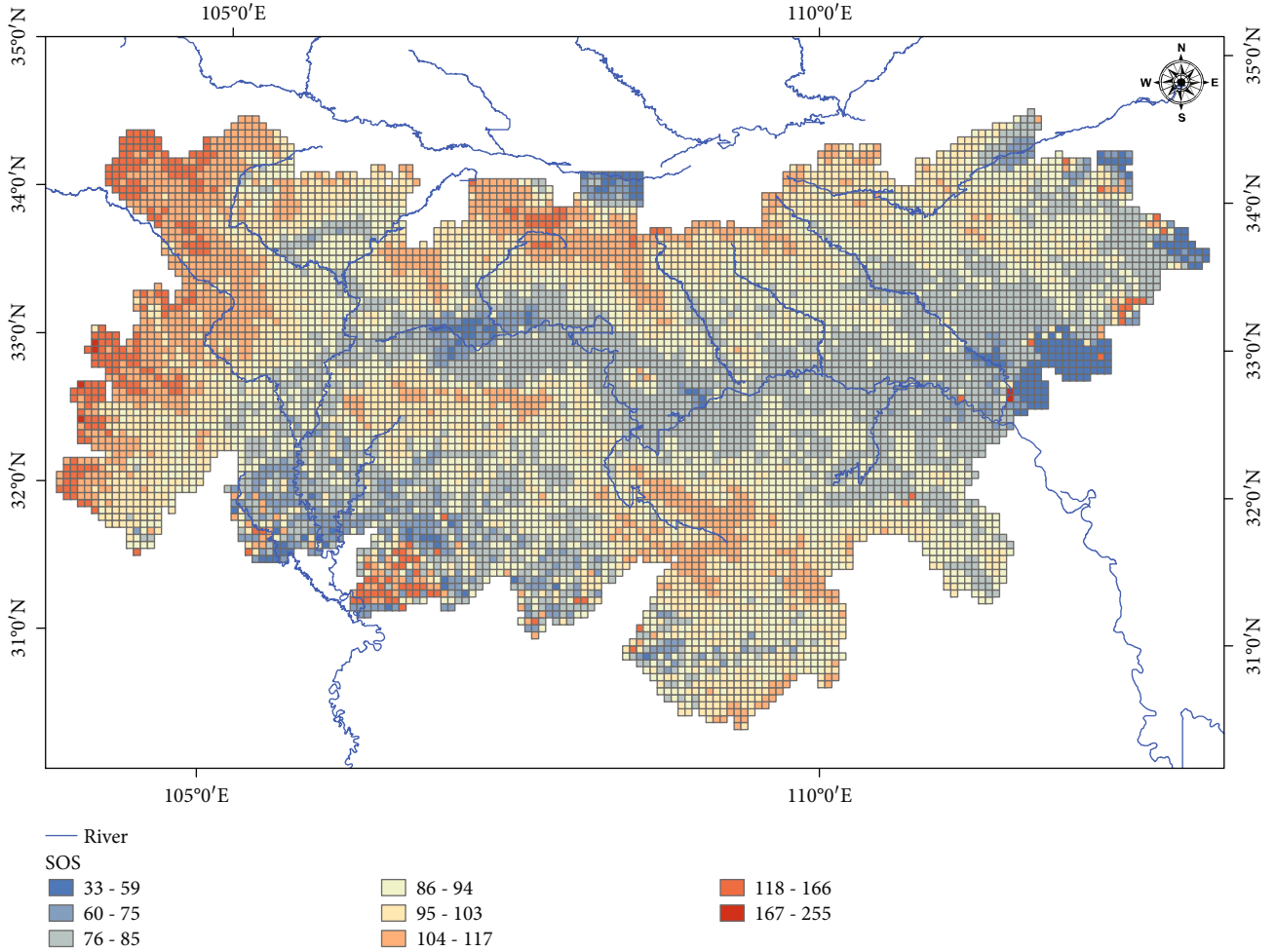


FIGURE 4: Spatial distribution of SOS between years 1981-2016.

elevation distribution of SOS shown in Figure 5(b) illustrates these changes more clearly, and it also indicates the SOS gets advancement year by year for the same elevation bins.

Slope is one of the important topographic factors that directly affects soil type, soil moisture, and nutrients and thus lead to different vegetation types. According to Figure 6(a), SOS increased significantly in the zone with a slope of 0° - 5° while growing slowly in 5° - 25° . When it reaches 25° , the growth rate becomes obvious. Figure 6(b) illustrates these changes in a 2D space. The tests demonstrated that the slope has a preventive effect on vegetation green-up.

The aspect is able to redistribute the sunlight, energy, and rainfall in a local environment. We define two aspect bins (south and north) and four elevation bins: (0, 600 m], (600 m, 1500 m], (1500 m, 2000 m], and (2000 m, 4000 m].

The SOS data cube was aggregated along both the aspect and elevation dimensions (Figure 7). The south-north slope differentiation of SOS is not obvious at an altitude of 1500 m or less. The SOS gap between the south slope and the north slope appears within the zone of (1500 m, 2000 m], but becomes smaller gradually until year 2000. In areas above 2000 m elevation, there have been significant SOS differences between the north and south slopes. The result reveals that the higher the altitude, the more obvious the south-north slope differentiation of SOS. However, the differentiation will gradually disappear with the global warming trend.

3.3. Trend Analysis. The Mann-Kendall trend test was performed on the SOS data cube for the period from 1981 to

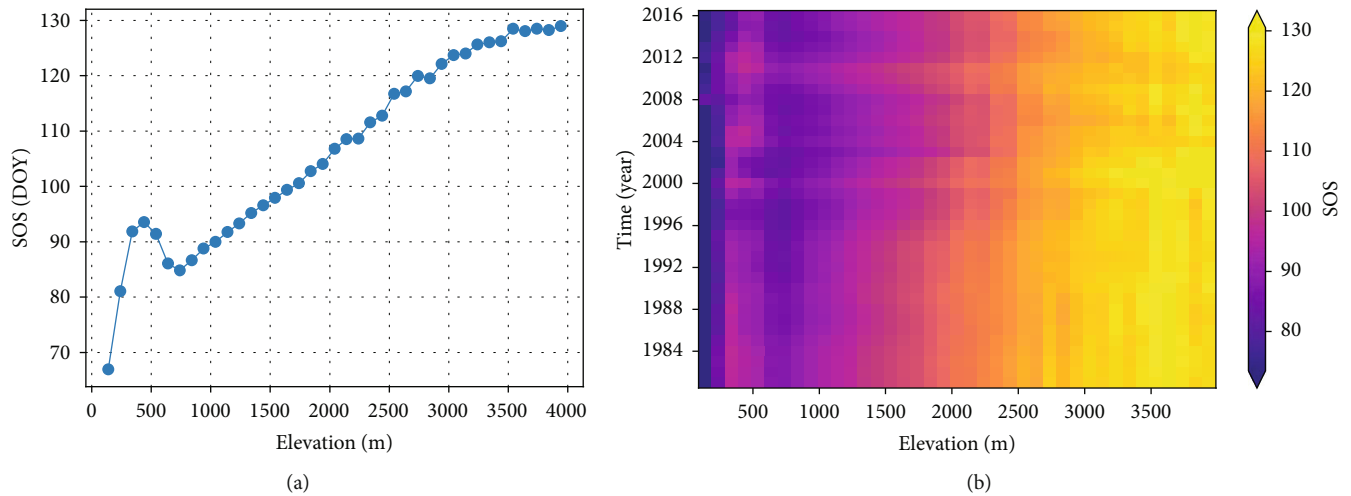


FIGURE 5: SOS changes with elevation differentiation. (a) Averaged SOS changes with elevation. (b) SOS changes in elevation-time space.

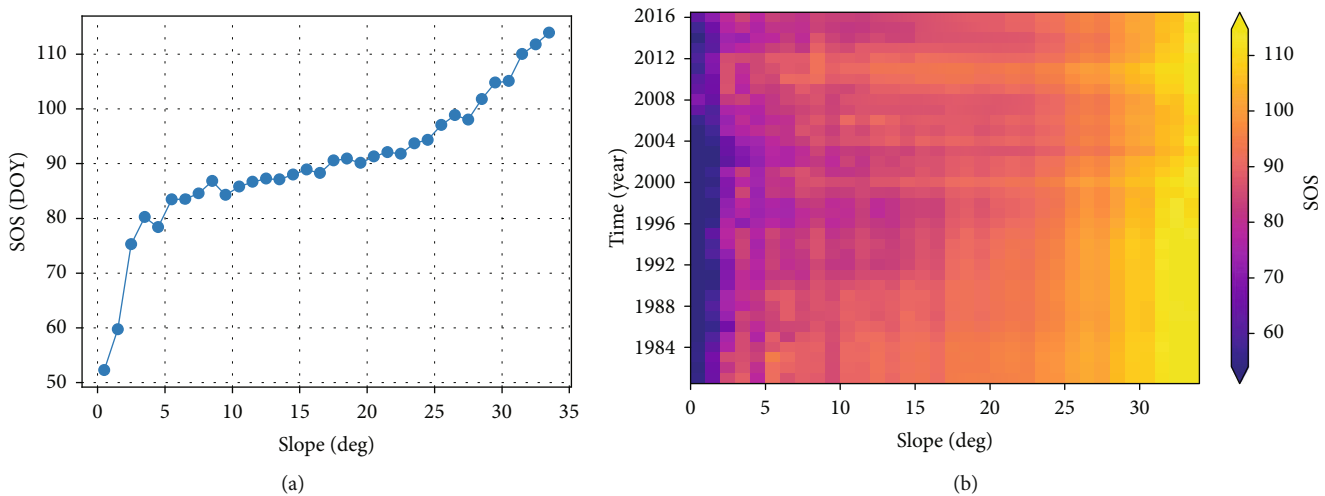


FIGURE 6: SOS changes with slope differentiation. (a) Averaged SOS changes with slope. (b) SOS changes in slope-time space.

2016 ($Z\text{-score} = -4.2906$, $p < 0.00001$). The slope of the Mann-Kendall trend is shown in Figure 8. It can be seen that SOS has an advance trend in most areas, except for the areas where human activities are more frequent.

In order to examine the response sensitivity of the SOS slope to different altitudes, we aggregated the trend slopes into different elevation bins (see Figure 9). The result shows that there is no significant change of the slope in the low-altitude area. When the elevation increases over 600 m, the negative slope gradually increased. At around 2000 m, the response of slope seems to be the most sensitive. It would decrease as the altitude continues to rise. The test demonstrates that SOS changes in high-altitude areas are more sensitive than those in low-altitude areas, and the effects of human activities on low-altitude areas on SOS changes are diverse.

The slope analysed above reflects the overall trend of SOS. In order to identify trends and investigate the change process, the Getis-Ord G_i^* statistic method is used in the SOS data cube (hot spot analysis). As shown in Figure 10,

the result has been categorized into eight clusters: persistent cold spot, intensified cold spot, diminishing cold spot, consecutive cold spot, oscillating cold spot, oscillating hot spot, diminishing hot spot, and persistent hot spot.

A persistent cold spot represents a statistically significant cold spot for 90% of the time-step intervals with no discernible trend. These types of spots are concentrated in the urban and small town area where the human activities are always frequent for a long time. The area is surrounded by intensified cold spot, diminishing cold spot, and constitutive cold spot. The intensified cold spot located in rural areas means the SOS is getting earlier while diminishing cold spot indicates the delaying trend. A consecutive cold spot describes a location with a single uninterrupted run of statistically significant cold spot bins in the final time-step intervals. The above different phenomena may be caused by different land use patterns by human in the region, such as bringing in exotic trees for city greening or planting different crops.

The area covered by oscillating cold spots is at medium and low altitudes, surrounding the residential areas. For this

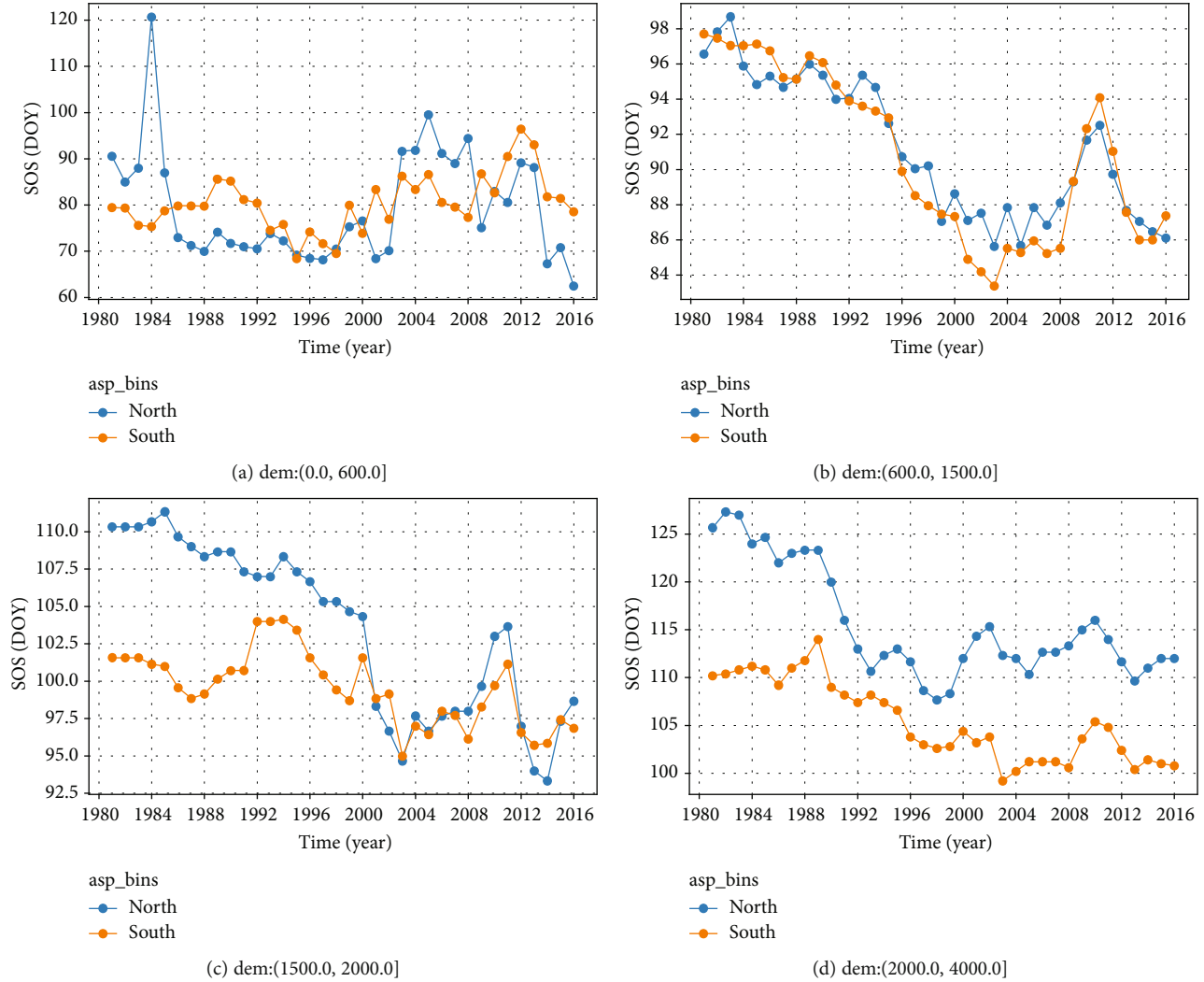


FIGURE 7: SOS changes with aspect differentiation. (a) SOS changes in elevation bin (0, 600]. (b) SOS changes in elevation bin (600, 1500]. (c) SOS changes in elevation bin (1500, 2000]. (d) SOS changes in elevation bin (2000, 4000].

type of area, there has been a statistically significant hot spot in the past, but a statistically significant cold spot recently. The result indicates this area may be affected by the superposition of climate change and human activities, so the SOS trend fluctuates greatly. Most of the high-altitude areas are covered by diminishing hot spots, and the edge area is distributed with an oscillating hot spot. Nonchanging hot spots only occupy a small part of the western region.

4. Discussions

Temperature and precipitation are direct factors affecting vegetation phenology. In mountainous areas, topography would cause differences in soil nutrients, soil water content, local temperature, and even rainfall distribution. Therefore, the spatial distribution would be affected by topography indirectly as shown in previous analysis. Based on the climate data cube and SOS data cube, this section gave exploratory analysis of potential influence factors by quantitative means, taking the data of year 2015 as an example.

Based on the least squares method, the linear relationships between temperature/rainfall/elevation/slope/aspect and SOS were calculated, respectively. The results are shown in Table 2 where the time bins of temperature are the month of SOS (0 m Lag), one month before SOS (1 m Lag), and the year of SOS (yearly). The time bins of precipitation are the month of SOS (0 m Lag), one month before SOS ($\Sigma 1$ m Lag), two months before SOS ($\Sigma 2$ m Lag), and the year of SOS (yearly). It can be obtained that the temperature of SOS's month and the accumulated precipitation before two months have a higher correlation with SOS. In addition, the correlation coefficient of elevation is the largest among all factors.

The least squares linear regression model and a geographically weighted regression model were established based on the four independent variables (temperature of 0 m Lag, precipitation of $\Sigma 2$ m Lag, slope, and aspect), resulting in the adjusted R^2 of 0.73 and 0.85, respectively. Since the temperature uses elevation as the covariate during the interpolation processing, it has a large collinearity with elevation, and then, we remove the elevation from independent variables.

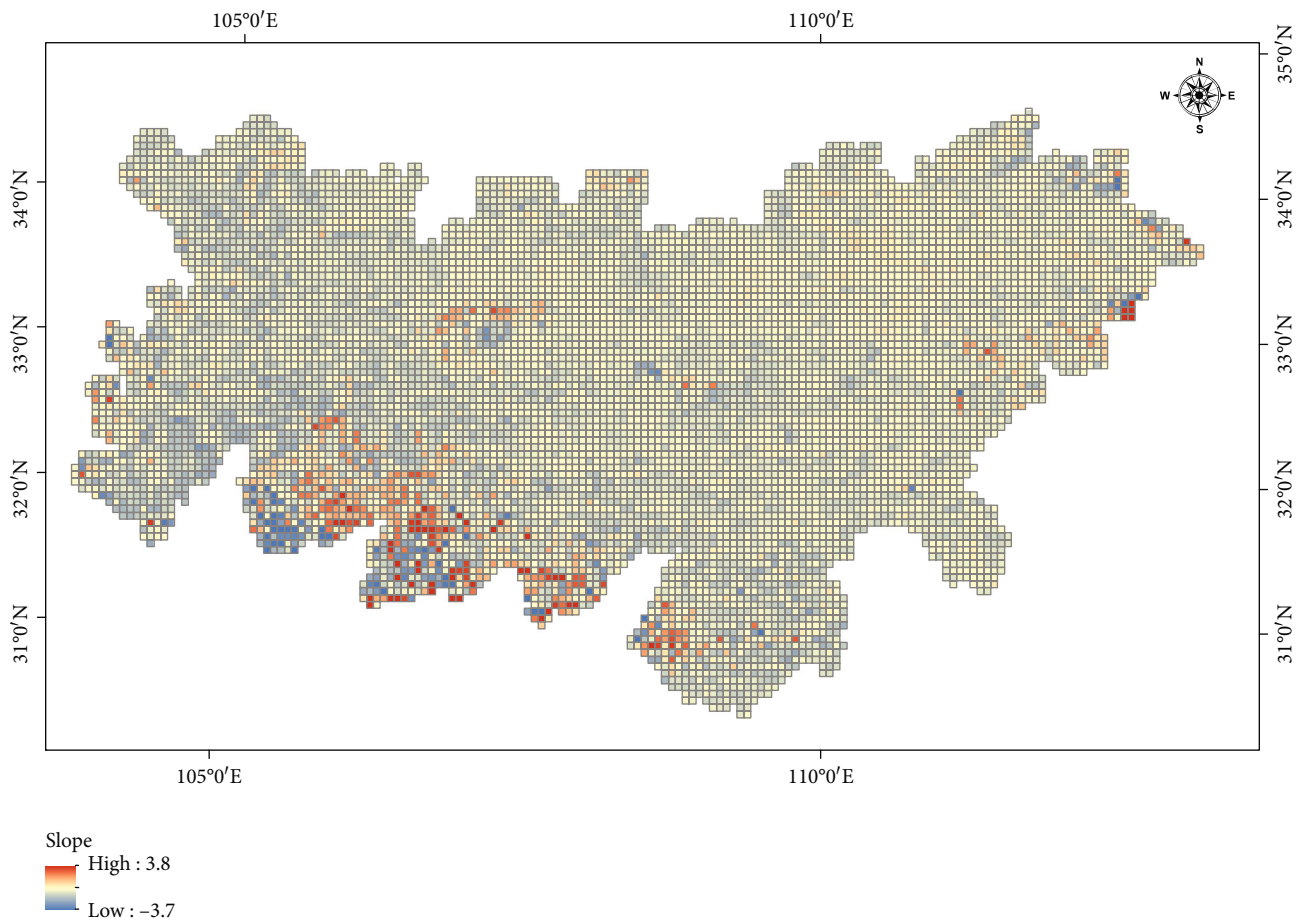


FIGURE 8: Spatial distribution of SOS slope.

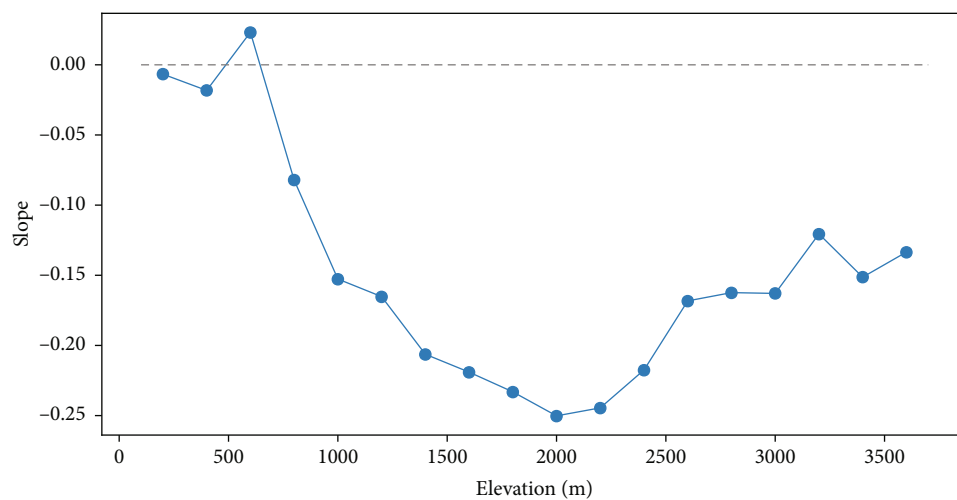


FIGURE 9: SOS slope changes with elevation.

Geographically weighted regression considers the nonstationarity of space and thus has a better overall fitting effect than linear regression as shown in Figure 11(a). However, the results in the southern and northern areas are not ideal that may be related to the vegetation disturbance caused by

human activities in these areas. We masked the area where a forest land accounted for less than 70% and performed the geographically weighted regression again. The adjusted R^2 reaches 0.91, indicating that this model is suitable for explaining the distribution of SOS in the forest land for the region

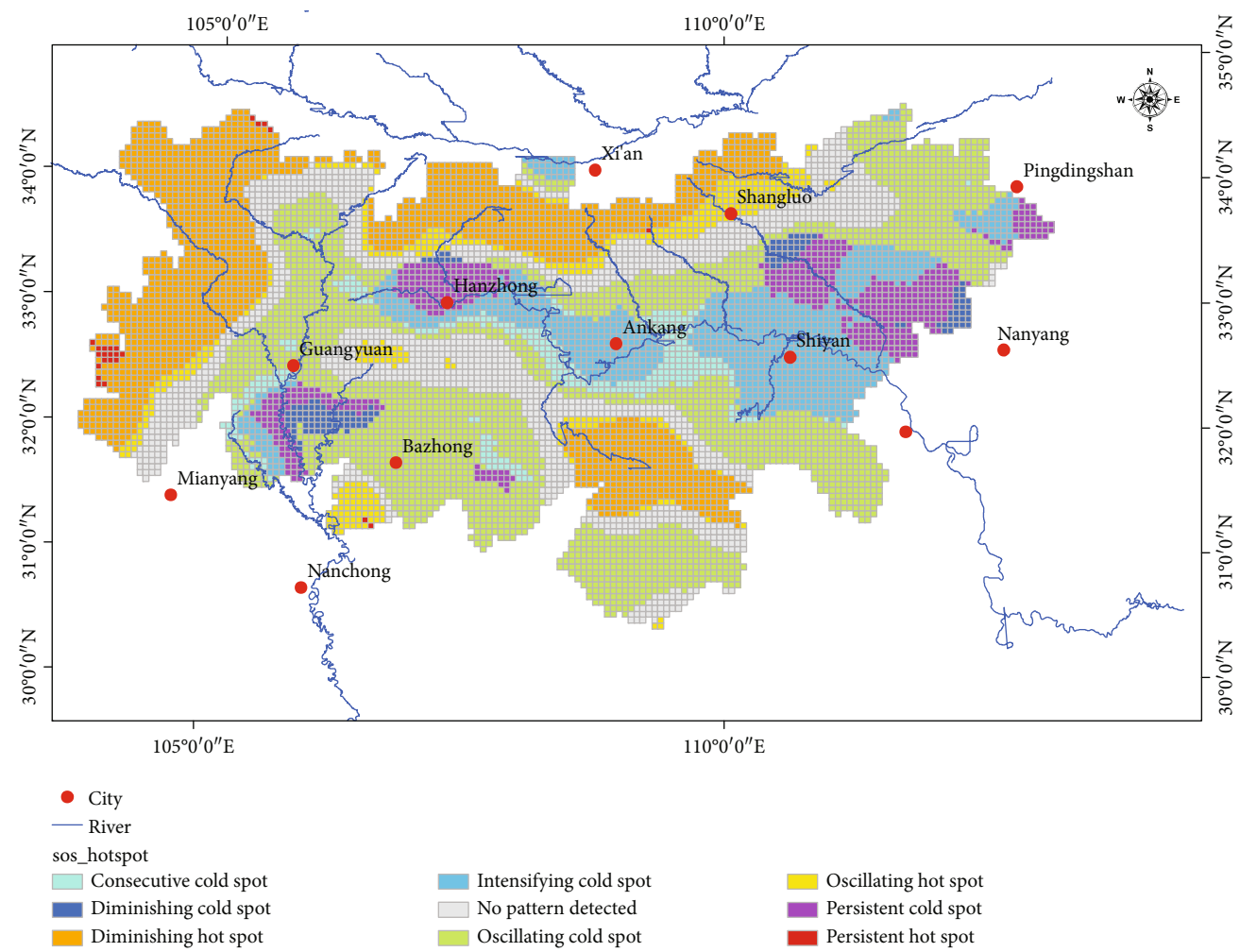


FIGURE 10: Hot spot analysis of SOS data cube.

TABLE 2: Correlation analysis of the factors and SOS.

Factors		Adjusted R^2	Negative (%)	Sig.
Temperature	0 m Lag	0.47	100	0.005**
	1 m Lag	0.16	100	0.021*
	Yearly	0.09	100	0.124
Precipitation	0 m Lag	0.06	68	0.153
	$\Sigma 1$ m Lag	0.21	70	0.015*
	$\Sigma 2$ m Lag	0.27	70	0.008**
	Yearly	0.20	50	0.047
Elevation		0.65	0	0.001**
Slope		0.18	0	0.007**
Aspect		0.12	80	0.006**

**Correlation is significant at the 0.001 level (2-tailed). *Correlation is significant at the 0.05 level (2-tailed).

(Figure 11(b)). The test further illustrates the climate of mountains has a strong dependence on the topography, and the temperature plays a leading role in the spring phenology

distribution of the region. For other areas, the land use/cover should be combined to measure the intensity of human activities for further attribution analysis in the future work.

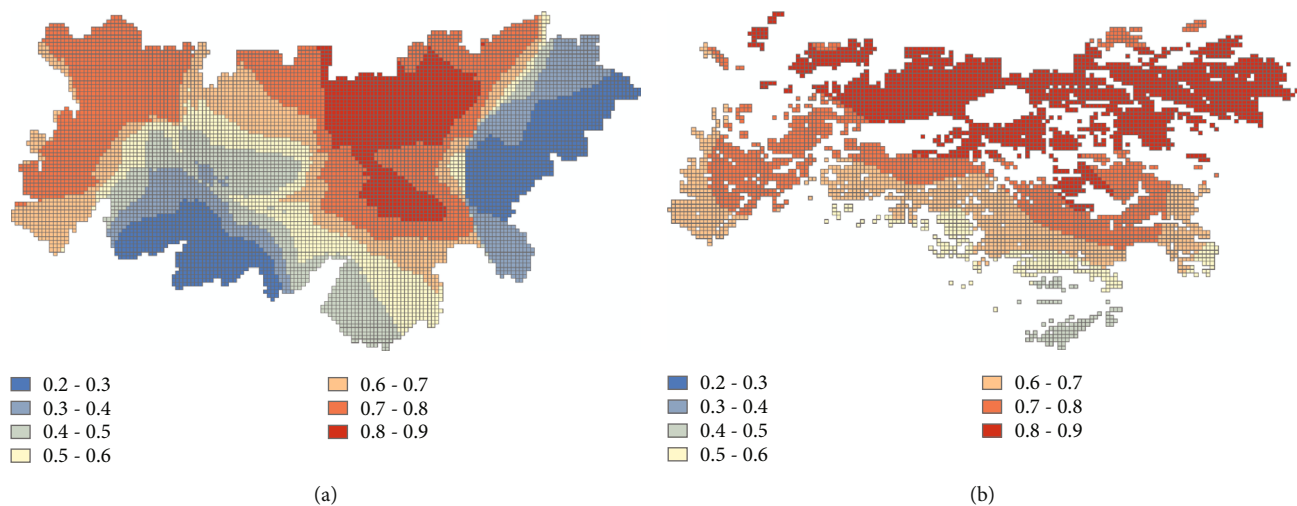


FIGURE 11: Results of geographically weighted regression for (a) the area with all types of land cover and (b) the area with only the forest cover.

5. Conclusions

The above analysis reveals the spatiotemporal differentiation and change characteristics of the spring phenology distribution in Qinba Mountains. The spatiotemporal data cube provides a good support for the whole analysis process in terms of data structure, multidimensional analysis, and exploratory analysis. Compared with traditional methods, this approach helps to explore hidden spatiotemporal pattern and its impacting factors. It provides a new perspective on studying phenology, which can be a complement to the current methods and techniques. In addition, the proposed data cube has the potential to connect to more exploratory analysis tools and spatial statistical algorithms.

The topography factors including elevation, slope, and aspect were considered in the paper. However, the mass elevation effect [32] and plant species are also the critical influence factors to the local climate, which have not been analysed here. The future work will include these factors in the study as well as land use/cover. In the absence of ground observation validation, the exploratory analysis of the relative change and trend in spatiotemporal distribution by using remote sensing data still has great advantages. For regional analysis, higher resolution remote sensing data of phenology is required.

Data Availability

The dataset of daily average temperature and precipitation used in this paper is publicly available from the Meteorological Science Data Sharing Service Network of China (<http://data.cma.cn>). The vegetation green-up products in the period of 1981–2016 are also provided freely by Vegetation Index and Phenology Lab, University of Arizona, USA (<https://vip.arizona.edu>).

Conflicts of Interest

The authors declare that they have no competing interests.

Acknowledgments

The studies presented here were developed within the research projects funded by the Fundamental Research Funds for the Central Universities of China (GK201903112), the National Natural Science Foundation of China (41831284), and the Natural Science Basic Research Plan in Shaanxi Province of China (2018JM4022), whose assistance is gratefully acknowledged.

References

- [1] Q. S. Ge, J. H. Dai, and J. Y. Zheng, "The progress of phenology studies and challenges to modern phenology research in China," *Bulletin of the Chinese Academy of Sciences*, vol. 25, no. 3, pp. 310–316, 2010.
- [2] J. Xia, S. Niu, P. Ciais et al., "Joint control of terrestrial gross primary productivity by plant phenology and physiology," *Proceedings of the National Academy of Sciences*, vol. 112, no. 9, pp. 2788–2793, 2015.
- [3] X. Wang, J. Xiao, X. Li et al., "No trends in spring and autumn phenology during the global warming hiatus," *Nature Communications*, vol. 10, no. 1, p. 2389, 2019.
- [4] A. J. H. van Vliet, R. S. de Groot, Y. Bellens et al., "The European phenology network," *International Journal of Biometeorology*, vol. 47, no. 4, pp. 202–212, 2003.
- [5] H. J. Wang, J. H. Dai, and Q. S. Ge, "The spatiotemporal characteristics of spring phenophase changes of *Fraxinus chinensis* in China from 1952 to 2007," *Science China Earth Sciences*, vol. 55, no. 6, pp. 991–1000, 2012.
- [6] A. D. Richardson, K. Hufkens, T. Milliman et al., "Tracking vegetation phenology across diverse North American biomes using PhenoCam imagery," *Scientific Data*, vol. 5, no. 1, 2018.
- [7] S. Jochner, A. Caffarra, and A. Menzel, "Can spatial data substitute temporal data in phenological modelling? A survey using birch flowering," *Tree Physiology*, vol. 33, no. 12, pp. 1256–1268, 2013.
- [8] C. Deng, H. Bai, X. Ma, T. Zhao, S. Gao, and X. Huang, "Spatiotemporal differences in the climatic growing season in the Qinling Mountains of China under the influence of global

- warming from 1964 to 2015,” *Theoretical and Applied Climatology*, vol. 138, no. 3–4, pp. 1899–1911, 2019.
- [9] X. Zhang, M. A. Friedl, C. B. Schaaf, and A. H. Strahler, “Climate controls on vegetation phenological patterns in northern mid- and high latitudes inferred from MODIS data,” *Global Change Biology*, vol. 10, no. 7, pp. 1133–1145, 2004.
 - [10] X. Li, Y. Zhou, L. Meng, G. R. Asrar, C. Lu, and Q. Wu, “A dataset of 30&thinspm annual vegetation phenology indicators (1985–2015) in urban areas of the conterminous United States,” *Earth System Science Data*, vol. 11, no. 2, pp. 881–894, 2019.
 - [11] C. Jeganathan, J. Dash, and P. M. Atkinson, “Remotely sensed trends in the phenology of northern high latitude terrestrial vegetation, controlling for land cover change and vegetation type,” *Remote Sensing of Environment*, vol. 143, pp. 154–170, 2014.
 - [12] G. M. Henebry and K. M. de Beurs, “Remote sensing of land surface phenology: a prospectus,” in *Phenology: An Integrative Environmental Science*, pp. 385–411, Springer, Dordrecht, 2013.
 - [13] X. Li, Y. Zhou, G. R. Asrar, J. Mao, X. Li, and W. Li, “Response of vegetation phenology to urbanization in the conterminous United States,” *Global Change Biology*, vol. 23, no. 7, pp. 2818–2830, 2017.
 - [14] D. Zhou, S. Zhao, L. Zhang, and S. Liu, “Remotely sensed assessment of urbanization effects on vegetation phenology in China’s 32 major cities,” *Remote Sensing of Environment*, vol. 176, pp. 272–281, 2016.
 - [15] X. P. Ma, H. Y. Bai, Y. N. He, and S. H. Li, “The vegetation remote sensing phenology of Qinling Mountains based on the NDVI and the response of temperature to it,” *Applied Mechanics and Materials*, vol. 700, pp. 394–399, 2014.
 - [16] H. P. Feng, H. Y. Bai, and X. P. Ma, “Research on vegetation phenological change based upon NDVI in Qinling area,” *Applied Mechanics and Materials*, vol. 700, pp. 350–359, 2014.
 - [17] Z. Wang, C. Xue, W. Quan, and H. He, “Spatiotemporal variations of forest phenology in the Qinling Mountains and its response to a critical temperature of 10°C,” *Journal of Applied Remote Sensing*, vol. 12, 2018.
 - [18] C. Deng, H. Bai, S. Gao, T. Zhao, and X. Ma, “Differences and variations in the elevation-dependent climatic growing season of the northern and southern slopes of the Qinling Mountains of China from 1985 to 2015,” *Theoretical and Applied Climatology*, vol. 137, no. 1–2, pp. 1159–1169, 2019.
 - [19] M. Lu, M. Appel, and E. Pebesma, “Multidimensional arrays for analysing geoscientific data,” *ISPRS International Journal of Geo-Information*, vol. 7, no. 8, p. 313, 2018.
 - [20] L. Yuan, Z. Yu, W. Luo, Y. Hu, L. Feng, and A. X. Zhu, “A hierarchical tensor-based approach to compressing, updating and querying geospatial data,” *IEEE Transactions on Knowledge and Data Engineering*, vol. 27, no. 2, pp. 312–325, 2015.
 - [21] G. Planthaber, M. Stonebraker, and J. Frew, “EarthDB: scalable analysis of MODIS data using SciDB,” in *Proceedings of the 1st ACM SIGSPATIAL International Workshop on Analytics for Big Geospatial Data*, pp. 11–19, 2012.
 - [22] Z. Tan, P. Yue, and J. Gong, “An array database approach for earth observation data management and processing,” *ISPRS International Journal of Geo-Information*, vol. 6, no. 7, p. 220, 2017.
 - [23] P. Baumann, P. Mazzetti, J. Ungar et al., “Big data analytics for earth sciences: the EarthServer approach,” *International Journal of Digital Earth*, vol. 9, no. 1, pp. 3–29, 2016.
 - [24] N. Gorelick, M. Hancher, M. Dixon, S. Ilyushchenko, D. Thau, and R. Moore, “Google Earth Engine: planetary-scale geospatial analysis for everyone,” *Remote Sensing of Environment*, vol. 202, pp. 18–27, 2017.
 - [25] S. Nativi, P. Mazzetti, and M. Craglia, “A view-based model of data-cube to support big earth data systems interoperability,” *Big Earth Data*, vol. 1, no. 1–2, pp. 75–99, 2017.
 - [26] S. Hoyer and J. Hamman, “xarray: N-D labeled arrays and datasets in Python,” *Journal of Open Research Software*, vol. 5, no. 1, 2017.
 - [27] J. Mennis, “Multidimensional map algebra: design and implementation of a spatio-temporal GIS processing language,” *Transactions in GIS*, vol. 14, no. 1, pp. 1–21, 2010.
 - [28] H. B. Mann, “Nonparametric tests against trend,” *Econometrica*, vol. 13, no. 3, pp. 245–263, 1945.
 - [29] M. G. Kendall, *Rank Correlation Methods*, Griffin, Oxford, England, 1948.
 - [30] P. K. Sen, “Estimates of the Regression Coefficient Based on Kendall’s Tau,” *Journal of the American statistical association*, vol. 63, no. 324, pp. 1379–1389, 1968.
 - [31] J. K. Ord and A. Getis, “Local spatial autocorrelation statistics: distributional issues and an application,” *Geographical Analysis*, vol. 27, no. 4, pp. 286–306, 1995.
 - [32] H. Fang, Z. Baiping, Y. Yonghui, Z. Yunhai, and P. Yu, “Mass elevation effect and its contribution to the altitude of snowline in the Tibetan Plateau and surrounding areas,” *Arctic, Antarctic, and Alpine Research*, vol. 43, no. 2, pp. 207–212, 2011.

Research Article

Variation Characteristics of Stem Water Content in *Lagerstroemia indica* and Its Response to Environmental Factors

Hao Liang^{1,2,3}, Meng Zhang^{1,3}, Hailan Wang^{1,2,3}, Chao Gao⁴, and Yandong Zhao^{1,2,3}

¹School of Technology, Beijing Forestry University, Beijing 100083, China

²Beijing Laboratory of Urban and Rural Ecological Environment, Beijing Municipal Education Commission, Beijing 100083, China

³Research Center for Intelligent Forestry, Beijing 10083, China

⁴School of Computer and Information Engineering, Beijing Technology and Business University, Beijing 100048, China

Correspondence should be addressed to Yandong Zhao; yandongzh@bjfu.edu.cn

Received 7 November 2019; Accepted 31 December 2019; Published 25 February 2020

Guest Editor: Zhenxing Zhang

Copyright © 2020 Hao Liang et al. This is an open access article distributed under the Creative Commons Attribution License, which permits unrestricted use, distribution, and reproduction in any medium, provided the original work is properly cited.

To achieve a rational allocation of limited water resources, and formulation of an appropriate irrigation system, this research studied the change characteristics of stem water content (StWC) in plant and its response to environmental factors. In this study, the StWC and environmental factors of *Lagerstroemia indica* in Beijing were continuously observed by a BD-IV plant stem water content sensor and a forest microclimate monitoring station from 2017 to 2018. The variation of StWC and its correlation with environmental factors were analyzed. The results showed that the StWC of *Lagerstroemia indica* varies regularly day and night during the growth cycle. Meanwhile, the rising time, valley time, and falling time of StWC were various at the different growth stages of *Lagerstroemia indica*. The results of correlation analysis between StWC and environmental factors indicated that the StWC of *Lagerstroemia indica* was positively correlated with air relative humidity, while it was negatively correlated with total radiation and air temperature. The multiple regression equation of StWC and environmental factors of *Lagerstroemia indica* was $\text{StWC} = 11.789 - 1.402R_n - 0.931T - 1.132W_s + 0.933RH - 3.368ST + 2.168SMC$, and the coefficient of determination of the equation was of 0.87. Furthermore, the results illustrated that the irrigation should pay attention to supplementing irrigation in time during the peak growing season of fruit.

1. Introduction

The stem is one of the two main structural axes of vascular plants, which plays a variety of roles in plants, such as mechanical support of leaves, flowers, and fruits, water transport between root and shoots in xylem and phloem, and water storage [1, 2]. The variation of steam water content (StWC) is an important segment of water transport in soil-plant-atmosphere continuum and also affects the transport of nutrients and the storage of carbohydrates. StWC is the result of interaction and feedback between different organs and their environment. A good understanding of StWC contributes to solving forestry research hotspots, such as cold resistance [3], drought resistance [4], and health assessment [5]. Moreover, accurately mastering the characteristics of

StWC and its environmental coupling mechanism is of great significance for formulating a reasonable irrigation system and making efficient use of water resources [6].

As a drought-resistant and pollution-resistant tree species, *Lagerstroemia indica* (Crape myrtle) has been widely used in the nursery cultivation and landscape use of cities in China. Water is one of the main factors restricting the growth and yield of *Lagerstroemia indica*; to assure the survival rate of *Lagerstroemia indica*, the irrigation strategies can be formulated more precisely according to the pattern of StWC of trees in different growth stages and the response to different environments, which also can improve the utilization rate of irrigation. In recent years, the research on the change of StWC in trees mainly focuses on fruit tree species such as jujube, walnut, and grape [7–9]. However, the research

TABLE 1: Growth periods of *Lagerstroemia indica*.

Flowering stage	Fruit growth stage	Fruit maturity stage	Dormancy stage
2017.3–2017.5	2017.6–2017.8	2017.9–2017.11	2017.12–2018.2

on tree species used in landscape greening is rare. In addition, the relationship between StWC and environmental factors in the whole growth cycle of plants has not been thoroughly explored.

Researchers have proposed many methods for measuring the StWC of plants. Oven-drying method is a traditional way to estimate the water content in stem. The StWC can be directly calculated by measuring the weight difference between the original wet stem and the stem dried by an oven. The method is the most accurate but destructive way, which cannot be used for in situ detection and also cost a long period for measurement. Therefore, oven-drying is commonly used as a calibration of the other measurements. To achieve nondestructive and in situ measurement, some image analysis methods are introduced, including gamma-ray densitometry [10], X-ray computer tomography [11], and magnetic resonance imaging (MRI) [12]. Both gamma-ray densitometry and X-ray computer tomography are highly sensitive, which can acquire the StWC of plants accurately, while the potential safety risks restricted further application of them [13]. Although the MRI system can safely obtain the StWC of plants accurately, it still cannot achieve in situ and real-time detection, which is not suitable for long-term monitoring at a fixed site in the field. With the development of electronic detection technology, dielectric constant method has been widely used in StWC real-time and in situ monitoring, including time-domain reflection (TDR) technology [14–16] and frequency-domain (FD) [17–19] technology, and the TDR method has been the most commonly used. On the basis of TDR method, Constantz and Murphy used a parallel waveguide probe to detect the volume moisture content of pine stem [20]. Wullschlegel and Hanson used a double-needle parallel stainless steel probe to monitor the seasonal variation of water content of four deciduous broad-leaved tree species. The calibration formulas suitable for the relationship between volume water content of stem and effective dielectric constant of tree species were summarized [21]. By summarizing the results of the previous studies of the researchers, it was feasible to detect StWC based on plant dielectric constant, but the length of the TDR probe restricted the detection effect. A short probe can reduce the damage to plants and the errors caused by the difference of water distribution, but the system resolution will be reduced, too. On the other hand, if the probes are too long, the signal attenuation will be very large. In addition, the TDR technology has high requirements and high production costs. Therefore, we used a nondestructive and real-time detection method of StWC on standing wave rate principle.

In this paper, *Lagerstroemia indica* growing in Beijing is selected as the research object. The area is affected by the cold wave, and the winter is cold and long, and the annual sunshine hours are significantly lower than other regions. The environmental conditions in Beijing vary widely, which leads the requirements of irrigation management for trees to be

high. The aims of our research were to monitor the StWC of *Lagerstroemia indica* trees in situ continuously based on the theory of standing wave ratio (SWR) and analyze the variation characteristics of StWC and its response to meteorological factors at different scales. Furthermore, we studied the correlation between StWC and meteorological factors by using cross-correlation, path analysis methods, and modeling, to provide more empirical data for *Lagerstroemia indica* trees for planting and management by revealing the patterns of StWC changes. Our results will be of significance in the management of guiding the scientific irrigation of the nursery garden reasonably and efficiently and providing a scientific basis for the comprehensive evaluation of ecological and hydrological processes and influencing factors of garden tree species in Beijing, China.

2. Materials and Methods

2.1. Study Site. The study site is located in the Sanqingyuan nursery garden in Haidian District, Beijing, China (40°0'N, 116°20'E). The region is characterized by a semihumid warm temperate continental monsoon climate zone, with an annual temperature of 12.6°C and annual precipitation of 620 mm, for which 80% of rainfall occurs primarily from June to August. With monthly percent possible sunshine ranging from 47% in July to 65% in January and February, the region receives 2,671 hours of bright sunshine annually. The mean annual evaporation of this area is 1,800 mm, which is greater than precipitation by a factor of 3. The climate information of the study site was collected by the forest microclimate monitoring station (School of Technology, Beijing Forestry University, Beijing, China). The height of the nursery is about 50 meters above sea level, and the terrain is flat, covering an area of about 31,200 m². The soil of the site is clay loam with a pH between 7 and 8. Vegetation at the site consists of deciduous broad-leaved trees dominated by *Lagerstroemia indica*, *Juglans mandshurica*, and *Malus spectabilis*.

2.2. Tree Material Preparation. We selected twelve *Lagerstroemia indica* tree samples with a similar diameter at breast height (DBH) for stem water content monitoring, which were determined to be healthy, straight, nonstressed, and well-grown specimens, for each year of the experimental period. The DBH is a standard method of expressing the diameter of the trunk or bole of a standing tree, which is measured at 1.3 m above ground [22, 23]. The DBH of the tree samples ranged from approximately 4.5 ± 0.5 cm, and the average tree height was 250 ± 5 cm. Irrigation in the site was carried out by small tube outflow, once a month for 1–2 days. In case of persistent high temperature and drought weather, irrigation was added 1–2 times a month. The amount of irrigation depended on the workers' experience. Weed control and pesticide spraying were carried out timely. The growth stages of *Lagerstroemia indica* trees are shown in

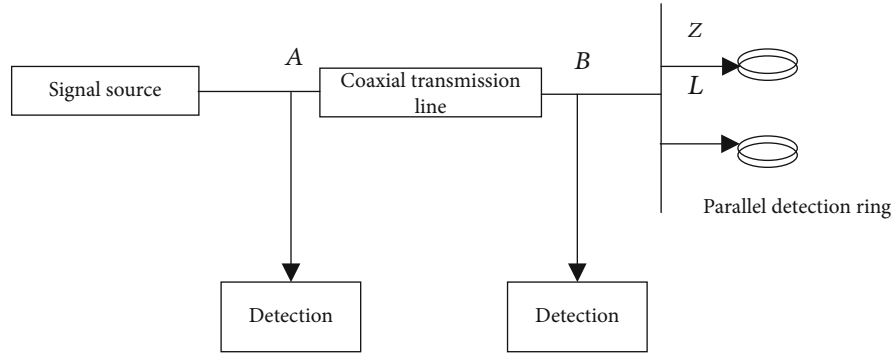


FIGURE 1: Schematic view of the BD-IV.

Table 1. Experiments were carried out under the existing conditions, and monitoring was performed from November 2017 to November 2018.

2.3. Stem Water Content Sensors. The BD-IV plant stem water content sensor (researched and developed by School of Technology, Beijing Forestry University, China) was implemented to measure the StWC of *Lagerstroemia indica* samples. The BD-IV, based on SWR, consisted of a 100 MHz sinusoidal oscillator, a coaxial transmission line, a high-frequency detector circuit, and a pair of parallel stainless steel metallic electrodes [2, 24]. The electrodes were designed to wrap around stems like an upper and a lower strap ring (Figure 1). The electromagnetic wave provided by the sinusoidal oscillator spreads along the coaxial transmission line into the strap ring, and because the impedance of the strap ring is different from that of the transmission line, a proportion of the incident wave would be reflected back along the line to the oscillator. As a result of the reflected wave interfering with the incident wave, a voltage standing wave would be set up on the transmission line. According to the measuring principle of SWR, the differential voltage of A and B is taken as the output of the transducer conversion circuit, which can be expressed as a function of the strap ring impedance [25, 26]:

$$U_{AB} = 2A_1 \frac{Z_L - Z_C}{Z_L + Z_C}, \quad (1)$$

where A_1 is the amplitude of the electromagnetic wave (V), Z_L is the impedance (Ω) of the strap ring, and Z_C is the impedance (Ω) of the transmission line. In this study, the Z_C is equal to 50 Ω . When A_1 and Z_C are constant, the potential difference U_{AB} at both ends of the transmission line is only related to the impedance of Z_L . The variation of StWC can affect the impedance of stem, which leads the change of the impedance of the strap ring (Z_L), and the output voltage (U_{AB}) of the sensor will be changed. In other words, Z_L is determined by StWC of the measured living tree. Therefore, the StWC of living standing trees can be quantified by measuring the output voltage difference of the transmission line (U_{AB}).

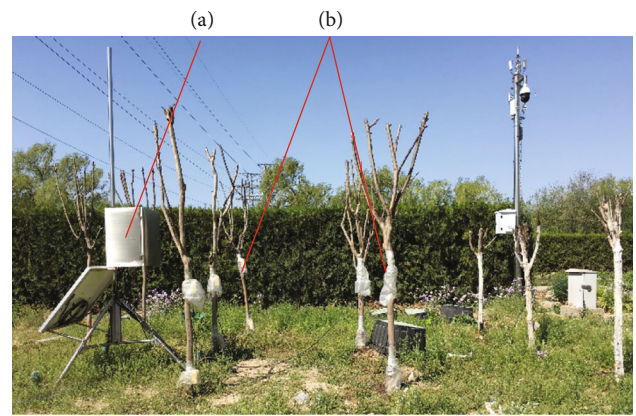


FIGURE 2: Monitoring station of stem water content: (a) digital collector and (b) SWR sensor (BD-IV).

2.4. Data Collection. StWC sensors (BD-IV) were installed on the trunks of 12 selected *Lagerstroemia indica* tree samples. The installation position of the BD-IV was close to the first bifurcation of the main trunk of the tree sample. A self-designed multichannel digital collector based on AVR 128 was used to connect the StWC sensors of each trunk. A monitoring station in the experiment is shown in Figure 2. The collector automatically collected and stored a data packet every 10 minutes and collected 144 data packets in one day. Thus, the collector can record 144 of StWC of each sample every day. During the whole experimental process, the same cultivation and management mode was adopted to ensure the supply of water and nutrients for all the samples. At the same time, the change process of StWC of the samples was recorded.

In the study site, a forest microclimate monitoring station (researched and developed by School of Technology, Beijing Forestry University, China) was built to measure the parameters of micrometeorological factors in the ecological micro-environment in real time, including air temperature, air relative humidity, global radiation, and wind speed. The station measured and collected the micrometeorological factors every 10 minutes. In addition, soil temperature sensors DS18B20 (Dallas Semiconductor, Dallas, Texas, United States) and soil volume moisture content sensors HYSWR-ARC (researched and developed by School of Technology,

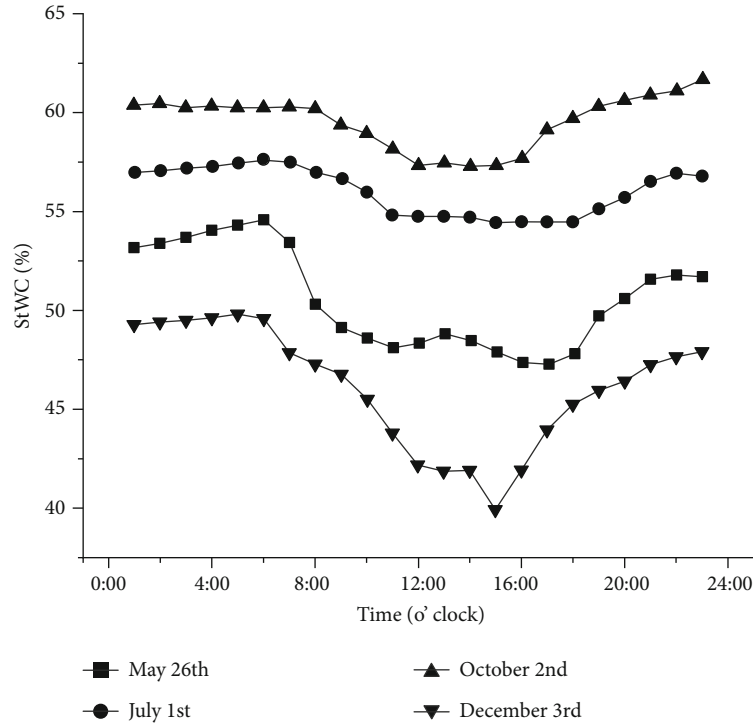


FIGURE 3: Daily variation of StWC in different growth stages of *Lagerstroemia indica*.

TABLE 2: Intermontly dynamic change of StWC on sunny days and environmental factor daily mean of *Lagerstroemia indica*.

Month	Date	Daily mean of environmental factor					Falling time	Valley time	Valley value	Rising time	Mean StWC
		Rn	T	RH	Ws	10 SMC					
5	2018.5.26	305.05	23.53	44.29	0.97	7.58	8:00	13:00	47.13	15:30	50.69
7	2018.7.1	249.54	31.68	59.07	0.73	8.56	7:00	10:30	54.47	19:30	56.15
10	2018.10.2	185.59	16.01	60.19	0.61	9.98	6:00	10:50	57.23	18:00	59.78
12	2018.12.2	139.78	0.95	50.85	0.50	7.66	7:30	12:00	39.79	14:00	46.18

Rn: total radiation ($\text{W}\cdot\text{m}^{-2}$); T: air temperature ($^{\circ}\text{C}$); RH: relative humidity (%); 10 SMC: 10 cm soil moisture content (%); falling time: time of StWC to fall; valley time: time of StWC to reach the minimum value; rising time: time of StWC to rise.

Beijing Forestry University, China) were installed at four different locations in the study site to monitor the soil temperature and soil volume moisture content, respectively.

2.5. Data Processing. The StWC of *Lagerstroemia indica* samples were calculated by

$$V = 1022.1 * St + 324.36 \quad (R^2 = 0.998), \quad (2)$$

where V is the output voltage difference of the transmission line and St is the StWC of *Lagerstroemia indica* samples. It is a linear relation between the StWC of the *Lagerstroemia indica* and the sensor output with the high sensitivity equal to $1022.1 \text{ mV} (\text{cm}^3\cdot\text{cm}^{-3})^{-1}$. The value of coefficient of determination (R^2) indicated that the sensor was able to measure the StWC of trees precisely.

Microsoft Excel (Microsoft Inc., Redmond, USA) was used to collate and calculate the StWC data of *Lagerstroemia indica* samples; SPSS 19.0 (SPSS Inc., Chicago, USA) and

MATLAB 2015b (MathWorks Inc., Natick, MA) were used to analyze the variance, regression, and correlation of the StWC and meteorological factors; and Origin (OriginLab Inc., USA) software was used to draw the charts and graphs.

3. Results and Discussion

3.1. Diurnal Variation Characteristics of Stem Water Content. The StWC data were selected from the typical sunny days. Figure 3 illustrates the diurnal variation characteristics of StWC of *Lagerstroemia indica* in its flowering stage (2017.5.26), fruit growth stage (2017.7.1), fruit maturity stage (2017.10.2), and dormancy period (2017.12.3). It can be found that the diurnal variation of StWC follows the overall trend of first decreasing and then increasing. Take the StWC data of October 2, 2017, as an example: StWC started to rapidly decrease at 6:00; after reaching the first trough at 11:00, the StWC was relatively stable till reaching the minimum value at 15:00; then, it began to increase smoothly. The rising

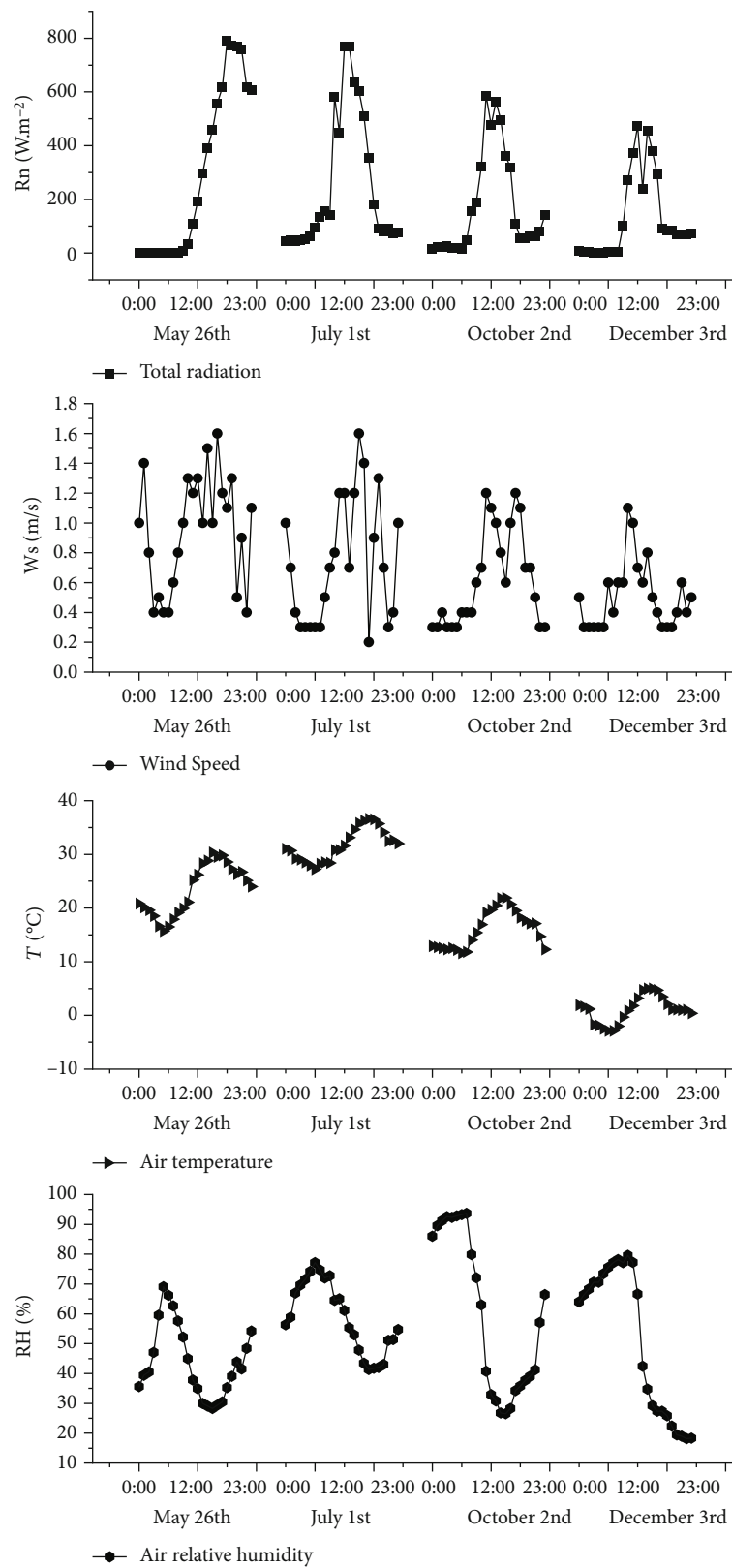


FIGURE 4: Daily variation of the main meteorological factors in different growth stages of *Lagerstroemia indica*.

process of StWC lasted nearly 16 hours until 5:00 the next day, and then, the falling process of StWC happened again. At different growth stages of *Lagerstroemia indica*, the valley

time, falling time, and rising time of StWC were also variant. It can be seen from Table 2 that the valley time of StWC reached early, and the falling time of StWC started late in July

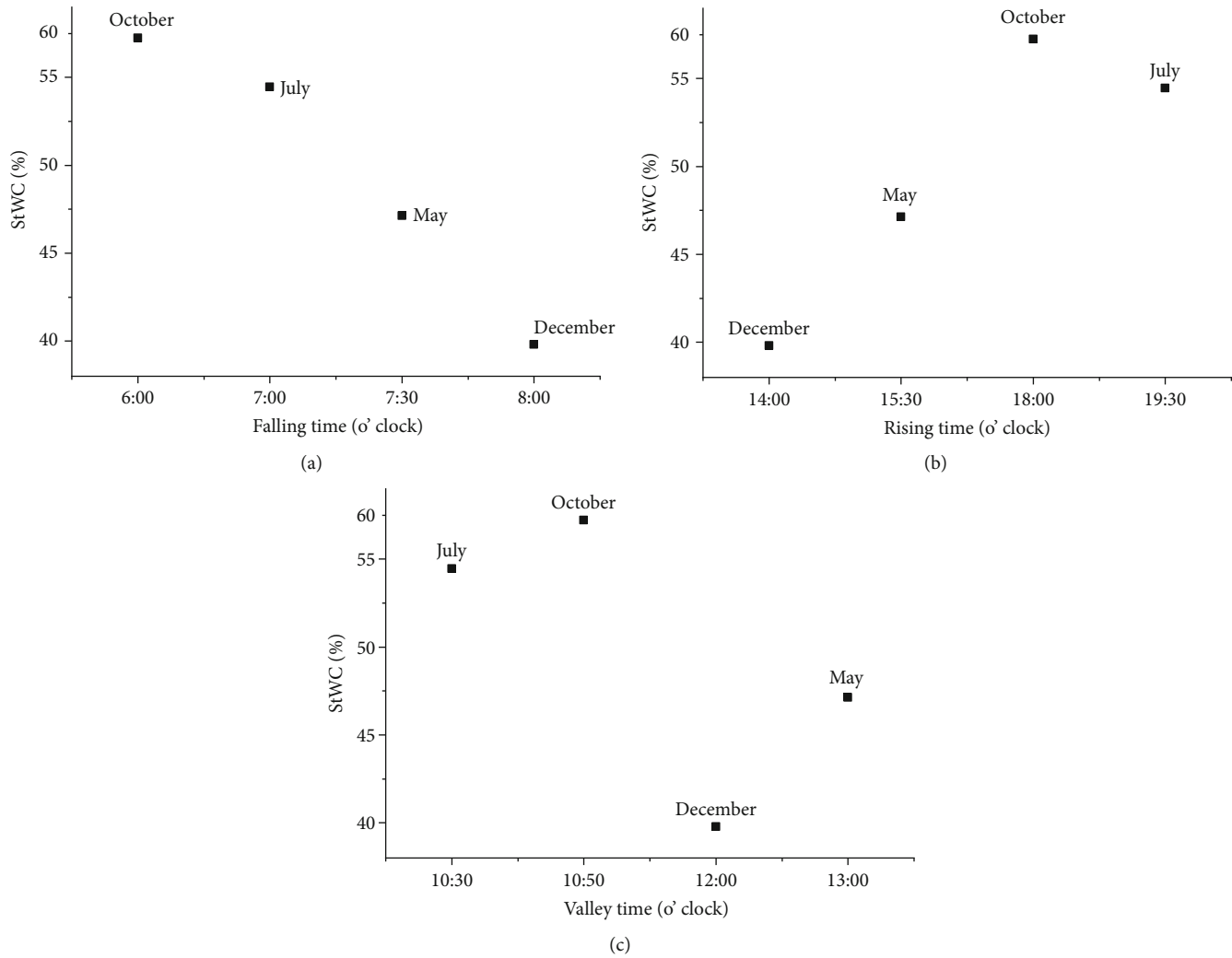


FIGURE 5: Relationship between valley StWC and StWC status. (a) Falling time of StWC. (b) Rising time of StWC. (c) Valley time of StWC.

and October. However, the pattern of StWC in March and December was conversely. This phenomenon may be related to the variation of meteorological factors during the growth period of the sample trees. The diurnal variation of the main meteorological factors on observation days at different growth periods is shown in Figure 4. The results indicate that the falling time of StWC in the fruit growth stage and fruit maturity stage was early, and the rising time of StWC was late, which was conducive to the accumulation of photosynthates, while the opposite was found in the deciduous dormancy period and germination stage. Figure 5 shows the rising time, falling time, and valley time of StWC in the growth cycle of *Lagerstroemia indica*, which illustrates that the growth stage influenced the times of StWC greatly. The valley value of StWC was October > July > May > December, the maximum StWC was 57.23% in October, and the minimum StWC was 39.79% in December. In addition, the mean of StWC was October > July > May > December, the maximum StWC was 59.78% in October, and the minimum StWC was 46.18% in December. As a result, StWC of *Lagerstroemia indica* was the most at the fruit stage and the least at the deciduous dormancy period.

3.2. Response of Stem Water Content to Environmental Factors. The StWC of *Lagerstroemia indica* at different growth stages was significantly different under the influence of external environmental factors. We selected the data of StWC and meteorological factors for 7 consecutive days (from July 24 to 30, 2017) to analyze the relationship between StWC and environmental factors in *Lagerstroemia indica*. The variation curve of StWC and meteorological factors of *Lagerstroemia indica* is shown in Figure 6. It can be concluded that the StWC had strong correlation with total radiation, air temperature, air relative humidity, wind speed, and soil moisture content, but not with soil temperature. Moreover, StWC was contrary to that of total radiation, wind speed, and air temperature but similar to the change trend of relative air humidity, which indicated that the increase of air relative humidity would increase the StWC and have a negative effect on fruit tree transpiration, while the increase of total radiation and air temperature would decrease the water content of stem, which can promote the transpiration of *Lagerstroemia indica*. The photosynthate rate was influenced by the changes of radiation and air temperature in a reasonable range [27–29]. Since the tree samples were in

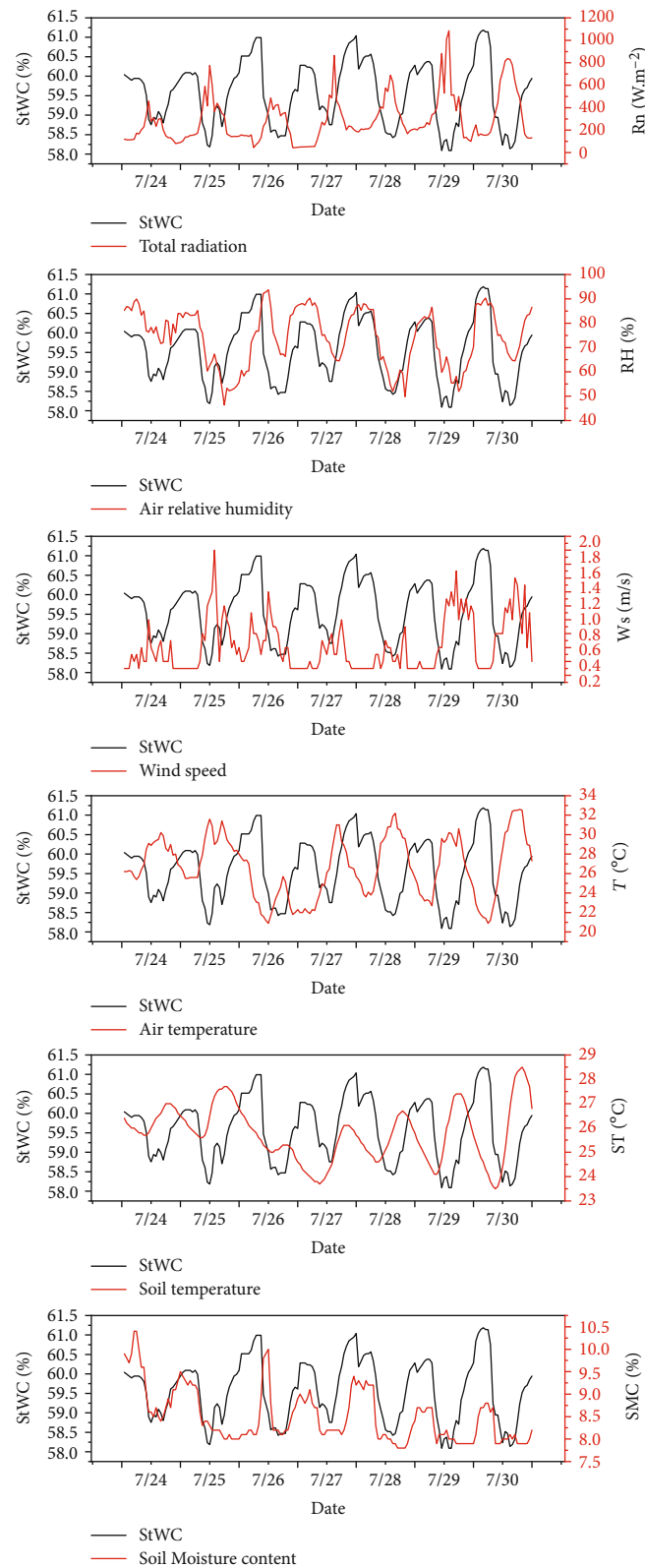


FIGURE 6: Relationship between StWC and environmental factors of *Lagerstroemia indica*.

the fruit growth stage, the accumulation of photosynthate would be increased with the increase of radiation and air temperature in a reasonable range [27–29].

The analysis results of correlation between StWC and environmental factors of *Lagerstroemia indica* are shown in Table 3. It can be seen that the StWC of *Lagerstroemia*

TABLE 3: Correlation between StWC of *Lagerstroemia indica* and environmental factors.

	Rn	RH	Ws	T	ST	SMC	StWC
Rn	1						
RH	-0.455**	1					
Ws	0.550**	-0.530**	1				
T	0.566**	-0.718**	0.481**	1			
ST	-0.033	-0.475**	0.405**	0.681**	1		
10 SMC	-0.427**	0.739**	-0.488**	-0.465**	-0.194**	1	
StWC	-0.732**	0.505**	-0.549**	-0.556**	-0.141**	0.414**	1

Rn: total radiation ($\text{W}\cdot\text{m}^{-2}$); RH: air relative humidity (%); Ws: wind speed (m/s); T: air temperature ($^{\circ}\text{C}$); ST: soil temperature ($^{\circ}\text{C}$); SMC: 15 cm soil moisture content (%); StWC: stem water content(%). **Significant correlation at 0.01 level. *Significant correlation at 0.05 level.

TABLE 4: Path analysis results between StWC and environmental factors.

Independent variable	Simple correlation coefficient	Direct path coefficient	Indirect path coefficient						Total
			X_1	X_2	X_3	X_4	X_5	X_6	
X_1	-0.732	-0.411	—	0.187	0.127	0.169	0.007	0.032	0.522
X_2	0.505	0.137	0.187	—	0.122	0.219	0.106	0.055	0.689
X_3	-0.549	-0.230	0.226	0.073	—	0.146	0.091	0.036	0.572
X_4	-0.556	-0.305	0.229	0.098	0.111	—	0.153	0.034	0.625
X_5	-0.141	0.224	0.014	0.065	0.093	0.208	—	0.014	0.394
X_6	0.414	-0.074	0.175	0.101	0.112	0.142	0.043	—	0.573

X_1 : total radiation ($\text{W}\cdot\text{m}^{-2}$); X_2 : air relative humidity (%); X_3 : wind speed (m/s); X_4 : air temperature ($^{\circ}\text{C}$); X_5 : soil temperature($^{\circ}\text{C}$); X_6 : 15 cm soil moisture content (%).

indica was significantly correlated with total radiation, air temperature, air relative humidity, wind speed, soil temperature, and 15 cm soil moisture content at level 0.01. The StWC was negatively correlated with air relative humidity and 15 cm soil moisture content but positively correlated with the other factors. The StWC had the strongest correlation with total radiation, and the correlation coefficient was 0.732. The degree of correlation was $r(\text{Rn}) = -0.732^{**} > r(T) = -0.556^{**} > r(\text{Ws}) = -0.549^{**} > r(\text{RH}) = 0.505^{**} > r(10 \text{ SMC}) = 0.414^{**} > r(\text{ST}) = -0.141^{**}$ (**significant bilateral correlation at 0.01 level).

3.3. Quantitative Correlation Analysis between Stem Water Content and Environmental Factors

3.3.1. Multiple Regression Analysis. The experiment took the StWC of *Lagerstroemia indica* as dependent variable and environmental factors as independent variable and established a comprehensive relationship model between StWC and environmental factors based on the multiple regression analysis. The model was optimal to reflect the effect of environmental factors on StWC of *Lagerstroemia indica*. The multiple regression equation of StWC and environmental factors of *Lagerstroemia indica* is as follows:

$$\text{StWC} = 11.789 - 1.402\text{Rn} - 0.931\text{T} - 1.132\text{Ws} + 0.933\text{RH} - 3.368\text{ST} + 2.168\text{SMC},$$

(3)

where St is the StWC of *Lagerstroemia indica*. The coefficient of determination of the equation is 0.87 (R^2). The environmental factors could explain 87.0% of the StWC changes of *Lagerstroemia indica*. The coefficient of determination of the residual factor is 0.49 ($e = \sqrt{1 - R^2}$), which indicates that there are other factors having certain influence on StWC of *Lagerstroemia indica*, such as stomatal conductance and leaf area index.

Furthermore, the path analysis was implemented to study the way of influence and its magnitude of environmental factors on StWC of *Lagerstroemia indica* (Table 4). The direct effect of environmental factors on StWC is $\text{Rn}(-0.411) > T(-0.305) > \text{Ws}(-0.230) > \text{ST}(0.224) > \text{RH}(0.137) > \text{Hs}(-0.074)$, and the indirect effect of environmental factors on StWC is $\text{RH}(0.689) > T(0.625) > \text{Hs}(0.573) > \text{Ws}(0.572) > \text{Rn}(0.522) > \text{ST}(0.394)$. As a result, it shows that the direct effect of total radiation (Rn) is the largest, while that of 15 cm soil moisture content (SMC) is the smallest. Air temperature mainly affected the StWC through the combined action of total radiation, relative humidity, and soil temperature. The total radiation mainly affected the StWC through the combined effects of air temperature, wind speed, and relative humidity.

4. Conclusions

This study confirms that the environmental factors can be significant predictors of daily stem water content (StWC) of

Lagerstroemia indica in Beijing. According to the experimental results, the following conclusions can be drawn:

- (1) The StWC of *Lagerstroemia indica* varies regularly day and night and follows the overall trend of first rising and then falling, which shows a typical valley curve. The rising time, valley time, and falling time of StWC are different at the different growth stages of the *Lagerstroemia indica*. Specifically, the falling time of the fruit growth stage and fruit maturity stage is ahead of the other stages, while the rising time of the fruit growth stage and fruit maturity stage is later than that of the other stages
- (2) The StWC of *Lagerstroemia indica* is positively correlated with air relative humidity and 15 cm soil moisture content and negatively correlated with total radiation, wind speed, air temperature, and soil temperature which is the most important factor affecting StWC of *Lagerstroemia indica*. Moreover, the multiple regression equation of StWC and environmental factors of *Lagerstroemia indica* is $\text{StWC} = 11.789 - 1.402R_n - 0.931T - 1.132W_s + 0.933RH - 3.368ST + 2.168SMC$, and the coefficient of determination of the equation is 0.87
- (3) The transpiration of *Lagerstroemia indica* in the region of Beijing, China, is larger in June–September. The transpiration is highly influenced by environmental factors such as solar radiation and wind speed. The solar radiation is stronger in July and August in this region, and the air temperature is higher. Therefore, the irrigation should pay attention to supplementing irrigation in time during the peak growing season of fruit, i.e., during the period of fruit expansion, especially in the continuous sunny days of July and August. Irrigation frequency ensures that *Lagerstroemia indica* are not affected by water stress during the critical period of growth, and irrigation time should be chosen before sunrise or after sunrise to reduce the loss of irrigation water caused by evaporation

Data Availability

The data used to support the findings of this study are available from the corresponding author upon request.

Conflicts of Interest

The authors declare no conflict of interest.

Authors' Contributions

For this research article, Hao Liang and Yandong Zhao conceived and designed the experiments; Meng Zhang and Hailan Wang performed the experiments; Meng Zhang and Chao Gao analyzed the data; Hao Liang, Meng Zhang, and Hailan Wang wrote the paper; Hao Liang and Yandong Zhao reviewed and edited the paper.

Acknowledgments

This research was funded by the Fundamental Research Funds for the Central Universities (grant number BLX201717), the Special Fund for Beijing Common Construction Project, and the Science and Technology Program of the Inner Mongolia Autonomous Region (grant number 201802085).

References

- [1] T. W. J. Scheenen, F. J. Vergeldt, A. M. Heemskerk, and H. van As, "Intact plant magnetic resonance imaging to study dynamics in long-distance sap flow and flow-conducting surface area," *Plant Physiology*, vol. 144, no. 2, pp. 1157–1165, 2007.
- [2] C. Gao, Y. Zhao, and Y. Zhao, "A novel sensor for noninvasive detection of in situ stem water content based on standing wave ratio," *Journal of Sensors*, vol. 2019, Article ID 3594964, 10 pages, 2019.
- [3] P. E. Verslues, M. Agarwal, S. Katiyar-Agarwal, J. Zhu, and J. K. Zhu, "Methods and concepts in quantifying resistance to drought, salt and freezing, abiotic stresses that affect plant water status," *Plant Journal*, vol. 45, no. 4, pp. 523–539, 2006.
- [4] M. Farooq, A. Wahid, N. Kobayashi, D. Fujita, and S. M. A. Basra, "Plant drought stress: effects, mechanisms and management," *Agronomy for Sustainable Development*, vol. 29, no. 1, pp. 185–212, 2009.
- [5] R. Spotts and A. Photosynthesis, "Photosynthesis, Transpiration, and water potential of apple leaves infected by *Venturia inaequalis*," *Phytopathology*, vol. 69, no. 7, pp. 717–719, 1979.
- [6] A. Patakas, B. Noitsakis, and A. Chouzouri, "Optimization of irrigation water use in grapevines using the relationship between transpiration and plant water status," *Agriculture Ecosystems & Environment*, vol. 106, no. 2–3, pp. 253–259, 2005.
- [7] L. I. Hong, L. Bang, and L. I. Chang-Cheng, "Characteristics of stem flow of young jujube tree at different reproductive periods and their relationship with environmental factors," *Agricultural Research in the Arid Areas*, vol. 34, no. 5, pp. 54–61, 2016.
- [8] Z. Fuyong, Z. Jinghua, and M. Yingjie, "The variation of stem flow and photosynthesis of walnut trees under drip irrigations," *China Rural Water & Hydropower*, vol. 3, pp. 31–40, 2017.
- [9] Y. Bai, G. F. Zhu, K. Zhang, and T. Ma, "Analysis of variation of sap flow velocity and water consumption of grapevine in the Nanhuoasis, Dunhuang," *China. Journal of Desert Research*, vol. 35, no. 1, pp. 175–181, 2015.
- [10] W. R. N. Edwards and P. G. Jarvis, "A method for measuring radial differences in water content of intact tree stems by attenuation of gamma radiation," *Plant Cell and Environment*, vol. 6, no. 3, pp. 255–260, 1983.
- [11] A. RASCHI, R. TOGNETTI, H.-. W. RIDDER, and C. BÉRES, "Water in the stems of sessile oak (*Quercus petraea*) assessed by computer tomography with concurrent measurements of sap velocity and ultrasound emission," *Plant Cell & Environment*, vol. 18, no. 5, pp. 545–554, 2010.
- [12] V. De Schepper, D. van Dusschoten, P. Copini, S. Jahnke, and K. Steppe, "MRI links stem water content to stem diameter variations in transpiring trees," *Journal of Experimental Botany*, vol. 63, no. 7, pp. 2645–2653, 2012.

- [13] H. G. Jones, "Irrigation scheduling: advantages and pitfalls of plant-based methods," *Journal of Experimental Botany*, vol. 55, no. 407, pp. 2427–2436, 2004.
- [14] A. Nadler, E. Raveh, U. Yermiyahu, and S. R. Green, "Evaluation of TDR use to monitor water content in stem of lemon trees and soil and their response to water stress," *Soil Science Society of America Journal*, vol. 67, no. 2, pp. 437–448, 2003.
- [15] M. Persson and S. Haridy, "Estimating water content from electrical conductivity measurements with short time-domain reflectometry probes," *Soil Science Society of America Journal*, vol. 67, no. 2, pp. 478–482, 2003.
- [16] J. Irvine and J. Grace, "Non-destructive measurement of stem water content by time domain reflectometry using short probes," *Journal of Experimental Botany*, vol. 48, no. 3, pp. 813–818, 1997.
- [17] N. M. Holbrook, M. J. Burns, and T. R. Sinclair, "Frequency and Time-Domain dielectric measurements of stem water content in the arborescent Palm, *Sabal palmetto*," *Journal of Experimental Botany*, vol. 43, no. 1, pp. 111–119, 1992.
- [18] M. Stacheder, F. Koeniger, and R. Schuhmann, "New dielectric sensors and sensing techniques for soil and snow moisture measurements," *Sensors*, vol. 9, no. 4, pp. 2951–2967, 2009.
- [19] W. Skierucha and A. Wilczek, "A FDR sensor for measuring complex soil dielectric permittivity in the 10–500 MHz frequency range," *Sensors*, vol. 10, no. 4, pp. 3314–3329, 2010.
- [20] J. Constantz and F. Murphy, "Monitoring moisture storage in trees using time domain reflectometry," *Journal of Hydrology*, vol. 119, no. 1–4, pp. 31–42, 1990.
- [21] S. D. Wullschleger, P. J. Hanson, and D. E. Todd, "Measuring stem water content in four deciduous hardwoods with a time-domain reflectometer," *Tree Physiology*, vol. 16, no. 10, pp. 809–815, 1996.
- [22] C. P. Brack, *Standard point on tree bole for measurement. Forest measurement and modelling*, Computer-based course resources for Forest Measurement and Modeling (FSTY2009) at the Australian National University, Canberra, Australia, 2009.
- [23] T. R. Feldpausch, L. Banin, O. L. Phillips et al., "Height-diameter allometry of tropical forest trees," *Biogeosciences*, vol. 8, no. 5, pp. 1081–1106, 2011.
- [24] Y. Zhao, C. Gao, X. Zhang, and Q. Xu, "Non-destructive measurement of plant stem water content based on standing wave ratio," *Transactions of the Chinese Society for Agricultural Machinery*, vol. 40, pp. 310–316, 2016.
- [25] G. J. Gaskin and J. D. Miller, "Measurement of soil water content using a simplified impedance measuring technique," *Journal of Agricultural Engineering Research*, vol. 63, no. 2, pp. 153–159, 1996.
- [26] H. Zhou, Y. Sun, M. T. Tyree et al., "An improved sensor for precision detection of in situ stem water content using a frequency domain fringing capacitor," *New Phytologist*, vol. 206, no. 1, pp. 471–481, 2015.
- [27] Z. Hong-jin, Z. Zhong-yuan, W. Xi-xi, S. Xiao-yuan, W. Hui, and J. Wei, "Effect of ecological factors and physiological factors on the net photosynthetic rate of *Ulmus pumila* at various growth stages," *Acta Ecologica Sinica*, vol. 36, pp. 1645–1651, 2016.
- [28] Q. Han, T. Kawasaki, T. Nakano, and Y. Chiba, "Spatial and seasonal variability of temperature responses of biochemical photosynthesis parameters and leaf nitrogen content within a *Pinus densiflora* crown," *Tree Physiology*, vol. 24, no. 7, pp. 737–744, 2004.
- [29] L. Gonzalez-Paleo and D. A. Ravetta, "Relationship between photosynthetic rate, water use and leaf structure in desert annual and perennial forbs differing in their growth," *Photosynthetica*, vol. 56, no. 4, pp. 1177–1187, 2018.

Review Article

Sensors Applied for the Detection of Pesticides and Heavy Metals in Freshwaters

Hongyong Xiang^{1,2}, Qinghua Cai³, Yuan Li⁴, Zhenxing Zhang^{1,5}, Lina Cao⁶, Kun Li⁷, and Haijun Yang^{1,2,8}

¹Key Laboratory of Vegetation Ecology, Ministry of Education, Institute of Grassland Science, Northeast Normal University, Changchun, Jilin 130024, China

²Institute for Ecological Research and Pollution Control of Plateau Lakes, School of Ecology and Environmental Science, Yunnan University, Kunming, Yunnan 650500, China

³State Key Laboratory of Freshwater Ecology and Biotechnology, Institute of Hydrobiology, Chinese Academy of Sciences, Wuhan 430072, China

⁴Northwest Land and Resources Research Center, Shaanxi Normal Northwest University, China

⁵State Environmental Protection Key Laboratory of Wetland Ecology and Vegetation Restoration, Northeast Normal University, Changchun, Jilin 130024, China

⁶Ecology and Environment Department of Jilin Province, Changchun, Jilin 130024, China

⁷Heilongjiang Provincial Key Laboratory of Ecological Restoration and Resource Utilization for Cold Region, Heilongjiang University, Harbin 150080, China

⁸School of Life Science and Geology, Yili Normal University, Yili, Xinjiang 835000, China

Correspondence should be addressed to Zhenxing Zhang; zhangzx725@nenu.edu.cn and Haijun Yang; yang@nenu.edu.cn

Received 29 October 2019; Accepted 20 January 2020; Published 11 February 2020

Academic Editor: Alberto J. Palma

Copyright © 2020 Hongyong Xiang et al. This is an open access article distributed under the Creative Commons Attribution License, which permits unrestricted use, distribution, and reproduction in any medium, provided the original work is properly cited.

Water is essential for every life living on the planet. However, we are facing a more serious situation such as water pollution since the industrial revolution. Fortunately, many efforts have been done to alleviate/restore water quality in freshwaters. Numerous sensors have been developed to monitor the dynamic change of water quality for ecological, early warning, and protection reasons. In the present review, we briefly introduced the pollution status of two major pollutants, i.e., pesticides and heavy metals, in freshwaters worldwide. Then, we collected data on the sensors applied to detect the two categories of pollutants in freshwaters. Special focuses were given on the sensitivity of sensors indicated by the limit of detection (LOD), sensor types, and applied waterbodies. Our results showed that most of the sensors can be applied for stream and river water. The average LOD was 72.53 ± 12.69 ng/ml ($n = 180$) for all pesticides, which is significantly higher than that for heavy metals (65.36 ± 47.51 ng/ml, $n = 117$). However, the LODs of a considerable part of pesticides and heavy metal sensors were higher than the criterion maximum concentration for aquatic life or the maximum contaminant limit concentration for drinking water. For pesticide sensors, the average LODs did not differ among insecticides (63.83 ± 17.42 ng/ml, $n = 87$), herbicides (98.06 ± 23.39 ng/ml, $n = 71$), and fungicides (24.60 ± 14.41 ng/ml, $n = 22$). The LODs that differed among sensor types with biosensors had the highest sensitivity, while electrochemical optical and biooptical sensors showed the lowest sensitivity. The sensitivity of heavy metal sensors varied among heavy metals and sensor types. Most of the sensors were targeted on lead, cadmium, mercury, and copper using electrochemical methods. These results imply that future development of pesticides and heavy metal sensors should (1) enhance the sensitivity to meet the requirements for the protection of aquatic ecosystems and human health and (2) cover more diverse pesticides and heavy metals especially those toxic pollutants that are widely used and frequently been detected in freshwaters (e.g., glyphosate, fungicides, zinc, chromium, and arsenic).

1. Introduction

Seventy-one percent of our planet is covered by water which is a vital necessity to the organisms living on the earth. Even though freshwater only occupied less than 3% of all the water on earth, our daily life is more associated with freshwater than saltwater. However, many freshwater ecosystems have been polluted by anthropogenic activities including the three most dominating contributors: human settlements, industries, and agriculture [1–3]. For example, more than 100,000 chemicals (e.g., pesticides) are registered nowadays, and most of them are related to our daily life; these chemicals can inevitably enter freshwaters [4]. In addition, more than half of the total production of chemicals is harmful to the environment [5]. In Latin America, Africa, and Asia, 1/3, 1/7, and 1/10 of all the streams and rivers have already been affected by pathogen (e.g., fecal coliform bacteria), organic (e.g., biochemical oxygen demand (BOD)), and salinity (e.g., total dissolved solids (TDS)) pollution [6]. At a national scale survey, the water quality of ~1/3 of US' streams and rivers was assessed by the Environmental Protection Agency (EPA), and the results revealed that 55% of the streams were categorized as impaired. Bacteria, sediment, and nutrients were identified as the three most significant causes for stream pollution in this survey [7]. Freshwaters in developing countries such as China are facing more serious pollution situation. It was estimated that ~60% of China's groundwater was classified as poor or very poor, and the number is even higher (~80%) in 17 northern provinces [8]. The impaired water quality negatively affected aquatic organisms and generates major threats to waterbodies, with great consequences on aquatic ecosystems at levels ranging from individuals to watershed [9–13]. More importantly, human health is also at risk if clean drinking water cannot be accessed [4]. It was estimated that the freshwater resources for 82% of the world's population are under high levels of threats, and the situation is more serious in developing countries than in developed countries [14]. Consequently, more than 1/3 of the population in the world lacks safe drinking water [4]. Freshwaters (e.g., streams, rivers, lakes, and ponds) receive large quantity of various pollutants including pesticides [15], heavy metals [16], and nutrients [17]. It was estimated that 80% of municipal wastewater that flows into waterbodies is untreated, and millions of tonnes of heavy metals and other pollutants were dumped into waterbodies every year [18]. In China, human activities introduced 14.5 ± 3.1 mega tonnes of nitrogen to freshwaters each year which are 2.7 times of the predicted safety threshold [19]. Excess nutrients such as nitrogen and phosphorus in freshwaters usually lead to eutrophication, one of the most common reasons for water quality degradation [20, 21]. Many efforts have been done to improve the water quality of freshwaters via direct or indirect ways [22, 23]. Monitoring water quality in freshwaters is still the first priority for many ecological studies, water quality control, and restoration projects [24, 25].

Monitoring water quality is especially important for the provision of clean drinking water and the protection of aquatic ecosystems [26, 27]. After the development of decades, numerous kinds of sensors, including chemical

sensors, biosensors, and electronical sensors, have been developed to detect water quality [28, 29]. A sensor is a device that is capable of providing selective quantitative or semiquantitative analytical information via a biological/chemical/electronical recognition element; it usually is composed of a transducer and a processor [30]. Generally, the requirements of water quality sensors are confined to many factors such as the waterbodies to be monitored, water quality parameters to be tested, and the objects of the monitoring system [31]. The projection of future sensors targets on higher sensitivity, rapider detection, smaller size, inexpensiveness, disposability, ease of manipulation, durability for longer time, and suitability for multiple environments. For example, in a newly published review, Parra et al. [29] summarized several requirements of physical sensors for precision aquaculture: low maintenance, low cost, low battery consumption, nonmetal, robust, waterproof, withstand biofouling, and no effects on aquatic organisms. Previous review papers focus on either one type/category of sensors [32] or one analyte (or one group of analytes) [33]. This review paper will focus on the sensors applied to test two of the most common pollutants in freshwaters, i.e., pesticides and heavy metals. The general contamination status of these parameters in freshwaters and a simple analysis of sensors are also discussed. The sensitivity of sensors (limit of detection (LOD)) and sensor types are especially discussed. The present review paper differs from previous review papers in the following ways: (1) we unified the unit of LOD to make the comparison between studies possible and visualized; (2) only the data collected from freshwaters were used; and (3) not only the sensor types but also the detected analyte categories were discussed.

2. Materials and Methods

2.1. Database Compilation. We build the database of pesticide sensors by searching Web of Science using the following topics: “sensor” and “pesticide or herbicide or fungicide or insecticide” and “freshwater or river or stream or lake or reservoir or pond”. Most of the collected papers were published during the last five years which composed almost half of the publications (2015–2019). The data collected before 2015 were mainly based on previous review papers [34–36]. For each publication, we extracted the following information: tested analytes, sensor types (e.g., biosensors and electronical sensors), LODs, and the applicable waterbodies. For the optical sensors, we included fluorescent sensors, luminescent sensors, and colorimetric sensors. The tested analytes were grouped into three categories of pesticides (i.e., herbicides, insecticides, and fungicides). All the units of LODs were unified as ng/ml. The same method was used to build the database of heavy metal sensors by replacing “pesticide OR herbicide OR fungicide OR insecticide” with “heavy metal”. For heavy metal sensors, we only collected data during the year 2017–2019 (updated until October) which composed ~1/3 of all the publications.

TABLE 1: Summary of studies employing sensors for the detection of pesticides in freshwaters.

Analytes	Sensor types	LOD (ng/ml)	Waterbodies	Ref.
Picloram	Bioelectrochemical	5	Paddy field water	[55]
Malathion	Biosensor	1	Tap water	[56]
Methamidophos	Biosensor	0.01 0.013	Tap water River water	[57]
Monocrotophos	Biosensor	0.015	River and tap water	[58]
Mevinphos		0.009		
Phosphamidon		0.012		
Omethoate		0.032		
Bentazone	Electronical	262.3	River water	[59]
Carbaryl	Electrochemical	5.3	Wastewater	[60]
Heptenophos		3.6		
Fenitrothion		160		
Carbofuran	Electronical	2	Tap water and farmland water	[61]
Fenobucarb		2		
Paraoxon	Bioelectronical	2.8	Lagoon water	[62]
Carbaryl		8.0		
Chlorpyrifos	Biosensor	0.004	Lake water	[63]
Chlorfenvinfos		0.004		
Atrazine	Electrochemical	2.2	River water	[64]
Atrazine	Electrochemical	4.5	River water	[65]
Atrazine	Electrochemical	1.9	River water	[66]
Atrazine	Electrochemical	13	River water	[67]
Atrazine	Electrochemical	3.1	River water	[68]
Ametryne		3.8		
Atrazine	Electrochemical	30.2	Natural waters	[69]
Chlorpyrifos oxon	Bioelectronical	1.1	River water	[70]
Paraoxon		30		
Malaoxon		25		
Chlormequat	Bioelectronical	502.74	River and ground water	[71]
Carbofuran	Bioelectronical	20	Well water	[72]
Carbaryl		300		
Paraoxon	Bioelectronical	5.5	Well water	[73]
Methyl parathion		5.8		
Omethoate	Bioelectronical	21.3	Lake water	[74]
Atrazine	Biooptical	0.15	Drinking, lake, and agricultural wastewater	[75]
Isoproturon	Bio-Opt	3	Well water	[76]
Carbaryl	Biooptical	0.029	Drinking water	[77]
Carbendazim	Biooptical	15	Environmental water	[78]
Carbofuran		68		
Benomyl		35		
Carbaryl	Biooptical	0.27	River water	[79]
Fuberidazole	Biooptical	0.09	River, well, dam, irrigation water	[80]
Carbaryl		6		
Benomyl		9		
Fuberidazole	Biooptical	0.18	River and well water	[81]
O-Phenylphenol		6.1		
Linuron	Biooptical	130	Tap, underground, mineral, and river water	[82]
Metsulfuron methyl	Optical	0.14	River, well, and irrigation water	[83]

TABLE 1: Continued.

Analytes	Sensor types	LOD (ng/ml)	Waterbodies	Ref.
α -Naphthol	Optical	2	Tap and river water	[84]
O-Phenylphenol		2		
Thiabendazole		2		
Triazine	Biooptical	0.0013	River water	[85]
Thiabendazole	Optical	2.8	Tap, underground, mineral, and river water	[86]
Warfarin	Optical	2	River, lake, and spring water	[87]
Thiabendazole	Optical	2.5	Well, river, and irrigation water	[88]
Metsulfuron methyl		3.3		
N-1-Naphthylphthlamic acid	Optical	8.1	Drinking and mineral water	[89]
1-Naphthylamine		11.2		
Thiabendazole	Optical	4.5	Tap, underground, mineral, and river water	[90]
Carbaryl	Biooptical	1.38	Groundwater, tap, and river water	[91]
1-Naphthylamine	Optical	1.1	Well, tap, and urban wastewater	[92]
Paraquat	Optical	0.11	Tap, well, lake, river, and rain water	[93]
Paraquat	Optical	1.6	Wastewater	[94]
Paraquat	Optical	0.003	Tap, mineral, waste, and ground water	[95]
Paraquat	Optical	0.7	Drinking water	[96]
Paraquat	Bioelectrochemical	0.926	River and groundwater	[97]
Paraquat	Biooptical	0.036	River water	[98]
Paraquat	Electronical	23.92	River water	[99]
Paraquat	Electronical	2	Dam, river, and tap water	[100]
Paraquat	Optical	22	River, dam, and mineral water	[101]
Paraquat	Ele-optical	0.1	River water	[102]
Diquat		0.2		
Paraquat	Ele-optical	0.2	Tap, lake, river, ground, and bog water	[103]
Diquat		0.1		
Paraquat	Ele-optical	5		[104]
Diquat		1		
Dipterex	Che-optical	5.152	Wastewater	[105]
Dursban		7.012		
Paraquat		5.143		
Methyl thiophanate		6.84		
Cartap		5.476		
Paraoxon	Optical	0.05	Tap and river water	[106]
Diniconazole	Biooptical	6.4	River and wastewater	[107]
Diuron	Electrochemical	0.00125	Lake water	[108]
Diazinon	Biooptical	36.3	River water	[109]
Iprobenfos		53.6		
Edifenphos		27.9		
Paraoxon	Bioelectronical	2	River water	[110]
2,4-D		50		
Atrazine		10		
Diazinon	Bioelectrochemical	0.039	Tap and river wastewater	[111]
Metamitron	Electrochemical	7.28	River water	[112]
Carbamate	Biooptical	3.3	Lake water	[113]
Diuron	Bioelectrochemical	2.1	River water	[114]
Mesotrione	Electrochemical	8.822	Lake and tap water	[115]
Paraquat	Electrochemical	3.086	River water	[116]
Fenoxanil	Electronical	0.0092	River water	[117]

TABLE 1: Continued.

Analytes	Sensor types	LOD (ng/ml)	Waterbodies	Ref.
Malathion		0.01		
Parathion methyl	Bioelectrochemical	0.02		
Monocrotophos	Bioelectrochemical	0.01	Tap and river water	[118]
Dichlorvos		0.01		
Dicloran	Bioelectrochemical	0.099	Tap and river water	[119]
Fenitrothion	Electrochemical	0.036	Tap and lake water	[120]
Carbamate	Optical	0.023	River water	[121]
Fenoxycarb	Biooptical	949.221	River water	[122]
Malathion	Ele-optical	0.0991	Pond water	[123]
Methomyl	Electronical	126.192	River and tap water	[124]
Diuron		8.1585		
2,4-D	Electronical	26.405	Lake and well water	[125]
Tebuthiuron		77.625		
Pyrethroids	Biooptical	42.64	River water	[126]
2,4-D	Electronical	44.008	River water	[127]
Fomesafen	Electrochemical	89	Lake water	[128]
Glyphosate		338		
Dimethoate		458.52		
Atrazine		431.36		
Cyanazine		481.39		
Diuron		466.2		
Imidacloprid		511.32		
Malathion		660.72		
Imazethapyr	Biooptical	578	Lake water	[50]
Mecoprop-P		429.3		
2,4-D		440.08		
Trifluralin		670.56		
Paraquat		514.32		
Metolachlor		567.6		
Carbaryl		402.44		
Acephate		366		
Dichlorophen	Electronical	3.768	River water	[129]
Hexazinone	Bioelectronical	0.00066	River water	[130]
Malathion	Optical	1.84×10^{-7}	Agricultural runoff water and lake water	[131]
Fenitrothion	Optical	1.677	Well, river, and tap water	[132]
Pendimethalin	Electronical	10.408	Tap and river water	[133]
Metol		0.344		
Bisphenol A	Electrochemical	0.685	River water	[134]
Azinphos methyl	Che-optical	0.549	Tap and river water	[135]
Fenvalerate pyrethroid	Optical	0.01	Tao, river, well, distilled, and draining water	[136]
Propham	Electrochemical	0.789	River water	[137]
Propham	Electrochemical	0.179	River water	[138]
Cyanazine	Electrochemical	0.06	Tap, river, and ground water	[139]
Tau-fluvalinate	Biooptical	6.105	Lake water	[140]
Methyl parathion	Optical	291.3	Lake water	[141]
Pymetrozine	Optical	2.172	Tap and lake water	[142]
Imidacloprid	Electronical	106.1	River water	[143]
Pyrethroid	Biooptical	6.568	River water	[144]
Paraquat	Electronical	0.8	River water	[145]
Clopyralid	Electrochemical	0.154	River water	[146]
Carbendazim	Electronical	37.473	River water	[147]

TABLE 1: Continued.

Analytes	Sensor types	LOD (ng/ml)	Waterbodies	Ref.
Quinalphos	Electrochemical	0.378	Tap and lake water	[148]
Methyl parathion	Biooptical	1.87	River water	[149]
2,4-D	Optical	0.0045	Tap, bottle, and lake water	[150]
Diethofencarb	Electronical	320	River water	[151]
Diazinon	Bioelectrochemical	57.827	River water	[152]
Naptalam	Electrochemical	4.37	River water	[153]
Phosmet	Biooptical	0.0004	Lake water	[154]
Phoxim	Che-optical	298.298	River water	[155]
Bentazone	Electrochemical	8.918	Lake and ground water	[156]
Fenitrothion	Electronical	0.155	Well water	[157]
Chlorpyrifos	Bioelectrochemical	0.07	Lake water	[158]
Lindane	Ele-optical	0.585	River and tap water	[159]
Difenzoquat	Electrochemical	102.225	River and deionized water	[160]
Diquat	Electrochemical	37.844	River and drinking water	[161]
Methyl parathion	Optical	27.674	Pond water	[162]
Glyphosate	Optical	5.07	Lake water	[48]
Aminomethylphosphonic acid		1.666		
Atrazine	Opt-electrochemical	25.882	River water	[163]
Chlorpyrifos		10.167		
Lindane		40.716		
Tetradifon		14.242		
Imidacloprid		3.322		
Glyphosate	Optical	845	River water	[49]
Methyl parathion	Electrochemical	0.012	River water	[164]
Amitrole	Electrochemical	58.856	River water	[165]
Paraoxon	Optical	0.014	Tap and river water	[166]
Malathion		0.033		
Methamidophos		0.017		
Carbaryl	Electronical	0.026	River water	[167]
Fenitrothion		0.0526		
Carbendazim		5.736		
Ofloxacin	Optical	0.123	River and tap water	[169]

2.2. Data Analysis. One-way ANOVA (analysis of variation) was conducted to test the differences of LODs among the pesticide groups/heavy metals and among the sensor types. All data were checked for normality before conducting the ANOVA tests and were log-transformed to meet normality and homogeneity assumptions [37]. One case (1.84×10^{-7}) was deleted from the pesticide sensor dataset due to the outlier when conducting the ANOVA. If significant effects present in the ANOVA, then Tukey's multiple comparison was used for *post hoc* analysis of significant differences among sensor types or analyte groups [38]. All statistical analyses were carried out using SPSS 24.0.

3. Results and Discussion

3.1. Pesticide Sensors

3.1.1. Pesticides in Freshwaters. Pesticides are usually classified into three major categories: herbicides, insecticides, and fungicides/bactericides. The application of pesticides is used to con-

trol weeds, pest outbreaks, and fungal infestations for the security of global food supply [15, 39, 40]. The worldwide pesticide expenditures increased from \$48.8 billion in 2008 to \$55.9 billion in 2012 [41]. After application, these pesticides can enter freshwaters via numerous ways such as wastewater effluent and surface runoff [15]. In a national (US) monitoring network for pesticides in streams and rivers during 1992-2011, the concentrations of one or more pesticides exceeded the aquatic organism benchmark in 61%-69%, 45%, and 53%-90% of the streams in agricultural, mixed-land-use, and urban areas, respectively [42]. In Europe, atrazine (herbicide) is among the most frequently detected chemicals in groundwaters [5]. Due to their high frequency of being detected in freshwaters and the toxicity effects on aquatic organisms, pesticides are one of the most common monitored water quality parameters [43-45]. During the last few decades, many sensors have been developed to detect pesticides in freshwaters [46, 47].

Most of the sensor data we collected can be applied in rivers and streams which correspond to the fact that most studies focused on these waterbodies and indicated the needs

TABLE 2: Criterion maximum concentration and maximum contaminant concentration of some pesticides and heavy metals in freshwaters in the United States.

	CMCs (ng/ml)	MCLs (ng/ml)
<i>Pesticides</i>		
Carbaryl	2.1	—
Chlorpyrifos	0.083	—
Diazinon	0.17	—
Parathion	0.065	—
Dieldrin	0.24	—
Lindane	0.95	0.2
Atrazine	—	3
2,4-D	—	70
Diquat	—	20
<i>Heavy metals</i>		
Arsenic	340 (1.0)	10
Cadmium	1.8 (1.14)	5
Chromium ³⁺	570 (0.316)	50
Chromium ⁶⁺	16 (0.982)	50
Copper	- (0.96)	130
Lead	82 (1.46)	15
Mercury	1.4 (0.85)	2
Nickel	470 (0.998)	—
Silver	3.2 (0.85)	100
Zinc	120 (0.978)	500

Note: CMC: criterion maximum concentration for the recommended aquatic life in the United States. Numbers in parentheses of CMCs for heavy metals are conversion factors for dissolved metals. MCL: maximum contaminant limit concentration for drinking water in the United States.

to monitoring pesticides in streams and rivers. The most frequently detected pesticides are paraquat, followed by atrazine and carbaryl (Table 1). This result is in accordance with the most common pesticide contamination in freshwaters [5]. However, only three studies detected glyphosate [48–50], the most widely used herbicide worldwide [51, 52]. Therefore, more studies should target on the development of glyphosate sensors to get a clearer understanding of the glyphosate contamination in freshwaters. Although the production of herbicides is the highest worldwide [53], more studies focus on insecticide sensors than herbicide sensors (Table 1), probably because organophosphorus pesticides, the most frequently detected analytes, are highly toxic to organisms [54]. Therefore, priority was given to those with relatively high toxicity rather than those used in large quantity when monitoring water quality.

3.1.2. Sensitivity of Pesticide Sensors. The average LOD of pesticide sensors included in this review was 72.53 ± 12.69 ng/ml ($n = 180$, mean \pm SE). Not all of sensors for the detection of pesticides in freshwaters were sensitive enough for ecological and monitoring requirements. The proposed maximum contaminant level, i.e., the maximum permissible level (MCL) of a contaminant in water that is delivered to any user of a public waterbody, for many pesticides (e.g., atrazine and aldicarb) is at the level of ng/ml or

even less than 1 ng/ml [170]. For example, the criterion maximum concentrations (CMC) of carbaryl, chlorpyrifos, diazinon, and parathion for aquatic life in freshwaters of the United States are 2.1, 0.083, 0.17, and 0.065 ng/ml, respectively (Table 2). Moreover, more than 5% of the MCLs for the top 29 commonly regulated pesticides in drinking water exceed the computed upper thresholds for human health risk uncertainty [171], which means that the MCLs for pesticides in drinking water should be stricter and higher sensitive sensors are needed. However, our results indicated that the LODs for 32.8% of the sensors are higher than 10 ng/ml, and <50% of the sensors can reach the level of 3 ng/ml. Therefore, many sensors may not be sensitive enough for the detection of pesticides in freshwaters regarding the requirements for the protection of aquatic life and human health. In addition, there are more than 1,000 pesticides used worldwide to ensure food security. Nevertheless, this review paper only included 97 kinds of pesticides/active ingredients which cover less than 10% of all pesticides. Therefore, future studies should focus on the largely ignored pesticides because many pesticides have toxic effects on aquatic organisms [172] and human health [173, 174]. For example, many sensors were developed to analyze organophosphorus pesticides (e.g., chlorpyrifos and carbaryl) while fewer sensors were targeted on organochlorine pesticides such as dichlorodiphenyl-trichloroethane (DDT). DDT was widely used for the control of pest and fungus in the last century. Even though DDT has been banned for decades in many countries, it can still be found in 8–100% of the sampled small streams in three South American countries [175]. Therefore, DDT is still a global concern due to the toxicity, not easy to be degraded, and the tendency to be accumulated in organisms [176]. The LOD of one biooptical sensor used for the detection of DDT in river water can be as low as 0.015 ng/ml [177].

LODs in this study showed thousands of orders for different analytes and sensors. Among all the sensors been checked, the most sensitive sensor was developed by Kumar et al. [131], in which the indirect detection of malathion through an enzyme-based fluorometric method was applied. This system can achieve an ultrasensitive LOD which is as low as 1.84×10^{-7} ng/ml and can be spiked for lake water and agricultural runoff water [131]. By contrast, some sensors are relatively “insensitive” with the LODs at the level of 100 ng/ml [50, 122, 141]. Although, the average LOD for herbicide sensors is higher than that of insecticides and fungicides, there is no significant difference among the three categories of pesticides ($F_{2,176} = 2.717$, $P = 0.069$, Figure 1). The sensitivity of sensors collected in this paper is similar to that of previous review papers [34, 178]. Only 22 cases (12.22%) were related to fungicide sensors. This extremely low percentage indicated the urgency to improve the monitoring of fungicides in freshwaters, because fungicides are widely occurring in freshwaters and are highly toxic to numerous aquatic organisms [15, 179]. For the sensor types, we found a similar pattern (Table 1) as some previous review papers that electrochemical [180], optical [33, 35], and biological [181] sensors are among the most widely used sensors for the detection of pesticides in freshwaters. Regarding the sensitivity of different types of sensors, biosensors showed

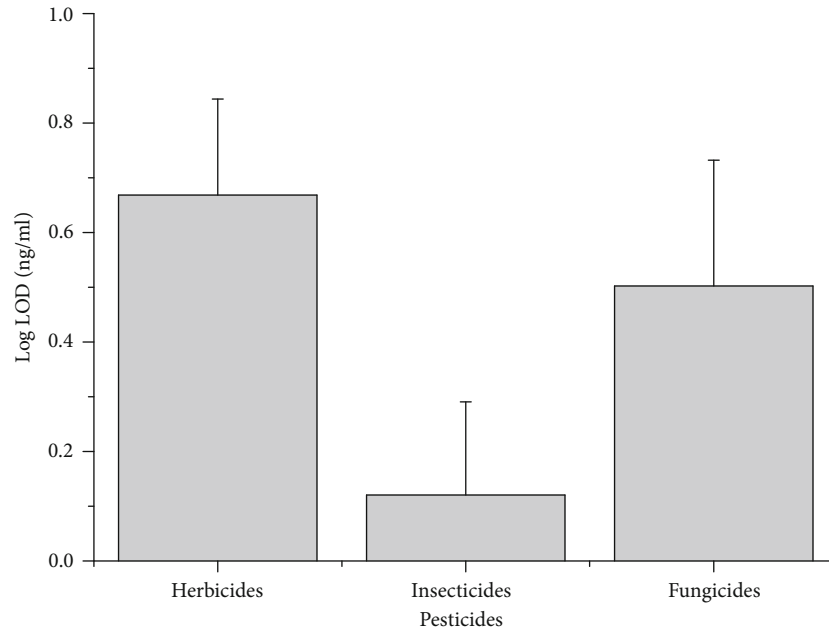


FIGURE 1: Averages of limit of detection of sensors for herbicides, insecticides, and fungicides. Values are the mean \pm SE.

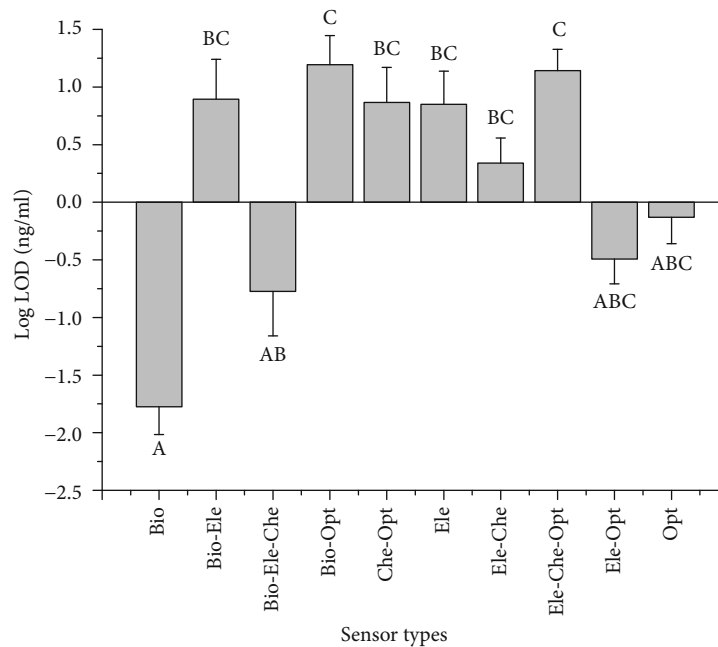


FIGURE 2: Averages of limit of detection of pesticide sensors based on different detection methods. Values are the mean \pm SE. Different uppercase letters above each bar indicate significant differences after one-way ANOVA and *post hoc* Tukey (parameters with the same letter are not significantly different between sensors).

the highest sensitivity compared with other sensors, while the biooptical and electrochemical optical sensors indicated the lowest sensitivity ($F_{9,169} = 7.239$, $P < 0.001$, Figure 2). Biosensors have been widely used in the environmental monitoring [5], given the advantages of biosensors in detecting pesticides and other pollutants over conventional methods: high stability (e.g., they can operate at high temperature), inexpensiveness, possibility for real-time monitoring, high selectivity, and disposability, just to name some of them

[181–183]. Biosensors could be a promising direction for pesticide detection in freshwaters. For example, diatoms, which were popular for the assessment of water quality [184], may be a suitable tool for biosensors.

3.2. Heavy Metal Sensors

3.2.1. Heavy Metals in Freshwaters. Heavy metals refer to metallic elements that have a high atomic weight and with a

TABLE 3: Summary of sensors used to detect heavy metals in freshwaters during the year 2017-2019.

Analytes	Sensors	LOD (ng/ml)	Waterbodies	Ref.
As ³⁺	Biosensor	0.005	Tap, lake, and pond water	[203]
As ³⁺	Electrochemical	75	River water	[204]
Cd ²⁺	Electrochemical	0.068	Tap and lake water	[205]
Pb ²⁺		0.105		
Pb ²⁺	Electrochemical	0.15	Tap and lake water	[206]
Pb ²⁺	Optical	0.029	River water	[207]
Hg ²⁺		0.044		
Cu ²⁺	Electrochemical	9.532	Tap and river water	[208]
Fe ³⁺	Optical	200	Tap and lake water	[209]
Ni ²⁺		300		
Cr ⁶⁺		100		
Cu ²⁺		30		
Al ³⁺		80		
Zn ²⁺		40		
Cd ²⁺	Electrochemical	0.337	River water	[210]
Pb ²⁺	Electrochemical	0.2	Lake water	[211]
Cu ²⁺		0.2		
Hg ²⁺		0.2		
Pb ²⁺	Electrochemical	0.6	River water	[212]
Cu ²⁺		0.3		
Ag ⁺	Biosensor	0.006	Tap, drinking, pond, and soil water	[213]
Cd ²⁺	Electrochemical	0.0056	River water	[214]
Pb ²⁺		0.0166		
Cu ²⁺		0.001		
Hg ²⁺		0.010		
As ³⁺	Electrochemical biosensor	0.000003	Lake and well water	[215]
Cd ²⁺	Electrochemical	0.17	Lake water	[216]
Hg ²⁺	Optical	0.6	Tap water	[217]
Pb ²⁺	Electrochemical	0.17	River, lake, and wastewater	[218]
Cd ²⁺		0.21		
Hg ²⁺	Electrochemical	6.018	River water	[219]
Cu ²⁺	Electronical	0.02	River, tap, and well water	[220]
Pb ²⁺		0.03		
Cr ³⁺		0.15		
Ag ⁺	Electrochemical	0.098	Pond, tap, drinking, and soil water	[221]
Hg ²⁺	Biofluorescent	0.261	River water	[222]
Cd ²⁺	Electrochemical	0.05	Tap, pond, and river water	[223]
Ni ²⁺	Electrochemical	0.12	Tap and river water	[224]
Cu ²⁺	Electrochemical	3	River water	[225]
Cd ²⁺		4		
Pb ²⁺		2.5		
Cd ²⁺		1.012		
Pb ²⁺	Electrochemical	0.207	River water	[226]
Cu ²⁺		0.508		
Hg ²⁺		0.181		
Ni ²⁺	Electrochemical	240	Lake water	[227]
Cr ⁶⁺		180		
Hg ²⁺		190		
Pb ²⁺	Electrochemical	0.5	River water	[228]

TABLE 3: Continued.

Analytes	Sensors	LOD (ng/ml)	Waterbodies	Ref.
Hg ²⁺	Optical	0.261	Tap and river water	[229]
As ³⁺	Biooptical	0.005	Groundwater	[203]
Hg ²⁺	Biooptical	0.241	Lake and deionized water	[230]
Pb ²⁺	Bioelectrochemical	0.000001	River water	[231]
Cd ²⁺	Electrochemical	3.372	Lake water	[232]
Hg ²⁺	Optical	7.422	River water	[233]
Cu ²⁺		6.672		
Pb ²⁺	Electrochemical	0.15	Lake and river water	[234]
Cu ²⁺		0.07		
Hg ²⁺		0.13		
Pb	Electrochemical	1.68	Tap and lake water	[235]
Cd		1.24		
Cu ²⁺	Optical	0.0064	River water	[236]
Fe ³⁺		0.056		
Pb ²⁺	Biooptical	1.036	Lake water	[237]
Hg ²⁺		3.731		
Cd ²⁺	Electrochemical	1.16	Lake water	[238]
		0.152	Deionized water	
Pb ²⁺	Optical	0.216	River and tap water	[239]
Pb ²⁺	Optical	0.011	River water	[240]
As ³⁺	Bioelectronical	2.248	River, tap, and wastewater	[241]
Cd ²⁺		7.869		
Cd ²⁺	Electrochemical	0.5	River water	[242]
Pb ²⁺		1		
Cu ²⁺		5		
Cr ³⁺	Biosensor	0.35	River and tap water	[243]
Pb ²⁺	Electrochemical	4.144	Lake and mining effluent water	[244]
Cd ²⁺	Electrochemical	7.45	Lake and tap water	[245]
Pb ²⁺		1.17		
Zn ²⁺	Electrochemical	0.327	Tap and river water	[246]
Cd ²⁺		0.225		
Pb ²⁺		0.166		
Cu ²⁺	Electrochemical	25.418	River, tap, and dam water	[247]
Cd ²⁺	Electrochemical	0.0025		[248]
Pb ²⁺		0.0518		
Ni ²⁺		0.0002		
Zn ²⁺	Electrochemical	0.05	Lake water	[249]
Pb ²⁺		0.02		
Cu ²⁺		0.03		
Pb ²⁺	Electrochemical	2.486	Tap, lake, and river water	[250]
Ag ⁺	Bioelectrochemical	0.00000005	Tap and lake water	[251]
Cd ²⁺	Electrochemical	0.2	River water	[252]
Pb ²⁺		0.3		
Pb ²⁺	Bioelectronical	3.937	River water	[253]
Hg ²⁺		3.611		
Cu ²⁺	Electrochemical	19.064	Tap and river water	[254]
Pb ²⁺	Optical	192.696	Lake water	[255]
Cr ³⁺		48.356		
Hg ²⁺		186.549		

TABLE 3: Continued.

Analytes	Sensors	LOD (ng/ml)	Waterbodies	Ref.
Cd ²⁺	Chemical	0.001	Wastewater	[256]
Cu ²⁺		0.006		
Hg ²⁺		0.020		
Pb ²⁺		0.021		
Mn ²⁺	Optical	16	River water	[257]
Fe ²⁺		11		
Cu ²⁺		12		
Fe ³⁺		50		
Hg ²⁺	Optical	0.233	River and tap water	[258]
Hg ²⁺		0.509		
Hg ²⁺	Biooptical	0.602	Lake water	[259]
Ag ⁺		0.324		
Cd ²⁺	Optical-electronical	0.152	River water	[260]
Pb ²⁺		0.029		
Cd ²⁺	Electrochemical	0.315	River and tap water	[261]
Pb ²⁺		0.292		
As ³⁺		0.172		
Hg ²⁺		0.321		
Cu ²⁺	Biooptical	5547.566	Pond wand tap water	[262]

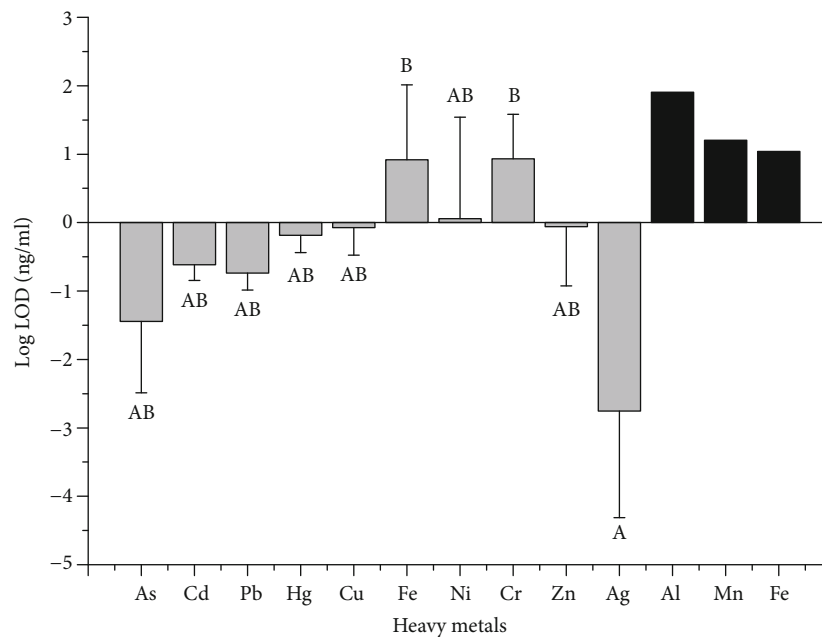


FIGURE 3: Averages of limit of detection of sensors for the detection of heavy metals in freshwaters. Values are the mean \pm SE. Different uppercase letters above each bar indicate significant differences after one-way ANOVA and *post hoc* Tukey (parameters with the same letter are not significantly different between heavy metal sensors). Only one sensor was included in this review for the detection of Al, Mn, and Fe. Therefore, these three heavy metal sensors were excluded from the ANOVA. The data of Cr³⁺ and Cr⁶⁺ were combined for the ANOVA.

density of at least five times greater than that of water [185]. Aquatic ecosystems can be polluted by heavy metals through multiple ways such as mining, weathering of soils and rocks, industrial wastewater, and surface runoff [186–188]. Natural concentrations of Pb and Cd are less than 0.003 ng/ml in

streams [189]. However, heavy metal concentrations may be two or three orders of the natural concentrations or even higher in polluted waterbodies [190, 191]. The most common heavy metal pollutants found in aquatic ecosystems are As, Cd, Cr, Cu, Ni, Pb, Hg, and Zn [192]. For instance, Cu, Fe,

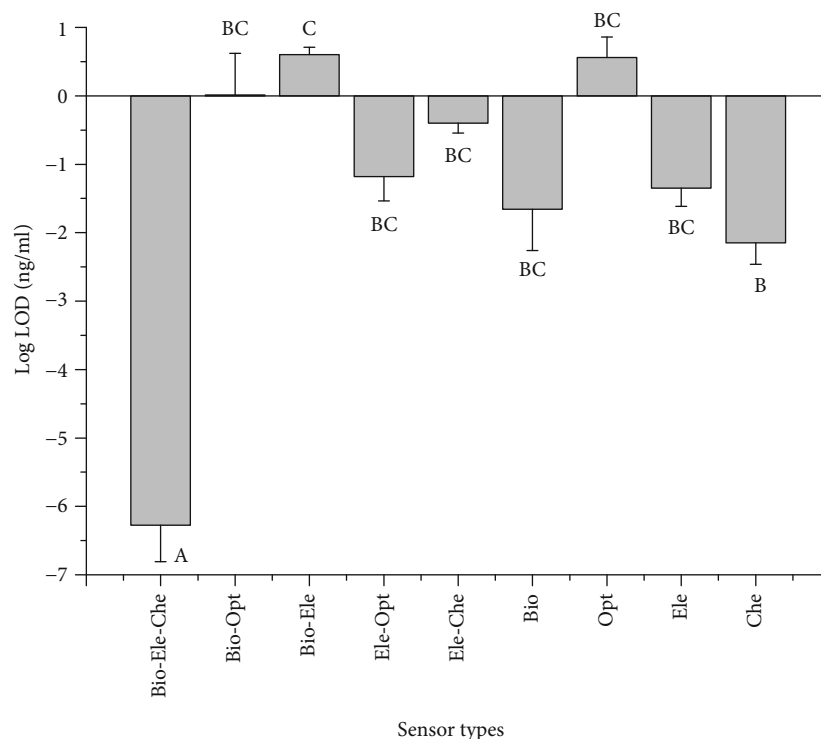


FIGURE 4: Averages of limit of detection of heavy metal sensors based on different methods. Values are the mean \pm SE. Different uppercase letters above each bar indicate significant differences after one-way ANOVA and *post hoc* Tukey (parameters with the same letter are not significantly different between sensors).

Zn, Mn, and Cr were the top five heavy metals of concern in freshwaters in Bohai Region, China, while Hg showed the lowest risk [193]. The concentrations of many heavy metals in the river Ganga water and sediment exceeded the acceptable concentrations and threatened human health and aquatic organisms [194]. Three countries, i.e., the United States, Germany, and Russia, consume 3/4 of the world's most widely used metals. Human health and aquatic ecosystems can be threatened by heavy metals especially by Pb, Cd, Hg, and As [195, 196]. For example, groundwaters contaminated by As threatened millions of people's drinking water safety in developing countries such as India, Cambodia, and Vietnam [4]. Aquatic organisms still suffer from the toxic effects of heavy metals even though upstream mining activities ceased for decades [197]. Due to the high toxicity and them commonly found in freshwaters [198, 199], heavy metals are among the most important indices when monitoring water quality [45, 200].

3.2.2. Sensitivity of Heavy Metal Sensors. Altogether, 61 publications were selected during the years 2017-2019 (the data were updated until October 2019), with nine types of sensors used for the detection of 13 heavy metals in freshwaters (Table 3). The average LOD for all sensors is 65.36 ± 47.51 ng/ml ($n = 117$, mean \pm SE). The sensitivity of sensors differed among the detected heavy metals ($F_{9,104} = 2.289$, $P = 0.022$, Figure 3). Sensors targeted on Ag had the highest sensitivity while the sensors used to detect Fe and Cr showed the lowest sensitivity. The sensitivity of many sensors can satisfy the requirements for drinking water and wild life

protection. The LODs of some sensors were still higher than CMCs or MCLs. Especially for mercury sensors, 30% of the collected sensors failed to satisfy the CMC or MCL requirements. It reminds us that higher sensitivity sensors should be developed to protect human health and aquatic organisms. In addition, the CMC/MCL may be changed due to the national regulation [201, 202] which means that the higher sensitivity sensors may be needed to detect lower concentrations of heavy metals. As mentioned above, As, Cr, Ni, and Zn are among the highest concentrations of heavy metals in freshwaters [192]. However, limited sensors were developed to detect these heavy metals. Therefore, more diverse sensors should be developed to analyze these heavy metals.

Regarding the sensor types, more than half of the heavy metal sensors were based on electrochemical methods, while few studies applied biological ways (Table 3). The sensitivity of sensors for heavy metal detection varied among sensor types ($F_{8,108} = 12.5$, $P < 0.001$, Figure 4). Bioelectrochemical sensors had the highest sensitivity, while bioelectronic sensors showed the lowest sensitivity. The most sensitive sensor was a bioelectrochemical sensor which was developed by Zhang et al. [251] for the detection of silver in tap and lake water, and the LOD was as low as 5.0×10^{-8} ng/ml. On the contrary, a pigment-based whole-cell biosensor developed for the analysis of copper in pond and tap water showed the highest LOD (5547.6 ng/ml) [262]. The average LOD of heavy metals based on electrochemical methods was 12.187 ± 5.446 ng/ml ($n = 65$, mean \pm SE). The LOD of

electrochemical sensors in this review is higher than the LODs of electrochemical sensors in previous review papers [210, 263, 264]. This probably is because the LODs of four electrochemical sensors were higher than 50 ng/ml which increased the average LOD. Electrochemical sensors have the advantages such as easy to manipulate, cheap, suitable for field monitoring, and portable which make it suitable for heavy metal detection [263]. However, the optical sensors in this review did not show higher sensitivity than electrochemical sensors as mentioned in a previous study [263]. This is caused by two studies which used colorimetric and luminescent detection; the LODs in these two studies are 30–300 ng/ml [209, 255].

4. Conclusion

This review presents the general information on sensors for the detection of pesticides and heavy metals in freshwaters. The studied sensors covered less than 10% of all registered pesticides/ingredients. Most of the selected pesticide sensors were used to analyze insecticides and herbicides while limited studies were focused on fungicides. The LODs of ~30% of the pesticide sensors failed to meet the maximum permissible concentrations for aquatic life and drinking water. Biosensors showed the highest sensitivity and appeared to be a promising technology in future development for the detection of pesticides in freshwaters. The average LOD of sensors for the detection of heavy metals is 65.36 ng/ml during the last three years. The LODs of a small fraction of sensors such as mercury sensors were higher than the upper threshold concentrations for the protection of wild life and drinking water safety. Most of the heavy metal sensors were designed to detect mercury, cadmium, lead, and copper based on electrochemical methods. These results imply us that higher sensitivity sensors should be developed in the future. In addition, future sensors should cover more pesticides and heavy metals (e.g., glyphosate and zinc) which are commonly detected in waterbodies and are highly toxic to aquatic organisms and human health.

Conflicts of Interest

The authors declare that there is no conflict of interest regarding the publication of this paper.

Acknowledgments

This work was supported by the National Natural Science Foundation of China (grant numbers 41501566 and 41601576), Fundamental Research Funds for the Central Universities (grant number 2412018JC002), Program of Introducing Talents of Discipline to Universities (grant number B16011), Foundation of Education Department of Jilin Province (grant number 2014 B050), and Basal Research Fund for Undergraduate Universities of Heilongjiang Province of China (grant number 2019-KYYWF-0598).

References

- [1] J. Mateo-Sagasta, S. M. Zadeh, H. Turrall, and J. Burke, *Water Pollution from Agriculture: A Global Review*, the Food and Agriculture Organization of the United Nations; the Water Land and Ecosystems research program, Rome, Italy; Colombo, Sri Lanka, 2017.
- [2] K. Li, Z. Zhang, H. Yang et al., “Effects of instream restoration measures on the physical habitats and benthic macroinvertebrates in an agricultural headwater stream,” *Ecological Engineering*, vol. 122, pp. 252–262, 2018.
- [3] T. Mani, S. Primpke, C. Lorenz, G. Gerdt, and P. Burkhardt-Holm, “Microplastic pollution in benthic midstream sediments of the Rhine River,” *Environmental Science & Technology*, vol. 53, no. 10, pp. 6053–6062, 2019.
- [4] R. P. Schwarzenbach, T. Egli, T. B. Hofstetter, U. von Gunten, and B. Wehrli, “Global water pollution and human health,” *Annual Review of Environment and Resources*, vol. 35, no. 1, pp. 109–136, 2010.
- [5] M. Gavrilescu, K. Demnerová, J. Aamand, S. Agathos, and F. Fava, “Emerging pollutants in the environment: present and future challenges in biomonitoring, ecological risks and bioremediation,” *New Biotechnology*, vol. 32, no. 1, pp. 147–156, 2015.
- [6] UNEP, *A Snapshot of the World's Water Quality: Towards a Global Assessment*, Nairobi, United Nations Environment Programme, 2016.
- [7] EPA, *Water Quality Assessment and TMDL Information*, United States Environmental Protection Agency, 2015.
- [8] D. Hou, G. Li, and P. Nathanail, “An emerging market for groundwater remediation in China: policies, statistics, and future outlook,” *Frontiers of Environmental Science & Engineering*, vol. 12, no. 1, p. 16, 2018.
- [9] B. Grizzetti, D. Lanza, C. Lique, A. Reynaud, and A. C. Cardoso, “Assessing water ecosystem services for water resource management,” *Environmental Science & Policy*, vol. 61, pp. 194–203, 2016.
- [10] J. Turunen, J. Markkula, M. Rajakallio, and J. Aroviita, “Riparian forests mitigate harmful ecological effects of agricultural diffuse pollution in medium-sized streams,” *Science of the Total Environment*, vol. 649, pp. 495–503, 2019.
- [11] H. M. Valett and D. T. Ely, “Acidification, stress, and detrital processing: implications for ecosystem function in headwater streams,” *Hydrobiologia*, vol. 826, no. 1, pp. 233–246, 2019.
- [12] K. Li, C. He, J. Zhuang et al., “Long-term changes in the water quality and macroinvertebrate communities of a subtropical river in South China,” *Water*, vol. 7, no. 12, pp. 63–80, 2015.
- [13] Z. Zhang, H. Yang, H. Yang, Y. Li, and T. Wang, “The impact of roadside ditches on juvenile and sub-adult Bufo melanostictus migration,” *Ecological Engineering*, vol. 36, no. 10, pp. 1242–1250, 2010.
- [14] P. A. Green, C. J. Vörösmarty, I. Harrison, T. Farrell, L. Sáenz, and B. M. Fekete, “Freshwater ecosystem services supporting humans: pivoting from water crisis to water solutions,” *Global Environmental Change*, vol. 34, pp. 108–118, 2015.
- [15] J. P. Zubrod, M. Bundschuh, G. Arts et al., “Fungicides: an overlooked pesticide class?,” *Environmental Science & Technology*, vol. 53, no. 7, pp. 3347–3365, 2019.
- [16] K. Sekabira, H. O. Origa, T. A. Basamba, G. Mutumba, and E. Kakudidi, “Assessment of heavy metal pollution in the urban stream sediments and its tributaries,” *International*

- Journal of Environmental Science & Technology*, vol. 7, no. 3, pp. 435–446, 2010.
- [17] G. Woodward, M. O. Gessner, P. S. Giller et al., “Continental-scale effects of nutrient pollution on stream ecosystem functioning,” *Science*, vol. 336, no. 6087, pp. 1438–1440, 2012.
 - [18] WWAP, *The United Nations World Water Development Report 2017: Wastewater, the Untapped Resource*, In Place de Fontenoy Paris, France, 2017.
 - [19] C. Yu, X. Huang, H. Chen et al., “Managing nitrogen to restore water quality in China,” *Nature*, vol. 567, no. 7749, pp. 516–520, 2019.
 - [20] M. Le Moal, C. Gascuel-Oudou, A. Ménesguen et al., “Eutrophication: a new wine in an old bottle?,” *Science of the Total Environment*, vol. 651, pp. 1–11, 2019.
 - [21] V. H. Smith, “Eutrophication of freshwater and coastal marine ecosystems a global problem,” *Environmental Science and Pollution Research*, vol. 10, no. 2, pp. 126–139, 2003.
 - [22] Z. Zhang, L. Cao, Z. Zhu et al., “Evaluation on soil bioengineering measures in agricultural areas: poorer durability of wooden structures and better aboveground habitat improvements,” *Ecological Engineering*, vol. 129, pp. 1–10, 2019.
 - [23] L. L. Osborne and D. A. Kovacic, “Riparian vegetated buffer strips in water-quality restoration and stream management,” *Freshwater Biology*, vol. 29, no. 2, pp. 243–258, 1993.
 - [24] J. S. Bash and C. M. Ryan, “Stream restoration and enhancement projects: is anyone monitoring?,” *Environmental Management*, vol. 29, no. 6, pp. 877–885, 2002.
 - [25] S. C. Mukhopadhyay and A. Mason, *Smart Sensors for Real-Time Water Quality Monitoring*, Springer, 2013.
 - [26] M. V. Storey, B. van der Gaag, and B. P. Burns, “Advances in on-line drinking water quality monitoring and early warning systems,” *Water Research*, vol. 45, no. 2, pp. 741–747, 2011.
 - [27] J. Bartram and R. Ballance, *Water Quality Monitoring: A Practical Guide to the Design and Implementation of Freshwater Quality Studies and Monitoring Programmes*, CRC Press, 1996.
 - [28] P. Kruse, “Review on water quality sensors,” *Journal of Physics D: Applied Physics*, vol. 51, no. 20, p. 25, 2018.
 - [29] L. Parra, G. Lloret, J. Lloret, and M. Rodilla, “Physical sensors for precision aquaculture: a review,” *IEEE Sensors Journal*, vol. 18, no. 10, pp. 3915–3923, 2018.
 - [30] M. Farré, L. Kantiani, S. Pérez, D. Barceló, and D. Barceló, “Sensors and biosensors in support of EU Directives,” *TrAC Trends in Analytical Chemistry*, vol. 28, no. 2, pp. 170–185, 2009.
 - [31] N. A. Cloete, R. Malekian, and L. Nair, “Design of smart sensors for real-time water quality monitoring,” *IEEE Access*, vol. 4, pp. 3975–3990, 2016.
 - [32] N. de Acha, C. Elosúa, J. M. Corres, and F. J. Arregui, “Fluorescent sensors for the detection of heavy metal ions in aqueous media,” *Sensors*, vol. 19, no. 3, p. 599, 2019.
 - [33] E. J. Llorent-Martínez, P. Ortega-Barrales, M. L. Fernández-Córdova, and A. Ruiz-Medina, “Trends in flow-based analytical methods applied to pesticide detection: a review,” *Analytica Chimica Acta*, vol. 684, no. 1–2, pp. 30–39, 2011.
 - [34] G. A. Ibañez and G. M. Escandar, “Luminescence sensors applied to water analysis of organic pollutants—an update,” *Sensors*, vol. 11, no. 12, pp. 11081–11102, 2011.
 - [35] S. A. Nsibandé and P. B. C. Forbes, “Fluorescence detection of pesticides using quantum dot materials - a review,” *Analytica Chimica Acta*, vol. 945, pp. 9–22, 2016.
 - [36] A. Gahlaut, A. Gothwal, A. K. Chhillar, and V. Hooda, “Electrochemical biosensors for determination of organophosphorus compounds: review,” *Open Journal of Applied Biosensor*, vol. 1, no. 1, pp. 1–8, 2012.
 - [37] Z. Yuan and H. Y. H. Chen, “Global trends in senesced-leaf nitrogen and phosphorus,” *Global Ecology and Biogeography*, vol. 18, no. 5, pp. 532–542, 2009.
 - [38] J. Liu, C. Feng, D. Wang, L. Wang, B. J. Wilsey, and Z. Zhong, “Impacts of grazing by different large herbivores in grassland depend on plant species diversity,” *Journal of Applied Ecology*, vol. 52, no. 4, pp. 1053–1062, 2015.
 - [39] B. Rashid, T. Husnain, and S. Riazuddin, “Herbicides and pesticides as potential pollutants: a global problem,” in *Plant Adaptation and Phytoremediation*, M. Ashraf, M. Ozturk, and M. S. A. Ahmad, Eds., pp. 427–447, Springer Netherlands, Dordrecht, 2010.
 - [40] W. Zhang, “Global pesticide use: profile, trend, cost/benefit and more,” *Proceedings of the International Academy of Ecology and Environmental Sciences*, vol. 8, no. 1, pp. 1–27, 2018.
 - [41] D. Atwood and C. Paisley-Jones, *Pesticides Industry Sales and Usage: 2008–2012 Market Estimates*, US Environmental Protection Agency, Washington, DC, USA, 2017.
 - [42] W. W. Stone, R. J. Gilliom, and K. R. Ryberg, “Pesticides in U.S. streams and rivers: occurrence and trends during 1992–2011,” *Environmental Science & Technology*, vol. 48, no. 19, pp. 11025–11030, 2014.
 - [43] P. Palma, M. Kuster, P. Alvarenga et al., “Risk assessment of representative and priority pesticides, in surface water of the Alqueva reservoir (south of Portugal) using on-line solid phase extraction-liquid chromatography-tandem mass spectrometry,” *Environment International*, vol. 35, no. 3, pp. 545–551, 2009.
 - [44] J. Robles-Molina, B. Gilbert-López, J. F. García-Reyes, and A. Molina-Díaz, “Monitoring of selected priority and emerging contaminants in the Guadalquivir River and other related surface waters in the province of Jaen, South East Spain,” *Science of the Total Environment*, vol. 479–480, pp. 247–257, 2014.
 - [45] S. Zgheib, R. Moilleron, and G. Chebbo, “Priority pollutants in urban stormwater: part 1 - case of separate storm sewers,” *Water Research*, vol. 46, no. 20, pp. 6683–6692, 2012.
 - [46] P. Joshi, A. Bisht, T. Tyagi, S. Mehtab, and M. Zaidi, “Electrochemical sensor for the detection of pesticides in environmental sample: a review,” *IJCS*, vol. 6, no. 2, pp. 3199–3205, 2018.
 - [47] C. Steffens, J. Steffens, A. Marcia Graboski, A. Manzoli, and F. Lima Leite, “16- nanosensors for detection of pesticides in water,” in *New Pesticides and Soil Sensors*, A. M. Grumezescu, Ed., pp. 595–635, Academic Press, 2017.
 - [48] E. A. O. Pereira, V. F. Melo, G. Abate, and J. C. Masini, “Determination of glyphosate and aminomethylphosphonic acid by sequential-injection reversed-phase chromatography: method improvements and application in adsorption studies,” *Analytical and Bioanalytical Chemistry*, vol. 411, no. 11, pp. 2317–2326, 2019.
 - [49] L. B. Jennings, S. Shuvaev, M. A. Fox, R. Pal, and D. Parker, “Selective signalling of glyphosate in water using europium luminescence,” *Dalton Transactions*, vol. 47, no. 45, pp. 16145–16154, 2018.
 - [50] H. Kwon, K. M. Chan, and E. T. Kool, “DNA as an environmental sensor: detection and identification of pesticide

- contaminants in water with fluorescent nucleobases," *Organic & Biomolecular Chemistry*, vol. 15, no. 8, pp. 1801–1809, 2017.
- [51] R. Annett, H. R. Habibi, and A. Hontela, "Impact of glyphosate and glyphosate-based herbicides on the freshwater environment," *Journal of Applied Toxicology*, vol. 34, no. 5, pp. 458–479, 2014.
- [52] N. M. van Straalen and J. Legler, "Decision-making in a storm of discontent," *Science*, vol. 360, no. 6392, pp. 958–960, 2018.
- [53] W. Zhang, F. Jiang, and J. Ou, "Global pesticide consumption and pollution: with China as a focus," *Proceedings of the International Academy of Ecology and Environmental Sciences*, vol. 1, no. 2, pp. 125–144, 2011.
- [54] S. Y. Wee and A. Z. Aris, "Ecological risk estimation of organophosphorus pesticides in riverine ecosystems," *Chemosphere*, vol. 188, pp. 575–581, 2017.
- [55] L. Tang, G.-M. Zeng, G.-L. Shen, Y.-P. Li, Y. Zhang, and D.-L. Huang, "Rapid detection of picloram in agricultural field samples using a disposable immunomembrane-based electrochemical sensor," *Environmental Science & Technology*, vol. 42, no. 4, pp. 1207–1212, 2008.
- [56] H. G. Zuo, J. X. Zhu, C. R. Zhan et al., "Preparation of malathion MIP-SPE and its application in environmental analysis," *Environmental Monitoring and Assessment*, vol. 187, no. 7, p. 394, 2015.
- [57] Z.-L. Shen, D. Yuan, Q.-D. Su et al., "Selective solid-phase extraction using molecularly imprinted polymer for analysis of methamidophos in water and soil samples," *Bioscience, Biotechnology, and Biochemistry*, vol. 75, no. 3, pp. 473–479, 2011.
- [58] X. Zhu, J. Yang, Q. Su, J. Cai, and Y. Gao, "Selective solid-phase extraction using molecularly imprinted polymer for the analysis of polar organophosphorus pesticides in water and soil samples," *Journal of Chromatography A*, vol. 1092, no. 2, pp. 161–169, 2005.
- [59] R. P. Cerejeira, C. Delerue-Matos, and C. M. Vaz, "Development of an FIA system with amperometric detection for determination of bentazone in estuarine waters," *Analytical and Bioanalytical Chemistry*, vol. 373, no. 4-5, pp. 295–298, 2002.
- [60] R. Solná, S. Sapelnikova, P. Skládal et al., "Multienzyme electrochemical array sensor for determination of phenols and pesticides," *Talanta*, vol. 65, no. 2, pp. 349–357, 2005.
- [61] M. G. F. Sales, M. C. V. F. Vaz, C. Delerue-Matos, S. A. A. Almeida, M. F. Barroso, and H. A. O. Ferreira, "Flow amperometric determination of carbofuran and fenobucarb," *International Journal of Environmental Analytical Chemistry*, vol. 88, no. 1, pp. 37–49, 2008.
- [62] C. La Rosa, F. Pariente, L. Hernández, and E. Lorenzo, "Amperometric flow-through biosensor for the determination of pesticides," *Analytica Chimica Acta*, vol. 308, no. 1-3, pp. 129–136, 1995.
- [63] G. Istamboulie, R. Durbiano, D. Fournier, J.-L. Marty, and T. Noguer, "Biosensor-controlled degradation of chlorpyrifos and chlorfenvinfos using a phosphotriesterase-based detoxification column," *Chemosphere*, vol. 78, no. 1, pp. 1–6, 2010.
- [64] L. Švorc, M. Rievaj, and D. Bustin, "Green electrochemical sensor for environmental monitoring of pesticides: determination of atrazine in river waters using a boron-doped diamond electrode," *Sensors and Actuators B: Chemical*, vol. 181, pp. 294–300, 2013.
- [65] L. B. O. dos Santos, M. S. P. Silva, and J. C. Masini, "Developing a sequential injection-square wave voltammetry (SI-SWV) method for determination of atrazine using a hanging mercury drop electrode," *Analytica Chimica Acta*, vol. 528, no. 1, pp. 21–27, 2005.
- [66] L. B. O. dos Santos, G. Abate, and J. C. Masini, "Determination of atrazine using square wave voltammetry with the hanging mercury drop electrode (HMDE)," *Talanta*, vol. 62, no. 4, pp. 667–674, 2004.
- [67] C. M. P. Vaz, S. Crestana, S. A. S. Machado, L. H. Mazo, and L. A. Avaca, "Electroanalytical determination of the herbicide atrazine in natural waters," *International Journal of Environmental Analytical Chemistry*, vol. 62, no. 1, pp. 65–76, 1996.
- [68] D. De Souza, R. A. de Toledo, A. Galli et al., "Determination of triazine herbicides: development of an electroanalytical method utilizing a solid amalgam electrode that minimizes toxic waste residues, and a comparative study between voltammetric and chromatographic techniques," *Analytical and Bioanalytical Chemistry*, vol. 387, no. 6, pp. 2245–2253, 2007.
- [69] L. C. S. Figueiredo-Filho, D. C. Azzi, B. C. Janegitz, and O. Fatibello-Filho, "Determination of atrazine in natural water samples by differential pulse adsorptive stripping voltammetry using a bismuth film electrode," *Electroanalysis*, vol. 24, no. 2, pp. 303–308, 2012.
- [70] G. Jeanty, A. Wojciechowska, J.-L. Marty, and M. Trojanowicz, "Flow-injection amperometric determination of pesticides on the basis of their inhibition of immobilized acetylcholinesterases of different origin," *Analytical and Bioanalytical Chemistry*, vol. 373, no. 8, pp. 691–695, 2002.
- [71] A. H. Kamel, F. T. C. Moreira, S. A. A. Almeida, and M. G. F. Sales, "Novel potentiometric sensors of molecular imprinted polymers for specific binding of chlormequat," *Electroanalysis*, vol. 20, no. 2, pp. 194–202, 2008.
- [72] S. Suwansa-ard, P. Kanatharana, P. Asawatreratanakul, C. Limsakul, B. Wongkittisuksa, and P. Thavarungkul, "Semi disposable reactor biosensors for detecting carbamate pesticides in water," *Biosensors and Bioelectronics*, vol. 21, no. 3, pp. 445–454, 2005.
- [73] P. Mulchandani, W. Chen, and A. Mulchandani, "Flow injection amperometric enzyme biosensor for direct determination of organophosphate nerve agents," *Environmental Science & Technology*, vol. 35, no. 12, pp. 2562–2565, 2001.
- [74] B. Bucur, M. Dondoi, A. Danet, and J.-L. Marty, "Insecticide identification using a flow injection analysis system with biosensors based on various cholinesterases," *Analytica Chimica Acta*, vol. 539, no. 1-2, pp. 195–201, 2005.
- [75] M. Á. González-Martínez, Á. Maquieira, and R. Puchades, "Analysis of atrazine in water and vegetables using immunosensors working in organic media," *International Journal of Environmental Analytical Chemistry*, vol. 83, no. 7-8, pp. 633–642, 2003.
- [76] P. Pulido-Tofiño, J. M. Barrero-Moreno, and M. C. Pérez-Conde, "Flow-through fluoroimmunosensor for isoproturon determination in agricultural foodstuff: evaluation of antibody immobilization on solid support," *Analytica Chimica Acta*, vol. 417, no. 1, pp. 85–94, 2000.
- [77] M. A. González-Martínez, S. Morais, R. Puchades, A. Maquieira, A. Abad, and A. Montoya, "Development of an automated controlled-pore glass flow-through

- immunosensor for carbaryl," *Analytica Chimica Acta*, vol. 347, no. 1-2, pp. 199-205, 1997.
- [78] E. J. Llorent-Martínez, J. F. García-Reyes, P. Ortega-Barrales, and A. Molina-Díaz, "Flow-through fluorescence-based optosensor with on-line solid-phase separation for the simultaneous determination of a ternary pesticide mixture," *Journal of AOAC International*, vol. 88, no. 3, pp. 860-865, 2005.
- [79] I. Sánchez-Barragán, K. Karim, J. M. Costa-Fernández, S. A. Piletsky, and A. Sanz-Medel, "A molecularly imprinted polymer for carbaryl determination in water," *Sensors and Actuators B: Chemical*, vol. 123, no. 2, pp. 798-804, 2007.
- [80] J. F. García Reyes, E. J. Llorent Martínez, P. Ortega Barrales, and A. Molina Díaz, "Multiwavelength fluorescence based optosensor for simultaneous determination of fuberidazole, carbaryl and benomyl," *Talanta*, vol. 64, no. 3, pp. 742-749, 2004.
- [81] E. J. Llorent-Martínez, P. Ortega-Barrales, and A. Molina-Díaz, "Multi-commutated flow-through multi-optosensing: a tool for environmental analysis," *Spectroscopy Letters*, vol. 39, no. 6, pp. 619-629, 2006.
- [82] G. N. Piccirilli, G. M. Escandar, F. C. Cañada, I. D. Merás, and A. M. de la Peña, "Flow-through photochemically induced fluorescence optosensor for the determination of linuron," *Talanta*, vol. 77, no. 2, pp. 852-857, 2008.
- [83] J. López Flores, M. L. Fernández de Córdova, and A. Molina Díaz, "Flow-through optosensing device implemented with photochemically-induced fluorescence for the rapid and simple screening of metsulfuron methyl in environmental waters," *Journal of Environmental Monitoring*, vol. 11, no. 5, pp. 1080-1085, 2009.
- [84] A. Domínguez-Vidal, P. Ortega-Barrales, and A. Molina-Díaz, "Environmental water samples analysis of pesticides by means of chemometrics combined with fluorimetric multi-optosensing," *Journal of Fluorescence*, vol. 17, no. 3, pp. 271-277, 2007.
- [85] S. Herranz, J. Ramón-Azcón, E. Benito-Peña, M. D. Marazuela, M. P. Marco, and M. C. Moreno-Bondi, "Preparation of antibodies and development of a sensitive immunoassay with fluorescence detection for triazine herbicides," *Analytical and Bioanalytical Chemistry*, vol. 391, no. 5, pp. 1801-1812, 2008.
- [86] G. N. Piccirilli and G. M. Escandar, "A novel flow-through fluorescence optosensor for the determination of thiabendazole," *Analytica Chimica Acta*, vol. 601, no. 2, pp. 196-203, 2007.
- [87] R. Badía and M. E. Díaz-García, "Cyclodextrin-based optosensor for the determination of warfarin in waters," *Journal of Agricultural and Food Chemistry*, vol. 47, no. 10, pp. 4256-4260, 1999.
- [88] J. L. Flores, M. L. Fernández De Córdova, and A. Molina Díaz, "Simultaneous flow-injection solid-phase fluorometric determination of thiabendazole and metsulfuron methyl using photochemical derivatization," *Analytical Sciences*, vol. 25, no. 5, pp. 681-686, 2009.
- [89] A. Salinas-Castillo, J. F. Fernández-Sánchez, A. Segura-Carretero, and A. Fernández-Gutiérrez, "A facile flow-through phosphorimetric sensing device for simultaneous determination of naptalam and its metabolite 1-naphthylamine," *Analytica Chimica Acta*, vol. 522, no. 1, pp. 19-24, 2004.
- [90] G. N. Piccirilli and G. M. Escandar, "Flow injection analysis with on-line nylon powder extraction for room-temperature phosphorescence determination of thiabendazole," *Analytica Chimica Acta*, vol. 646, no. 1-2, pp. 90-96, 2009.
- [91] E. Mauriz, A. Calle, A. Abad et al., "Determination of carbaryl in natural water samples by a surface plasmon resonance flow-through immunosensor," *Biosensors and Bioelectronics*, vol. 21, no. 11, pp. 2129-2136, 2006.
- [92] J. L. Guzmán Mar, L. López Martínez, P. L. López de Alba, J. E. Castrejón Durán, and V. Cerdà Martín, "Optical fiber reflectance sensor coupled to a multisyringe flow injection system for preconcentration and determination of 1-naphthylamine in water samples," *Analytica Chimica Acta*, vol. 573-574, pp. 406-412, 2006.
- [93] M. Agudo, A. Ríos, and M. Valcárcel, "Automatic continuous-flow determination of paraquat at the subnanogram per millilitre level," *Analytica Chimica Acta*, vol. 281, no. 1, pp. 103-109, 1993.
- [94] Q.-Q. Bian, Y.-F. Liu, and J.-S. Yu, "CdTe/CdS semiconductor quantum dots as a highly sensitive sensor for pesticide paraquat," *Chemical Journal of Chinese Universities*, vol. 6, 2010.
- [95] G. M. Durán, A. M. Contento, and Á. Ríos, "Use of CdSe/ZnS quantum dots for sensitive detection and quantification of paraquat in water samples," *Analytica Chimica Acta*, vol. 801, pp. 84-90, 2013.
- [96] F. Maya, J. M. Estela, and V. Cerdà, "Improved spectrophotometric determination of paraquat in drinking waters exploiting a multisyringe liquid core waveguide system," *Talanta*, vol. 85, no. 1, pp. 588-595, 2011.
- [97] N. Mai, X. Liu, W. Wei, S. Luo, and W. Liu, "Electrochemical determination of paraquat using a DNA-modified carbon ionic liquid electrode," *Microchimica Acta*, vol. 174, no. 1-2, pp. 89-95, 2011.
- [98] Y. Li, G. Yao, C. Ma, M. Gong, C. Yu, and N. Jie, "Determination of paraquat in water, rice, and urine samples by resonance light scattering technique with DNA," *Analytical Letters*, vol. 44, no. 4, pp. 709-716, 2011.
- [99] L. C. S. de Figueiredo-Filho, V. B. dos Santos, B. C. Janegitz et al., "Differential pulse voltammetric determination of paraquat using a bismuth-film electrode," *Electroanalysis*, vol. 22, no. 11, pp. 1260-1266, 2010.
- [100] L. B. O. dos Santos, C. M. C. Infante, and J. C. Masini, "Development of a sequential injection-square wave voltammetry method for determination of paraquat in water samples employing the hanging mercury drop electrode," *Analytical and Bioanalytical Chemistry*, vol. 396, no. 5, pp. 1897-1903, 2010.
- [101] C. M. C. Infante, A. Morales-Rubio, M. de la Guardia, and F. R. P. Rocha, "A multicommutated flow system with solenoid micro-pumps for paraquat determination in natural waters," *Talanta*, vol. 75, no. 5, pp. 1376-1381, 2008.
- [102] M. Takino, S. Daishima, and K. Yamaguchi, "Determination of diquat and paraquat in water by liquid chromatography/electrospray-mass spectrometry using volatile ion-pairing reagents," *Analytical Sciences*, vol. 16, no. 7, pp. 707-711, 2000.
- [103] V. Y. Taguchi, S. W. D. Jenkins, P. W. Crozier, and D. T. Wang, "Determination of diquat and paraquat in water by liquid chromatography-(electrospray ionization) mass spectrometry," *Journal of the American Society for Mass Spectrometry*, vol. 9, no. 8, pp. 830-839, 1998.

- [104] J. C. Marr and J. B. King, "A simple high performance liquid chromatography/ion spray tandem mass spectrometry method for the direct determination of paraquat and diquat in water," *Rapid Communications in Mass Spectrometry*, vol. 11, no. 5, pp. 479–483, 1997.
- [105] Y. Fan, L. Liu, D. Sun et al., "'Turn-off' fluorescent data array sensor based on double quantum dots coupled with chemometrics for highly sensitive and selective detection of multi-component pesticides," *Analytica Chimica Acta*, vol. 916, pp. 84–91, 2016.
- [106] X. Wu, Y. Song, X. Yan et al., "Carbon quantum dots as fluorescence resonance energy transfer sensors for organophosphate pesticides determination," *Biosensors and Bioelectronics*, vol. 94, pp. 292–297, 2017.
- [107] M. Amjadi and R. Jalili, "Molecularly imprinted mesoporous silica embedded with carbon dots and semiconductor quantum dots as a ratiometric fluorescent sensor for diniconazole," *Biosensors and Bioelectronics*, vol. 96, pp. 121–126, 2017.
- [108] N. Shams, H. N. Lim, R. Hajian et al., "A promising electrochemical sensor based on Au nanoparticles decorated reduced graphene oxide for selective detection of herbicide diuron in natural waters," *Journal of Applied Electrochemistry*, vol. 46, no. 6, pp. 655–666, 2016.
- [109] M. S. Kim, G. W. Kim, and T. J. Park, "A facile and sensitive detection of organophosphorus chemicals by rapid aggregation of gold nanoparticles using organic compounds," *Biosensors and Bioelectronics*, vol. 67, pp. 408–412, 2015.
- [110] F. Arduini, S. Cinti, V. Caratelli, L. Amendola, G. Palleschi, and D. Moscone, "Origami multiple paper-based electrochemical biosensors for pesticide detection," *Biosensors and Bioelectronics*, vol. 126, pp. 346–354, 2019.
- [111] M. Khadem, F. Faridbod, P. Norouzi et al., "Modification of carbon paste electrode based on molecularly imprinted polymer for electrochemical determination of diazinon in biological and environmental samples," *Electroanalysis*, vol. 29, no. 3, pp. 708–715, 2017.
- [112] R. Šeleševská, L. Janíková, and J. Chýlková, "Green electrochemical sensors based on boron-doped diamond and silver amalgam for sensitive voltammetric determination of herbicide metamitron," *Monatshfte für Chemie-Chemical Monthly*, vol. 146, no. 5, pp. 795–805, 2015.
- [113] X. Wang, T. Hou, S. Dong, X. Liu, and F. Li, "Fluorescence biosensing strategy based on mercury ion-mediated DNA conformational switch and nicking enzyme-assisted cycling amplification for highly sensitive detection of carbamate pesticide," *Biosensors and Bioelectronics*, vol. 77, pp. 644–649, 2016.
- [114] A. Wong, M. V. Foguel, S. Khan, F. M. . Oliveira, C. R. T. Tarley, and M. D. P. T. Sotomayor, "Development of an electrochemical sensor modified with MWCNT-COOH and MIP for detection of diuron," *Electrochimica Acta*, vol. 182, pp. 122–130, 2015.
- [115] P. B. Deroco, B. C. Lourencao, and O. Fatibello-Filho, "The use of modified electrode with carbon black as sensor to the electrochemical studies and voltammetric determination of pesticide mesotrione," *Microchemical Journal*, vol. 133, pp. 188–194, 2017.
- [116] T. Nasir, G. Herzog, M. Hébrant, C. Despas, L. Liu, and A. Walcarius, "Mesoporous silica thin films for improved electrochemical detection of paraquat," *ACS Sensors*, vol. 3, no. 2, pp. 484–493, 2018.
- [117] M. Brycht, S. Skrzypek, J. Robak et al., "Ultra trace level determination of fenoxanil by highly sensitive square wave adsorptive stripping voltammetry in real samples with a renewable silver amalgam film electrode," *Journal of Electroanalytical Chemistry*, vol. 738, pp. 69–76, 2015.
- [118] B. Kaur, R. Srivastava, and B. Satpati, "Nanocrystalline titanosilicate-acetylcholinesterase electrochemical biosensor for the ultra-trace detection of toxic organophosphate pesticides," *ChemElectroChem*, vol. 2, no. 8, pp. 1164–1173, 2015.
- [119] M. Khadem, F. Faridbod, P. Norouzi, A. R. Foroushani, M. R. Ganjali, and S. J. Shahtaheri, "Biomimetic electrochemical sensor based on molecularly imprinted polymer for dicloran pesticide determination in biological and environmental samples," *Journal of the Iranian Chemical Society*, vol. 13, no. 11, pp. 2077–2084, 2016.
- [120] N. Shams, H. N. Lim, R. Hajian et al., "Electrochemical sensor based on gold nanoparticles/ethylenediamine-reduced graphene oxide for trace determination of fenitrothion in water," *RSC Advances*, vol. 6, no. 92, pp. 89430–89439, 2016.
- [121] Q. J. Luo, Y. X. Li, M. Q. Zhang, P. Qiu, and Y. H. Deng, "A highly sensitive, dual-signal assay based on rhodamine B covered silver nanoparticles for carbamate pesticides," *Chinese Chemical Letters*, vol. 28, no. 2, pp. 345–349, 2017.
- [122] E. Caballero-Díaz, S. Benítez-Martínez, and M. Valcárcel, "Rapid and simple nanosensor by combination of graphene quantum dots and enzymatic inhibition mechanisms," *Sensors and Actuators B: Chemical*, vol. 240, pp. 90–99, 2017.
- [123] N. F. M. Rodrigues, S. Y. Neto, R. D. C. S. Luz, F. S. Damos, and H. Yamanaka, "Ultrasensitive determination of malathion using acetylcholinesterase immobilized on chitosan-functionalized magnetic iron nanoparticles," *Biosensors*, vol. 8, no. 1, p. 16, 2018.
- [124] D. J. E. Costa, J. C. S. Santos, F. A. C. Sanches-Brandão, W. F. Ribeiro, G. R. Salazar-Banda, and M. C. U. Araujo, "Boron-doped diamond electrode acting as a voltammetric sensor for the detection of methomyl pesticide," *Journal of Electroanalytical Chemistry*, vol. 789, pp. 100–107, 2017.
- [125] E. H. Duarte, J. Casarin, E. R. Sartori, and C. R. T. Tarley, "Highly improved simultaneous herbicides determination in water samples by differential pulse voltammetry using boron-doped diamond electrode and solid phase extraction on cross-linked poly(vinylimidazole)," *Sensors and Actuators B: Chemical*, vol. 255, pp. 166–175, 2018.
- [126] H. Li, X. Wei, Y. Xu et al., "A thin shell and 'sunny shape' molecular imprinted fluorescence sensor in selective detection of trace level pesticides in river," *Journal of Alloys and Compounds*, vol. 705, pp. 524–532, 2017.
- [127] K. Skrzypczyńska, K. Kuśmierk, and A. Świątkowski, "Carbon paste electrodes modified with various carbonaceous materials for the determination of 2,4-dichlorophenoxyacetic acid by differential pulse voltammetry," *Journal of Electroanalytical Chemistry*, vol. 766, pp. 8–15, 2016.
- [128] E. Demir and R. İnam, "Square wave voltammetric determination of fomesafen herbicide using modified nanostructure carbon paste electrode as a sensor and application to food samples," *Food Analytical Methods*, vol. 10, no. 1, pp. 74–82, 2017.
- [129] K. Sipa, M. Brycht, A. Leniart et al., "β-Cyclodextrins incorporated multi-walled carbon nanotubes modified electrode for the voltammetric determination of the pesticide dichlorophen," *Talanta*, vol. 176, pp. 625–634, 2018.

- [130] M. J. U. Toro, L. D. Marestoni, and M. D. P. T. Sotomayor, "A new biomimetic sensor based on molecularly imprinted polymers for highly sensitive and selective determination of hexazinone herbicide," *Sensors and Actuators B: Chemical*, vol. 208, pp. 299–306, 2015.
- [131] D. N. Kumar, S. A. Alex, R. S. S. Kumar, N. Chandrasekaran, and A. Mukherjee, "Acetylcholinesterase inhibition-based ultrasensitive fluorometric detection of malathion using unmodified silver nanoparticles," *Colloids and Surfaces A: Physicochemical and Engineering Aspects*, vol. 485, pp. 111–117, 2015.
- [132] J. Nebu, J. S. A. Devi, R. S. Aparna, B. Aswathy, G. M. Lekha, and G. Sony, "Fluorescence turn-on detection of fenitrothion using gold nanoparticle quenched fluorescein and its separation using superparamagnetic iron oxide nanoparticle," *Sensors and Actuators B-Chemical*, vol. 277, pp. 271–280, 2018.
- [133] G. G. Gerent, C. Q. Gonçalves, P. S. da Silva, and A. Spinelli, "In situ bismuth-film electrode for square-wave cathodic voltammetric detection of pendimethalin at nanomolar level," *Electrochimica Acta*, vol. 168, pp. 379–385, 2015.
- [134] B. Kaur, B. Satpati, and R. Srivastava, "ZrO₂ supported nano-ZSM-5 nanocomposite material for the nanomolar electrochemical detection of metol and bisphenol A," *RSC Advances*, vol. 6, no. 70, pp. 65736–65746, 2016.
- [135] R. Kaur and N. Kaur, "A novel cation ensembled fluorescent organic nanoparticle for selective detection of organophosphorus insecticides," *Dyes and Pigments*, vol. 139, pp. 310–317, 2017.
- [136] D. D. Thiare, A. Coly, D. Sarr et al., "Determination of the fenvalerate insecticide in natural waters by a photochemically-induced fluorescence method," *Macedonian Journal of Chemistry and Chemical Engineering*, vol. 34, no. 2, pp. 245–254, 2015.
- [137] A. Ozcan, M. Gurbuz, and A. Ozbal, "Preparation of a double-step modified carbon paste electrode for the voltammetric determination of propham via bulk modification with fumed silica and drop-casting of maghemite-modified fumed silica nanocomposite," *Sensors and Actuators B-Chemical*, vol. 255, pp. 1517–1524, 2018.
- [138] A. Ozcan, M. Gurbuz, and A. A. Ozcan, "Preparation of a disposable and low-cost electrochemical sensor for propham detection based on over-oxidized poly(thiophene) modified pencil graphite electrode," *Talanta*, vol. 187, pp. 125–132, 2018.
- [139] M. B. Gholivand, N. Karimian, and M. Torkashvand, "A graphene-based electrochemical sensor for sensitive determination of cyanazine," *Journal of Analytical Chemistry*, vol. 70, no. 3, pp. 384–391, 2015.
- [140] J. Wang, Y. Wang, H. Qiu et al., "A novel sensitive luminescence probe microspheres for rapid and efficient detection of τ -fluvialinate in Taihu Lake," *Scientific Reports*, vol. 7, no. 1, 2017.
- [141] H. Wu, Y. Luo, C. Hou et al., "Rapid and fingerprinted monitoring of pesticide methyl parathion on the surface of fruits/leaves as well as in surface water enabled by gold nanorods based casting-and-sensing SERS platform," *Talanta*, vol. 200, pp. 84–90, 2019.
- [142] J. Kang, Y. Zhang, X. Li et al., "Rapid and sensitive colorimetric sensing of the insecticide pymetrozine using melamine-modified gold nanoparticles," *Analytical Methods*, vol. 10, no. 4, pp. 417–421, 2018.
- [143] W. D. A. Paiva, T. M. B. F. Oliveira, C. P. Sousa et al., "Electroanalysis of imidacloprid insecticide in river waters using functionalized multi-walled carbon nanotubes modified glassy carbon electrode," *Journal of the Electrochemical Society*, vol. 165, no. 10, pp. B431–B435, 2018.
- [144] H. Li, X. Wang, Z. Wang et al., "A high-performance SERS-imprinted sensor doped with silver particles of different surface morphologies for selective detection of pyrethroids in rivers," *New Journal of Chemistry*, vol. 41, no. 23, pp. 14342–14350, 2017.
- [145] R. Faramarzi, A. R. Taheri, and M. Roushani, "Determination of paraquat in fruits and natural water using Ni(OH)₂ nanoparticles-carbon nanotubes composite modified carbon ionic liquid electrode," *Analytical & Bioanalytical Electrochemistry*, vol. 7, no. 6, pp. 666–683, 2015.
- [146] A. Özcan and M. Gürbüz, "Development of a modified electrode by using a nanocomposite containing acid-activated multi-walled carbon nanotube and fumed silica for the voltammetric determination of clopyralid," *Sensors and Actuators B: Chemical*, vol. 255, pp. 262–267, 2018.
- [147] M. Brycht, O. Vajdle, K. Sipa et al., " β -Cyclodextrin and multi-walled carbon nanotubes modified boron-doped diamond electrode for voltammetric assay of carbendazim and its corrosion inhibition behavior on stainless steel," *Ionics*, vol. 24, no. 3, pp. 923–934, 2018.
- [148] N. G. Khare, R. A. Dar, and A. K. Srivastava, "Adsorptive stripping voltammetry for trace determination of quinalphos employing silicon carbide nanoparticles modified glassy carbon electrode," *Electroanalysis*, vol. 27, no. 2, pp. 503–509, 2015.
- [149] S. Lan, X. Wang, Q. Liu et al., "Fluorescent sensor for indirect measurement of methyl parathion based on alkaline-induced hydrolysis using N-doped carbon dots," *Talanta*, vol. 192, pp. 368–373, 2019.
- [150] X. Feng, G. Zhang, L. K. Chin, A. Q. Liu, and B. Liedberg, "Highly sensitive, label-free detection of 2,4-dichlorophenoxyacetic acid using an optofluidic chip," *ACS Sensors*, vol. 2, no. 7, pp. 955–960, 2017.
- [151] A. Sinha, Y. Huang, and H. Zhao, "Preparation of 3D assembly of mono layered molybdenum disulfide nanotubules for rapid screening of carbamate pesticide diethofencarb," *Talanta*, vol. 204, pp. 455–464, 2019.
- [152] M. Arvand and M. Dehsaraei, "Amperometric determination of diazinon by gold nanorods/ds-DNA/graphene oxide sandwich-modified electrode," *Ionics*, vol. 24, no. 8, pp. 2445–2454, 2018.
- [153] M. Brycht, A. Leniart, J. Zavašnik et al., "Synthesis and characterization of the thermally reduced graphene oxide in argon atmosphere, and its application to construct graphene paste electrode as a naptalam electrochemical sensor," *Analytica Chimica Acta*, vol. 1035, pp. 22–31, 2018.
- [154] L. Zhou, Y. Cao, B. Lin, S. Song, Y. Yu, and L. Shui, "In-situ visual and ultrasensitive detection of phosmet using a fluorescent immunoassay probe," *Sensors and Actuators B: Chemical*, vol. 241, pp. 915–922, 2017.
- [155] J. Feng, G. Yang, Y. Mei et al., "Macroscopic visual detection of phoxim by calix[4]arene-based host-guest chemistry," *Sensors and Actuators B: Chemical*, vol. 271, pp. 264–270, 2018.
- [156] A. Geto, J. S. Noori, J. Mortensen, W. E. Svendsen, and M. Dimaki, "Electrochemical determination of bentazone using simple screen-printed carbon electrodes," *Environment International*, vol. 129, pp. 400–407, 2019.

- [157] N. Y. Sreedhar, M. S. Kumar, and K. Krishnaveni, "Enhanced electrocatalytic determination of fenitrothion at graphene and silver-zirconia nanosensor," *Monatshefte für Chemie - Chemical Monthly*, vol. 146, no. 9, pp. 1385–1393, 2015.
- [158] W. Cheng, Z. Zheng, J. Yang et al., "The visible light-driven and self-powered photoelectrochemical biosensor for organophosphate pesticides detection based on nitrogen doped carbon quantum dots for the signal amplification," *Electrochimica Acta*, vol. 296, pp. 627–636, 2019.
- [159] K. K. Masibi, O. E. Fayemi, A. S. Adekunle, E. S. M. Sherif, and E. E. Ebenso, "Electrocatalysis of lindane using antimony oxide nanoparticles based-SWCNT/PANI nanocomposites," *Frontiers in Chemistry*, vol. 6, 2018.
- [160] J. Gajdár, J. Barek, and J. Fischer, "Electrochemical microcell based on silver solid amalgam electrode for voltammetric determination of pesticide difenzoquat," *Sensors and Actuators B: Chemical*, vol. 299, article 126931, 2019.
- [161] N. A. Zambianco, T. A. Silva, H. Zanin, O. Fatibello-Filho, and B. C. Janegitz, "Novel electrochemical sensor based on nanodiamonds and manioc starch for detection of diquat in environmental samples," *Diamond and Related Materials*, vol. 98, article 107512, 2019.
- [162] X. Hu, F. Wang, Q. Peng et al., "Construction of a luminescent sensor based on a lanthanide complex for the highly efficient detection of methyl parathion," *RSC Advances*, vol. 9, no. 23, pp. 13048–13053, 2019.
- [163] P. Mandal, D. Sahoo, P. Sarkar, K. Chakraborty, and S. Das, "Fluorescence turn-on and turn-off sensing of pesticides by carbon dot-based sensor," *New Journal of Chemistry*, vol. 43, no. 30, pp. 12137–12151, 2019.
- [164] X. C. Fu, C. Zhang, X. H. Li, J. Zhang, and G. Wei, "Mono-6-thio- β -cyclodextrin-functionalized AuNP/two-dimensional TiO₂nanosheet nanocomposite for the electrochemical determination of trace methyl parathion in water," *Analytical Methods*, vol. 11, no. 37, pp. 4751–4760, 2019.
- [165] S. Zhou, H. Xu, Y. Wei et al., "Platelet nitrogen and sulfur co-doped ordered mesoporous carbon with inexpensive methylene blue as a single precursor for electrochemical detection of herbicide amitrole," *Nano*, vol. 14, no. 8, article 1950104, 2019.
- [166] J. Korram, L. Dewangan, R. Nagwanshi, I. Karbhal, K. K. Ghosh, and M. L. Satnami, "A carbon quantum dot-gold nanoparticle system as a probe for the inhibition and reactivation of acetylcholinesterase: detection of pesticides," *New Journal of Chemistry*, vol. 43, no. 18, pp. 6874–6882, 2019.
- [167] A. Özcan, D. Topçuoğulları, and A. Atılır Özcan, "Fenitrothion sensing with reduced graphene oxide decorated fumed silica nanocomposite modified glassy carbon electrode," *Sensors and Actuators B-Chemical*, vol. 284, pp. 179–185, 2019.
- [168] J. G. M. Yanke, G. K. Dedzo, and E. Ngameni, "Solvent effect on the grafting of an organophilic silane onto smectite-type clay: application as electrode modifiers for pesticide detection," *Electroanalysis*, vol. 29, no. 8, pp. 1894–1902, 2017.
- [169] H. Yi, Z. Yan, L. Wang et al., "Fluorometric determination for ofloxacin by using an aptamer and SYBR Green I," *Microchimica Acta*, vol. 186, no. 10, 2019.
- [170] L. H. Nowell and E. A. Resek, "National standards and guidelines for pesticides in water, sediment, and aquatic organisms: application to water-quality assessments," in *Reviews of Environmental Contamination and Toxicology: Continuation of Residue Reviews*, G. W. Ware, Ed., pp. 1–154, Springer New York, New York, NY, USA, 1994.
- [171] Z. Li and A. Jennings, "Worldwide regulations of standard values of pesticides for human health risk control: a review," *International Journal of Environmental Research and Public Health*, vol. 14, no. 7, p. 826, 2017.
- [172] L. Pisa, D. Goulson, E.-C. Yang et al., "An update of the Worldwide Integrated Assessment (WIA) on systemic insecticides. Part 2: impacts on organisms and ecosystems," *Environmental Science and Pollution Research*, 2017.
- [173] P. Nicolopoulou-Stamati, S. Maipas, C. Kotampasi, P. Stamatis, and L. Hens, "Chemical pesticides and human health: the urgent need for a new concept in agriculture," *Frontiers in Public Health*, vol. 4, no. 148, 2016.
- [174] K.-H. Kim, E. Kabir, and S. A. Jahan, "Exposure to pesticides and the associated human health effects," *Science of the Total Environment*, vol. 575, pp. 525–535, 2017.
- [175] L. Hunt, C. Bonetto, V. H. Resh et al., "Insecticide concentrations in stream sediments of soy production regions of South America," *Science of the Total Environment*, vol. 547, pp. 114–124, 2016.
- [176] B. B. Prasad and D. Jauhari, "A dual-template biomimetic molecularly imprinted dendrimer-based piezoelectric sensor for ultratrace analysis of organochlorine pesticides," *Sensors and Actuators B: Chemical*, vol. 207, pp. 542–551, 2015.
- [177] E. Mauriz, A. Calle, J. J. Manclús et al., "Optical immunosensor for fast and sensitive detection of DDT and related compounds in river water samples," *Biosensors and Bioelectronics*, vol. 22, no. 7, pp. 1410–1418, 2007.
- [178] P. F. P. Barbosa, E. G. Vieira, L. R. Cumba et al., "Voltammetric techniques for pesticides and herbicides detection-an overview," *International Journal of Electrochemical Science*, vol. 14, pp. 3418–3433, 2019.
- [179] T. A. McMahon, N. T. Halstead, S. Johnson et al., "Fungicide-induced declines of freshwater biodiversity modify ecosystem functions and services," *Ecology Letters*, vol. 15, no. 7, pp. 714–722, 2012.
- [180] R. Ramachandran, V. Mani, S. M. Chen, G. G. Kumar, and M. Govindasamy, "Recent developments in electrode materials and methods for pesticide analysis-an overview," *International Journal of Electrochemical Science*, vol. 10, no. 1, pp. 859–869, 2015.
- [181] S. Boulanouar, S. Mezzache, A. Combès, and V. Pichon, "Molecularly imprinted polymers for the determination of organophosphorus pesticides in complex samples," *Talanta*, vol. 176, pp. 465–478, 2018.
- [182] J. Chouler and M. Di Lorenzo, "Water quality monitoring in developing countries; can microbial fuel cells be the answer?," *Biosensors*, vol. 5, no. 3, pp. 450–470, 2015.
- [183] A. ElMekawy, H. M. Hegab, D. Pant, and C. P. Saint, "Bio-analytical applications of microbial fuel cell-based biosensors for onsite water quality monitoring," *Journal of Applied Microbiology*, vol. 124, no. 1, pp. 302–313, 2018.
- [184] Y. Zhang, J. Tao, J. Wang et al., "Trends in diatom research since 1991 based on topic modeling," *Microorganisms*, vol. 7, no. 8, p. 213, 2019.
- [185] P. B. Tchounwou, C. G. Yedjou, A. K. Patlolla, and D. J. Sutton, "Heavy metal toxicity and the environment," in *Molecular, Clinical and Environmental Toxicology: Volume 3: Environmental Toxicology*, A. Luch, Ed., pp. 133–164, Springer Basel, Basel, 2012.

- [186] J. O. Duruibe, M. Ogwuegbu, and J. Egwurugwu, "Heavy metal pollution and human biotoxic effects," *International Journal of Physical Sciences*, vol. 2, no. 5, pp. 112–118, 2007.
- [187] Y. Yi, Z. Yang, and S. Zhang, "Ecological risk assessment of heavy metals in sediment and human health risk assessment of heavy metals in fishes in the middle and lower reaches of the Yangtze River basin," *Environmental Pollution*, vol. 159, no. 10, pp. 2575–2585, 2011.
- [188] C. Sun, Z. Zhang, H. Cao, M. Xu, and L. Xu, "Concentrations, speciation, and ecological risk of heavy metals in the sediment of the Songhua River in an urban area with petrochemical industries," *Chemosphere*, vol. 219, pp. 538–545, 2019.
- [189] Y. Erel, J. J. Morgan, and C. C. Patterson, "Natural levels of lead and cadmium in a remote mountain stream," *Geochimica et Cosmochimica Acta*, vol. 55, no. 3, pp. 707–719, 1991.
- [190] A. O'Sullivan, D. Wicke, and T. Cochrane, "Heavy metal contamination in an urban stream fed by contaminated air-conditioning and stormwater discharges," *Environmental Science and Pollution Research*, vol. 19, no. 3, pp. 903–911, 2012.
- [191] M. S. Islam, M. K. Ahmed, M. Raknuzzaman, M. Habibullah-Al-Mamun, and M. K. Islam, "Heavy metal pollution in surface water and sediment: a preliminary assessment of an urban river in a developing country," *Ecological Indicators*, vol. 48, pp. 282–291, 2015.
- [192] V. Masindi and K. L. Muedi, "Environmental contamination by heavy metals," in *Heavy Metals*, pp. 115–133, IntechOpen, Aglan, France, 2018.
- [193] C. Su, Y. Lu, A. C. Johnson et al., "Which metal represents the greatest risk to freshwater ecosystem in Bohai Region of China?," *Ecosystem Health and Sustainability*, vol. 3, no. 2, article e01260, 2017.
- [194] D. Paul, "Research on heavy metal pollution of river Ganga: a review," *Annals of Agrarian Science*, vol. 15, no. 2, pp. 278–286, 2017.
- [195] L. Järup, "Hazards of heavy metal contamination," *British Medical Bulletin*, vol. 68, no. 1, pp. 167–182, 2003.
- [196] M. S. Schuler and R. A. Relyea, "A review of the combined threats of road salts and heavy metals to freshwater systems," *Bioscience*, vol. 68, no. 5, pp. 327–335, 2018.
- [197] H. Lefcort, J. Vancura, and E. L. Lider, "75 years after mining ends stream insect diversity is still affected by heavy metals," *Ecotoxicology*, vol. 19, no. 8, pp. 1416–1425, 2010.
- [198] S. Cheng, "Heavy metal pollution in China: origin, pattern and control," *Environmental Science and Pollution Research*, vol. 10, no. 3, pp. 192–198, 2003.
- [199] I. Razo, L. Carrizales, J. Castro, F. Díaz-Barriga, and M. Monroy, "Arsenic and heavy metal pollution of soil, water and sediments in a semi-arid climate mining area in Mexico," *Water, Air, and Soil Pollution*, vol. 152, no. 1–4, pp. 129–152, 2004.
- [200] G. Teijon, L. Candela, K. Tamoh, A. Molina-Díaz, and A. R. Fernández-Alba, "Occurrence of emerging contaminants, priority substances (2008/105/CE) and heavy metals in treated wastewater and groundwater at Depurbaix facility (Barcelona, Spain)," *Science of the Total Environment*, vol. 408, no. 17, pp. 3584–3595, 2010.
- [201] J. McKay and A. Moeller, "Are mandatory regulations required for water quality in Australia?," *Water Policy*, vol. 4, no. 2, pp. 95–118, 2002.
- [202] F. W. Pontius, "Future directions in water quality regulations," *Journal-AWWA*, vol. 89, no. 3, pp. 40–54, 1997.
- [203] J. Pan, Q. Li, D. Zhou, and J. Chen, "Ultrasensitive aptamer biosensor for arsenic (III) detection based on label-free triple-helix molecular switch and fluorescence sensing platform," *Talanta*, vol. 189, pp. 370–376, 2018.
- [204] M. M. Marei, K. L. Kaht, T. J. Roussel, R. S. Keynton, and R. P. Baldwin, "Measurement of As(III) with in situ subtraction of background and interferent signals by double potential step-anodic stripping coulometry," *Sensors and Actuators B: Chemical*, vol. 301, article 127005, 2019.
- [205] D. Qin, A. Chen, X. Mamat et al., "Double-shelled yolk-shell microspheres based electrochemical sensor for determination of cadmium and lead ions," *Analytica Chimica Acta*, vol. 1078, pp. 32–41, 2019.
- [206] X. Hu, H. Guo, T. Qi et al., "Miniaturized electrochemical sensor with micropillar array working electrode for trace lead online measurement in tap water," *Journal of Micromechanics and Microengineering*, vol. 29, no. 10, article 105005, 2019.
- [207] Z. Liu, W. Jin, F. Wang et al., "Ratiometric fluorescent sensing of Pb²⁺ and Hg²⁺ with two types of carbon dot nanohybrids synthesized from the same biomass," *Sensors and Actuators B: Chemical*, vol. 296, p. 126698, 2019.
- [208] P. Wei, Z. Zhu, R. Song, Z. Li, and C. Chen, "An ion-imprinted sensor based on chitosan-graphene oxide composite polymer modified glassy carbon electrode for environmental sensing application," *Electrochimica Acta*, vol. 317, pp. 93–101, 2019.
- [209] F. Li, Y. Hu, Z. Li, J. Liu, L. Guo, and J. He, "Three-dimensional microfluidic paper-based device for multiplexed colorimetric detection of six metal ions combined with use of a smartphone," *Analytical and Bioanalytical Chemistry*, vol. 411, no. 24, pp. 6497–6508, 2019.
- [210] Y. Chen, D. Zhang, D. Wang, L. Lu, X. Wang, and G. Guo, "A carbon-supported BiSn nanoparticles based novel sensor for sensitive electrochemical determination of Cd (II) ions," *Talanta*, vol. 202, pp. 27–33, 2019.
- [211] N. Q. Giao, V. H. Dang, P. T. H. Yen et al., "Au nanodendrite incorporated graphite pencil lead as a sensitive and simple electrochemical sensor for simultaneous detection of Pb(II), Cu(II) and Hg(II)," *Journal of Applied Electrochemistry*, vol. 49, no. 8, pp. 839–846, 2019.
- [212] S. Singh, A. Pankaj, S. Mishra, K. Tewari, and S. Pratap Singh, "Cerium oxide-catalyzed chemical vapor deposition grown carbon nanofibers for electrochemical detection of Pb(II) and Cu(II)," *Journal of Environmental Chemical Engineering*, vol. 7, no. 4, article 103250, 2019.
- [213] W. Xiao, Y. Gao, Y. Zhang et al., "Enhanced 3D paper-based devices with a personal glucose meter for highly sensitive and portable biosensing of silver ion," *Biosensors and Bioelectronics*, vol. 137, pp. 154–160, 2019.
- [214] W. Wu, M. Jia, Z. Zhang et al., "Sensitive, selective and simultaneous electrochemical detection of multiple heavy metals in environment and food using a lowcost Fe₃O₄ nanoparticles/fluorinated multi-walled carbon nanotubes sensor," *Ecotoxicology and Environmental Safety*, vol. 175, pp. 243–250, 2019.
- [215] R. Yadav, V. Kushwah, M. S. Gaur et al., "Electrochemical aptamer biosensor for As³⁺ based on apta deep trapped Ag-Au alloy nanoparticles-impregnated glassy carbon electrode," *International Journal of Environmental Analytical Chemistry*, pp. 1–12, 2019.
- [216] X. Zhao, W. Bai, Y. Yan, Y. Wang, and J. Zhang, "Core-shell self-doped polyaniline coated metal-organic-framework

- (SPAN@ UIO-66-NH₂) screen printed electrochemical sensor for Cd²⁺ ions,” *Journal of the Electrochemical Society*, vol. 166, no. 12, pp. B873–B880, 2019.
- [217] S. Sajed, K. Vafaei, F. Arefi et al., “Instant sensitive measurement of Hg concentration using lab-on-a-phone colorimetry,” *Physica Status Solidi A*, vol. 216, no. 14, article 1800871, 2019.
- [218] B. Maleki, M. Baghayeri, M. Ghanei-Motlagh et al., “Polyamidoamine dendrimer functionalized iron oxide nanoparticles for simultaneous electrochemical detection of Pb²⁺ and Cd²⁺ ions in environmental waters,” *Measurement*, vol. 140, pp. 81–88, 2019.
- [219] A. Sánchez-Calvo, M. T. Fernández-Abedul, M. C. Blanco-López, and A. Costa-García, “Paper-based electrochemical transducer modified with nanomaterials for mercury determination in environmental waters,” *Sensors and Actuators B: Chemical*, vol. 290, pp. 87–92, 2019.
- [220] M. Ghorbani, T. Pedramrad, M. Aghamohammadhasan, O. Seyedin, H. Akhlaghi, and N. Afshar Lahoori, “Simultaneous clean-up and determination of Cu(II), Pb(II) and Cr(III) in real water and food samples using a magnetic dispersive solid phase microextraction and differential pulse voltammetry with a green and novel modified glassy carbon electrode,” *Microchemical Journal*, vol. 147, pp. 545–554, 2019.
- [221] H. Fu, Q. Yin, H. Wang et al., “Target-triggered in situ autocatalysis in nanopore membrane for point-of-care testing of sub-nanomolar Ag⁺,” *Sensors and Actuators B: Chemical*, vol. 287, pp. 290–295, 2019.
- [222] S. Venkateswarlu, S. Govindaraju, R. Sangubotla, J. Kim, M.-H. Lee, and K. Yun, “Biosynthesized highly stable Au/C nanodots: ideal probes for the selective and sensitive detection of Hg²⁺ ions,” *Nanomaterials*, vol. 9, no. 2, p. 245, 2019.
- [223] Y. Song, C. Bian, J. Hu et al., “Porous polypyrrole/graphene oxide functionalized with carboxyl composite for electrochemical sensor of trace cadmium (II),” *Journal of the Electrochemical Society*, vol. 166, no. 2, pp. B95–B102, 2019.
- [224] R. Tekanya, K. Pokpas, N. Jahed, and E. I. Iwuoha, “Enhanced specificity and sensitivity for the determination of nickel(II) by square-wave adsorptive cathodic stripping voltammetry at disposable graphene-modified pencil graphite electrodes,” *Analytical Letters*, vol. 52, no. 2, pp. 373–398, 2019.
- [225] L. Liu, K. Zhang, and Y. Wei, “A simple strategy for the detection of Cu(II), Cd(II) and Pb(II) in water by a voltammetric sensor on a TC4A modified electrode,” *New Journal of Chemistry*, vol. 43, no. 3, pp. 1544–1550, 2019.
- [226] M. Lu, Y. Deng, Y. Luo et al., “Graphene aerogel–metal–organic framework-based electrochemical method for simultaneous detection of multiple heavy-metal ions,” *Analytical Chemistry*, vol. 91, no. 1, pp. 888–895, 2019.
- [227] J. P. Devadhasan and J. Kim, “A chemically functionalized paper-based microfluidic platform for multiplex heavy metal detection,” *Sensors and Actuators B: Chemical*, vol. 273, pp. 18–24, 2018.
- [228] M. Finšgar, D. Majer, U. Maver, and T. Maver, “Reusability of SPE and Sb-modified SPE sensors for trace Pb(II) determination,” *Sensors*, vol. 18, no. 11, article 3976, 2018.
- [229] D. Wu, Y. Huang, S. Hu, X. Yi, and J. Wang, “Sensitive Hg²⁺ sensing via quenching the fluorescence of the complex between polythymine and 5, 10, 15, 20-tetrakis(*N*-methyl-4-pyridyl) porphyrin (TMPyP),” *Sensors*, vol. 18, no. 11, article 3998, 2018.
- [230] S. Wang, B. Lin, L. Chen et al., “Branch-migration based fluorescent probe for highly sensitive detection of mercury,” *Analytical Chemistry*, vol. 90, no. 20, pp. 11764–11769, 2018.
- [231] W. Cai, S. Xie, J. Zhang, D. Tang, and Y. Tang, “Immobilized-free miniaturized electrochemical sensing system for Pb²⁺ detection based on dual Pb²⁺-DNAzyme assistant feedback amplification strategy,” *Biosensors and Bioelectronics*, vol. 117, pp. 312–318, 2018.
- [232] A. Aravind and B. Mathew, “Tailoring of nanostructured material as an electrochemical sensor and sorbent for toxic Cd (II) ions from various real samples,” *Journal of Analytical Science and Technology*, vol. 9, no. 1, p. 22, 2018.
- [233] X. Pang, L. Gao, H. Feng, X. Li, J. Kong, and L. Li, “A peptide-based multifunctional fluorescent probe for Cu²⁺, Hg²⁺ and biothiols,” *New Journal of Chemistry*, vol. 42, no. 19, pp. 15770–15777, 2018.
- [234] V. H. Dang, P. T. H. Yen, N. Q. Giao et al., “A versatile carbon fiber cloth-supported Au nanodendrite sensor for simultaneous determination of Cu(II), Pb(II) and Hg(II),” *Electroanalysis*, vol. 30, no. 10, pp. 2222–2227, 2018.
- [235] L. Wang, G. Jing, and T. Cui, “Nafion coated flexible bismuth sensor for trace lead and cadmium determination,” *Microsystem Technologies*, vol. 24, no. 9, pp. 3697–3704, 2018.
- [236] S. Tang, J. Sun, Y. Li et al., “pH-dependent selective ion exchange based on (ethylenediaminetetraacetic acid- nickel)-layered double hydroxide to catalyze the polymerization of aniline for detection of Cu²⁺ and Fe³⁺,” *Talanta*, vol. 187, pp. 287–294, 2018.
- [237] Q. Zhu, L. Liu, Y. Xing, and X. Zhou, “Duplex functional G-quadruplex/NMM fluorescent probe for label-free detection of lead(II) and mercury(II) ions,” *Journal of Hazardous Materials*, vol. 355, pp. 50–55, 2018.
- [238] W.-T. Tsai, M.-H. Nguyen, J.-R. Lai, H.-B. Nguyen, M.-C. Lee, and F.-G. Tseng, “ppb-level heavy metal ion detection by electrochemistry-assisted nanoporous silicon (ECA-NPS) photonic sensors,” *Sensors and Actuators B: Chemical*, vol. 265, pp. 75–83, 2018.
- [239] P. Li, J. Li, M. Bian et al., “A redox route for the fluorescence detection of lead ions in sorghum, river water and tap water and a desk study of a paper-based probe,” *Analytical Methods*, vol. 10, no. 26, pp. 3256–3262, 2018.
- [240] J. Xu, X. Jie, F. Xie, H. Yang, W. Wei, and Z. Xia, “Flavonoid moiety-incorporated carbon dots for ultrasensitive and highly selective fluorescence detection and removal of Pb²⁺,” *Nano Research*, vol. 11, no. 7, pp. 3648–3657, 2018.
- [241] M. B. Gumpu, M. Veerapandian, U. M. Krishnan, and J. B. B. Rayappan, “Amperometric determination of As(III) and Cd(II) using a platinum electrode modified with acetylcholinesterase, ruthenium(II)-tris(bipyridine) and graphene oxide,” *Microchimica Acta*, vol. 185, no. 6, p. 297, 2018.
- [242] S. Liu, T. Wu, F. Li, Q. Zhang, X. Dong, and L. Niu, “Disposable graphene sensor with an internal reference electrode for stripping analysis of heavy metals,” *Analytical Methods*, vol. 10, no. 17, pp. 1986–1992, 2018.
- [243] M. Xiao, H. Shen, Q. Fu et al., “Practical immune-barometer sensor for trivalent chromium ion detection using gold core platinum shell nanoparticle probes,” *Analyst*, vol. 143, no. 6, pp. 1426–1433, 2018.
- [244] M. Sebastian and B. Mathew, “Ion imprinting approach for the fabrication of an electrochemical sensor and sorbent for lead ions in real samples using modified multiwalled carbon

- nanotubes," *Journal of Materials Science*, vol. 53, no. 5, pp. 3557–3572, 2018.
- [245] L. Li, D. Liu, A. Shi, and T. You, "Simultaneous stripping determination of cadmium and lead ions based on the N-doped carbon quantum dots-graphene oxide hybrid," *Sensors and Actuators B: Chemical*, vol. 255, pp. 1762–1770, 2018.
- [246] W. Ren, Y. Zhang, and M. J. Li, "Sensitive determination of Zn^{2+} , Cd^{2+} and Pb^{2+} at electrochemically reduced nanoporous graphene oxide/bismuth film electrode," *International Journal of Electrochemical Science*, vol. 13, no. 2, pp. 1331–1342, 2018.
- [247] C. Topcu, G. Lacin, V. Yilmaz et al., "Electrochemical determination of copper(II) in water samples using a novel ion-selective electrode based on a graphite oxide-imprinted polymer composite," *Analytical Letters*, vol. 51, no. 12, pp. 1890–1910, 2018.
- [248] A. Zazoua, N. Khedimallah, and N. Jaffrezic-Renault, "Electrochemical determination of cadmium, lead, and nickel using a polyphenol-polyvinyl chloride—boron-doped diamond electrode," *Analytical Letters*, vol. 51, no. 3, pp. 336–347, 2018.
- [249] Z. Lu, J. Zhang, W. Dai, X. Lin, J. Ye, and J. Ye, "A screen-printed carbon electrode modified with a bismuth film and gold nanoparticles for simultaneous stripping voltammetric determination of Zn(II) , Pb(II) and Cu(II) ," *Microchimica Acta*, vol. 184, no. 12, pp. 4731–4740, 2017.
- [250] A. Maity, X. Sui, C. R. Tarman et al., "Pulse-driven capacitive lead ion detection with reduced graphene oxide field-effect transistor integrated with an analyzing device for rapid water quality monitoring," *ACS Sensors*, vol. 2, no. 11, pp. 1653–1661, 2017.
- [251] Y. Zhang, H. Li, M. Chen et al., "Ultrasensitive electrochemical biosensor for silver ion based on magnetic nanoparticles labeling with hybridization chain reaction amplification strategy," *Sensors and Actuators B: Chemical*, vol. 249, pp. 431–438, 2017.
- [252] D. Martin-Yerga, I. Alvarez-Martos, M. C. Blanco-Lopez, C. S. Henry, and M. T. Fernandez-Abedul, "Point-of-need simultaneous electrochemical detection of lead and cadmium using low-cost stencil-printed transparency electrodes," *Analytica Chimica Acta*, vol. 981, pp. 24–33, 2017.
- [253] M. B. Gumpu, U. M. Krishnan, and J. B. B. Rayappan, "Design and development of amperometric biosensor for the detection of lead and mercury ions in water matrix—a permeability approach," *Analytical and Bioanalytical Chemistry*, vol. 409, no. 17, pp. 4257–4266, 2017.
- [254] X. Qi, J. Qian, T. Chen, D. Lu, and B. Chen, "Electrochemical determination of Cu(II) ions based on Ag/Pd alloy for water quality early warning," *International Journal of Electrochemical Science*, vol. 12, no. 6, pp. 5511–5520, 2017.
- [255] J. Liu, G. Lv, W. Gu, Z. Li, A. Tang, and L. Mei, "A novel luminescence probe based on layered double hydroxides loaded with quantum dots for simultaneous detection of heavy metal ions in water," *Journal of Materials Chemistry C*, vol. 5, no. 20, pp. 5024–5030, 2017.
- [256] L.-R. Popescu Mandoc, I. Moldoveanu, R.-I. Stefan-van Staden, and E. M. Ungureanu, "Pattern recognition of Cu(II) , Pb(II) , Hg(II) , and Cd(II) in waste waters," *Microsystem Technologies*, vol. 23, no. 5, pp. 1141–1145, 2017.
- [257] N. Youngvises, K. Suwannasaroj, J. Jakmunee, and A. AlSuhaimi, "Multi-reverse flow injection analysis integrated with multi-optical sensor for simultaneous determination of Mn(II) , Fe(II) , Cu(II) and Fe(III) in natural waters," *Talanta*, vol. 166, pp. 369–374, 2017.
- [258] G. Chen, J. Hai, H. Wang, W. Liu, F. Chen, and B. Wang, "Gold nanoparticles and the corresponding filter membrane as chemosensors and adsorbents for dual signal amplification detection and fast removal of mercury(ii)," *Nanoscale*, vol. 9, no. 9, pp. 3315–3321, 2017.
- [259] W. Zhou, J. Ding, and J. Liu, "2-aminopurine-modified DNA homopolymers for robust and sensitive detection of mercury and silver," *Biosensors and Bioelectronics*, vol. 87, pp. 171–177, 2017.
- [260] K. Tyszczyk-Rotko and K. Domańska, "Simple and sensitive voltammetric procedure for determination of Cd (II) and Pb (II) using bismuth-coated screen-printed carbon electrode prepared with mediator," *Journal of the Electrochemical Society*, vol. 164, no. 7, pp. H537–H544, 2017.
- [261] M. B. Gumpu, M. Veerapandian, U. M. Krishnan, and J. B. B. Rayappan, "Simultaneous electrochemical detection of Cd(II) , Pb(II) , As(III) and Hg(II) ions using ruthenium(II)-textured graphene oxide nanocomposite," *Talanta*, vol. 162, pp. 574–582, 2017.
- [262] P.-H. Chen, C. Lin, K.-H. Guo, and Y.-C. Yeh, "Development of a pigment-based whole-cell biosensor for the analysis of environmental copper," *RSC Advances*, vol. 7, no. 47, pp. 29302–29305, 2017.
- [263] B. Bansod, T. Kumar, R. Thakur, S. Rana, and I. Singh, "A review on various electrochemical techniques for heavy metal ions detection with different sensing platforms," *Biosensors and Bioelectronics*, vol. 94, pp. 443–455, 2017.
- [264] D. Omanović, C. Garnier, K. Gibbon-Walsh, and I. Pižeta, "Electroanalysis in environmental monitoring: tracking trace metals—a mini review," *Electrochemistry Communications*, vol. 61, pp. 78–83, 2015.

Research Article

Stem Water Content for Crape Myrtle in Response to Drought, Cold, and Disease Stress

Chao Gao ^{1,2}, Yue Zhao ^{3,4} and Yandong Zhao ^{3,4}

¹School of Computer and Information Engineering, Beijing Technology and Business University, Beijing 100048, China

²Beijing Key Laboratory of Big Data Technology for Food Safety, Beijing Technology and Business University, Beijing 100048, China

³School of Technology, Beijing Forestry University, Beijing 100083, China

⁴Beijing Laboratory of Urban and Rural Ecological Environment, Beijing Municipal Education Commission, Beijing 100083, China

Correspondence should be addressed to Chao Gao; gaochao9158@sina.com

Received 27 October 2019; Revised 28 December 2019; Accepted 8 January 2020; Published 7 February 2020

Guest Editor: Zhenxing Zhang

Copyright © 2020 Chao Gao et al. This is an open access article distributed under the Creative Commons Attribution License, which permits unrestricted use, distribution, and reproduction in any medium, provided the original work is properly cited.

The abiotic and biotic stresses including drought, cold, and disease stress are linked by the fact that they all decrease the availability of water to plant cells. In previous studies, some physiological factors related with plant water status, such as stem sap flow, leaf transpiration rate, and water potential, were used to assess the effects of these stresses on plants. But there are few studies about the effects of these stresses on stem water content (StWC) which can be measured by a novel SWR sensor. In this study, crape myrtle was selected as an experimental subject and its StWC was observed in four experiments including no stress, drought, cold, and disease stress. Before conducting stress experiments, the StWC and environmental and physiological parameters were synchronously monitored under unstressed conditions on a typical day in summer. In the experiment of drought stress, the StWC was monitored under different gradients of soil moisture. In the experiment of cold stress, the StWC was monitored in warm and cold weather, respectively. In the experiment of disease stress, the StWC was monitored under different frequencies of disease treatment. The results showed that the correlation coefficients between StWC and PAR and VPD were larger than 0.5 and the correlation coefficients between StWC and Pn, Tr, Gs, and Ci were larger than 0.8 under no stress. The diurnal mean of StWC decreased firstly, then remained stable for a period of time, and eventually continued to fall under drought stress. On the whole, there was a negative correlation between the diurnal mean of StWC and the degree of drought stress. The StWC showed opposite diurnal variation rules in warm and cold weather. There was a positive correlation between the diurnal range of StWC and the degree of cold stress. The diurnal minimum, maximum, and mean of StWC showed a positive correlation with the health level of plants and the diurnal range of StWC showed a negative correlation with the health level of plants. In conclusion, the StWC can be used as a qualitative evaluation index of the degree of the three types of stress.

1. Introduction

Plants often suffer from continuous exposure to various abiotic and biotic stresses in natural and agricultural settings. The stresses, such as drought, cold, and disease stress are serious threats to plants and result in the deterioration of the environment. Hence, it is important to distinguish whether plants are under a certain stress.

Drought stress usually occurs when available water in soil is reduced and meteorological conditions cause continuous loss of water by evaporation or transpiration [1]. Drought stress can be quantified as a decrease in water potential (ψ_w)

[2]. In most cases, the first response of plants for drought stress is to avoid low ψ_w by adjusting stomatal conductance such that the rates of water loss and water uptake remain balanced [3]. As the drought stress becomes severe, the plant is no longer able to keep a balance between water loss and uptake. Under this condition, some additional mechanisms, such as solutes accumulation [4, 5] and cell wall hardening [6] play an important role in keeping plants from dehydration. As the drought stress becomes more severe, it is increasingly difficult for the plant to avoid dehydration. In this case, some additional mechanisms, including protective proteins [7], metabolic changes [8], and reactive oxygen

species (ROS) detoxification [9] become important for plants in enduring dehydration. In the process of continuous dehydration, plant tissues and organs may suffer from damages, indicating that the plant need to be irrigated immediately.

Cold stress usually can be classified into two types, chilling stress and freezing stress [10]. Compared with chilling stress, freezing stress is more harmful to plants. From the macro perspective, water begins to freeze in the large vessels of the xylem in leaves and stems where dilute sap has a higher freezing point than other solutions in plant [11]. From the micro perspective, water begins to freeze in the extracellular space and then ice crystals dehydrate the cell [12, 13]. As water begins to freeze in plant, liquid water is converted into solid water which is hard to be used by plants, ultimately causing the available water for plants to decrease sharply. Moreover, freezing stress can induce various damages for plants, including cellular dehydration, structural changes in tissues or organs, embolisms in xylem vessels, frost cracks, and plant diseases [14]. In the process of freezing stress, some protection measures should be adapted against cold damages, such as pruning branches, wrapping the trunk, and painting the trunk with white latex paint.

Disease stress usually occurs after plants are infected with various bacteria, fungus, virus, or insects [15]. Upon infection, the plant's water status would also be affected [16–21]. Roberts and Schreiber investigated the changes of root resistance to water flow in American elm seedlings inoculated with *Ceratocystis ulmi* and concluded that the water flow of infected plants was reduced to about 40% as compared with healthy plants [17]. Parke et al. and Collins et al. indicated that tanoak infected with *Phytophthora ramorum* had significantly more tyloses than noninfected trees in xylem vessels, resulting in the reduction of water transport and hydraulic conductivity [18, 19]. Park et al. reported that sap flow velocity was significantly lower in bitternut hickory infected with *Ceratocystis smalleyi* than that in noninfected trees [20]. Ploetz et al. claimed that avocado infected with *Raffaelea lauricola* had significantly smaller net photosynthetic rate, stomatal conductance, transpiration rate, water use efficiency, and xylem sap flow rate than noninfected trees [21]. In the process of disease stress, plant water status is disturbed, indicating that some preventive measure should be adapted against disease stress.

Based on the above analysis, it can be concluded that plant water status is significantly affected by drought, cold, and disease stress. Therefore, measuring plant water status contributes to a better understanding of these stresses. So far, most researchers use stem sap flow, leaf transpiration rate, and water potential to assess various abiotic and biotic stresses [10, 22]. But there are few studies about the effects of these stresses on stem water content (StWC) = (volume of water):(volume of stem). In this study, we monitored the StWC of crape myrtle trees. Meanwhile, some environmental and physiological parameters were synchronously monitored. The main objectives were to (1) analyze the response of StWC to environmental and physiological parameters, (2) analyze the response of StWC to drought stress, (3) analyze the response of StWC to cold stress, and (4) analyze the response of StWC to disease stress.

2. Materials and Methods

2.1. Studying Site. This study was conducted in a nursery (116°20' 43.62" E, 40°0' 41.92" N) near Beijing Forestry University. The study area has a temperature monsoon climate with warm summers and cold winters. The main soil type is clay loam with pH values ranging from 7 to 8. Since 2015, the mean annual air temperature was 12.6°C, and the mean maximum and minimum annual air temperature of the warmest and the coldest months were 36.5 and -12.8°C, respectively. The mean annual precipitation was 620 mm and the mean annual sunshine duration was 2569 hours. A large number of crape myrtle trees were planted in the nursery. These trees with similar morphological characteristics (approx. 2.5 m in tree height, 4 cm in diameter at breast height, 1 m² in crown projection area) were selected as experimental subjects.

2.2. Measuring Methods

2.2.1. Measurement of Stem Water Content. StWC was monitored by a self-made high-frequency standing wave ratio (SWR) sensor which had been developed in our previous researches and can detect StWC noninvasively in situ and in real time [23]. Based on the previous researches, the performance indexes of SWR sensor can be concluded as follows: axial sensitive distance ≤ 53 mm, radial sensitive distance ≤ 20 mm, measuring range for StWC 1~100%, measuring sensitivity ≥ 10 mV/1% and average measuring error ≤ 1%.

2.2.2. Measurement of Environmental and Physiological Parameters. Root-water-uptake rate is related with soil temperature (ST) and moisture (SM). Leaf transpiration rate is influenced by air temperature (AT), humidity (AH), and vapor pressure deficit (VPD). Photosynthetic rate is directly determined by photosynthetically active radiation (PAR). Hence, it is necessary to monitor the six environmental parameters which are external factors to affect the regulation of plant water status. Soil temperature and moisture were measured by 5TM sensor (Decagon, America, temperature range -40~60°C, temperature accuracy ±1°C, moisture range 0~100%, moisture accuracy ±2%). Air temperature and humidity were measured by HMP50-L6 sensor (Vaisala, Finland, temperature range -10~50°C, temperature accuracy ±0.25°C, humidity range 0~100%, humidity accuracy ±2%). PAR was measured by LI-190R sensor (Li-Cor, America, range 0~10000 μmol m⁻² s⁻¹, accuracy ±5%). VPD can be calculated using air temperature and humidity based on the Goff-Gratch formulation [24].

Plant physiological parameters, such as net photosynthetic rate (Pn), transpiration rate (Tr), stomatal conductance (Gs), and intercellular CO₂ concentration (Ci) are internal factors to affect the regulation of plant water status. The four physiological parameters were synchronously measured and recorded by LI-6400XT portable photosynthesis system (Li-Cor, America, CO₂ range 0~3100 μmol mol⁻¹, CO₂ accuracy ±10 μmol mol⁻¹, H₂O range 0~75 mmol mol⁻¹, H₂O accuracy ±1 mmol mol⁻¹). Considering the fact that Tr measured by LI-6400XT just represents the leaf transpiration

rate, the whole-tree transpiration was measured by electronic balance (UWA-T-030, LangKe XingYe Weighing Equipment Ltd., China, range 0–30 kg, accuracy ± 1 g).

2.3. Experimental Methods. Before conducting the experiments of drought, cold, and disease stress, we monitored StWC of crape myrtle trees under unstressed conditions on a typical day in summer. In this experiment, three well-grown crape myrtle trees were chosen as experimental samples in the nursery. In the meantime, environmental parameters were automatically measured by self-developed data logger in the whole day and plant physiological parameters were manually measured by LI-6400XT portable photosynthesis system from 6:00 to 18:00 at intervals of an hour.

In the experiment of drought stress, crape myrtle trees were divided into experimental and control group with three trees in each group. Each tree was cultivated in a polyresin pot with the volume of 10.2 L. The textural compositions of the soil in the pots were sand 0.61 g g^{-1} , silt 0.28 g g^{-1} , and clay 0.11 g g^{-1} . The soil surface in the experimental group was covered by plastic wrap to prevent water from evaporating. Compared with the experimental trees without irrigation, the trees in the control group were fully irrigated every day. This experiment was conducted in a greenhouse and lasted for ten days between April and May. In the start stage, the drought stress was slight with soil moisture between 9% and 14%. In the middle stage, the drought stress was moderate with soil moisture between 7% and 11%. In the end stage, the drought stress was severe with soil moisture between 5% and 9%. During the three stages of drought stress, StWC and environmental parameters of all samples were monitored. In addition, the weight of the pot in experimental group was synchronously monitored to calculate the whole-tree transpiration.

In the experiment of cold stress, three crape myrtle trees were chosen as experimental samples in the nursery. In order to observe the responses of StWC to warm and cold weather, respectively, under natural environment, the experiment was divided into two stages. In the first stage, the experiment was carried out in early September when the trees were in growth period and the air temperature ranged from 17.9 to 30.9°C. In the second stage, the experiment was carried out in late November when the trees were in dormancy period and the air temperature ranged from -5.6 to 7.9°C. During both stages, StWC and environmental parameters of all samples were monitored.

Based on historical cultivation experience in the nursery, *Eriococcus legerstroemiae* Kuwana usually parasitize in the cracks of the trunk in winter, thus causing the crape myrtle trees suffering from sooty blotch in June. In order to obtain different disease degree of samples, crape myrtle trees were divided into three groups with 24 trees in each group and disease treatments, such as pruning branches and spraying lime-sulfur mixture, were adopted for the three groups with different frequencies. In the first group, disease treatments were taken both in winter and spring and then the trees were healthy without disease (no black spots on leaves). In the second group, the same disease treatments were taken only in spring and then the trees were slightly infected with sooty

blotch (black spot area less than 1/3 of leaf area). In the third group, no disease treatment was taken at any time and then the trees were severely infected with sooty blotch (black spot area more than 1/3 of leaf area). During the germination process of crape myrtle tree, StWC and environmental parameters of all samples were monitored. This experiment was conducted in the nursery from May to July.

2.4. Data Collection and Preprocessing. The data including StWC and environmental parameters were collected using the self-developed data logger (8 MB flash, 16-channel, and 12-bit ADC, 0–2.5 V range, 2-channel RS-232, 2-channel RS-485) at intervals of 10 minutes. The sensors measuring environmental parameters were installed on the self-designed bracket (Figure 1(a)) and the SWR sensor measuring StWC was installed on the tree stem at breast height which is set to 1.3 m above the ground in forestry (Figure 1(b)). Then, all sensors mentioned above were connected to the data logger. In the process of data collection, the sensor data was affected by missing data and abnormal values due to instrumental error or some other external factors like severance of connectivity or power shutdown. These missing data was interpolated using rolling average of available data of past three samples. These abnormal values lying outside the permissible range for the corresponding parameter were also replaced by rolling average of past three samples. Then, all data was further denoised using mean filtering with the window length of three.

3. Results and Discussion

3.1. Response of StWC to Environmental and Physiological Parameters. Drought and cold stress are essentially determined by environmental parameters. Then, these stresses in turn will affect plant physiological parameters. Therefore, it is necessary to analyze the response of StWC to environmental and physiological parameters under natural environment before analyzing other experiments including drought and cold stress.

The correlations between StWC and environmental parameters were analyzed under unstressed conditions on a typical day in summer (Table 1). Correlation analysis suggests that AT, PAR, and VPD were significantly negatively correlated with StWC and AH was significantly positively correlated with StWC. Considering that AT and AH can be characterized by VPD, we further analyzed the diurnal variation rule between StWC and environmental parameters including PAR and VPD. As can be seen from Figure 2, when PAR or VPD increased in the morning, water loss rate by leaf transpiration was greater than water absorption rate by root, thus resulting in the fall of StWC. Nevertheless, as PAR or VPD reached a certain threshold at midday, there was a dynamic balance between water loss and water absorption due to the midday depression, thus resulting in small fluctuations of StWC. When PAR or VPD decreased in the afternoon, water loss rate by leaf transpiration was smaller than water absorption rate by root, thus resulting in the raise of StWC [25, 26].



FIGURE 1: (a) The installation of environmental sensors. (b) The installation of SWR sensor.

TABLE 1: Correlations between StWC and environmental parameters under unstressed conditions on a typical day in summer.

Variables		Environmental parameters				
		ST	SM	AT	AH	PAR
StWC	Correlation coefficient	-0.0284	-0.1873	-0.5875	0.5372	-0.9132
	Significance probability	0.8954	0.3809	0.0025	0.0068	0.0000
	Sample size	24	24	24	24	24

ST: soil temperature; SM: soil moisture; AT: air temperature; AH: air humidity; PAR: photosynthetically active radiation; VPD: vapor pressure deficit.

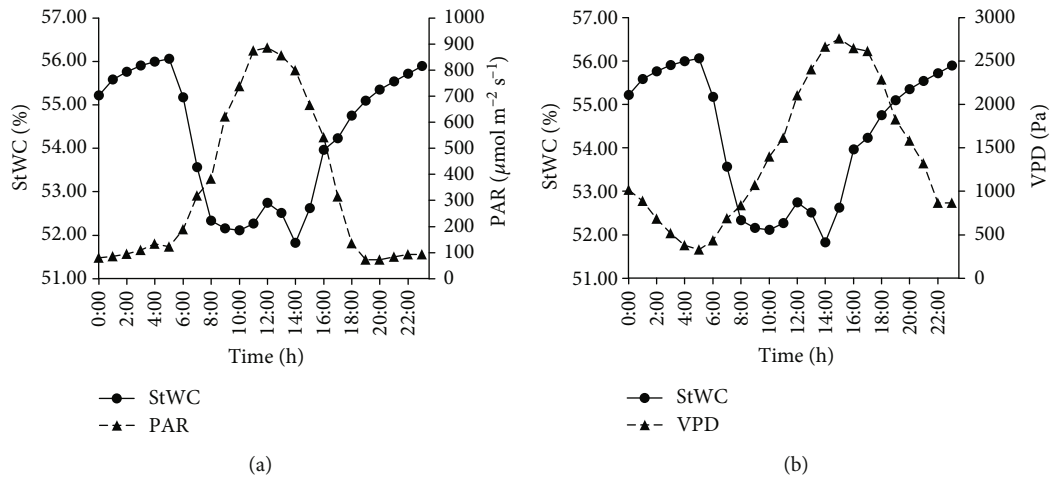


FIGURE 2: Diurnal variation rule between StWC and environmental parameters including PAR (a) and VPD (b) under unstressed conditions on a typical day in summer.

The correlations between StWC and physiological parameters were synchronously analyzed in the same case (Table 2). Correlation analysis suggests that Pn, Tr, and Gs

were significantly negatively correlated with StWC and Ci was significantly positively correlated with StWC. Comparing Table 1 with Table 2, it can be concluded that the

TABLE 2: Correlations between StWC and physiological parameters under unstressed conditions on a typical day in summer.

Variables	Physiological parameters			
	Pn	Tr	Gs	Ci
Correlation coefficient	-0.8402	-0.8374	-0.8535	0.9457
Significance probability	0.0003	0.0004	0.0002	0.0000
Sample size	13	13	13	13

Pn: net photosynthetic rate; Tr: transpiration rate; Gs: stomatal conductance; Ci: intercellular CO₂ concentration.

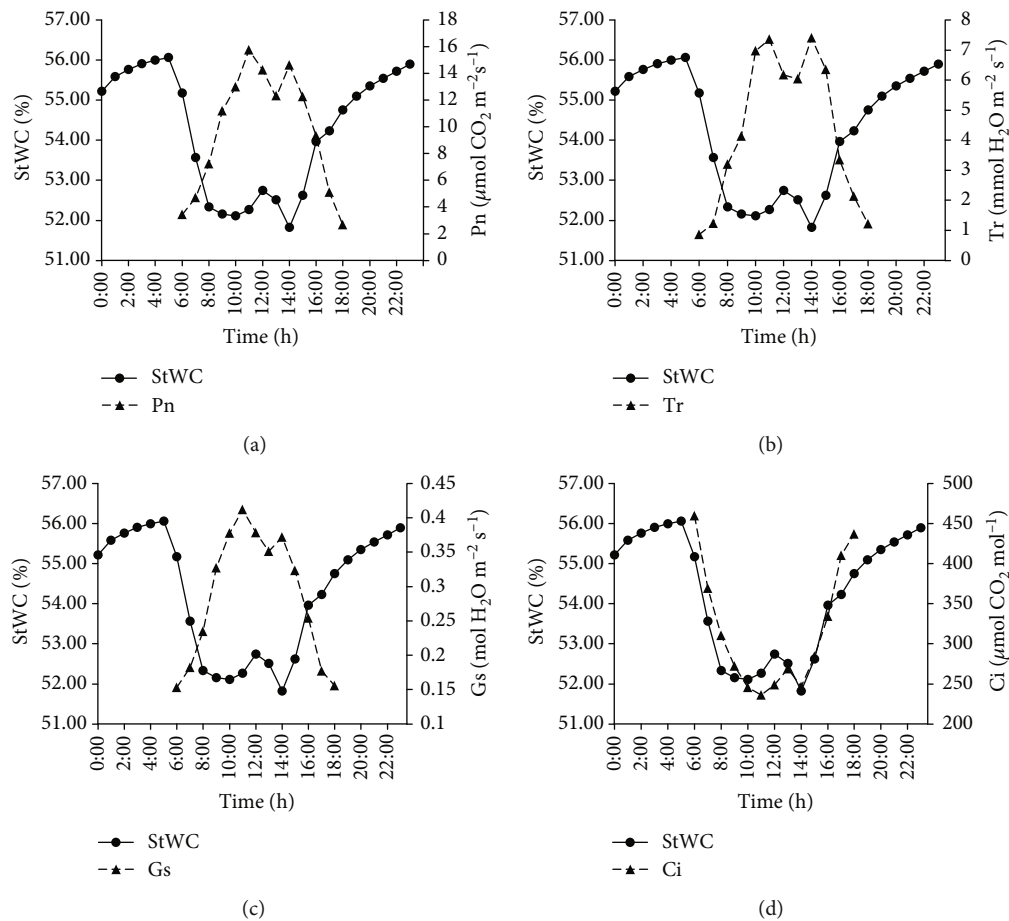


FIGURE 3: Diurnal variation rule between StWC and environmental parameters including Pn (a), Tr (b), Gs (c), and Ci (d) under unstressed conditions on a typical day in summer.

correlation coefficients between StWC and physiological parameters were generally greater than that between StWC and environmental parameters. The reason for the difference may be that the physiological parameters directly affect StWC, but the environmental parameters indirectly affect StWC by changing the physiological parameters [27, 28]. In addition, we further analyzed the diurnal variation rule between StWC and the four physiological parameters (Figure 3). Comparing Figure 2 with Figure 3, the diurnal variation rule between StWC and physiological parameters excluding Ci was similar with that between StWC and environmental parameters. And there was an obvious midday

depression of Pn and Gs, thus resulting in the rise of Ci and the fall of Tr, respectively [29, 30]. Therefore, the StWC also increased at midday. The Tr decreased from 11:00 to 13:00, during which time water loss rate by leaf transpiration was smaller than water absorption rate by root, thus resulting in the rise of StWC from 10:00 to 12:00. The Tr increased from 13:00 to 14:00, during which time water loss rate by leaf transpiration was greater than water absorption rate by root, thus resulting in the fall of StWC from 12:00 to 14:00. And the change of StWC was ahead of the change of Tr about an hour. Based on the above analysis, the conclusion can be drawn that StWC

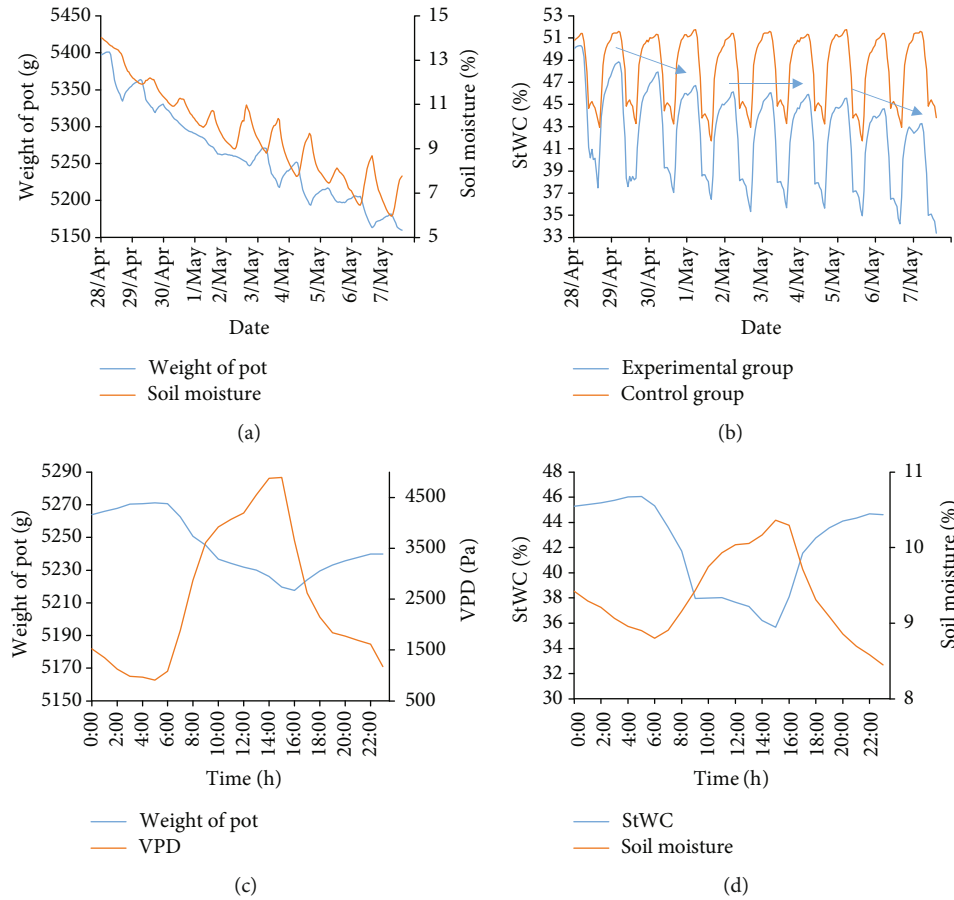


FIGURE 4: Response of StWC to drought stress. (a) Periodic variation rule between weight of pot and soil moisture in the experimental group. (b) Periodic variation rule of StWC in the experimental and control groups. (c) Diurnal variation rule between weight of pot and VPD in the experimental group on May 3. (d) Diurnal variation rule between StWC and soil moisture in the experimental group on May 3.

can characterize the environmental and physiological information to some extent.

3.2. Response of StWC to Drought Stress. The response of StWC to drought stress is shown in Figure 4. From an overall perspective, the weight of pot and soil moisture continuously declined throughout the period of drought stress (Figure 4(a)). As shown in Figure 4(b), the diurnal mean StWC of the tree in the control group with adequate irrigation was steady and the diurnal mean StWC of the tree in the experimental group without irrigation showed diversity which can be divided into three stages. In the start stage of drought stress (from April 28 to May 1), the water potential of the tree was higher than that of the soil and then the water content of the tree would decrease, resulting in the reduction of the diurnal mean StWC. In the middle stage of drought stress (from May 2 to May 4), as the drought stress became severe (soil moisture less than 11%), the water potential of the tree would equilibrate with that of the soil by accumulation of solutes and cell wall hardening [10], resulting in the stabilization of the diurnal mean StWC (approx. 42%). The length of stable time was dependent on the drought resistance of crape myrtle. In the end stage of drought stress (from

May 5 to May 7), as the drought stress became more severe (soil moisture less than 9%), the balance of water potential between tree and soil was destroyed, resulting the further decline of the diurnal mean StWC. When plants are in the end stage of drought stress, some morphological and biochemical responses of plants will cause negative effects on plants [31]. In terms of morphological response, drought stress can cause impaired mitosis, cell elongation, and expansion resulting in reduced growth and yield traits [32, 33]. In terms of biochemical response, drought stress can cause the increase of ROS level resulting in oxidative damage to proteins, DNA, and lipids [9]. Hence, in order to reduce the damages for plants, the diurnal mean StWC in the middle stage of drought stress can be regarded as the critical threshold of irrigation.

In this experiment, some interesting phenomena were observed. As shown in Figure 4(a), the weight of pot showed a downward fluctuation trend. Compared with the period from April 30 to May 2, the weight of pot changed more significantly between May 3 and May 4. As shown in Figure 4(c), the weight of the pot appeared to have an obvious increase (approx. 29 g) at night. This phenomenon may be caused by two factors. One factor was that the VPD is usually

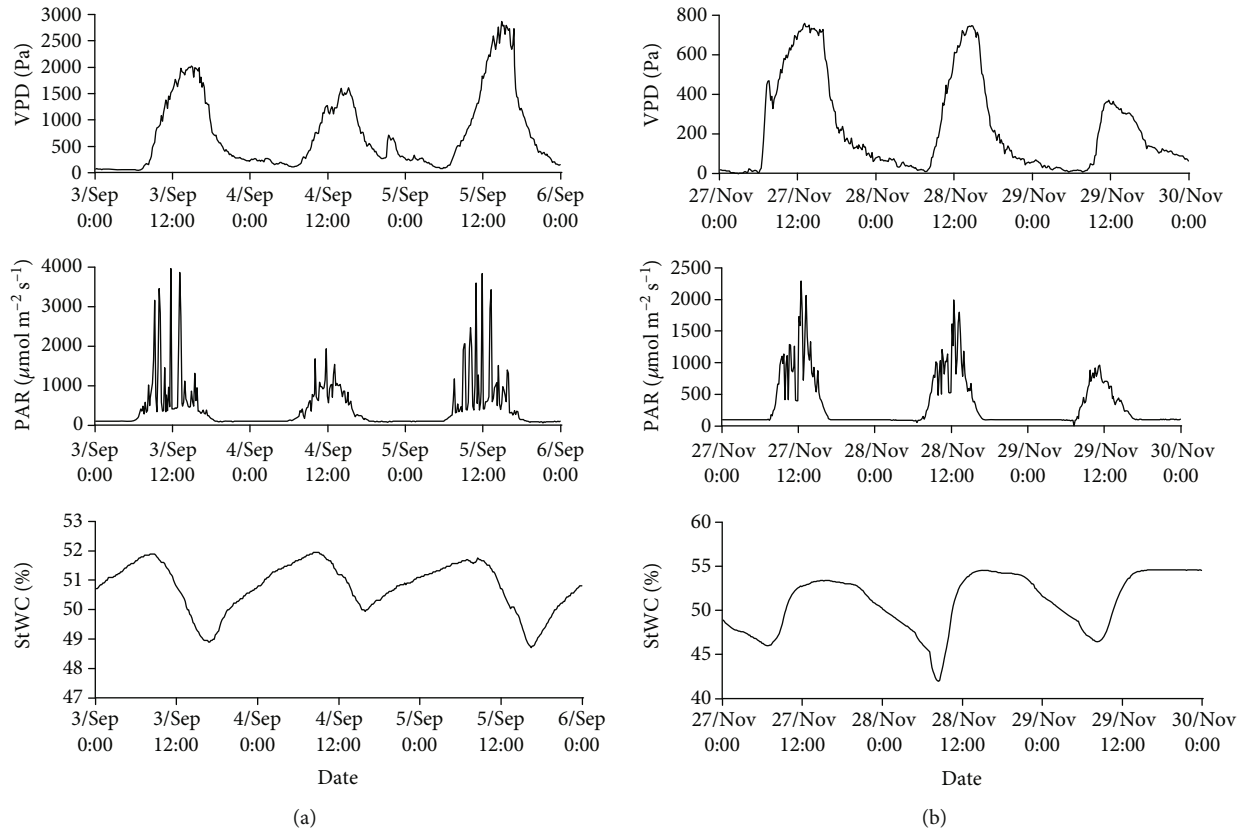


FIGURE 5: Responses of VPD, PAR, and StWC to temperature stress. (a) Periodic variation rules of VPD, PAR, and StWC in warm weather. (b) Periodic variation rules of VPD, PAR, and StWC in cold weather.

very low in the greenhouse at night resulting in the formation of condensation water on leaves [34]. The other factor was that the transpiration of plants is usually extremely weak at night and the growth rate of plants at night is faster than that in the daytime resulting in the accumulation of biomass [35]. Meanwhile, as shown in Figure 4(d), the soil moisture in pot appeared to have a slight increase (approx. 1.6%) during the daytime. This phenomenon may be caused by strong transpiration resulting in the increase of soil moisture near the roots where the 5TM sensor was placed [36].

3.3. Response of StWC to Cold Stress. The responses of VPD, PAR, and StWC to temperature stress are shown in Figure 5. As shown in Figure 5(a), in warm weather with high VPD and PAR, StWC gradually increased at night and decreased during the daytime. As shown in Figure 5(b), in cold weather with low VPD and PAR, StWC gradually decreased at night and increased during the daytime. Therefore, it can be concluded that the StWC showed opposite diurnal variation rules in warm and cold weather, respectively. In addition, the mean diurnal range of StWC in cold weather (approx. 9.4%) was significantly larger than that in warm weather (approx. 2.7%). In order to further analyze the response of StWC to cold stress, the periodic variation rule between StWC and air temperature in cold weather is shown in Figure 6. When the air temperature fell below 0°C at night, the StWC slowly decreased. When the air temperature rose

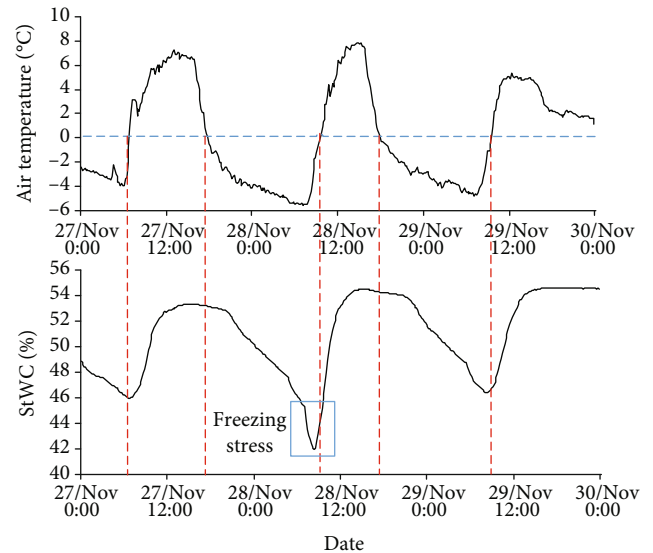


FIGURE 6: Periodic variation rule between StWC and air temperature in cold weather.

above 0°C during the daytime, the StWC gradually increased. Considering that chilling stress can restrict root water uptake by decreasing the VPD [37] and increasing the viscosity of soil moisture [38], then it caused the slow decrease of the

StWC. Hence, the conclusion can be drawn that the plant may suffer from chilling stress when the air temperature is lower than 0°C . When the air temperature fell below -5°C on November 28, the StWC sharply decrease by 5.5% in 210 minutes. When the air temperature rose above -5°C on November 28, the StWC sharply increased by 9.8% in 160 minutes. Considering that freezing stress can induce the formation of ice in the large vessels of the xylem in stems [11], then it caused the sharp decrease of the StWC. Therefore, it can be concluded that the plant may suffer from freezing stress when the air temperature is lower than -5°C . Based on the above analysis, we can conclude that cold stress can weaken the water regulation ability of plants and then result in the larger diurnal fluctuation of StWC.

3.4. Response of StWC to Disease Stress. The StWC changing curves of crape myrtle with different health levels during the period of germination are shown in Figure 7. In the long term, the diurnal mean StWC of healthy and mild disease tree decreased firstly then increased. However, the diurnal mean StWC of severe disease tree decreased all the time. Considering that the better understanding of the effects of disease on StWC can contribute to the early diagnosis of the disease, we further analyzed the diurnal variation rule of StWC under disease stress. The diurnal minimum value, maximum value, mean value, and range value of StWC were selected as feature parameters which were used to represent the diurnal variation rule of StWC. The means and standard deviations of the four feature parameters among different health level groups on June 1 are shown in Figure 8. The health level of the groups, in descending order, was healthy group > mild disease group > severe disease group. The diurnal minimum value, maximum value and mean value of StWC showed a positive correlation with the health level of the group and the diurnal range value of StWC showed a negative correlation with the health level of the group. Meanwhile, the effects of disease on the four feature parameters were tested using one-way ANOVA analysis. As can be seen from Table 3, the four feature parameters differed significantly ($p < 0.001$) among different health level groups, indicating that the health status of the tree can be diagnosed by analyzing the four feature parameters. The effects of disease on StWC also can be interpreted based on plant physiology. The cankers caused by disease can induce the formation of tyloses which can cause the reduced hydraulic conductivity, xylem function [39], and water transport [40] in affected stems, ultimately resulting in the decrease of diurnal mean value of StWC and the increase of diurnal range value of StWC.

4. Conclusions

In this study, the novel SWR sensor was used to monitor the StWC of crape myrtle trees. The responses of StWC to environmental and physiological parameters, drought, cold, and disease stress were analyzed, respectively. In the meantime, the effects of the three types of stress on StWC were interpreted based on related mechanisms. The results proved that the StWC was simultaneously affected by both environmen-

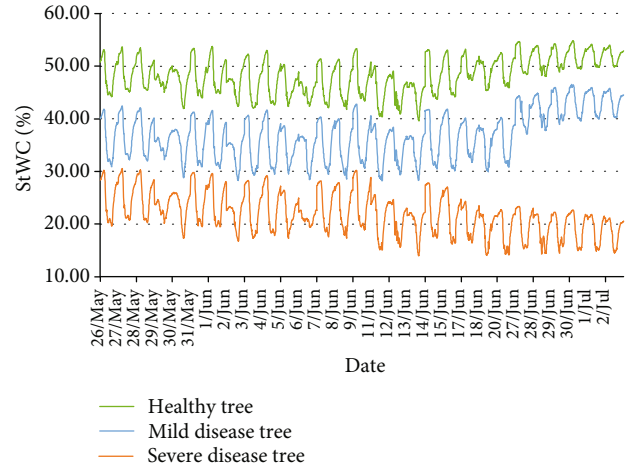


FIGURE 7: StWC changing curves of crape myrtle with different health levels during the period of germination.

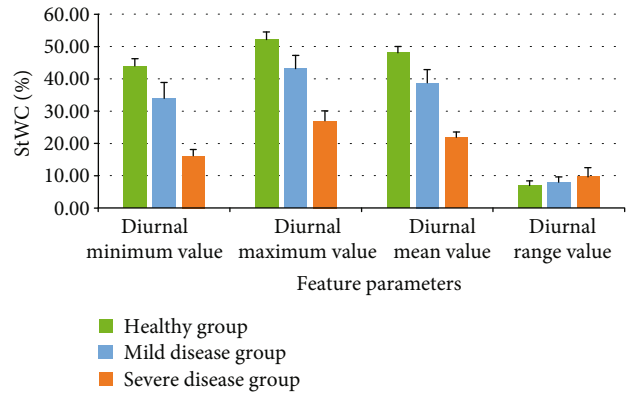


FIGURE 8: The means and standard deviations of four feature parameters among different groups on June 1.

tal parameters determined by stress degree and physiological parameters. To some extent, both were coupled with each other and difficult to separate. Therefore, it was difficult to quantitatively evaluate the effects of drought, cold, and disease stress on StWC. But the StWC still can be used as a qualitative evaluation index of the degree of the three types of stress.

- (1) In the start and end stage of drought stress, there was a negative correlation between the diurnal mean of StWC and the degree of drought stress. In the middle stage, the diurnal mean of StWC remained stable for a period of time; the length of which can characterize the drought resistance of plants
- (2) In the case of cold stress, the StWC showed opposite diurnal variation rules in warm and cold weather, respectively. There was a positive correlation between the diurnal range of StWC and the degree of cold stress. The decline rate of StWC under chilling stress was significantly less than that under freezing stress

TABLE 3: Tests for disease effects on four feature parameters using one-way ANOVA analysis.

Feature parameters	Source	Sum of squares	Df	Mean square	F	Sig.
Diurnal minimum StWC	Between groups	0.953	2	0.476	421.562	<0.001
	Within groups	0.078	69	0.001		
Diurnal maximum StWC	Between groups	0.778	2	0.389	368.243	<0.001
	Within groups	0.073	69	0.001		
Diurnal mean StWC	Between groups	0.842	2	0.421	534.468	<0.001
	Within groups	0.054	69	0.001		
Diurnal range StWC	Between groups	0.009	2	0.004	10.350	<0.001
	Within groups	0.029	69	<0.001		

- (3) In the case of disease stress, the diurnal minimum, maximum, and mean of StWC showed a positive correlation with the health level of plants and the diurnal range of StWC showed a negative correlation with the health level of plants

Data Availability

The data used to support the findings of this study are available from the corresponding author upon request.

Conflicts of Interest

The authors declare that they have no conflicts of interest.

Authors' Contributions

For this research article, Chao Gao and Yandong Zhao conceived and designed the experiments. Chao Gao performed the experiments. Chao Gao and Yue Zhao analyzed the data. Chao Gao, Yue Zhao, and Yandong Zhao wrote the paper.

Acknowledgments

This research was funded by the Research Foundation for Youth Scholars of Beijing Technology and Business University (Grant No. QNJ2020-23), the National Key Research and Development Program of China (Grant No. 2017YFD0600901), the Beijing Municipal Science and Technology Commission (Grant No. Z161100000916012), and the Special Fund for Beijing Common Construction Project.


References

- [1] C. A. Jaleel, P. Manivannan, A. Wahid et al., "Drought stress in plants: a review on morphological characteristics and pigments composition," *International Journal of Agriculture and Biology*, vol. 11, no. 1, pp. 100–105, 2009.
- [2] R. M. Augé, "Water relations, drought and vesicular-arbuscular mycorrhizal symbiosis," *Mycorrhiza*, vol. 11, no. 1, pp. 3–43, 2001.
- [3] J. S. Sperry, Y. Wang, B. T. Wolfe et al., "Pragmatic hydraulic theory predicts stomatal responses to climatic water deficits," *New Phytologist*, vol. 212, no. 3, pp. 577–589, 2016.
- [4] J. Zhang, H. T. Nguyen, and A. Blum, "Genetic analysis of osmotic adjustment in crop plants," *Journal of Experimental Botany*, vol. 50, no. 332, pp. 291–302, 1999.
- [5] M. P. Apse and E. Blumwald, "Engineering salt tolerance in plants," *Current Opinion in Biotechnology*, vol. 13, no. 2, pp. 146–150, 2002.
- [6] R. Murphy and J. K. E. Ortega, "A new pressure probe method to determine the average volumetric elastic modulus of cells in plant tissue," *Plant Physiology*, vol. 107, no. 3, pp. 995–1005, 1995.
- [7] T. J. Close, "Dehydrins: a commonality in the response of plants to dehydration and low temperature," *Physiologia Plantarum*, vol. 100, no. 2, pp. 291–296, 1997.
- [8] D. K. Hincha and M. Hagemann, "Stabilization of model membranes during drying by compatible solutes involved in the stress tolerance of plants and microorganisms," *Biochemical Journal*, vol. 383, no. 2, pp. 277–283, 2004.
- [9] K. Apel and H. Hirt, "Reactive oxygen species: metabolism, oxidative stress, and signal transduction," *Annual Review of Plant Biology*, vol. 55, pp. 373–399, 2004.
- [10] P. E. Verslues, M. Agarwal, S. Katiyar-Agarwal, J. Zhu, and J. K. Zhu, "Methods and concepts in quantifying resistance to drought, salt and freezing, abiotic stresses that affect plant water status," *The Plant Journal*, vol. 45, no. 4, pp. 523–539, 2006.
- [11] N. S. Arias, F. G. Scholz, G. Goldstein, and S. J. Bucci, "The cost of avoiding freezing in stems: trade-off between xylem resistance to cavitation and supercooling capacity in woody plants," *Tree Physiology*, vol. 37, no. 9, pp. 1251–1262, 2017.
- [12] R. S. Pearce, "Extracellular ice and cell shape in frost-stressed cereal leaves: a low-temperature scanning-electron-microscopy study," *Planta*, vol. 175, no. 3, pp. 313–324, 1988.
- [13] R. S. Pearce and E. N. Ashworth, "Cell shape and localisation of ice in leaves of overwintering wheat during frost stress in the field," *Planta*, vol. 188, no. 3, pp. 324–331, 1992.
- [14] R. S. Pearce, "Plant freezing and damage," *Annals of Botany*, vol. 87, no. 4, pp. 417–424, 2001.
- [15] S. Sankaran, A. Mishra, R. Ehsani, and C. Davis, "A review of advanced techniques for detecting plant diseases," *Computers and Electronics in Agriculture*, vol. 72, no. 1, pp. 1–13, 2010.
- [16] J. Urban and M. Dvořák, "Sap flow-based quantitative indication of progression of Dutch elm disease after inoculation with *Ophiostoma novo-ulmi*," *Trees*, vol. 28, no. 6, pp. 1599–1605, 2014.

- [17] B. R. Roberts and L. R. Schreiber, "Influence of Dutch elm disease on resistance to water flow through roots of American elm," *Phytopathology*, vol. 77, no. 1, pp. 56–59, 1977.
- [18] J. L. Parke, E. Oh, S. Voelker, E. M. Hansen, G. Buckles, and B. Lachenbruch, "Phytophthora ramorum colonizes tanoak xylem and is associated with reduced stem water transport," *Phytopathology*, vol. 97, no. 12, pp. 1558–1567, 2007.
- [19] B. R. Collins, J. L. Parke, B. Lachenbruch, and E. M. Hansen, "The effects of Phytophthora ramorum infection on hydraulic conductivity and tylosis formation in tanoak sapwood," *Canadian Journal of Forest Research*, vol. 39, no. 9, pp. 1766–1776, 2009.
- [20] J. H. Park, J. Juzwik, and J. Cavender-Bares, "Multiple Ceratocystis smalleyi infections associated with reduced stem water transport in bitternut hickory," *Phytopathology*, vol. 103, no. 6, pp. 565–574, 2013.
- [21] R. C. Ploetz, B. Schaffer, A. I. Vargas, J. L. Konkol, J. Salvatierra, and R. Wideman, "Impact of laurel wilt, caused by Raffaelea lauricola, on leaf gas exchange and xylem sap flow in avocado, Persea americana," *Phytopathology*, vol. 105, no. 4, pp. 433–440, 2015.
- [22] A. Stöhr and R. Lösch, "Xylem sap flow and drought stress of Fraxinus excelsior saplings," *Tree Physiology*, vol. 24, no. 2, pp. 169–180, 2004.
- [23] C. Gao, Y. Zhao, and Y. Zhao, "A Novel Sensor for Noninvasive Detection of In Situ Stem Water Content Based on Standing Wave Ratio," *Journal of Sensors*, vol. 2019, Article ID 3594964, 10 pages, 2019.
- [24] J. A. Goff, "Saturation pressure of water on the new kelvin temperature scale," in *Proc. Semi-annual Meeting of the American Society of Heating and Ventilating Engineers*, pp. 347–354, American Society of Heating and Ventilating Engineers, Murray Bay, QC, Canada, 1957.
- [25] P. J. Kramer, "The relation between rate of transpiration and rate of absorption of water in plants," *American Journal of Botany*, vol. 24, no. 1, pp. 10–15, 1937.
- [26] M. J. Aston and D. W. Lawlor, "The relationship between transpiration, root water uptake, and leaf water potential," *Journal of Experimental Botany*, vol. 30, no. 1, pp. 169–181, 1979.
- [27] D. A. Grantz, D. Zinsmeister, and J. Burkhardt, "Ambient aerosol increases minimum leaf conductance and alters the aperture–flux relationship as stomata respond to vapor pressure deficit (VPD)," *New Phytologist*, vol. 219, no. 1, pp. 275–286, 2018.
- [28] R. Terada, Y. Watanabe, M. Fujimoto, I. Tatamidani, S. Kokubu, and G. N. Nishihara, "The effect of PAR and temperature on the photosynthetic performance of a freshwater red alga, Thorea gaudichaudii (Thoreales) from Kagoshima, Japan," *Journal of Applied Phycology*, vol. 28, no. 2, pp. 1255–1263, 2016.
- [29] G. Ren, X. Liu, and Y. Shi, "Effects of Plant Growth Regulator S-Y on Diurnal Changes in Photosynthetic Parameters and Yield of Stevia Rebaudina Bertoni," *Energy Procedia*, vol. 5, pp. 429–434, 2011.
- [30] L. V. Chengguo, M. Lei, and S. Yan, "Study on the diurnal changes of net photosynthetic rate and the impact factors of Stevia rebaudiana Bertoni in autumn," *American Journal of Plant Physiology*, vol. 4, no. 1, pp. 18–23, 2009.
- [31] S. A. Anjum, X. Y. Xie, L. C. Wang, M. F. Saleem, C. Man, and W. Lei, "Morphological, physiological and biochemical responses of plants to drought stress," *African Journal of Agricultural Research*, vol. 6, no. 9, pp. 2026–2032, 2011.
- [32] H. Nonami, "Plant water relations and control of cell elongation at low water potentials," *Journal of Plant Research*, vol. 111, no. 3, pp. 373–382, 1998.
- [33] M. Hussain, M. A. Malik, M. Farooq, M. Y. Ashraf, and M. A. Cheema, "Improving drought tolerance by exogenous application of glycinebetaine and salicylic acid in sunflower," *Journal of Agronomy and Crop Science*, vol. 194, no. 3, pp. 193–199, 2008.
- [34] D. Piscia, J. I. Montero, E. Baeza, and B. J. Bailey, "A CFD greenhouse night-time condensation model," *Biosystems Engineering*, vol. 111, no. 2, pp. 141–154, 2012.
- [35] A. Graf, A. Schlereth, M. Stitt, and A. M. Smith, "Circadian control of carbohydrate availability for growth in Arabidopsis plants at night," *Proceedings of the National Academy of Sciences*, vol. 107, no. 20, pp. 9458–9463, 2010.
- [36] H. J. Tromp-van Meerveld and J. J. McDonnell, "On the interrelations between topography, soil depth, soil moisture, transpiration rates and species distribution at the hillslope scale," *Advances in Water Resources*, vol. 29, no. 2, pp. 293–310, 2006.
- [37] R. Aroca, "Involvement of abscisic acid in leaf and root of maize (Zea mays L.) in avoiding chilling-induced water stress," *Plant Science*, vol. 165, no. 3, pp. 671–679, 2003.
- [38] A. J. Bloom, M. A. Zwieniecki, J. B. Passioura, L. B. Randall, N. M. Holbrook, and D. A. St Clair, "Water relations under root chilling in a sensitive and tolerant tomato species," *Plant, Cell and Environment*, vol. 27, no. 8, pp. 971–979, 2004.
- [39] S. A. Inch and R. C. Ploetz, "Impact of laurel wilt, caused by Raffaelea lauricola, on xylem function in avocado, Persea americana," *Forest Pathology*, vol. 42, no. 3, pp. 239–245, 2012.
- [40] T. Kirisits and I. Offenthaler, "Xylem sap flow of Norway spruce after inoculation with the blue-stain fungus Ceratocystis polonica," *Plant Pathology*, vol. 51, no. 3, pp. 359–364, 2002.

Research Article

***Leymus chinensis* Tolerates Mowing Disturbance by Maintaining Photosynthesis in Saline-Alkali Heterogeneous Habitats**

Nan Lu,¹ Luhao Qu,¹ Jun Liu ,^{1,2} Jiyun Yang,¹ Long Bai,¹ Yue Huang,³ and Yanchun Zhou²

¹College of Horticulture, Shenyang Agricultural University, Shenyang 110866, China

²Institute of Grassland and Ecology Sciences of Jilin Academy of Agricultural Sciences, Changchun 130033, China

³Key Laboratory of Forest Ecology and Management, Institute of Applied Ecology, Chinese Academy of Sciences, Shenyang 110016, China

Correspondence should be addressed to Jun Liu; liuj@syau.edu.cn

Received 17 November 2019; Accepted 23 December 2019; Published 4 February 2020

Guest Editor: Zhenxing Zhang

Copyright © 2020 Nan Lu et al. This is an open access article distributed under the Creative Commons Attribution License, which permits unrestricted use, distribution, and reproduction in any medium, provided the original work is properly cited.

Leymus chinensis is a perennial rhizomatous clonal plant with strong tolerance to mowing, grazing, drought, and salt-alkali. However, with patchy soil environment, how mowing affect the photosynthesis of *L. chinensis* in heterogeneous patches is largely unknown. In this experiment, we tested the effects of mowing intensity (0, 35%, and 70% removal of aboveground biomass) on plant photosynthesis under different heterogeneous patches with different saline-alkali soil. We found that moderate concentrations of salt-alkali under heterogeneous patches have no significant effect on the photosynthesis of *L. chinensis*. Moderate mowing can maintain photosynthesis under no heterogeneity soil and moderate salt-alkali patch condition. In addition, heavy mowing and high salt-alkali soil under heterogeneous patches both inhibited net photosynthetic rate (P_N) and transpiration rate (E), reduced leaf area, and plant height. *L. chinensis* responded to extreme soil conditions and strong disturbance by increasing water-use efficiency (WUE), reducing relative water content (RWC), and changing stomatal conductance (Gsw). Therefore, our results imply that moderate grazing or mowing can be used to maintain the productivity and economic benefits of grassland when the soil heterogeneous patches with moderate saline-alkali conditions.

1. Instruction

Salinization and alkalization of soil is a major environmental problem worldwide [1–3]. Soil salinization represents an increasing environmental problem [4], and the salinities are heterogeneously distributed in natural habitats. There are about 932 million hectares of saline-alkalized land in the world, and about 10×10^6 hm² of irrigated farmland is abandoned every year [5]. There are many reasons for the formation of saline-alkalized land in the natural environment. In addition to the natural environmental factors, the formation of saline-alkali land has human causes [6, 7] and mainly refers to the overuse of grassland resources among them. In the Songnen Plain of Northeast China, about 70% of the natural grassland has been seriously degraded due to soil salinization and alkalization, and this trend is still increasing [8, 9].

It is generally considered that saline-alkali stress inhibits plant growth by water deficiency or ion toxicity, high concentrations of salts in the soil make it harder for roots to extract water, and high concentrations of salts within the plant can be toxic [4]. But in salt-tolerant species (e.g., *L. chinensis*), plant growth is only moderately inhibited, or even stimulated at certain levels of salinity [10]. Tolerance to osmotic stress is a feature of most clonal plants; it has been suggested to be perceived partly by stretch-activated channels. The integration by clonal plant may cause a reduction in leaf area and a development in clonal growth, which allows plant to conserve soil moisture and prevent an escalation in the salt concentration in the soil [4]. Early studies demonstrated that cloned plants have the ability to modify their morphology in response to habitat heterogeneity habitat which is one kind of phenotypic plasticity [11, 12]. The morphological plasticity

of *L. chinensis* simultaneously occurs at above- and below-ground; these responses to stimuli most in a way by compensatory growth or shoot and root biomass allocation. In addition, saline-alkali stress also affects the physiological characteristics of plants.

Saline-alkali stress affects every stage of plant growth and development [13]. It can also slow down the growth rate of plant, reduce individual size, decrease leaf area, and decrease root activity and yellowing leaves, resulting in the reduction of biomass accumulation and other physiological characteristics [14]. Photosynthesis of plants is sensitive to salinity and alkali stress and can be used as one of the important indicators of plant response to stress [15]. The photosynthesis of tomato seedlings was inhibited by salt-alkali stress [16]. The net photosynthetic rate and stomatal conductance of barley were also inhibited under salt-alkali stress [17]. But there are many plants having tolerance to saline-alkali. Some studies have shown that clonal plants have high tolerance to adverse habitats (e.g., saline-alkali, low nutrition, and drought) due to the presence of stolon and rhizomes [18–20]. *L. chinensis*, a clonal plant, showed good tolerance to saline-alkali environment [21]. It evades and resists the damage caused by saline-alkali environment by selectively distributing, expanding, and utilizing rhizomes for clonal integration [11, 22]. And low concentration of saline-alkali can also promote the growth of *L. chinensis* [10]. The main challenge to be solved is to unravel the relationship between morphological and physiological characteristics of cloned plants under heterogeneous saline-alkali conditions.

In natural communities, the resource distributions within environment (i.e., light, water, and nutrients) are usually heterogeneous in a spatial and temporal pattern. Previous studies have shown that clonal plants possess a particularly foraging behavior of rhizome or stolon responses to heterogeneity, such as higher proportional allocation of biomass to stolon under low light patches [23], greater production of ramet, and above-ground biomass in the nutrient-rich environment [19]. Plants should maximize benefits and minimize costs subject to certain constraints. The experimental evidences are still lacking to understand the mechanisms of clonal plant adaptability under heterogeneous environment. A number of studies have shown that connections among ramets of clonal plants by rhizome allow transport of photosynthates, water, and nutrients from established genet (parent plant) to developing ramet (daughter plant) [22, 24, 25]. However, the photosynthesis of plant would explain more on the physiological responses.

Moreover, grazing and mowing are the two major ways of grassland utilization [26]. It is generally believed that grazing and mowing have many adverse effects on plant growth by defoliation and indirectly by modifying growth allocation (e.g., enhancing total production, altering relative growth rate, and enhancing tiller compensatory growth due to leaf removal) and resource availability (e.g., altering water uptake and redistribution of nutrients) [23, 27]. With the increase of grazing intensity, in order to better adapt to grazing, plants not only change morphological indicators but also change physiological indicators such as photosynthesis and redistribution of nutrients in plants [28, 29]. Grazing reduces the leaf area of plants, directly affects photosynthesis [30], and even

directly impairs some functions of plants [31]. In addition, grazing can affect the water situation in plants, thus changing the relationship between net photosynthetic rate and water, leading to the decline of net photosynthetic rate [30]. However, many studies have found that moderate grazing and mowing can stimulate plants to produce compensatory growth, thus restoring their lost biomass, and even produce more biomass. In the study of *Festuca arundinacea*, the result suggested that moderate grazing could promote its quality and yield [32]. Similar results were also found in the experiment of cutting *L. chinensis*, under mild and moderate mowing intensities, overcompensatory growth appeared, and aboveground biomass accumulation, relative growth rate, and root tillering were all higher [18]. Particularly under the condition of sufficient resources, both mild and moderate mowing can promote the accumulation of biomass and the growth of buds of *L. chinensis* [24]. Grazing can stimulate plants and compensate them, thus promoting photosynthesis [33, 34]. Photosynthesis affects productivity and is important for grazing and mowing; studies in Hunshandak Sandland showed that moderate grazing intensity promoted photosynthesis [29]. However, some studies have also found that grazing has little effect on plants and no changes in physiological indicators such as photosynthesis [35].

Previous studies on the effects of salinity and grazing on the clone growth and photosynthesis of *L. chinensis* almost have not considered the interaction between these two factors. However, in the salinized grassland, these two kinds of stress exist simultaneously. In addition, most experiments in the field have difficulty distinguishing the growth, expansion, and biomass distribution of belowground roots of rhizome clones, especially in heterogeneous habitats with large numbers of other species. Therefore, we conducted to set pot experiments in greenhouse, to explore the changes of photosynthetic characteristics and resistance mechanism of *L. chinensis* under saline-alkali heterogeneous patches and mowing disturbance.

2. Materials and Methods

2.1. Species and Site Description. The experiment was conducted in a greenhouse located at the Research Station of Shenyang Agricultural University (41°50'N, 123°34'E). The station base belongs to temperate semihumid continental climate with average annual temperature of 8.1°C and average annual precipitation of 721.9 mm. The greenhouse was controlled with natural photoperiod, 42%/69% day/night relative humidity and 26°C/20°C day/night temperature, and an average day/night vapor-pressure deficit of 1.75/0.35 kPa. The total experimental period of this study was 120 days and was conducted from mid-May to the end of September. We chose the clonal plant *L. chinensis*, which seeds were collected from the natural grasslands of the Songnen Plains, as our experimental material. *L. chinensis* is a typical rhizomatous perennial Gramineae clonal plant [20] distributed in the eastern part of the Eurasian steppe, including the northern and eastern parts of the Mongolian People's Republic, the Lake Baikal region of Russia, the North China Plain, the Inner Mongolia Plateau, and the Northeast Plain [36, 37]. It is rich

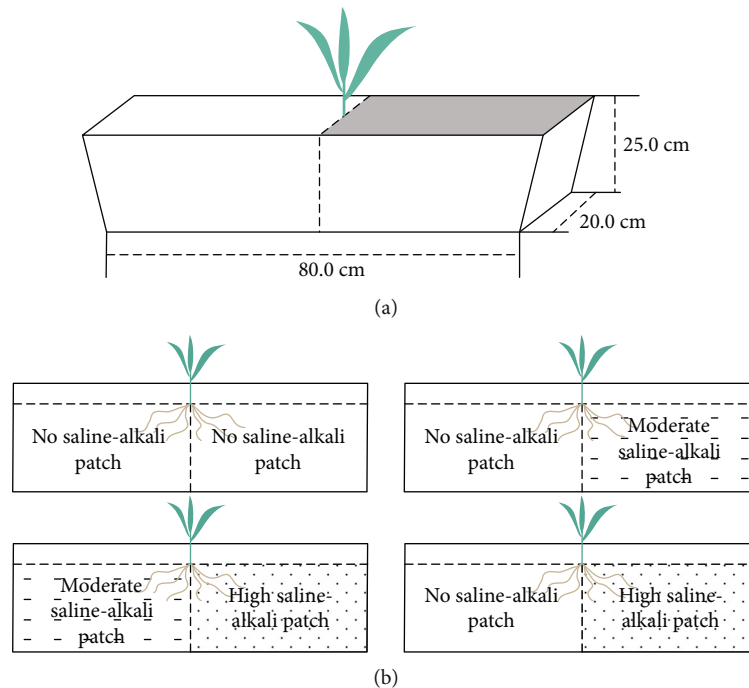


FIGURE 1: The planting configuration of the plants. Each long trough pot has one plant, which is planted in the middle of the pot (directly above the baffle), and the plant roots can grow left and right. Schematic representation of saline-alkali stress treatments given to different patches.

in protein, minerals, and carbohydrates, with strong palatability, drought resistance, cold tolerance, barren tolerance, and high tolerance to saline-alkali soil. It is also resistant to mowing and grazing, commonly known as “alkali grass” in Northeast China [38]. It has strong ecological adaptability and plasticity. As the dominant species in this area, it has great significance for grassland restoration.

2.2. Experimental Design. A 3×4 factorial, completely randomized design was used with three mowing levels and four heterogeneity patches. There were three levels of mowing treatment: no mowing (NM), moderate mowing (MM) which was 35% of aboveground biomass harvested, and heavy mowing (HM) which was 70% of aboveground biomass harvested. Four heterogeneity patches was conducted with sand as culture medium and long trough pot (80 cm length \times 20 cm width \times 25 cm depth), as shown in Figure 1(a), these containers were used to ensure that the clonal growth of *L. chinensis* individuals was not limited by the size of the pot, and the new ramets can find enough space to establish and grow. A baffle retaining was placed into the center of each trough pot to blocking the lower 2/3 of a culture medium layer, and remaining the super 1/3 to allowing the plants root system grow. Therefore, the install baffle of each long trough pot divided the container into two patches. Similar or different concentrations of saline-alkali solution were added into both patches of one same pot to simulate homogeneous or heterogeneous soil saline-alkali habitats. There are four combinations of soil saline-alkali heterogeneity patches: nonheterogeneity (no saline-alkali on both patches, recorded as NS-NS), heterogeneity (no saline-alkali and moderate saline-alkali patches, recorded as NS-MS;

moderate saline-alkali and high saline-alkali patches, recorded as MS-HS; no saline-alkali and high saline-alkali patches, recorded as NS-HS), such as Figure 1(b). Saline-alkali stress was realized by using different concentrations of compound saline-alkali solution with varying salinity and pH, which was set as three gradients: non-saline-alkali (NS), moderate saline-alkali (MS), and high saline-alkali (HS). Two neutral salts (NaCl and Na_2SO_4) and two alkaline salts (NaHCO_3 and Na_2CO_3) were selected based on the salt components in the extent saline-alkali soil of northeast China [10]. The medium concentration of moderate saline-alkali was 100 mmol/L, the high concentration of saline-alkali was 200 mmol/L, and the ratios of four salts were $\text{NaCl}:\text{Na}_2\text{SO}_4:\text{NaHCO}_3:\text{Na}_2\text{CO}_3 = 1:1:1:1$ [1, 10].

At the beginning of the experiment, *L. chinensis* seeds were germinated in seedling trays for four weeks. At about 30-day age, each long trough pot was transplanted with one *L. chinensis* seedling, which was placed into the middle of the pot directly perpendicular above the baffle. By this design, the root system of plant could grow random direction of the long pot. The saline-alkali solution and nutrient liquid were added into culture medium from the either side edges of each long trough to ensure the solution not confused. There are total 36 long troughs with 12 treatments, 3 replications for each treatment. Saline-alkali and mowing treatments were carried out at intervals of 30 days. Indicators were measured and sampled at 20 days after treatment. Total three times of mowing and saline-alkali additions were implemented from June to August in 2019. A total of about 29.286 g and 58.572 g solid salt mixture were added into each moderate and high salt-alkaline patch, respectively. Water availability was controlled by the water capacity test (Moisture

TABLE 1: Statistical summary of two-way ANOVA evaluating the effects of salt-alkali heterogeneity of soil and clipping their combined effects on the net photosynthetic rate (P_N), intercellular CO_2 concentration (C_i), ambient CO_2 concentration (C_a), intercellular CO_2 /ambient CO_2 (C_i/C_a), stomatal conductance (G_{sw}), and stomatal limitation (LS) of *L. chinensis*. Values are F ratios and their significance for effects.

Treatment	df	P_N ($\mu\text{mol m}^{-2} \text{s}^{-1}$)		C_i/C_a		C_i ($\mu\text{mol mol}^{-1}$)		C_a ($\mu\text{mol l}^{-1}$)		G_{sw} ($\text{mol m}^{-2} \text{s}^{-1}$)		LS (%)	
		F		F		F		F		F		F	
		P		P		P		P		P		P	
Mowing (M)	2	14.867	<0.001**	1.871	0.176	4.903	0.016*	24.934	<0.001**	0.389	0.682	1.871	0.176
Saline-alkali heterogeneity (S)	7	3.262	0.039*	2.638	0.073	1.360	0.279	10.321	<0.001**	4.104	0.017*	2.638	0.073
S×M	14	5.709	0.001**	4.664	0.003**	6.173	0.001**	6.679	<0.001**	1.893	0.123	4.664	0.003**

F values and significance levels (** $P < 0.01$; * $P < 0.05$) are given.

Meter type HH2, Delta-T Devices Ltd., UK) of trays every 2 days and by adding tap water until a prefixed sand water content was reached (75% of field capacity for well-watered). During the experiment, all pots received adequate fertilized of Hoagland's nutrient solution once a week. The experiment was started on May 5, 2019, and harvested on September 25, 2019.

2.3. Measurements and Calculations. The individual height of each genet plant and daughter plants was measured every week and was averaged for each pot. The clipped biomasses after each time of mowing treatment as well as the final living biomass were collected and oven-dried at first 1 h at 105°C and then 65°C for 48 h to determine the accumulated aboveground biomass. The leaf area was measured by a portable laser leaf area meter (CI-202, USA). Leaf mass per area (LMA) was calculated as leaf biomass/leaf area.

2.4. Leaf Relative Water Content. Weigh the fresh leaves (about 0.1 g) to obtain the fresh weight (FW), then immerse the leaves in distilled water, put them under 4°C , stay overnight in the dark, weigh their apparent turgid fresh weight (TW) the next day, and finally put them in the oven, dry them to constant weight at 65°C , and weigh their dry weight (DW). The relative water content (RWC) of leaves is $\text{RWC} = [(FW - DW)/(TW - DW)] \times 100\%$.

2.5. Leaf Gas Exchange. Photosynthesis-related indexes were measured from 8:00 to 11:00 in a clear morning, included the net photosynthetic rate (P_N), intercellular CO_2 concentration (C_i), ambient CO_2 concentration (C_a), intercellular CO_2 /ambient CO_2 (C_i/C_a), stomatal conductance (G_{sw}), transpiration rate (E), water-use efficiency (WUE), and stomatal limitation (LS), by a portable photosynthesis system (LI-6800, USA).

2.6. Plant Height. After 20 days of the third treatment, 3 pots were randomly selected for each treatment, and 5 *L. chinensis* plants for each pot were randomly selected for plant height determination.

2.7. Statistical Analysis. For plant photosynthesis, variables performed two-way ANOVA to evaluate the effects of mowing, saline-alkali, and their interaction. Data were further analyzed within each factor when the interaction was not significant. *Post hoc* tests (Tukey's HSD test) were performed to

compare the means between clipping treatments at each saline-alkali intensity levels. All statistical analyses were performed using the SPSS statistical package.

3. Result

3.1. Gas Exchange. The net photosynthetic rate (P_N) was significantly affected by mowing and soil saline-alkali heterogeneity and their interaction ($P < 0.05$, Table 1). Without mowing, the heterogeneity patches of different soil saline-alkali concentrations had no significant effect on P_N . Under moderate mowing treatment, P_N were significantly decreased in MS-HS and NS-HS patches. The P_N of *L. chinensis* with heavy mowing showed a similar pattern as no mowing (Figure 2(a)).

The intercellular carbon dioxide concentration (C_i) was significantly affected by mowing and the interaction between mowing and saline-alkali patches ($P < 0.05$). In NS-NS and NS-MS patches, the C_i was significantly increased with heavy mowing. Furthermore, under heavy mowing, the C_i in NS-HS patches was significantly lower than that of other soil patches (Table 1, Figure 2(b)).

Mowing treatment, soil saline-alkali heterogeneity, and their interaction have significant effects on the concentration of ambient carbon dioxide (C_a) ($P < 0.05$). The C_a in NS-NS and NS-MS was similar as C_i ; it was significantly higher under heavy mowing than moderate and no mowing treatments. However, in NS-HS patches, the C_a was significantly lower only under no mowing condition (Table 1, Figure 2(c)).

The C_i/C_a was only significantly affected by the interaction of soil saline-alkali heterogeneity and mowing ($P < 0.05$, Table 1). In homogeneous environment (NS-NS), heavy mowing was significantly increased C_i/C_a . Under heavy mowing, the C_i/C_a was significantly decreased in NS-HS patches, Figure 2(e). The limiting value of stomata (LS) followed an opposite pattern to the C_i/C_a (Figure 2(f)) and was significantly affected by the interaction of soil saline-alkali heterogeneity and mowing (Table 1). The stomatal conductance (G_{sw}) was only affected by the heterogeneity of soil saline-alkali patches (Table 1) and significantly decreased in NS-HS patches (Figure 2(d)).

3.2. Moisture Change. The soil saline-alkali heterogeneity and the interaction between saline-alkali and mowing had a significant effect on transpiration rate (E) ($P < 0.05$, Table 2).

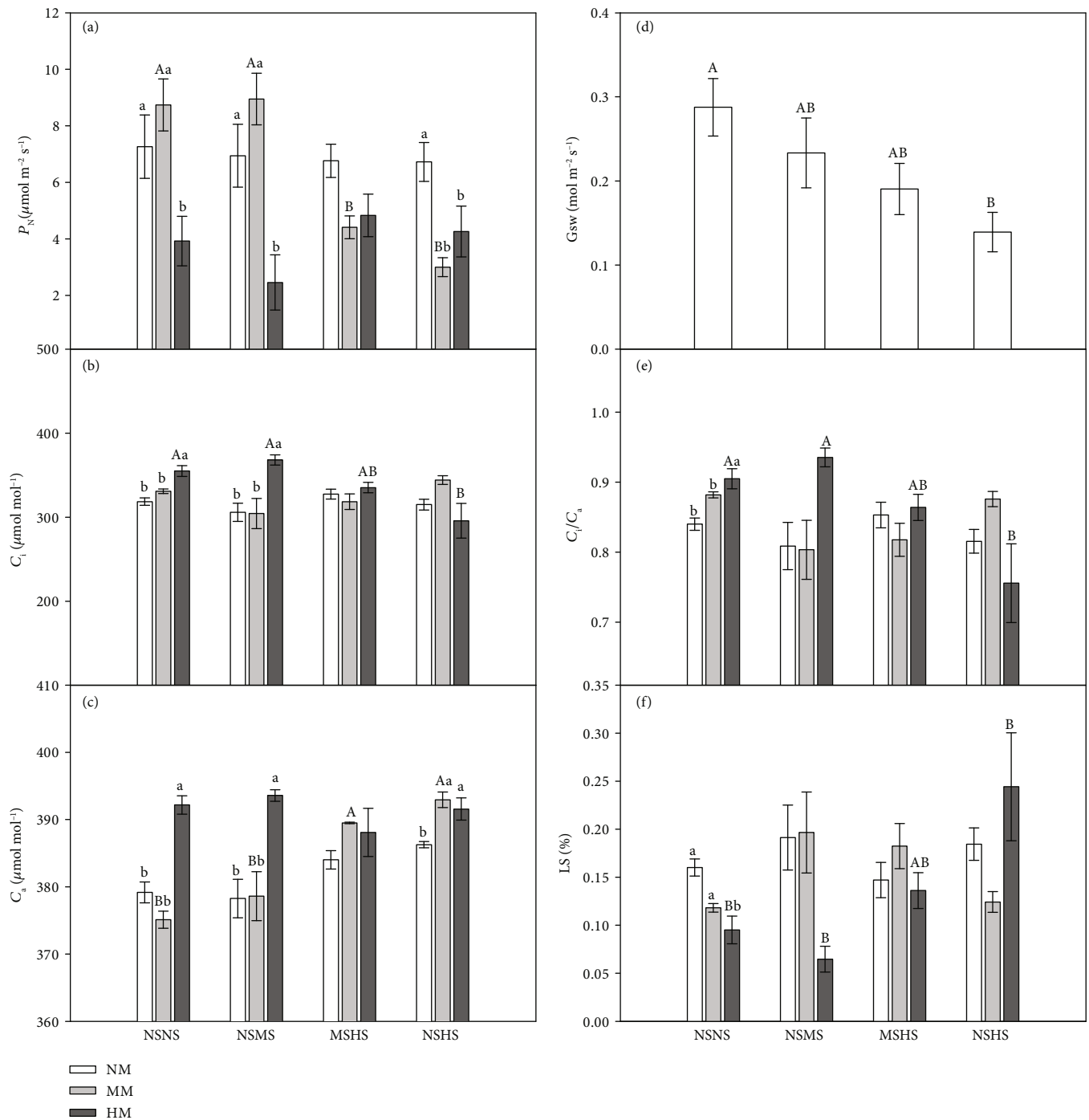


FIGURE 2: Effects of saline-alkali and clipping stress on the net photosynthetic rate (P_N), intercellular CO_2 concentration (C_i), ambient CO_2 concentration (C_a), the intercellular CO_2 /ambient CO_2 (C_i/C_a), stomatal limitation (LS), and stomatal conductance (G_{sw}) of *L. chinensis*. Different lowercase letters represent significant difference ($P < 0.05$) among the saline-alkali and clipping treatments.

In homogeneous environment (NS-NS), the transpiration rate under moderate mowing was significantly higher than that of no mowing and heavy mowing. Meanwhile, the transpiration rate was also significantly decreased in saline-alkali heterogeneous patches NS-MS under moderate mowing (Figure 3(b)).

Water-use efficiency (WUE) was significantly affected by the interaction between soil saline-alkali heterogeneity

and mowing ($P < 0.05$, Table 2). Under heavy mowing, WUE in NS-HS patches was significantly higher than other patches (Figure 3(a)). There were no significant effects of mowing and soil saline-alkali heterogeneity and their interaction on relative water content (RWC, Table 2).

3.3. Growth Situation. The plant height of *L. chinensis* only showed significant difference in different mowing treatments

TABLE 2: Statistical summary of two-way ANOVA evaluating the effects of salt-alkali heterogeneity of soil and clipping their combined effects on the transpiration rate (E), water-use efficiency (WUE), leaf area, leaf mass per area (LMA), relative water content (RWC), and plant height of *L. chinensis*. Values are F ratios and their significance for effects.

Treatment	df	E ($\text{mol m}^{-2} \text{s}^{-1}$)		WUE (P_N/E)		Leaf area (cm^2)		LMA (g/cm^2)		RWC (%)		Plant height (cm)	
		F	P	F	P	F	P	F	P	F	P	F	P
Mowing (M)	2	2.003	0.157	1.614	0.220	22.746	<0.001**	0.015	0.985	0.859	0.436	23.508	<0.001**
Saline-alkali heterogeneity (S)	7	5.667	0.004**	3.709	0.025*	5.063	0.007**	0.647	0.592	0.608	0.617	1.281	0.304
S×M	14	2.518	0.049*	4.492	0.003**	1.161	0.359	0.735	0.626	2.507	0.050	1.594	0.192

F values and significance levels (** $P < 0.01$; * $P < 0.05$) are given.

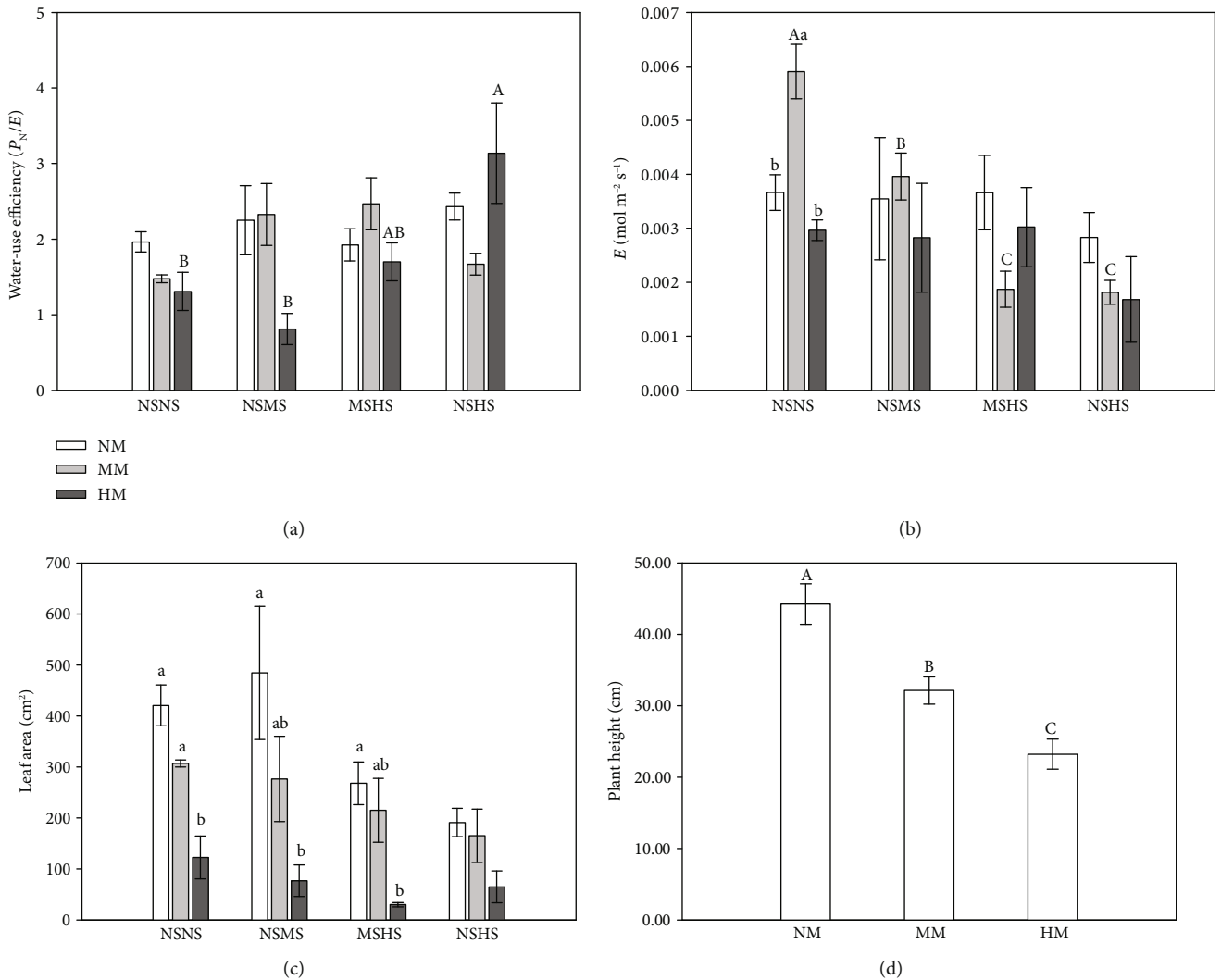


FIGURE 3: Effects of saline-alkali and clipping stress on the leaf area, plant height, transpiration rate (E), and water-use efficiency (WUE) of *L. chinensis*. Different lowercase letters represent significant difference ($P < 0.05$) among the saline-alkali and clipping treatments.

($P < 0.05$). With the increase of mowing intensity, plant height decreased gradually (Table 2, Figure 3(d)).

Mowing treatment and soil saline-alkali heterogeneity had a significant effect on the leaf area of *L. chinensis* ($P < 0.05$). Under each patches, with the increase of cutting

intensity, the leaf area decreased, and HM significantly reduced the leaf area, except the NS-HS patches which mowing have no effect on the leaf area (Table 2, Figure 3(c)). There was no significant effect on the leaf mass per area (LMA) of *L. chinensis* under different treatments (Table 2).

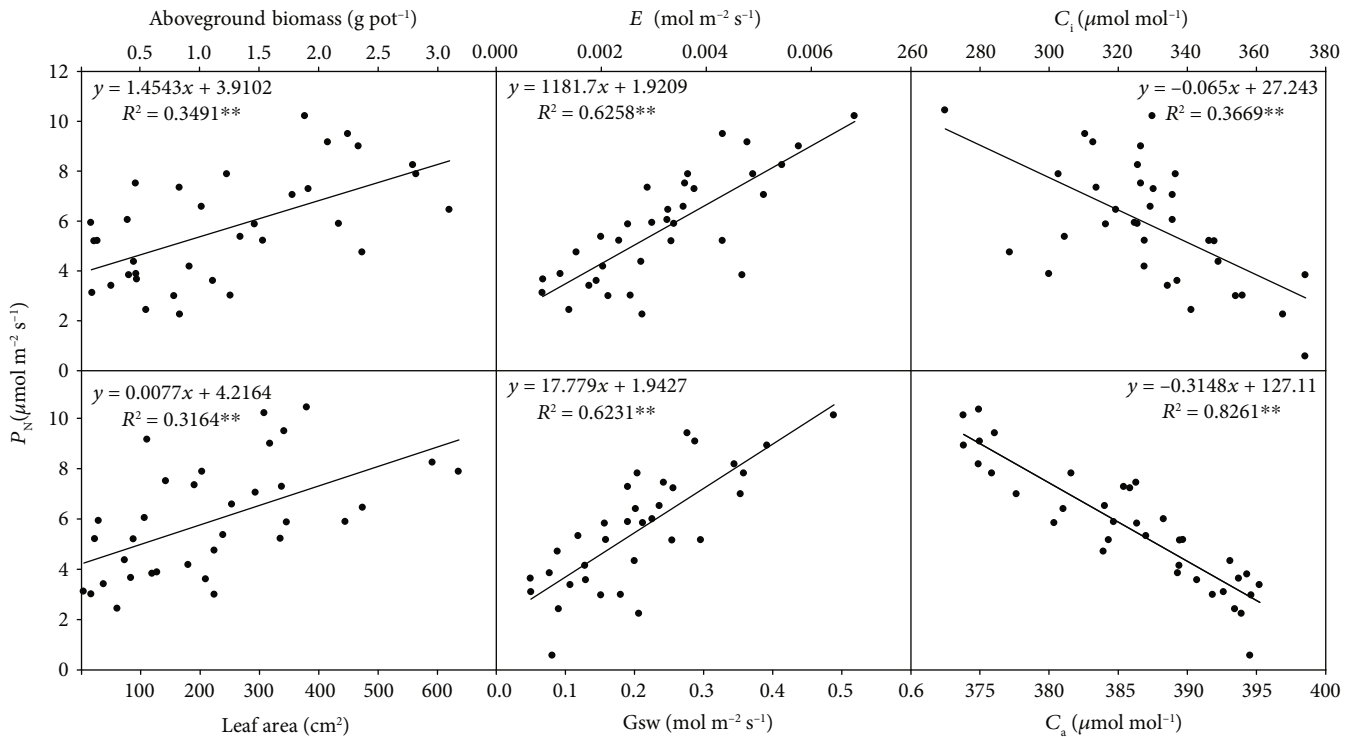


FIGURE 4: Correlation of aboveground biomass, leaf area, and gas exchange parameters of *L. chinensis*.

3.4. Correlation of Gas Exchange. The P_N of *L. chinensis* was positively correlated with aboveground biomass, leaf area, transpiration rate (E), and stomatal conductance (G_{sw}) and negatively correlated with intercellular CO_2 concentration and ambient CO_2 concentration (Figure 4).

4. Discussion

Photosynthesis can fix the solar energy, which is an important physiological activity of plants, affects the growth and development of plants, and determines the productivity of plants [39]. The results showed that under moderate mowing, *L. chinensis* could maintain the net photosynthetic rate (P_N) and transpiration rate in the NS-NS and NS-MS of soil saline-alkali patches (Figures 2(a) and 3(b)). This was similar to Yan et al. who study on *Stipa baicalensis* in Grassland of Hulun Buir, Inner Mongolia [40]. This may be due to the reduction of leaf area by mowing, and in order to compensate for defoliation losses, *L. chinensis* chose to increase the photosynthetic rate to compensate, which is in line with the statement that the loss of leaf area will increase photosynthesis found in other studies [18, 32]. And photosynthesis has a significant positive correlation with aboveground biomass (Figure 4), so the photosynthesis is maintained and the aboveground biomass is maintained. Our experiment found that the compensation of aboveground biomass may be through the compensation of leaf area. The results showed that there was a significant positive correlation between leaf area and net photosynthesis (Figure 4). Moreover, there is no significant difference between the leaf area of moderate mowing (MM) and that of no mowing (NM) when there is no salt-alkali (NS-NS) or low salt-alkali (NS-MS) content in

soil patches (Figure 3(c)). This proves that the growth of leaf area is compensated. The reason for this compensatory growth may be related to mowing or grazing promoted the growth of the rhizome of *L. chinensis* [41]. It is also possible that moderate mowing or grazing promoted tiller growth and increased bud number of *L. chinensis*, resulting in compensatory growth of daughter plant and increased photosynthetic rate [42]. As the place where photosynthesis takes place, the compensation of leaf area will also ensure the progress of photosynthesis. There are many conditions for photosynthesis to go on normally, one of which is the opening degree of stomata. Stomata are the channels of gas exchange between leaves and the outside world, which can supplement CO_2 for photosynthesis and affect transpiration rate. Our results show that photosynthesis is negatively correlated with intercellular CO_2 concentration and ambient CO_2 concentration, positively correlated with transpiration (Figure 4). If the stomatal opening degree is low, the transpiration rate is reduced and the carbon dioxide outside the cell cannot enter the cell normally; photosynthesis will be inhibited. The stomatal conductance reflects the degree of stomatal opening, so as our results, there is a significant positive correlation between stomatal conductance and net photosynthesis (Figure 4).

When the salt concentration of soil saline-alkali patches is high (MS-HS and NS-HS), compared with the other two saline-alkali environments, the compensation growth disappears and the net photosynthetic rate decreases significantly when cutting moderately (Figure 2(a)). We speculate that high concentration of salt and alkali has an overwhelming adverse effect on plant growth. This may be due to the high concentration of salt and alkali plaque on the plant to produce osmotic stress or affect the ion balance around the root

system, so as to reduce the photosynthetic rate [1]. One study of the photosynthetic characteristics of cotton seedlings found that the main reason for the decline of photosynthesis under saline-alkali stress was the stomatal factor, but when the saline-alkali concentration increased or the effects lasted for a long time, the influencing factors gradually became nonstomatal factors [43]. Our results showed that the stomatal conductance decreased with the increase of saline-alkali stress concentration (Figure 2(f)). This is consistent with the positive correlation between the stomatal conductance and the index of plant assimilation ability found by Drake et al. [44]. Therefore, under the stress caused by the saline-alkali concentration, the main factor limiting the photosynthesis of *L. chinensis* might be a stomatal factor. Stomata closing forced by saline-alkali stress, which reduced the stomatal conductance, hindered CO₂ from entering the leaves and also reduced the evaporation of water, thus reducing the transpiration rate and net photosynthetic rate. However, the change of stomatal limit (LS) value did not increase with the increase of saline-alkali concentration. This changing trend was different under different mowing treatments, which may be due to the influence of nonstomatal factors on photosynthesis under the combined stress of saline-alkali stress and mowing treatment [45]. The results of this experiment showed that the stomatal limit value was low (Figure 2(f)), but the net photosynthetic rate was low as well (Figure 2(a)), which may be because under these conditions, the nonstomatal factors have more prominent influence on the photosynthetic rate. As some studies have found that there is a nonlinear relationship between net photosynthetic rate and stomatal conductance, that is, the net photosynthetic rate increases with the increase of stomatal conductance, but the increase rate decreases gradually, which may be due to the aggravation of nonstomatal factors on photosynthetic rate [46]. Under heavy mowing, the leaf area, plant height, transpiration rate, and net photosynthetic rate of *L. chinensis* decreased significantly (Figures 3(c) and 3(d)). Mowing greatly reduced leaf area and plant height, resulted in loss of photosynthetic organs, thus reduced photosynthetic rate, which is similar to the results of Rhodes et al. [33]. Moreover, photosynthesis has a significant positive correlation with aboveground biomass (Figure 4), so the decrease of photosynthesis may reduce aboveground biomass, thus plant height. Water-use efficiency (WUE) refers to the amount of organic matter assimilated by plants in time of losing unit water [47], which can reflect the water consumption and adaptation of plants to stress [48]. The results showed that the water-use efficiency of NS-HS soil salt and alkali patches increased under heavy mowing (Figure 3(a)). This may be due to the existence of mowing treatment which reduces water-use efficiency, or it may be that these treatments have made *L. chinensis* unable to survive. Some studies have shown that there is a positive correlation between net photosynthetic rate and water-use efficiency of *L. chinensis* after grazing. It improved water-use efficiency by increasing net photosynthetic rate and reducing transpiration rate and adapted to grazing stress [29, 49]. However, with the continuous grazing time, perennial grasses can survive by reducing water-use efficiency to respond to stress [28, 50]. Moreover,

under saline-alkali stress, plants will limit water loss, improve water-use efficiency, and fix more CO₂ but reduce the overall growth rate [51].

5. Conclusion

Maintaining photosynthetic characteristics is the primary integration strategy by clonal plants to tolerated or escaped highly stresses. In moderate saline-alkali heterogeneity site, moderate mowing or grazing can maintain photosynthesis, resulting in the promotion of compensatory growth. However, high saline-alkali patches have an overriding detrimental impact on plant compensatory growth and extremely inhibit net photosynthetic rate. In the future research, we should focus on the nonstomatal factors limiting photosynthesis and combined with the biomass distribution model of plant in field experiments, to explore the photosynthetic characteristics and growth strategy of *Leymus chinensis* under mowing and soil saline-alkali heterogeneity environments, so as to provide effective reference for the rational utilization of grassland.

Data Availability

All materials used in this paper are public, and the data used to support the results of this study are available on request from the corresponding author.

Conflicts of Interest

The authors declare that there is no conflict of interests regarding the publication of this paper.

Authors' Contributions

Nan Lu and Luhao Qu are joint first authors.

Acknowledgments

The research was funded by the National Natural Science Foundation of China (Nos. 31600327 and 31300345), the Scientific and Technological Innovation Talent Training Program of Science and Technology Department of Jilin Province (20160520056JH), and the Program for Introducing Talents to Shenyang Agricultural University (880416047).

References

- [1] J. Y. Yang, W. Zheng, Y. Tian, Y. Wu, and D. W. Zhou, "Effects of various mixed salt-alkaline stresses on growth, photosynthesis, and photosynthetic pigment concentrations of *Medicago ruthenica* seedlings," *Photosynthetica*, vol. 49, no. 2, pp. 275–284, 2011.
- [2] J. Lin, C. Mu, Y. Wang, Z. Li, and X. Li, "Physiological adaptive mechanisms of *Leymus chinensis* during germination and early seedling stages under saline and alkaline conditions," *Journal of Animal and Plant Sciences*, vol. 24, no. 3, pp. 904–912, 2014.
- [3] J. Lin, Z. Li, Y. Wang, and C. Mu, "Effects of various mixed salt-alkaline stress conditions on seed germination and early seedling growth of *Leymus chinensis* from songnen grassland

- of China," *Notulae Botanicae Horti Agrobotanici Cluj-Napoca*, vol. 42, no. 1, pp. 154–159, 2014.
- [4] R. Munns and M. Tester, "Mechanisms of salinity tolerance," *Annual Review of Plant Biology*, vol. 59, no. 1, pp. 651–681, 2008.
 - [5] P. S. Rao, B. Mishra, S. R. Gupta, and A. Rathore, "Reproductive stage tolerance to salinity and alkalinity stresses in rice genotypes," *Plant Breeding*, vol. 127, no. 3, pp. 256–261, 2008.
 - [6] G. I. Metternicht and J. A. Zinck, "Remote sensing of soil salinity: potentials and constraints," *Remote Sensing of Environment*, vol. 85, no. 1, pp. 1–20, 2003.
 - [7] Y. T. Song, D. W. Zhou, H. X. Zhang, G. D. Li, Y. H. Jin, and Q. Li, "Effects of vegetation height and density on soil temperature variations," *Chinese Science Bulletin*, vol. 58, no. 8, pp. 907–912, 2013.
 - [8] J. T. Zhang and C. S. Mu, "Effects of saline and alkaline stresses on the germination, growth, photosynthesis, ionic balance and anti-oxidant system in an alkali-tolerant leguminous *forage-Lathyrus quinquenervius*," *Soil Science & Plant Nutrition*, vol. 55, no. 5, pp. 685–697, 2009.
 - [9] C. Yang, D. Shi, and D. Wang, "Comparative effects of salt and alkali stresses on growth, osmotic adjustment and ionic balance of an alkali-resistant halophyte *Suaeda glauca* (bge.)," *Plant Growth Regulation*, vol. 56, no. 2, pp. 179–190, 2008.
 - [10] D. Shi and D. Wang, "Effects of various salt-alkaline mixed stresses on *Aneurolepidium chinense* (Trin.) Kitag," *Plant and Soil*, vol. 271, no. 1–2, pp. 15–26, 2005.
 - [11] H. de Kroons and M. J. Hutchings, "Morphological plasticity in clonal plants: the foraging concept reconsidered," *Ecology*, vol. 83, no. 1, pp. 143–152, 1995.
 - [12] S. W. Kembel and J. F. Cahill Jr, "Plant phenotypic plasticity belowground: a phylogenetic perspective on root foraging trade-offs," *The American Naturalist*, vol. 166, no. 2, pp. 216–230, 2005.
 - [13] P. Parihar, S. Singh, R. Singh, V. P. Singh, and S. M. Prasad, "Effect of salinity stress on plants and its tolerance strategies: a review," *Environmental Science and Pollution Research*, vol. 22, no. 6, pp. 4056–4075, 2015.
 - [14] Y. Wei, M. Dong, Z. Y. Huang, and D. Y. Tan, "Factors influencing seed germination of *Salsola affinis* (Chenopodiaceae), a dominant annual halophyte inhabiting the deserts of Xinjiang, China," *Flora - Morphology, Distribution, Functional Ecology of Plants*, vol. 203, no. 2, pp. 134–140, 2008.
 - [15] M. M. Chaves, J. Flexas, and C. Pinheiro, "Photosynthesis under drought and salt stress: regulation mechanisms from whole plant to cell," *Annals of Botany*, vol. 103, no. 4, pp. 551–560, 2009.
 - [16] X. Wang, S. Geng, Y. Ma, D. Shi, C. Yang, and H. Wang, "Growth, photosynthesis, solute accumulation, and ion balance of tomato plant under sodium- or potassium-salt stress and alkali stress," *Agronomy Journal*, vol. 107, no. 2, p. 651, 2015.
 - [17] E. Tavakkoli, F. Fatehi, S. Coventry, P. Rengasamy, and G. K. McDonald, "Additive effects of Na⁺ and Cl⁻ ions on barley growth under salinity stress," *Journal of Experimental Botany*, vol. 62, no. 6, pp. 2189–2203, 2011.
 - [18] W. Zhao, S. P. Chen, and G. H. Lin, "Compensatory growth responses to clipping defoliation in *Leymus chinensis* (Poaceae) under nutrient addition and water deficiency conditions," *Plant Ecology*, vol. 196, no. 1, pp. 85–99, 2008.
 - [19] Y. Gao, F. Xing, Y. Jin, D. Nie, and Y. Wang, "Foraging responses of clonal plants to multi-patch environmental heterogeneity: spatial preference and temporal reversibility," *Plant and Soil*, vol. 359, no. 1–2, pp. 137–147, 2012.
 - [20] W. J. Zhang, Y. J. Zhang, J. J. Song, and G. W. Yang, "Clonal integration for the *L. chinensis* in a heterogeneous alkaline stress environment," *Journal of Animal and Veterinary Advances*, vol. 11, no. 20, pp. 3796–3799, 2012.
 - [21] Z. Li, J. Lin, T. Zhang, N. Zhang, C. Mu, and J. Wang, "Effects of summer nocturnal warming on biomass production of *Leymus chinensis* in the Songnen grassland of China: from bud bank and photosynthetic compensation," *Journal of Agronomy and Crop Science*, vol. 200, no. 1, pp. 66–76, 2014.
 - [22] P. Alpert, "Effects of clonal integration on plant plasticity in *Fragaria chiloensis*," *Plant Ecology*, vol. 141, no. 1/2, pp. 99–106, 1999.
 - [23] J. S. Chen, D. Yu, Q. Liu, and M. Dong, "Clonal integration of the stoloniferous herb *Fragaria vesca* from different altitudes in Southwest China," *Flora*, vol. 199, no. 4, pp. 342–350, 2004.
 - [24] Y. Gao, D. Wang, L. Ba, Y. Bai, and B. Liu, "Interactions between herbivory and resource availability on grazing tolerance of *Leymus chinensis*," *Environmental and Experimental Botany*, vol. 63, no. 1–3, pp. 113–122, 2008.
 - [25] J. F. Wang, S. Gao, J. X. Lin, Y. G. Mu, and C. S. Mu, "Summer warming effects on biomass production and clonal growth of *Leymus chinensis*," *Crop and Pasture Science*, vol. 61, no. 8, pp. 670–676, 2010.
 - [26] Z. Wang, L. Li, X. Han, and M. Dong, "Do rhizome severing and shoot defoliation affect clonal growth of *Leymus chinensis* at ramet population level?," *Acta Oecologica*, vol. 26, no. 3, pp. 255–260, 2004.
 - [27] J. Liu, C. Feng, D. Wang, L. Wang, B. J. Wilsey, and Z. Zhong, "Impacts of grazing by different large herbivores in grassland depend on plant species diversity," *Journal of Applied Ecology*, vol. 52, no. 4, pp. 1053–1062, 2015.
 - [28] S. P. Chen, Y. F. Bai, G. H. Lin, Y. Liang, and X. G. Han, "Effects of grazing on photosynthetic characteristics of major steppe species in the xilin river basin, Inner Mongolia, China," *Photosynthetica*, vol. 43, no. 4, pp. 559–565, 2005.
 - [29] Y. Peng, G. M. Jiang, X. H. Liu, S. L. Niu, M. Z. Liu, and D. K. Biswas, "Photosynthesis, transpiration and water use efficiency of four plant species with grazing intensities in hunshandak sandland, China," *Journal of Arid Environments*, vol. 70, no. 2, pp. 304–315, 2007.
 - [30] W. Ren, N. Hu, X. Hou et al., "Long-term overgrazing-induced memory decreases photosynthesis of clonal offspring in a perennial grassland plant," *Frontiers in Plant Science*, vol. 8, p. 419, 2017.
 - [31] D. Wang, J. Du, B. Zhang, L. Ba, and K. C. Hodgkinson, "Grazing Intensity and Phenotypic Plasticity in the Clonal Grass *Leymus chinensis*," *Rangeland Ecology & Management*, vol. 70, no. 6, pp. 740–747, 2017.
 - [32] A. J. Graaf, J. Stahl, and J. P. Bakker, "Compensatory growth of *Festuca rubra* after grazing: can migratory herbivores increase their own harvest during staging?," *Functional Ecology*, vol. 19, no. 6, pp. 961–969, 2005.
 - [33] A. C. Rhodes, V. Anderson, and S. B. St Clair, "OUP accepted manuscript," *Tree Physiology*, vol. 37.3, no. 3, pp. 402–413, 2017.
 - [34] G. B. Jones, J. B. Alpuerto, B. F. Tracy, and T. Fukao, "Physiological effect of cutting height and high temperature on

- regrowth vigor in orchardgrass," *Frontiers in Plant Science*, vol. 8, p. 805, 2017.
- [35] D. Hattas, P. F. Scogings, and R. Julkunen-Tiitto, "Does the growth differentiation balance hypothesis explain allocation to secondary metabolites in *Combretum apiculatum*, an African savanna woody species?," *Journal of Chemical Ecology*, vol. 43, no. 2, pp. 153–163, 2017.
- [36] Y. Song, C. A. Busso, Y. Yu et al., "Regrowth, yield and nutrition of *Leymus chinensis* and *Hordeum brevisubulatum* in response to defoliation intensity and frequency," *Pyton-International Journal of Experimental Botany*, vol. 87, pp. 242–251, 2018.
- [37] Y. Song, R. Turkington, and D. Zhou, "Soil fissures help in the restoration of vegetation on secondary bare alkali-saline soil patches on the Songnen Plain, China," *Journal of Soil and Water Conservation*, vol. 67, no. 1, pp. 24A–25A, 2012.
- [38] H. Yan, D. C. Shi, S. J. Yin, and W. Zhao, "Effects of Ca^{2+} ABA and H_3PO_4 on relaxing stress of Na_2CO_3 and NaCl ," *The Journal of Applied Ecology*, vol. 11, no. 6, pp. 889–892, 2000.
- [39] J. Lin, Y. Wang, S. Sun, C. Mu, and X. Yan, "Effects of arbuscular mycorrhizal fungi on the growth, photosynthesis and photosynthetic pigments of *Leymus chinensis* seedlings under salt-alkali stress and nitrogen deposition," *Science of the Total Environment*, vol. 576, pp. 234–241, 2017.
- [40] X. Yan, J. R. Gong, Z. Y. Zhang et al., "Responses of photosynthetic characteristics of *stipa baicalensis* to grazing disturbance," *Chinese Journal of Plant Ecology*, vol. 37, no. 6, pp. 530–541, 2013.
- [41] Y. H. Li and S. P. Wang, "Response of plant and plant community to different stocking rates," *Grassland of China*, no. 3, pp. 11–19, 1999.
- [42] P. Wang, H. Li, X. Y. Pang et al., "Clonal integration increases tolerance of a phalanx clonal plant to defoliation," *Science of the Total Environment*, vol. 593–594, pp. 236–241, 2017.
- [43] Q. Huang, L. Qi, and X. Bai, "Effects of rhizosphere aeration on photosynthesis and ion absorption in cotton seedlings under salt stress," *Acta Ecologica Sinica*, vol. 38, no. 2, pp. 1–9, 2018.
- [44] P. L. Drake, R. H. Froend, and P. J. Franks, "Smaller, faster stomata: scaling of stomatal size, rate of response, and stomatal conductance," *Journal of Experimental Botany*, vol. 64, no. 2, pp. 495–505, 2013.
- [45] U. C. Shukla, P. C. Joshi, and P. Kakkar, "Synergistic action of ultraviolet-B radiation and cadmium on the growth of wheat seedlings," *Ecotoxicology and Environmental Safety*, vol. 51, no. 2, pp. 90–96, 2002.
- [46] D. J. Yu, S. J. Kim, and H. J. Lee, "Stomatal and non-stomatal limitations to photosynthesis in field-grown grapevine cultivars," *Biologia Plantarum*, vol. 53, no. 1, pp. 133–137, 2009.
- [47] S. Zhang and S. Lun, "Research progress on water use efficiency of plant," *Agricultural Research in the Arid Areas*, vol. 20, no. 4, pp. 1–5, 2002.
- [48] B. Martin, C. G. Tauer, and R. K. Lin, "Carbon isotope discrimination as a tool to improve water-use efficiency in tomato," *Crop Science*, vol. 39, no. 6, pp. 1775–1783, 1999.
- [49] S. Zheng, Z. Lan, W. Li et al., "Differential responses of plant functional trait to grazing between two contrasting dominant C_3 and C_4 species in a typical steppe of Inner Mongolia, China," *Plant and Soil*, vol. 340, no. 1–2, pp. 141–155, 2011.
- [50] B. Vandoorne, A. S. Mathieu, W. van den Ende et al., "Water stress drastically reduces root growth and inulin yield in *Cichorium intybus* (var. *sativum*) independently of photosynthesis," *Journal of Experimental Botany*, vol. 63, no. 12, pp. 4359–4373, 2012.
- [51] G. D. Farquhar and T. D. Sharkey, "Stomatal conductance and photosynthesis," *Annual Review of Plant Physiology*, vol. 33, no. 1, pp. 317–345, 1982.

Research Article

Effects on Local Temperature and Energy of Oasis City Expansion in Arid Area of Northwest China

Miao Zhang ¹, Geping Luo ², Peng Cai,² and Rafiq Hamdi³

¹Northwest Land and Resources Research Center, Shaanxi Normal University, No. 620, West Chang'an Avenue, Chang'an District, Xi'an 710119, China

²State Key Laboratory of Desert and Oasis Ecology, Xinjiang Institute of Ecology and Geography, Chinese Academy of Sciences, No. 818 South Beijing Road, Urumqi, 830011 Xinjiang, China

³Royal Meteorological Institute, Avenue Circulaire 3, B-1180 Brussels, Belgium

Correspondence should be addressed to Geping Luo; luogp@ms.xjb.ac.cn

Received 16 July 2019; Revised 29 October 2019; Accepted 10 January 2020; Published 1 February 2020

Guest Editor: Jingwei Wang

Copyright © 2020 Miao Zhang et al. This is an open access article distributed under the Creative Commons Attribution License, which permits unrestricted use, distribution, and reproduction in any medium, provided the original work is properly cited.

The land surface model SURFEX 7.3 was used to study climate effect of urban expansion located in oasis in arid area of Northwest China by surface and 2 m urban heat island (UHI) intensity and available energy ratio (B). We performed a true regional development scenario and three assumed scenario simulations in 1978, 1993, 2004, and 2014, respectively. The results show that 2 m UHI always displays positive twin peaks during whole day, while surface UHI only displays a positive single peak with several hours during daytime at four seasons in the four years. Moreover, 2 m UHI intensity during night is higher than that during daytime, indicating that UHI intensity is contributed more by “trap effect” from urban complex geometry or anthropogenic heat and that surface UHI according to land surface temperature cannot reflect UHI comprehensively. The oasis-urban development resulted in local warming and increasing of B , and compared with the original undeveloped environment, local climate in the study area was in a relatively balanced state in 1978 and 1993 due to the “heating effect” of urban area and the “cooling effect” of oasis, but the offsetting effect from oasis would become weaker after 1993.

1. Introduction

Research on local climate change caused by urban expansion has received increasing interest due to the fact that it is closely related to the living quality for humans in the past few years [1–6]. But studies with respect to the climate effect of urban expansion in the oasis-desert system in arid area is relatively rare [7, 8]. Northwest China has a special mountain-basin geomorphology, and urban are in this region is usually converted from surrounding oasis area, while oasis is usually from a difficult reclamation in the surrounding desert. Both urban and oasis development in this region are greatly limited by local water and soil resources in the basin [9, 10], since the main water resource is from the limited melting of snow and glaciers and the precipitation in tall mountain ranges and the desert background also makes oasis and urban compete for the limited fertile soil on alluvial fan out of the mountains [11]. Urban expansion

on such oasis will inevitably increase instability of oasis and the integrated ecosystem [12, 13]. Based on our previous studies, the oasis plays a role of wet-cold island compared with the surrounding desert and drives local atmospheric circulation between oasis and desert, which plays an important role in maintaining the existence of oases [14, 15]. However, what we do not know is whether this urban expansion will affect the wet-cold island effects of oasis and local climate and how? Thus, exploring climate effects of urban expansion in this region will provide beneficial information to regional sustainable development [16].

Expansion of impervious surface area (ISA) is a representative of urban development [17], and the urban heat island (UHI) has been considered as the most obvious feature that resulted from the ISA expansion [18]. However, we found that the understanding for UHI and the relation with the increasing of ISA in previous studies are incomplete, unilateral, and controversial. For example, some researchers

determined that city center is sometimes cooler than the rural environment, such as in the morning in the summer [19]. Others believed that the city center was always warmer than rural area in whole year [20]. Except for difference in urban scale and urban geometry description [21], one possible important reason for these controversial conclusions is from the different UHI definitions. As we all know, the UHI is defined as the temperature difference between urban and rural areas. But some researchers calculated the UHI using air temperature difference between the urban and rural areas [2, 19, 22–24], while others calculated the UHI from land surface temperature (LST) difference between urban and rural areas [1, 20, 25].

Therefore, in this paper, we compared the two different UHI intensities at hour scale with the increasing of ISA in a typical middle-scale oasis-urban Fukang (FK for short) in the north slope of Tianshan Mountains. The vertical temperature difference between land surface and its over and available energy ratio in the urban center were also studied for understanding further the mechanism of UHI.

2. Method

2.1. Study Area. The particularity of the study area was mainly that such urban area expanded on artificial oases [9, 10], while the formation of these oases rely on the geomorphic characteristics of high mountain-basin systems. The limited water resources from melting of snow and glaciers and the precipitation in mountain ranges maintain oasis and urban survival in these mountain-basin systems. Water resources are scarce for both human livelihoods and ecosystems here, and urban development will certainly increase the instability of regional sustainable development.

We selected FK in SanGong River Basin (SGRB) in the north slope of the Tianshan Mountains as the study area, which has an area of 304 km². The FK with central latitude and longitude of 44°09′ and 87°58′. The SGRB has a gentle slope from the southeast to the northwest with the average altitude of 575 m, and the famous Gurbantonggut desert is located in the northern areas. Before the year 1958, FK is just a small village, and the dominant plant species of the SGRB were desert shrubs, grassland, and saline [26]. The area and population of FK have dramatically increased approximately to 60.87 km² and 220,000 (population density of oasis reached 71 persons/km²) in the past 60 years. The dominant plant species become crops such as wheat, cotton, and surrounding sparse desert shrubs. The SGRB belongs to continental arid and semiarid climate with average evapotranspiration of 2292 mm and average precipitation of 145 mm. The average annual temperature is 6.7°C, and there had been the historical extreme highest temperature of 41.5°C and the lowest temperature -37°C.

2.2. Model. The externalized surface scheme SURFEX 7.3 was used in this paper. The SURFEX actually includes various modules to describe the exchanges of water, momentum, and energy over four universal surface area titles: sea, lake, vegetation, and town [27]. In this paper, we used the Town Energy Balance (TEB) [28] scheme to parameterize the local

scale energy and water exchanges between urban surfaces and the atmosphere and simultaneously coupled with the Interactions between Soil, Biosphere, and Atmosphere (ISBA) scheme [29, 30] to simulate the energy and water budget of soil and vegetation. TEB simulates the urban energy and water exchange over three generic and comprehensive surfaces (road, roof, and wall). Although TEB is a single-layer canopy module with simplification hypotheses on the canopy shape and direction, it is enough to accurately describe the change trend of surface energy, canyon air temperature, and surface temperature. The coupling of ISBA and TEB was run in offline mode.

2.3. Input Data

2.3.1. Impervious Surface Area Estimation. In this study, both aviation photos and satellite images were used to access the fraction of impervious surface area (ISA): scanned aviation photos in 1958 and 1978, Landsat 5 TM in 1993 (30 m), SPOT 4 in 2004 (10 m), and Landsat 8 in 2014 (15 m). All of the satellite images were acquired from July to September. Since vegetation grows vigorously in this period, it is easy to distinguish different land cover types on the basis of obvious spectral difference. The images in 1993, 2004, and 2014 were first radiometrically and atmospherically corrected using the ENVI/FLAASH module, and geometric corrections were also performed. The projection of all images was projected using the Universal Transverse Mercator with WGS-84 coordinate system. The main method to extract ISA is referenced from the studies [17, 31–33]. First of all, water was masked according to the Normalized Difference Water Index. Three abundant spectral information bands were extracted by minimum noise fraction, which were used to select the four quite different and classical endmembers (vegetation, low albedo, high albedo composition, and soil composition). Finally, ISA fractions were obtained using the Decision Tree classification. For the photos in 1958 and 1978, the ISA was extracted by sketching city boundaries digitally and calculating the ISA by the grayscale difference of aviation photos and referenced to the FK yearbook. The ISA expansion can be seen in Figure 1.

2.3.2. Forcing and Observed Data. Reanalysis Modern-Era Retrospective Analysis for Research and Applications (MERRA) was selected as forcing data. This product is produced at one-hour intervals, and the full spatial resolution is 1/2 degrees (latitude) × 2/3 degrees (longitude), which were downloaded from the Goddard Earth Sciences Data and Information Services Center (MERRA). MERRA was generated with version 5.2.0 of the Goddard Earth Observing System (GEOS) atmospheric model and data assimilation system (DAS). The MERRA used the ensemble assimilation methods [34] and had high quality [35]. The forcing variables consist of hourly downward direct shortwave radiation, downward longwave radiation, rainfall rate, 10 m air temperature, northward wind and eastward wind at 10 m above displacement height, surface pressure, specific humidity at 10 m above the displacement height for the years of 1978 and 1993, but at 50 m in the years of 2004 and 2014, and equivalent

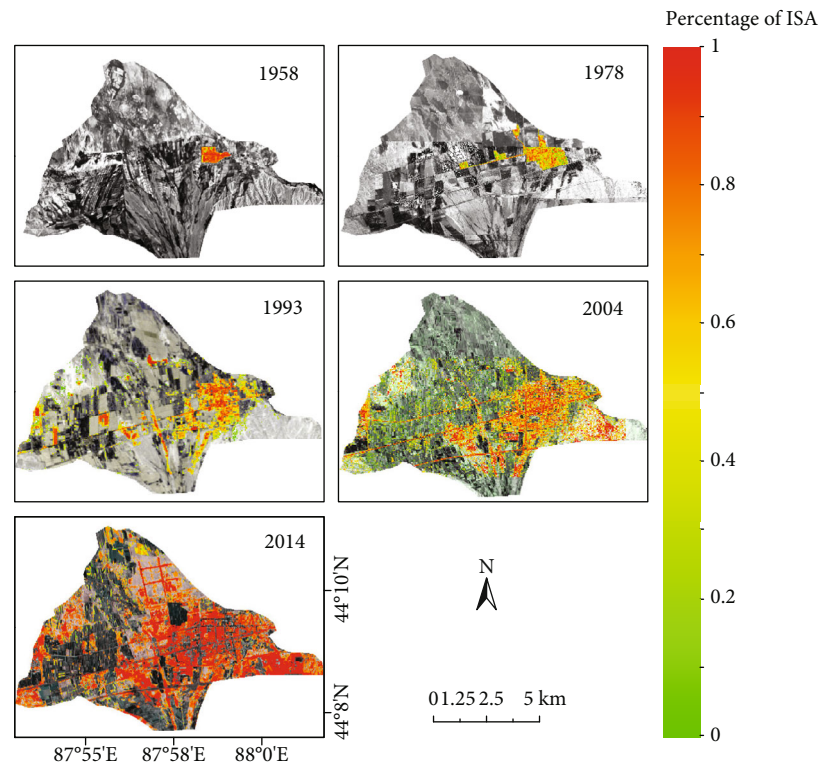


FIGURE 1: Impervious surface area (ISA) in 1958, 1978, 1993, 2004, and 2014.

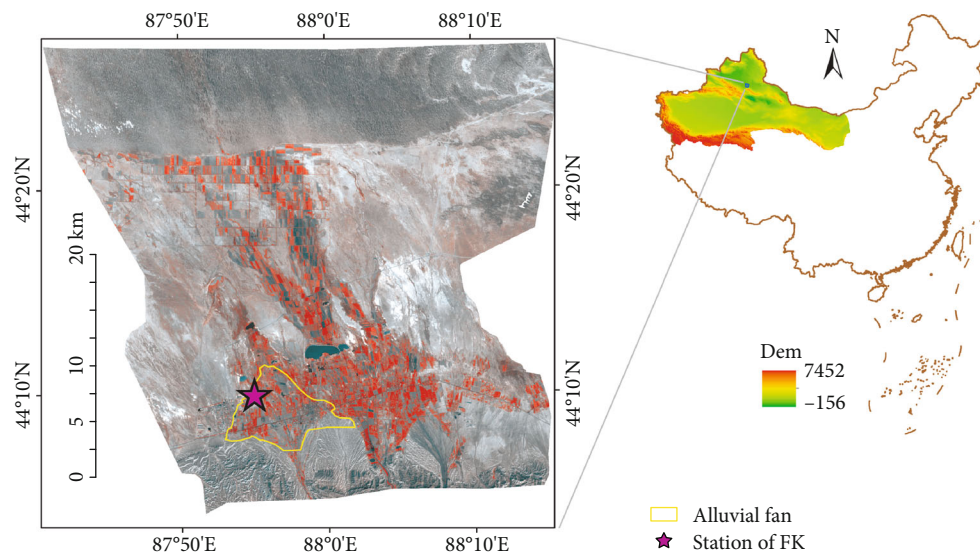


FIGURE 2: Location of FK station and SanGong River Basin (SGRB).

density of CO_2 (350 ppm) during the simulation. In situ observations from a meteorological station FK are used to validate the simulated hourly temperature (Figure 2). The original underlying surface of the FK station is irrigated crop, but with the expansion of FK, the observation is influenced more by the urban area.

2.4. Simulation Scenarios. Because there is smaller ISA (Figure 1) and a lack of forcing data in 1958, we performed a true control scenario and three assumed scenario simu-

lations only in 1978, 1993, 2004, and 2014, respectively. Table 1 displays the land use change in different scenarios and explains the details of different scenarios. CDISA scenario represented the true evolution of land cover in the historical four years. CDC scenario assumed that the ISA in the true scenario was converted from surrounding oasis and the desert was still the same with CDISA scenario. Thus, the difference between CDISA and CDC can explain the contribution of ISA on local climate when urban area developed at the expense of oasis. CDD referred that the ISA in CDISA

TABLE 1: Simulation scenarios.

	ISA	Oasis	Desert
CDISA	True	True	True
CDC	No	Original oasis+ISA area	True
CDD	No	True	Original desert+ISA area
D	No	No	Original desert+ISA+oasis
CDISA-CDC	The effect on local climate of ISA expansion when the ISA area was converted from oasis		
CDISA-CDD	The effect on local climate of ISA expansion when the ISA area was converted from desert		
CDISA-D	The effect on local climate when both oasis and ISA developed (true regional development)		
CDC-D	The effect on local climate when oasis only developed		

was converted from the desert, and the difference between CDISA and CDD can explain the ISA effect when urban area developed from the surrounding desert. We also assumed that there is no urban and oasis expansion in the past (D scenario) and the climate from the D scenario represented assumed climatic environment of the undeveloped state. Thus, the difference between CDC and D will give climate effect when the oasis only developed, and the difference between CDISA and D gives climate effect of true development. Because of the same forcing data and parameters used in the different simulation scenarios, we can deduce that the local climate difference between different scenarios at the same year resulted from regional development.

2.5. Model Parameters. The dominant crop types of the SGRB were cotton and wheat according to fieldwork ([36]). The leaf area index (LAI) values in 12 months were set as 0, 0, 0.5, 1.06, 2.38, 3.4, 4.2, 4.3, 3, 1.33, 0, and 0 based on the average of MERRA LAI data (MERRA), dominant crop phenology [37–39], and fieldwork. Road in oasis city generally can be divided into surface layer, base layer, and the cushion. According to survey, the thickness of the surface layer is about 3–15 cm and the layer is composed of the combination of asphalt and concrete layer. The thickness of base layer approaches to 50 cm, and the layer is mainly composed of concrete to keep the stability of road. The cushion is the layer between the base layer and soil and is also mainly composed of concrete. Wall in oasis city can be composed of plaster and layer on both sides and internal insulation and adiabatic layer (200–300 cm) of hollow brick, aerated concrete, or benzene board. Roof in oasis city can be divided into surface waterproof layer, insulation and adiabatic layer, and reinforced concrete layer [40, 41]. In this study, parameters of roof, wall, and road were set as three layers referenced from fieldwork and papers [3, 23, 40–43]. The details can be seen in Table 2.

3. Results

3.1. Simulation Evaluation. We used Pearson correlation coefficient (r), index of agreement (d), mean bias (Bias), root mean square error (RMSE), standard deviations (SDT), and proportions of systematic and unsystematic error (S/U) to comprehensively evaluate the simulation result. These measures describe the direction of the error bias and indicate the average error magnitude. Table 3 shows SURFEX perfor-

mance in simulating 2 m daily average temperature from the true (CDISA) simulation at the FK station. A strong linear relationship is obtained at all seasons in the three years from simulation with coefficients of determination (d) larger than 0.74 ($p < 0.05$) and Pearson correlation coefficient (r) larger than 0.66 ($p < 0.05$) (Table 3). Simulation in warm seasons (summer and autumn) was better than that in cold seasons (spring and winter). The proportions of systematic and unsystematic errors were much less than 30%; this means that physical processes that the model routinely simulate are relatively well [44]. The 2 m temperatures simulated using the SURFEX in three years were well consistent with observation. Considering that the UHI intensity is different between urban center and rural area, the simulated errors were counteracted to some extent, and acceptable bias and mean absolute error were obtained except for the spring and winter in the years 1993 and 2004.

3.2. The 2 m and Surface UHI and Energy Partition in the True Scenario. The hourly and yearly intensity of UHI in 1978, 1993, 2004, and 2014 was calculated at a height of 2 m (T2MD for short) and land surface (TSD for short). T2MD refers to the 2 m air temperature difference between the city center and the rural area, and TSD means the difference of average temperature of three urban surfaces (road, roof, and wall) and the rural surface temperature. At the same time, we also computed the vertical temperature difference at 2 m from the city surface to its over (TUD) and from rural area to its over (TVD) in these four years with the purpose of further understanding the reasons and physical process of UHI.

From Figure 3, the following rules can be obviously obtained. (1) T2MD always displays positive twin peaks during whole day at four seasons in the four years, and the twin peak in the winter becomes weaker than the other three seasons (Figure 3 solid line), while the TSD displays a single peak and the temperature of the city surface is higher than that of the rural surface several hours during daytime in the four seasons in the four years, but displaying a cooler surface during deep night (Figure 3 dotted line). This means that 2 m air temperature of city environment is indeed warmer than that in rural environment in whole day, but surface temperature of the city is not always warmer than that of the rural area. The UHI defined by air temperature difference has different rules with UHI calculated by land surface temperature

TABLE 2: Morphometric parameters and the physical properties of city elements in the modelling.

	1978	1993	2004	2014
Land cover fraction				
C3 crop	47.09	59.46	46.51	44.00
Sparse desert plant	49.99	20.43	13.58	10.45
ISA	2.92	20.11	39.91	45.55
Morphometric parameters				
Mean building height	10	10	20	30
Height/width	1	1	2	3
Road properties				
Main materials	Asphalt, concrete	Asphalt, concrete	Asphalt, concrete	Asphalt, concrete
Albedo	0.08	0.08	0.08	0.08
Emissivity	0.94	0.94	0.94	0.94
Roughness length	0.05 m	0.05 m	0.05 m	0.05 m
Roof properties				
Main materials	Asphalt, mortar, concrete	Asphalt, mortar, concrete	Asphalt, mortar, concrete	Asphalt, mortar, concrete
Albedo	0.14	0.14	0.14	0.14
Emissivity	0.90	0.90	0.90	0.90
Roughness length	0.15 m	0.15 m	0.15 m	0.15 m
Wall properties				
Main materials	Plaster, concrete, brick	Plaster, concrete, brick	Plaster, concrete, brick	Plaster, concrete, brick
Albedo	0.14	0.14	0.14	0.14
Emissivity	0.90	0.90	0.90	0.90

TABLE 3: The Pearson correlation coefficient (r), index of agreement (d), mean bias error (Bias), and root mean square error (RMSE) between the simulated and observed for winter (DJF), spring (MAM), summer (JJA), and fall (SON) in 1978, 1993, and 2004.

Year		r	d	Bias (°C)	RMSE (°C)	S/U
1978	Spring	0.95	0.97	-0.562	2.46	21%
	Summer	0.67	0.82	-0.046	2.27	32%
	Autumn	0.98	0.99	0.2286	1.84	23%
	Winter	0.96	0.97	0.7246	1.94	25%
1993	Spring	0.92	0.95	-1.1652	3.14	24%
	Summer	0.86	0.90	-0.8438	1.8	29%
	Autumn	0.95	0.97	0.3199	3.25	21%
	Winter	0.66	0.74	2.216	5.04	26%
2004	Spring	0.98	0.98	-1.608	2.38	31%
	Summer	0.91	0.94	-0.903	1.98	28%
	Autumn	0.97	0.97	-0.0811	2.75	11%
	Winter	0.92	0.95	1.2073	2.98	25%

*S/U means proportions of systematic and unsystematic errors.

difference. Some researchers think that remotely sensed UHIs are usually stronger and exhibit the greatest spatial variability of UHIs [45]. However, why do 2 m UHI and surface UHI have different diurnal variation patterns rather than just quantity differences in this study? The main reason is that UHI is not only from the difference of specific heat capacity

for the averaged urban surface and rural area surface, which results in larger difference between surface and its over air evidenced by the greater range of TUD than TVD (Figure 4), but is also closely related with the complex and heterogeneous three-dimensional structure, which makes it difficult for energy to spread out. Anthropogenic heat is a major contributor to the formation of the UHI. Sources include heat generated by the combustion process in vehicles, heat created by industrial processes, the conduction of heat through building walls or emitted directly into the atmosphere by air-conditioning systems, and the metabolic heat produced by humans [46]. Therefore, surface UHI can only reflect responsibility of land surface to energy, while 2 m UHI reflected land-atmosphere interaction status including effects of atmospheric pollution on absorption and scattering of longwave shortwave radiation, anthropogenic heating, “trap effect” from urban complex geometry, and energy interaction between surface and over air. This further implies that the main reason of UHI resulted from “trap effect” of urban complex geometry or anthropogenic heat and also implies that surface UHI according to the inversion temperature from remote sensing data cannot reflect UHI comprehensively. (2) T2MD during night is higher than that during the day, which indicates that the intensity of 2 m UHI during the night is stronger than that during the day. The reason might be that 2 m air temperature in both city environment and rural environment is increasing and the difference of the increasing rate between the two environments is relatively less during daytime. While the 2 m air temperature in both

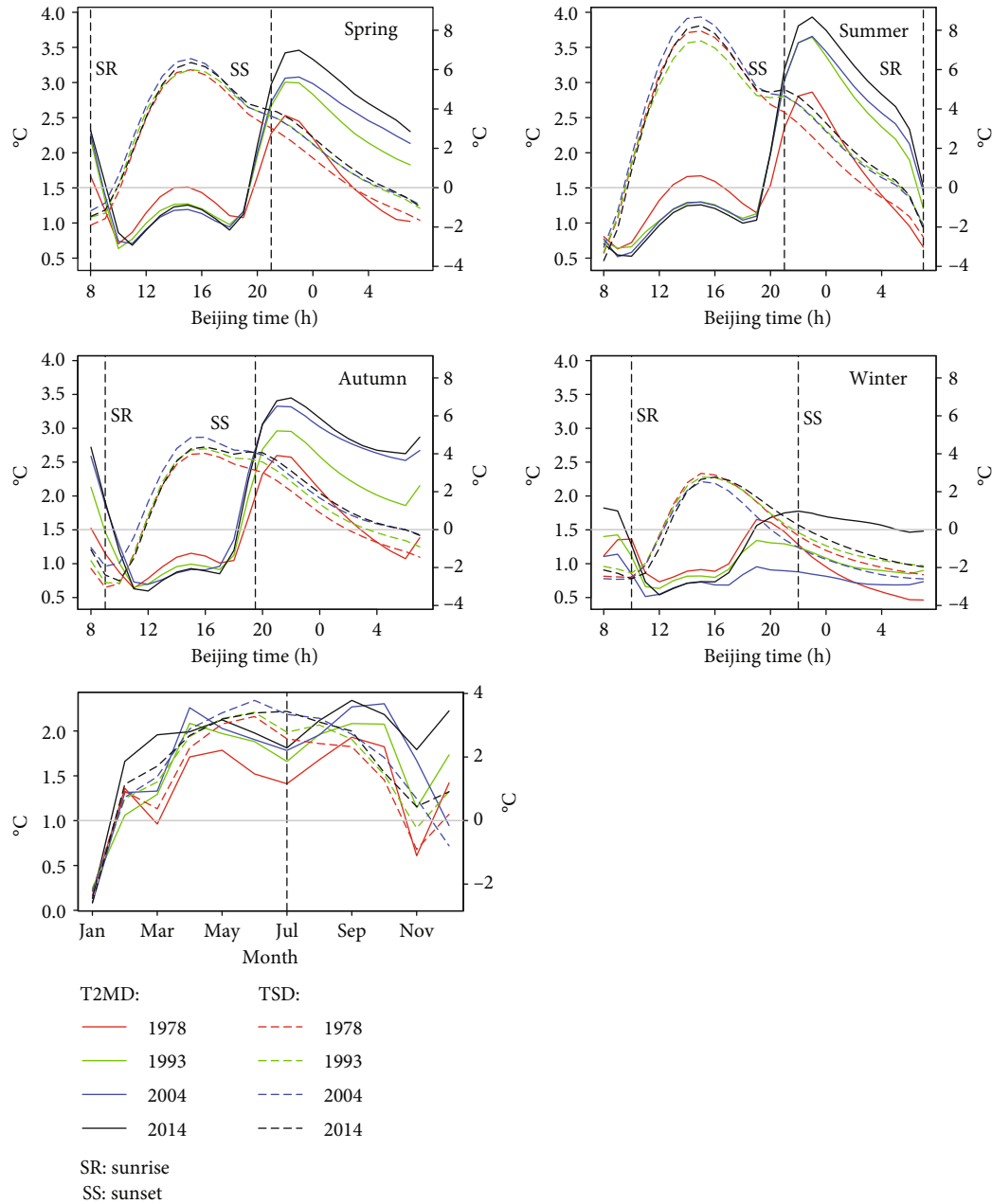


FIGURE 3: Comparison of daily and yearly T2MD (solid lines reference to the left axis) and TSD (dotted lines reference to the right axis) in 1978, 1993, 2004, and 2014.

city environment and rural environment is decreasing after sunset, the decreasing rate of 2m air temperature in rural environment is much quick than that in city environment (the slow release due to “trap effect” from urban complex geometry), which makes the temperature difference between the city and the rural environment continue to increase. These indicate that the intensity of 2m UHI during daytime mainly resulted from the difference of energy absorption rate of the city and rural area, while the UHI intensity during night is decided by energy release rate of these two environments. This further confirms the above conclusion that the UHI intensity is determined more by “trap effect” from

urban complex geometry or anthropogenic heat after urban expansion. (3) Both T2MD and TSD at sun rising time are the lowest in a day, which illustrates that the UHI is the weakest at sun rising time. (4) The intensity of 2m UHI in the whole year displays similar twin peak trends. The strongest period of 2m UHI is April, September, and October in this region and relatively weaker during July, when it is the warmest period in the study area. The reason is that the evapotranspiration difference between the rural area and the urban area in July significantly decreased, thereby the temperature difference between them also decreased. The range of hourly and yearly averaged surface UHI is from

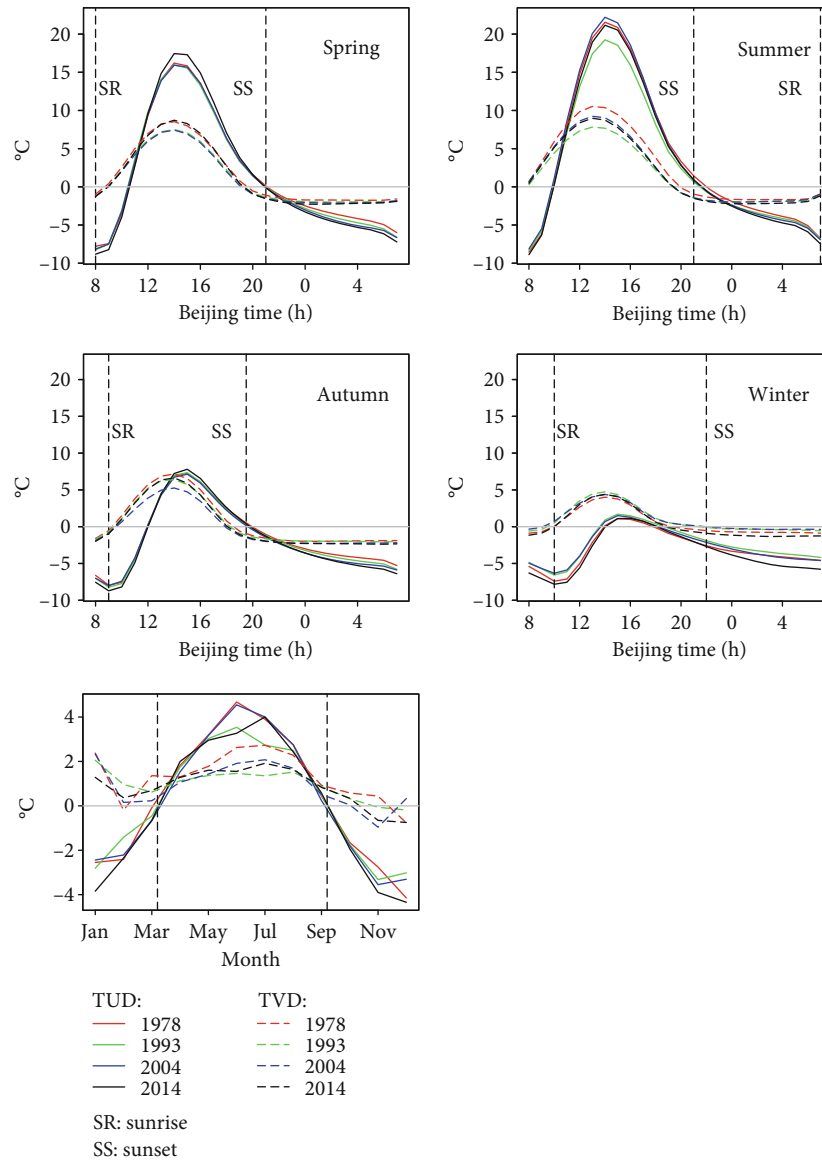


FIGURE 4: Comparison of daily and yearly TUD (solid lines) and TVD (dotted lines) with the increasing of ISA in 1978, 1993, 2004, and 2014.

-4°C to 7°C and from -3°C to 3°C, respectively, which were greater than that of 2 m UHI, with the range from 0°C to 3.5°C and 0°C to 2°C, respectively.

3.3. Effects on Local Climate Resulted from Increasing of ISA. 2 m temperature difference between the true scenario and the three assumed scenarios can quantitatively reveal the contribution to local climate of regional land use change. The red and green dotted lines in Figure 5 represented the change of 2 m temperature that resulted from the expansion of ISA in the four years at the expense of crop and desert, respectively. And black solid line and dark-green dotted line in Figure 5 represented the change of 2 m temperature that resulted from true regional development and without urban development, respectively. No matter if ISA was converted from oasis or desert, this conversion would increase local temperature in this region (red and green dotted lines in Figure 5), and increased magnitude of annual temperature

that resulted from crop to ISA conversion from 1978 to 2014 was 0.02°C, 0.16°C, 0.23°C, and 0.31°C, which was more than desert-ISA conversion directly. This confirms that urban development in the past 60 years resulted in the increasing of local temperature. Moreover, according to the true regional development, both urban and city are expanded in the past 60 years, but the “cooling effect” caused by expansion of oasis to local climate in the study region (dark-green dotted lines) was counteracted by the effect from urban expansion.

Bowen ratio (B) difference is important to understand the local climate change of land use change from the view point of available energy. If B is greater than 1, a greater proportion of the available energy at the surface is passed to the atmosphere as sensible heat than as latent heat, vice versa [47]. Figure 6 displays B in the true scenario and the B differences between the true and the three assumed scenarios in 1978, 1993, 2004, and 2014. No matter if the ISA was converted

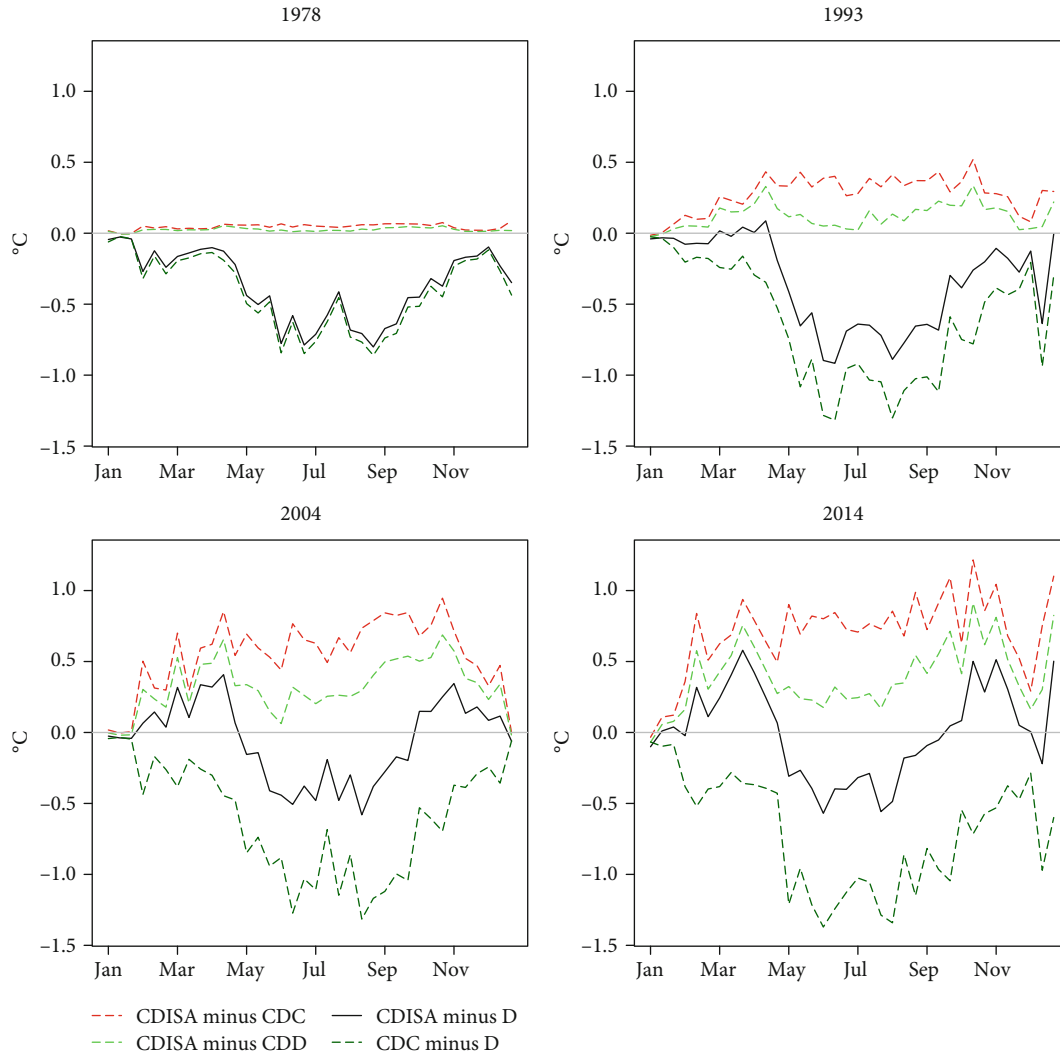


FIGURE 5: 2 m mean temperature difference in simulation area between the true and assumed scenarios in 1978, 1993, 2004, and 2014.

from land cover of crop or desert, there is no doubt that city development resulted in the increasing of B in a year (red and green dotted lines). The reason might be from the double effects of rising in sensible heat and declining in latent heat. Increased sensible heat flux was caused by more heat storage due to “trap effect” which resulted from rough three-dimensional shape of urban area, relatively smaller reflectivity and heat capacity, and decreased latent heat flux was due to rare vegetation in the city. Thus, the increasing of B was a positive correlation with the increasing of ISA, which implies that B can also be an indicator of urbanization. Oasis development can lead to decreased B in a year except for the growing peak season, which can be seen from the different comparison between CDC and D scenario (dotted dark-green line in Figure 6). Compared with the original undeveloped environment, local thermal environment was in a relatively balanced state based on equivalent increased sensible heat and decreased latent heat in 1978 and 1993 due to combined effects of urban and oasis expansion, but local climate becomes warmer due to dominant increased sensible heat after 1993.

In order to explore the quantitative effects of oasis and urban expansion on the local climate, 2 m averaged temperature and B difference between true scenario (CDISA) and undeveloped environment (D) were compared in the years 1978, 1993, 2004, and 2014 (Figures 7(a) and 7(b)). B difference is almost greater than zero in the four years (Figure 7(a)); both B and local temperature increased from 1978 to 2014 (Figures 7(a) and 7(b)). The relation between both annual B and temperature with extended ISA is a positive correlation (see Figure 7(c)), the conclusion that regional land development in the study area, especially the growth of ISA, resulted in the increased B and local temperature.

4. Discussion

In this study, the effects of oasis-urban (regional) development on local climate in arid area of Northwest China from viewpoints of surface and 2 m UHI intensity and the change of available energy partition, using SURFEX land surface model, were discussed.

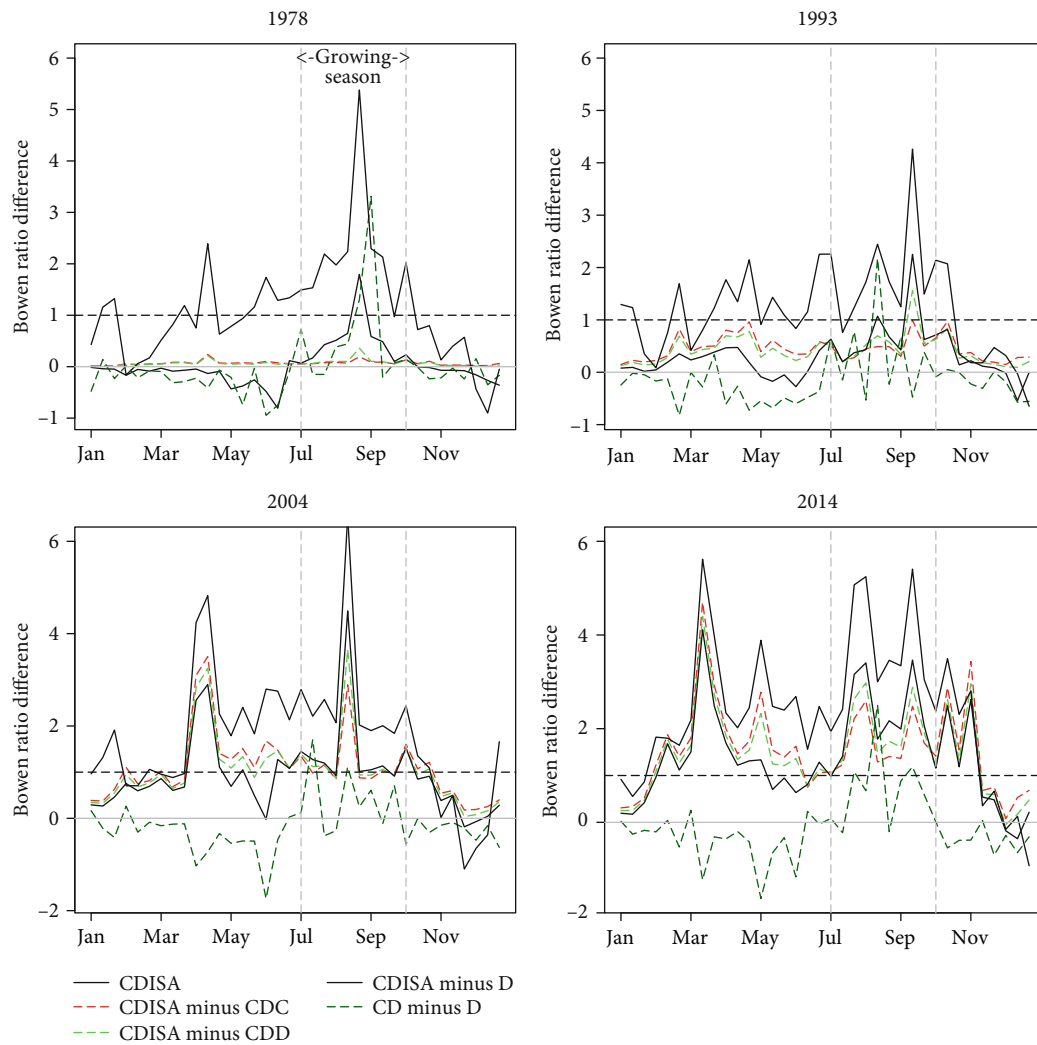


FIGURE 6: Bowen ratio (B) and its differences between the true and assumed scenarios in 1978, 1993, 2004, and 2014.

Our study also contributes certain new findings. The differences between surface and 2 m UHI show different diurnal variation patterns, rather than just quantity differences in this study. This conclusion is different from papers [1, 20, 25]; they indicate that surface and 2 m UHI have similar diurnal variations and differ only in magnitude. In addition, compared with the original undeveloped environment, local thermal environment was in a relatively balanced state in 1978 and 1993 due to the combined effects of urban and oasis expansion, but local climate becomes warmer due to the dominant increased sensible heat after 1993. This result is consistent with the findings reported in previous investigation [48], in which the author considered that the urbanization of most cities in northwestern China resulted in considerable negative warming effects before 1978, but in evidently positive effects after this year.

However, the report is only partly supplementary to the effects of urban development in the arid area; there are still many aspects that need to be studied or explored in depth, such as modelling uncertainty. Although we think it is feasible to use a grid forcing data in plain area, we plan that the

further research focus on the sensitivity analysis for uncertainty of different forcing data and model parameters and larger ISA, to explore the response of oasis-urban heat island to these parameters. As we all know, the poor choice of parameter values can cause a large drop in performance for models [49]; if better observed information about FK city such as annual air pollution, average building height, building materials, and larger cities are available in this study, then the simulated accuracy of this model can be improved and the conclusions in this study are more convincing. In addition, the simulations in this paper are unidirectional, not bidirectional, and these will bring some unpredictable uncertainty.

5. Conclusion

The SURFEX 7.3 was used to simulate effects of oasis-urban development on local climate in arid area of Northwest China from viewpoints of surface and 2 m UHI intensity and available energy partition. We performed a true scenario and four assumed scenario simulations in each year of 1978,

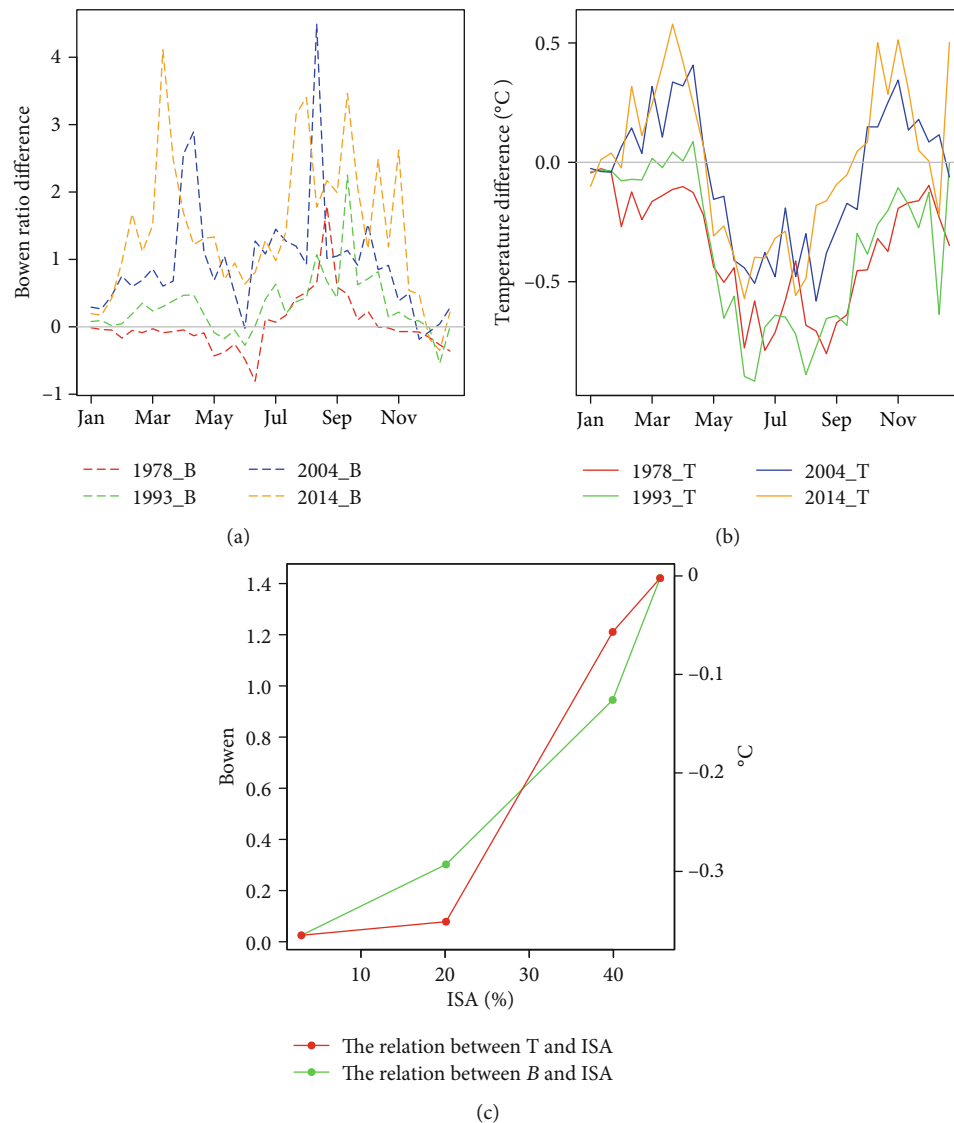


FIGURE 7: Local thermal environment change with the increasing of ISA.

1993, 2004, and 2014 and obtained the following conclusions. (1) 2 m UHI always displays positive twin peaks during whole day, while surface UHI displays a positive single peak during daytime at the four seasons in the four years, displaying a cooler surface during deep night. Surface UHI can only reflect responsibility of land surface to energy, while 2 m UHI reflects a comprehensive and three-dimensional land-atmosphere interaction after urban development. The UHI is determined more by “trap effect” from urban complex geometry or anthropogenic heat after urban expansion and that surface UHI according to the inversion temperature from remote sensing data cannot reflect UHI truly and comprehensively. (2) The urban development increased local temperature and available energy ratio (B) no matter if the ISA was converted by oasis or desert. Compared with the original undeveloped environment, local climate was in a relatively balanced state in 1978 and 1993 due to “heating effect” of urban and “cooling effect” of oasis, but the offsetting effect from oasis would become weaker

with the increasing of ISA. We hope the report can not only be beneficial to local planners but be helpful to regional climate researchers.

Data Availability

The data including validating data, forcing data for land surface model, code for processing output from land surface model, et al. used to support the findings of this study have been deposited in the “GitHub” repository (<https://github.com/mmzpb/Urban-in-arid-area>).

Additional Points

Highlights. 2 m urban heat island (UHI) intensity during night is higher than that during the day. UHI intensity is contributed more by “trap effect” from urban complex geometry or anthropogenic heat. Surface UHI according to land surface temperature from remote sensing data cannot reflect

UHI truly and comprehensively. Local climate in the study area was in a relatively balanced state in 1978 and 1993 due to “heating effect” of urban and “cooling effect” of oasis.

Conflicts of Interest

The authors declare that they have no conflicts of interest.

Acknowledgments

This work was financially supported by the National Natural Science Foundation of China (Grant Nos. 41801095 and 4167112) and the Fundamental Research Funds for the Central Universities (Grant No. GK201903117).

References

- [1] M. V. K. Aparna Dwivedi and B. K. Mohan, “Estimation of land surface temperature to study urban heat island effect in Mumbai using Landsat ETM+ image,” *International Journal of Remote Sensing and GIS*, vol. 4, no. 1, pp. 8–16, 2015.
- [2] S. Grossman-Clarke, J. A. Zehnder, T. Loridan, and C. S. B. Grimmond, “Contribution of land use changes to near-surface air temperatures during recent summer extreme heat events in the Phoenix metropolitan area,” *Journal of Applied Meteorology and Climatology*, vol. 49, no. 8, pp. 1649–1664, 2010.
- [3] R. Hamdi, A. Deckmyn, P. Termonia et al., “Effects of historical urbanization in the Brussels capital region on surface air temperature time series: a model study,” *Journal of Applied Meteorology and Climatology*, vol. 48, no. 10, pp. 2181–2196, 2009.
- [4] R. Hamdi, O. Giot, R. De Troch, A. Deckmyn, and P. Termonia, “Future climate of Brussels and Paris for the 2050s under the A1B scenario,” *Urban Climate*, vol. 12, pp. 160–182, 2015.
- [5] D. Li, T. Sun, M. Liu, L. Yang, L. Wang, and Z. Gao, “Contrasting responses of urban and rural surface energy budgets to heat waves explain synergies between urban heat islands and heat waves,” *Environmental Research Letters*, vol. 10, no. 5, 2015.
- [6] T. Loridan, F. Lindberg, O. Jorba, S. Kotthaus, S. Grossman-Clarke, and C. S. B. Grimmond, “High resolution simulation of the variability of surface energy balance fluxes across Central London with urban zones for energy partitioning,” *Boundary-Layer Meteorology*, vol. 147, no. 3, pp. 493–523, 2013.
- [7] Z. Hu, C. Zhang, Q. Hu, and H. Tian, “Temperature changes in Central Asia from 1979 to 2011 based on multiple datasets,” *Journal of Climate*, vol. 27, no. 3, pp. 1143–1167, 2014.
- [8] C. Li, C. Zhang, G. Luo et al., “Carbon stock and its responses to climate change in Central Asia,” *Global Change Biology*, vol. 21, no. 5, pp. 1951–1967, 2015.
- [9] C. Gao, J. Lei, and F. Jin, “The classification and assessment of vulnerability of man-land system of oasis city in arid area,” *Frontiers of Earth Science*, vol. 7, no. 4, pp. 406–416, 2013.
- [10] Y. Yang and Y. Liu, “Spatio-temporal analysis of urbanization and land and water resources efficiency of oasis cities in Tarim River Basin,” *Journal of Geographical Sciences*, vol. 24, no. 3, pp. 509–525, 2014.
- [11] G. Luo, Y. Feng, B. Zhang, and W. Cheng, “Sustainable land-use patterns for arid lands: a case study in the northern slope areas of the Tianshan Mountains,” *Journal of Geographical Sciences*, vol. 20, no. 4, pp. 510–524, 2010.
- [12] B. Lamptey, E. Barron, and D. Pollard, “Impacts of agriculture and urbanization on the climate of the northeastern United States,” *Global and Planetary Change*, vol. 49, no. 3–4, pp. 203–221, 2005.
- [13] S. Z. Qi, X. Y. Li, and H. P. Duan, “Oasis land-use change and its environmental impact in Jinta Oasis, arid northwestern China,” *Environmental Monitoring and Assessment*, vol. 134, no. 1–3, pp. 313–320, 2007.
- [14] M. Zhang, G. Luo, P. De Maeyer, P. Cai, and A. Kurban, “Improved atmospheric modelling of the oasis-desert system in Central Asia using WRF with actual satellite products,” *Remote Sensing*, vol. 9, no. 12, p. 1273, 2017.
- [15] M. Zhang, G. Luo, R. Hamdi et al., “Numerical simulations of the impacts of mountain on oasis effects in arid Central Asia,” *Atmosphere*, vol. 8, no. 12, p. 212, 2017.
- [16] J. W. Yan, J. Y. Liu, B. Z. Chen et al., “Changes in the land surface energy budget in eastern China over the past three decades: contributions of land-cover change and climate change,” *Journal of Climate*, vol. 27, no. 24, pp. 9233–9252, 2014.
- [17] D. S. Lu, G. Y. Li, E. Moran, M. Batistella, and C. C. Freitas, “Mapping impervious surfaces with the integrated use of Landsat Thematic Mapper and radar data: a case study in an urban-rural landscape in the Brazilian Amazon,” *Isprs Journal of Photogrammetry and Remote Sensing*, vol. 66, no. 6, pp. 798–808, 2011.
- [18] F. Yuan and M. E. Bauer, “Comparison of impervious surface area and normalized difference vegetation index as indicators of surface urban heat island effects in Landsat imagery,” *Remote Sensing of Environment*, vol. 106, no. 3, pp. 375–386, 2007.
- [19] E. Vardoulakis, D. Karamanis, A. Fotiadis, and G. Mihalakakou, “The urban heat island effect in a small Mediterranean city of high summer temperatures and cooling energy demands,” *Solar Energy*, vol. 94, pp. 128–144, 2013.
- [20] M. L. Imhoff, P. Zhang, R. E. Wolfe, and L. Bounoua, “Remote sensing of the urban heat island effect across biomes in the continental USA,” *Remote Sensing of Environment*, vol. 114, no. 3, pp. 504–513, 2010.
- [21] P. A. Mirzaei, “Recent challenges in modeling of urban heat island,” *Sustainable Cities and Society*, vol. 19, pp. 200–206, 2015.
- [22] E. M. Fischer, K. W. Oleson, and D. M. Lawrence, “Contrasting urban and rural heat stress responses to climate change,” *Geophysical Research Letters*, vol. 39, no. 3, 2012.
- [23] R. Hamdi and G. Schayes, “Sensitivity study of the urban heat island intensity to urban characteristics,” *International Journal of Climatology*, vol. 28, no. 7, pp. 973–982, 2008.
- [24] L. Wang, Z. Gao, S. Miao et al., “Contrasting characteristics of the surface energy balance between the urban and rural areas of Beijing,” *Advances in Atmospheric Sciences*, vol. 32, p. 10, 2015.
- [25] R. Hamdi, “Estimating urban heat island effects on the temperature series of Uccle (Brussels, Belgium) using remote sensing data and a land surface scheme,” *Remote Sensing*, vol. 2, no. 12, pp. 2773–2784, 2010.
- [26] G. Luo, C. Zhou, and X. Chen, “Process of land use/land cover change in the oasis of arid region,” *Acta Geographica Sinica Chinese Edition*, vol. 58, pp. 63–72, 2003.

- [27] P. Le Moigne, A. Boone, J. Calvet, B. Decharme, S. Faroux, and A. Gibelin, "SURFEX scientific documentation," in *Note de centre (CNRM/GMME)*, Météo-France, Toulouse, France, 2009.
- [28] V. Masson, C. S. B. Grimmond, and T. R. Oke, "Evaluation of the town energy balance (TEB) scheme with direct measurements from dry districts in two cities," *Journal of Applied Meteorology*, vol. 41, pp. 1011–1026, 2002.
- [29] V. Masson, P. Le Moigne, E. Martin et al., "The SURFEXv7.2 land and ocean surface platform for coupled or offline simulation of earth surface variables and fluxes," *Geoscientific Model Development*, vol. 6, no. 4, pp. 929–960, 2013.
- [30] J. Noilhan and J. F. Mahfouf, "The ISBA land surface parameterisation scheme," *Global and Planetary Change*, vol. 13, no. 1–4, pp. 145–159, 1996.
- [31] C. Deng and C. Wu, "A spatially adaptive spectral mixture analysis for mapping subpixel urban impervious surface distribution," *Remote Sensing of Environment*, vol. 133, pp. 62–70, 2013.
- [32] D. Lu and Q. Weng, "Use of impervious surface in urban land-use classification," *Remote Sensing of Environment*, vol. 102, no. 1–2, pp. 146–160, 2006.
- [33] D. S. Lu and Q. H. Weng, "Spectral mixture analysis of ASTER images for examining the relationship between urban thermal features and biophysical descriptors in Indianapolis, Indiana, USA," *Remote Sensing of Environment*, vol. 104, no. 2, pp. 157–167, 2006.
- [34] M. M. Rienecker, M. J. Suarez, R. Gelaro et al., "MERRA: NASA's modern-era retrospective analysis for research and applications," *Journal of Climate*, vol. 24, no. 14, pp. 3624–3648, 2011.
- [35] Z. Hu, Q. Hu, C. Zhang, X. Chen, and Q. Li, "Evaluation of reanalysis, spatially interpolated and satellite remotely sensed precipitation data sets in Central Asia," *Journal of Geophysical Research: Atmospheres*, vol. 121, no. 10, pp. 5648–5663, 2016.
- [36] Y. Shen, S. Li, Y. Chen, Y. Qi, and S. Zhang, "Estimation of regional irrigation water requirement and water supply risk in the arid region of Northwestern China 1989–2010," *Agricultural Water Management*, vol. 128, pp. 55–64, 2013.
- [37] N. Dağdelen, E. Yılmaz, F. Sezgin, and T. Gürbüz, "Water-yield relation and water use efficiency of cotton (*Gossypium hirsutum*) and second crop corn (*Zea mays* L.) in western Turkey," *Agricultural Water Management*, vol. 82, no. 1–2, pp. 63–85, 2006.
- [38] D. Haboudane, "Hyperspectral vegetation indices and novel algorithms for predicting green LAI of crop canopies: modeling and validation in the context of precision agriculture," *Remote Sensing of Environment*, vol. 90, no. 3, pp. 337–352, 2004.
- [39] S. K. Hicks and R. J. Lascano, "Estimation of leaf area index for cotton canopies using the LI-COR LAI-2000 plant canopy analyzer," *Agronomy Journal*, vol. 87, no. 3, pp. 458–464, 1995.
- [40] C. Romeo and M. Zinzi, "Impact of a cool roof application on the energy and comfort performance in an existing non-residential building. A Sicilian case study," *Energy and Buildings*, vol. 67, pp. 647–657, 2013.
- [41] A. Takano, S. K. Pal, M. Kuittinen, K. Alanne, M. Hughes, and S. Winter, "The effect of material selection on life cycle energy balance: a case study on a hypothetical building model in Finland," *Building and Environment*, vol. 89, pp. 192–202, 2015.
- [42] J. S. Golden and K. E. Kaloush, "Mesoscale and microscale evaluation of surface pavement impacts on the urban heat island effects," *International Journal of Pavement Engineering*, vol. 7, no. 1, pp. 37–52, 2006.
- [43] R. Hamdi and V. Masson, "Inclusion of a drag approach in the town energy balance (TEB) scheme: offline 1D evaluation in a street canyon," *Journal of Applied Meteorology and Climatology*, vol. 47, no. 10, pp. 2627–2644, 2008.
- [44] C. J. Willmott, "Some comments on the evaluation of model performance," *Bulletin of the American Meteorological Society*, vol. 63, no. 11, pp. 1309–1313, 1982.
- [45] A. J. Arnfield, "Two decades of urban climate research: a review of turbulence, exchanges of energy and water, and the urban heat island," *International Journal of Climatology*, vol. 23, no. 1, pp. 1–26, 2003.
- [46] L. Allen, F. Lindberg, and C. S. B. Grimmond, "Global to city scale urban anthropogenic heat flux: model and variability," *International Journal of Climatology*, vol. 31, no. 13, pp. 1990–2005, 2011.
- [47] R. Khatun, M. Farukh, A. Miyata, and M. Baten, "Bowen ratio measurements of energy budget components over various ecosystems in Mymensingh, Bangladesh," *Journal of Environmental Science and Natural Resources*, vol. 7, no. 1, p. 4, 2015.
- [48] F. Fang, J. Guo, L. Sun, J. Wang, and X. Wang, "The effects of urbanization on temperature trends in different economic periods and geographical environments in northwestern China," *Theoretical and Applied Climatology*, vol. 116, no. 1–2, pp. 227–241, 2013.
- [49] C. S. B. Grimmond, M. Blackett, M. J. Best et al., "Initial results from phase 2 of the international urban energy balance model comparison," *International Journal of Climatology*, vol. 31, no. 2, pp. 244–272, 2011.

Research Article

Optimized Cluster-Based Dynamic Energy-Aware Routing Protocol for Wireless Sensor Networks in Agriculture Precision

Kashif Naseer Qureshi¹,¹ Muhammad Umair Bashir,¹ Jaime Lloret²,² and Antonio Leon²

¹Department of Computer Science, Bahria University, Islamabad, Pakistan

²Universitat Politècnica de Valencia, Spain

Correspondence should be addressed to Kashif Naseer Qureshi; kashifnq@gmail.com and Jaime Lloret; jlloret@dcom.upv.es

Received 28 October 2019; Accepted 2 December 2019; Published 31 January 2020

Guest Editor: Zhenxing Zhang

Copyright © 2020 Kashif Naseer Qureshi et al. This is an open access article distributed under the Creative Commons Attribution License, which permits unrestricted use, distribution, and reproduction in any medium, provided the original work is properly cited.

Wireless sensor networks (WSNs) are becoming one of the demanding platforms, where sensor nodes are sensing and monitoring the physical or environmental conditions and transmit the data to the base station via multihop routing. Agriculture sector also adopted these networks to promote innovations for environmental friendly farming methods, lower the management cost, and achieve scientific cultivation. Due to limited capabilities, the sensor nodes have suffered with energy issues and complex routing processes and lead to data transmission failure and delay in the sensor-based agriculture fields. Due to these limitations, the sensor nodes near the base station are always relaying on it and cause extra burden on base station or going into useless state. To address these issues, this study proposes a Gateway Clustering Energy-Efficient Centroid- (GCEEC-) based routing protocol where cluster head is selected from the centroid position and gateway nodes are selected from each cluster. Gateway node reduces the data load from cluster head nodes and forwards the data towards the base station. Simulation has performed to evaluate the proposed protocol with state-of-the-art protocols. The experimental results indicated the better performance of proposed protocol and provide more feasible WSN-based monitoring for temperature, humidity, and illumination in agriculture sector.

1. Introduction

Precision agriculture refers to a science using advance technologies to provide cost management, crop growth, and production in agriculture fields. One of the major driver of agriculture precision is wireless sensor networks (WSNs) where the sensor nodes are monitoring the physical or environmental conditions including humidity, temperature, and illumination and send the sensed data to the base station (BS) via single-hop or multihop coordinator nodes [1–3]. This technology has various beneficial applications in other fields like healthcare, military, transportation, security, and agriculture. In healthcare, sensor nodes have deployed to collect the patient physiological or biometric information such as ECG, heart rate, and blood pressure [4]. In the military, sensor nodes are deployed to track the soldiers on the battlefield, for monitoring, find the location of platoons, and protect the forces. In security, sensor nodes can offer a careful

watch to track and monitor the dangerous situation and remain alert against terrorist attacks [5]. In agriculture, sensor nodes are deployed to sense the temperature, pressure, humidity, and wind speed. In addition, the sensor nodes also sense environmental conditions for weather forecast and natural disaster happening probability. In these networks, the sensor nodes are categorized into coordinator and normal nodes to collect the data from the agricultural field [6]. The sensor nodes sense the required parameters and analyze the distance threshold (d_{Th}) and then forward the sensed data to the sink node by single-hop or multihop communication. The role of the sink node is to collect the data from sensor nodes and further transmit to gateway or BS and then further send to the central management system for decision making as shown in Figure 1.

Sensor nodes are small in size with low computational power and energy resources [7]. Sensor nodes are used for monitoring the environmental conditions like crop conditions

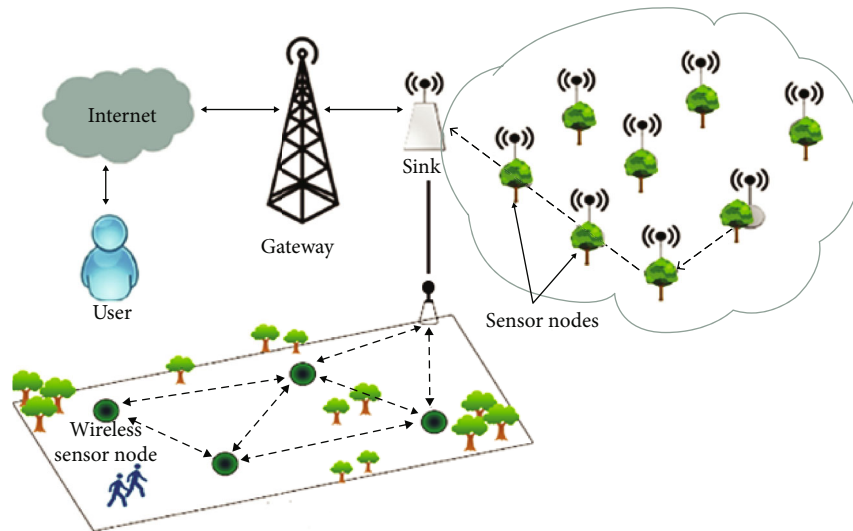


FIGURE 1: Architecture field with WSN deployment.

and other environmental parameters. The sensor nodes are deployed on the surface of soil or inside the soil. There are different technologies and standards which have been adopted based on applications and data rate, frequency band, power consumption, and distance. Some common technologies are Wibree, Wifi, GPRS, WiMAX, Bluetooth, and ZigBee [2, 8]. Monitored data was obtained from the deployed sensor nodes and then was wirelessly forwarded to the BS for data collection. The BS initiates the decision for further processes. Users received the crop growth information or other information related to the drip irrigation and take further initiatives to improve the microenvironment for their product [9]. In agriculture, for achieving the precision control, the sensor nodes monitored different parameters, analysis of monitored data for decision making and applying the control mechanism [10, 11]. There are various efforts to improve the cultivation in agriculture, precision farming, collecting, and sending the monitored data [12, 13]. The monitored data is about environmental conditions including weather, wind speed, temperature, soil humidity, chemical and physical properties of soil like the pH level, crop identification, leaf area index, leaf moisture content, and weed-disease detection. There is another way in which the sensor nodes captured the images of fruits, for automated harvesting, and predicted the soil moisture and organic contents [14, 15]. Mobility-based sensor nodes are used to measure the plant mass of crops and analyze the fertilization characteristics for best production. Soil strength measurement and prediction-based harvesting time are evaluated through special sensors [16, 17].

In addition, most of the agriculture precision WSN-based applications need in time and reliable data communication in the network. Due to limited battery resources, sensor nodes are not able to maintain their operations; recharging and replacement of batteries are not possible especially in dense forests and large areas [18, 19]. For data communication, the routing protocols are used to maintain the load balancing and maximize network lifetime. There are two main types of

protocol flat and hierarchical. In flat routing protocols, all the nodes in the network play an identical role. The main issue in flat routing protocols is scalability, load balancing, route maintenance, and not feasible for the large networks [20, 21]. To address the scalability and load balancing issues in flat routing, hierarchical routing protocols are introduced. It is also called cluster-based routing, in which all sensor nodes in the network are separated into layers based on residual energy and assigned the different roles. In the entire network, the sensor nodes are divided into a group called clusters [22]. Each cluster has cluster members (CMs) and one cluster head (CH). The CH is responsible for coordination within the cluster and forwarding the data to other CHs or BS. Hierarchical routing protocols or clustering protocols are helpful especially for large-scale agriculture precision-based WSN. It utilized fewer resources, save more energy of sensor nodes, scalable, less packet overhead, and efficiently balances the load among the network as compared to flat routing protocol [23–25].

Complex routing processes and data transmission are the main causes of energy depletion among sensor nodes in agricultural precision WSN [26, 27]. Aiming at a higher energy efficiency for the entire network, a new protocol named Gateway Clustering Energy-Efficient Centroid (GCEEC) routing protocol is proposed to manage the energy resources. The main contributions of this paper is to minimize the energy consumption of sensor nodes and to reduce the load on CHs. The proposed protocol selects and rotates the CH on efficient location, i.e., near the energy centroid position in the cluster to reduce the energy consumption of sensor nodes in cluster and maximize the CH coverage. Furthermore, the protocol selects gateway node in cluster to facilitate the CH in agriculture environment and significantly reduces the load on CH.

The main objectives of this paper are as follow:

- (i) To minimize the energy consumption and load balancing of the CH by the help of gateway node

- (ii) Edge node becomes a gateway node to receive more than one joining message from adjacent CHs

The rest of the paper is organized as follows: Section 2 presents the related work in the area of agriculture-based WSN and its existing energy-based routing protocols. Section 3 presents the proposed work design and all steps including flow chart and algorithm. Section 4 presents the experimental results and analysis with state-of-the-art protocols. Last section concludes the paper with future direction.

2. Related Work

This section discussed the existing energy-efficient routing protocols for agriculture precession-based WSN and critically analyzed to find their limitations. Energy-efficient routing protocols are categorized into two categories, flat routing protocol and hierarchical routing protocols which are discussed in detail.

2.1. Flat Routing Protocol. In flat routing, all nodes in the network have the same role and perform the same tasks [24].

In [28], the authors proposed the dynamic distributed framework protocol known as Energy and Trust-Aware Mobile Agent Migration (ETMAM), in which a mobile agent is used to making route among sensor nodes for data aggregation based on energy and trust metric evaluation. A mobile agent is a self-determined software agent that can move autonomously among sensor nodes and carry the data for aggregation. To protect a mobile agent from malicious sensor nodes, ETMAM framework provides trust evaluation to the mobile agent and bypass the malicious sensor nodes. Furthermore, the framework also provides optimize migration route based on energy metrics as well as cloning method to aggregate the data from the sensor node. However, the proposed framework supports small route mobile agent and is where response time is low. Power-Aware Heterogeneous AODV (PHAODV) in [29] was proposed for the resource that should be utilized efficiently. In this protocol, the optimized routing path is created by considering the energy status of every sensor node to achieve the load balancing among heterogeneous networks. The path which consumes the least energy is selected as a routing path for data communication from the existing path in the routing table. Therefore, all the sensor nodes are keeping aware of the instantaneous change in energy level. Furthermore, link-aware dynamic threshold prevents from route exhausting and reduces the route error message. However, this protocol has more overhead which leads to energy depletion issues in the network.

An Optimal Base Transmission Strategy (OTDS) [30] is proposed in which transmission distance is calculated to balance the energy consumption of the entire network. Data mule concept is proposed in which data is collected from sensor nodes and transmits to the BS. Data mule is a mobile node having sufficient storage and energy and collects the data from sensor nodes while roaming across the sensor field and sends it to the BS. PEGASIS-DSR Optimized Routing Protocol (PDORP) is proposed in [31] based on a hybrid

approach having both characteristics of proactive (PEGASIS) and reactive (DSR) approach. Utilization of directional transmission scheme helps reduce the communication distance which ensures energy efficiency. Furthermore, a trust list is generated by each node to avoid acknowledgment of receiving packets; this will be updated at each round and randomly checked at any time. Besides this, PDROP also adopts a Genetic Algorithm (GA) and Bacterial Foraging Optimization (BFO) to discover the optimized path. However, complex routing processes consume more energy and have a serious impact on the network.

2.2. Hierarchical Routing Protocol. It is also called clustering routing protocols. In these protocols, the whole network nodes are divided into a group of nodes called clusters. Each cluster selects CH node which is responsible for transmitting the data to the BS.

In [32], the authors proposed a Mobile Sink-based Adaptive Immune Energy-Efficient clustering Protocol (MSIEEP) and addressed the energy hole problem. The protocol uses Adaptive Immune Algorithm (AIA) to find the sojourn path for the mobile sink. Moreover, the algorithm also finds the optimize number of CHs based on their dissipated energy and favorable location. AIA acts as a guide of the mobile sink. The significance of mobile sink is to collect the data from the isolated region of the CH which improved the connectivity of the network. The protocol does not fully address the hole problem due to load balancing issue. In [33], the authors proposed a distributed clustering algorithm, namely, Delay-Constrained Energy Multihop (DCEM) in which CH is selected in a distributed manner. BS initiates the protocol by broadcasting ADV message among network sensor nodes; therefore, each node calculates the distance between itself and BS using receive signal strength technique. After that, every sensor node broadcasts the advertisement message that contains its ID and energy level to its neighbor sensor nodes so that every neighbor node on receiving advertisement message compares its energy level with energy level information in receiving advertisement message. If the energy level is greater, then the sensor node becomes candidate CH; otherwise, it remains a cluster member. Similarly, the candidate CH elects by broadcasting an advertisement message procedure and becomes CH. The candidate CH with the same energy level is further proceeded by computing the trade-off energy and delay (TED) value. After computing, the candidate CH waits for the TED value to receive an advertisement message otherwise becomes the CH. Furthermore, the DCEM protocol uses intercluster multihop routing cost function to achieve a minimum cost route from CH to BS. DCEM does not consider the optimal location of the CH in cluster intercluster multihop routing among CH which consumes more energy.

In [23], the authors proposed the PSO-ECHS (Particle Swarm Optimization-Energy Efficient-based Cluster Head Selection) protocol that enhanced the network lifetime. In the PSO-ECHS algorithm, the CH is selected by fitness functions that consider the distance between sensor node and BS, as well as sensor node and neighbor nodes, and the residual energy of sensor nodes. By a minimum value of fitness

function, the CH selected and start cluster formation by broadcasting the joining message. Each sensor node after receiving and joining messages calculates the joining weight value. The sensor node joins the CH which has the highest joining weight value. In [34], the authors proposed the Energy-Efficient Centroid-based Routing Protocol (EECRP) for data routing using wireless sensor devices. The term “centroid” is the mechanical engineering term which means the imaginary central point of mass concentration. Initially in protocol, the BS computes the energy centroid position among the network and divides the network into a cluster based on energy centroid position. The node near the energy centroid position is selected as the CH. At the time of CH rotation, the CH recomputed the energy centroid position and the node which is near to the energy centroid position elected as the next CH. Furthermore, the protocol also fixed the threshold distance called MAX distance between the CH and the BS where the CH transmits the data to the CM. If CH and BS distance are less than MAX distance, then the CH stores the information in the cache and deliver to the next elected CH at the time of CH rotation.

In [35], the authors proposed the Distributed Unequal Size Optimize Cluster (DUSOC) base technique to resolve the load balancing issue in the CH. According to the protocol, the BS elects the CH node based on an energy level as well as the distance from BS. The CH near the BS chooses the least number of sensor nodes as compared to the CH which is far away from the BS during the cluster formation stage. Furthermore, intercluster multihop routing among the CH approach is adopted for data transmission towards the BS. In [36], the authors proposed the Mobile Energy-Aware Cluster-Based Multihop (MEACBM) routing protocol in which heterogeneous WSN is divided into clusters, selecting the CH with the highest residual energy. Furthermore, the protocol maintains the coverage and connectivity in the network by constructing a subcluster for nodes that deployed far away in the network and compute the multihop route for interclustering combination among clusters and subclusters. After selecting CH, the algorithm divides the network into sectors and each sector is assigned with Mobile Data Cluster (MDC) node that collects the data from the CH. MDC node computes an efficient route that is found by Expectational Maximization (EM) algorithm. According to the EM algorithm, MDC computes the route by considering the CH residual energy and location. MDC moves to collect the data from the CH first, whose residual energy is minimum. Similarly, the MDC node collects data from other CH on an efficient route and delivered to the BS.

The authors in [37] proposed a Cluster Aided Multipath Routing (CAMP) protocol which divided the region of interest into virtual zones and assign one CH for each cluster. The noncluster member's nodes have adopted the trade-off method for residual energy evaluation between itself and neighbor nodes and take decision. During this process, if the cluster member node is selected as the next forwarder, then it cancels the trade-off method and forwards the data to the CH via multihop communication. The authors claimed that the proposed CAMP protocol improves the energy consumption due to randomly selection of CH or

based on residual energies of the nodes. In addition, CAMP also adjusts the tuning factors including remaining energy, node degree, and distance towards the sink node. However, with many benefits, this protocol has significant delay due to its energy calculation and randomly selection of CH in the network.

All the discussed studies mainly focused on energy-efficient routing for WSN that reveal the strength and limitations that lead to the development of the research problem. Based on the literature review, it is revealed that the CH has a heavy responsibility for data transmission of the cluster data towards the BS directly or relaying through other CH. The CH which directly sends data towards the BS consumes more energy. The CH far from the BS required more energy in transmitting cluster data towards the BS in a single hop. Consequently, these issues lead to the early energy depletion of CH's which are far from the BS. Moreover, in many schemes such as DUSOC [35], and DCEM [33], CAMP [37] CH sends the data towards the BS via intercluster multihopping. The CH near the sink continuously forwards the CH data towards the BS. Therefore, uneven load distribution among CHs tend to deplete their energy resources rapidly which leads to disrupt the data dissemination process and generate routing holes. The CH node selection and CH responsibility rotation are one of the most important features. Therefore, network coverage of CH among cluster nodes reduces and consumes more energy for data transmission to their CH. The optimal location of CH is an important factor which enhances the network coverage among clusters. The optimal location of CH must consider the position where energy density nodes found so that the CH responsibility rotation is must among the nodes that are rich in energy. It is discussed above that most of the existing clustering schemes such as DCEM [33] must improve their intercluster multihopping process to overcome load on the CH. Table 1 presents the protocol comparison in terms of their strategies and limitations.

3. Gateway Clustering Energy-Efficient Centroid (GCEEC) Protocol

The Gateway Energy-Efficient Centroid (GCEEC) routing protocol is proposed for agriculture precision WSN to improve the load balancing among CHs and energy consumption of the whole network. The GCEEC protocol selects the efficient location of CH near the energy centroid position and for gateway node selection for transmitting the data towards the BS via multihop communication which maximizes the CH coverage and reduces the transmission power of CH. This section is divided into two subsection network setup modules and process module. The network setup module presents the energy consumption model, energy centroid position, gateway node weight, and CH joining weight used in GCEEC protocol. The processing module explains the setup phase, transmission phase, and rotation phase of GCEEC.

3.1. Network Setup Module. The network model consists of 100 sensor nodes and one BS. Figure 2 shows the sensor

TABLE 1: Protocol strategies and limitations.

S#	Authors	Cluster	Strategies	Limitations
Flat routing protocols				
1	ETMAM [28] 2014	✗	Mobile agent route among the sensor for data aggregation considering energy and trust metrics	Framework support small route mobile agent and response time is low
2	PHADOV [29] 2014	✗	Link condition for optimize path, prevent route exhausting, and reduce route error message	Routing overhead increase
3	OTDS [30] 2015	✗	Data mule (mobile node) that has the ability to collect and store data from sensor node and transmit towards BS	In sufficient for different constraint and energy hole problem
4	PDORP [31] 2016	✗	Generate trust list to avoid acknowledgement	Cause significant delay
Hierarchical routing protocol				
5	MISSEEP [32] 2015	✓	Mobile sink for collecting data to alleviate hole	Protocol not fully addressed hole problem due to load balancing issue
6	DCEM [33] 2016	✓	Minimum inter cluster multihop routing cost function	DCEM not consider the optimal location of CH in cluster Intercluster multihop routing among CH consume more energy of CH
7	PSO-ECHS [23] 2017	✓	CH is selected by fitness functions that consider the distance between sensor node and BS, as well as sensor node and neighbor nodes, and the residual energy of sensor nodes	Robustness of the algorithm, however, needs to be verified with the heterogeneous nature of nodes
8	EECRP [34] 2017	✓	CH selected in energy density node region	MAX-dist consume more energy of CH in caching and transferring data
9	Awan et al. [35] 2018	✓	Cluster size reduction	Not focus on energy-efficient optimize route among cluster head
10	MEACBM [36] 2019	✓	Mobile data cluster node utilizes as CH data collection and transfer to BS	Subcluster nodes are taking more processes and lead to network overhead
5	CAMP [37] 2019	✓	Adjusts the tuning factors including remaining energy, node degree, distance towards the sink node.	Has significant delay due to its energy calculation and randomly selection of CH in the network.

nodes which are randomly distributed in the sensor field. Each sensor node after sensing sends the data to the regional CH, then transfer the data towards the BS via single-hop direct transmission or multihop gateway nodes; it depends on the distance between CH and BS.

3.1.1. Energy Consumption Model. Most of the energy is consumed by the sensor node during data transmission and receiving. The most popular and common energy model is proposed in [34] as shown in the following:

$$E = \begin{cases} l(e_r + e_t + \epsilon_{fs}d^2), & \text{if } d \leq d_{Th}, \\ l(e_r + e_t + \epsilon_{mp}d^4), & \text{if } d \geq d_{Th}, \end{cases} \quad (1)$$

where l is the packet size, e_r and e_t are the transmitting and receiving energy, ϵ_{fs} and ϵ_{mp} are required energy to send in free space and multipath, respectively. The transmission energy consumption depends on distance d .

3.1.2. Energy Centroid. Centroid is the mechanical term, which means the imaginary central point of mass concentration. It is the central point where the entire mass of object is concentrated. Similarly, energy centroid in cluster is the point where sensor node is having massive energy concentration which is distributed. Energy centroid [34] can be mathematically represented as in Equations (2) and (3), respectively.

$$X_{ec} = \frac{\sum_{i=0}^n (E_{i_{rs}}/E_o)X}{N}, \quad (2)$$

$$Y_{ec} = \frac{\sum_{i=0}^n (E_{i_{rs}}/E_o)Y}{N}, \quad (3)$$

where $E_{i_{rs}}$ = residual energy of node i , E_o = initial energy, X and Y are the coordinate of node i , N = total number of nodes in cluster, X_{ec} and Y_{ec} are the energy centroid.

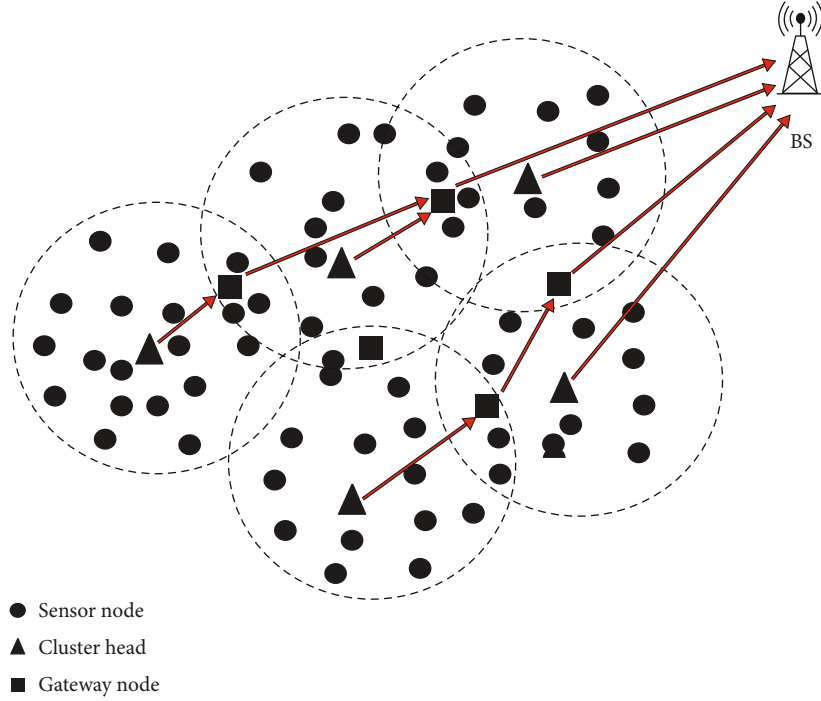


FIGURE 2: Network topology.

1-byte	1-byte	1-byte	1-byte	2-bytes
Message type	Sender's ID	X coordinate	Y coordinate	Energy level

FIGURE 3: LOCATION message.

Distance from the energy centroid position to the i^{th} sensor node for calculating candidate CH can be shown below.

$$d = \sqrt{(X_{ec} - X_i)^2 + (Y_{ec} - Y_i)^2}. \quad (4)$$

3.1.3. Gateway Node. Information gathering from sensor nodes and transmitting towards the BS is the main function of CH. Due to heavy responsibilities on CH due to the management of cluster data, the CH consumes more energy and sends the data directly to the BS or itself relaying on other CH and forwards the data towards the BS. Therefore, gateway node is formed in each cluster by CH which relay data towards the BS. The nodes in cluster which are adjacent to neighbor CH are called gateway nodes. Every CH computes the gateway node weight [38] by considering the CH residual energy, distance between the nodes in particular cluster and adjacent neighbor CH. The function is as follows:

$$G(i, j) = \left[\frac{S(i).E}{S(i).Max} \right] + \left[d(i, j)^2 + d(i, x)^2 + d(j, x)^2 + \frac{d(j, s)^2}{d(i, s)^2} \right], \quad (5)$$

where $S(i).E$ = residual energy of CH, $S(i).Max$ = initial energy, $d(i, j)$ = distance between CH i and CH j , $d(i, x)$ = distance between CH i to cluster member node x which are

adjacent to neighbor CH j , $d(j, x)$ = distance between adjacent CH j to cluster member node x of CH i , $d(j, s)$ = distance between CH j to BS, and $d(i, s)$ = distance between CH i to BS.

Higher weightage of node becomes a cluster gateway node.

3.1.4. Cluster Head Joining Weight Function. When CH sends join request to neighbors, then in response, sensor nodes decide to be part of cluster or not base on CH joining weight function. The function consists the following parameter, CH residual energy $E_{\text{residual}}(\text{CH}_j)$, distance from CH to sensor node $\text{dist}(s_i, \text{CH}_j)$, distance from CH to BS $\text{dist}(\text{CH}_j, \text{BS})$ [23].

$$\text{CH joining weight}(s_i, \text{CH}_j) = \frac{E_{\text{residual}}(\text{CH}_j)}{\text{dist}(s_i, \text{CH}_j) * \text{dist}(\text{CH}_j, \text{BS})}. \quad (6)$$

3.2. Process Module. In most of the agriculture precision WSNs, energy is the main concern due to limited resources of sensor nodes. The main objective of this study is design the protocol for energy-saving and efficiently utilize the resource during data processing. Clustering protocols

1-byte	1-byte	2-byte
Message type	CH ID	Avg energy

FIGURE 4: FEEDBACK message.

consist of three main phases: CH selection phase, gateway selection phase, data transmission, and CH rotation phase.

3.2.1. CH Selection Phase. Initially, the BS broadcasts the HELLO-MSG across the network. Hello message contains the BS ID and location. BS has more energy than ordinary sensor nodes, and if we use the BS to broadcast the Hello messages to other sensor nodes, it will decrease the load on other member nodes in the network. The sensor nodes send a reply with LOCATION message as shown in Figure 3. Message type contains the type of message. The “sender ID” contains the sensor node ID. The “X coordinate and Y coordinate” are the locations of the sensor node. The energy level contains the state of the sensor node. The LOCATION message size is 6 bytes as shown in Figure 3.

BS computes the average energy of the network and calculates the energy centroid positions in the network. After the calculation of energy centroid positions, BS divides the network into a cluster around the energy centroid position and chooses the CH. The BS chooses the CH node from the cluster which is nearest to the energy centroid position. After selecting the CH, the BS broadcasts the FEEDBACK message to the specific cluster as shown in Figure 4. The FEEDBACK message contains the message type and the information of feedback message, CH’s ID, and average energy of the network.

After the first CH selection by the BS, the CH transmits joining message containing the CH ID, energy level, and location to the neighbor sensor nodes. The sensor node that receives the joining message calculates the joining weight value of CH. If the highest CH joining weight value is reached, then the sensor node joins the CH as a CM. Figure 5 shows the CH selection process.

3.2.2. Gateway Selection Phase. After selection of CHs, each CM who receive adjacent CH joining request computes the gateway node weight. The gateway node weight is then sent to CH. Higher gateway node weight value is selected for a gateway node. Gateway node then informs the adjacent CH by sending gateway message containing its location and its CH ID as shown in Figure 6 showing the gateway message for requesting the adjacent CH for its gateway node. When adjacent CH gateway node receives, it then computes the route towards the BS via adjacent gateway node multihopping.

The data transmission of CH via gateway node depends on distance between itself and BS. If distance is less than threshold distance (d_{Th}), then CH sends directly to BS; otherwise, CH uses gateway node for data transmission towards BS. Figure 7 shows the gateway selection process.

3.2.3. Data Transmission and CH Rotation Phase. After the selection of CH and gateway node, the data communication

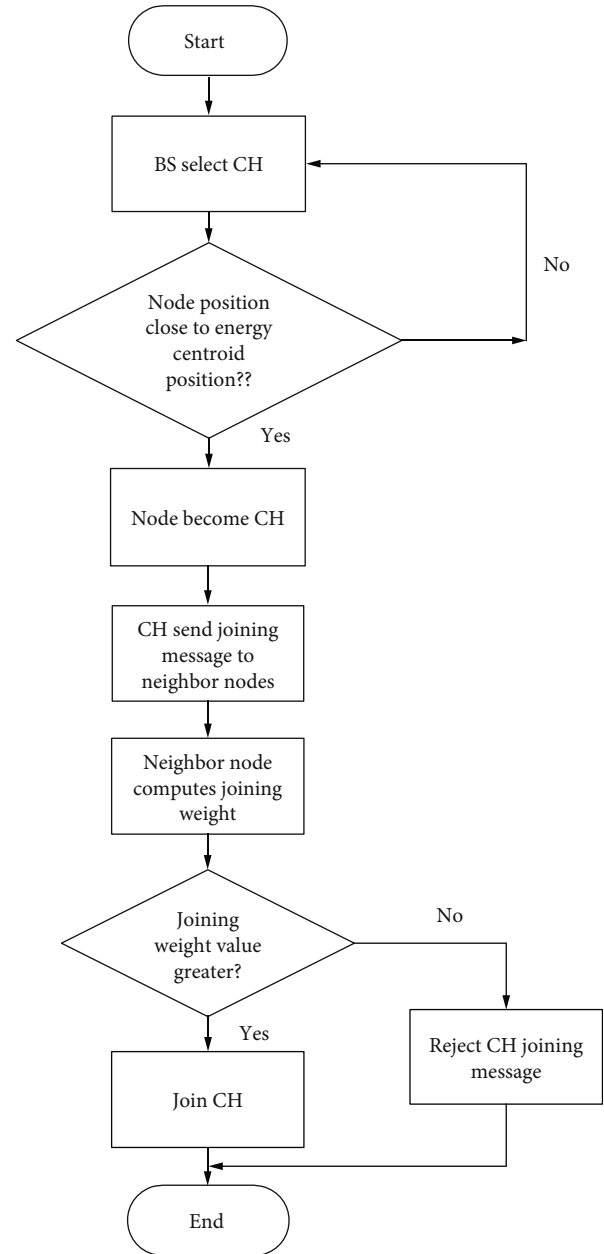


FIGURE 5: CH selection flow chart.

begins. CM senses the data and transmits to their particular CH. The CH then sends towards the BS via gateway nodes or directly transmits depending on threshold distance d_{Th} . Just before the end of the round, each CM sends their residual energy and location to CH. After that, the CH node calculates the average energy and energy centroid position. The CM that is near to the energy centroid position will be the next candidate CH. The following conditions for the CM can become the CH for the next round.

- (i) Its energy level is greater than the average energy of cluster
- (ii) Its distance from the energy centroid position of cluster is the smallest


```

1. Input: N=Total number of nodes
2. Output: BS divide entire network into Cluster
3. for i=1:N
4.   Node transmit their ID, Location and Energy level to BS
5. end for
6.  $E$  = Average Energy of entire network calculate by BS
7.  $c$  = centroid position of cluster calculate by BS =  $(X_c, Y_c)$ 
8. for i = 1 : C
9.    $c_i = (X_{ci}, Y_{ci})$ 
10.  for j = 1 : N
11.     $d_i = \text{dist}(\text{node}(i), c_i)$ 
12.    if (node(j) very close to  $c_i$ )
13.      Select as  $CH_j$ 
14.    end if
15.  end for
16. end for
17. BS Broadcast Feedback Message contain Message Type, CH ID, Avg Energy  $E$ 
18. for i = 1 : N
19.  node(i) receive Feedback Message from BS
20.  if (node(i) == CH ID)
21.    node(i) state =  $CH_i$ 
22.    Broadcast joining message  $CH_i$  to neighbor nodes
23.  else
24.    Wait for CH joining message
25.  end if
26. end for
27. Neighbor nodes calculates joining weight
28.    $CH \text{ Joining Weight } (s_i, CH_j) = E_{\text{residual}}(CH_j) / \text{dist}(s_i, CH_j) * \text{dist}(CH_j, BS)$ 
29. if (neighbor node CH Joining Weight greater)
30.   Join CH
31. else
32.   Reject CH joining message
33. end if

```

ALGORITHM 1: CH Selection Phase.

1-byte	1-byte	1-byte
Message type	Gateway node ID	CH ID

FIGURE 6: Gateway message.

Figure 8 shows the data transmission and CH rotation flow chart.

The detail of GCEEC data transmission and CH rotation is discussed in Algorithm 2. Lines 1 to 8 show the data transmission directly or via gateway node towards the BS from the CH. From lines 8 to 11, wait till just a few moments before the end of round, each CM sends residual energy and location to respective CH. From line 12 to 16, it calculates the average energy of cluster, recalculate energy centroid position, and distance between each node among cluster from energy centroid position. Lines 18 to 23 select the CH for next round if the energy level of node is greater than the average energy and distance between CH when centroid position is smaller. Algorithm 3 shows the gateway node selection process.

4. Simulation Setup and Experimental Results

To evaluate the performance of GCEEC with other relevant algorithms, simulator selection is one of the challenge. A number of simulation environments have been developed for wireless networks such as Objective Modular Network Testbed in C++ (OMNET++) [39], Network Simulator2 (NS2) [40], and MATLAB [41]. NS2 is an event-driven, open-source simulator and is the best tool for analyzing communication networks. The NS2 provides executable ns script file name “Tool Command Language (TCL).” A simulation trace file is generated after running TCL file which is used for plotting graphs or result analysis. NS2 provides a tool called NAM (Network Animator) to execute the animation files.nam. NS2 comprises of two main languages, i.e., C++ and Object-Oriented Tool command language (OTcl). C++ provides user facility to describe interior working mechanisms (executed at back-end) of the stimulation objects, while OTcl provides the facility to setup the stimulation scripts and configuration of objects (executed at front) [40, 42]. In addition, NS2 has open-source modules and widely exploits in the

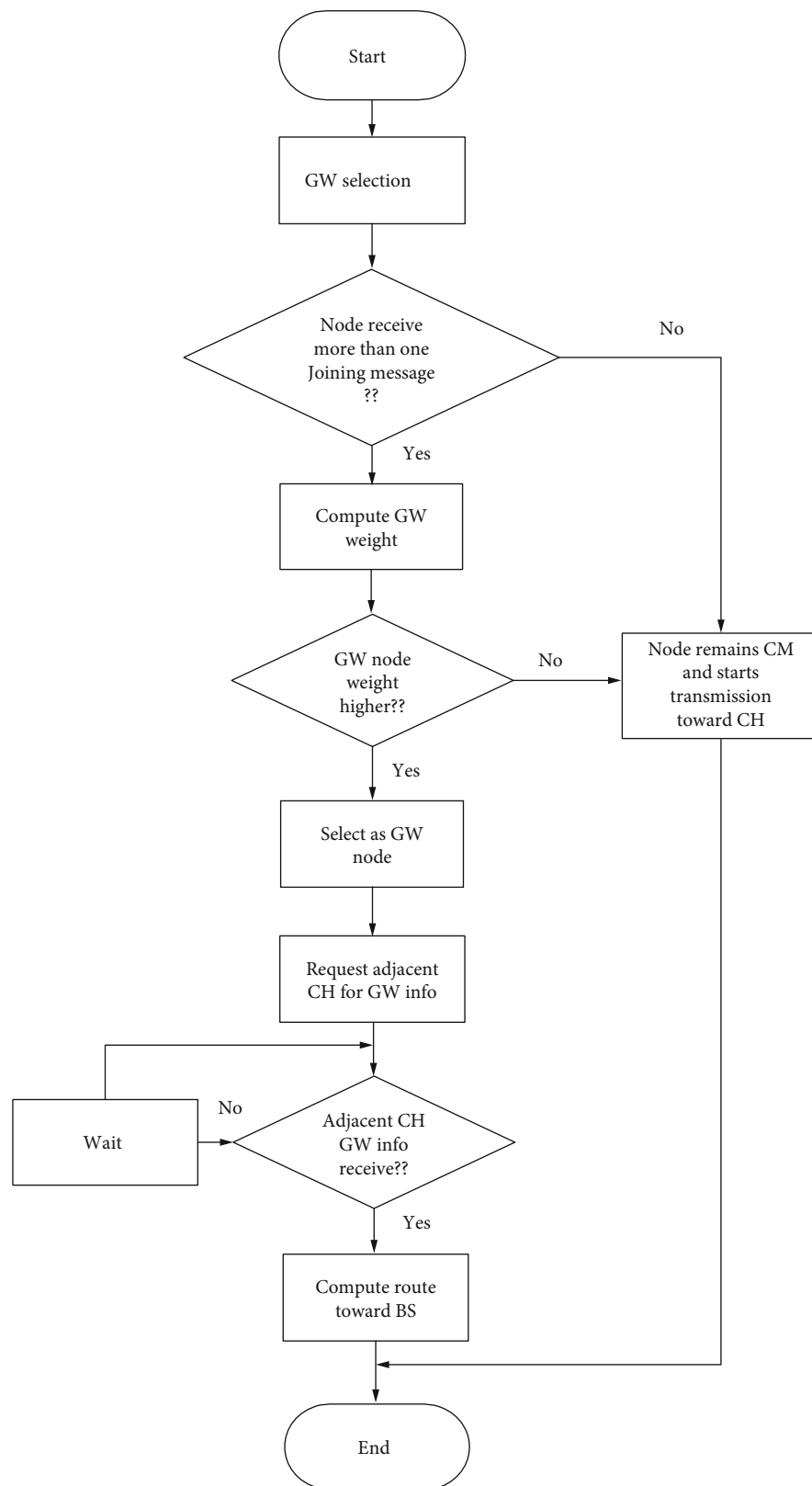


FIGURE 7: Gateway selection flow chart.

research community; new objects can be easily added using OTcl interpreter via corresponding objects in C++ class. In this research work, NS2 simulator is used to eval-

uate the performance of proposed GCEEC protocol with relevant scheme in terms of different performance parameters.

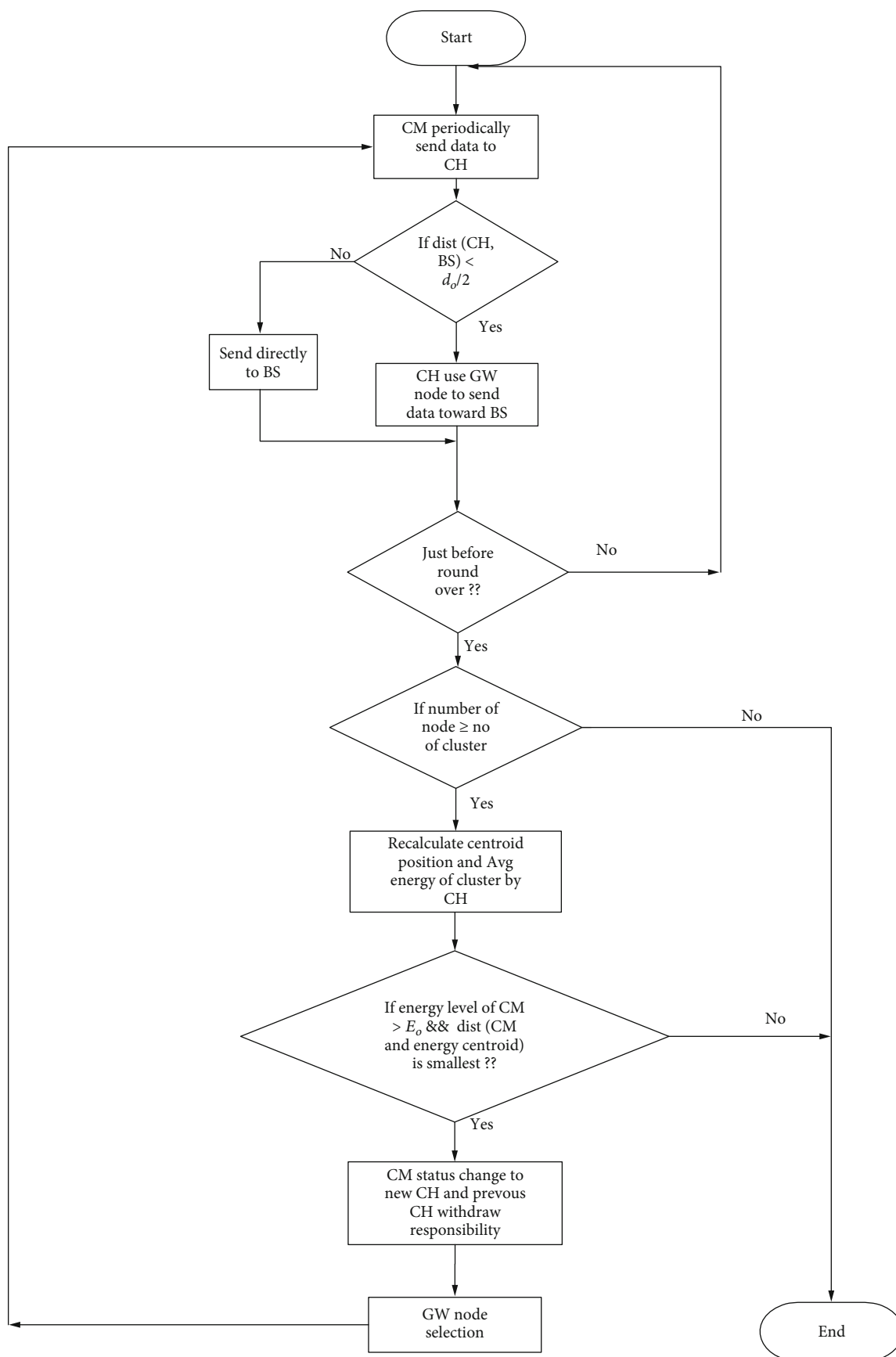


FIGURE 8: Data transmission and CH rotation flow chart.

```

1. do
2.   CM sense and transmit sense data to CH
3.   if ( $dist(CH, BS) < d_o/2$ )
4.     CH directly transmit data to BS in single hope
5.   else
6.     CH use GW node to transmit data to BS in multi-hop
7.   end if
8. while (just before round over)
9.   for  $j = 0 : CM$ 
10.    each CM  $node(k)$  send residual energy and location to their CH
11.   end for
12.   CH calculate avg energy of cluster
13.    $E_o = \sum_{k=0}^{CM} E_k / CM$ 
14.   CH calculate energy centroid of cluster
15.    $X_{ec} = \sum_{i=0}^{CM} (E_{i-rs} / E_o) X_i / CM$ 
16.    $Y_{ec} = \sum_{i=0}^{CM} (E_{i-rs} / E_o) Y_i / CM$ 
17.    $d = \sqrt{(X_{ec} - X_i)^2 + (Y_{ec} - Y_i)^2}$ 
18.   for  $k = 0 : CM$ 
19.     if ( $energy\ level\ of\ node(k) > E_o$  &&  $d$  is smallest )
20.       current CH change the status of node(k) =  $CH_k$ 
21.       current CH withdraw responsibility
22.     end if
23.   end for
24.    $CH_k$  transmit joining message as same as Algorithm 1

```

ALGORITHM 2: Data Transmission and Cluster Head Rotation.

4.1. Simulation Setup. This section presents the simulation setup to measure the performance of the proposed protocol design. The simulation is performed in the network, where we set 100 * 100 m area with 100 sensor nodes. All the sensor nodes are static and know their location by means of GPS. The BS is located outside the network at position of (100,100). We have considered three network scenarios which are discussed as follow: 2%, 5%, and 10% of sensor nodes as CH. To analyze the performance of network by varying the number of CH in sensor nodes, we ran the simulation 5 times; the average of these instances of data is used for plotting the results. The simulation parameters used to evaluate the proposed protocol with existing protocols are in Table 2.

4.1.1. Performance Metrics. To determine the efficiency of the proposed schemes against specified objectives, the following performance metrics are used.

Network lifetime. The network lifetime is the expiration of the network life when the number of nodes depleted their energy when data transmission begins; the cluster nodes sense the data and send to their CH and then to BS via gateway node. In these experiments, the initial energy of node is 2 J which is reducing while transmitting and receiving control messages and data.

Network throughput. Network throughput refers to the receiving of packets by the BS. It is a successful transmission of sensing the data from CM of clusters to the BS via the CHs and gateway nodes.

Energy consumption. Energy consumption is the most valuable parameters for wireless sensor network in which sensor nodes utilize their battery resources in transmission and

reception of data packets. In experiments, the energy consumes per round and consumes energy in clustering, assigning gateway node, sensing, and transmitting of data from CM of the cluster to the BS via the involvement of CH and gateway node. The confidence interval refers to possible range or values for the simulation parameters which are based on the simulation results. The 90% confidence level is the probability that the interval contains the value of the parameter. For this study, simulation confidence interval is at 90%.

4.1.2. Assumptions and Limitations

- (1) Sensor nodes are static and are deployed randomly in field
- (2) All nodes adjust their transmission power according to distance
- (3) Communication channel is reliable and free of error
- (4) The sensor nodes are aware of their locations through some localization techniques
- (5) The BS is placed outside the network (100,100) location
- (6) Every gateway node is in the range of its neighboring gateway node

4.2. Results and Discussion

4.2.1. Effect on Number of Alive Nodes. The number of alive nodes which indicates the network lifetime is as shown in Figures 9–11. This comparison is based on the alive nodes

```

1. for  $j = 0 : CM$ 
2.   if (node(j) receive adjacent CH joining request)
3.     Compute GW node Weight for Adjacent Cluster Head
4.      $G(i, j) = [S(i).E/S(i).Max] + [d(i, j)^2 + d(i, x)^2 + d(j, x)^2 + (d(j, s)^2/d(i, s)^2)]$ 
5.     Send GW weight value to CH
6.   else
7.     Round Start, CM periodically send data to their CH
8.   end if
9. end for
10. if (node(j) GW weight value higher)
11.   node(j) select as Gateway Node by CH
12. else
13.   node(j) Reject as Gateway node by CH
14. end if
15. Gateway node inform its status to adjacent CH and request for Adjacent CH Gateway node
16. while (Adjacent CH Gateway Node Information Receive)
17.   Compute Route
18. end while
19. if ( $dist(CH, BS) < d_{Th}$ )
20.   CH directly transmit data to BS in single-hop
21. else
22.   CH use GW node to transmit data to BS in multi-hop
23. end if

```

ALGORITHM 3: Gateway Node Selection.

TABLE 2: Simulation parameters.

Parameter	Values
Network area	100 m * 100 m
BS location	At the edge of the area
Number of sensor nodes	100
Initial energy (J)	2 J
Data aggregation energy	5 nJ/bit/signal
Transmission energy	50 nJ/bit
Reception energy	50 nJ/bit
Data transmission rate	5000 bps
ϵ_{fs}	10 pJ/bit/m ²
ϵ_{amp}	0.0013 pJ/bit/m ⁴
Round time	2 sec/round
Packet size	200 bits
MAC	802.11

vs. the number of rounds at 2%, 5%, and 10%, respectively. As it is shown that the proposed protocol GCEE performs better as compared to EECRP, CAMP, and MEACBM. The first node dies in the proposed scheme approximately in between 700 and 800 rounds. Similarly, the first node dies in EECRP very shortly because data transmitted by CH is on a single hop, while the proposed scheme utilizes multihop gateway nodes for data transmission from CH to BS. Moreover, as shown in the results that the CAMP protocol has almost the same results as MEACBM and the nodes

die approximately at 550-800 rounds, these results are showing early depletion of sensor nodes. In addition, the results also indicated that at 2% and 10% of CH, the CH consumes more energy, so that node dies earlier. While in 5%, nodes die slowly. Therefore, 5% of nodes that are CHs have better conditions.

4.2.2. Average Data Transmission. Figure 12 shows the result of average data transmission by changing the number of CH nodes in the network. As compared to EECRP, CAMP, and MEACBM schemes, the proposed scheme of GCEE performs better because CM data are transmitting towards the BS via the CH and multihop gateway node. Therefore, average data transmission enhances by increasing the number of CH. Furthermore, a lot of fluctuations in EECRP scheme is due to the concept of MAX-dist. MAX-dist is the threshold distance in which the CH sends the data to the BS successfully if the distance is less than the data forwarded; otherwise, CH stores the data in cache and wait for the next round due to which average data transmission reduces. In addition, Figure 12 also reveals when the number of CH is small, the average data transmission is less because the distance between the sensor nodes and the BS is large, and large amount of energy was consumed by all sensor nodes. As number of CH increases, the average data transmission increases. But as the number of CH increases by 5%, the average data transmission also reduces because amount of data to increase in network which creates energy dissipation is quicker among sensor nodes. The results indicate that the proposed protocol has stable data transmission as compared to EECRP, CAMP, and MEACBM.

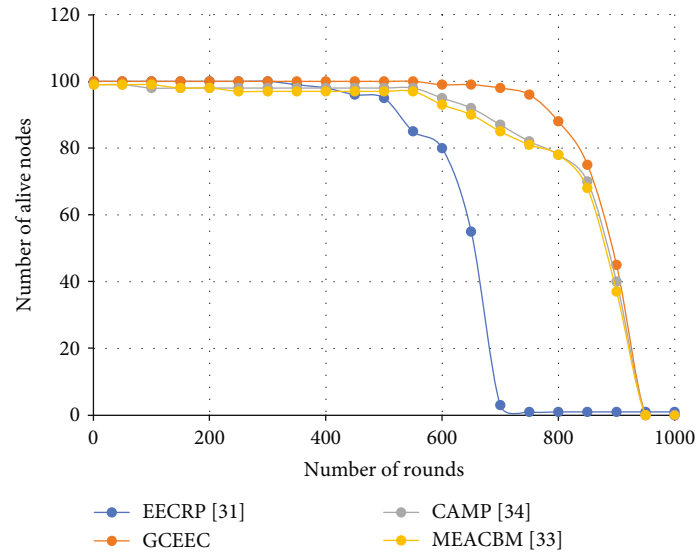


FIGURE 9: Number of alive nodes at 2% CH.

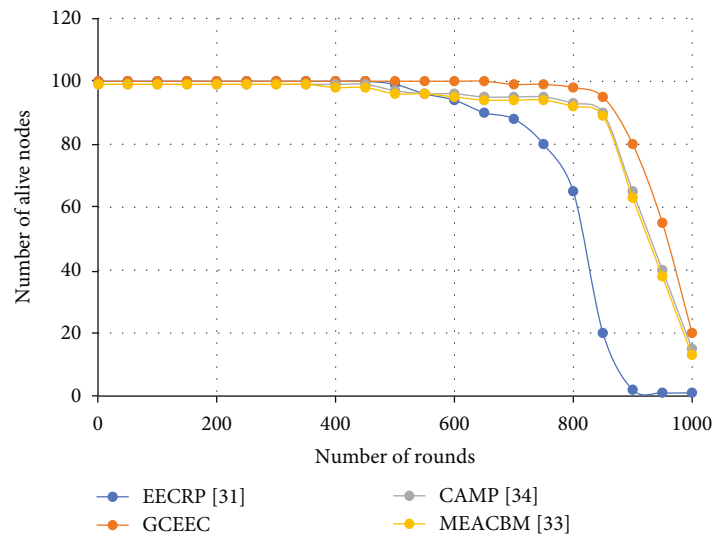


FIGURE 10: Number of alive nodes at 5% CH.

4.2.3. Round vs. Packet Received by Base Station. Number of data packet received by BS which is taken into consideration at different number of rounds. Figures 13–15 show the data packet received by BS at 2%, 5%, and 10% of CH, respectively. As it is shown, EECRP considerably receives fewer data packet to BS than GCEEC. Furthermore, packet received by BS in EECRP scheme is slower than GCEEC because of the adjustment of MAX-dist in EECRP where as in GCEEC, gateway nodes relay data from the CH to the BS. As compared to CAMP and MEACBM, the proposed protocol GCEEC has better data transmission. However, the MEACBM is better than EECRP due to the use of coverage and connectivity in the network by constructing a subcluster and computing the multihop route for interclustering combination among clusters and subclusters. In addition, the pro-

posed scheme at 5% of CH performs better transmission of packet than 2% and 10% because in 5% of CH, nodes die slowly and have better coverage and have less burden on gateway nodes. While in 2% of CH, the distance between nodes and BS is greater so large amount of energy is consumed. Similarly, in 10% of CH, data transmission in network enhances; more data is relaying on gateway nodes which shorten network lifetime.

4.2.4. Rounds vs. Energy Consumption. As shown in Figures 16–18, the total energy consumption in EECRP is high as compared to the proposed schemes. It is due to the fact that EECRP scheme uses single-hop transmission by CH as well as threshold distance name MAX-dist. The single-hop transmission towards the BS causes load on the

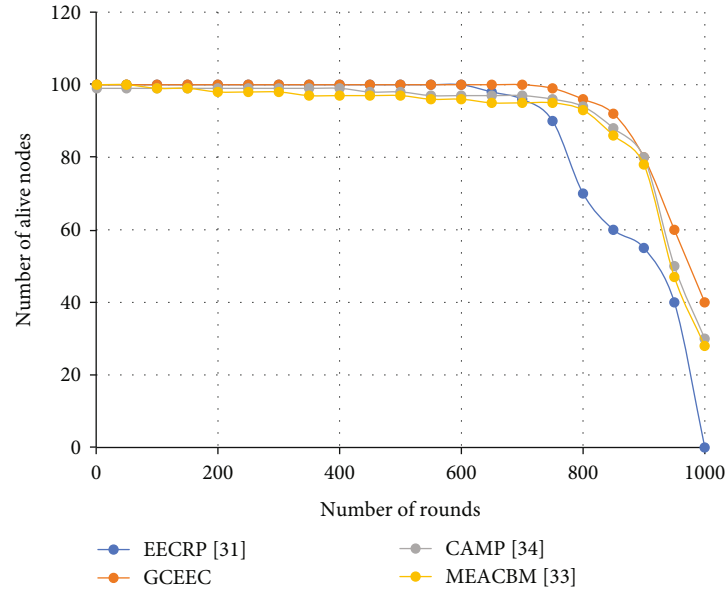


FIGURE 11: Number of alive nodes at 10% CH.

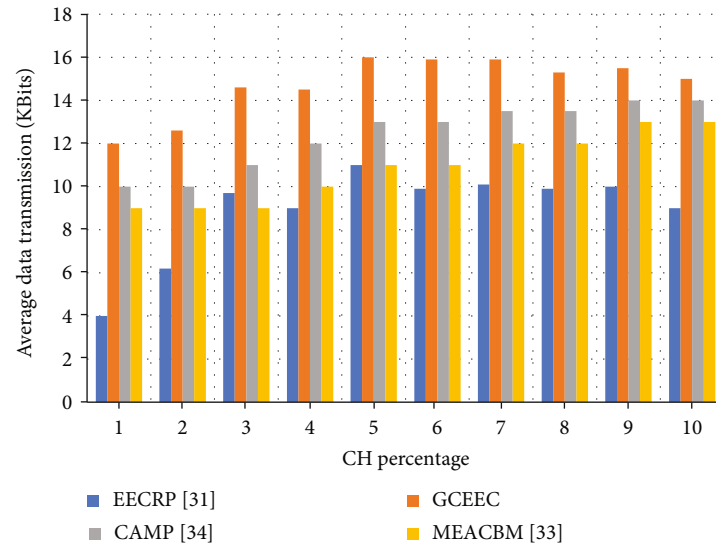


FIGURE 12: Average data transmission with different numbers of CHs.

CH, which consumes more energy. Furthermore, due to MAX-dist concept, i.e., CH stops transmission, stores data in cache when distance between CH and BS is greater than MAX-dist, and transmits all cache data to incoming CH during rotation phase. This MAX-dist cache process consumes more energy of CH during transmission and reception. In GCEEC, the load of CH is distributed due to selection of multihop gateway node which significantly reduces energy consumption. Therefore, overall energy consumption is reducing in the proposed protocol as compared to EECRP, CAMP, and MEACBM.

The objective of these experiments is to select the CH on efficient location in cluster and to reduce the load on CH. The proposed GCEEC protocol for agriculture precision selects

the CH near the energy centroid position which maximizes the network coverage of cluster nodes and reduces the energy consumption. Furthermore, gateway nodes are selected among clusters which relays itself as well as other CHs and forward the data towards the BS which significantly reduces load on CH. The experimental results indicated that GCEEC performs better than EECRP, CAMP, and MEACBM protocols. All sensor nodes transmit limited amount of data to the CH, and the CH can bear all cluster node data in his memory. It can easily transfer to its gateway, and gateway can easily transfer the data to the next gateway and then further transmit towards the BS. Therefore, there will be more transmissions as compare to EECRP, CAMP, and MEACBM protocols, but it reduces the load on CH with the help of

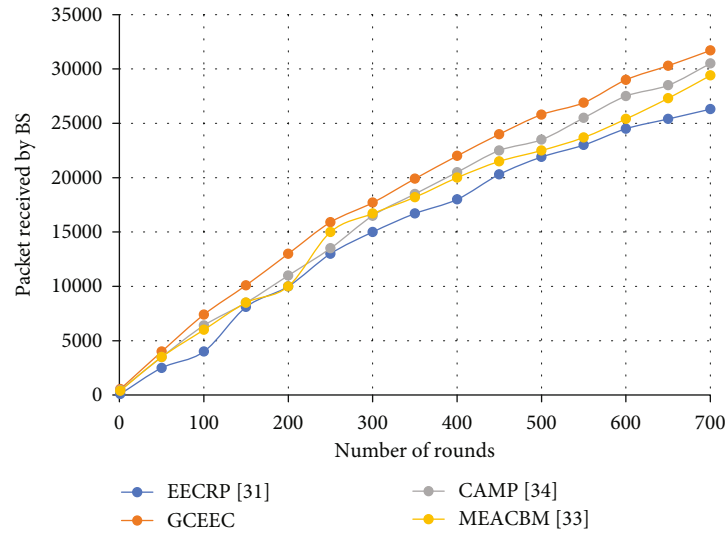


FIGURE 13: Packet received by BS 2% CH.

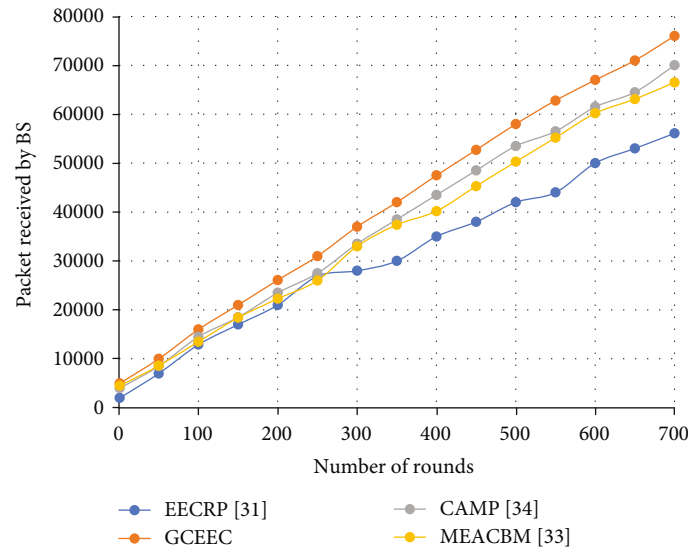


FIGURE 14: Packet received by BS 5% CH.

gateway node. Hence, we say that the proposed GCEEC protocol has much more energy and efficient as compared to state-of-the-art routing protocols.

The applications for precision agriculture have deployed to analyze the environmental parameters such as humidity, crop conditions, and soil monitoring. All the data communication process among small sensor nodes is based on feasible and energy-efficient sensor systems to improve the monitoring systems for further decision making. Routing protocols are playing a very crucial role for data collection in field. Complex routing protocols lead to consuming more energy, overhead, and packet dropping. In this paper, after designing the proposed GCEEC routing protocol, we analyze the performance with state-of-the-art routing protocols and observed that proposed protocol consumes less energy which impacts on better data delivery in agriculture fields.

After designing the protocol, now we compare the whole system performance with existing systems in agriculture precision field. Table 3 presents the comparison of some of the existing agriculture precision systems and proposed system in terms of overhead, coverage area, energy consumption, network lifetime, scalability, and other performance parameters. Table 3 indicates that most of the existing systems have more overhead and not scalable to adjust in other agriculture fields like [43, 44]. The proposed system is scalable especially for agriculture precision applications such as precision farming, horticulture, orchard, precision agriculture, precision fruticulture, precision horticulture, quality, tree fruits, and vegetables. The table below also indicates the different parameters to evaluate the existing agriculture precision system and their possible applications in terms of network overhead, coverage area, energy consumption

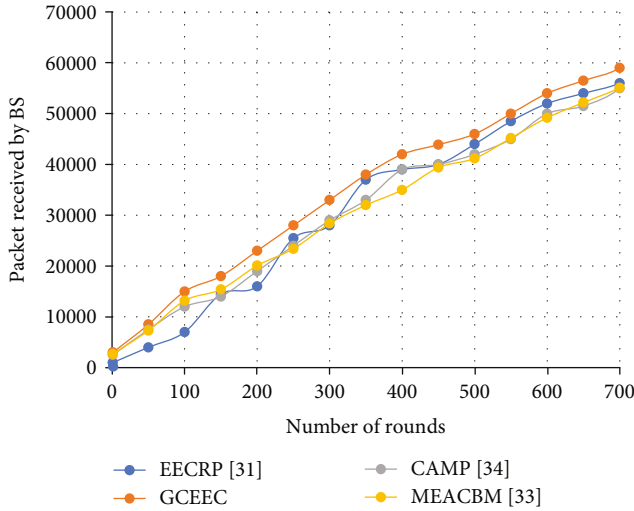


FIGURE 15: Packet received by BS 10% CH.

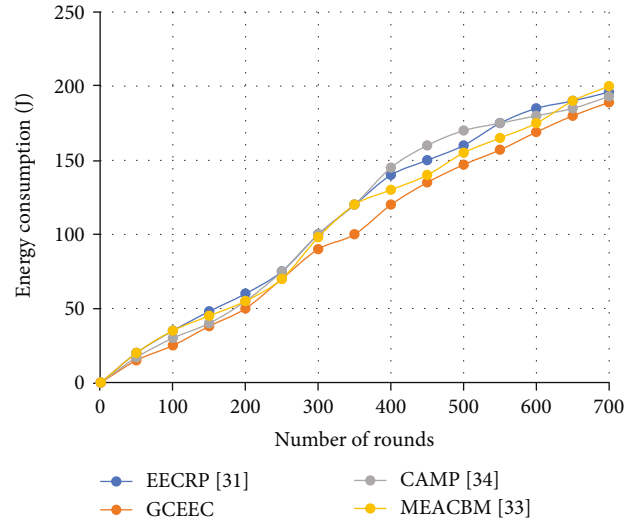


FIGURE 17: Energy consumption at 5% CH.

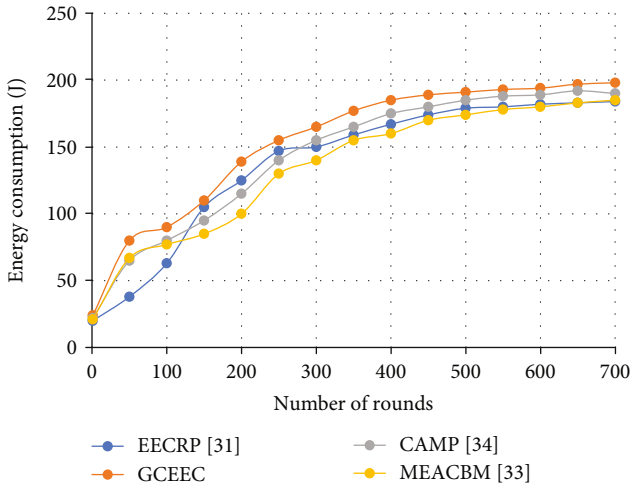


FIGURE 16: Energy consumption at 2% CH.

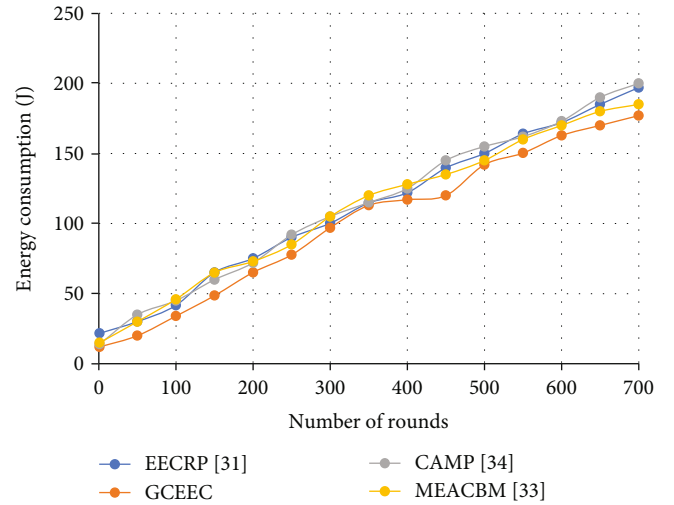


FIGURE 18: Energy consumption at 10% CH.

reduction, network lifetime, scalability, and system limitations. Some systems have moderate but still suffered with other parameters such as [41] which is moderate but still suffered in network lifetime. The system in [42] has high overhead and also not considered energy consumption and scalability. The systems [39, 40, 44] are not scalable and also suffered in overhead issues. The proposed system GCEEC is scalable and offers moderate network lifetime.

5. Conclusion

Wireless sensor network (WSN) is one of the emerging technique and technology especially for agriculture sector. In WSN, sensor nodes sense the physical and environmental conditions of soil and crop and send the data to the sink node by single-hop or multihop communication. Due to low computational power and limited battery resources, complex routing processes may cause energy depletion of the sensor

nodes. Most of the routing protocols do not consider load balancing for a feasible routing path. This research improves load among the sensor nodes especially on the cluster head (CH). Furthermore, research also improves the optimized location and rotation of CH among energy density sensor nodes. In this research, Gateway Clustering Energy-Efficient Centroid-based Routing Protocol (GCEEC) is proposed for WSN. The proposed protocol selects and rotates the CH near the energy centroid position of the cluster. In addition, each CH chooses the gateway node for multihopping itself and other CH data towards the BS which reduce load among the CH. We performed the experiment on a well-known network simulator named NS-2.35 to analyze the performance of GCEEC for different criterion which includes network lifetime, network throughput, and energy consumption. The experimental result revealed that network lifetime, throughput, and energy consumption of our protocol is better than EECRP protocol. In the future, we will analyze the proposed

TABLE 3: Comparison table.

S#	Agriculture precision system references	Applications	Overhead	Coverage area	Energy consumption reduction	Network lifetime	Scalability	Limitation
1	[45]	Greenhouse	Moderate	50 m	Moderate	Limited	Moderate	Time consuming, synchronization accuracy
2	[46]	Agriculture	High	150 m	Not considered	Moderate	Not considered	Not feasible for other quality of services parameters
3	[47]	Crop farming	Moderate	180 m	20 times more compared to traditional systems without CH	Limited	Not considered	Not reliable communication beyond 80 m
4	[44]	Tree monitoring	High	180 m	High	Limited	Not considered	Its solar system has irregularity on different aspects
5	[48]	Precision agriculture	Moderate	40 m	High	Limited	Not considered	System is more complex and leads to predefined path issues
6	[43]	Forest monitoring	High	672 m	High	Moderate	Not considered	Packet loss, energy consumption
7	Proposed system (GCEEC)	Precision agriculture	Low	200 m	Low	Long	Considered	Fixed for agriculture precision only

protocol with other environments like drone-assisted WSN, wireless body area networks, and sensor-based transportation systems.

Data Availability

No data have to be included.

Conflicts of Interest

The authors declare that they have no conflict of interest.

Acknowledgments

This work has also been partially supported by the European Union through the ERANETMED (Euromediterranean Cooperation through ERANET joint activities and beyond) project ERANETMED3-227 SMARTWATIR.

References

- [1] K. Sneha, R. Kamath, M. Balachandra, and S. Prabhu, "New gossiping protocol for routing data in sensor networks for precision agriculture," in *Soft Computing and Signal Processing: Proceeding*, pp. 139–152, Springer, 2019.
- [2] K. N. Qureshi and A. H. Abdullah, "Adaptation of wireless sensor network in industries and their architecture, standards and applications," *World Applied Sciences Journal*, vol. 30, no. 10, pp. 1218–1223, 2014.
- [3] K. N. Qureshi, A. H. Abdullah, F. Bashir, S. Iqbal, and K. M. Awan, "Cluster-based data dissemination, cluster head formation under sparse, and dense traffic conditions for vehicular ad hoc networks," *International Journal of Communication Systems*, vol. 31, no. 8, article e3533, 2018.
- [4] M. Salayma, A. Al-Dubai, I. Romdhani, and Y. Nasser, "New dynamic, reliable and energy efficient scheduling for wireless body area networks (WBAN)," in *2017 IEEE International Conference on Communications (ICC)*, pp. 1–6, Paris, France, May 2017.
- [5] T. Rault, A. Bouabdallah, and Y. Challal, "Energy efficiency in wireless sensor networks: a top-down survey," *Computer Networks*, vol. 67, pp. 104–122, 2014.
- [6] K. O. Flores, I. M. Butaslaç, J. E. M. Gonzales, S. M. G. Dumlaio, and R. S. J. Reyes, "Precision agriculture monitoring system using wireless sensor network and Raspberry Pi local server," in *2016 IEEE Region 10 Conference (TENCON)*, pp. 3018–3021, Singapore, Singapore, November 2016.
- [7] X. Feng, J. Zhang, C. Ren, and T. Guan, "An unequal clustering algorithm concerned with time-delay for internet of things," *IEEE Access*, vol. 6, pp. 33895–33909, 2018.
- [8] D. M. Omar and A. M. Khedr, "ERPLBC-CS: energy efficient routing protocol for load balanced clustering in wireless sensor networks," *Adhoc & Sensor Wireless Networks*, vol. 42, 2018.
- [9] C. Savaglio, P. Pace, G. Aloï, A. Liotta, and G. Fortino, "Light-weight reinforcement learning for energy efficient communications in wireless sensor networks," *IEEE Access*, vol. 7, pp. 29355–29364, 2019.
- [10] M. Srbinovska, C. Gavrovski, V. Dimcev, A. Krkoleva, and V. Borozan, "Environmental parameters monitoring in precision agriculture using wireless sensor networks," *Journal of Cleaner Production*, vol. 88, pp. 297–307, 2015.
- [11] J. Lloret, M. Garcia, D. Bri, and J. Diaz, "A cluster-based architecture to structure the topology of parallel wireless sensor networks," *Sensors*, vol. 9, no. 12, pp. 10513–10544, 2009.
- [12] T. Kalaivani, A. Allirani, and P. Priya, "A survey on Zigbee based wireless sensor networks in agriculture," in *3rd International Conference on Trendz in Information Sciences & Computing (TISC2011)*, pp. 85–89, Chennai, India, December 2011.
- [13] K. N. Qureshi, S. Din, G. Jeon, and F. Piccialli, "Link quality and energy utilization based preferable next hop selection routing for wireless body area networks," *Computer Communications*, vol. 149, pp. 382–392, 2020.
- [14] S. A. Kumar and P. Ilango, "The impact of wireless sensor network in the field of precision agriculture: a review," *Wireless Personal Communications*, vol. 98, no. 1, pp. 685–698, 2018.
- [15] M. H. Anisi, G. Abdul-Salaam, and A. H. Abdullah, "A survey of wireless sensor network approaches and their energy consumption for monitoring farm fields in precision agriculture," *Precision Agriculture*, vol. 16, no. 2, pp. 216–238, 2015.
- [16] D. S. Long and J. D. McCallum, "On-combine, multi-sensor data collection for post-harvest assessment of environmental stress in wheat," *Precision Agriculture*, vol. 16, no. 5, pp. 492–504, 2015.
- [17] X. Fu, G. Fortino, W. Li, P. Pace, and Y. Yang, "WSNs-assisted opportunistic network for low-latency message forwarding in sparse settings," *Future Generation Computer Systems*, vol. 91, pp. 223–237, 2019.
- [18] S. Palaniappan and P. Periyasamy, "WISSEN: mote as an innovative approach in precision agriculture monitoring using wireless sensor network," *International Journal of Printing, Packaging & Allied Sciences*, vol. 4, no. 5, pp. 3475–3487, 2016.
- [19] A. Mehmood, S. Khan, B. Shams, and J. Lloret, "Energy-efficient multi-level and distance-aware clustering mechanism for WSNs," *International Journal of Communication Systems*, vol. 28, no. 5, pp. 972–989, 2015.
- [20] N. A. Pantazis, S. A. Nikolidakis, and D. D. Vergados, "Energy-efficient routing protocols in wireless sensor networks: a survey," *IEEE Communications Surveys & Tutorials*, vol. 15, no. 2, pp. 551–591, 2013.
- [21] A. Mehmood, J. L. Mauri, M. Noman, and H. Song, "Improvement of the wireless sensor network lifetime using LEACH with vice-cluster head," *Ad Hoc & Sensor Wireless Networks*, vol. 28, no. 1–2, pp. 1–17, 2015.
- [22] C. M. de Farias, L. Pirmez, G. Fortino, and A. Guerrieri, "A multi-sensor data fusion technique using data correlations among multiple applications," *Future Generation Computer Systems*, vol. 92, pp. 109–118, 2019.
- [23] P. C. S. Rao, P. K. Jana, and H. Banka, "A particle swarm optimization based energy efficient cluster head selection algorithm for wireless sensor networks," *Wireless Networks*, vol. 23, no. 7, pp. 2005–2020, 2017.
- [24] K. Guravaiah and R. L. J. A. Velusamy, "BEACH: balanced energy and adaptive cluster head selection algorithm for wireless sensor networks," *Ad Hoc & Sensor Wireless Networks*, vol. 42, 2018.
- [25] X. Fu, G. Fortino, P. Pace, G. Aloï, and W. Li, "Environment-fusion multipath routing protocol for wireless sensor networks," *Information Fusion*, vol. 53, pp. 4–19, 2020.
- [26] X. Liu, "Atypical hierarchical routing protocols for wireless sensor networks: a review," *IEEE Sensors Journal*, vol. 15, no. 10, pp. 5372–5383, 2015.

- [27] N. Jan, N. Javaid, Q. Javaid et al., "A balanced energy-consuming and hole-alleviating algorithm for wireless sensor networks," *IEEE Access*, vol. 5, pp. 6134–6150, 2017.
- [28] G. P. Gupta, M. Misra, and K. Garg, "Energy and trust aware mobile agent migration protocol for data aggregation in wireless sensor networks," *Journal of Network and Computer Applications*, vol. 41, pp. 300–311, 2014.
- [29] H. Safa, M. Karam, and B. Moussa, "PHAODV: power aware heterogeneous routing protocol for MANETs," *Journal of Network and Computer Applications*, vol. 46, pp. 60–71, 2014.
- [30] X. Liu, "An optimal-distance-based transmission strategy for lifetime maximization of wireless sensor networks," *IEEE Sensors Journal*, vol. 15, no. 6, pp. 3484–3491, 2015.
- [31] G. S. Brar, S. Rani, V. Chopra, R. Malhotra, H. Song, and S. H. Ahmed, "Energy efficient direction-based PDORP routing protocol for WSN," *IEEE Access*, vol. 4, pp. 3182–3194, 2016.
- [32] M. Abo-Zahhad, S. M. Ahmed, N. Sabor, and S. Sasaki, "Mobile sink-based adaptive immune energy-efficient clustering protocol for improving the lifetime and stability period of wireless sensor networks," *IEEE Sensors Journal*, vol. 15, no. 8, pp. 4576–4586, 2015.
- [33] T.-T. Huynh, A.-V. Dinh-Duc, and C.-H. Tran, "Delay-constrained energy-efficient cluster-based multi-hop routing in wireless sensor networks," *Journal of Communications and Networks*, vol. 18, no. 4, pp. 580–588, 2016.
- [34] J. Shen, A. Wang, C. Wang, P. C. K. Hung, and C. F. Lai, "An efficient centroid-based routing protocol for energy management in WSN-assisted IoT," *IEEE Access*, vol. 5, pp. 18469–18479, 2017.
- [35] K. M. Awan, A. Ali, F. Aadil, and K. N. Qureshi, "Energy efficient cluster based routing algorithm for wireless sensors networks," in *2018 International Conference on Advancements in Computational Sciences (ICACS)*, pp. 1–7, Lahore, Pakistan, February 2018.
- [36] K. M. Awan, P. A. Shah, K. Iqbal, S. Gillani, W. Ahmad, and Y. Nam, "Underwater wireless sensor networks: a review of recent issues and challenges," *Wireless Communications and Mobile Computing*, vol. 2019, Article ID 6470359, 20 pages, 2019.
- [37] M. Sajwan, D. Gosain, and A. K. Sharma, "CAMP: cluster aided multi-path routing protocol for wireless sensor networks," *Wireless Networks*, vol. 25, no. 5, pp. 2603–2620, 2019.
- [38] F. Amin and M. Zubair, "Energy-efficient clustering scheme for multihop wireless sensor network (ECMS)," in *17th IEEE International Multi Topic Conference 2014*, pp. 131–136, Karachi, Pakistan, December 2014.
- [39] A. Varga, "OMNeT++," in *Modeling and Tools for Network Simulation*, K. Wehrle, M. Güneş, and J. Gross, Eds., pp. 35–59, Springer Berlin Heidelberg, Berlin, Heidelberg, 2010.
- [40] T. Issariyakul and E. Hossain, *Introduction to Network Simulator NS2*, Springer Publishing Company, Incorporated, 2010.
- [41] O. Lartillot, P. Toiviainen, and T. Eerola, "A Matlab toolbox for music information retrieval," in *Data Analysis, Machine Learning and Applications*, pp. 261–268, Springer, Berlin Heidelberg, 2008.
- [42] K. Fall and K. Varadhan, "The ns manual," 2011, <https://www.isi.edu/nsnam/ns/ns-documentation.html>.
- [43] P. Mathur, R. H. Nielsen, N. R. Prasad, and R. Prasad, "Data collection using miniature aerial vehicles in wireless sensor networks," *IET Wireless Sensor Systems*, vol. 6, no. 1, pp. 17–25, 2016.
- [44] T. Zou, S. Lin, Q. Feng, and Y. Chen, "Energy-efficient control with harvesting predictions for solar-powered wireless sensor networks," *Sensors*, vol. 16, no. 1, p. 53, 2016.
- [45] Y. Song, J. Ma, X. Zhang, and Y. Feng, "Design of wireless sensor network-based greenhouse environment monitoring and automatic control system," *Journal of Networks*, vol. 7, no. 5, p. 838, 2012.
- [46] S. Nikolidakis, D. Kandris, D. Vergados, and C. Douligeris, "Energy efficient routing in wireless sensor networks through balanced clustering," *Algorithms*, vol. 6, no. 1, pp. 29–42, 2013.
- [47] D. L. Ndzi, A. Harun, F. M. Ramli et al., "Wireless sensor network coverage measurement and planning in mixed crop farming," *Computers and Electronics in Agriculture*, vol. 105, pp. 83–94, 2014.
- [48] T. H. F. Khan and D. S. Kumar, "Mobile collector aided energy reduced (MCER) data collection in agricultural wireless sensor networks," in *2016 IEEE 6th International Conference on Advanced Computing (IACC)*, pp. 629–633, Bhimavaram, India, February 2016.

Research Article

Elite Immune Ant Colony Optimization-Based Task Allocation for Maximizing Task Execution Efficiency in Agricultural Wireless Sensor Networks

Mengying Xu  and Jie Zhou 

College of Information Science and Technology, Shihezi University, Shihezi, China

Correspondence should be addressed to Jie Zhou; jiezhou@shzu.edu.cn

Received 31 October 2019; Revised 29 December 2019; Accepted 11 January 2020; Published 31 January 2020

Guest Editor: Zhenxing Zhang

Copyright © 2020 Mengying Xu and Jie Zhou. This is an open access article distributed under the Creative Commons Attribution License, which permits unrestricted use, distribution, and reproduction in any medium, provided the original work is properly cited.

The research of agricultural wireless sensor networks (AWSNs) plays an important role in the field of facility agricultural technology. The temperature and humidity nodes in AWSNs are so tiny that they are limited on computation, network management, information collection, and storage size. Under this condition, task allocation plays a key role in improving the performance of AWSNs to reduce energy consumption and computational constraints. However, the optimization of task allocation is a nonlinearly constrained optimization problem whose complexity increases when constraints such as limited computing capabilities and power are undertaken. In this paper, an elite immune ant colony optimization (EIACO) is proposed to deal with the problem of task allocation optimization, which is motivated by immune theory and elite optimization theory. The EIACO uses ant colony optimization (ACO) to combine the clone operator and elite operator together for the optimization of task allocation. The performances of EIACO with different numbers of temperature and humidity sensor nodes and tasks have been compared by both genetic algorithm (GA) and simulated annealing (SA) algorithm. Simulation results show that the proposed EIACO has a better task execution efficiency and higher convergence speed than GA and SA. Furthermore, the convergence speed of EIACO is faster than GA and SA. Therefore, the whole system efficiency can be improved by the proposed algorithm.

1. Introduction

With the rapid progress in the research and development of efficient software algorithms, electronics and mobile networking have shown a great potential in computation, managing network, collecting information, low-cost, and self-adaptation [1]. Agricultural wireless sensor networks (AWSNs) are composed of some wireless sensors for monitoring temperature and humidity in the environment [2]. Each temperature and humidity sensing unit consists of the data acquisition, the computing capability, the short-range radio transmitter, the data storage, and the power supply [3–7]. AWSNs have been applied in many important areas such as intelligent family, military, automated assistance for the elderly monitors, environmental, multimedia surveillance, and traffic avoidance [8, 9].

Recent success of emerging AWSN technology has encouraged researchers to develop new task allocation algorithm in this field. Generally, temperature and humidity sensors are small and have limited abilities of computing [10]. Careful task allocation scheme can be an effective optimization mean for achieving the desired high-energy consumption goals, comprising computing capability constraints. The task allocation problem is combinatorial in nature and consists of numerous hard constraints such as computing capabilities and limited computing power [11, 12].

In this paper, an EIACO-based task allocation approach for maximizing task execution efficiency is proposed. To assess the efficiency of algorithms, the mathematical model of task allocation is given firstly. After that, the immune and elite selection mechanism is introduced into ant colony optimization (ACO). The fitness function for task allocation

is designed to optimize the task execution efficiency. The results show that the proposed immune strategy and elite strategy improved the global search ability of EIACO.

In the simulation, EIACO has shown a great ability to find optimal individuals. It can also avoid local optima. Simulations demonstrate that the EIACO has a better performance when implemented into AWSNs.

The rest of the paper is organized as follows. Section 2 discusses the related work. Section 3 presents the task allocation model and our problem description. The proposed EIACO is then extended to optimize the performance of task allocation in Section 4. Simulation and results are given in Section 5. Finally, conclusions are drawn in Section 6.

2. Related Work

In wireless sensor networks, an effective task allocation scheme can attain low total computational time as well as low energy costs, increase network reward, and improve lifetime of networks. In [13], a distributed task allocation strategy based on particle swarm optimization (PSO) is proposed. Furthermore, task can be allocated quickly and directly. In order to reduce energy consumption and extend lifetime, a heuristic-based algorithm is proposed. The task is distributed to sensor nodes in different allocation phases to balance the workload [14]. In [15], a social network optimization algorithm is given to deal with task allocation issue for reducing total computational time and the energy costs.

Exhaustive search can achieve high task execution efficiency compared with other schemes, but its computational complexity is too high for practical implementations. For this reason, many heuristics have been proposed for the practical situation [16], such as genetic algorithm (GA), ant colony optimization (ACO), and particle swarm optimization. Aiming at this problem in heterogeneous wireless sensor networks, GA is first found and its capability is evaluated through the task execution efficiency in [17]. It has been used for the task allocation in WSNs in which the resources and computing power of sensors are limited. It turns out that the computational complexity of limited computing power increases exponentially with the number of sensor nodes and targets. In [18], SA can achieve high task execution efficiency when dealing with task allocation issue. In [19], authors proposed a GA scheme to improve system performance for better total system efficiency in WSNs. GA is adaptable but has many problems, computational complexity for instance. In their work, they maximize the task execution efficiency but neglect the ability constraint of computing [20, 21].

3. Task Allocation Model

In this section, a mathematical model of the task allocation in AWSNs is given with respect to the constraints of computing capabilities and limited computing power. In [22], authors used a max-min type model with nonlinear constraints to demonstrate the task allocation problem in AWSNs. Later in [23], the authors showed a similar model by a fewer num-

ber of sensor nodes and targets. The model is more flexible than the first and more suitable to different requirements of flows.

In this paper, an optimizing model comprising wireless sensor nodes located at the coordinates is described. The model can be expressed simply as assuming that there are n tasks and m temperature and humidity sensor nodes in AWSN system. m sensor nodes are randomly deployed in a certain area, and the task allocation is executed on the gateway. The gateway node stores the location information of all sensors; m sensors allocate n tasks.

It is assumed that the urgency of the task being assigned has been assessed and ranked. The advantage of assigning tasks has been assessed and evaluated. The urgency of the j_{th} task being assigned is w_j , and the advantage of the j_{th} task assigned to the i_{th} sensor is estimated to be b_{ij} , so that each sensor assigns a benefit value to the task as c_j . In equation (1), c_j represents the benefit value of assigning a task. In equation (2), the reward of all tasks being allocated is calculated and the maximum reward C_{max} needs to be pursued.

$$c_j = w_j B_j, \quad (1)$$

$$C = \sum_{j=1}^n c_j. \quad (2)$$

Here, an ant, 3 sensor nodes, and 4 tasks are assumed in the model. The ant randomly generates a solution in (5).

The advantage of the j_{th} task being allocated to the i_{th} sensor is estimated to be b_{ij} .

$$b_{ij} = \begin{bmatrix} b_{11} & b_{12} & b_{13} & b_{14} \\ b_{21} & b_{22} & b_{23} & b_{24} \\ b_{31} & b_{32} & b_{33} & b_{34} \end{bmatrix} (i \in [1, 3], j \in [1, 4]). \quad (3)$$

Each task has the value of urgency as

$$w_j = [w_1 \ w_2 \ w_3 \ w_4]. \quad (4)$$

One solution is randomly generated in order to store the allocation results in (5). The encoding method is described in Section 4.

$$X = [2 \ 1 \ 3 \ 2]. \quad (5)$$

Real coding needs to be converted to a binary encoding method in order to perform the next operation. The binary allocation matrix is shown as

$$X^* = \begin{bmatrix} 0 & 1 & 0 & 0 \\ 1 & 0 & 0 & 1 \\ 0 & 0 & 1 & 0 \end{bmatrix}. \quad (6)$$

According to (3) and (6), b_{ij}^* is calculated in (7). It represents the advantage of the j_{th} task being allocated to the i_{th}

sensor. X^* is the binary allocation matrix. $X^*_{ij} = 1$ represents that j_{th} task is allocated to i_{th} sensor. Otherwise, j_{th} task is not allocated to i_{th} sensor. b_{ij} is the advantage matrix. The value in the advantage matrix represents the advantage value of the j_{th} task being allocated to the i_{th} sensor.

$$b^*_{ij} = b_{ij} \cdot X^*, \quad (7)$$

$$b^*_{ij} = \begin{bmatrix} 0 & b_{12} & 0 & 0 \\ b_{21} & 0 & 0 & b_{24} \\ 0 & 0 & b_{33} & 0 \end{bmatrix}. \quad (8)$$

The identity matrix with i columns is generated in B_j in the following formulas. The number of sensors corresponds to the number of columns of a_i . The calculated B_j can be shown in (11).

$$a_i = [1 \quad 1 \quad 1], \quad (9)$$

$$B_j = a_i \times b^*_{ij}, \quad (10)$$

$$B_j = [b_{21} \quad b_{12} \quad b_{33} \quad b_{24}]. \quad (11)$$

c_j represents the benefit value of assigning a task; it can be calculated as

$$c_j = B_j \times w'_j. \quad (12)$$

In AWSNs, task allocation not only needs to meet the requirements of application quality of service but should also increase the total task execution efficiency as much as possible. The efficiency of task execution refers to the sum of execution efficiency of each sensor node to complete tasks. Since the temperature and humidity nodes in the AWSNs are heterogeneous, the execution efficiency of sensor nodes is different, so the total task execution efficiency generated by the task mapping of sensor nodes may also be different. The allocation of tasks usually achieves better performance and higher total task execution efficiency for the application. Therefore, the gateway needs to perform a task schedule according to the execution capability of each sensor node and the load size of each task.

4. EIACO-Based Task Allocation for Maximizing Task Execution Efficiency in AWSNs

To solve the problem of task allocation in AWSNs, an optimization scheme based on EIACO is proposed. It was inspired by the real ants in nature [24]. By taking advantage of the ACO, it combines the merits of both elite operator and immune operator. This strategy enables EIACO to deal with the task allocation and direct the search toward an optimal solution. In our strategy of EIACO, the important improvement is that elite operator and immune operator are added to the traditional ACO algorithm.

The traditional ACO algorithm was proposed by the Italian scholar Dorigo M. in the 1990s. Later, people paid more attention to the application and development of this new algorithm in bionics [25]. The traditional ACO algorithm was derived from the behavior of the ant community. The ants use pheromones to communicate information with others, so that each ant can find a path from the nest to the food location with the shortest distance [26]. Dorigo M. found that the famous traveling salesman problem (TSP) is quite similar to the ant foraging behavior. After efforts, the ACO algorithm was successfully used to solve the TSP problem [27, 28]. It uses the characteristics of ant colony foraging, such as discrete optimization which can be solved by the EIACO algorithm.

EIACO is a technique for approximate optimization caused by swarm intelligence. The process of finding the optimal reward can be divided into the early adaptation phase and the later collaboration phase. In the early adaptation phase, the pheromone changes continuously with the number of time that the ants pass. The more time the ants pass, the higher the pheromone, so the tasks with higher task execution efficiency are more likely to be allocated to the sensor nodes. In the later stage of cooperation, the problem of task allocation is solved through the pheromone in the environment, which will form a self-organized collaborative relationship. The self-organized collaborative relationship between individuals will result in a better performance.

The main parts of the EIACO are described in terms of initialization, fitness evaluation, path selection, pheromone update, and termination condition.

4.1. Solution Encoding. Encoding is the primary step to be solved by EIACO. In the process of EIACO, it will directly affect the fitness calculation, path selection, and pheromone update. Encoding methods include binary encoding and real encoding. In this paper, real encoding is employed to facilitate searching for larger space. Assume that there are s ants and the numbers of sensors and tasks are m and n , respectively. Each ant generates a solution after visiting all the tasks. The population can be described as follows. In formula (13), $x_{s,n}$ represents the relationship between s_{th} ant, m_{th} sensor node, and n_{th} task. In formula (14), the number of ants is 5, and the number of sensors and tasks is 8 and 10, respectively. Therefore, 5 individuals are randomly generated in order to store the allocation results.

$$X = \begin{bmatrix} x_{1,1} & x_{1,2} & x_{1,3} & \cdots & x_{1,n} \\ x_{2,1} & x_{2,2} & x_{2,3} & \cdots & x_{2,n} \\ \cdots & \cdots & \cdots & \cdots & \cdots \\ x_{k,1} & x_{k,2} & x_{k,3} & \cdots & x_{k,n} \\ \cdots & \cdots & \cdots & \cdots & \cdots \\ x_{s,1} & x_{s,2} & x_{s,3} & \cdots & x_{s,n} \end{bmatrix} \quad (x_{s,n} \in [1, m], k \in [1, s]), \quad (13)$$

$$X = \begin{bmatrix} 1 & 5 & 8 & 4 & 4 & 3 & 8 & 5 & 3 & 5 \\ 4 & 7 & 5 & 6 & 4 & 2 & 1 & 7 & 5 & 1 \\ 3 & 6 & 4 & 6 & 7 & 4 & 1 & 3 & 1 & 8 \\ 5 & 1 & 4 & 3 & 5 & 4 & 8 & 7 & 4 & 1 \\ 7 & 3 & 2 & 3 & 4 & 3 & 2 & 2 & 7 & 5 \end{bmatrix}. \quad (14)$$

4.2. Ant Initialization. The population is created on the basis of encoding. It aims to create a link between the problem of task allocation and the EIACO. Before the initial irritation, s individuals are randomly generated as an initial population. Initial population contains m individuals that can be described as $X = \{x_1, x_2, \dots, x_k, \dots, x_s\} (k \in [1, s])$. Formula (14) shows the initial population that contains 5 individuals. It represents the allocated relationship between 8 sensors and 10 tasks.

4.3. Fitness Evaluation. The objective function has a greater influence on the convergence of the EIACO. Each ant has a solution of path selection. In other words, each ant has its corresponding objective fitness. The reward is compared with the fitness of different ants. The fitness in this paper is to calculate the reward between the sensor nodes and tasks. The fitness of EIACO can be evaluated as (2). The aim of the fitness is to pursue the best reward with high task execution efficiency. Therefore, it is aimed at maximizing the reward to obtain task execution efficiency. According to (1) and (2), if b_{ij} is bigger, then B_j is bigger, and c_j becomes better.

4.4. Path Selection. There are s ants and each ant has the following characteristics: the advance value and the number of pheromones on path determine which sensor node will be selected by the ant. τ_{ij} is the total amount of pheromone on the connection path between the two nodes at the moment. The walking rules of ants are as follows: the ants must complete the travel, and they cannot visit the same node twice. When the ant completes a travel, it leaves a certain number of pheromones on the road that it has traveled. In the beginning, the number of pheromones on the path of two nodes is the same. When the k_{th} ant selects the next node, the number of pheromones on the path and the benefit value determine which node will be selected by the ants. P_{ef}^{ij+1} represents the probability that the ant will choose the next sensor node on the path (e, f) from the j_{th} task to the $(j+1)_{th}$ task in each generation. e and f are two selected adjacent nodes on the path, respectively.

When the ant selects the next node, the pheromone and benefit value of the path are used to calculate the probability of selecting the next node. If the condition is met, the node can be selected. The probability P of the ant visiting from node e to node f in the t_{th} generation is calculated from equation (15). According to formula (15), the roulette wheel strange is used to select the sensor nodes on each path.

TABLE 1: Rewards with different number of tasks and sensor nodes.

	8 sensors 15 tasks	15 sensors 30 tasks	20 sensors 40 tasks	50 sensors 100 tasks
EIACO	6.81	13.09	19.25	48.58
GA	6.27	11.94	17.23	41.25
SA	5.72	10.92	14.89	36.66

$$P_{ef}^{ij+1}(t) = \frac{\tau_{ef}^\alpha(t) g_f^\beta(t)}{\sum_{l=1}^m \tau_{el}^\alpha(t) g_{l,j+1}^\beta(t)} \left(e \in [1, m], f \in [1, m], g_f \in g_{ij}, g_{l,j+1} \in g_{ij} \right), \quad (15)$$

$$W_{ij} = \begin{bmatrix} w_{11} & w_{12} & w_{13} & \cdots & w_{1n} \\ w_{21} & w_{22} & w_{23} & \cdots & w_{2n} \\ w_{31} & w_{32} & w_{33} & \cdots & w_{3n} \\ \cdots & \cdots & \cdots & \cdots & \cdots \\ w_{m1} & w_{m2} & w_{m3} & \cdots & w_{mn} \end{bmatrix} \quad (i \in [1, m], j \in [1, n]), \quad (16)$$

$$g_{ij} = W_{ij} \cdot b_{ij}. \quad (17)$$

In equation (15), t represents iteration time. $\tau_{ef}(t)$ denotes the pheromone on the path (e, f) at the t_{th} generation; $g_f(t)$ is the benefit value of assigning the f_{th} sensor node to the $(j+1)_{th}$ task that can be calculated by equation (17). α and β represent the weight of pheromone and the weight of benefit value, respectively. They determine the proportion of the pheromone and the benefit value. When the value of α is large, the probability of choosing this sensor node is great, and when the value of β is large, ants are more likely to choose the sensor node based on the benefit value of the j_{th} task assigned to the i_{th} sensor. In equation (15), when the concentration of the pheromone and the benefit value are large, the probability that ants select the sensor nodes will increase.

In equation (16), the matrix W_{ij} is the urgency degree of the j_{th} task being assigned, and it is composed of m identical matrixes, which is $[w_1 \ w_2 \ w_3 \ \cdots \ w_n]$. According to (3) and (16), g_{ij} is a matrix of benefit value that can be calculated in (17).

4.5. Pheromone Update. In the process of finding the best solution, it is necessary to calculate pheromones. Ants leave pheromones from the e_{th} sensor node to the f_{th} sensor node when they visit sensor nodes. As the number of iterations increases, the pheromone also volatilizes while accumulating. Similarly, in the EIACO algorithm, each ant updates the pheromone on the path after one step or one travel. The pheromone concentration on the path (e, f) during $(t, t+1)$ generation is updated in

$$\tau_{ef}(t, t+1) = \rho \times \tau_{ef}(t) + \Delta \tau_{ef}(t, t+1), \quad (18)$$

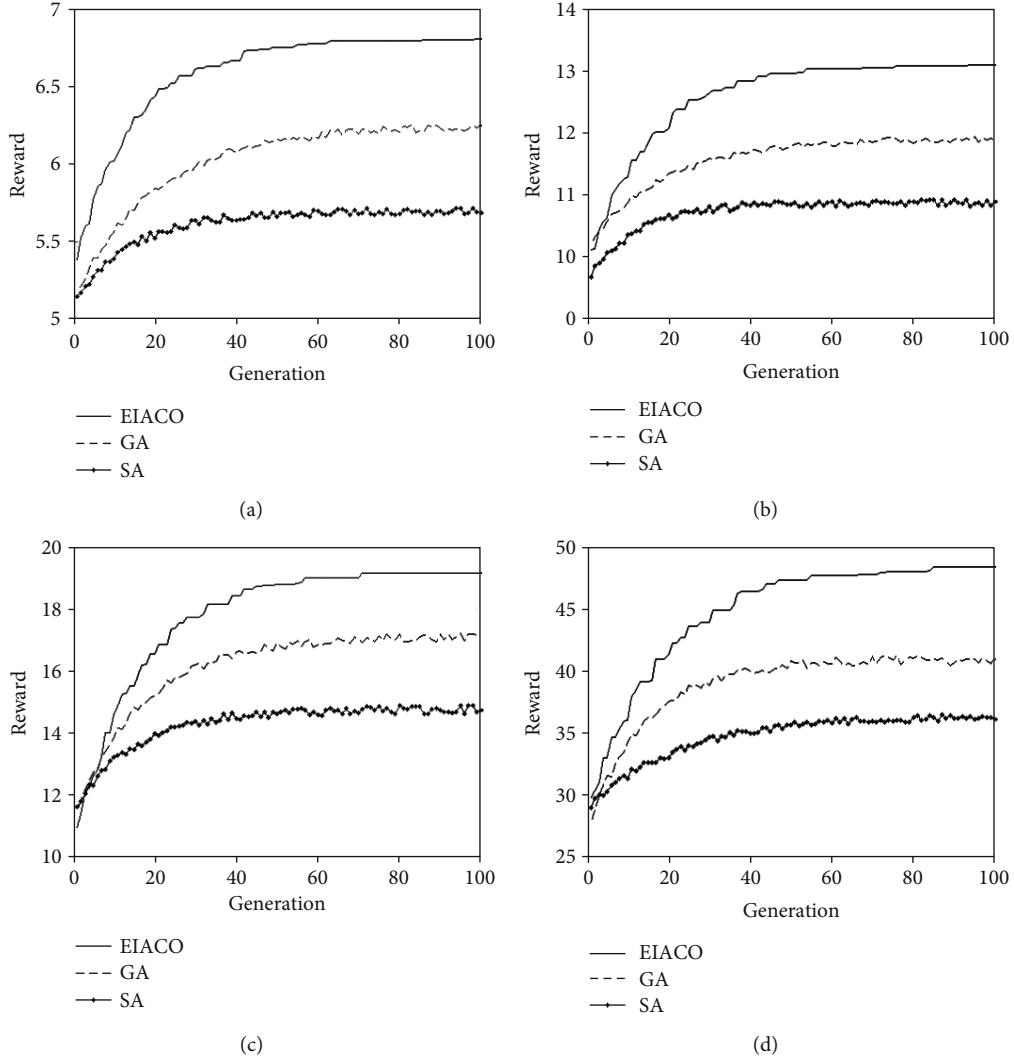


FIGURE 1: (a) Reward for comparison of three algorithms when the number of tasks is 15 and the number of sensors is 8 after 100 generations. (b) Reward for comparison of three algorithms when the number of tasks is 30 and the number of sensors is 15 after 100 generations. (c) Reward for comparison of three algorithms when the number of tasks is 40 and the number of sensors is 20 after 100 generations. (d) Reward for comparison of three algorithms when the number of tasks is 100 and the number of sensors is 50 after 100 generations.

$$\Delta\tau_{ef}(t, t+1) = \sum_{k=1}^s \Delta\tau_{ef}^k(t, t+1). \quad (19)$$

In formula (18), $\Delta\tau_{ef}(t, t+1)$ indicates the value of pheromones that the ant left on the path (e, f) during the generation $(t, t+1)$. ρ is the evaporation coefficient of pheromone to avoid infinite growth of pheromone on the path. And $\Delta\tau_{ef}^k(t, t+1)$ in equation (19) represents the increment of pheromone information that the k_{th} ant left on the path (e, f) during the $(t, t+1)$ generation.

Formula (20) shows the ant-cycle system model of the EIACO to calculate $\Delta\tau_{ef}^k$.

$$\Delta\tau_{ef}^k = g_f Q. \quad (20)$$

In formula (20), Q is a constant and the pheromone released by the ant on the path is the intensity per unit Q . g_f

represents the benefit value that the task is assigned to the f_{th} sensor node. In the ant-cycle system model, the ants release the pheromone when the ant has found an optimal solution. The ant-cycle system model utilizes the overall information.

4.6. Termination Condition. After irritations, EIACO will check whether the condition is satisfied. If the number of iterations is reached, the algorithm will be terminated.

4.7. Elite Strategy. The elitist strategy is introduced to EIACO. In EIACO, the pheromone quantity update formulas are as follows:

$$\tau_{ef}(t, t+1) = \rho \times \tau_{ef}(t) + \Delta\tau_{ef}(t, t+1) + \Delta\tau_{ef}^*, \quad (21)$$

$$\Delta\tau_{ef}^* = \sigma \cdot g_f^* Q. \quad (22)$$

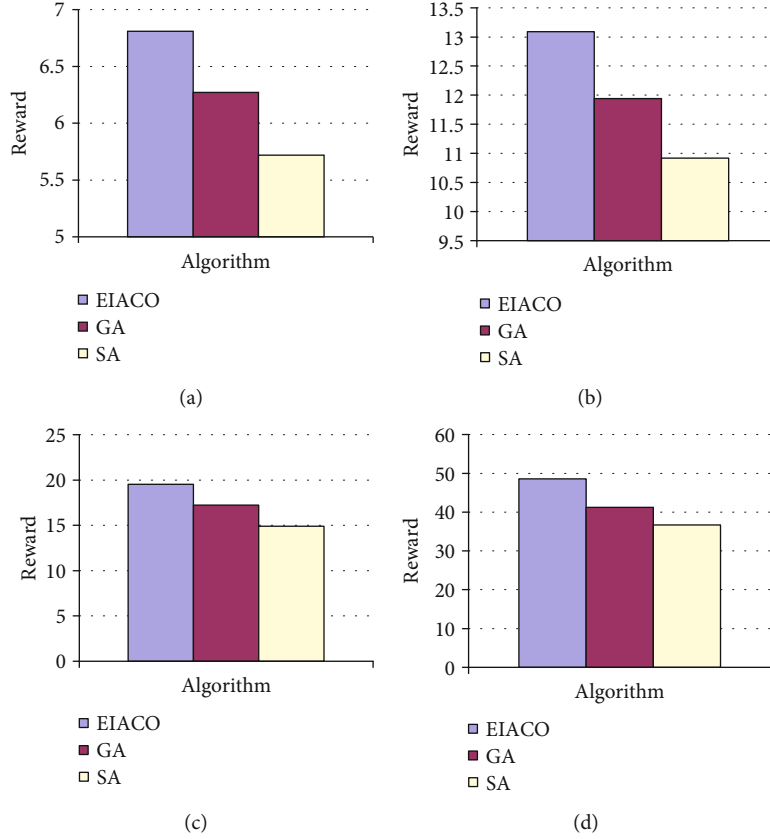


FIGURE 2: (a) Reward for comparison of three algorithms with 15 tasks and 8 sensors. (b) Reward for comparison of three algorithms with 30 tasks and 15 sensors. (c) Reward for comparison of three algorithms with 40 tasks and 20 sensors. (d) Reward for comparison of three algorithms with 100 tasks and 50 sensors.

In formulas (21) and (22), $\Delta\tau_{ef}^*$ represents the increased amount of pheromone on the path (e, f) found by elite ants. σ represents the number of elite ants. g_f^* represents the benefit value of assigning a task with elite strategy.

4.8. Immune Strategy. Unlike the traditional ACO, the EIACO is proposed in this paper for the task allocation problem with immune strategy. The main mechanisms in the immune system, which have been developed in the field of wireless sensor networks based on the immune theory, are applied in the problem of task allocation. The immune strategy is a global optimization method. It has the advantages of strong global search ability, maintaining antibody diversity and robustness. Therefore, the immune strategy is used to deal with the problem of task allocation.

Principles of immune operator in EIACO are as follows. The first step is to identify the antigen. Antigen can be described as the problem of task allocation. Then, create the initial population from the memory cells. The affinity needs to be calculated to evaluate the reward generated by the ants. If the terminal condition is not satisfied, it is necessary to perform immune selection, cloning, mutation and inhibition of mutation, etc. The next step is to refresh the population. A reward of solution with lower performance is replaced by a new generated solution to form an antibody.

The immune operator in EIACO uses the immune mechanism to accelerate convergence. At the same time, the similarity between individuals is used to ensure the diversity of the population, so as to avoid falling into local optimum.

4.9. Basic Steps. The steps of the EIACO algorithm are as follows.

Step 1. Initialize the parameters. The maximum number of iterations is $N_{c,max}$. The initial number of iterations $N_c = 0$. Set the pheromone value, benefit value, and pheromone volatilization coefficient. The number of ants is s . τ_{ef} is used to initialize the pheromone information on the edge (e, f) , $\tau_{ef}(0) = 1$.

Step 2. Add the number of iterations, $N_c = N_c + 1$.

Step 3. Add one number of ants, $k = k + 1$.

Step 4. Calculate the probability of selecting the next node based on formula (15).

Step 5. If $k < m$, turn to Step 3; otherwise, perform Step 6.

Step 6. Update pheromone.

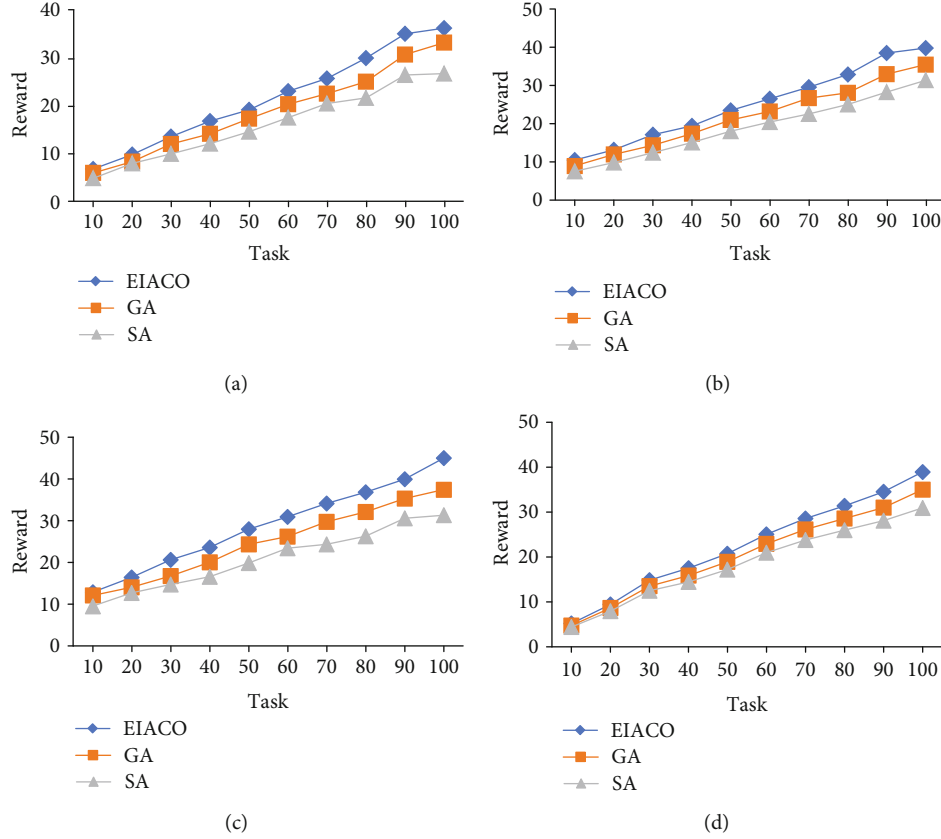


FIGURE 3: (a) Reward for comparison of three algorithms with different tasks and 10 sensors. (b) Reward for comparison of three algorithms with different tasks and 20 sensors. (c) Reward for comparison of three algorithms with different tasks and 30 sensors. (d) Reward for comparison of three algorithms with different tasks and 40 sensors.

Step 7. If the condition is satisfied, that is, the number of irritations $N_c > N_{c_max}$, output the reward. Otherwise, turn to Step 2.

5. Simulation and Results

In this section, the performance of the proposed EIACO method is tested and compared with the GA and SA methods for task allocation in AWSNs. The performance of EIACO is compared with different quantity of temperature and humidity sensor nodes and targets. All cases are run by a computer with a Pentium 2.4 GHz CPU. As indicated earlier, the objective function in Section 3 is to demonstrate the effectiveness of schemes in optimizing the task allocation.

In our simulation, the performance of EIACO will be compared with the GA and the SA. All the runs of the EIACO, GA, and SA algorithms were terminated after 100 generations and the population size is 50. In EIACO, the weight of pheromone is 2 and the weight of benefit value is 2; pheromone volatilization coefficient is employed as 0.98. In GA, the crossover probability is 0.85 and mutation probability is employed as 0.05. In SA, the value of the original temperature is defined as 200 and the value of annealing temperature is defined as 0.85.

The rewards for the EIACO, GA, and SA with different sensors and tasks are listed in Table 1. It shows the task exe-

cution efficiency versus the number of iterations of EIACO, GA, and SA on the task allocation problem with different quantity of sensors and tasks, respectively.

Figures 1(a)–1(d) show the convergence for EIACO, GA, and SA, respectively. Figure 1(a) illustrates obviously that EIACO has a better performance than GA and SA when the number of the sensors is 8 and the number of the tasks is 15. Figure 1(a) shows that the optimal reward of SA is lower than GA as EIACO performs better than GA. Within the initial 50 iterations, the reward of EIACO varies greatly and the convergence speed improves as the generations increase. From 50 to 100 iterations, the reward of EIACO is close to 6.81; however, GA is still far from it and the value of reward is 6.27. The reward of SA is 5.72. EIACO outperforms GA and SA in task execution efficiency after about 50 generations; the population diversity of EIACO with elite operator and immune operator will boost. Over all 100 iterations, the reward of SA is lower than GA, and the convergence rate of EIACO is greater. In Figures 1(b)–1(d), the rewards of EIACO perform better than those of GA and SA with solving the problem of task allocation when the numbers of the sensors are 15, 20, and 50, respectively, and the numbers of the tasks are 30, 40, and 100, respectively. GA and SA show a slower convergence rate than EIACO, and they converge to a suboptimal solution. EIACO displayed no premature convergence in average profits, which are a

common feature of GA and SA. Overall, EIACO is more successful and ideal for task allocation and its convergence is faster than GA and SA when the number of generations is the same.

The performance of EIACO, GA, and SA is compared with a histogram in Figure 2. In Figure 2(a), EIACO yielded much better results compared with GA and SA when the number of the sensors is 8 and the number of tasks is 15 after 100 generations. The reward of SA is smaller than the reward of GA, and EIACO provides a better performance than GA. In Figures 2(b)–2(d), similar conclusions are concluded when the numbers of the sensors are 15, 20, and 50, respectively, and the numbers of the tasks are 30, 40, and 100, respectively. Overall, the performance of EIACO is better than that of the other two algorithms.

In Figure 3, 10 sensors, 20 sensors, 30 sensors, and 40 sensors are considered. The objective function in equations (1) and (2) is used to evaluate the reward. In Figure 3(a), after 100 iterations, the sensors of EIACO, GA, and SA are 10, and the reward increases when the number of tasks is from 10 to 100. It shows that EIACO is more effective than GA and the performance of GA is better than SA. In Figures 3(b)–3(d), comparable results are given when the numbers of the sensors are 20, 30, and 40, respectively. EIACO always performs better than GA and SA.

6. Conclusion

Hence, an elite immune ant colony optimization (EIACO) is proposed in this paper for task allocation in AWSNs. By introducing EIACO into the problem of task allocation, a mathematical model that evaluates the efficiency of task execution is designed to maximize task execution efficiency for AWSNs. Rewards of EIACO in simulation results validate the task execution efficiency, with comparison of GA and SA. In Section 5, the proposed algorithm has higher task execution efficiency than the conventional GA and SA approaches, especially for AWSNs that have numerous targets and temperature and humidity sensor nodes. It further validates the effectiveness of EIACO-based task allocation for maximizing task execution efficiency in AWSNs.

Data Availability

The data used to support the findings of this study are available from the corresponding author upon request.

Conflicts of Interest

The authors declare that they have no conflicts of interest.

Acknowledgments

This paper is supported by the National Nature Science Foundation of China (No. 61662063), High-Level Talent Research Project of Shihezi University (No. RCZX201530), and Major Scientific and Technological Projects of Corps (No. 2017AA005-04).

References

- [1] Z. Sun, Y. Liu, and L. Tao, "Attack localization task allocation in wireless sensor networks based on multi-objective binary particle swarm optimization," *Journal of Network and Computer Applications*, vol. 112, pp. 29–40, 2018.
- [2] W. Yu, Y. Huang, and A. Garcia-Ortiz, "Distributed optimal on-line task allocation algorithm for wireless sensor networks," *IEEE Sensors Journal*, vol. 18, no. 1, pp. 446–458, 2018.
- [3] M. Okhovvat, M. R. Kangavari, and H. Zarrabi, "An analytical task assignment model in wireless sensor actor networks," in *2017 IEEE 7th International Conference on Consumer Electronics - Berlin (ICCE-Berlin)*, pp. 195–199, Berlin, Germany, September 2017.
- [4] Y. Sun, W. Dong, and Y. Chen, "An improved routing algorithm based on ant colony optimization in wireless sensor networks," *IEEE Communications Letters*, vol. 21, no. 6, pp. 1317–1320, 2017.
- [5] J. Jiang, G. Han, and C. Zhu, "A complicated task solution scheme based on node cooperation for wireless sensor networks," in *2016 IEEE 22nd International Conference on Parallel and Distributed Systems (ICPADS)*, pp. 264–269, Wuhan, China, December 2016.
- [6] X. Wang and Q. Liang, "Efficient sensor selection schemes for wireless sensor networks in microgrid," *IEEE Systems Journal*, vol. 12, no. 1, pp. 539–547, 2015.
- [7] A. A. Ferjani, N. Liouane, and I. Kacem, "Task allocation for wireless sensor network using logic gate-based evolutionary algorithm," in *2016 International Conference on Control, Decision and Information Technologies (CoDIT)*, pp. 654–658, St. Julian's, Malta, April 2016.
- [8] P. Neamatollahi, M. Naghibzadeh, and S. Abrishami, "Fuzzy-based clustering-task scheduling for lifetime enhancement in wireless sensor networks," *IEEE Sensors Journal*, vol. 17, no. 20, pp. 6837–6844, 2017.
- [9] S. Aroua, I. Korbi, Y. Ghamri-Doudane, and L. A. Saidane, "A distributed unselfish spectrum assignment for smart microgrid cognitive wireless sensor networks," in *2017 IEEE Wireless Communications and Networking Conference (WCNC)*, pp. 1–6, San Francisco, CA, USA, March 2017.
- [10] V. Raae, M. D. Naboulsi, and R. Glitho, "Energy efficient task assignment in virtualized wireless sensor networks," in *2018 IEEE Symposium on Computers and Communications (ISCC)*, pp. 976–979, Natal, Brazil, June 2018.
- [11] W. Yu, Y. Huang, E. Ding, and A. Garcia-Ortiz, "Joint task allocation approaches for hierarchical wireless sensor networks," in *2018 7th International Conference on Modern Circuits and Systems Technologies (MOCASST)*, pp. 1–4, Thessaloniki, Greece, May 2018.
- [12] M. M. Hassan and A. Alsanad, "Resource provisioning for cloud-assisted software defined wireless sensor network," *IEEE Sensors Journal*, vol. 16, no. 20, pp. 7401–7408, 2016.
- [13] X. Yin, W. Dai, B. Li, L. Chang, and C. Li, "Cooperative task allocation in heterogeneous wireless sensor networks," *International Journal of Distributed Sensor Networks*, vol. 13, no. 10, Article ID 155014771773574, 2017.
- [14] X. Yin, K. Zhang, B. Li, A. K. Sangaiah, and J. Wang, "A task allocation strategy for complex applications in heterogeneous cluster-based wireless sensor networks," *International Journal Of Distributed Sensor Networks*, vol. 14, no. 8, Article ID 155014771879535, 2018.

- [15] A. Niccolai, F. Grimaccia, M. Mussetta, and R. Zich, "Optimal task allocation in wireless sensor networks by means of social network optimization," *Mathematics*, vol. 7, no. 4, p. 315, 2019.
- [16] J. Zhang, R. Heusdens, and R. C. Hendriks, "Rate-distributed spatial filtering based noise reduction in wireless acoustic sensor networks," *IEEE/ACM Transactions on Audio, Speech, and Language Processing*, vol. 26, no. 11, pp. 2015–2026, 2018.
- [17] Y. Jiao and I. Joe, "Energy-efficient resource allocation for heterogeneous cognitive radio network based on two-tier cross-over genetic algorithm," *Journal of Communications and Networks*, vol. 18, no. 1, pp. 112–122, 2016.
- [18] K. Wang, L. Yuan, T. Miyazaki, D. Zeng, S. Guo, and Y. Sun, "Strategic antieavesdropping game for physical layer security in wireless cooperative networks," *IEEE Transactions on Vehicular Technology*, vol. 66, no. 10, pp. 9448–9457, 2017.
- [19] R. Han, Y. Gao, C. Wu, and D. Lu, "An effective multi-objective optimization algorithm for spectrum allocations in the cognitive-radio-based internet of things," *IEEE Access*, vol. 6, pp. 12858–12867, 2018.
- [20] W. Chien, H. Cho, H. Chao, and T. K. Shih, "Enhanced SA-based charging algorithm for WRSN," in *2016 International Wireless Communications and Mobile Computing Conference (IWCMC)*, pp. 1012–1017, Paphos, Cyprus, September 2016.
- [21] M. Ye, Y. Wang, C. Dai, and X. Wang, "A hybrid genetic algorithm for the minimum exposure path problem of wireless sensor networks based on a numerical functional extreme model," *IEEE Transactions on Vehicular Technology*, vol. 65, no. 10, pp. 8644–8657, 2016.
- [22] S. Bi and Y. J. Zhang, "Computation rate maximization for wireless powered mobile-edge computing with binary computation offloading," *IEEE Transactions on Wireless Communications*, vol. 17, no. 6, pp. 4177–4190, 2018.
- [23] W. Li, D. Liu, B. Zhu, X. Wei, W. Xiao, and L. Yang, "SDN control model for intelligent task execution in wireless sensor and actor networks," in *2016 IEEE 83rd Vehicular Technology Conference (VTC Spring)*, pp. 1–5, Nanjing, China, May 2016.
- [24] P. Neamatollahi, M. Naghibzadeh, S. Abrishami, and M. H. Yaghmaee, "Distributed clustering-task scheduling for wireless sensor networks using dynamic hyper round policy," *IEEE Transactions on Mobile Computing*, vol. 17, no. 2, pp. 334–347, 2018.
- [25] P. Bhardwaj, A. Panwar, O. Ozdemir et al., "Enhanced dynamic spectrum access in multiband cognitive radio networks via optimized resource allocation," *IEEE Transactions on Wireless Communications*, vol. 15, no. 12, pp. 8093–8106, 2016.
- [26] S. Marano and P. Willett, "Resource allocation in energy-harvesting sensor networks," *IEEE Transactions on Signal and Information Processing over Networks*, vol. 4, no. 3, pp. 585–598, 2018.
- [27] F. Li, L. Wang, L. Meng, Y. Zhang, and Q. Pan, "Time-pattern design for transmission energy allocation in wireless sensor networks," *IET Communications*, vol. 11, no. 7, pp. 1028–1035, 2017.
- [28] Y. Zhuang, C. Wu, and Y. Zhang, "Non-preference bi-objective compound event barrier coverage algorithm in 3-D sensor networks," *IEEE Access*, vol. 6, pp. 34086–34097, 2018.

Research Article

Colloidal Influence Factor of Bioflocculant in Coagulation of Chromium and Nitrobenzene

Renshi Ma ¹, Guang Chen ¹, Kai Liu ¹ and Shihuan Cheng ²

¹Department of Vascular Surgery, First Hospital of Jilin University-Eastern Division, Changchun City, Jilin Province, China

²Department of Rehabilitation, First Hospital of Jilin University, Changchun City, Jilin Province, China

Correspondence should be addressed to Shihuan Cheng; riely2001@163.com

Received 7 November 2019; Accepted 9 December 2019; Published 30 January 2020

Guest Editor: Yuan Li

Copyright © 2020 Renshi Ma et al. This is an open access article distributed under the Creative Commons Attribution License, which permits unrestricted use, distribution, and reproduction in any medium, provided the original work is properly cited.

The aim of this study is to investigate the flocculation capacity of activated sludge flocculant in chromium ion and nitrobenzene solutions. Besides comparing with activated carbon, we changed some potential factors which may influence the flocculation, such as solution pH value, reaction time, flocculant dosage, and solution initial concentration, and tested the flocculation capacity of this bioflocculant for both chromium and nitrobenzene. In addition, the flocculation of activated sludge after acidic or alkali modification for double solutions was also estimated. Compared with activated carbon, the activated sludge flocculant showed a good flocculation capacity for nitrobenzene, but poor flocculation for chromium following the initial concentration increase. The flocculation for nitrobenzene or chromium increased at initial stage and decreased gradually following the primary dosage of flocculant increase. The flocculation for nitrobenzene increased at the primary stage and decreased after peak, while the flocculation for chromium increased following the pH increase of both solutions. Although the flocculation for nitrobenzene decreased, the flocculation for chromium increased obviously, when we prolonged the reaction time. The flocculant showed a gradual increasing trend in double kinds of solution when they were heating. The flocculation for both nitrobenzene and chromium decreased after acid modification of activated sludge flocculant, while the flocculation increased after basic modification. The present research provided further theoretical basis of the biosorption of heavy metal waste water and nitrobenzene organic toxicants.

1. Introduction

With the rapid development of chemical industry, mining, and metallurgy, emissions of industrial wastewater usually contains an excess of heavy metals [1] and organic toxicants, such as nitrobenzene, which have threatened the environment and human health seriously [2]. The biological flocculation method has been paid more attention due to its efficient and low cost in treating wastewater [3, 4]. The flocculation of some living or dead biomass has been explored in heavy metals and organic compounds [5] by many researchers, such as activated sludge, bacteria, fungi, or algae [6]. Activated sludge is not only for green environmental protection, but also for circular economy in wastewater treatment field. It can decompose organic substances in industrial wastewater by the biochemical meta-

bolic reactions of aerobic microbial substances, which is related to the flocculation, coagulation, and precipitation of activated sludge [7]. In addition, activated sludge can effectively remove colloidal and dissolved substances in waste water and purify the wastewater [3, 8, 9].

Starch is the most widely used synthetic flocculant with a long molecular chain structure. Its amide group (CONH_2) can adsorb many substances to form hydrogen bonds [10]. There have been experiments in which alumina hydrate was added into partially hydrolyzed starch solution, and the anions of the polymerization were adsorbed on the cations of alumina and the viscosity was increased rapidly or colonialized [6, 11, 12]. This enables it to bridge the adsorbed particles, connect several or even dozens of particles together, form flocs, accelerate the descent of particles, and make it the most ideal flocculant. The main reasons for improving

flocculation efficiency by modifying starch are as follows [13]: firstly, because of its polar gene-amide group, it is easy to adsorb on the surface of sediment particles by its hydrogen-binding effect. Secondly, because of its long molecular chains and huge adsorption surface area in water, long chains of large orders of magnitude have good flocculation effect [14]. They can bridge the particles by using long chains to form large particles of flocculants and accelerate sedimentation. Thirdly, with the aid of flocculation-coagulation aid of starch, double ionization compression may occur during the mud coagulation process of water purification, which reduces the stability of particle aggregation [15]. Under the action of molecular gravity, the simple anions of dispersed phase can be replaced by polymer anion groups. Fourthly, the chemical interaction between macromolecule and suspended matter in natural water, or between ions of hydrolytic coagulant added before it, may be a complexation reaction. Finally, because the molecular chains are fixed on the surface of different particles, a polymer bridge is formed between the solid particles [16].

Ionic biomacromolecular flocculants have the following characteristics compared with traditional organic macromolecular flocculants because they carry various anionic and cationic functional groups: the flocculation performance is less affected by the fluctuation of water pH value and salt [17, 18]; the clarification performance is mainly obtained by charge neutralization. The function of this kind of flocculant is mainly to flocculate colloids with positive and negative charges. It has the functions of turbidity removal and decolorization. It is suitable for water treatment with high content of organic colloids [19, 20]. In the present study, we prepared activated sludge flocculant by industrial heavy water and evaluated its flocculation properties for nitrobenzene and heavy metals such as chromium ion. After the comparison of flocculation with activated carbon, we changed some factor which can influence the flocculation potentially, such as primary concentration of chromium and nitrobenzene, pH value of solution, reaction time, flocculant dosage, or solution temperature, and evaluated the flocculation properties of activated sludge flocculant [5–8]. In addition, we modified the flocculant with acid or alkali in order to optimize the flocculation ability.

2. Materials and Methods

2.1. The Experimental Equipment and Reagents

- (1) The main equipment includes a centrifuge (Beckman 6700, USA), constant temperature water tank, UV spectrophotometer (Model-T6, PGENERAL Ltd., Beijing, China), atomic absorption spectrophotometer (4530 Jingke Ltd., Shanghai, China), and electronic scales. The conventional experimental instrument included various ranges of beaker, pipette, volumetric flask, round bottom flask, and glass rod.

- (2) The main reagents are activated sludge of wastewater treatment plant, ammonium sulfamate, N-(1-naphthyl)ethylenediamine, acetone, potassium dichromate, diphenyl hydrazine, nitrobenzene, ethanol, sodium hydroxide, zinc powder, hydrochloric acid, sulfuric acid, nitrate, copper sulfate, sodium nitrite, and sodium chloride.

2.2. Preparing Activated Sludge Biological Flocculant. We made the activated sludge, which has been cultured for some time, standing for 20 minutes and washed twice by distilled water. The supernatant was removed after centrifugation of the sludge at 3000 r/min centrifuge. The remaining material is the activated sludge biological flocculant.

2.3. Preparation of Biological Flocculant from Activated Sludge. The activated sludge was washed with tap water and air-dried at room temperature. After pulverization and screening by a 0.5 mm sieve, the material was mixed well by deionized water and stored for 24 hours. After removal of the suspended matter and soluble material, the sludge was dried at 105°C into powder. We mixed the activated sludge powder (100 g weighted) with phosphoric acid solution or sodium hydroxide solution (1000 mL, 1 mol/L) and stirred for 1 hour in a beaker. After standing, the supernatant was removed from the mixture, which was then dried at 105°C. Next, the sludge was heated at 180°C for 1 hour and washed by deionized water (75°C). After removing the free phosphoric acid and drying at 105°C, the acid- or base-modified activated sludge was prepared finally [21].

2.4. Preparing Different Concentrations of Nitrobenzene Solution and Chromium Ion Solution. A little ether was mixed with nitrobenzene (100 mg) in a 100 mL volumetric flask. After dissolution, the volumetric flask was filled with benzene. The concentration of initial nitrobenzene solution was 1000 mg/L. Different concentrations of nitrobenzene solution was gained by dilution to the initial nitrobenzene solution with benzene.

2.5. Batch Experiment of Colloidal Stability of Chromium Adsorbed by Bioflocculants. Bioflocculants was diluted to 60 mg/L by the addition of distilled water for flocculation of chromium and nitrobenzene. The effects of flocculation conditions (temperature (°C), pH, flocculation time (hour), bioflocculant dosage (mg/L), solutional zeta potential (mg/L), and flocculant dosage) were studied. The pH was adjusted to approximately 3.0–11.0 by 0.1 M HCl and 0.1 M NaOH. Likewise, the effect of temperature was incubated at desired temperatures.

After setting up of fixed parameters, tubes containing the mixture of the bioflocculant solution with chromium ion and nitrobenzene were shaken in an orbital shaker (Model-HZQ-X100, HDL APPARATUS Ltd., China) and stirred at a constant speed of 250 rpm. The initial nitrobenzene concentration was chosen with 2 mg/L. Zeta potential detection value of samples was determined at the liquid surface height of the beaker. The zeta potential of the solution without bioflocculant was set as the

control. Change efficiency of colloid stability of the flocculant was calculated by Equation (1) [22, 23]:

$$\text{Change efficiency of colloid stability (\%)} = \frac{|(A - B)|}{|A|} \times 100, \quad (1)$$

where A is value of the sample and B is value of the control which is determined by an atomic absorption spectrometer.

2.6. ANOVA Analysis of Colloidal Stability of Chromium Adsorbed by Biofloculants. Statistical design of the experiments and data analysis was used by The Design-Expert Software (version 8.3) [24]. The central composite design (CCD) and response surface methodology (RSM) were chosen and applied to optimize the five factors: temperature, pH, flocculation time, flocculant dosage, and chromium ion concentration (see supplementary data S2).

3. Experimental Protocols

3.1. Comparison of Flocculation between Activated Sludge Flocculant and Carbon. In the present studies, we compared the flocculation of activated sludge and carbon in different concentration solutions of nitrobenzene or chromium ion.

1000 mL nitrobenzene solution of different concentrations (500 mg/L, 300 mg/L, 100 mg/L, 50 mg/L, 30 mg/L, 10 mg/L, 1 mg/L, and 0.5 mg/L; 8 kinds of concentration) were mixed with 100 g activated sludge. The suspension were agitated in a beaker for 1 h at 25°C and left to stand for 72 hours. The nitrobenzene concentrations were determined by high-performance liquid chromatography and the removal rates were calculated.

1000 mL nitrobenzene solutions of different concentrations (500 mg/L, 300 mg/L, 100 mg/L, 50 mg/L, 30 mg/L, 10 mg/L, 1 mg/L, and 0.5 mg/L; 8 kinds of concentration) were mixed with 100 g activated carbon. The suspension were agitated in a beaker for 1 h at 25°C and left to stand for 72 hours. The nitrobenzene concentrations were determined by high-performance liquid chromatography and the removal rates were calculated.

We mixed 1000 mL chromium ion solutions of different concentrations (500 mg/L, 300 mg/L, 100 mg/L, 50 mg/L, 30 mg/L, 10 mg/L, 1 mg/L, and 0.5 mg/L; 8 kinds of concentration) with 100 g activated sludge. All the suspensions were agitated in the beaker for 1 hour at 25°C. After standing for 72 hours, the chromium ion concentrations were determined by atomic absorption spectroscopy and the removal rates were calculated.

We mixed 1000 mL chromium ion solutions of different concentrations (500 mg/L, 300 mg/L, 100 mg/L, 50 mg/L, 30 mg/L, 10 mg/L, 1 mg/L, and 0.5 mg/L; 8 kinds of concentration) with 100 g activated carbon. All suspensions were stirred in the beaker for 1 hour at 25°C. After standing for 72 hours, the chromium ion concentrations were determined by atomic absorption spectroscopy and the removal rates were calculated.

3.2. Flocculation of Activated Sludge Flocculant after Changes of Experimental Conditions. In the following experiments, we changed some experimental conditions, such as activated sludge dosage, solutions' pH value, suspension standing time, and solution temperature, in order to demonstrate whether the conditions could affect the flocculation of activated sludge (refer to supplementary data S3 for details of the experiment).

3.3. Flocculation Performance of Modified Activated Sludge Flocculant. In the following research, we changed the pH value of activated sludge for acid or basic modification and determined the flocculation in nitrobenzene or chromium ion solutions.

The activated sludge (100 g) after acid modification, pH value of 2, 3, 4, 5, and 6, were mixed with 1000 mL solutions of nitrobenzene (10 mg/L) or chromium ion (100 mg/L). The suspensions were stirred for 1 hour at 25°C and left to stand for 72 hours. Finally, the remaining concentration of nitrobenzene or chromium ion were determined and the removal rates were calculated.

The activated sludge (100 g) after basic modification, pH value of 8, 9, 10, 11, and 12, were mixed with 1000 mL solutions of nitrobenzene (10 mg/L) or chromium ion (100 mg/L). The suspensions were stirred for 1 hour at 25°C and left to stand for 72 hours. Then, we determined the remaining concentration of nitrobenzene or chromium ion by chromatography or spectroscopy and calculate the removal rates.

3.4. High-Performance Liquid Chromatography

(1) Instruments and reagents

Instrument and reagents include the following: Waters 600 high-performance liquid chromatography (Waters Inc., USA), Waters 2487 Ultraviolet Detector (Waters Inc., USA), methanol (chromatographic purity), distilled water, glacial acetic acid, and nitrobenzene.

(2) Chromatographic conditions (see supplementary data and Figures S1 and S2)

3.5. Analytical Methods. Flocculation&removal rate = $((A - B)/A) \times 100\%$, where A was the concentration of nitrobenzene or chromium ion solution before flocculation, while B was the concentration after flocculation by carbon or activated sludge.

Zeta potential measurement of colloids and flocculant solution was conducted by a zeta potential analyzer (Malvern Nano ZS, Malvern, England).

Fourier-transform infrared spectrometer (Nicolet 6700, ThermoFisher, USA) for space atmospheric component detecting of colloids and flocculants.

4. Results and Discussion

4.1. Comparison of Flocculation between Activated Sludge Flocculant and Carbon. With the increase of initial concentration of nitrobenzene, the activated sludge and carbon

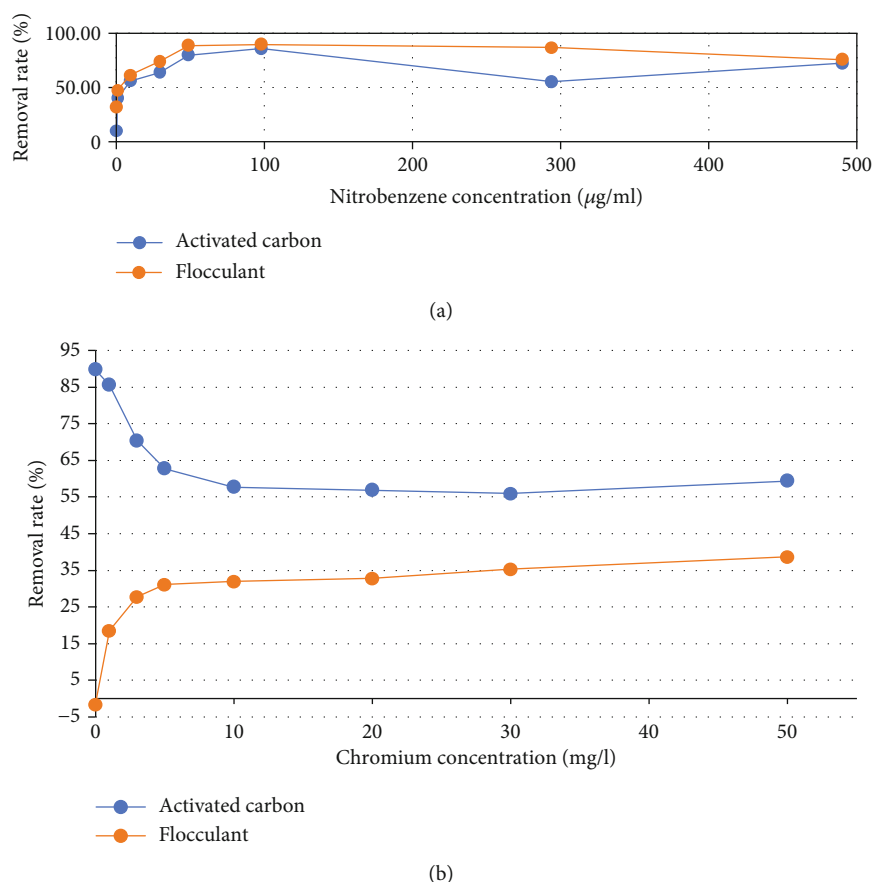


FIGURE 1: (a) Flocculation of activated carbon or flocculant in nitrobenzene. (b) Flocculation of activated carbon or flocculant in chromium.

provided an increased flocculation when the concentration was lower than 100 $\mu\text{g/mL}$. However, with the increasing of concentration, the sludge showed a gradual decreasing flocculation, while the flocculation of carbon increased when the concentration was higher than 300 $\mu\text{g/mL}$. In general, the sludge showed a predominant flocculation than carbon in the nitrobenzene solution (Figure 1(a)). In the chromium solution, the sludge showed a decreased elimination rate of chromium, while the elimination rate increase was shown in activated carbon. In general, the activated carbon showed a predominant flocculation than activated sludge (Figure 1(b)). When the amount of activated sludge was relatively small, the area used for adsorption was relatively small. Because the adsorption site cannot be provided, the removal rate decreased in the chromium solution. On the contrary, the removal rate of activated sludge increased gradually, which proved that the amount of flocculant to remove certain chromium was less. The macromolecule flocculant can provide enough coordination through modification and molecular conformation change.

4.2. Flocculation of Activated Sludge Flocculant after Changes of Experimental Conditions. In the present experiment, we tried to determine the optimal dosage of activated sludge which could absorb the nitrobenzene or chromium at most. Six weights of dosage were tested in the nitrobenzene or chromium solution. The dosage of the flocculant on the flocculation

efficiency did not show a single trend in the present experiment. Nearly 80 percent of nitrobenzene was absorbed by 30 g activated sludge. Too much flocculant (more than 100 g) just provided less than 50 percent removal rate (Figure 2(a)). In the chromium ion solution, the absorption peak was shown at a weight of 50 g activated flocculant. Unlike high dose of nitrobenzene, nearly 80 percent of chromium was absorbed by more than 100 g sludges (Figure 2(b)).

The difference of solution pH value showed a totally different flocculation of sludge in nitrobenzene or chromium ion solution. An acid or weak circumstance could provide more than 80 percent removal rate in nitrobenzene, while a sharp decline of flocculation was shown with very alkaline in solution. The flocculant showed a proximal 100 percent absorption rate when the pH value was 5 (Figure 2(c)). In the chromium solution, the sludge also showed an obvious increasing flocculation with the pH ranging from 2 to 8. The flocculation of sludge approached the maximum even if the pH value raised continuously (Figure 2(d)). The chromium ions existed in an alkaline state as precipitate or complexes, which could not represent the biological removal flocculant. Therefore, the flocculant showed a greater flocculation property in acidic condition.

In the present research, we mixed the sludge with nitrobenzene or chromium solution and was left standing for 72 hours usually. However, we hypothesized that different

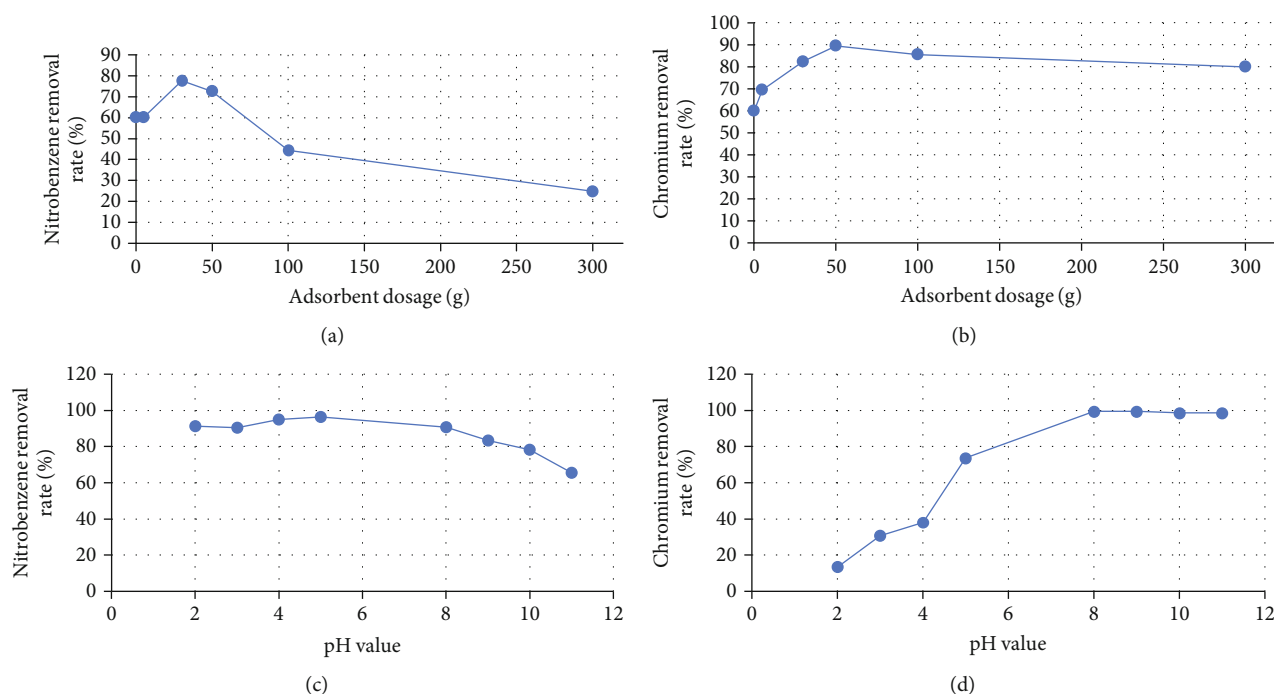


FIGURE 2: (a) Flocculation of different dosage flocculants in nitrobenzene. (b) Flocculation of different dosage flocculants in chromium. (c) Flocculation of different solution pH values in nitrobenzene. (d) Flocculation of different solution pH values in chromium.

standing time or reaction time may affect the flocculation and gave some tests. The sludge showed a total difference in absorption with the time increasing. A gradual flocculation decline was detected after standing within 10 hours, while severe decrease was shown after 12 hours in nitrobenzene solution (Figure 3(a)). In the chromium solution, most ion, nearly 80 percent, was absorbed by sludge within 8 hours, while a platform in flocculation was observed after 12 hours (Figure 3(b)). The interpretation of this phenomenon was that the elimination rate changed following the change of its initial concentration.

In temperature-flocculation tests, the sludge showed a similar trend in both solutions of nitrobenzene and chromium ions with the temperature increasing. From room temperature to 40°C, an obvious incline of absorption was observed in the double solutions. When the temperature was above 40°C, saturation phenomena were shown, with proximal 80 percent in nitrobenzene and 90 percent in chromium of removal rate (Figures 3(c) and 3(d)). The increased temperature could aggravate the thermal motion of molecules, which is in contact with the activated sludge more frequently. Hence, the activated sludge may overcome the barriers to chemical flocculation activation energy and enhance the diffusion rate of particles, which led to an increased elimination rate finally.

4.3. Flocculation Performance of Modified Activated Sludge Flocculant. Finally, we modified the activated sludge with acid or baseline and tested the flocculation in the nitrobenzene and chromium solution. Interestingly, the acidic modified sludge showed a similar flocculation capacity in the double solutions. When the sludge was very acidic (pH value was below 4), nearly 80 percent of nitrobenzene and 85 per-

cent of chromium was absorbed by the flocculant (Figures 4(a) and 4(b)). Although the peak rate was shown at the pH of 2, there was no serious difference of the rate with the pH ranging from 2 to 4. Considering the economy or efficiency, pH value of 4 is more profitable in dealing with too many samples due to its investment reduction in information technology for strong acid.

The basic modified activated sludge showed an increased trend in the elimination of nitrobenzene and chromium ion following the increased pH value. Differently, the flocculation of basic modified sludge was a little more predominant in nitrobenzene than in chromium (Figures 4(c) and 4(d)). Although the peak absorption was shown at the pH of 12, proximal 60 percent of nitrobenzene or chromium was absorbed by modified sludge at the pH of 10. Considering the economy or efficiency, pH value of 10 is more reasonable in dealing with mixture. Nevertheless, basic modified sludge generally showed a weaker flocculation than acidic modification in both nitrobenzene and chromium solution.

4.3.1. Effects of Flocculant Dosage, Temperature, pH, and Flocculation Time on Colloidal Stability of Chromium and Nitrobenzene Adsorbed by Flocculants. The experiment assignment and the collected response data are shown in Table S1 and Table S2. As shown in Table S3, the linear terms for flocculant dosage (C) and flocculation time (D) had significant effects on the change efficiency of colloid stability (F value < 0.05), but temperature (A) and pH (B) had no significant effects on the change efficiency of colloid stability. The relationship between temperature in the range of 10–40°C and change efficiency of colloid stability was studied. Figure 5 shows that the highest change efficiency of colloid stability was achieved at 17.58°C. With the

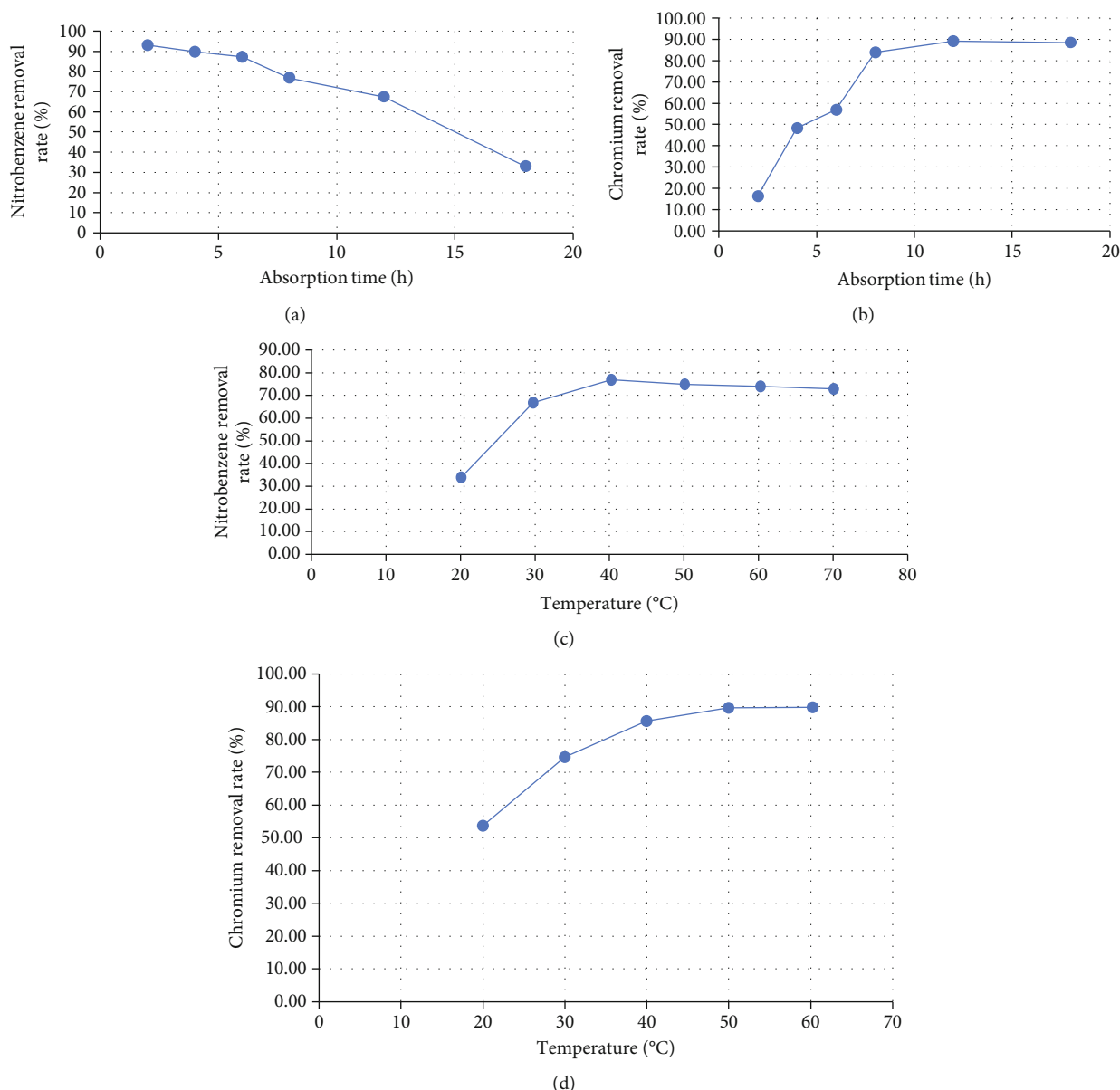


FIGURE 3: (a) Flocculation of different absorption time in nitrobenzene. (b) Flocculation of different absorption time in chromium. (c) Flocculation of different temperature in nitrobenzene. (d) Flocculation of different temperature in chromium.

temperature rising from 10 to 17.58°C, change efficiency of colloid stability increased from 69.87% to 71.81% and decreased to 60.72% with temperature rising to 30°C.

Table S3 and Figure 4 (above) shows that the influence of pH on flocculation was not significant, the change efficiency of colloid stability just increased by 1%, with pH raising from 5 to 9. As shown in Figure 5 (below), zeta potential measurement of flocculant illustrated that it was mainly negatively charged in alkaline condition and in acidic condition. Flocculant has been reported to have different electric states at different pH; it is positively charged in acidic condition (pH below 4) and negatively charged in neutral and alkaline conditions (pH above 4). It could be concluded that electrostatic repulsion effect was not the main factor affecting the change efficiency of colloid stability.

For these reasons, we chose the most conventional condition viz pH 6.5-8 and temperature 15-25°C in the optimized experimental condition [25]. According to the experimental results, the main factors affecting the change efficiency of colloid stability are flocculant dosage (C) and flocculation time (D). The optimization of the operating conditions was conducted by the quadratic models of the experimental design. Figure 5 illustrates that all the selected optimum solutions had a desired prediction of the change efficiency of colloid stability with the maximum experimental data. By triplicates of the experiments, the validated experimental results of the change efficiency of colloid stability and the values predicted by the models were shown in Figure 5. Therefore, the model was considered to fit the experimental data very well.

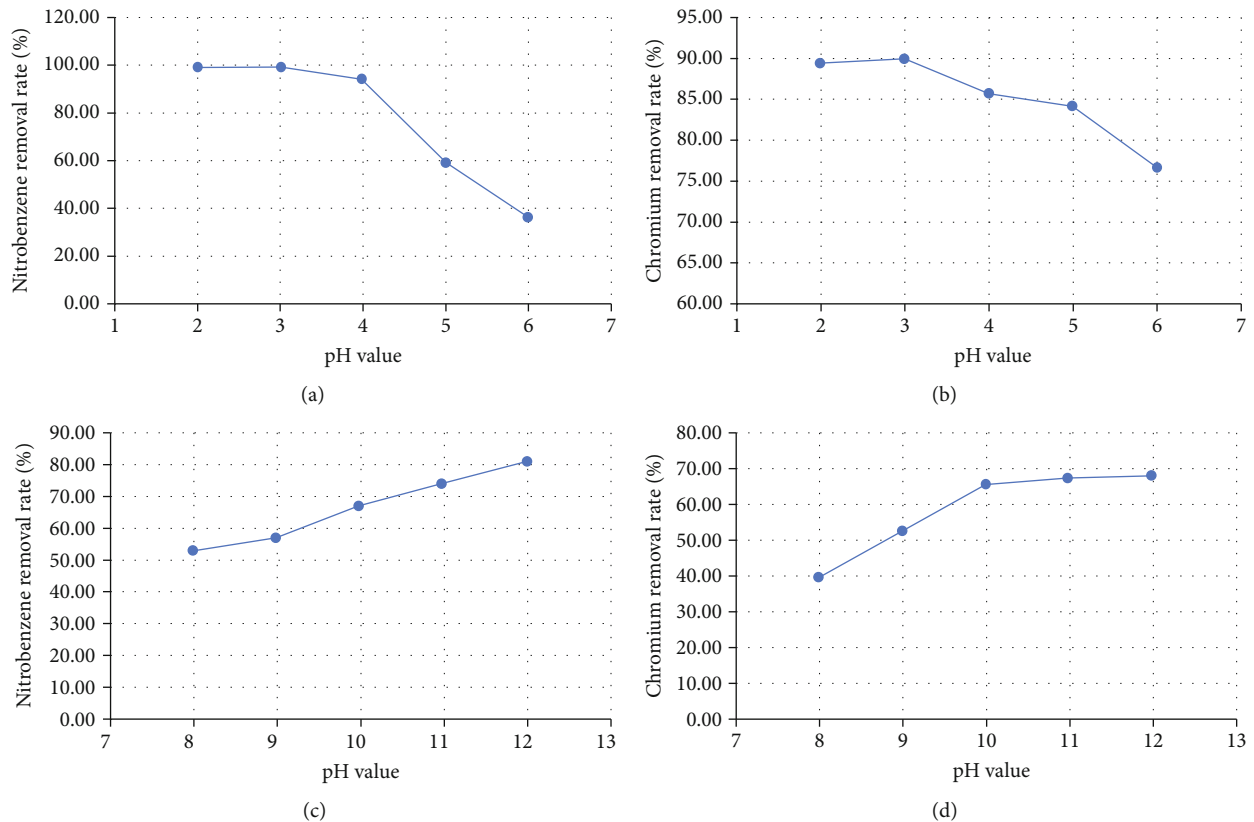


FIGURE 4: (a) Flocculation after acid modification in nitrobenzene. (b) Flocculation after acid modification in chromium. (c) Flocculation after basic modification in nitrobenzene. (d) Flocculation after basic modification in chromium.

4.4. Zeta Potential and Fourier-Transform Infrared Spectrometer Analysis of Colloids and Flocculant Solution. Infrared radiation (IR) spectrum was investigated. The IR spectrum of flocculant exhibited a hydroxyl stretching peak at 3700 cm^{-1} and a carboxyl band at 1750 , 1500 , and 1400 cm^{-1} as presented in Figure 6. The C-O-H stretching vibration displayed adsorption peak at 700 cm^{-1} . 1750 , 1500 , and 1400 and 700 cm^{-1} indicated the deformation vibration of C-O-H and the bending vibration of Cr-O, respectively. Oxygen-containing groups above [26], especially the strong polar groups such as -OH, are abundant on the surface of the bioflocculant, which makes the materials water soluble. Shock and displacement of the absorption peak showed that the dispersion is good and the polarity is enhanced, and the adsorption of chromium by bioflocculant is promoted [27]. The migration and change of the infrared peak show that the existence of flocculant may destroy the stability of the colloid, which may be caused by adsorption, but it may also be caused by the role of net catching.

Zeta potential measurement of flocculant (Figure 6) indicated that it was negatively charged in both alkaline solution and acidic solution; however, zeta potential of colloids after flocculation was electrically neutral ($2 < \text{pH} < 7$) and was decreased by bioflocculant in alkaline ($10 < \text{pH} < 7$) (Figure 6).

5. Conclusions

In activated sludge wastewater treatment process, the degradation of pollutants is divided into two stages: the first stage is that sludge flocs adsorb organic pollutants from wastewater outside the cell wall of bacteria (adsorption stage); the second stage is that bacteria transport pollutants to the substances and energy required for cell metabolism (degradation stage) through active transportation. Physical effect plays a decisive role, and extracellular polymer (EPS) is the main component of sludge flocs, accounting for 50% to 90% of the total organic matter of activated sludge [22]. EPS has a significant impact on the physical and chemical properties of sludge flocs, such as floc structure, surface charge, flocculation, sedimentation, dewatering, and adsorption properties. Many domestic scholars and abroad have discussed the influence of sludge EPS adsorption, but they mainly focus on the adsorption of heavy metals by activated sludge EPS [23]. Studies on extracting EPS from aerobic granular sludge by cation exchange resin found that the presence of EPS significantly increased the bacterial adsorption performance. Colloidal stability is directly related to the flocculation efficiency of pollutants. As the research shows, bridging, netting and compressing double electric layer can make the colloid lose stability, so that the pollutants can be removed from the water by flocculation or air flotation.

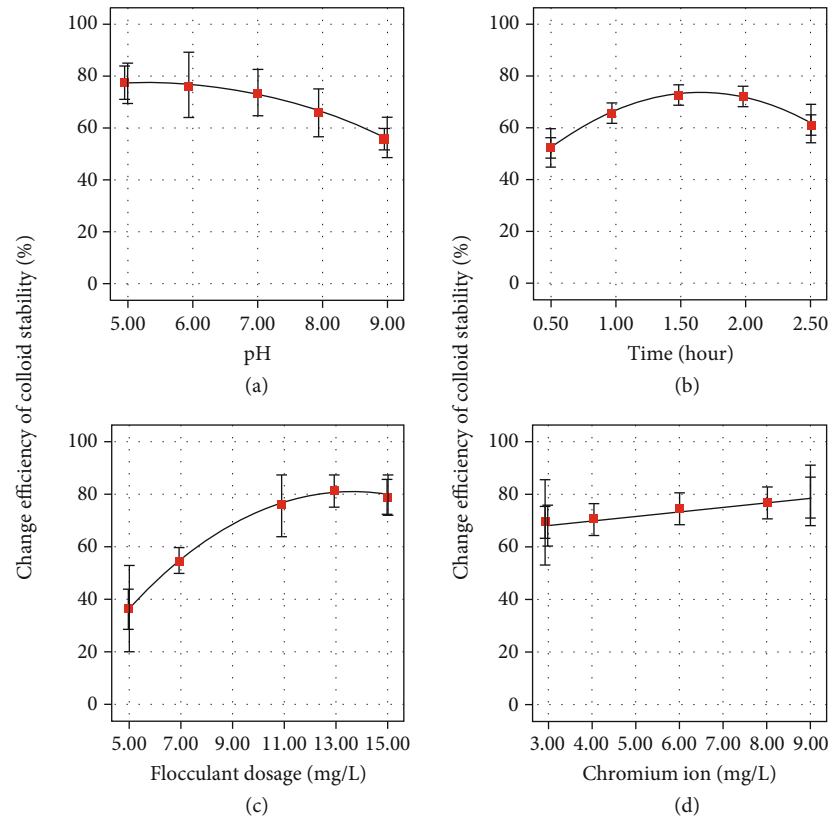


FIGURE 5: Effect of four single variables on the change efficiency of colloid stability, which include the following: (A) pH, (B) time, (C) flocculant dosage (G value was 0 s^{-1}), and (E) chromium ion. Red field square: verified change efficiency of colloid stability under selected conditions.

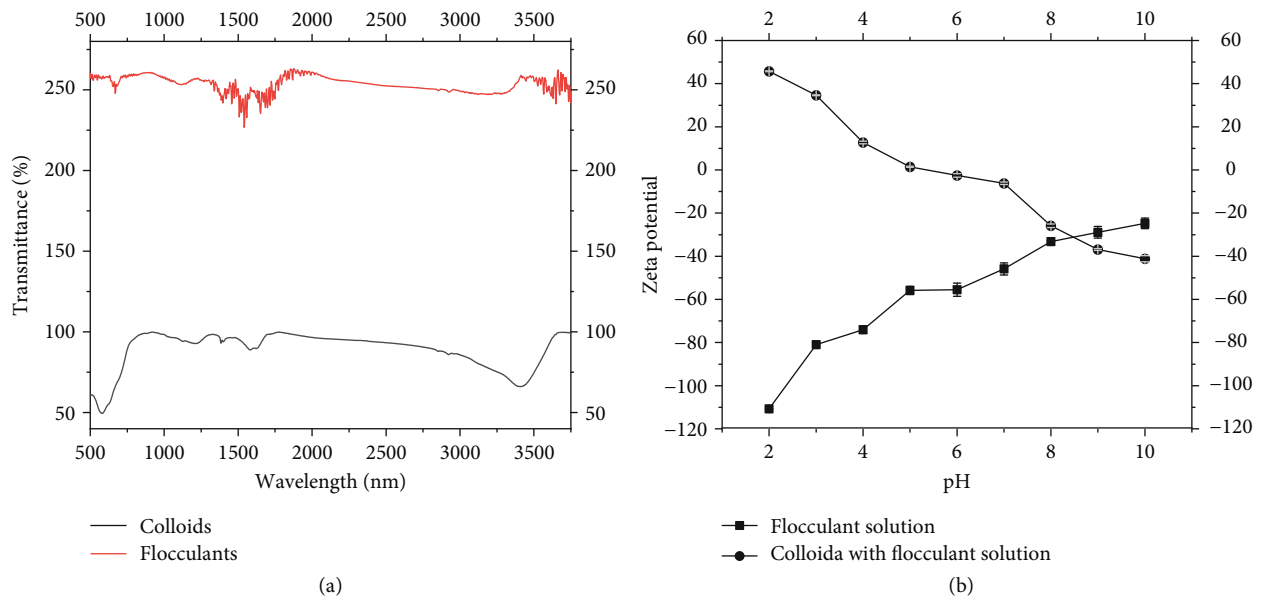


FIGURE 6: Zeta potential and Fourier-transform infrared spectrometer analysis of colloids and flocculants solution (dry precipitate).

Previous studies have focused on one pollutant, which can be easily explained by the principle and model of flocculation. However, when two pollutants exist, especially organic pollutants and inorganic ions, the colloidal stability and destabi-

lization process become very complex. This paper studies the influence of different conditions on the system. However, it must be acknowledged that the methods used in this paper, such as zeta potential and Fourier infrared scanning, are

not enough to explain the molecular role in this complex system. Therefore, further research is needed.

Little research has been done on the adsorption of organic pollutants by sludge EPS; the analysis of experimental results obtained the following conclusions:

- (1) Compared with activated carbon, the activated sludge showed a greater flocculation capacity on heavy metals or organics
- (2) The appropriate pH modification, acidic or basic, could increase the elimination rate, while the acid modification is more effective
- (3) Activated sludge process should strictly follow the reduction, recycling, and innocuity principles

Data Availability

The data used to support the findings of this study are included within the article.

Conflicts of Interest

The authors declare that they have no conflicts of interest.

Supplementary Materials

SI-1: chromatographic conditions and standard curve. SI-2: ANOVA analysis of colloidal stability of chromium adsorbed by biofloculants. SI-3: flocculation of activated sludge flocculant after changes of experimental conditions. SI-4: transcription analyses procedure. Table S1: independent variables and their levels in the experimental design. Table S2: experimental design and results of the central composite design. Table S3: ANOVA analysis for responses Y (change efficiency of colloid stability (%)). (Supplementary Materials)

References

- [1] J. Lin and C. Harichund, "Short communication: industrial effluent treatments using heavy-metal removing bacterial bio-floculants," *Water SA*, vol. 37, no. 2, pp. 265–270, 2011.
- [2] Y. Deng, K. Lei, A. Critto, F. Qiao, Z. Li, and G. Fu, "Improving optimization efficiency for the total pollutant load allocation in large two-dimensional water areas: Bohai Sea (China) case study," *Marine Pollution Bulletin*, vol. 114, no. 1, pp. 269–276, 2017.
- [3] Q. Yu, Y. Hu, and Z. Lei, "Flocculation properties of the compound biofloculant," *Huanjing Kexue Xuebao/Acta Scientiae Circumstantiae*, vol. 33, no. 11, pp. 2999–3006, 2013.
- [4] J. Sun, X. Zhang, X. Miao, and J. Zhou, "Preparation and characteristics of biofloculants from excess biological sludge," *Bioresource Technology*, vol. 126, pp. 362–366, 2012.
- [5] A. E. C. Botero, M. L. Torem, and L. M. S. De Mesquita, "Trends on the use of bioreagents in mineral flotation," *Revista Escola de Minas*, vol. 61, no. 1, pp. 57–61, 2008.
- [6] B. R. Sharma, N. C. Dhuldhoya, and U. C. Merchant, "Flocculants - an ecofriendly approach," *Journal of Polymers and the Environment*, vol. 14, no. 2, pp. 195–202, 2006.
- [7] S. L. Guo, X. Q. Zhao, C. Wan et al., "Characterization of flocculating agent from the self-flocculating microalga *Scenedesmus obliquus* AS-6-1 for efficient biomass harvest," *Bioresource Technology*, vol. 145, pp. 285–289, 2013.
- [8] A. K. Lee, D. M. Lewis, and P. J. Ashman, "Microbial flocculation, a potentially low-cost harvesting technique for marine microalgae for the production of biodiesel," *Journal of Applied Phycology*, vol. 21, no. 5, pp. 559–567, 2009.
- [9] H. Zou, G. Pan, and H. Chen, "Effects of ionic strength on the flocculation and removal of cyanobacterial cells of *Microcystis aeruginosa* by clays," *Huanjing Kexue/Environmental Science*, vol. 26, no. 2, pp. 148–151, 2005.
- [10] D. O. Krentz, C. Lohmann, S. Schwarz et al., "Properties and flocculation efficiency of highly cationized starch derivatives," *Starch/Staerke*, vol. 58, no. 3–4, pp. 161–169, 2006.
- [11] M. Salgot, E. Huertas, S. Weber, W. Dott, and J. Hollender, "Wastewater reuse and risk: definition of key objectives," *Desalination*, vol. 187, no. 1–3, pp. 29–40, 2006.
- [12] S. Majam and P. A. Thompson, "Polyelectrolyte determination in drinking water," *Water SA*, vol. 32, no. 5, pp. 705–707, 2006.
- [13] K. J. Howe, D. W. Hand, J. C. Crittenden, R. R. Trussell, and G. Tchobanoglous, *Principles of Water Treatment*, Wiley, 2012.
- [14] S. S. F. Filho, "Water treatment: principles and design," *Engenharia Sanitaria E Ambiental*, vol. 10, no. 3, pp. 184–184, 2005.
- [15] R. D. Holbrook, J. H. Yen, and T. J. Grizzard, "Characterizing natural organic material from the Occoquan Watershed (Northern Virginia, US) using fluorescence spectroscopy and PARAFAC," *Science of the Total Environment*, vol. 361, no. 1–3, pp. 249–266, 2006.
- [16] C. Park, C. D. Muller, M. M. Abu-Orf, and J. T. Novak, "The effect of wastewater cations on activated sludge characteristics: effects of aluminum and iron in floc," *Water Environment Research*, vol. 78, no. 1, pp. 31–40, 2006.
- [17] D. M. Bortz, T. L. Jackson, K. A. Taylor, A. P. Thompson, and J. G. Younger, "Klebsiella pneumoniae flocculation dynamics," *Bulletin of Mathematical Biology*, vol. 70, no. 3, pp. 745–768, 2008.
- [18] Z. Zhang, B. Lin, S. Xia, X. Wang, and A. Yang, "Production and application of a novel biofloculant by multiple-microorganism consortia using brewery wastewater as carbon source," *Journal of Environmental Sciences*, vol. 19, no. 6, pp. 667–673, 2007.
- [19] W. Wei, R. Yu, Y. Yuan, and G. Wang, "Research on the flocculation mechanism of microbial flocculants," in *2010 4th International Conference on Bioinformatics and Biomedical Engineering*, Chengdu, China, June 2010.
- [20] L. S. Kim, S. J. Hong, M. K. Son, and Y. H. Lee, "Polymeric and compositional properties of novel extracellular microbial poly-glucosamine biopolymer from new strain of *Citrobacter* sp. BL-4," *Biotechnology Letters*, vol. 28, no. 4, pp. 241–245, 2006.
- [21] L. Ge, H. Deng, H. Gao, and F. Wu, "Optimized extraction protocol for extracellular polymeric substances (EPS) from two activated sludges," *Research Journal of Chemistry and Environment*, vol. 14, no. 2, pp. 78–82, 2010.
- [22] C. Xu, S. Zhang, C. Y. Chuang, E. J. Miller, K. A. Schwehr, and P. H. Santschi, "Chemical composition and relative hydrophobicity of microbial exopolymeric substances (EPS) isolated by anion exchange chromatography and their actinide-binding affinities," *Marine Chemistry*, vol. 126, no. 1–4, pp. 27–36, 2011.

- [23] D. Kumar, L. K. Pandey, and J. P. Gaur, "Metal sorption by algal biomass: from batch to continuous system," *Algal Research*, vol. 18, pp. 95–109, 2016.
- [24] L. Xu, R. Ma, C. Sun, and D. Sun, "Enterococcus faecalis bio-flocculant enhances recovery of graphene oxide from water," *Polish Journal of Environmental Studies*, vol. 27, no. 6, pp. 1–10, 2018.
- [25] H. Ding, P. M. Feng, W. Chen, and H. Lin, "Identification of bacteriophage virion proteins by the anova feature selection and analysis," *Molecular BioSystems*, vol. 10, no. 8, pp. 2229–2235, 2014.
- [26] G. A. Pitsevich, A. E. Malevich, E. N. Kozlovskaya et al., "Theoretical study of the C-H/O-H stretching vibrations in malonaldehyde," *Spectrochimica Acta Part A: Molecular and Biomolecular Spectroscopy*, vol. 145, pp. 384–393, 2015.
- [27] Y. L. Pei, Z. S. Wu, X. Y. Shi, X. N. Pan, Y. F. Peng, and Y. J. Qiao, "NIR assignment of magnolol by 2D-COS technology and model application Huoxiangzhengqi oral liquid," *Guang pu xue yu guang pu fen xi = Guang pu*, vol. 35, no. 8, pp. 2119–2123, 2015.

Research Article

Evaluation of the Spatial Pattern of the Resolution-Enhanced Thermal Data for Urban Area

Xiao Feng¹ and Jiyuan Li²

¹School of Highway, Chang'an University, Middle of South Er'huan Road, Xi'an, Shaanxi, China 710064

²Northwest Land and Resources Research Center, Shaanxi Normal University, No. 620 West Chang'an Street, Xi'an, Shaanxi, China 710119

Correspondence should be addressed to Jiyuan Li; vip@snnu.edu.cn

Received 31 October 2019; Accepted 14 December 2019; Published 28 January 2020

Guest Editor: Zhifeng Yu

Copyright © 2020 Xiao Feng and Jiyuan Li. This is an open access article distributed under the Creative Commons Attribution License, which permits unrestricted use, distribution, and reproduction in any medium, provided the original work is properly cited.

With the development of urbanization, land surface temperature (LST), as a vital variable for the urban environment, is highly demanded by urban-related studies, especially the LST with both fine temporal and spatial resolutions. Thermal sharpening methods have been developed just under this demand. Until now, there are some thermal sharpening methods proposed especially for urban surface. However, the evaluation of their accuracy still stopped at the level that only considers the statistical aspect, but no spatial information has been included. It is widely acknowledged that the spatial pattern of the thermal environment in an urban area is relatively critical for urban-related studies (e.g., urban heat island studies). Thus, this paper chose three typical methods from the limited number of thermal sharpening methods designed for the urban area and made a comparison between them, together with a newly proposed thermal sharpening method, superresolution-based thermal sharpener (SRTS). These four methods are analyzed by data from different seasons to explore the seasoning impact. Also, the accuracy for different land covers is explored as well. Furthermore, accuracy evaluation was not only taken by statistical variables which are commonly used in other studies; evaluation of the spatial pattern, which is equally important for urban-related studies, was also carried out. This time, the spatial pattern not only was analyzed qualitatively but also has been quantified by some variables for the comparison of accuracy. It is found that all methods obtained lower accuracies for data in winter than for data in other seasons. Linear water features and areas along it are difficult to be detected correctly for most methods.

1. Introduction

It is widely acknowledged that urban heat island (UHI) is becoming a detrimental phenomenon, leading to several social and environmental issues such as poor air quality, high energy demand, and even human mortality [1, 2]. Land surface temperature (LST), which can be derived from remote sensing data, is an essential variable for UHI studies and has been widely used in the literature [3]. Unfortunately, it is still reported that the current satellite sensor data are of inadequate detail for urban-related studies, which demands data with fine resolution in both spatial and temporal dimensions [4]. Sobrino et al. [5] carried out a study exploring the suitable spatial and temporal resolutions for UHI studies and finally suggested that spatial resolution finer than 50 m

and a 1-2-day revisit frequency would be the desired resolutions. According to the current satellite thermal data, it is impossible to achieve this requirement because there is a trade-off between the spatial and temporal resolutions of the current remote sensing data. Moreover, this trade-off is difficult to address through the advancement of hardware due to the physical principles of remote sensing [6–8]. Thus, thermal sharpening techniques have been proposed.

It is found that the accuracy of thermal sharpening usually relies much on the physical meaning behind the relationship between LST and the sharpening predictors. This means that if the relationship and sharpening predictors have a strong physical meaning (e.g., the strong correlation between vegetation and LST in summer), the accuracy of a thermal sharpening method is usually acceptable. In light of this,

researchers used more land cover information in thermal sharpening, especially for areas with complicated surface compositions such as urban areas [9, 10]. Studies based on regression models for downscaling have often used spectral indices (e.g., normalized difference water index (NDWI), normalized difference built-up index (NDBI)) to represent different land covers [8, 11, 12], while some others directly made use of land cover data in the process of downscaling [13, 14]. The accuracy assessment shows that methods considering more land covers gained a higher accuracy than methods based on only NDVI-LST relationship for urban areas. However, although the priority of bringing more land cover information in thermal sharpening has been demonstrated, as Sismanidis et al. [15] pointed out, the evaluation system of current thermal sharpening methods for urban areas may still need some improvements.

First, results of many studies are carried out by only one image and hence may be of limited generalizability [8, 16, 17], particularly when images acquired at different times or under different conditions are used (e.g., summer or winter) or used for different land cover mosaics. Therefore, it is better to use more than one image as the testing dataset to reduce the occurrence of bias. Furthermore, LST is a highly changeable variable which changes hourly, daily, and seasonally. Sismanidis et al. [15] pointed out that most spatial-resolution-enhanced LST actually would be used for UHI monitoring and analyzing which are the time series applications. Thus, the evaluation should at least consider the performance of a new method in different biomes, seasons, topography, and climatic conditions which will impact the relationship between LST and its predictors in time series studies. Until now, though there were some studies that reported the use of thermal sharpened LST for time series application, they mainly used the images collected between June and September [15, 18, 19]. This is because these studies usually used the methods relying on NDVI-LST relationship, and thus, they need to choose the months that have a reliable NDVI-LST relationship to guarantee the accuracy. Therefore, there is still a lack of research exploring the accuracy of thermal sharpening methods for data in different seasons.

The second issue is the evaluation of the spatial pattern of the thermal sharpened LST. Currently, most studies rely on the statistical methods for the assessment (e.g., RMSE, mean absolute error (MAE), and correlation coefficient) which focus on the accuracy of the absolute LST value of each pixel but do not consider any spatial information [9, 15, 20, 21]. However, spatial pattern information is equally critical for UHI studies [15]. How to evaluate it quantitatively and adequately is always a challengeable issue. Researchers tried to measure the spatial extent and magnitude of the UHI or use some variables (e.g., Local Moran I) to quantify the spatial information from LST images [15, 22]. Unfortunately, until now, there is no widely acknowledged method to define the similarity of the spatial pattern between the predicted and reference LSTs.

The third issue is the evaluation of accuracy for different land cover types. Although it is acknowledged that more land cover information can enhance the accuracy of thermal sharpening for urban areas, it is rare to see the analyses for

the accuracy of the sharpened LST of different land covers. Based on the definition of heat capacity, it is known that heat capacity is a significant impacting factor for LST. Different materials have different heat capacities. Thus, different land covers have different LSTs. Furthermore, land covers may have different changing features in different seasons. For example, the LST of water will not decrease as many as that of an impervious surface from summer to winter, because the heat capacity of water is larger than that of the impervious surface. LST of land covers has a direct impact on the spatial pattern of LST. Thus, this difference may further lead to questions such as the following: Will the spatial pattern of LST, which influenced significantly by land covers, in different seasons change? Is the spatial pattern of LST in summer the same as it is in winter? If it changes, how does it change? There is a lack of answer to these questions because there is little spatial analysis of LST for different land covers in different seasons.

This research tried to provide a comprehensive comparison both statistically and spatially in a quantitative way, considering all the impacting factors to the accuracy of the thermal sharpening methods, such as seasons and land covers. It illustrated the advantage of a newly proposed thermal sharpening method and analyzed the accuracy of different thermal sharpening methods proposed for urban areas, including the new method, by data in different seasons, which corresponds to the aforementioned first issue. Not only the statistical assessment of the accuracy was taken; the evaluation of spatial pattern, which is equally important for urban-related studies, was also carried out. This study tried to use quantitative variables to compare the accuracy of the spatial pattern of LST and not only qualitative description for the spatial analyses of LST, which provided a potential way to deal with the second issue. Furthermore, the spatial analysis was also conducted for different land cover types, which refers to the third evaluation issue discussed above.

2. Data and Methods

2.1. Data. Great London is chosen as the study area, since it provides a complex surface composition. Testing data used in this research includes Landsat ETM+ and MODIS, while the validation data is ASTER images (Figure 1).

2.2. Experiment Design. The target of this study is to provide a comprehensive comparison for different methods in both statistical and spatial aspects and also to analyze the reliability and accuracy of the newly proposed thermal sharpening method SRTS. Thus, other three thermal sharpening methods proposed for the urban surface, which are Emissivity Modulation (EM) [14], Pixel Block Intensity Modulation (PBIM) [23, 24], and adjusted stratified stepwise regression method (Stepwise) [11], were chosen as the comparison of SRTS. Those three methods were chosen because they consider more than three land cover types which are essential impacting factors in thermal sharpening. Another reason is that their study areas are also metropolitans that are comparable with each other (i.e., Hong Kong, Athens, Shanghai, and

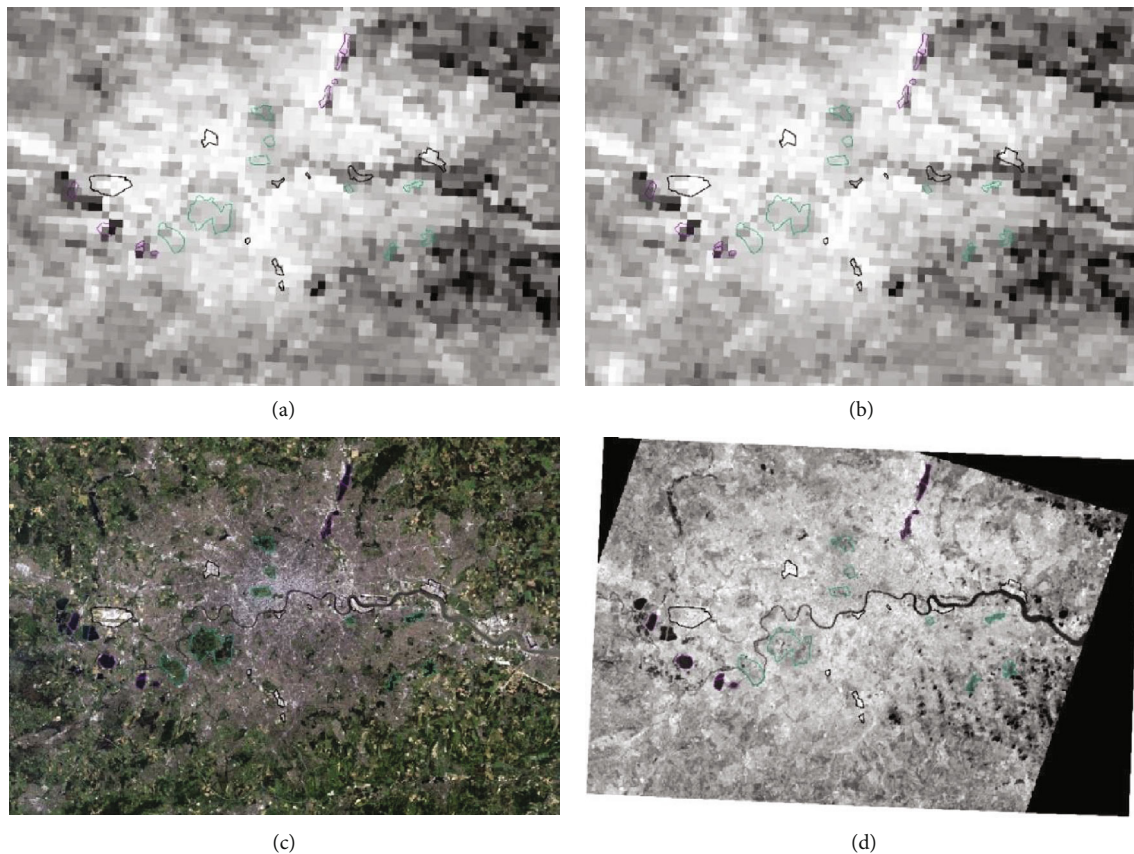


FIGURE 1: Illustration of the study area by the main data sources obtained in April used in this study. (a, b) are the MODIS thermal band images of Greater London with 1 km resolution. (c) is the true color image of Landsat ETM+ image with 30 m resolution, which is prepared for methods requiring fine resolution input. This image is obtained in June due to the unavailability of data in April 2000. (d) is the reference LST obtained from ASTER with 90 m resolution. The objects representing impervious surface (black boundary), vegetation (green boundary), and water (purple boundary) are also presented in each image.

London). All four methods were tested by data from different seasons. Moreover, LSTs for different land cover types were also compared and analyzed.

The evaluation of thermal sharpening methods was conducted in two perspectives: evaluation by statistical variables, including RMSE and correlation coefficient of result produced by each method, and evaluation of the spatial pattern of thermal sharpened LST results. In this study, fuzzy similarity, which considers the spatial characteristics in the neighborhood of each pixel, was used for evaluation of the spatial pattern of LST [25]. It calculated a similarity value for each pixel of the predicted LST images based on the reference image. In addition, visual comparison with vector boundaries of some selected objects representing different land covers was also taken for evaluation of the spatial pattern of LST. Here, the impervious surface, water, and vegetation are considered as the main land cover types of the urban surface [26]. The objects chosen for water or vegetation are relatively easy, as lakes and parks can be used which usually have a fairly clear closed boundary. The impervious surface, which is usually built as open areas or connected to other impervious surfaces (e.g., roads), is difficult to define a closed boundary. Therefore, in visual comparison, the analysis of the impervious surface was focused on the relative comparison

between the LSTs of pixels in and outside the objects representing the impervious surface, for instance, whether the pixels in the impervious surface objects obtained, if in summer, the higher LST than its surroundings that are not impervious surface in the daytime. This can, though qualitatively, still support the accuracy assessment of the predicted spatial pattern of the LST image to some extent and can reflect the sensitivity of all methods to the LST variation between different land covers.

2.3. Superresolution-Based Thermal Sharpener. Currently, there are two main strategies to enhance the spatial resolution of LST. The first one is to process the coarse spatial resolution LST directly with its fine resolution impacting factors by using their experience relationship extracted by statistical algorithms, while the second strategy is to enhance the spatial resolution of the retrieving elements of LST (e.g., thermal radiance, atmospheric profiles). The newly proposed SRTS actually proposed a framework within which enhances the spatial resolution of the retrieving elements first by superresolution mapping (SRM) and superresolution reconstruction (SRR) and then derives the LST based on the resolution-enhanced elements. The framework has been shown in Figure 2.

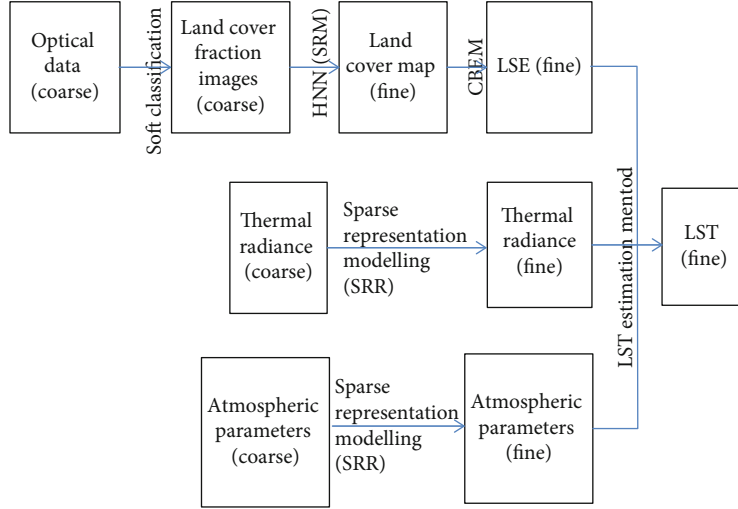


FIGURE 2: Framework of the proposed SRTS. SRR means superresolution reconstruction. SRM means superresolution mapping. LSE means land surface emissivity. HNN means Hopfield neural network. CBEM means classification-based emissivity method.

2.3.1. Hopfield Neural Network-Based SRM. One of the retrieving elements of the LST is the land surface emissivity which can be derived by land cover map. SRM could enhance the spatial resolution of the classification and thus can enhance the resolution of the emissivity.

The HNN is a fully connected recurrent network and thus can be used to represent the image in image processing [27].

The energy function of HNN for SRM is defined as

$$E = - \sum_{k=1}^N \sum_i \sum_j \left(k_1 G_{kij}^1 + k_2 G_{kij}^0 + k_p P_{kij} + k_M M_{kij} \right), \quad (1)$$

where G_{kij}^1 and G_{kij}^0 are the goal functions at a neuron (i, j, k) ; P_{kij} and M_{kij} are the proportional information constraint and the multiclass constraint, respectively; N is the number of land cover types; and k_1 , k_2 , k_p , and k_M are the weight constants for each element of the energy function. The rate of change for the energy function for neuron (i, j) is defined as

$$\frac{dE_{kij}}{dv_{kij}} = k_1 \frac{dG_{kij}^1}{dv_{kij}} + k_2 \frac{dG_{kij}^0}{dv_{kij}} k_p \frac{dP_{kij}}{dv_{kij}} + k_M \frac{dM_{kij}}{dv_{kij}}. \quad (2)$$

The two goal functions, G_{ij}^1 and G_{ij}^0 , in the energy function for SRM represent two forces pushing the output to 1 or 0. The aim of the increasing function G_{ij}^1 is to raise the value of the neuron when the average of the eight neighboring subpixels is greater than a threshold and becomes 0 when the average is less than the threshold.

The proportion constraint dP_{kij}/dv_{kij} is used to guarantee that the proportional information derived from soft classification is maintained while the goal functions and other constraints are satisfied, or this constraint will impact on the output of the energy function.

The multiclass constraint dM_{kij}/dv_{kij} plays a similar role as the proportional constraint which adds another limitation that needs to be satisfied when goal functions achieve the aim. The basic idea is to ensure that each subpixel has been assigned with only one land cover type, which means that no subpixel will be unclassified or overlaid by different types.

It can be seen that the rate of change of the neuron can be obtained after the rate of change for the energy function is derived. Then, HNN for SRM could be updated at each time step, Δt , until $\sum_{ij} (u_{ij}(t + \Delta t) - u_{ij}(t)) < \varepsilon$, where ε is a very small value, or the number of iterations reaches a certain amount using the Euler method.

2.3.2. Sparse Representation-Based SRR. SRR is to enhance the coarse spatial resolution image through one or a series of images by the experience relationship extracted by training algorithms. The basic idea of this model is that a vector (signal/image) can be represented by a sparse linear combination of some vectors (prototypes) contained in a dictionary matrix (D) which contains all the possible arrangements of the elements in a vector (signal/image) [28]:

$$x = D\alpha, \quad \text{subject to } \|D\alpha - x\|_2 \leq \varepsilon, \quad (3)$$

where x is the signal or image that needs to be represented by the sparse representation model and α is a vector containing a small number of nonzero elements, recording the coefficients of the sparse linear combination. To make the features, which are also called the prototypes in a dictionary, to be as typical as possible, the dictionary is usually trained by the dictionary training methods in patches.

This model is primarily popular among data compression techniques, as it reduces the records for images/signals to the minimum. However, researchers have found that images covering the same area but with different spatial resolutions share the same sparse vector but use different dictionaries [28, 29]. This means that for each image patch pair containing a coarse spatial resolution patch (x_c) and its

corresponding fine spatial resolution patch (x_f), they can be represented as

$$\begin{aligned} x_c &= D_c \alpha, \\ x_f &= D_f \alpha, \end{aligned} \quad (4)$$

where α is the sparse vector they share.

This discovery provides the possibility for spatial resolution enhancement. If D_c and D_f are known by training, they can be used directly with a coarse spatial resolution image to derive the corresponding fine spatial resolution image patch-by-patch. However, this time, the dictionary training is actually for an image pair, which is different from the traditional training process just for one single image. So, there are some modifications made to train the dictionary.

Firstly, because D_c and D_f share the same sparse vector α , the training for D_c and D_f cannot be taken separately as two images. Or they may obtain the different vector α . The strategy used for dictionary training in this condition is the joint dictionary training [28].

The second modification is the extraction strategy for training samples. It is known that for traditional SRR, the training images actually should be the image pairs covering the same area in different spatial resolutions. However, to make the preparation of training data simple, the sparse representation modelling-based SRR uses each training image as the fine spatial resolution image and generates its corresponding coarse spatial resolution image by blurring and downsampling. Furthermore, the sparse representation SRR does not use the whole training image for training but just randomly extracted some sample patches from the training images to save the training time and reduce the training database.

Finally, the third modification is to add the feature extraction for coarse spatial resolution patches. To make the derived sparse coefficients fit the most relevant part of the coarse spatial resolution signal, feature extraction is adopted to highlight the features concerned. Generally, this process could be some kind of high-pass filter [30].

3. Results and Analyses

3.1. Statistical Analyses. To compare with other studies, which usually use statistical variables to assess their results, statistical analyses were also taken firstly. Table 1 listed the RMSE and correlation coefficient of each method to the reference LST derived by ASTER data.

Table 1 shows that the RMSEs of PBIM and Stepwise seem to be unacceptable, which are much higher than what is usually reported in previous studies. Even for EM and SRTS, RMSE around 5°C seems not a good result either (normally <5°C) [9, 11, 20]. However, previous studies used degraded data but not the real data sources for all inputs and reference data. Some studies claimed that using degraded data could avoid the small crossscale georeferencing inaccuracies caused by the usage of data from different sources [16, 31, 32]. However, it is almost unavoidable to use data from different platforms in real applications of thermal

TABLE 1: Correlation coefficient and RMSE of results of all compared methods in different seasons.

	Correlation coefficient between sharpened and reference LST			RMSE of LST image produced by each method		
	Jan	Apr	Oct	Jan	Apr	Oct
EM	0.395	0.647	0.63	5.1706	4.05	5.0236
SRTS	0.361	0.632	0.554	5.1112	4.3352	5.1585
PBIM	0.285	0.585	0.493	79.0189	45.8235	45.1414
Stepwise	0.066	0.497	-0.015	54.0901	47.8465	39.1645

sharpened LST [15, 18]. Therefore, those accuracies reported by degraded data, although ideal, may not be practical in real applications. In contrary, accuracy assessment reported by this study, though not as good as reported in the previous studies, can be a more practical and reliable reference to those who would like to use the thermal data in real applications because all the experiments are based on real data from different sources.

The reason for the large RMSEs of PBIM and Stepwise might be explained by the correlation analyses (Figure 3). The LST ranges of PBIM or Stepwise are much wider than that of the reference LST. Given that the study area has a temperate oceanic climate, it should be impossible to have some extreme LSTs such as 160K or 430K. The reference LST also suggested that the range of LST should not be that extreme. Thus, the correlation plots indicate that PBIM and Stepwise produced some extreme points which are not correct and these points significantly increased the RMSEs.

However, the number of those extreme points is not very large, as the correlation coefficients of PBIM and Stepwise are generally similar to those of the others as shown in Table 2. Differences of the correlation coefficient between compared methods seem to be impacted mainly by seasons, because almost all the results for winter (January) obtained the lowest correlation coefficients among the three seasons. This may mainly be due to the heat capacity of surface materials which makes the characteristics of LST in winter relatively different from those in other seasons. The temperature of a material with a larger heat capacity changes slower than that of a material with a smaller heat capacity along with the change of the external temperature. Thus, LST contrast in winter would be much smaller than that in other seasons because LST of water will not change as much as others from summer to winter. This phenomenon will be shown later in Visual Comparison where the reference images of all three seasons are presented. Therefore, the reason why the correlation coefficients of PBIM and Stepwise are lower than those of the other two is because they failed to predict the small LST contrast in winter while EM and SRTS did better than them.

The only one minus value in Table 1 is produced by Stepwise for data in October. From Figure 3, it shows that the main body of its scatter points actually shows a relative clear positive trend, which means that the regression line should be from the bottom left corner to the upright corner in the feature space. However, there is a small green cluster of points (means a relatively large number of points) located

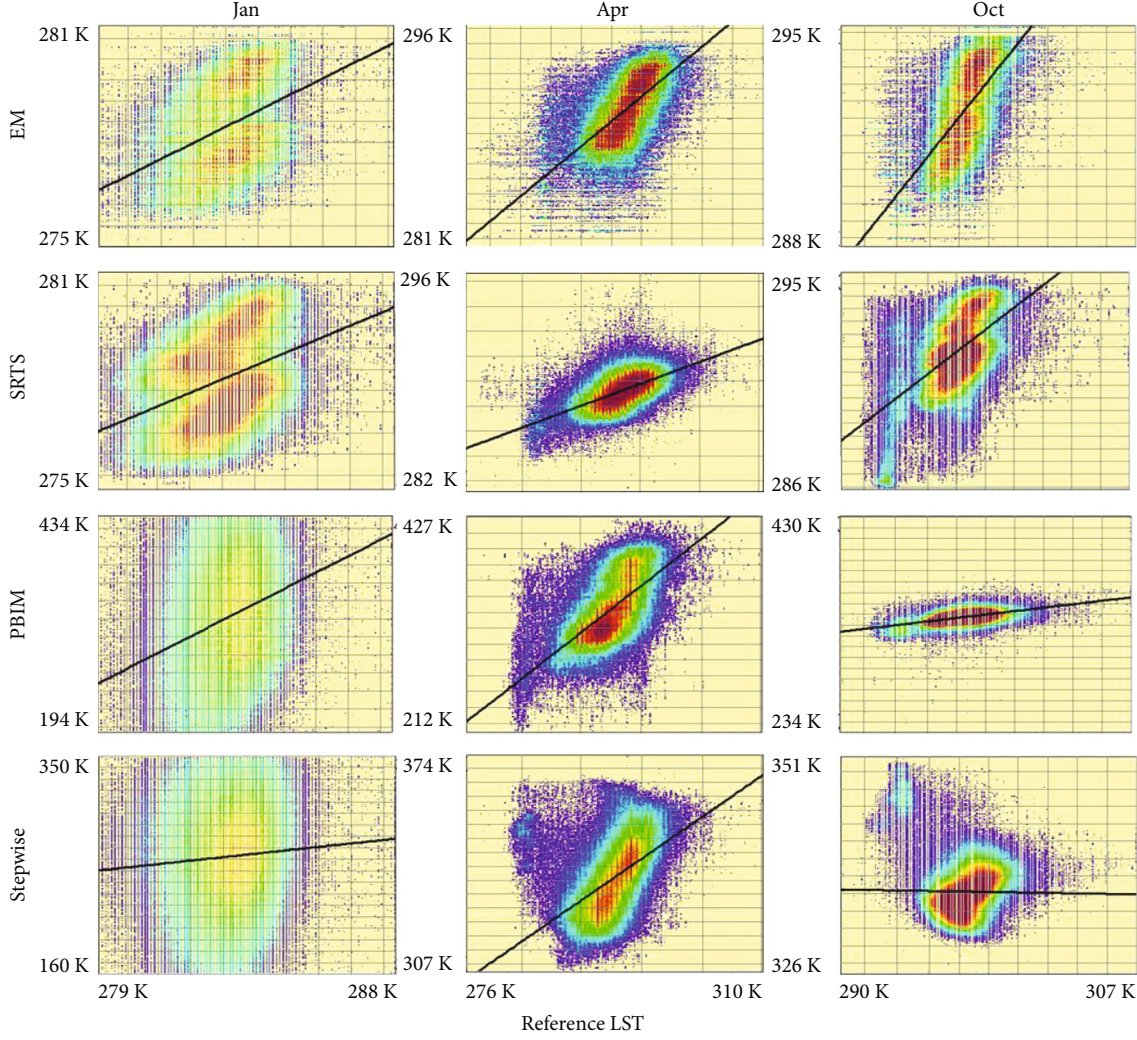


FIGURE 3: Scatter plot of the sharpened LST produced by each method in different seasons. Different colors represent different locating frequencies of points. From blue to red, it means that the frequency is from the lowest to the highest. X-axis represents the reference LST while Y-axis is the sharpened LST.

TABLE 2: Mean fuzzy similarity, standard error of the mean of results produced by EM, SRTS, PBIM, and Stepwise for data in different seasons.

	Jan		Apr		Oct		All seasons	
	Mean	SE	Mean	SE	Mean	SE	Mean	SE
EM	0.419	0.000571	0.688	0.000331	0.673	0.000377	0.623	0.000244
SRTS	0.668	0.000329	0.605	0.000414	0.686	0.000341	0.656	0.000208
PBIM	0.612	0.000566	0.652	0.00039	0.685	0.000383	0.654	0.000251
Stepwise	0.602	0.000559	0.625	0.000415	0.485	0.000468	0.568	0.000277
All methods	0.594	0.000243	0.645	0.000193	0.638	0.0002		

at the top left corner, and this cluster impacted the trend of the regression line significantly, making it even slightly negative. The small green cluster indicates that several points with low LST in reference dataset are predicted to have a much higher LST in the predicted dataset. If analyzed with the images in Visual Comparison (Figure 4), it can be seen that almost all the water pixels are predicted to have the highest

LST in the result of Stepwise for data in October which are not consistent with the reference of October, leading to a low correlation with the reference. This error is mainly because Stepwise adopted an automatic mechanism of choosing sharpening indices [11]. For the image in October 2001, although the candidate indices include NDVI, MNDWI, NDBI, and albedo, only MNDWI was chosen as the

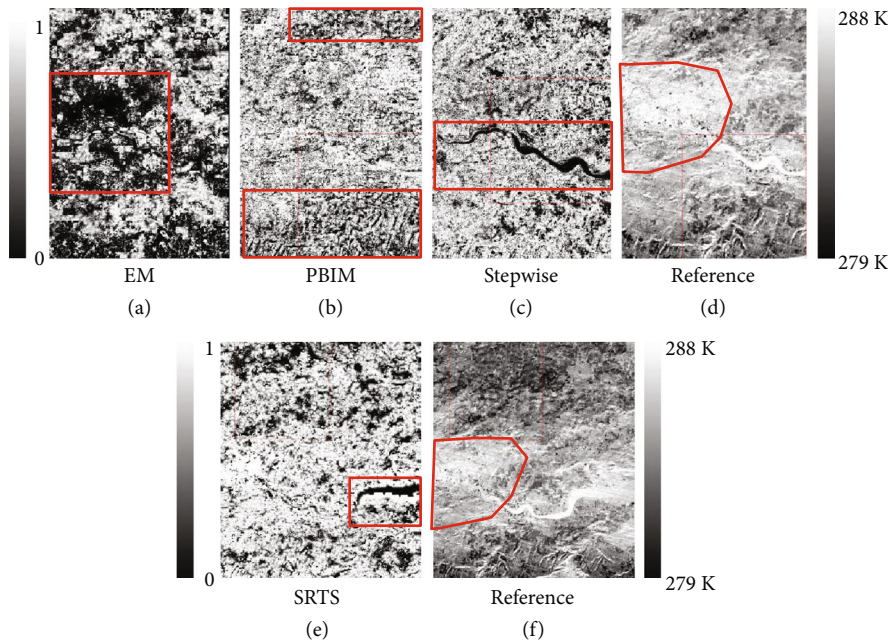


FIGURE 4: Fuzzy similarity image for LST in January sharpened by each method. The coverage area in the figure is the east part of Great London which is near the estuary of the River Thames. The corresponding references are provided. The red polygons in the reference images illustrated the central urban area. The red boxes in sharpened LST images highlighted the area with distinctively low similarity.

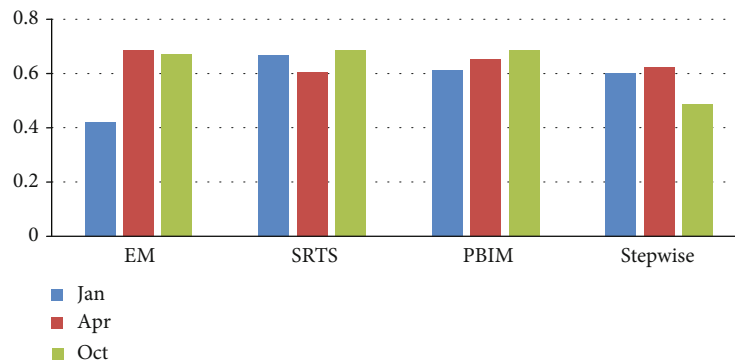


FIGURE 5: The mean fuzzy similarity of each method based on data in all tested seasons.

sharpening index for stepwise regression and this cannot be controlled manually. Therefore, the water surface pixels were all given a high, even higher than the impervious surface, LST value in that LST image, though the shape of most water bodies (e.g., lakes, rivers) is predicted relatively well (as shown in Figure 4). This may reflect the limitation of the autoselection mechanism for sharpening indices to some extent. Although the autoselection may avoid the human interference in the process, it causes the risk that the chosen indices might be unsuitable but cannot be controlled manually.

3.2. Evaluation of Spatial Pattern. As Keramitsoglou et al. [22] claimed, the spatial pattern information from LST images is also important for the UHI studies. Sobrino et al. [5] pointed out that to use the mean LST as the representation of an urban area or a rural surrounding area is not reasonable, as, in their experiment, it is apparent that different

districts in the city have different LSTs. Thus, the description on the details of the thermal structure of the UHI effect should be considered. Unfortunately, there is a lack of in-depth evaluation of the thermal spatial patterns [15]. Thus, this research considers the spatial pattern as another essential aspect in the evaluation of the compared methods. Fuzzy similarity was employed as the assessment variables as it can not only provide a mean value as the representation of the entire image but also produce an image of which each pixel has a similarity value for the spatially corresponding pixel of the original result.

3.2.1. Evaluation by Mean Fuzzy Similarity and the Standard Error of the Mean. Figure 5 illustrated the mean fuzzy similarity of the result produced by each method in each season. It shows that most result obtained a mean similarity above 0.6 except for the result of EM in January and result of

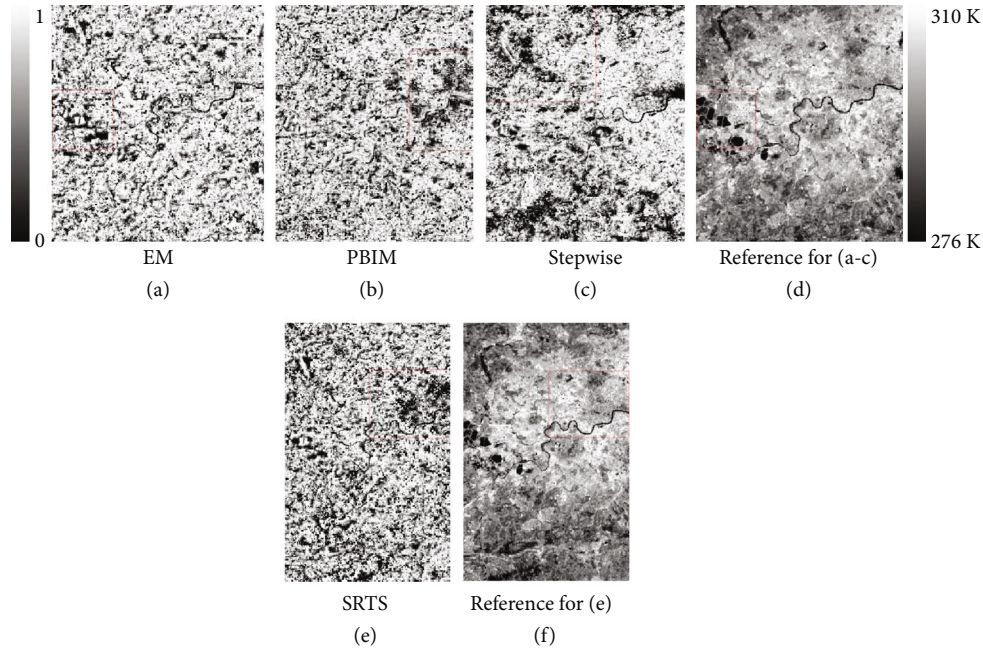


FIGURE 6: Fuzzy similarity image of LST in April sharpened by each method. The references for the similarity image covering the same area are also provided. The coverage area in the figure is the west part of Great London which includes the lakes near Heathrow Airport.

Stepwise in October. This may suggest that SRTS and PBIM are better for detecting the correct spatial pattern than EM and Stepwise.

Table 2 listed more details on the mean fuzzy similarity and the standard error (SE) of the mean for every result. It shows that the SEs of all the results are very small, which means that almost all the mean values are significantly different from each other. In addition, it is known that lower values of SE indicate more precise estimates of the population mean. In Table 2, SRTS obtained the lowest SEs of the mean among results in January and October, while EM obtained the lowest SE of the mean among results in April. In the comparison of the mean values and the SE of the mean based on data in all three seasons for each method, it also shows that SRTS obtained the lowest SE of the mean and the highest mean fuzzy similarity compared with other methods. This may suggest that SRTS has a higher accuracy in the evaluation of the spatial pattern than other three methods.

When compared for different seasons, it can be seen that the mean similarity and SE of the mean based on results of all methods in January obtained the lowest similarity and the highest SE among the compared three seasons. Thus, even though not shown apparently in Figure 5, the figures in Table 2 may still suggest that the data in January tends to be difficult for thermal sharpening methods to get a correct spatial pattern of LST compared with data in other seasons.

3.2.2. Evaluation by Fuzzy Similarity Imagery. Figures 4–6 showed the fuzzy similarity image of the result produced by each method for each season. Fuzzy similarity images can reflect the spatial distribution of areas with high or low similarity to the reference. In the fuzzy similarity image, the brighter the pixel is, the higher the similarity value it has, which indicates that it is more similar to the reference pixel.

Otherwise, through comparing the similarity image to the reference image, the shortage of each method on predicting different land covers might be found.

Figures 6 and 7 illustrated the fuzzy similarity images of LST results not in winter. It might be found that the illustrated coverage area of the result produced by SRTS is different from other methods. For EM, PBIM, and Stepwise, their experiment data should be the common area among scenes of three platforms (MODIS, ETM+, and ASTER), while SRTS, which does not require fine spatial resolution input, just needs two sources (MODIS and ASTER). This makes the coverage area in experiment of SRTS different from, usually larger than, those of the other three methods.

Through comparison in Figures 6 and 7, which represent the performance of each method on detecting the LST spatially correct for data not in winter, it might be said that Stepwise is not recommended among the compared methods, as its accuracy is not stable due to the automechanism of predictor choice of the algorithm. Its result in Figure 7 obtained apparently more dark pixels than in Figure 6, indicating a lower spatial similarity. Although there are the advantages of this mechanism such as to reduce the human interference and to make the process more automatic, it still lacks the mechanism to guarantee that the most optimal predictors can be selected. For EM, PBIM, and SRTS, their performances in evaluation by fuzzy similarity images seem to be similar. Dark pixels tend to gather in or around the river area, indicating that the narrow linear water bodies are difficult to be detected correctly. This is mainly because the linear features tend to be in the mixed pixels in the coarse spatial resolution images. Thus, in thermal sharpening, even the fine spatial resolution information has been brought in or generated by algorithms; the accuracy of the spatial distribution of those fine resolution details is easily impacted by the

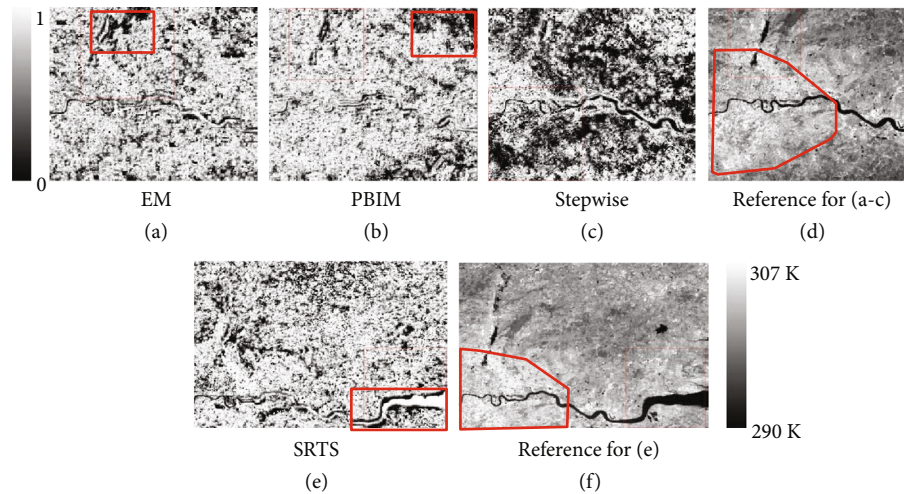


FIGURE 7: Fuzzy similarity image for LST in October sharpened by each method. The coverage area in the figure included the most proportion of the central London and the north-east part of the surrounding areas. The red polygons in references highlighted the central urban area of London. The red boxes in sharpened results highlighted the area with distinctively low similarity.

original coarse resolution mixed pixels. Otherwise, vegetation in rural areas tends to be predicted wrongly as well for all compared methods.

When it comes to Figure 4 which represents the performance of each method for data in winter, there are two apparent findings. The first is that EM obtained much more dark areas than other methods, which is consistent with its low mean fuzzy similarity in the previous evaluation. The second is that almost all the water pixels in the result of Stepwise are predicted incorrectly.

Based on the reference data, the LST contrast of the entire study area in winter is much smaller than that in other seasons because of the heat capacities of different land covers. From the reference image for LST in winter (Figures 4(d) and 4(f)), it can be seen that the LST difference for the whole image is only 9K, including water, which is much smaller than those in other seasons. The incorrections that happened for vegetation and impervious surface in the result of EM are mainly because the LST for the impervious surface was predicted to be higher and LST for vegetation was predicted to be lower than their reference LSTs for winter. For the incorrections that occurred for water or areas along it (as the red boxes shown in Figures 4(c) and 4(e)), similarly, it is because of the large heat capacity of water and the original coarse resolution mixed pixels. In winter, the LST of water in winter is not significantly lower than most other materials according to the reference. However, in the sharpened LST, water still gets the lowest LST in the result of Stepwise, leading to a low similarity for the water surface.

In Figure 4, it seems like PBIM and SRTS obtained less dark areas than the other two methods. The dark pixels in the result of PBIM are evenly distributed in the study area while the dark pixels in the result of SRTS tend to be gathered mainly near the edge of the river and vegetated areas in the upper and lower parts of the image. According to the reference, there are much less dark pixels that occurred in the central urban area in the result of SRTS (as illustrated by the red polygon in the reference image).

Even for the part of the river in the urban area, dark pixels in or at the edge of the river are reduced significantly compared to those of the river edge in the rural area (as shown in the red box in Figure 7(e)). This may suggest that SRTS is more suitable to be used for urban studies than others in winter as it tends to produce less unsimilar pixels for the impervious surface which is the main land cover type of the urban surface.

Through analyses of Figures 4–6, the following conclusions can be derived:

- (1) Vegetated area, water, and areas near water tend to be wrongly predicted for all compared methods as more dark pixels in the fuzzy similarity image tend to occur in these areas
- (2) Among all the compared methods, PBIM and SRTS tend to obtain less dark pixels than other methods, which indicates a higher accuracy for the predicted spatial pattern generated by PBIM and SRTS than those of others
- (3) Result of SRTS for data in winter obtained much less dark pixels for the impervious surface area in the fuzzy similarity image. This may indicate that SRTS is suitable for urban studies as the main land cover type of the urban area is the impervious surface
- (4) Stepwise tends to have a lower accuracy for water than other land cover types. In the experiments, results of Stepwise for LST in October and January obviously obtained the incorrect LST for the water surface (as shown in Figures 6 and 7). This may suggest that Stepwise is not suitable to be used for the area containing a large amount of water

3.3. Visual Comparison. The general spatial pattern of the entire study area processed by each method in different seasons will be compared visually, to let the readers get a

straightforward view about the accuracy of the spatial pattern of each sharpened LST. It is assumed to be used as a support to the evaluation of the spatial pattern, especially to see the accuracy performance of each method for the main land cover types of urban areas, including vegetation, water, and impervious surface.

To understand the thermal response of each land cover type is also valuable for a district level study, as the LST can vary significantly between different land covers [33]. Particularly, land cover composition in urban areas is highly complicated and variable in the spatial dimension, which makes the thermal environment more complex. Anniballe et al. [19] also pointed out that the intraurban UHI spatial variability is closely related to the distribution of buildings, surface materials, and density of green areas. Therefore, some objects are chosen in this research for three land cover types.

Those highly built-up areas might be the airport, commercial areas with intensive roof-related impervious surface, and so forth.

Figure 8 illustrated the results of all compared methods for data not in winter (i.e., April and October). It can be seen that the general spatial pattern of LST produced by EM is consistent with the reference, yet blocky effect exists in both results of EM, which actually is impacted by the original coarse resolution data. One apparent evidence for the rough description of the spatial pattern is that the shape of the river and the lakes is not well described, which almost maintained the characteristics of the original coarse pixels.

For results of SRTS, blocky effect is eliminated, and the general spatial pattern of LST is consistent with the reference as well. However, it seems like the pattern has been smoothed too much, resulting in several small round hot spots in the edging area of the central urban area. This is mainly due to the SRM algorithm used by SRTS. If SRM is overdone, it is common to produce this sparsely distributed round shapes. Nevertheless, variations of LST between different land covers are still distinguishable in results of SRTS. Most impervious surface objects obtained the highest LST, while parks are allocated to the lower LST. Water bodies are generally located in the blue or yellow areas.

Even though the general pattern that the central urban areas are red and the surrounding areas are blue can be distinguished in the result of PBIM, it seems like a large amount of blue fragments exist in the central area while several red fragments appear in the rural areas as well. This might be because the regression method it used tries to bring the fine spatial resolution information extracted from predictors into the result, while the residual extracted from the original coarse resolution pixels is still used to correct the final sharpened LST. These residual data brought back the impact of coarse resolution pixels. In the results of PBIM, the shape of the river and some lakes is described fairly well. However, the relationship between LSTs of vegetation and impervious surface, where LST of vegetation should be lower than that of impervious surface, was not described well.

Results of Stepwise for data in October are apparently inconsistent with the reference, where the LST of water should not be that high. This is due to the automechanism of predictor choice. And here again confirmed that the

accuracy of Stepwise is not stable when used for different applications.

Figure 9 illustrated the result of each method for data in winter (January). Due to the limited common area between ASTER and ETM+ imagery for this date, not all the objects have the reference background LSTs here. However, from the reference, it can be seen that the LST contrast of the entire area is much smaller than in other seasons.

In Figure 9, the spatial pattern of LST produced by EM and SRTS showed the consistency with the reference, where the LST contrast is generally small. In contrast, the result of PBIM obtained a fragmented LST spatial pattern and even shows a trend that the central area is cooler than the surrounding rural area. Stepwise still predicted the water pixels to have the lowest LSTs, which actually should have the similar LST to other land covers.

Through comparison in Figure 9, the priority of using the classification information, instead of a limited number of spectral indices, to provide fine spatial resolution details in thermal sharpening is highlighted. As introduced in Data and Methods, EM extracted fine spatial resolution details from emissivity data which actually are produced by classification information, and SRTS uses the SRM to sharpen the land cover information first and then bring it into LST estimation. In this section, the results produced by EM and SRTS do not have extreme points like in results of PBIM and Stepwise and are more sensitive to the changes of the spatial pattern in different seasons than those of PBIM and Stepwise.

4. Discussions

4.1. The Evaluation of Spatial Pattern. As Sismanidis et al. [15] mentioned, most current studies on thermal sharpening methods lack the evaluation of spatial patterns which is equally significant for UHI studies. Instead, they prefer to use statistical variables to do the evaluation. This might be because these variables are easy to be calculated from the absolute LST values and can be a quantitative way to describe the accuracy performance. However, they consider little spatial information of the entire LST map. Quan et al. [21] found that the conclusion derived from the evaluation based on the absolute LST values might be inconsistent with that derived from the evaluation of LST spatial distribution. In their experiment, they found the result with the most similar spatial pattern and texture to the reference image obtained the highest RMSE. Therefore, they suggested that to use which evaluation or both of them should depend on the application of the sharpened LST. If the sharpened LST is used as input to a quantified model, the accuracy of the absolute LST values should be emphasized. If the application focuses on the description of the spatial pattern of the entire thermal environment, evaluation of LST distribution and texture might be preferred. Therefore, for a comprehensive evaluation of a method, it is better to evaluate both aspects.

The lack of evaluation of the LST spatial pattern might be partly due to the difficulty of defining the spatial pattern of LST. What usually derived from thermal remote sensing data is the raster LST images which consist of pixels. On the contrary, the spatial pattern is a relatively “vectorial” concept

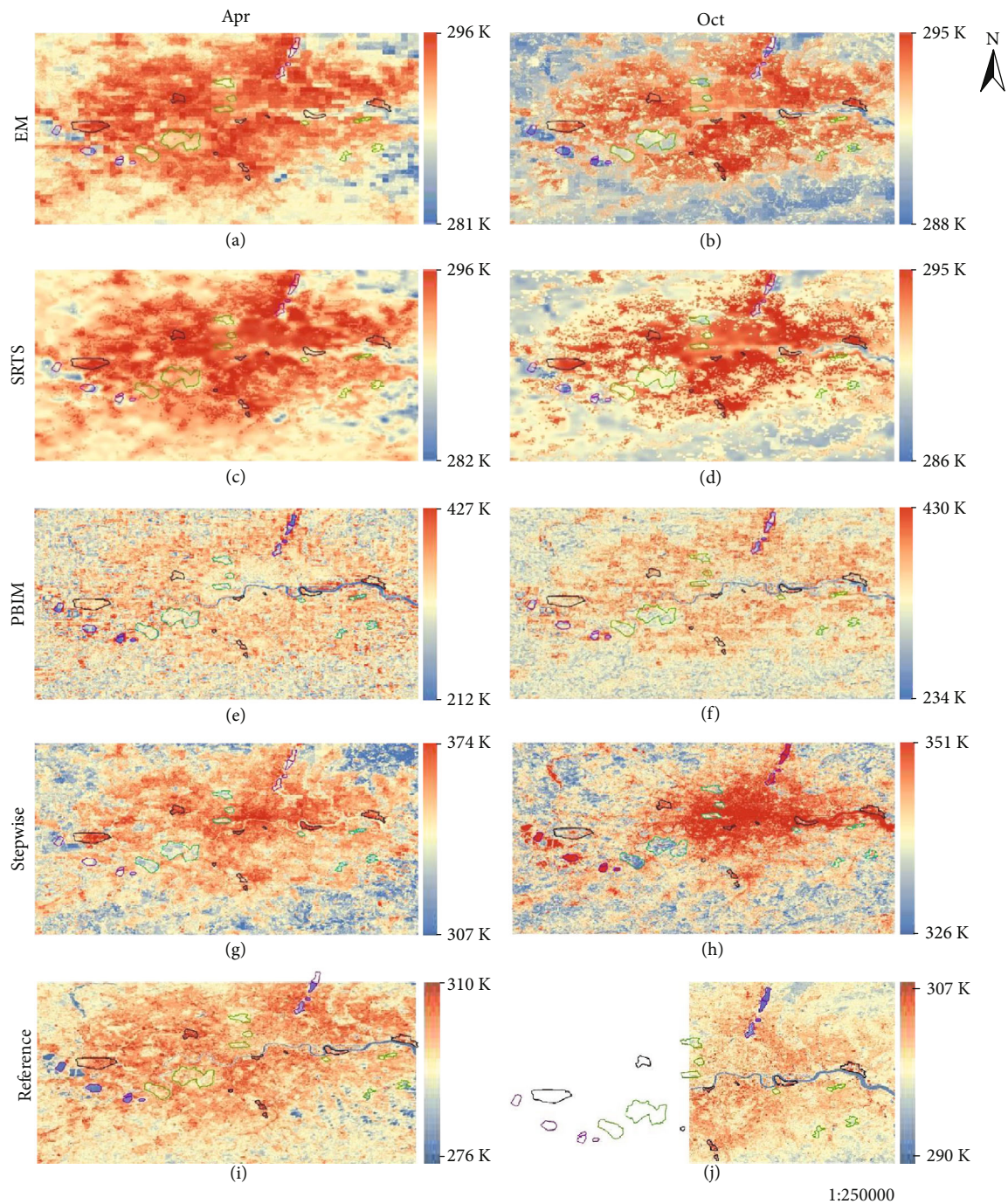


FIGURE 8: (a–h) are the sharpened LST images for data acquired not in winter by all compared methods. Reference LST images ((i, j)) are provided to show the general spatial pattern of part of the study area for the visual comparison. Vector boundaries in each image represent the chosen objects for different land cover types. The objects with black, green, and purple lines represent the impervious surface, vegetated areas, and water bodies, respectively.

which may need to define a boundary of an area. As Keramitsoglou et al. [22] reported, they extracted the hot spot pixels and then treat them as objects. However, in their study, the extracted objects were more like the LST classification but lost the gradual change of the entire LST pattern. Voogt and Oke [34] have already criticized that the slow development of thermal remote sensing of urban areas is due largely

to the qualitative description of thermal patterns. It is common to find in literature that, for comparison of LST spatial patterns or texture, people usually present a number of results in an illustration and then use a limited number of words for the description [35–37]. This revealed the lack of a widely acknowledged quantifying method for evaluation of the LST spatial pattern. Currently, three indices have been

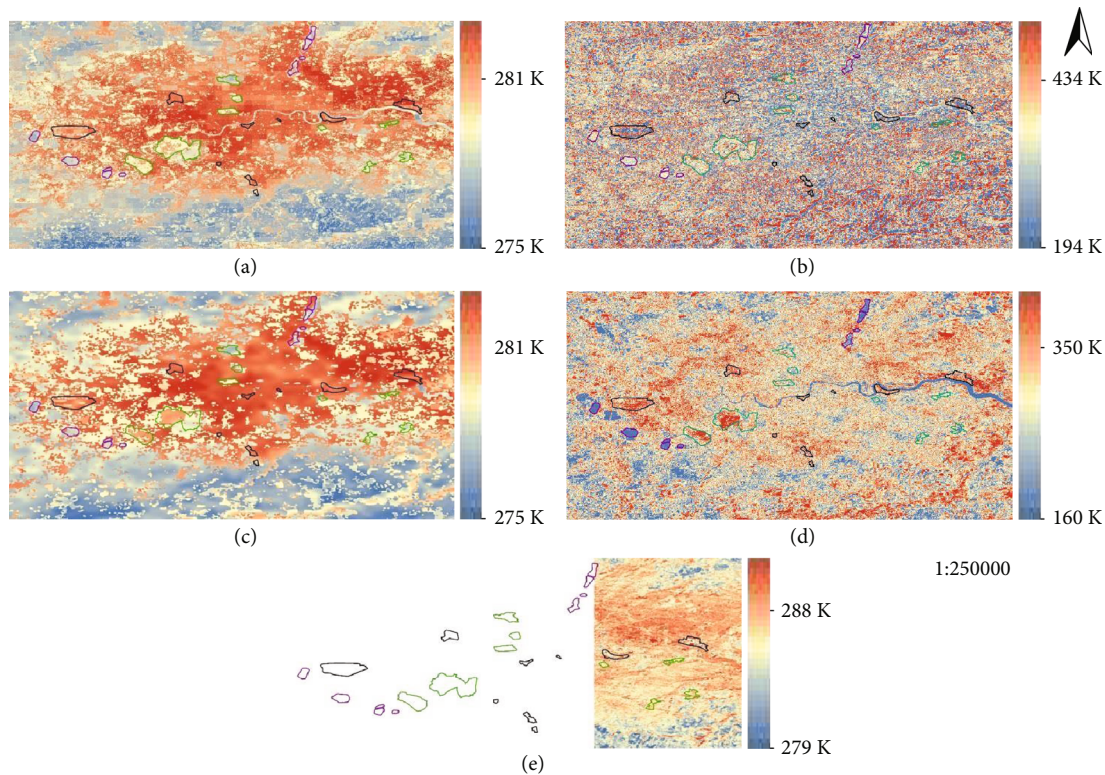


FIGURE 9: LST images for MODIS image acquired in January 2001 sharpened by (a) EM, (b) PBIM, (c) SRTS, and (d) Stepwise. Reference LST image (e) is provided to show the general spatial pattern of part of the study area for the visual comparison. Vector boundaries in each image represent the chosen objects for different land covers. The objects with black, green, and purple lines represent the impervious surface, vegetated areas, and water bodies, respectively.

tried in the relative evaluations. The Local Moran Index (LMI) has been tried in studies of Sismanidis et al. [15] because this is a classic statistical tool for detection of the spatial cluster [38]. To evaluate the spatial pattern, CO-RMSE, which is based on the comparison between the LST cooccurrence matrix of sharpened LST and the reference, was proposed and used in studies of Quan et al. [21]. Fuzzy similarity allocated a similarity value to each pixel based on the information of its neighborhood pixels around the central pixel. The reason we adopted fuzzy similarity in this research is that it not only provides a value representing for the entire study area (e.g., mean fuzzy similarity of an image) but also provides a similarity image which can further provide spatial information on the location of error occurrence and its relationship to the land cover or other spatial factors. This type of information did help the analyses in our study, making us understand the impact of different land cover types to the accuracy performance of each method. Also, it is found in our study that the accuracies of PBIM and Stepwise in evaluation of the spatial pattern were not affected by the extreme points too much like in the statistical evaluation. This might be because those extreme values are smoothed by their neighborhoods in calculation of fuzzy similarity and thus do not show a significant reduction in the accuracy of PBIM and Stepwise in evaluation of the spatial pattern. This reflected the priority of fuzzy similarity and the necessity to do evaluation of the spatial pattern for a method as it may reveal

accuracy performance from a different aspect. The evaluation and analyses of the spatial pattern in this study may provide some ideas for the further related researches.

4.2. Application of Thermal Sharpening for Urban Area. In early years of development of thermal sharpening technology, most studies emphasize on the sharpening for the large area covered mainly by vegetation [17, 37, 39]. Also, the predictors commonly used in thermal sharpening algorithms are vegetation indices. Thermal sharpening was found to be especially suitable for urban thermal environment studies because there is an urgent requirement of both fine spatial and temporal resolution data [5, 26, 40]. However, it was found that those methods proposed for large vegetated areas were not suitable for urban areas because the main impacting factor of LST in urban is not the vegetation [12, 41]. Therefore, more impacting factors, including impervious surface fractions, water indices, and albedo, were considered. Until years after 2010, more proposal studies and application reports of thermal sharpening methods were found in literature [8, 11, 15, 35, 42, 43]. However, it is found that for most of them, the scale factor (or zoom factor) of downscaling is still limited (<10) and the aiming sharpening resolutions, especially for applications of thermal sharpening data, are 1 km [15, 44], 90 m [35], or 30 m [42], which are the spatial resolutions of MODIS, ASTER, and TM/ETM+, respectively.

This might be due to the limited data sources for fine spatial resolution input. Also, it might be the strategy to guarantee the accuracy of the sharpened data, because studies usually reported that a larger scaling factor corresponds to a lower accuracy of the sharpened data [5, 8, 31]. Another possible reason might be the processing time. For applications which would like to dynamically monitor the thermal environment of several urban areas, they need data with very fine temporal resolution which usually are acquired from geostationary platforms (e.g., SEVERI with 15 min resolution). If the spatial resolution is also required to be relatively fine, there might be a burden for the processing system.

Although the applications of sharpened LST seem to be limited, that does not mean that the efforts made on expanding the diversity of the thermal sharpening methods are insignificant. On the contrary, the limited applications may reflect that the current methods are still insufficient or unsuitable for various real applications. Efforts may still be needed to ease the data preparation, optimize the algorithm to reduce the processing time and burden, and make the whole process be as automatic as possible. These requirements of practical applications are still challenging the research world, and some of the researchers have started to try to deal with the above issues. SRTS tried to simplify the data preparation by moving out the requirement of fine spatial resolution input [13]. Weng et al. [42] and Yang et al. [35] are advancing some models which try to generate TM-like and ASTER-like daily LST automatically based on a number of inputs. The above attempts are still in the beginning and have some limitations. However, they showed the efforts made on diversity of thermal sharpening development and on filling the gap between the research and the real applications.

5. Conclusions

This study compared four thermal sharpening methods proposed especially for urban areas through evaluation of two aspects. Particularly, not only statistical evaluation, which is commonly used by most thermal sharpening methods, but also evaluation of the LST spatial pattern is carried out.

In both evaluations, it is found that the accuracy performances of all methods are worse in winter than in other seasons. This is mainly because the LST contrast in winter decreased significantly compared to that in other seasons. Most thermal sharpening methods cannot detect this change very well, leading to a decreased accuracy. For comparison of different methods, Stepwise is not recommended for areas with a large amount of water, and EM and SRTS performed better than the other two methods. However, SRTS removed the requirement of fine spatial resolution input data which eased the data preparation and thus is considered to be more useful than EM. It is also found that linear water features and areas along it are commonly detected wrongly by most thermal sharpening methods. Vegetation in rural areas is also easy to be detected incorrectly.

In this study, we focused on the evaluation of the spatial pattern in accuracy assessment to make the evaluation of each method be comprehensive. Though the accuracy of the spatial pattern has been recognized as an essential factor

for LST map, it is difficult to be quantified for a long time. This research may provide an idea on how to evaluate the spatial pattern for the further relative studies. Also, other assessing variables, such as LMA and CO-RMSE, are the good alternatives. It is urgent to develop a variable which can be widely accepted to quantitatively evaluate the spatial pattern and texture of an image. In addition, it is also encouraged to develop more thermal sharpening methods that could be used in real applications especially for urban areas in the future.

Data Availability

Thanks for the free data access to the MODIS images used in this study which were downloaded from https://lpdaac.usgs.gov/data_access/data_pool and the Landsat images which were downloaded from <https://landsat.usgs.gov/landsat-data-access>.

Conflicts of Interest

The authors declare that they have no conflicts of interest.

Acknowledgments

Thanks are due to Dr. Anuar Muad and Yang et al. for providing the MATLAB codes of SRM and SRR. This work is supported by the “Fundamental Research Funds for the Central Universities” (Grant Nos. 310821171014 and GK201903112) in China.

References

- [1] S. N. Gosling, J. A. Lowe, G. R. McGregor, M. Pelling, and B. D. Malamud, “Associations between elevated atmospheric temperature and human mortality: a critical review of the literature,” *Climatic Change*, vol. 92, no. 3–4, pp. 299–341, 2009.
- [2] E. Ashley and L. Lemay, “Concrete’s contribution to sustainable development,” *Journal of Green Building*, vol. 3, no. 4, pp. 37–49, 2008.
- [3] Q. Weng, “Thermal infrared remote sensing for urban climate and environmental studies: methods, applications, and trends,” *ISPRS Journal of Photogrammetry and Remote Sensing*, vol. 64, no. 4, pp. 335–344, 2009.
- [4] S. Mukherjee, P. K. Joshi, and R. D. Garg, “Evaluation of LST downscaling algorithms on seasonal thermal data in humid subtropical regions of India,” *International Journal of Remote Sensing*, vol. 36, no. 10, pp. 2503–2523, 2015.
- [5] J. A. Sobrino, R. Oltra-Carrió, G. Sòria, R. Bianchi, and M. Paganini, “Impact of spatial resolution and satellite overpass time on evaluation of the surface urban heat island effects,” *Remote Sensing of Environment*, vol. 117, pp. 50–56, 2012.
- [6] X. Feng, “Enhancing the spatial resolution of satellite-derived land surface temperature mapping for urban areas,” PhD thesis of University of Nottingham, 2016.
- [7] F. Gao, W. P. Kustas, and M. C. Anderson, “A data mining approach for sharpening thermal satellite imagery over land,” *Remote Sensing*, vol. 4, no. 11, pp. 3287–3319, 2012.

- [8] A. Dominguez, J. Kleissl, J. C. Luvall, and D. L. Rickman, "High-resolution urban thermal sharpener (huts)," *Remote Sensing of Environment*, vol. 115, no. 7, pp. 1772–1780, 2011.
- [9] B. Bechtel, K. Zaksek, and G. Hoshyaripour, "Downscaling land surface temperature in an urban area: a case study for Hamburg, Germany," *Remote Sensing*, vol. 4, no. 10, pp. 3184–3200, 2012.
- [10] I. F. Trigo, I. T. Monteiro, F. Olesen, and E. Kabsch, "An assessment of remotely sensed land surface temperature," *Journal of Geophysical Research Atmospheres*, vol. 113, no. D17, article 11611165, 2008.
- [11] S. Zhu, H. Guan, A. C. Millington, and G. Zhang, "Disaggregation of land surface temperature over a heterogeneous urban and surrounding suburban area: a case study in Shanghai, China," *International Journal of Remote Sensing*, vol. 34, no. 5, pp. 1707–1723, 2013.
- [12] W. Essa, B. Verbeiren, J. van der Kwast, T. van de Voorde, and O. Batelaan, "Evaluation of the DisTrad thermal sharpening methodology for urban areas," *International Journal of Applied Earth Observation and Geoinformation*, vol. 19, pp. 163–172, 2012.
- [13] X. Feng, G. Foody, P. Aplin, and S. N. Gosling, "Enhancing the spatial resolution of satellite-derived land surface temperature mapping for urban areas," *Sustainable Cities and Society*, vol. 19, pp. 341–348, 2015.
- [14] J. Nichol, "An emissivity modulation method for spatial enhancement of thermal satellite images in urban heat island analysis," *Photogrammetric Engineering and Remote Sensing*, vol. 75, no. 5, pp. 547–556, 2009.
- [15] P. Sismanidis, I. Keramitsoglou, C. Kiranoudis, and B. Bechtel, "Assessing the capability of a downscaled urban land surface temperature time series to reproduce the spatiotemporal features of the original data," *Remote Sensing*, vol. 8, no. 4, p. 274, 2016.
- [16] W. Essa, J. van der Kwast, B. Verbeiren, and O. Batelaan, "Downscaling of thermal images over urban areas using the land surface temperature-impervious percentage relationship," *International Journal of Applied Earth Observation and Geoinformation*, vol. 23, no. 23, pp. 95–108, 2013.
- [17] N. Agam, W. P. Kustas, M. C. Anderson, F. Li, and C. M. U. Neale, "A vegetation index based technique for spatial sharpening of thermal imagery," *Remote Sensing of Environment*, vol. 107, no. 4, pp. 545–558, 2007.
- [18] P. Sismanidis, I. Keramitsoglou, and C. T. Kiranoudis, "A satellite-based system for continuous monitoring of surface urban heat islands," *Urban Climate*, vol. 14, pp. 141–153, 2015.
- [19] R. Anniballe, S. Bonafoni, and M. Pichierri, "Spatial and temporal trends of the surface and air heat island over Milan using MODIS data," *Remote Sensing of Environment*, vol. 150, pp. 163–171, 2014.
- [20] P. Qi, S. Hu, H. Zhang, and G. Guo, "Sharpening method of satellite thermal image based on the geographical statistical model," *Journal of Applied Remote Sensing*, vol. 10, no. 2, article 025013, 2016.
- [21] J. Quan, W. Zhan, Y. Chen, and W. Liu, "Downscaling remotely sensed land surface temperatures: a comparison of typical methods," *Journal of Remote Sensing*, vol. 17, no. 2, pp. 361–387, 2013.
- [22] I. Keramitsoglou, C. T. Kiranoudis, G. Ceriola, Q. Weng, and U. Rajasekar, "Identification and analysis of urban surface temperature patterns in Greater Athens, Greece, using MODIS imagery," *Remote Sensing of Environment*, vol. 115, no. 12, pp. 3080–3090, 2011.
- [23] M. Stathopoulou and C. Cartalis, "Downscaling AVHRR land surface temperatures for improved surface urban heat island intensity estimation," *Remote Sensing of Environment*, vol. 113, no. 12, pp. 2592–2605, 2009.
- [24] L. J. Guo and J. M. Moore, "Pixel block intensity modulation: adding spatial detail to TM band 6 thermal imagery," *International Journal of Remote Sensing*, vol. 19, no. 13, pp. 2477–2491, 1998.
- [25] A. Hagen, "Fuzzy set approach to assessing similarity of categorical maps," *International Journal of Geographical Information Science*, vol. 17, no. 3, pp. 235–249, 2003.
- [26] S. Bonafoni, R. Anniballe, B. Gioli, and P. Toscano, "Downscaling Landsat land surface temperature over the urban area of Florence," *European Journal of Remote Sensing*, vol. 49, no. 1, pp. 553–569, 2017.
- [27] A. J. Tatem, H. G. Lewis, P. M. Atkinson, and M. S. Nixon, "Multiple-class land-cover mapping at the sub-pixel scale using a Hopfield neural network," *International Journal of Applied Earth Observation and Geoinformation*, vol. 3, no. 2, pp. 184–190, 2001.
- [28] J. Yang, J. Wright, T. S. Huang, and Y. Ma, "Image super-resolution via sparse representation," *IEEE Transactions on Image Processing*, vol. 19, no. 11, pp. 2861–2873, 2010.
- [29] J. Yang, J. Wright, T. Huang, and Y. Ma, "Image super-resolution as sparse representation of raw image patches," in *2008 IEEE Conference on Computer Vision and Pattern Recognition*, Anchorage, AK, USA, June 2008.
- [30] W. T. Freeman, E. C. Pasztor, and O. T. Carmichael, "Learning low-level vision," *International Journal of Computer Vision*, vol. 40, no. 1, pp. 25–47, 2000.
- [31] C. Hutengs and M. Vohland, "Downscaling land surface temperatures at regional scales with random forest regression," *Remote Sensing of Environment*, vol. 178, pp. 127–141, 2016.
- [32] B. Tan, C. E. Woodcock, J. Hu et al., "The impact of gridding artifacts on the local spatial properties of MODIS data: implications for validation, compositing, and band-to-band registration across resolutions," *Remote Sensing of Environment*, vol. 105, no. 2, pp. 98–114, 2006.
- [33] R. Gluch, D. A. Quattrochi, and J. C. Luvall, "A multi-scale approach to urban thermal analysis," *Remote Sensing of Environment*, vol. 104, no. 2, pp. 123–132, 2006.
- [34] J. A. Voogt and T. R. Oke, "Thermal remote sensing of urban climates," *Remote Sensing of Environment*, vol. 86, no. 3, pp. 370–384, 2003.
- [35] G. Yang, Q. Weng, R. Pu et al., "Evaluation of ASTER-like daily land surface temperature by fusing ASTER and MODIS data during the HiWATER-MUSOEXE," *Remote Sensing*, vol. 8, no. 1, p. 75, 2016.
- [36] P. Wu, H. Shen, L. Zhang, and F. M. Göttsche, "Integrated fusion of multi-scale polar-orbiting and geostationary satellite observations for the mapping of high spatial and temporal resolution land surface temperature," *Remote Sensing of Environment*, vol. 156, pp. 169–181, 2015.
- [37] S. Mukherjee, P. K. Joshi, and R. D. Garg, "A comparison of different regression models for downscaling Landsat and MODIS land surface temperature images over heterogeneous landscape," *Advances in Space Research*, vol. 54, no. 4, pp. 655–669, 2014.

- [38] L. Anselin, "Local indicators of spatial association—LISA," *Geographical Analysis*, vol. 27, no. 2, pp. 93–115, 1995.
- [39] W. P. Kustas, J. M. Norman, M. C. Anderson, and A. N. French, "Estimating subpixel surface temperatures and energy fluxes from the vegetation index-radiometric temperature relationship," *Remote Sensing of Environment*, vol. 85, no. 4, pp. 429–440, 2003.
- [40] R. Eswar, M. Sekhar, and B. K. Bhattacharya, "A simple model for spatial disaggregation of evaporative fraction: comparative study with thermal sharpened land surface temperature data over India," *Journal of Geophysical Research: Atmospheres*, vol. 118, no. 21, pp. 12,029–12,044, 2013.
- [41] F. Yuan and M. E. Bauer, "Comparison of impervious surface area and normalized difference vegetation index as indicators of surface urban heat island effects in Landsat imagery," *Remote Sensing of Environment*, vol. 106, no. 3, pp. 375–386, 2007.
- [42] Q. Weng, P. Fu, and F. Gao, "Generating daily land surface temperature at Landsat resolution by fusing Landsat and MODIS data," *Remote Sensing of Environment*, vol. 145, no. 8, pp. 55–67, 2014.
- [43] K. Zakšek and K. Oštir, "Downscaling land surface temperature for urban heat island diurnal cycle analysis," *Remote Sensing of Environment*, vol. 117, pp. 114–124, 2012.
- [44] Q. Weng and P. Fu, "Modeling diurnal land temperature cycles over Los Angeles using downscaled GOES imagery," *ISPRS Journal of Photogrammetry and Remote Sensing*, vol. 97, pp. 78–88, 2014.

Research Article

Development of an IoT-Based Indoor Air Quality Monitoring Platform

JunHo Jo ¹, ByungWan Jo ¹, JungHoon Kim ¹, SungJun Kim,¹ and WoonYong Han²

¹Department of Civil and Environmental Engineering, Hanyang University, 04763 Seoul, Republic of Korea

²Smart IS, 22101 Incheon, Republic of Korea

Correspondence should be addressed to ByungWan Jo; joycon@hanmail.net

Received 21 October 2019; Accepted 5 December 2019; Published 14 January 2020

Guest Editor: Zhenxing Zhang

Copyright © 2020 JunHo Jo et al. This is an open access article distributed under the Creative Commons Attribution License, which permits unrestricted use, distribution, and reproduction in any medium, provided the original work is properly cited.

In this paper, an IoT-based indoor air quality monitoring platform, consisting of an air quality-sensing device called “Smart-Air” and a web server, is demonstrated. This platform relies on an IoT and a cloud computing technology to monitor indoor air quality in anywhere and anytime. Smart-Air has been developed based on the IoT technology to efficiently monitor the air quality and transmit the data to a web server via LTE in real time. The device is composed of a microcontroller, pollutant detection sensors, and LTE modem. In the research, the device was designed to measure a concentration of aerosol, VOC, CO, CO₂, and temperature-humidity to monitor the air quality. Then, the device was successfully tested for reliability by following the prescribed procedure from the Ministry of Environment, Korea. Also, cloud computing has been integrated into a web server for analyzing the data from the device to classify and visualize indoor air quality according to the standards from the Ministry. An application was developed to help in monitoring the air quality. Thus, approved personnel can monitor the air quality at any time and from anywhere, via either the web server or the application. The web server stores all data in the cloud to provide resources for further analysis of indoor air quality. In addition, the platform has been successfully implemented in Hanyang University of Korea to demonstrate its feasibility.

1. Introduction

Atmospheric conditions continue to deteriorate each year due to the growth of civilization and increasing unclean emissions from industries and automobiles. Although air is an indispensable resource for life, many people are indifferent to the severity of air pollution or have only recently recognized the problem [1–3]. Among various types of pollutants such as water, soil, thermal, and noise, air pollution is the most dangerous and severe, causing climate change and life-threatening diseases. According to the World Health Organization (WHO), 90 percent of the population now breathes polluted air, and air pollution is the cause of death for 7 million people every year [4, 5]. The health effects of pollution are very severe that causes stroke, lung cancer, and heart disease. Furthermore, air pollutants have a negative impact on humans and the earth’s ecosystem, as observed in recent global air pollution problems like ozone depletion

[6–8]. Therefore, air quality monitoring and management are main subjects of concern.

According to the United States Environmental Protection Agency (EPA), indoor air is 100 times more contaminated than outside air. Most modern populations spend 80 to 90 percent of their time indoors; therefore, indoor air has a greater direct impact on human health than outside air [9–12]. Moreover, in contrast to atmospheric pollution, indoor pollutants are about 1000 times more likely to be transmitted to the lungs, causing diseases such as sick building syndrome, multiple chemical sensitivities, and dizziness. Indoor air quality management is very important, as it can prevent exposure through proactive precautionary measures [9, 13–15]. Therefore, efficient and effective monitoring of indoor air is necessary to properly manage air quality.

To reduce exposure to air contamination (especially aerosols), new measures have been pursued, including development of air quality measuring devices and air purifiers. The

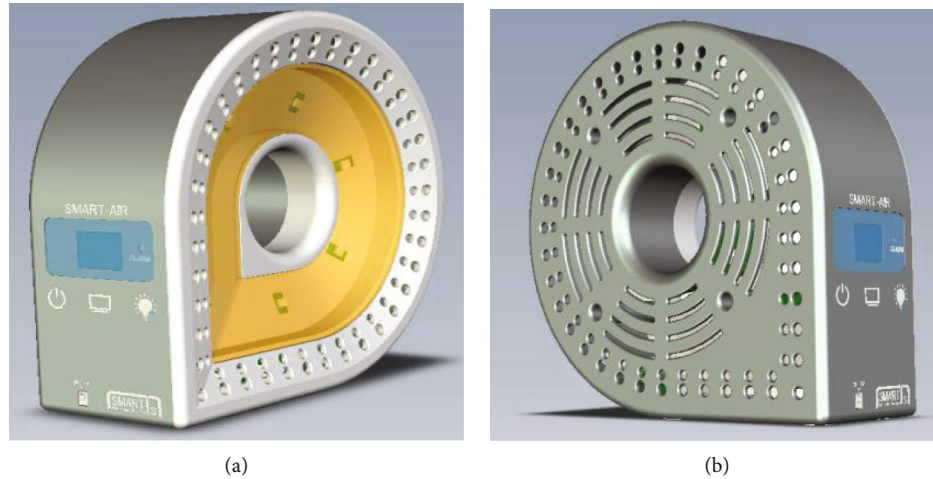


FIGURE 1: Primitive concept design of Smart-Air: (a) front and (b) back.

Ministry of the Environment in Korea assessed the efficacy of 17 widely used air quality measuring devices by analyzing their accuracy and reliability. The result showed that only two devices provided accurate readings of indoor air quality. The other devices did not present accurate measurements of aerosol and total volatile organic compounds except carbon dioxide. According to the report, the Ministry suggests that the low reliability of indoor air quality measurement values in most devices depended on many factors such as measurement methods, device structure, and data transmission. Thus, a technologically advanced air quality monitoring platform must be developed based on an understanding of the need for more accurate monitoring devices [16].

In recent years, introduction of technologies such as the Internet of Things (IoT) and cloud computing has revealed new capabilities of real-time monitoring in various fields. Thus, many scholars have studied integrating these technologies to indoor air quality monitoring system [17–21]. However, these studies were only focused on integrating an architecture of IoT platform to monitor the air quality in real time. Since the technologies feature a wireless sensor network to automatically transmit, process, analyze, and visualize data, merging these new technologies can also offer great advantages to improve indoor air quality [22–25].

Therefore, an IoT-based indoor air quality monitoring platform based on integration of cloud computing and IoT is presented in this research. Also, a device called “Smart-Air” was developed to precisely monitor indoor air quality and efficiently transmit real time data to a cloud computing-based web server using an IoT sensor network. The cloud computing based web server introduced in this platform analyzes real-time data and adds visual effects to illustrate the conditions of the indoor air quality. In addition, the web server was designed to issue alert mobile application users or facility managers of moderate or poor air quality so that responsible parties can take immediate remedial action. Real-time monitoring and a rapid alert system produce an efficient platform for improving indoor air quality. Major contributions of the proposed study are as follows:

- (i) We propose the use of the Smart-Air for the precise monitoring of indoor air quality
- (ii) We propose the utilization of an IoT for efficient monitoring of real-time data
- (iii) We propose the adoption of cloud computing for real-time analysis of indoor air quality
- (iv) We originally developed a mobile application to make the proposed IoT system with features of anytime, anywhere
- (v) The device has been tested for reliability of the data and the platform has been implemented in a building to test its feasibility

2. Smart-Air

An accurate data measurement of indoor air quality is the most important factor for the platform. Thus, Smart-Air was developed to collect accurate and reliable data for indoor air quality monitoring. Because the monitoring area is not constant, the device was designed to be easily customized to an environment by using an expandable interface. Thus, various types of sensors can be installed or adjusted based on the environment. Also, a Long-Term Evolution (LTE) modem is mounted in the device to transmit detected data directly to the web server for classifying and visualizing air quality. For most IoT platforms, gateway or data loggers are installed to gather and transmit data wirelessly to the web server. However, in this study, a microcontroller was installed in the device to gather the data from the sensors and transmit it to the web server using the LTE modem, eliminating the need for a gateway and a data logger.

The most important purpose of Smart-Air is to precisely detect air quality in the perception layer of the platform that a primitive concept design of the device is shown in Figure 1. This device has an expandable interface such that multiple sensors can be installed simultaneously or easily added according to monitoring requirements. In the present study,

TABLE 1: Specifications of the STM 32 F407IG microcontroller.

Specification	Value
Instruction set	ARM Cortex-M4 (32-bit)
Flash memory	1024 Kbytes
SRAM (system)	192 Kbytes
SRAM (system)	4 Kbytes
12-bit ADC number of channels	24
12-bit DAC number of channels	2
Maximum CPU frequency	168 MHz
Operating voltage	1.8 V to 3.6 V
Operating temperature range	-40 to 125 Celsius

the Smart-Air device consists of a laser dust sensor, a volatile organic compound (VOC) sensor, a carbon monoxide (CO) sensor, a carbon dioxide (CO₂) sensor, and a temperature-humidity sensor. Moreover, an LED strip was installed in the center of the device to visualize air quality using colors. When the quality of air changes, the device's LED changes color and wirelessly sends an alert message to the web server via LTE. Thus, the LTE modem transmits and receives data by communicating with the web server for detailed monitoring and determination of air quality as the presentation layer of the platform.

2.1. Microcontroller. The microcontroller is a compact integrated circuit used as an embedded system by receiving input from multiple sensors. In this paper, STM 32 F407IG from STMicroelectronics was selected, since it is designed for high performance and integration. The core of the microcontroller is the ARM 32-bit Cortex-M4 CPU that incorporates high-speed embedded memory. Table 1 summarizes the specifications of the STM 32 F407IG microcontroller [26].

2.2. Laser Dust Sensor. South Korean air space contains a very high level of aerosol, especially PM 2.5 and PM 10 [27–29]. A laser dust sensor, model PM2007 from Wuhan Cubic Optoelectronics Co., was installed in Smart-Air to measure and monitor concentrations of aerosol. This sensor can detect and output real-time particle mass concentrations for PM 2.5 and PM 10, which are defined as the fraction of particles with aerodynamic diameters smaller than 2.5 and 10 μm , respectively. The main features of the sensor are high sensitivity and accuracy in the range of 0 to 10000 $\mu\text{g}/\text{m}^3$ for 0.3 to 10 μm sized particles. This model also has a quick response time that can output real-time accurate particle mass concentration. The main specifications of the fine-dust sensor are provided in Table 2 [30].

2.3. Volatile Organic Compound Sensor. Volatile organic compounds (VOCs) are hydrocarbon-based products such as petroleum products and organic solvents that are easily vaporized in air due to high vapor pressure. Also, organic materials such as liquid fuels, paraffins, olefins, and aromatic compounds, which are commonly used in the living environment, are defined as VOCs. These compounds may cause damage to the nervous system through skin contact or

TABLE 2: Specifications of the laser dust sensor.

Specification	Value
Measurement particle size	0.3 to 10 μm
Measurement range	0 to 1000 $\mu\text{g}/\text{m}^3$
Time to first reading	≤ 8 s
Working temperature	-10 to 50 Celsius
Working humidity	0 to 95% RH (noncondensing)
Signal output	UART-TTL, PWM, IIC

TABLE 3: Specifications of the VOC sensor.

Specification	Value
Sensor input voltage	1 to 12 V
Operating temperature	-10 to 50 Celsius
Operating humidity	5 to 95% RH (noncondensing)
Reaction time	Less than 10 sec
Recovery time	Less than 30 sec
Power consumption	Below 460 mW
Sensitivity (β) for toluene	$0.30 \leq \beta \leq 0.60$ (concentration: 1.0 ppm)
Sensitivity (β) for H ₂	$0.35 \leq \beta \leq 0.70$ (concentration: 100 ppm)
Sensitivity (β) for i-butane	$0.20 \leq \beta \leq 0.60$ (concentration: 100 ppm)
Accuracy	$\pm 7\%$

* β = resistance after gas injection/resistance in a clean state.

respiratory inhalation, indicating the importance of monitoring [15, 31]. A VOC sensor module GSBT11-P110 from Ogam Technology is installed in Smart-Air. The sensor detects many types of VOCs, such as formaldehyde, toluene, benzene, xylene, and organic solvents, and the main specifications are illustrated in Table 3 [31].

2.4. Carbon Monoxide Sensor. Carbon monoxide is a toxic product of incomplete combustion of carbon compounds such as gas, petroleum, and coal. When CO gas is absorbed in the human body, it binds to hemoglobin in place of oxygen and induces hypoxia by obstructing the oxygen supply. CO gas can be generated from many sources, mainly human activities such as heating systems, cooking facilities, or burning fuel to power vehicles [8, 32]. Therefore, a CO sensor module GSET11-P110 from Ogam Technology is mounted in the device to detect and monitor CO. This sensor is a semiconductor-based gas sensor that is less expensive and easier to operate than a nondispersive infrared sensor. Additionally, it is possible to detect CO gas with high sensitivity; the specifications of the CO sensor are listed in Table 4 [33].

2.5. Carbon Dioxide Sensor. Although CO₂ is produced both naturally and through human activities, it is not classified as an air pollutant. However, it is treated as a pollutant because the amount of oxygen required for breathing becomes insufficient at high concentrations of CO₂ in an indoor space. CO₂ is a representative greenhouse gas that causes global warming

TABLE 4: Specifications of the CO sensor.

Specification	Value
Sensor input voltage	1 to 12 V
Operating temperature	-10 to 50 Celsius
Operating humidity	5 to 90% RH (non-condensing)
Reaction time	Less than 10 sec
Recovery time	Less than 30 sec
Power consumption	Below 380 mW
Sensitivity (β) for CO	$0.30 \leq \beta \leq 0.60$ (concentration: 100 ppm)
Sensitivity (β) for tobacco	$\beta \leq 0.60$ (concentration: 2000 ppm)
Sensitivity (β) for ethyl alcohol vapor	$\beta \leq 0.50$ (concentration: 50 ppm)
Accuracy	$\pm 7\%$

TABLE 5: Specifications of the CO₂ sensor.

Specification	Value
CO ₂ measurement range	0-2000 ppm up to 0-10000 ppm
Resolution	10 ppm
Accuracy	40 ppm + 2% reading
Response time	30 sec
Maximum drift	$\pm 2\%$ FS
Operating voltage	DC 5 V $\pm 5\%$
Operating current	Average: 70 mA, peak: 120 mA
Operating temperature	0 to 50 Celsius
Operating humidity	0 to 90% RH (noncondensing)

[22, 34]. Thus, the CO₂ gas sensor module CM1103 is installed to detect and monitor CO₂ concentrations. The sensor uses nondispersive infrared technology (NDIR) that have advantages of high precision, fast response, and factory calibration. Also, it features excellent long-term stability with low power consumption. The detailed specifications are listed in Table 5 [35].

2.6. Temperature-Humidity Sensor. According to the Ministry of the Environment Korea, comfort of the indoor environment is greatly influenced by temperature and humidity [36]. Thus, a temperature-humidity sensor, model DHT11 from OSEPP Electronics, is installed in Smart-Air to measure temperature and humidity. The sensor guarantees high reliability and excellent long-term stability using a digital signal acquisition technique. The sensor is strictly calibrated in the lab, and the calibration coefficients are stored as programs in the memory for application during the sensor's internal detection process. The specifications of the temperature-humidity sensor are listed in Table 6 [37].

2.7. Network Modem. Since networking is important in IoT technology to connect the Smart-Air with web servers for monitoring, determining, and visualizing indoor air quality,

TABLE 6: Specifications of the temperature-humidity sensor.

Specification	Value
Measurement range	0 to 50 Celsius 20 to 90% RH
Temperature accuracy	± 2 Celsius
Humidity accuracy	$\pm 5\%$ RH
Response time	6 to 15 sec

TABLE 7: Specifications of the LTE module.

Index	Specification
Communication method	LG U+ LTE B5/B7 FDD cat. 4
Band	LTE FDD 850 MHz(B5)/2.6 GHz(B7)
Interface	DB9 RS-232, RJ-45 ethernet, GPIO
Data speed	150 mbps DL/50 mbps UL
Input voltage	4.5 to 5.5 V
Operating temperature	-20 to 60 Celsius

a model RCU890L LTE modem from Woojin Networks was mounted in the device. The LTE modem is a mobile communication terminal device with widespread network coverage and can transmit, receive, and execute data anywhere in real time. Therefore, the modem provides a connection between the device and web server. The modem uses LG U+ LTE B5/B7 FDD Cat. 4 as the communication method; other characteristics are shown in Table 7 [38].

2.8. LED Strip. The proposed platform was designed to alert users and managers through the web server and mobile application when poor air quality is detected. However, the platform cannot alert everyone in the area. Therefore, a WS2812 LED strip from WorldSemi is mounted in the center of the device to immediately display colors depending on air quality defined based on the Ministry of Environment, Korea.

2.9. Reliability Tests. Since the accuracy of the sensors installed in Smart-Air is the most important factor in monitoring air quality, experimental efforts have focused on verifying the reliability of the sensors. The sensors were tested for the reliability according to the protocols from the Korea Testing Laboratory that was approved by the Ministry of Environment, Korea [16].

The VOC and CO sensors required calibration before the Smart-Air reliability test and were calibrated in a 1 m \times 1 m \times 1 m-sized acryl chamber. The CO₂ sensor and temperature-humidity sensor did not need extra calibration since they were precalibrated in the factory. In total, five sensors were tested based on the protocols of the Ministry: laser dust sensor, VOC sensor, CO sensor, CO₂ sensor, and temperature-humidity sensor. Two types of chambers were used to provide a constant environment for the experiments. For laser dust and VOC sensors, an acryl chamber was used because the experiment was not affected by temperature or humidity. A

TABLE 8: Measurements from the reliability test of the laser dust sensor.

	Inserted flow: 1 L/min			Inserted flow: 2.5 L/min		
	@ 1 minute	@ 30 minutes	@ 60 minutes	@ 1 minute	@ 30 minutes	@ 60 minutes
Smart-Air (A) ($\mu\text{g}/\text{m}^3$)	92	93	92	95	96	97
Smart-Air (B) ($\mu\text{g}/\text{m}^3$)	92	93	92	96	97	96
Smart-Air (C) ($\mu\text{g}/\text{m}^3$)	92	93	91	96	97	96
GRIMM 1109 ($\mu\text{g}/\text{m}^3$)		93			97	

temperature-humidity chamber was used with an accurate set temperature and humidity of 19°C and 55%, respectively, for the CO sensor, CO₂ sensor, and temperature-humidity sensor. Both chambers provided a constant environment suitable for the experiments. Then, the data were observed and extracted from the web server and application to assess the performance of the platform.

2.9.1. Laser Dust Sensor. The laser dust sensor was precalibrated in the factory, so only a reliability test was required to verify the data from Smart-Air. To test the accuracy of the laser dust sensor installed in the device, two types of experiments were performed based on aerosol concentration. The first method utilized a chamber experiment and was compared to a gravimetric method. The other method was a field test that compared the sensor data to that of a certified fine-dust measurement device to evaluate the reliability of real-time monitoring. In this study, a combination of the two methods was performed. The Ministry recommended and used GRIMM's light-scattering fine-dust measurement device because it used a light-scattering method for detection. This method is known to be the most reliable for detection due to the factory calibration. In the experiment, data from three Smart-Air devices were measured and compared to the data obtained from GRIMM 1109. The devices were placed in the acryl chamber, and external air was injected into the chamber at a flow rate of 1 L/min or 2.5 L/min. The data were measured at 1, 30, and 60 minutes after device installation. Then, the readings were compared to those of GRIMM 1109 to assess accuracy and reliability.

The results of the reliability test for the laser dust sensor installed in Smart-Air are shown in Table 8. A comparison of the data of GRIMM 1109 sensor, which was certified by the Ministry of Environment, Korea, with that of the sensor installed in Smart-Air was used to assess the accuracy of the sensors. The same experiment was conducted with the two different flows of 1 L/min and 2.5 L/min. For each experiment, GRIMM 1109 and three Smart-Air devices, which were presented as Smart-Air (A), (B), and (C), sensed the concentrations of fine dust. GRIMM 1109 showed its reading at 30 minutes after flow introduction as designed. Detection of fine dust by the sensors from Smart-Air devices was performed at 1, 30, and 60 minutes after flow insertion. The concentrations measured by the sensors showed constant and stable values independent of the model. The data measured by the sensor installed in Smart-Air and GRIMM 1109 were very similar 30 minutes after insertion. At a flow of 1 L/min, the concentration was 93 $\mu\text{g}/\text{m}^3$. At a flow of 2.5 L/min, the

concentration was 97 $\mu\text{g}/\text{m}^3$. The data collected from the sensors were similar to that from the certified devices, indicating the high reliability of the sensors.

2.9.2. VOC Sensor. The VOC sensor used in the study was selected based on an investigation by the Ministry of Environment, Korea. The sensor is a semiconductor type that can have a small diffusion effect and requires data verification. Accordingly, calibration and a chamber test were conducted to test the reliability of the VOC sensor. To calibrate the sensor, Smart-Air was placed in an acrylic chamber with a PID-type VOC sensor, i.e., MiniRAE 3000 from RAE Systems. The PID type VOC sensor was the most accurate and reliable type to detect VOCs. After the sensors were placed, about 1 inch of incense was burned to create a VOC compound to measure. The collected data from Smart-Air were calibrated against those from the PID-type VOC sensor. After calibration, a chamber test was performed to test the reliability of the VOC sensors, a common procedure adopted by the Ministry. After placing the Smart-Air in the chamber, N₂ was injected to clean the chamber. To test the accuracy of the measurement sensor, toluene gas was injected at different concentrations. In this study, three values of concentrations were selected and injected in ascending order: 480 $\mu\text{g}/\text{m}^3$, 1000 $\mu\text{g}/\text{m}^3$, and 1600 $\mu\text{g}/\text{m}^3$. After each injection, the data observed from the device were compared to the actual injected concentration to confirm the reliability of the measurement.

Both Smart-Air devices and MiniRAE 3000 were placed in the acryl chamber to obtain the data in the same conditions with a constant environment. As the incense was burned, the gas concentration increased as the voltage output signal of the VOC sensor increased, showing a linear relationship. This excludes any possible effects of gas concentration, and the relationship is illustrated in Figure 2.

After calibration, a reliability test was performed for the VOCs to test the accuracy of the data following the standards from the Ministry, and the results are shown in Figure 3. The measured value was very similar to the actual concentration of toluene. When a concentration of 480 $\mu\text{g}/\text{m}^3$ was injected at 14:24, the reading presented an accurate value at 15:10. When a concentration of 1000 $\mu\text{g}/\text{m}^3$ was injected at 15:22, the reading was accurate at 16:19. When a concentration of 1600 $\mu\text{g}/\text{m}^3$ was injected, an accurate measurement was observed at 17:40. At the highest concentration at 1600 $\mu\text{g}/\text{m}^3$, the reading was higher than the actual initial value because the gases required adequate time to uniformly mix in the chamber. The results showed that the

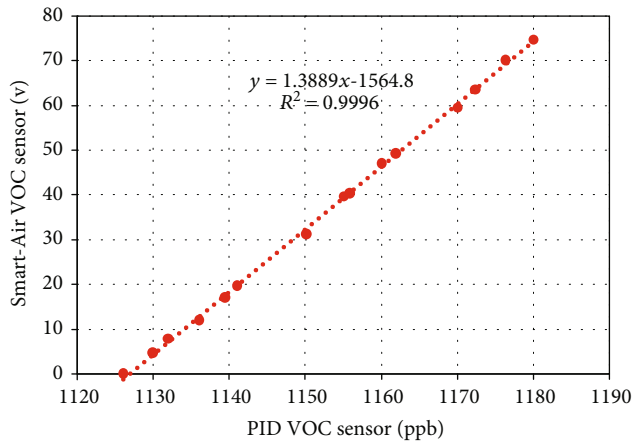


FIGURE 2: Calibration results of the VOC sensor.

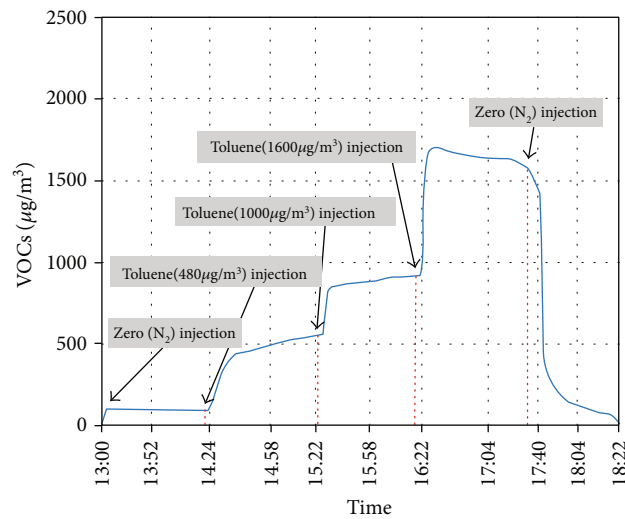


FIGURE 3: Reliability test results of the VOC sensor.

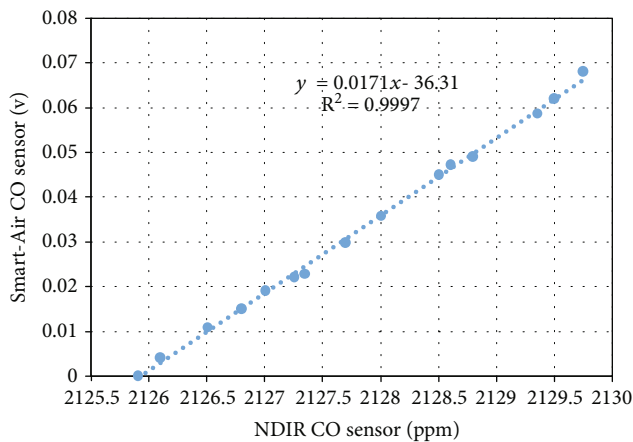
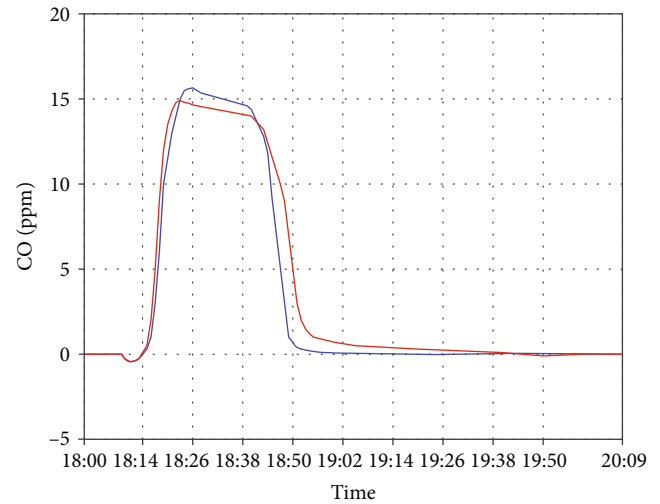
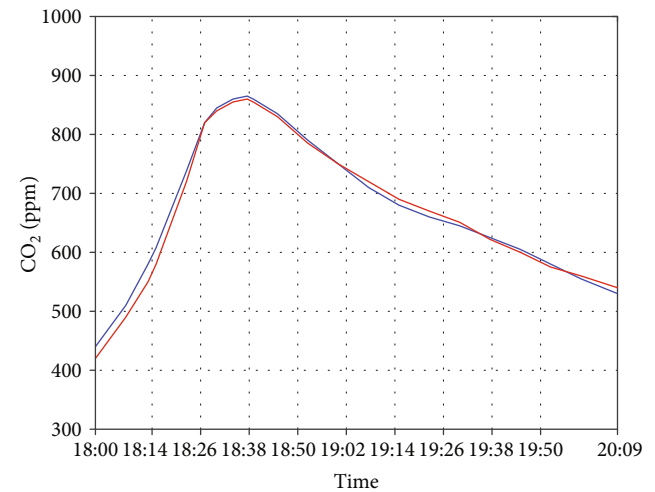


FIGURE 4: Calibration results of the CO sensor.



— TES-132
— Smart-Air

FIGURE 5: Reliability test results of the CO sensor.



— Testo-535
— Smart-Air

FIGURE 6: Reliability test results of the CO₂ sensor.

sensor can detect and present accurate readings in a short period of time. Thus, the device was suitable for monitoring indoor air quality.

2.9.3. CO Sensor. The CO sensor used in the study is also a semiconductor type, which is not the official standard CO sensor for indoor air quality measurements. TES-1372 from TES was used in the experiments for calibration and reliability testing because the Ministry recommended an NDIR-type measurement device. The same calibration method used for the VOC sensor was used for the CO sensor. A reliability test was performed after calibration. After the devices were placed in the sample chamber, incense (about 1-inch-long)

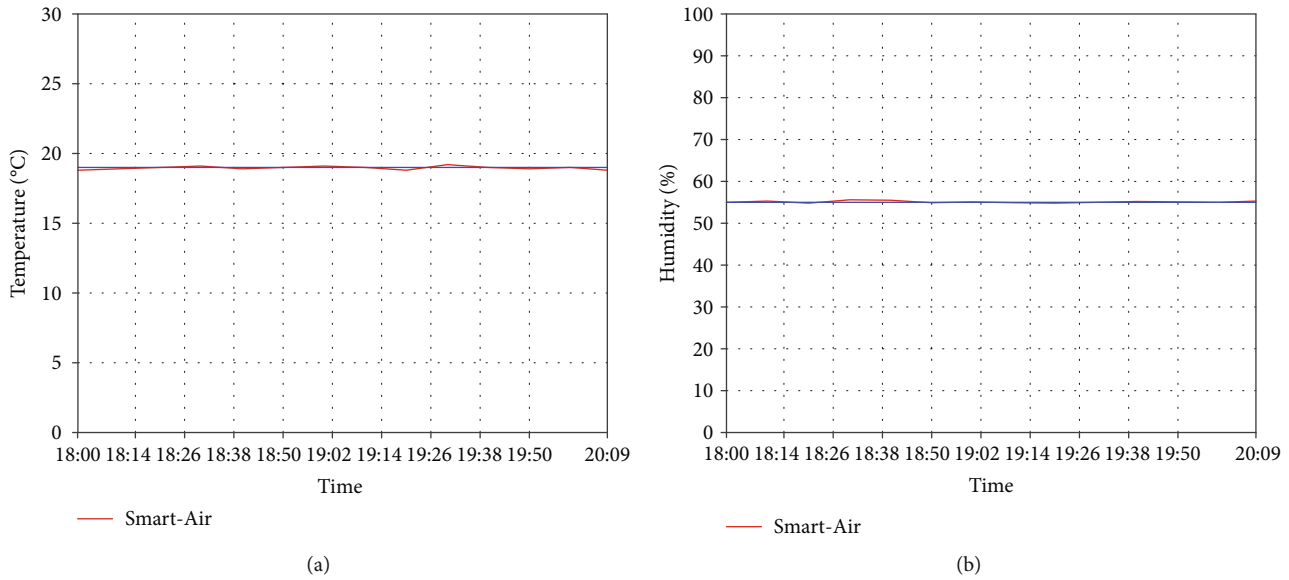


FIGURE 7: Reliability test results for (a) temperature and (b) humidity.

in a metal cup was placed inside and lighted. The CO sensor from Smart-Air and the NDIR-type device detected the increased concentration of CO associated with the combustion. The data collected from the two devices were compared to evaluate the accuracy of the CO sensor.

The CO sensor was calibrated with the same process used for the VOC sensor calibration. The Smart-Air and the TES-132, a certified device, were placed in the same chamber to measure the concentration of CO gas from the incense. Similar to the VOC sensor, the CO level increased as the voltage output signal increased. The linear conversion model for calibration of the CO sensor is presented in Figure 4.

After calibrating the CO sensor of Smart-Air, the device was placed in the chamber with TES-132 for reliability testing. The results of the reliability test for the CO sensor are provided in Figure 5. The data collected by the NDIR-type CO measurement device showed that the concentration of CO in the chamber dramatically increased with time after incense lighting, gradually decreased with completion of burning, and then dropped dramatically after loss of combustion. The data presented by the CO sensor were similar, indicating the efficacy of the CO sensor. If the device is to be used for a long period of time, periodic maintenance may be required to reduce the possibility of errors. As explained in the experimental method, the assessment of CO sensors followed the standard procedures performed and suggested by the Ministry of Environment, Korea. The contamination level detected from the sensor and certified device generally showed the same trends, supporting the high reliability of the sensor. However, further experiments are required to increase the accuracy of concentration measurement.

2.9.4. CO₂ Sensor. According to the Ministry of Environment, Korea, an NDIR-type sensor is used for verifying CO₂ measurement devices due to its high accuracy in detection

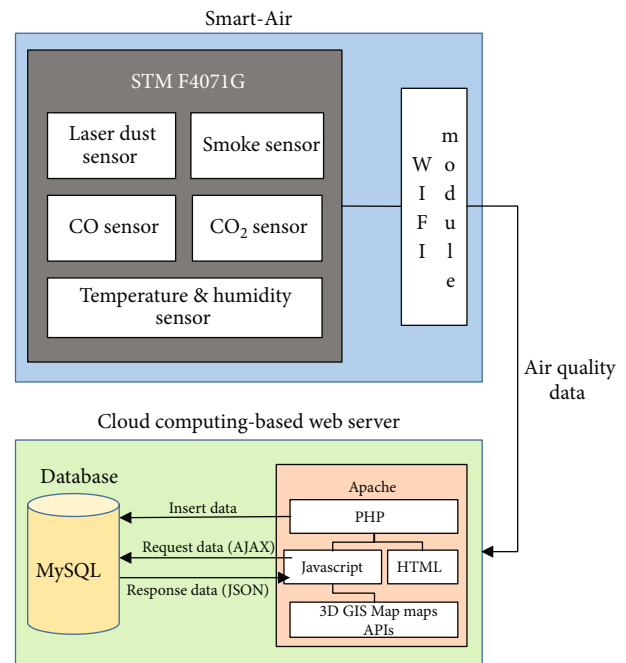


FIGURE 8: Configuration diagram for the IoT-based indoor air quality monitoring platform.

of CO₂. A CO₂ calibration is performed during sensor manufacturing and is not required for NDIR-type sensors after purchase. Furthermore, these sensors have high stability and do not deteriorate upon exposure to gases or experience sensor burnout. Since the sensor is precalibrated, only a reliability test was performed. A Testo-535, a commercial certified NDIR-type CO₂ measurement device, and the Smart-Air were placed in the temperature-humidity chamber to measure the concentration of CO₂. The reliability of the device was assessed by comparing its result to that of

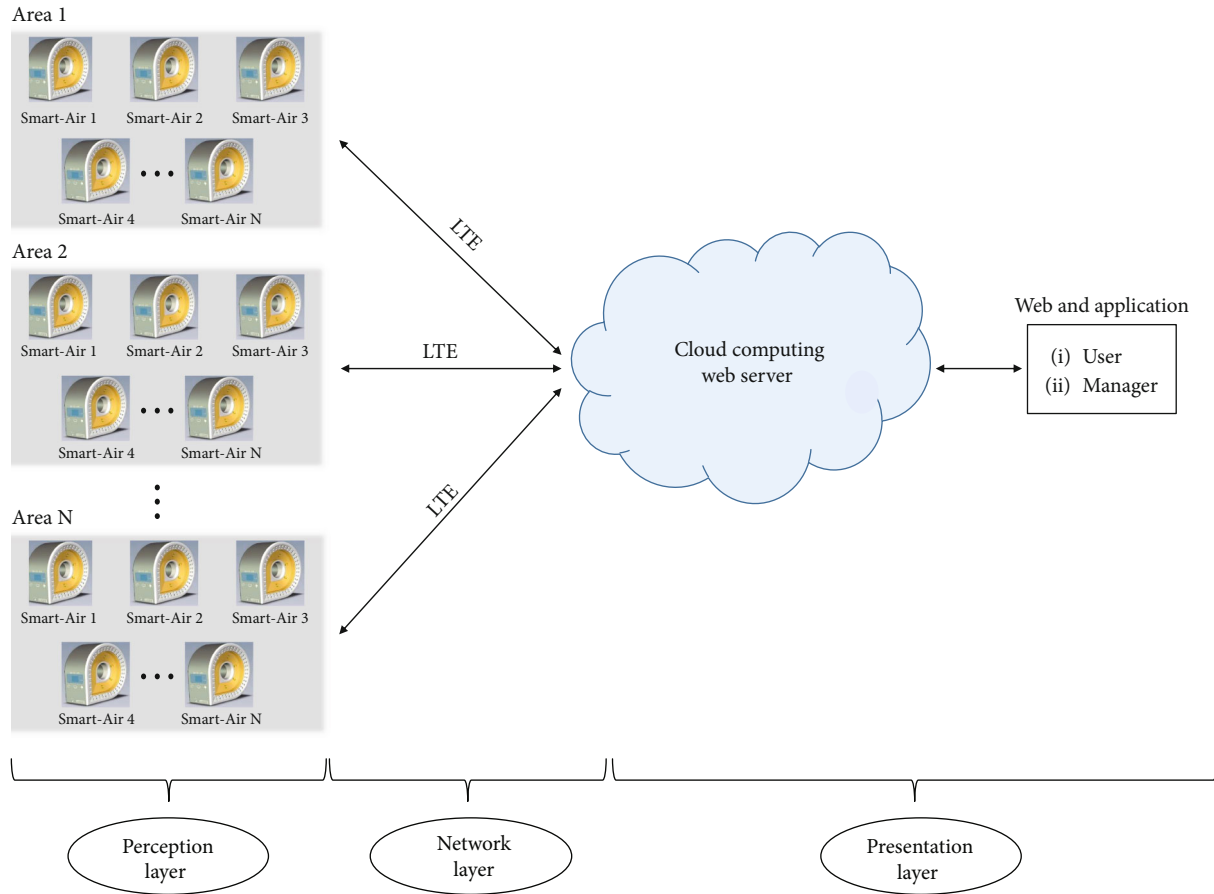


FIGURE 9: Block diagram of the IoT-based indoor air quality monitoring platform.

Testo-535. The experiment was conducted in the same manner as the method used for the CO sensor. About 1 inch of incense was lighted in a metal cup near the two devices placed in the chamber to sense the CO₂ concentration after incense lighting. The data presented by the two devices were compared to assess the reliability of the CO₂ sensor.

The CO₂ sensors from Smart Air and Testo-535 sensed an increase in CO₂ concentration after lighting until 18:38. As the incense burned, the CO₂ concentration gradually decreased. The two CO₂ sensors presented similar trends, indicating the high reliability of the device, as demonstrated in Figure 6. Therefore, the reliability of the sensor was verified through the experiment.

2.9.5. Temperature-Humidity Sensor. The temperature-humidity sensor was precalibrated in a factory instead of in a laboratory to produce greater accuracy and reliability. Although additional calibration of the sensor was not required, a reliability test was performed. Thus, Smart-Air was placed in the chamber for 2 hours with temperature and humidity set points of 19°C and 55%, respectively. The sensed temperature and humidity were compared to the initial set values for testing the accuracy of the sensor.

The chamber used in the experiment independently maintained specific humidity level and temperature of 19°C

and 55%, respectively. The measurements of temperature and humidity from the sensor were observed using an application, and the data were extracted from the web server, as shown in Figures 7(a) and 7(b), respectively. The data collected by the sensor were compared to the initial set values of the chamber. Smart-Air presented measurements as accurate as the set values, verifying the high reliability of the sensor and showing that it did not need extra calibration.

3. An IoT-Based Indoor Air Quality Monitoring Platform

The IoT-based indoor air quality monitoring platform is primarily divided (Figure 8) into the Smart-Air and the web server. The set of sensing devices necessary to collect the data to analyze air quality comprised a laser dust sensor, a CO sensor, a CO₂ sensor, a VOC sensor, and a temperature and humidity sensor. Each device transmitted data to the web server via the LTE module to determine air quality and visualize the result. Furthermore, cloud computing technology was integrated with a web server. The main benefits of the cloud computing-based web server are faster speed, flexibility, and greater accessibility. The web server provided faster and more flexible data processing functions with a large amount of data, which is essential for a monitoring platform. The cloud computing-based web server is easily accessible

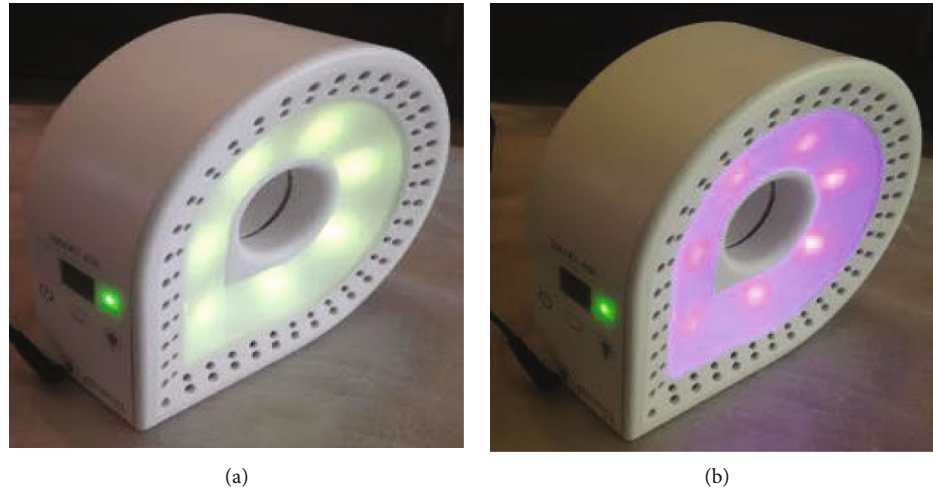


FIGURE 10: The Smart-Air (a) when indoor air quality is good and (b) when the light is set to purple.

through most browsers to allow ubiquitous monitoring. In this study, Amazon Web Services (AWS) was used as the web server to analyze, visualize, and present the data collected from Smart-Air. Also, the web server provides a database to store that data in the cloud. Furthermore, a mobile application was developed for the system to visualize air quality with the web server “anywhere, anytime” in real time.

The platform is designed based on an architecture of IoT platform that is mainly comprised of three components: (i) perception layer, (ii) a network layer, and (iii) presentation layer. The perception layer is the sensing component to collect data using sensors or any measuring devices. The network layer is responsible for transmitting the detected data using a wireless network module. Finally, the presentation layer allows data visualization and storage for efficient monitoring [39–41].

A block diagram of the IoT-based indoor air quality monitoring platform is shown in Figure 9. For the perception layer of the platform, multiple Smart-Air devices are used for detecting the data needed to analyze the air quality. Also, the LTE modem is mounted in the devices as the network layer. The data collected from each of these devices were sent to the web server via LTE. For the presentation layer, a cloud computing-based web server is used for the platform. The server gathered the data to evaluate air quality based on the Indoor Air Quality Control Act from the Ministry of Environment, Korea. Managers and users with specified access to the monitoring data can continuously monitor air quality anytime and anywhere via smart devices. Another feature of the server is that it automatically sends a warning message to managers and other related personnel whenever the quality of air decreases. Therefore, they can react immediately to improve the air quality.

3.1. Smart-Air. When a monitoring area has been determined, the specific types of air pollutants present must be considered. As mentioned above, Smart-Air has an expandable interface such that multiple sensors can be added to the microcontroller. Furthermore, the platform can monitor a large area or many areas simultaneously using multiple

TABLE 9: Specifications of the web server.

Index	Specification
Type of instance	T2 medium
Storage (GB)	EBS only
Memory (GiB)	4
vCPUs	2
Clock speed (GHz)	Maximum 3.3
CPU credits/hr	24
Networking performance	Low to medium

Smart-Air devices. Then, each device is classified by area to visualize the data. Each Smart-Air device transmits air quality data to the web server via LTE and automatically indicates the air quality for the specific area by LED color. Moreover, each device can be set to present a unique color of LED through the application or web server, as shown in Figure 10.

3.2. IoT Network. Since multiple Smart-Air devices can be used for efficient and precise monitoring, a wireless sensor network is very important for the platform. Although the network layer for most of the IoT-based air quality monitoring platform consists of the IoT gateway, the microcontroller is used as the IoT gateway to transmit and receive sensed data. Each Smart-Air device has its own microcontroller with an LTE modem. Thus, the data from each device are transferred wirelessly in the form of TCP/IP packets from the device to the web server via LTE [42, 43]. Then, the data are gathered and analyzed through the web server for visualization and storage.

3.3. Cloud Computing-Based Web Server. The IoT-based indoor air quality monitoring platform requires a server to efficiently analyze the data from Smart-Air and visualize the indoor air quality. To control and monitor multiple Smart-Air devices at the same time and save the data, AWS was used as the server. As AWS is a commercially certified cloud

TABLE 10: Standards for indoor air quality.

Condition	Aerosols ($\mu\text{g}/\text{m}^3$)	Type of air pollutant		
		CO (ppm)	CO ₂ (ppm)	VOCs ($\mu\text{g}/\text{m}^3$)
Good	≤ 100	≤ 10	≤ 1000	≤ 400
Moderate	$100 < * \alpha \leq 150$	$10 < * \alpha \leq 25$	N/A	$400 < * \alpha \leq 500$
Poor	> 150	> 25	> 1000	> 500

* α = measured value.

computing platform, significant amounts of time and money were saved in platform development, and errors were minimized. Furthermore, no separate database is needed to analyze and save data when using the AWS server.

The cloud computing-based port structure stability evaluation platform used the Elastic Compute Cloud (EC2) as the hypertext preprocessor (PHP) among the Amazon-supported application programming interfaces (APIs). EC2 is optimized for the platform because it offers stable support for dynamic instantiation and configuration of the virtual machine instance. The platform utilizes a T2 medium as an extensible instance, as specified and indexed in Table 9 [38, 44]. Also, the server was designed with the web programming language PHP, while MySQL was used as the database for data retention.

3.4. Application. An application for the IoT-based indoor air quality monitoring platform was developed to efficiently monitor the data and alert users and related personnel. Therefore, air quality was monitored both with the web server and with associated smart devices through the application. Air quality monitoring was easy and efficient using the application as it provided access anytime using smart devices. The application was designed to be very similar to the web server developed for Android OS version 4.1.1 using hypertext markup language, cascading style sheets, JavaScript, and PHP.

3.5. Conditions for Air Quality. To classify indoor air quality from the data, the IoT-based indoor air quality monitoring platform utilized standards for indoor air quality based on the indoor Air Quality Control Act. The act was instituted in 2007 by the Ministry of Environment, Korea to protect and manage indoor air quality to prevent health and environmental harm [36]. Based on the act, air quality is defined as good, moderate, or poor. The thresholds were automatically set as shown in Table 10 when Smart-Air was registered to the platform. However, the thresholds can be manually changed for a specific area via the web server based on user preferences.

Also, temperature and humidity are key factors affecting the comfort of indoor environments. Conditions for a comfortable indoor environment with respect to temperature and humidity were determined based on the Korea Meteorological Administration (KMA) and are listed in Table 11 [36]. If the temperature is neither good nor bad, the platform defines the condition as moderate. However, the thresholds for temperature and humidity are merely recommendations

TABLE 11: Recommended temperature and humidity by the KMA.

Condition	Temperature (Celsius)	Humidity (%)
Good	$18 \leq \alpha \leq 20$	$55 \leq \alpha \leq 65$
Poor	< 15 or > 30	< 30 or > 80

that can be edited according to user preferences for the desired indoor conditions.

3.6. Alert System. Although monitoring air quality in real time is important, the alert system is necessary to announce the need for change to prevent environmental harm. With the alert system, users or the manager of the platform can take immediate action to improve air quality. Therefore, AWS provides an application called Amazon Simple Notification Service for the alert system as an open library used in the IoT-based indoor air quality platform. Therefore, the web server was designed to issue a pop-up message in the application to alert the manager and users when the condition of the air was moderate or poor. Furthermore, semiconductor-type sensors that required inspection for calibration or deterioration due to long-term use were installed in Smart-Air. Therefore, the web server was designed to provide an automatic alert message when the device reached one year of use. The system automatically recommends inspections of the device via a pop-up message.

Furthermore, an LED strip was installed in the device such that the air quality conditions for the area can be recognized by nearby people. The device was designed to change the LED light color to match the current condition. Thus, the color will change to yellow and red when the conditions are moderate and poor, respectively.

4. Experimental Testing

Experimental efforts have focused on implementation of the IoT-based indoor air quality monitoring platform. Multiple Smart-Air devices were installed in the Jaesung Civil Engineering Building, Hanyang University, to test the feasibility of the platform. The entire installation consisted of the Smart-Air, cloud computing-based web server, and the application.

4.1. Installation. A total of seven Smart-Air instruments were installed to monitor indoor air quality in the Jaesung Civil Engineering Building, as shown in Figure 11. The building has two entrances, a main entrance and a back entrance located on the second floor, near which two Smart-Air

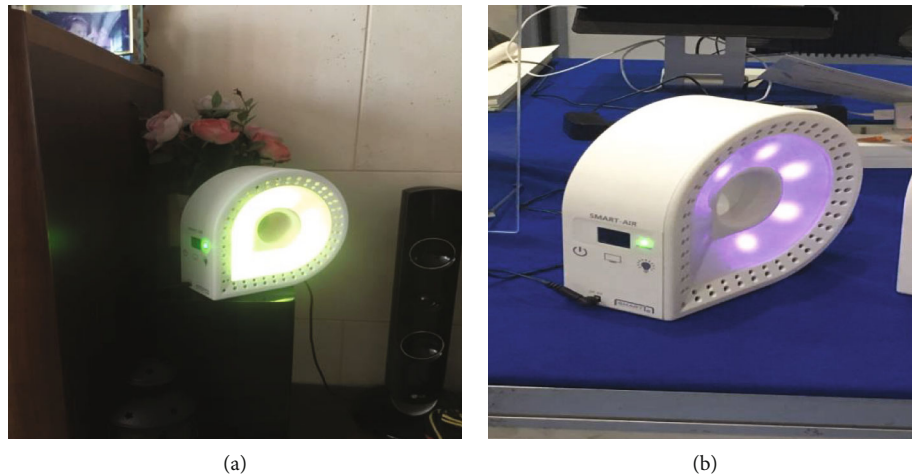


FIGURE 11: (a) Smart-Air ID No. 6 installed in the main entrance and (b) Smart-Air ID No. 1 installed in laboratory room 110.

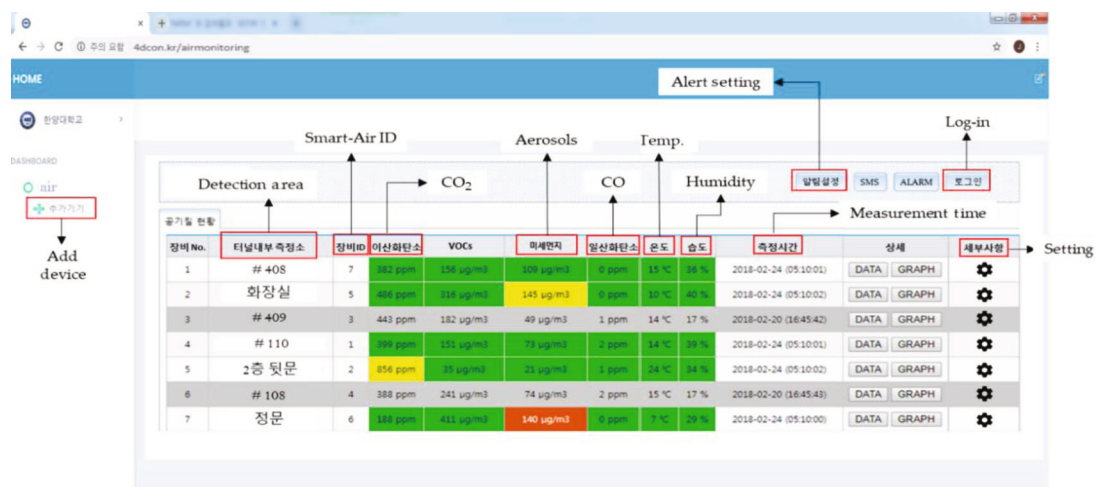


FIGURE 12: Cloud computing web server of the IoT-based indoor air quality monitoring platform.

devices, ID No. 6 and ID No. 2, were installed. Also, four devices (ID No. 4, ID No. 1, ID No. 7, and ID No. 3) were placed in four laboratories (rooms 108, 110, 408, and 409, respectively). The last Smart-Air, ID No. 5, was installed in a restroom located on the 1st floor.

4.2. Cloud Computing-Based Web Server. The cloud computing-based web server was enabled after installing the Smart-Air to analyze the detected data and visualize the indoor air quality for the platform. The web server used in the research is shown in Figure 12. The data from each device were classified by area and ID of the device. Also, the measured data from each sensor of the device were displayed in the web server. The server provided a datasheet and graph for the current set of stored data with measured times that can be extracted for review. Furthermore, the data were visualized and color-coded based on the current air quality. The color of the device changed to yellow or red along with activating the alert system when the air quality was moderate or poor. Therefore, the manager or user can take necessary

action to improve the air quality. Furthermore, the server stores the air quality data in the database of the cloud server to be reviewed when needed.

4.3. Application. To remotely monitor air quality, a mobile application was enabled after the web server was activated. After the desired monitoring device was selected, the condition of air quality was shown based on the types of air pollutants, as shown in Figure 13(a). Each component monitored as an air pollutant was displayed by color according to the web server. Additionally, when the specific types of air pollutants in the main page were selected, detailed monitoring of the pollutants was available based on a real-time graph as shown in Figure 13(b). Furthermore, the application alerts the user through a pop-up message when the condition of the air pollutant was moderate or poor.

5. Results

The goal of the experiment was to perform an initial implementation of the platform to monitor indoor air quality.

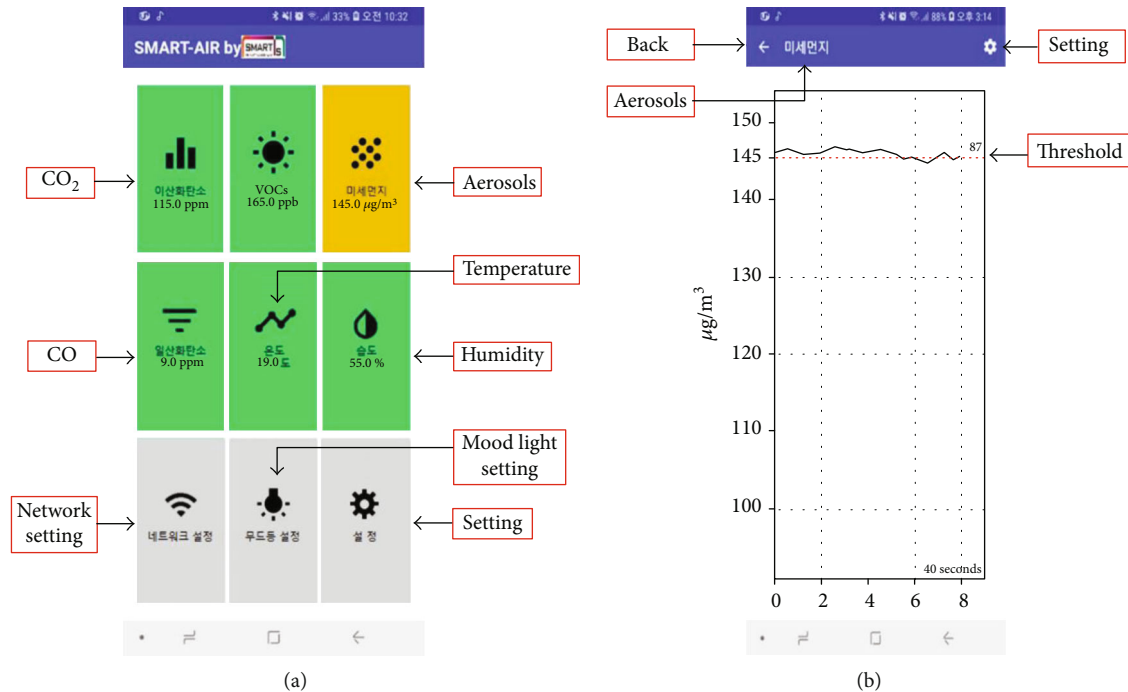


FIGURE 13: The application of the IoT-based air quality monitoring platform: (a) main page and (b) a real-time graph of aerosol data.

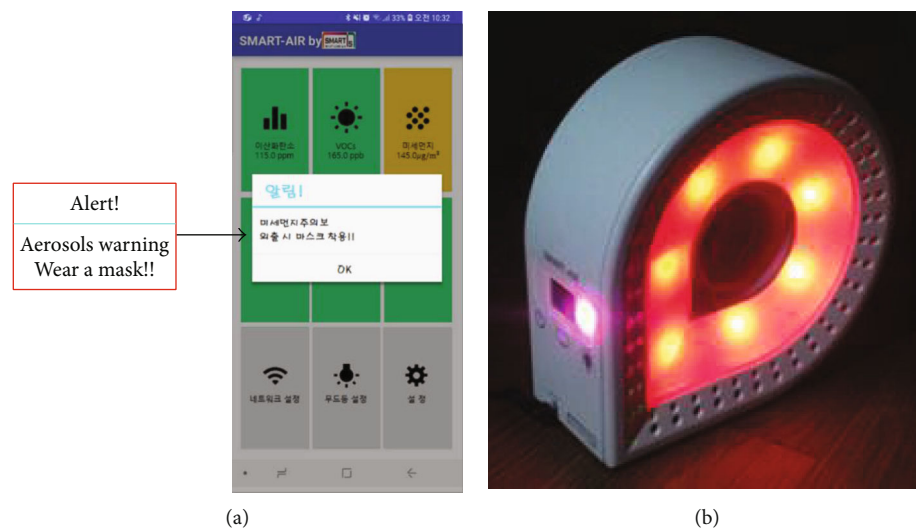


FIGURE 14: (a) A pop-up message from the application when the condition of aerosol was moderate. (b) Smart-Air response when the condition was poor.

Smart-Air wirelessly transmitted the detected data to the web server, which successfully classified the condition of indoor air quality and displayed it via both the web and the application. Also, the data were saved in the database of the web server as designed such that further studies can be performed on trends of air quality. The experiment showed poor conditions in entrances of the building because it is exposed to outside air more than other locations. However, the platform successfully alerted and visualized poor air quality, as shown in Figure 14. The device changed the LED light color to match the current condition and alerted the manager via a

pop-up message as shown in Figure 14(a). Also, LED lights installed in the device successfully displayed the condition especially when the air quality was poor as shown in Figure 14(b). Thus, the manager of the building was able to monitor the air quality of the building ubiquitously and take steps to improve the air quality.

Considering the nature of the platform, it is important to perform qualitative analysis based on user experience. In the experiment, interviews were conducted with building managers who used the platform to manage air quality. Interviewees were very satisfied with its ability to monitor air

quality. When air quality was moderate or poor, managers were alerted to the condition and able to react immediately to improve air quality. Positive comments were received from the managers regarding data precision and information collection in real time.

During the experiment, it was proven that the platform not only provided accurate data but also meaningful information in real time to save energy. The platform also monitors temperature and humidity to provide optimum environment for the area. By operating ventilation system when it is necessary along with the heating and air-conditioning system, people in the area were satisfied with the improved condition and saved energy.

6. Conclusions

In this paper, the development of an IoT-based indoor air quality monitoring platform is presented. Experiments were performed to verify the air quality measurement device used in the platform based a method suggested by the Ministry of Environment, Korea. We verified the accuracy of indoor air quality monitoring and the desirable performance of the device. Also, experiments making use of the platform were conducted and demonstrated suitable performance and convenience of the air quality monitoring platform. Several achievements of the platform were accomplished, including the following: (1) indoor air quality can be efficiently monitored anywhere and in real time by using an IoT and a cloud computing technologies; (2) the platform used Amazon Web Services as a certified web server for security of the platform and the data; (3) the Smart-Air device has an expandable interface, and the web server is also easily extendable, allowing easy application to various environments through the addition of appropriate sensors to the device or installing more Smart-Air devices to appropriate monitoring locations.

Future work will involve further testing of the device and the platform. In this paper, the experiment focused on testing the reliability of the device and implementing the platform, where more tests are necessary to ensure data accuracy for long time periods. In addition, ventilation system can be connected to the platform. Thus, the system can be automatically operated to improve the air quality whenever the air quality is not good.

Data Availability

The data used to support the findings of this study are available from the corresponding author upon request.

Disclosure

This research did not receive any specific grants from funding agencies in the public, commercial, or not-for-profit sectors.

Conflicts of Interest

The authors declare no conflict of interest.

Authors' Contributions

J.J. and B.J. conceptualized the study and J.J., J.K., and S.K. performed the investigations. J.J. and W.H. developed the methodology. JJ wrote the original draft of the manuscript while BJ supervised the research. J.J., J.K., and S.K. reviewed and edited the manuscript. All authors read and approved the final manuscript.

References

- [1] G. Parmar, S. Lakhani, and M. Chattopadhyay, "An IoT based low cost air pollution monitoring system," in *2017 International Conference on Recent Innovations in Signal processing and Embedded Systems (RISE)*, Bhopal, India, October 2017.
- [2] K. Okokpujie, E. Noma-Osaghae, O. Modupe, S. John, and O. Oluwatosin, "A smart air pollution monitoring system," *International Journal of Civil Engineering and Technology*, vol. 9, pp. 799–809, 2018.
- [3] K. A. Kulkarni and M. S. Zambare, "The impact study of houseplants in purification of environment using wireless sensor network," *Wireless Sensor Network*, vol. 10, no. 03, pp. 59–69, 2018.
- [4] World Health Organization, *Air Pollution and Child Health-Prescribing Clean Air*, WHO, Geneva, Switzerland, 2018, September 2018, https://www.who.int/ceh/publications/Advance-copy-Oct24_18150_Air-Pollution-and-Child-Health-merged-compressed.pdf.
- [5] G. Rout, S. Karuturi, and T. N. Padmini, "Pollution monitoring system using IoT," *ARPN Journal of Engineering and Applied Sciences*, vol. 13, pp. 2116–2123, 2018.
- [6] B. C. Kavitha, D. Jose, and R. Vallikannu, "IoT based pollution monitoring system using raspberry-PI," *International Journal of Pure and Applied Mathematics*, vol. 118, 2018.
- [7] D. Saha, M. Shinde, and S. Thadeshwar, "IoT based air quality monitoring system using wireless sensors deployed in public bus services," in *ICC '17 Proceedings of the Second International Conference on Internet of things, Data and Cloud Computing*, Cambridge, United Kingdom, March 2017.
- [8] J. Liu, Y. Chen, T. Lin et al., "Developed urban air quality monitoring system based on wireless sensor networks," in *2011 Fifth International Conference on Sensing Technology*, pp. 549–554, Palmerston North, New Zealand, December 2011.
- [9] United States Environmental Protection Agency, *Managing air quality - air pollutant types* October 2018, <https://www.epa.gov/air-quality-management-process/managing-air-quality-air-pollutant-types>.
- [10] C. Arnold, M. Harms, and J. Goschnick, "Air quality monitoring and fire detection with the Karlsruhe electronic micronose KAMINA," *IEEE Sensors Journal*, vol. 2, no. 3, pp. 179–188, 2002.
- [11] S. Abraham and X. Li, "A cost-effective wireless sensor network system for indoor air quality monitoring applications," *Procedia Computer Science*, vol. 34, pp. 165–171, 2014.
- [12] O. A. Postolache, D. J. M. Pereira, and S. P. M. B. Girão, "Smart sensors network for air quality monitoring applications," *IEEE Transactions on Instrumentation and Measurement*, vol. 58, no. 9, pp. 3253–3262, 2009.
- [13] Y. Jiangy, K. Li, L. Tian et al., "MAQS: a personalized mobile sensing system for indoor air quality monitoring," in

- Proceedings of the 13th international conference on Ubiquitous computing*, pp. 271–280, Beijing, China, September 2011.
- [14] S. Bhattacharya, S. Sridevi, and R. Pitchiah, “Indoor air quality monitoring using wireless sensor network,” in *2012 Sixth International Conference on Sensing Technology (ICST)*, pp. 422–427, Kolkata, India, December 2012.
 - [15] S. Zampolli, I. Elmi, F. Ahmed et al., “An electronic nose based on solid state sensor arrays for low-cost indoor air quality monitoring applications,” *Sensors and Actuators B: Chemical*, vol. 101, no. 1-2, pp. 39–46, 2004.
 - [16] Ministry of Environment, *Investigation results of Ministry of Environment* March 2019, <http://www.me.go.kr/home/web/board/read.do?boardMasterId=1&boardId=727840&menuId=286>.
 - [17] G. Marques, C. Ferreira, and R. Pitarma, “Indoor air quality assessment using a CO₂ monitoring system based on Internet of Things,” *Journal of Medical Systems*, vol. 43, no. 3, p. 67, 2019.
 - [18] M. Tastan and H. Gokozan, “Real-time monitoring of indoor air quality with internet of things-based E-nose,” *Applied Sciences*, vol. 9, no. 16, article 3435, 2019.
 - [19] A. Rackes, T. Ben-David, and M. S. Waring, “Sensor networks for routine indoor air quality monitoring in buildings: impacts of placement, accuracy, and number of sensors,” *Science and Technology for the Built Environment*, vol. 24, no. 2, pp. 188–197, 2018.
 - [20] M. Benammar, A. Abdaoui, S. Ahmad, F. Touati, and A. Kadri, “A modular IoT platform for real-time indoor air quality monitoring,” *Sensors*, vol. 18, no. 2, p. 581, 2018.
 - [21] S. Wang, S. Chew, M. Jusoh, A. Khairunissa, K. Leong, and A. Azid, “WSN based indoor air quality monitoring in classrooms,” *AIP Conference Proceedings*, vol. 1808, article 020063, 2017.
 - [22] S. Kamble, S. Mini, and T. Panigrahi, “Monitoring Air Pollution: An IoT Application,” in *2018 International Conference on Wireless Communications, Signal Processing and Networking (WiSPNET)*, Chennai, India, March 2018.
 - [23] GSMA, *Air quality monitoring using IoT and big data: a value generation guide for mobile operators*, 2018, September 2018, https://www.gsma.com/iot/wp-content/uploads/2018/02/iot_clean_air_02_18.pdf.
 - [24] H. Ghayvat, S. Mukhopadhyay, X. Gui, and N. Suryadevara, “WSN- and IOT-based smart homes and their extension to smart buildings,” *Sensors*, vol. 15, no. 5, pp. 10350–10379, 2015.
 - [25] K. Gupta and N. Rakesh, “IoT based automobile air pollution monitoring system,” in *2018 8th International Conference on Cloud Computing, Data Science & Engineering (Confluence)*, Noida, India, January 2018.
 - [26] STMicroelectronics, *STM32F407 specification*, 2016, October 2018, <https://www.st.com/en/microcontrollers/stm32f407-417.html?querycriteria=productId=LN11>.
 - [27] Y. Cho, E. Shin, K. Cho et al., “Study on the continuous monitoring of particulate matters concentrations in the subway station,” *Korean Society for Railway*, pp. 3242–3247, 2009.
 - [28] G. Kim, “Implementation of indoor air quality monitoring system for subway stations,” *Journal of the Institute of Electronics Engineers of Korea*, vol. 50, pp. 1610–1617, 2013.
 - [29] S. Kim, H. Kang, Y. Son et al., “Compensation of light scattering method for real-time monitoring of particulate matters in subway stations,” *Journal of Korean Society for Atmospheric Environment*, vol. 26, no. 5, pp. 533–542, 2010.
 - [30] Wuhan Cubic Optoelectronics Co, *Laser Dust Sensor Module PM2007* October 2018, http://www.gassensor.com.cn/product_detail_en/Particle_Sensor/PM2007.
 - [31] Ogam Technology, (2009) *Ogam Technology product information GSBT11* October 2018, https://www.eleparts.co.kr/data/goods_old/design/product_file/ogam-tech/GSBT11/GSBT11.pdf.
 - [32] J. Liu, Y. Chen, T. Lin et al., “An air quality monitoring system for urban areas based on the technology of wireless sensor networks,” *International Journal on Smart Sensing and Intelligent Systems*, vol. 5, no. 1, pp. 191–214, 2012.
 - [33] Ogam Technology, (2013) *Ogam Technology product information GSET11* October 2018, https://eleparts.co.kr/data/goods_old/data/GSET11_Kc.pdf.
 - [34] A. Mofarrh and T. Husain, “A holistic approach for optimal design of air quality monitoring network expansion in an urban area,” *Atmospheric Environment*, vol. 44, no. 3, pp. 432–440, 2010.
 - [35] Wuhan Cubic Optoelectronics Co, (2013) *User manual for carbon dioxide CO₂ sensor module* October 2018, <http://pdf.directindustry.com/pdf/wuhan-cubic-optoelectronics-co-ltd/ndir-carbon-dioxide-sensor-co2-sensor-cm1102-user-manual-dual-beam/54752-614013.html>.
 - [36] Ministry of Environment, *Indoor air quality control act for multi-use facilities* September 2018, [http://www.law.go.kr/%EB%B2%95%EB%A0%B9/%EB%8B%A4%EC%A4%91%EC%9D%B4%EC%9A%A9%EC%8B%9C%EC%84%A4%EB%93%B1%EC%9D%98%EC%8B%A4%EB%82%B4%EA%B3%B5%EA%B8%B0%EC%A7%88%EA%B4%80%EB%A6%AC%EB%B2%95/\(12216,20140107\)](http://www.law.go.kr/%EB%B2%95%EB%A0%B9/%EB%8B%A4%EC%A4%91%EC%9D%B4%EC%9A%A9%EC%8B%9C%EC%84%A4%EB%93%B1%EC%9D%98%EC%8B%A4%EB%82%B4%EA%B3%B5%EA%B8%B0%EC%A7%88%EA%B4%80%EB%A6%AC%EB%B2%95/(12216,20140107)).
 - [37] OSEPP Electronics, *DHT11 humidity & temperature sensor* October 2018, <https://www.mouser.com/ds/2/758/DHT11-Technical-Data-Sheet-Translated-Version-1143054.pdf>.
 - [38] B. Jo, J. Jo, R. M. A. Khan, J. Kim, and Y. Lee, “Development of a cloud computing-based pier type port structure stability evaluation platform using fiber Bragg grating sensors,” *Sensors*, vol. 18, no. 6, 2018.
 - [39] Y. J. Fan, Y. H. Yin, L. D. Xu, Y. Zeng, and F. Wu, “IoT-based smart rehabilitation system,” *IEEE Transactions on Industrial Informatics*, vol. 10, no. 2, pp. 1568–1577, 2014.
 - [40] D. Pavithra and R. Balakrishnan, “IoT based monitoring and control system for home automation,” in *2015 Global Conference on Communication Technologies (GCCT)*, Thuckalay, India, April 2015.
 - [41] C. Stergiou, K. Psannis, B. Kim, and B. Gupta, “Secure integration of IoT and cloud computing,” *Future Generation Computer Systems*, vol. 78, pp. 964–975, 2018.
 - [42] W. Lu, H. He, and L. Dong, “Performance assessment of air quality monitoring networks using principal component analysis and cluster analysis,” *Building and Environment*, vol. 46, no. 3, pp. 577–583, 2011.
 - [43] S. Devarakonda, P. Sevusu, H. Liu, R. Liu, L. Iftode, and B. Nath, “Real-time air quality monitoring through mobile sensing in metropolitan areas,” in *UrbComp '13 Proceedings of the 2nd ACM SIGKDD International Workshop on Urban Computing*, Chicago, Illinois, August 2013.
 - [44] J. Jo, B. Jo, R. M. A. Khan, and J. Kim, “A cloud computing-based damage prevention system for marine structures during berthing,” *Ocean Engineering*, vol. 180, pp. 23–28, 2019.

Research Article

A Novel Method for Broiler Abnormal Sound Detection Using WMFCC and HMM

Longshen Liu¹, Bo Li¹, Ruqian Zhao², Wen Yao³, Mingxia Shen¹ and Ji Yang¹

¹College of Engineering, Nanjing Agricultural University, Nanjing 210031, China

²College of Veterinary Medicine, Nanjing Agricultural University, Nanjing 210095, China

³College of Animal Science & Technology, Nanjing Agricultural University, Nanjing 210095, China

Correspondence should be addressed to Longshen Liu; liulongshen@njau.edu.cn

Received 14 August 2019; Accepted 28 October 2019; Published 13 January 2020

Guest Editor: Zhen-Xing Zhang

Copyright © 2020 Longshen Liu et al. This is an open access article distributed under the Creative Commons Attribution License, which permits unrestricted use, distribution, and reproduction in any medium, provided the original work is properly cited.

Broilers produce abnormal sounds such as cough and snore when they suffer from respiratory diseases. The aim of this research work was to develop a method for broiler abnormal sound detection. The sounds were recorded in a broiler house for one week (24/7). There were 20 thousand white feather broilers reared on the floor in a building. Results showed that the developed recognition algorithm, using wavelet transform Mel frequency cepstrum coefficients (WMFCCs), correlation distance Fisher criterion (CDF), and hidden Markov model (HMM), provided an average accuracy, precision, recall, and F1 of 93.8%, 94.4%, 94.1%, and 94.2%, respectively, for broiler sound samples. The results indicate that sound analysis can be used in broiler respiratory assessment in a commercial broiler farm.

1. Introduction

With the development of large-scale and intensive broiler industry, problems related to stocking density and poor management have emerged, resulting in increased incidences of respiratory diseases such as Newcastle disease, avian influenza, and infectious bronchitis. Broilers will have abnormal sounds such as cough and snore when they have respiratory diseases. Presently, the mode of detection of respiratory diseases in broilers is by manual sound distinction. However, this technique is time-consuming, labor-intensive, subjective, and has a low degree of real-time detection [1]. If respiratory diseases in broilers are detected manually, it will cause failure to detect and deal with the sick chicken in time. Therefore, effective real-time monitoring of abnormal sounds of broiler respiratory tracts has practical application value for early detection of broiler disease conditions, monitoring of broiler health status, and improving broiler productivity.

Vocalizations produced by animals contain a wide variety of information about their health, emotion, and behavior [2]. Based on these findings, there were different methods of animal vocalization analysis reported in recent years [3]. For

instance, acoustic technology has been used to assess pig sex, age, distress, heat stress [4–6], and piglet stressful conditions [7, 8]; recognize bovine and pig respiratory disease [9–12]; and monitor cattle, goat, and sheep behaviors and feed intake [13–18]. Similar work has been conducted with poultry. Vocalization-based avian influenza disease, respiratory disease, and abnormal night vocalization detection have also been reported in chickens [19, 20]. The short-term feeding behavior detection of broiler chickens based on a real-time sound processing technology has also been achieved [21, 22]. Goose behavior recognition based on vocalizations has also been demonstrated [23]. An advantage to the technology is the prospect of having noninvasive, real-time, quantitative, accurate devices to detect welfare issues at a relatively low cost [10]. Although these studies have shown that animal sound analysis was useful as an early warning tool to detect stress, behaviors, and diseases in some animal species, few studies have been reported on broiler abnormal sound detection in commercial buildings.

Numerous audio features and classifiers have been proposed for use in animal vocalization detection and classification [3]. In particular, Mel frequency cepstrum coefficients

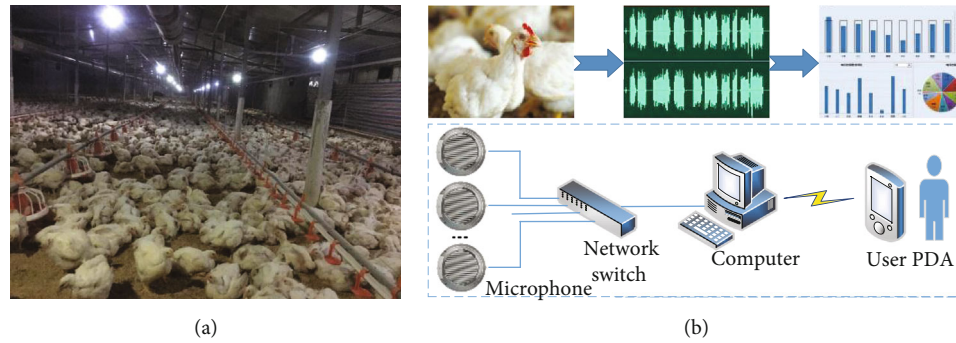


FIGURE 1: System structure. (a) Interior of the broiler building; (b) system model.

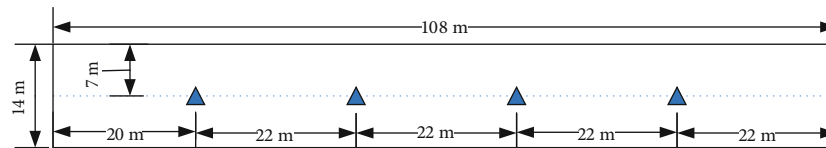


FIGURE 2: Top view of the four microphones' position in the broiler building. Blue triangles represent the network microphones.

(MFCCs) with the classifier such as support vector machine (SVM), hidden Markov model (HMM), or deep neural network (DNN) were commonly used features in animal sound recognition [24–27] because of its strong ability in sound distinction and robustness. However, MFCCs only reflected the static characteristics of acoustic signals. The dynamic characteristics of sound could be obtained by differentiating operation of MFCCs. This would produce more dimensional redundant characteristics. Sound feature selection and improvement should be carried out. Therefore, the objectives of this study were to develop an innovative method to detect abnormal broiler sounds for its respiratory assessment.

2. Materials and Methods

2.1. Acquisition of Sounds. For sound acquisition, four network microphones (HD-B-1001, Youanhong Technology Limited Company, Shenzhen, China) were used to record sounds of broiler. Sounds in the broiler building were recorded in mono at a sampling frequency of 48 kHz. Broiler sounds were sent to a computer over a local area network. The audio files in the .mp3 format were saved in a computer. The interior of the broiler building and system model was shown in Figure 1.

The microphones were positioned approximately 80 cm from the building floor. The four microphones' position in the broiler building was shown in Figure 2. The experiment was conducted in a commercial broiler farm located in Gaomi, Shandong Province, China. A group of 20 thousand Ross 308 white feather broilers aged 30 days was used for the experiment for one week starting from March 29, 2019. The body weight of the broilers was about 1.6–2.2 kg. The broilers were reared on the floor in the building of 14 m (W) × 108 m (L) (Figure 1). The temperature in the building was controlled at 20–22°C, and the humidity was 46% to 50%. Broilers were fed ad libitum with compound feed provided in hoppers with natural drinks. Feed was added daily

at 09:30 and 16:45. The building was illuminated with energy-saving lamps from 00:00 am to 21:00 for about 21 h of lighting daily during the whole experiment. The light intensity was set at 50 lux. The broiler building was ventilated using negative pressure fans during the experiment.

2.2. Sound Analysis and Recognition. In this paper, our task is to detect broiler abnormal sound in a commercial broiler building. The main steps of the proposed algorithm are illustrated in Figure 3. The detection system is composed of two parts: the model training part and the testing part for broiler abnormal sound detection. The algorithm was established in MATLAB R2014a (The MathWorks, Inc., Natick, MA).

2.2.1. Sound Sample Preparation. The sound analysis started with sound sample preparation. The abnormal respiratory broilers were assessed by the veterinary medicine professor and animal science & technology professor. The sound samples were detected and extracted manually from the recorded audio files randomly using Audition CS6 (Adobe Systems Inc., USA). The selected sound segments contained broiler cough, snore, and interfering sounds. The interfering sounds included background noises (e.g., room ventilation) and the sound created by broiler activities (e.g., crowing, feeding).

Eight thousand one hundred and fifty sound samples, including 2790 broiler cough samples, 2560 snore samples, and 2800 interfering sound, were manually selected from the sound segments. Four-fifths of the samples were used for training model, and the remaining was used for model testing.

2.2.2. Sound Preprocessing. Sound signal preprocessing included framing, filtering, and endpoint detection of the sound samples. The sound samples, which were nonstationary for longer timescales, were then framed by a moving Hamming window to obtain a short-time stationary signal (10–30 ms). Filtering was done to remove the ambient noise from the sound signals to improve the signal-to-noise ratios.

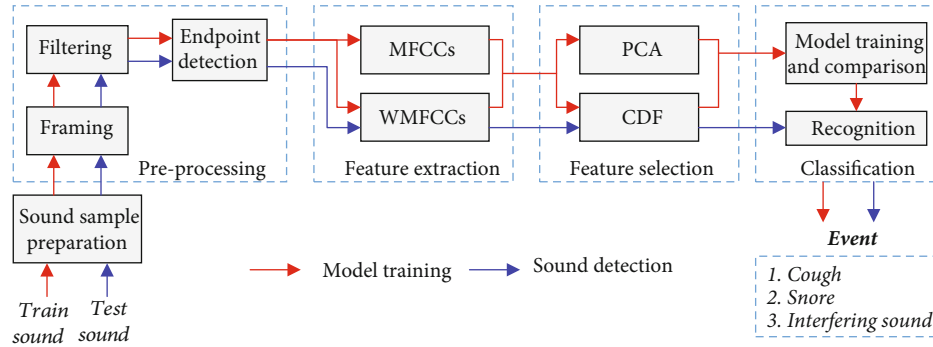


FIGURE 3: Brief flowchart of the broiler sound signal processing and recognition procedure. The red and blue paths denote the model training and sound detection processes.

This was performed using Spectral Subtraction method with Minimum Mean Square Error (MMSE) [28]. After that, broiler vocal signals from different sound samples were processed with endpoint detection. This was performed based on cepstrum distance.

Endpoint detection test was performed using six sound files. The sound segments were preprocessed by framing and filtering. Detection rate (DER) was used to evaluate the accuracy of endpoint detection algorithm with

$$DER = \frac{N_D}{N}, \quad (1)$$

where N represents the total number of the abovementioned three types of sounds; N_D is the number of sound endpoint detected successfully.

2.2.3. Sound Feature Extraction. In this study, Wavelet Transform (WT) replaced the fast Fourier Transform (FFT) in traditional MFCC feature extraction. The 48-dimensional WMFCCs were extracted from a continuous sound signal as follows:

- (1) Framed the continuous sound signal by a moving Hamming window into frames of 512 samples with a frameshift of 128 samples
- (2) Took the Wavelet Transform (WT) to convert each frame of samples from the time domain to the wavelet domain
- (3) Converted the wavelet scale of each frame from linear to Mel scale
- (4) Took the logarithm of the powers at the Mel frequencies
- (5) Took the discrete cosine transform (DCT) for the log Mel spectrum
- (6) Kept the 1-16 coefficients as the original 16-dimensional WMFCCs
- (7) Calculated the first-order delta coefficients (Δ WMFCC) and the second-order delta coefficients (Δ^2 WMFCC)

- (8) Combined the 16-dimensional original coefficients, 16-dimensional Δ WMFCCs, and 16-dimensional Δ^2 WMFCCs to get the final 48-dimensional WMFCCs for each sound sample

2.2.4. Sound Feature Selection and Improvement. There were some redundancy coefficients in the 48-dimensional WMFCCs. Because the contribution of different characteristic parameters in recognition is also different, dimensionality reduction was applied by selecting the high-contributing coefficients and excluding the low-contributing coefficients. In this study, principal component analysis (PCA) [29] and correlation distance Fisher criterion (CDF) [30] were, respectively, used and compared to calculate the contribution rate of each coefficient. The parameters were ranked in descending order according to the contribution rate. The top 24 dimensional coefficients were selected to use for the following sound classification.

For increasing the contribution of the high-contributing coefficients and reducing the influence of the low-contributing coefficients in classification, the weighted WMFCCs were calculated by multiplying each coefficient by its contribution rate after high-contributing WMFCC selection.

2.3. Sound Classification Algorithm. Hidden Markov model (HMM) has a strong capability of pattern classification due to its rich mathematical structure and proven accuracy on critical applications. It was widely used in signal recognition and classification [31, 32]. HMM was used to recognize abnormal broiler sound in this study. A complete specification of a HMM requires three sets of probability measures which are represented by $\lambda = (A, B, \pi)$. According to prior knowledge, the number of sound hidden states N was initialized to five. The state-transition probability matrix A and the initial state probability distribution π were initialized to non-zero numbers randomly. The observation probability matrix B was described by a Gaussian mixture distribution whose number was three. B was initialized by global mean and variance of training data. The output of HMM was the one with the highest output probability of the input sound sample in each model. There are three basic algorithms in HMM, namely, the Forward-Backward algorithm, Viterbi algorithm, and Baum-Welch algorithm. The details of these algorithms have been described by Rabiner [33]. The overall block

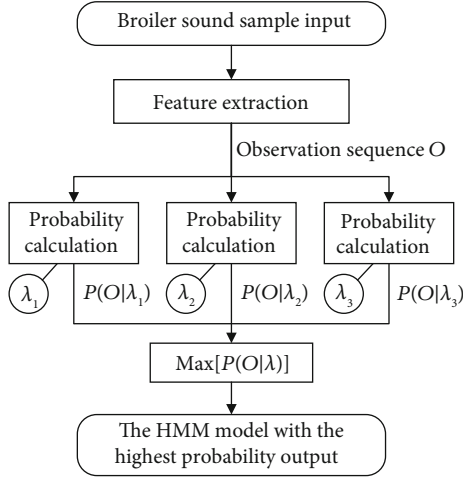


FIGURE 4: Block diagram of the HMM recognition algorithm.

diagram of the HMM recognition algorithm was shown in Figure 4.

The performance of the classification was measured with the accuracy, precision, recall, and F1 measure.

$$A_i = \frac{N_{TP}}{N} \times 100\%, \quad (2)$$

$$P_i = \frac{N_{TP}}{N_{TP} + N_{FP}} \times 100\%, \quad (3)$$

$$R_i = \frac{N_{TP}}{N_{TP} + N_{FN}} \times 100\%. \quad (4)$$

In these formulas, the cough and snore classified as cough and snore by the classifier were the true positives (TP), the unclassified cough and snore were the false negatives (FN), the correctly classified other sounds are the true negatives, and the wrongly classified other sounds were the false positives (FP). N was the total number of the i th class samples. Considering appraisal index P and R comprehensively, F1 measure was calculated according to

$$F1 = \frac{2PR}{P + R} \times 100\%. \quad (5)$$

3. Results and Discussion

3.1. Endpoint Detection Test. Endpoints of the three types of sound in the six sound files were detected using the algorithm based on cepstrum distance. The detection rate (DER) was calculated based on equation (1). The achieved results are shown in Table 1.

As seen from the table, the average detection rate was 98.7%. Test results show that the proposed endpoint detection algorithm performed well. It is also confirmed by other literature the role of the endpoint detection algorithm for MFCC distance in increasing accuracy [34]. The DER of snore was slightly lower than that of others. The reason was probably that the power of snore was lower than that of others.

TABLE 1: Test results of endpoint detection.

Sound types	Number of three types of sounds (N)	Number of successful endpoint detection (N_D)	Detection rate (DER)
Cough	1265	1248	98.7%
Snore	1315	1283	97.6%
Interfering	6451	6386	99.0%
Total	9031	8917	98.7%

3.2. Sound Characteristic Analysis. The different contribution rates calculated by PCA and CDF of 48 components were shown in Figure 5 in sequence. The contribution rate of the first principal component calculated by PCA and CDF was 13.3% and 11.7%, while the contribution rates of the rest were all lower than 10%. According to the selection criteria, the top half coefficients were selected for the following sound classification. The top 24 components calculated by PCA and CDF were named PWMFCCs and CWMFCCs, respectively. The cumulative contribution rate with 93.8% of PWMFCCs was higher than the cumulative rate with 86.4% of CWMFCCs. The PWMFCCs should be selected as the principal wavelet Mel frequency cepstrum coefficients. In this study, PWMFCCs and CWMFCCs were both selected as features for classification performance comparison.

The weighted PWMFCCs and CWMFCCs of the three sound samples were calculated by multiplying each coefficient by its contribution rate. The results of PWMFCCs are shown in Figure 6.

As can be seen from Figure 6, the dimensionality of coefficients after PCA and CDF selection is half of the origin. The surface chart of the CWMFCCs and the weighted CWMFCCs of cough is more rugged than that of the PWMFCCs and the weighted PWMFCCs, respectively. This shows that the discrimination of coefficients selected by CDF is better than that selected by PCA. Other literatures have also confirmed that CDF selection could select the components that were relatively divisible, because it considered not only the contribution of each dimension coefficient but also the correlation between the coefficients of each dimension coefficient [30].

3.3. Abnormal Sound Classification and Recognition Algorithm Evaluation. HMM were trained with different input characteristics, which included MFCCs, WMFCCs, PWMFCCs, CWMFCCs, and weighted PWMFCCs. The HMM were trained using 2232 cough, 2048 snore, and 2240 interfering sound samples. The performance of the HMM was tested by 1630 sound samples, including 558 cough, 512 snore, and 560 interfering sound samples. The classification accuracy of the different input characteristics is shown in Table 2.

The accuracy of classification using WMFCCs as the input characteristics was better than using MFCCs. Using the top 24 dimensional coefficients selected by PCA and CDF as the input characteristics, the average accuracy of classification was higher than using the 48-dimensional mixing

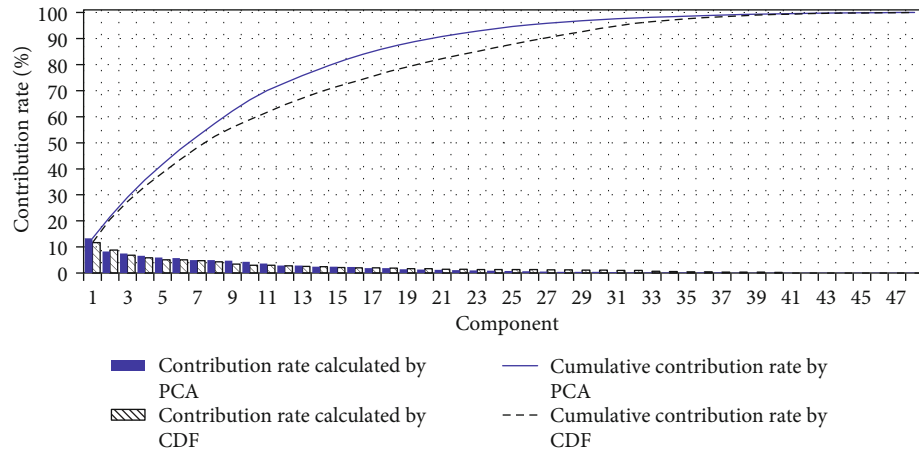


FIGURE 5: Contribution rate calculated by PCA and CDF of 48 components of WMFCCs.

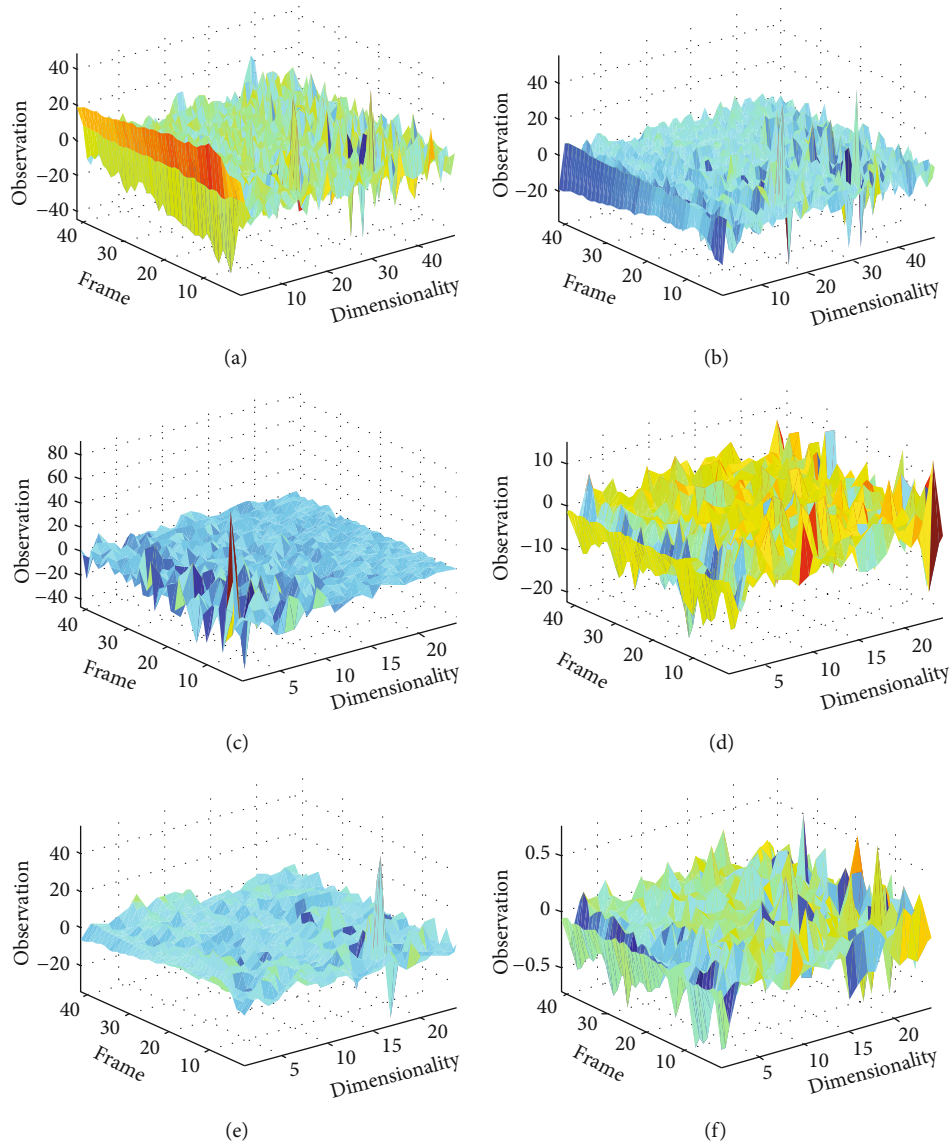


FIGURE 6: The characteristics of three sound samples of cough, snore, and interfering sound. (a) MFCCs of cough; (b) WMFCCs of cough; (c) PWMFCCs of cough; (d) CWMFCCs of cough; (e) weighted PWMFCCs of cough; (f) weighted CWMFCCs of cough.

TABLE 2: Classification accuracy of different input characteristics.

Input characteristics	Dimensions	Accuracy (%)			
		Cough	Snore	Interfering	Average
MFCCs	48	82.9	79.8	81.2	81.3
WMFCCs	48	87.1	86.5	81.3	85.0
PWMFCCs	24	87.8	84.2	86.5	86.2
CWMFCCs	24	91.3	87.9	90.3	89.8
Weighted CWMFCCs	24	96.7	93.3	91.5	93.8

TABLE 3: Classification performance of the HMM input weighted CWMFCCs.

Performance	P (%)	R (%)	F1 (%)
Cough	97.1	93.2	95.1
Snore	95.7	92.6	94.1
Interfering	90.3	96.5	93.3
Average	94.4	94.1	94.2

coefficients. The classification average accuracy of input CWMFCCs was 3.6% higher than input PWMFCCs, although the cumulative contribution rate of PWMFCCs was higher than CWMFCCs. The reason probably was that the CDF selection took into account the correlation between coefficients. The overall classification accuracy of input weighted CWMFCCs reached 93.8%. Therefore, the HMM of input weighted CWMFCCs worked well for broiler abnormal sound classification.

The classification performance of the HMM input weighted CWMFCCs is shown in Table 3.

For the HMM input weighted CWMFCCs, the precision, recall, and F1 on average reached 94.4%, 94.1%, and 94.2%, respectively. Other literatures have also used intelligence methodology to diagnose animal disease. Banakar et al. designed an intelligent device to diagnose avian diseases by using data mining methods and Dempster-Shafer evidence theory (D-S) with 91.15% accuracy [19]. Huang et al. developed an avian influenza detection method using MFCC and SVM with an accuracy rate that ranged between 84% and 90% [35]. Wang et al. assessed air quality based on pigs' cough sound analysis using MFCC and SVM with an accuracy of 95% [25]. The algorithm attained an accuracy of 94.4% which is lower than values reported for algorithms used to detect pig coughs [25]. It indicated that the classification algorithm could be used for broiler abnormal sound classification effectively.

The results of the novel method of abnormal sound detection were affected by many factors, such as ambient noise interference, quality of sound samples, and feature extraction algorithm. In this research, fan noise has some effect on sound quality. In addition, the age, body weight, and type of birds may affect the results of the abnormal sound detection. Other literature has investigated that pig vocalization was different according to age, sex, and distress [4]. Future work can also focus on the specific disease detec-

tion of different age, body weight, and types of chicken. The present research gives us inspiration that a lot of useful information can be discovered by analyzing the sound of animals. It is of great significance to the poultry farms.

4. Conclusions

This paper proposed a novel method to automatically detect broiler abnormal sounds based on a combination of WMFCC and HMM. Three types of sound of broilers were selected for detection including cough, snore, and interfering sounds. HMM were trained and compared with different input characteristics, which included MFCCs, WMFCCs, PWMFCCs, CWMFCCs, and weighted PWMFCCs. The results show that the algorithm could effectively identify broiler abnormal sounds. The classification accuracy, precision, recall, and F1 on average of HMM input weighted CWMFCCs reached 93.8%, 94.4%, 94.1%, and 94.2%, respectively. Therefore, the HMM of input weighted CWMFCCs worked well for broiler abnormal sound classification. Further studies will be the detection of specific disease of different age, body weight, and types of chicken.

Data Availability

All materials are publicly available.

Conflicts of Interest

The authors declare that there is no conflict of interest regarding the publication of this paper.

Acknowledgments

The authors want to thank Yi Xu and Hehua Zheng of New Hope Group and Gaomi broiler farm for their help in field experiment and data acquisition. This research was funded by the Key Projects of Intergovernmental Cooperation in International Scientific and Technological Innovation (project no. YS2017YFGH000712) and funded by the "13th Five-Year" National Key R&D Plan Project of China (project no. 2017YFD0701600). This research was also funded by the Young Scientists Fund of the National Natural Science Foundation of China (project no. 65103187).

References

- [1] K. Wang, X. Zhao, and Y. He, "Review on noninvasive monitoring technology of poultry behavior and physiological information," *Transactions of the Chinese Society of Agricultural Engineering*, vol. 33, no. 20, pp. 197–209, 2017.
- [2] E. F. Briefer and S. Le Comber, "Vocal expression of emotions in mammals: mechanisms of production and evidence," *Journal of Zoology*, vol. 288, no. 1, pp. 1–20, 2012.
- [3] R. V. Sharan and T. J. Moir, "An overview of applications and advancements in automatic sound recognition," *Neurocomputing*, vol. 200, pp. 22–34, 2016.
- [4] A. F. D. S. Cordeiro, I. D. A. Nääs, F. da Silva Leitão, A. C. de Almeida, and D. J. de Moura, "Use of vocalisation to identify

- sex, age, and distress in pig production," *Biosystems engineering*, vol. 173, pp. 57–63, 2018.
- [5] S. Ferrari, A. Costa, and M. Guarino, "Heat stress assessment by swine related vocalizations," *Livestock Science*, vol. 151, no. 1, pp. 29–34, 2013.
 - [6] S. Düpjan, P.-C. Schön, B. Puppe, A. Tuchscherer, and G. Manteuffel, "Differential vocal responses to physical and mental stressors in domestic pigs (*Sus scrofa*)," *Applied Animal Behaviour Science*, vol. 114, no. 1-2, pp. 105–115, 2008.
 - [7] A. da Silva Cordeiro, I. de Alencar Nääs, S. Oliveira, F. Violaro, A. de Almeida, and D. Neves, "Understanding vocalization might help to assess stressful conditions in piglets," *Animals*, vol. 3, no. 3, pp. 923–934, 2013.
 - [8] C. Manteuffel, E. Hartung, M. Schmidt, G. Hoffmann, and P. C. Schön, "Online detection and localisation of piglet crushing using vocalisation analysis and context data," *Computers and Electronics in Agriculture*, vol. 135, pp. 108–114, 2017.
 - [9] J. Vandermeulen, C. Bahr, D. Johnston et al., "Early recognition of bovine respiratory disease in calves using automated continuous monitoring of cough sounds," *Computers and Electronics in Agriculture*, vol. 129, pp. 15–26, 2016.
 - [10] D. Berckmans, M. Hemeryck, D. Berckmans, E. Vranken, and T. van Waterschoot, "Animal sound...talks! Real-time sound analysis for health monitoring in livestock," in *Animal Environment and Welfare - Proceedings of International Symposium*, J.-Q. Ni, T.-T. Lim, and C. Wang, Eds., pp. 215–222, China Agriculture Press, Chongqing, China, 2015.
 - [11] Y. Chung, S. Oh, J. Lee, D. Park, H. H. Chang, and S. Kim, "Automatic detection and recognition of pig wasting diseases using sound data in audio surveillance systems," *Sensors*, vol. 13, no. 10, pp. 12929–12942, 2013.
 - [12] V. Exadaktylos, M. Silva, J. M. Aerts, C. J. Taylor, and D. Berckmans, "Real-time recognition of sick pig cough sounds," *Computers and Electronics in Agriculture*, vol. 63, no. 2, pp. 207–214, 2008.
 - [13] G. H. Meen, M. A. Schellekens, M. H. M. Slegers, N. L. G. Leenders, E. van Erp-van der Kooij, and L. P. J. J. Noldus, "Sound analysis in dairy cattle vocalisation as a potential welfare monitor," *Computers and Electronics in Agriculture*, vol. 118, pp. 111–115, 2015.
 - [14] W. M. Clapham, J. M. Fedders, K. Beeman, and J. P. S. Neel, "Acoustic monitoring system to quantify ingestive behavior of free-grazing cattle," *Computers and Electronics in Agriculture*, vol. 76, no. 1, pp. 96–104, 2011.
 - [15] J. O. Chelotti, S. R. Vanrell, D. H. Milone et al., "A real-time algorithm for acoustic monitoring of ingestive behavior of grazing cattle," *Computers and Electronics in Agriculture*, vol. 127, pp. 64–75, 2016.
 - [16] J. O. Chelotti, S. R. Vanrell, J. R. Galli, L. L. Giovanini, and H. L. Rufiner, "A pattern recognition approach for detecting and classifying jaw movements in grazing cattle," *Computers and Electronics in Agriculture*, vol. 145, pp. 83–91, 2018.
 - [17] S. Navon, A. Mizrach, A. Hetzroni, and E. D. Ungar, "Automatic recognition of jaw movements in free-ranging cattle, goats and sheep, using acoustic monitoring," *Biosystems Engineering*, vol. 114, no. 4, pp. 474–483, 2013.
 - [18] J. R. Galli, C. A. Cangiano, D. H. Milone, and E. A. Laca, "Acoustic monitoring of short-term ingestive behavior and intake in grazing sheep," *Livestock Science*, vol. 140, no. 1-3, pp. 32–41, 2011.
 - [19] A. Banakar, M. Sadeghi, and A. Shushtari, "An intelligent device for diagnosing avian diseases: Newcastle, infectious bronchitis, avian influenza," *Computers and Electronics in Agriculture*, vol. 127, pp. 744–753, 2016.
 - [20] X. Du, F. Lao, and G. Teng, "A sound source localisation analytical method for monitoring the abnormal night vocalisations of poultry," *Sensors*, vol. 18, no. 9, p. 2906, 2018.
 - [21] A. Aydin, C. Bahr, S. Viazzi, V. Exadaktylos, J. Buyse, and D. Berckmans, "A novel method to automatically measure the feed intake of broiler chickens by sound technology," *Computers and Electronics in Agriculture*, vol. 101, pp. 17–23, 2014.
 - [22] A. Aydin and D. Berckmans, "Using sound technology to automatically detect the short-term feeding behaviours of broiler chickens," *Computers and Electronics in Agriculture*, vol. 121, pp. 25–31, 2016.
 - [23] K. A. Steen, O. R. Therkildsen, H. Karstoft, and O. Green, "A vocal-based analytical method for goose behaviour recognition," *Sensors*, vol. 12, no. 3, pp. 3773–3788, 2012.
 - [24] Y. Chung, J. Lee, S. Oh, D. Park, H. H. Chang, and S. Kim, "Automatic detection of cow's oestrus in audio surveillance system," *Asian-Australasian Journal of Animal Sciences*, vol. 26, no. 7, pp. 1030–1037, 2013.
 - [25] X. Wang, X. Zhao, Y. He, and K. Wang, "Cough sound analysis to assess air quality in commercial weaner barns," *Computers and Electronics in Agriculture*, vol. 160, pp. 8–13, 2019.
 - [26] R. V. Sharan and T. J. Moir, "Robust acoustic event classification using deep neural networks," *Information Sciences*, vol. 396, pp. 24–32, 2017.
 - [27] J. C. Bishop, G. Falzon, M. Trotter, P. Kwan, and P. D. Meek, "Livestock vocalisation classification in farm soundscapes," *Computers and Electronics in Agriculture*, vol. 162, pp. 531–542, 2019.
 - [28] B. L. Sim, Y. C. Tong, J. S. Chang, and C. T. Tan, "A parametric formulation of the generalized spectral subtraction method," *IEEE Transactions on Speech and Audio Processing*, vol. 6, no. 4, pp. 328–337, 1998.
 - [29] Y. Liu, X. Gao, Q. Gao, L. Shao, and J. Han, "Adaptive robust principal component analysis," *Neural Networks*, vol. 119, pp. 85–92, 2019.
 - [30] Z. Tang, W. Maorong, and P. Zhou, "Mixed parameters based on fisher criterion with correlation distance in speaker recognition," *Popular Science & Technology*, vol. 18, no. 1, pp. 13–16, 2016.
 - [31] T. Boutros and M. Liang, "Detection and diagnosis of bearing and cutting tool faults using hidden Markov models," *Mechanical Systems and Signal Processing*, vol. 25, no. 6, pp. 2102–2124, 2011.
 - [32] G. Zhai, J. Chen, C. Li, and G. Wang, "Pattern recognition approach to identify loose particle material based on modified MFCC and HMMs," *Neurocomputing*, vol. 155, pp. 135–145, 2015.
 - [33] L. R. Rabiner, "A tutorial on hidden Markov models and selected applications in speech recognition," *Proceedings of the IEEE*, vol. 77, no. 2, pp. 257–286, 1989.
 - [34] X. Zhao, L. Wang, and L. Peng, "Adaptive cepstral distance-based voice endpoint detection of strong noise," *Computer Science*, vol. 42, no. 9, 2015.
 - [35] J. Huang, W. Wang, and T. Zhang, "Method for detecting avian influenza disease of chickens based on sound analysis," *Biosystems Engineering*, vol. 180, pp. 16–24, 2019.

Review Article

A Review of Underwater Localization Techniques, Algorithms, and Challenges

Xin Su ¹, Inam Ullah ¹, Xiaofeng Liu,¹ and Dongmin Choi ²

¹The College of Internet of Things (IoT) Engineering, Hohai University (HHU), Changzhou 213022, China

²The Division of Undeclared Majors, Chosun University, Gwangju 61452, Republic of Korea

Correspondence should be addressed to Dongmin Choi; jdmcc@chosun.ac.kr

Received 14 October 2019; Revised 26 November 2019; Accepted 3 December 2019; Published 13 January 2020

Guest Editor: Yuan Li

Copyright © 2020 Xin Su et al. This is an open access article distributed under the Creative Commons Attribution License, which permits unrestricted use, distribution, and reproduction in any medium, provided the original work is properly cited.

Recently, there has been increasing interest in the field of underwater wireless sensor networks (UWSNs), which is a basic source for the exploration of the ocean environment. A range of military and civilian applications is anticipated to assist UWSN. The UWSN is being developed by the extensive wireless sensor network (WSN) applications and wireless technologies. Therefore, in this paper, a review has been presented which unveils the existing challenges in the underwater environment. In this review, firstly, an introduction to UWSN is presented. After that, underwater localizations and the basics are presented. Secondly, the paper focuses on the architecture of UWSN and technologies used for underwater acoustic sensor network (UASN) localization. Various localization techniques are discussed in the paper classified by centralized and distributed localizations. They are further classified into estimated and prediction-based localizations. Also, various underwater localization algorithms are discussed, which are grouped by the algorithms based on range and range-free schemes. Finally, the paper focuses on the challenges existing in underwater localizations, underwater acoustic communications with conclusions.

1. Introduction

Underwater wireless sensor networks (UWSNs) have shown increasing interest, in the latest years. For a variety of applications, underwater sensor networks (USNs) can be implemented. Each implementation is essential in its domain, but some of them can enhance ocean exploration to meet the variety of underwater applications, including a natural disaster alert scheme (i.e., tsunami and seismic tracking), aided navigation, oceanographic information collection, and underwater surveillance, ecological applications (i.e., quality of biological water, tracking of pollution), industrial applications (i.e., marine exploration), etc. For example, for offshore engineering applications, sensors can assess certain parameters such as base intensity and mooring tension to monitor the structural quality of the mooring environment [1]. Underwater acoustic sensors networks (UASNs) provide a new platform for under communication to explore the underwater environment. UASNs have also improved the understanding related to underwater environments such as

climate changes, animal life in underwater, and the population of coral reefs.

In [2], the authors present a localization technique for UASN in which the mobility of the sensor node is considered and all the unknown sensor nodes are successfully placed at different positions. The positioning system is recursive and the localization method involves distinct sensor nodes. UASNs also increase the underwater warfare capabilities of the naval forces so that they can be used for the detection of a submarine, unmanned operation system, surveillance, and mine countermeasure algorithms. UASNs can also help monitor or control the oil rigs that can take prevent the disaster's effects such as rigs explosion in the Gulf of Mexico once occurred (2010). Similarly, UASN technology also helps in tsunami and earthquake forewarning. A unique system is called 3-DUL, which originally consisted of only three anchor sensor nodes, such as buoys on the water surface, which defuse their worldwide position data in all three directions and 3-DUL follows a 2-phase operation [3–6]. The distances to nearby anchor nodes are determined by a node with

TABLE 1: Comparison table of electromagnetic, acoustic, and optical waves in underwater environment.

	Electromagnetic waves	Acoustic waves	Optical waves
Frequency band	~kHz	~MHz	$\sim 10^{14}$ - 10^{15} Hz
Bandwidth	~kHz	~MHz	~10-150 MHz
Power loss	>0.1 dB/m/Hz	~28 dB/1 km/100 MHz	\propto turbidity
Effective range	~1 m	~10 m	~10-100 m
Nominal speed (m/s)	~1,500	~33,333,333	~33,333,333
Antenna size	~0.1 m	~0.5 m	~0.1 m

an unknown place during the first stage. The anchor nodes are projected to their horizontal level in the second phase and form a virtual geometric shape using the depth information from these multivariate ranges. If the corresponding shape is robust, the sensor node will find itself and become an anchor sensor node through the dynamic trilateration method. In three-dimensional (3D) topology, this method iterates dynamically in all directions to locate as many sensors as possible. A 3D localization method takes into account the attenuation of electromagnetic (EM) waves over the reliable elevation angle spectrum. They pick the radiation patterns of dipole antennas to determine the reliable elevation range. The feasibility of this scheme is presented in distance estimation and 3D localization schemes by changing the elevation angle and distance. However, in [7], the writers suggest a fresh model that utilizes the benefits of the features of EM waves in water. The sensor node cannot only evaluate the distance with low environmental noise but also ensure precise localization output with elevated sampling rates. Using the sets of RF sensors, a UWSN is built for this localization system at the target docking location. A 3D underwater localization algorithm is also suggested in [8] for a marine near-sea surveillance scheme that utilizes a tiny amount of beacons for localization. Performance evaluations show that the worldwide localization of three surface anchor nodes is effectively spread by 3DUL. Its simple algorithm makes it possible for UASNs to adapt to the vibrant nature of the water globe [9, 10]. To this end, the ocean surveillance system is used that can gather information from the ocean and its surrounding areas and provide this information via satellite communication to the ship or on-shore center or sometimes use underwater wires. These are replaced by less expensive and small underwater nodes that use this equipment in UASN to house various nodes on board, such as pressure, temperature, and salinity. Underwater sensor nodes are networked and can interact using acoustic signals.

As we know, in underwater the radio signals can only travel to a short distance because the radio signal attenuates highly underwater and optical signals cannot travel in an inappropriate medium because of the dispersion of the optical signals. An acoustic signal scatters less as compared to radio and optical signals, resulting in an acoustic signal being more useful for underwater communication purposes as compared to radio and optical signals as shown in Table 1. However, the acoustic bandwidth in the underwater is smaller, resulting in reduced information rates. Multiple sensor nodes are needed to raise information rates and have

short-range communication, resulting in excellent coverage. The acoustic channel also has a low quality of connection [11, 12] owing to the time variability of the propagation of the medium and multipath. The underwater sound speed is approximately 1500 m/s, resulting in very elevated delay propagation. The UASNs are also energy-limited as WSN due to these difficulties. Also, localization is a fundamental task that is used to detect the location of a target in the underwater medium for various purposes such as data tagging, tracking nodes in the underwater and coordinating the movement of node groups. For the tracking of a target [6, 13, 14], research work proposes a semidefinite programming- (SDP-) based localization procedure that is achieved by measurements obtained via onboard pressure sensors. SDP enhances the point localization precision and provides quicker convergence for monitoring under the same system setup and environmental circumstances, particularly at low signal to noise ratio (SNR). On condition that geomagnetic anomaly can be reversed as a magnetic dipole target, the localization of an underwater vessel relative to the target is calculated by the magnitude of the magnetic field and target gradients. The magnetic field is calculated by the device mounted on a car comprised of ten magnetometers of one axis. Since the noise of magnetometers results in the coefficients of a six-order formula [15] with an unsuitable element, the localization accuracy will be influenced by the weather. In [16], USNs can modify ocean exploration to enable a list of new applications that are not presently feasible or expensive to implement, including oceanographic information collection, ecological applications, government security, underwater military tracking, and commercial operation.

For maritime defense purposes, USNs can provide immediate deployment and enhance coverage in coastal area surveillance applications. USNs mounted on the bottom of the ocean with underwater sensor nodes can detect earthquakes and tsunami formations before entering residential areas. A rough drawing of underwater node operation is shown in Figure 1. Mobile USNs can track polluted waters for water pollution detection devices as they propagate to clean water from their source and warn authorities to take action. USNs could be used to monitor coastal creatures and coral reefs, where there is limited data about human activity. The Gaussian noise injection detector (GNID) is proposed [17], to improve the probability of detection based on the noise-enhanced signal detection using a prewhitening filter, time frequency denoising technique with S-transform, in inverse whitening filter results in improving underwater signal

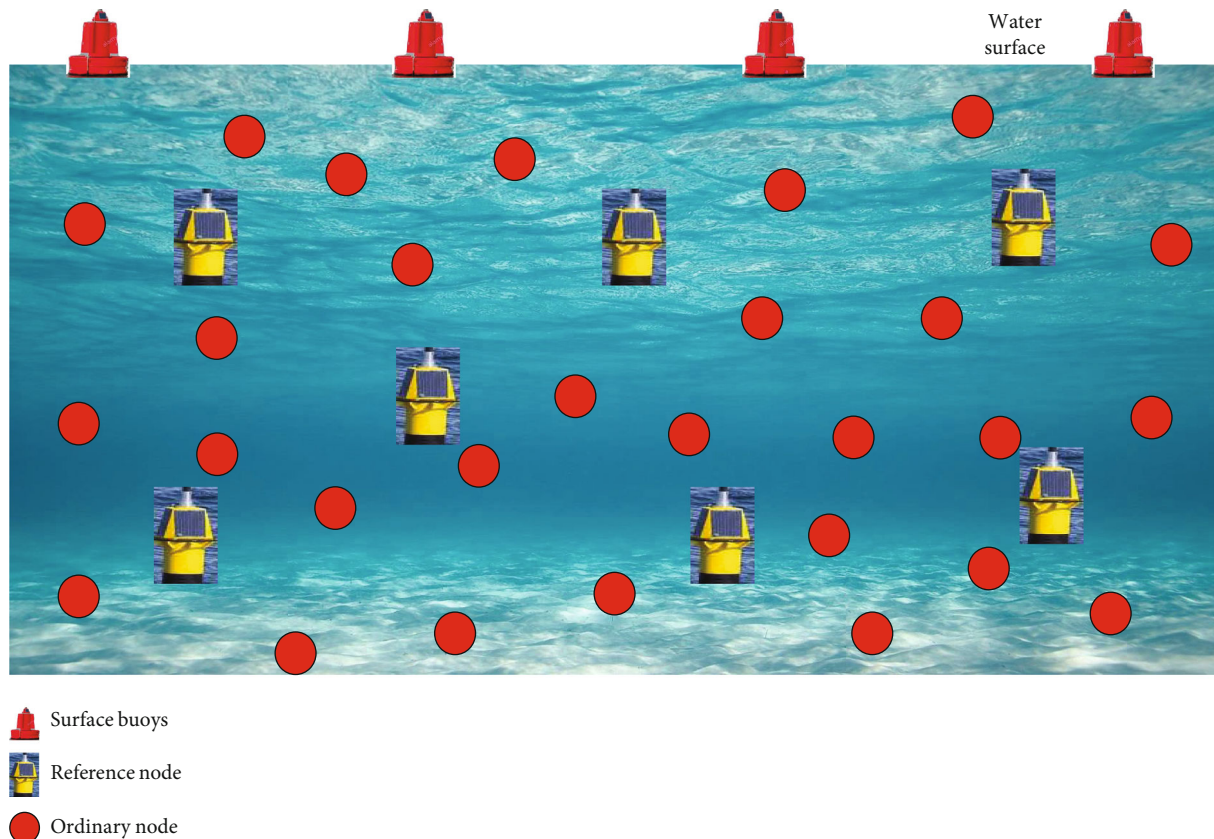


FIGURE 1: A rough sketch of the underwater node deployment.

detection. Environmental monitoring is also a vibrant aspect of determining safety and health problems for environmental or mankind's health. Environmental monitoring's main purpose is sampling soil, water, and atmospheric but they also need to take the air samples inside buildings to guarantee rules are met. The group of people working in environmental monitoring needs to looking for many things which are important in fact. The most obvious is the radioactivity or pollutants, especially in the case when looking to build a case of negligence against a distinct or for evidence of the effects of changes in climate.

The key objectives of this paper are to outlines a comprehensive review of underwater localization techniques and their algorithms. We attempt to review the different aspects of underwater communications and underwater localizations by considering various attributes. The main objective of this review is to provide a detailed knowledge of underwater localization techniques, localization algorithms, architecture, etc. We also highlight the weaknesses and strengths of the existing underwater localization techniques that can help the researchers to identify more efficient and accurate solutions for the existing challenges. Explicitly, this review aims to answer the following basic questions:

- (i) What are the state-of-the-art localization techniques?
- (ii) What are the main research challenges in underwater localization?

- (iii) What are the main defenses and their pros and cons?
- (iv) What are the promising solutions to improve underwater localization?

This review makes the following contributions:

- (i) This review provides a detail explanation of localization for the underwater environment which covers the localization basics, architecture, localization techniques, and algorithms used for localization
- (ii) This review rises the basic requirements for localization such as security attacks on underwater nodes
- (iii) Based on a detailed analysis of existing underwater localization techniques, we presented the existing challenges and future directions that need to be considered in the recent future

The paper is organized as follows. Section 2 presents the procedure and basics of localization. Next, Section 3 presents the architecture of UASN, Section 4 presents the related works, and Section 5 presents the techniques used for UASN localizations. Furthermore, Section 6 and Section 7 present range-based and range-free algorithms for localization, respectively. Section 8 presents the performance evaluation of underwater localization schemes. Finally, Section 9 presents the existing challenges and open issues in UWSNs and Section 10 concludes the paper.

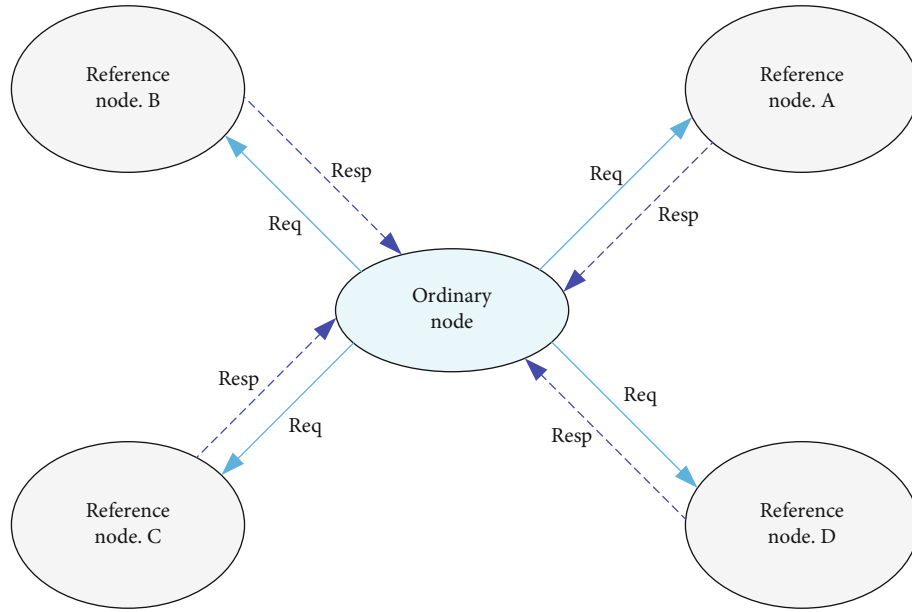


FIGURE 2: Two-way message exchange of reference and ordinary node.

2. Procedure and Basics of Localization

Assumptions for the localization operation need to take care of is that all antenna nodes have an ideal understanding of their position and should share clock information with the other sensor nodes worldwide synchronization. All nodes should meet to share data at any time, i.e., every individual sensor node can retrieve all readings and execute the process of localization before carrying all data back to the active or reference nodes. Each sensor node in the corresponding destination frame can communicate completely with other nodes and has no accident or interference problems [18]. At time t_0 , the active sensor node emits a single message requesting location through all of the listening nodes and each node gets message at the time $t_{n,m}$. On the given message, each node conducts a Doppler speed estimate. After gathering all data from sensors, a master node gets all estimates and performs the operation of localization and transmits the complete estimate back to the active node. Alternatively, it is possible to collect and relay the data to the active node where localization is done after that. The updates of the active node or master node estimate tracking and navigation algorithms as estimates of points are acquired. Localization is another difficult work; the use of Global Positioning System (GPS) is limited to surface nodes because in underwater, GPS signal does not propagate [19]. Alternative GPS fewer positioning approaches for terrestrial sensor networks have been provided, but they must be amended owing to the description of the acoustic channel. The acoustic channel has low bandwidth, high delay in propagation, and high error rate. Localization protocols, therefore, need to operate with the minimal feasible exchange of messages between nodes and exchange of messages such as two-way data exchange (see in Figure 2). This is also assessed by the sensor node's restricted battery

energy and the underwater sensor node battery recharge or replacement problem.

To execute localization in a better way, it requires several objects with known locations, i.e., anchors and distance or angle measurement between anchors and the object to be located underwater, i.e., unknown sensor node. The anchors can be placed in a fixed position and their coordinates may have been configured in the beginning, or they may have distinctive hardware to learn from the location server such as GPS. Using angle or distance measurement between the anchor and the unknown node to estimate the location of an unknown sensor node and also combining measurements occur. Sensors presently used for oceanographic studies are either located with long or short baseline (LBL/SBL) devices. With a set of receivers based on acoustic wave communication, sensor positions are described in both instances. Acoustic transponders are introduced in the LBL either on the seabed or underfloor moorings around the application region [20, 21]. The effects of multiple error sources on the LBL-based scheme's localization accuracy have been investigated and evaluated in detail. It shows that the more severe variables that may affect general accuracy are the calibration of the transmitters and the amounts of data about the sound speed in the operating area. A vessel follows the sensors in the SBL scheme and utilizes a short-range emitter to allow the process of localization.

UWSN is characteristically composed of various nodes that are anchored to the lowermost of the ocean wirelessly linked with underwater gateways [22–24]. The information from these sensors is transmitted within this network from the lowermost of the sea to the water surface station by applying multihop links. The gateways in underwater are furnished with definite nodes with both upright and straight transceivers. The first gateway is utilized to transfer instructions and constellation information to the nodes and receive

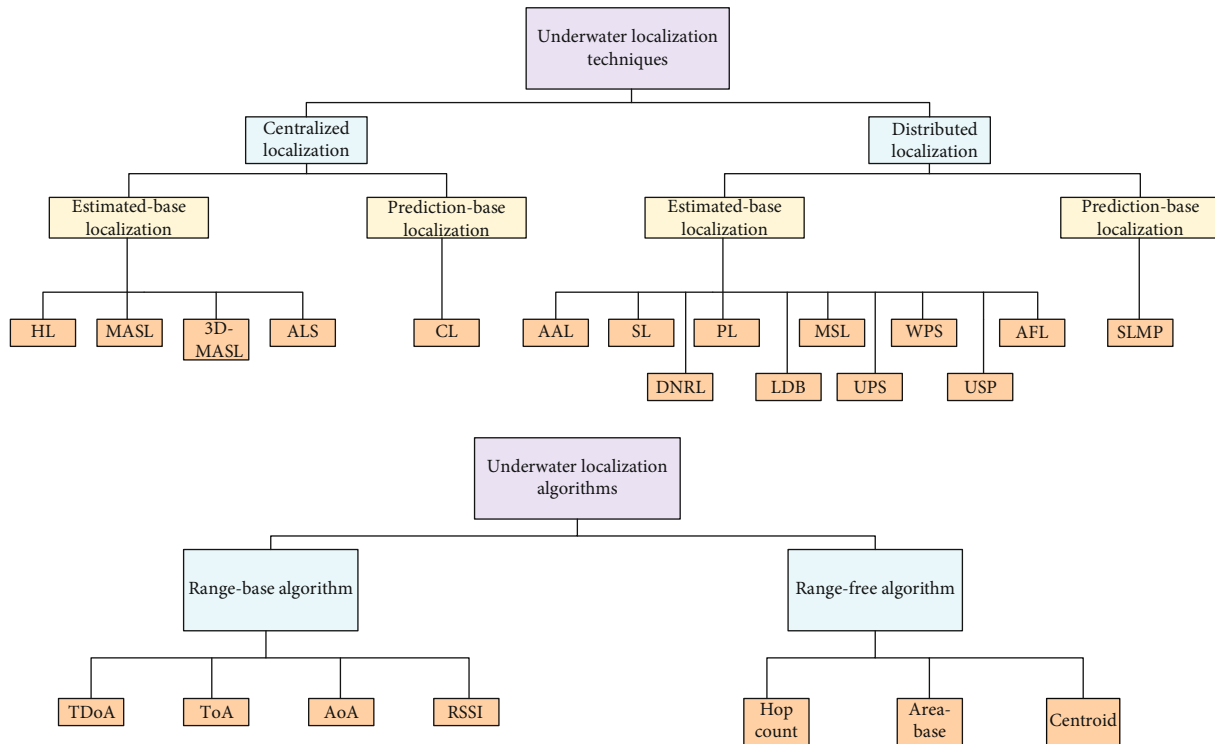


FIGURE 3: Architecture of underwater localization techniques and underwater localization algorithms.

the collected information back from the node. The second gateway is used to transmit the supervised information to the water surface station. Contrasting shallow water, upright communication is typically essential for a long range in deep water to attain the transfer of information to the water surface station. The acoustic communication is applied to accomplish multiple communications to collect the information from the nodes, where radio communication is generally conventional with satellite communication to transmit the collected information to the coastal sink. The underwater sensor nodes in the propagation range will sense a series of transmissions and decode packets. To compare the receiving time with the transmission time encoded in the packet, every sensor node can achieve the time of arrival (ToA) estimates of the packet message from various surface nodes, based on which it tries to calculate its particular location. The broadcast from the surface nodes to underwater nodes is one-way communication and the quality of localization is independent of the number of sensor nodes in underwater, and there is no extra interference between underwater sensor nodes. The underwater sensor nodes contain a controller to accommodate with an oceanographic sensor through a sensor pledge micro security [25]. The receiving data from the sensor through the controller is stored in the onboard memory. The controller can store, progress, and broadcast to the network devices.

3. Architecture of UASN

It is well known that energy consumption is more important in UWSN, which may limit long life cycles. Therefore, the network topology is the basic aspect that needs to be carefully

designed to reduce the serious impact on network performance. Also, the reliability and capacity of the network depend on the network topology. Therefore, how to organize such a network topology is a challenging task, and researchers need to pay more attention to network topology. Here, the architecture of UASN is classified according to two metrics: one is the motion capability of the sensor nodes, i.e., stationary, mobile, or hybrid; the other is the spatial coverage of UASN, i.e., 2D or 3D UASNs as shown in Figure 3. The nodes float freely under the water in the portable UASNs with unpropelled and untethered sensor nodes and drift with the water current. In UASN with powered sensor nodes, the node motion can be controlled by inertial navigation systems. Autonomous Underwater Vehicles (AUVs) and Unmanned Underwater Vehicles (UUV) are floats, drifters, gliders, and profiling float, along with examples of unpropelled portable machinery. Most of these instruments are used in oceanography to gather data and measurements from the various layers of the ocean environment. Drifters operate mostly on the ground and drift with winds and surface waves as floats move with the current of the water. They are used to acquire measurements from the surface of the ocean and send the information to the on-shore center via satellite or GPS. Gliders are devices driven by buoyancy, as they can travel vertically comparable to floats for profiling. Besides that, with the assistance of their body and wing design structure, they can move horizontally. Sensor nodes are linked to surface buoys or ocean floor units having a fixed position in the stationary UASNs. For example, the port entrance, stationary UASNs are applied for controlling a certain region. Mobile and stationary nodes coexist in hybrid UASN architectures. In [26, 27], using a hybrid architecture,

a portable sink node transverses the network and collects data from underwater sensor nodes.

The immediate domain with acoustic energy density is comparable to the density of the acoustic energy source in the resounding field and an open atmosphere with an acoustic energy density using acoustic waves such as W_r reflecting the various wall. Direct field acoustic energy density depends on the distance r to the source associated with:

$$W_d(r) = \left(\frac{P_s}{4\pi cr^2} \right), \quad (1)$$

where P_s is the source force and c is the sound velocity. It implicitly assumes an omnidirectional source; if the source is directional, the direct field relies on the direction.

And the acoustic energy density W_r and the acoustic intensity I_r are linked to an isotropic homogenous reverberated domain [28] by:

$$W_r = \left(\frac{4I_r}{c} \right). \quad (2)$$

The derivative of the complete acoustic power in the tank, $Q = W_r(V)$, is the variance between the acoustic power that is forced by the P_s source and the acoustic power is degenerated by the absorption or transmission on the wall aI_r .

$$\frac{dQ}{dt} = P_s - aI_r = P_s - \frac{ac}{4V} Q. \quad (3)$$

In Equation (3), a is the Sabine coefficient which represents the absorption and transmission due to the walls. When the balance is reached ($dQ/dt = 0$), then

$$P_s = \frac{ac}{4V} Q = \frac{ac}{4} W_r. \quad (4)$$

It represents the belonging between the source power P_s and the density of acoustic energy in the reverberation sector W_r .

In 2D UASNs, all sensor nodes are supposed to be on the same depth, e.g., they can be deployed on the seafloor and ocean surface, and each sensor node can float at an arbitrary depth in 3D UASNs [29]. Stationary sensor networks are generally regarded to be 2D as the sensor nodes are positioned on the ground buoys or anchors of the ocean floor. The wealth of UASN architecture is due in part to a conventional description of UASNs and in part to its application and particular design criteria. For example, GPS can be used for a 2D stationary UASN with nodes deployed on the sea surface, or for similar UASNs with ocean floor units, the sensor nodes can be deployed in predefined location is trivial. Furthermore, stationary UASNs do not involve regular localization as do portable UASNs, which implies that localization protocols with comparatively elevated overhead communication can still be used as they only operate at the moment of configuration. In [30], the authors also proposed the architecture of UASNs and divided it into different groups such as (a)

static architecture, (b) hybrid architectures, and (c) mobile UASNs and free-floating networks.

4. Related Works

In this section, we give a brief description of underwater acoustic communication. After that, we review some widely known schemes which are used for underwater localization. Currently, the underwater communication system utilizes EM, optics, and acoustic data transmission schemes to transfer data among the various locations of the nodes. EM communication scheme is influenced by the conducting nature of the underwater environment while optic waves are only able to move on very short distance because optic waves are easier to absorb in underwater environments [31, 32]. Therefore, an acoustic communication scheme is only one scheme that has better performance as compared to EM and optical due to less attenuation in the underwater environment. Acoustic signals also have less attenuation in the deep and thermally stable underwater field. Acoustic signals attenuate more in shallow as compared to deep water because of the temperature, noise, and multipath reflection and refraction. In the underwater field, the sound speed is not constant instead of this sound speed varies almost at every point. Near to the water surface, sound speed is almost 1500 that is four times higher than the sound speed in air and very slow as compared to the EM and optic speed in air.

Due to the unique challenges of the acoustic channel, it is highly variant, for example, high propagation delay, variable sound speed, narrow bandwidth, reflection, and refraction. Because of these unique properties, it creates more issues regarding MAC protocols. MAC protocols have two main groups such as content-based and scheduled-based protocols. Content-based nodes complete each other for the exchange of signals, while scheduled-based avoid collision among the transmission nodes. Content-based are not suitable for the underwater environment, while scheduled-based such as TDMA and FDMA are not efficient due to the high propagation delay and narrow bandwidth, respectively; however, CDMA is appropriate for UANs [33, 34].

A localization scheme for UWSN is presented for localization issues in large-scale UWSNs. Unlike in TWSN, GPS cannot work properly in underwater or attenuate highly [35]. Due to the costly equipment of underwater, limited bandwidth and harshly impaired channel all make the process of localization very challenging. Currently, most of the localization techniques are not well appropriate for the deep underwater field. The researchers presented a new scheme that mainly consists of four types of sensor nodes, such as DETs, surface buoys, ordinary nodes, and anchor nodes. DET is connected to the surface buoys and can dive and rise to the water surface for the broadcasting of its location. Surface buoys are supposed to connect with the GPS. Anchor node can estimate their locations based on location information from the DETs and estimation of the distance to the DETs. This localization scheme is scalable and can be applied to make balances on the accuracy and cost of localization.

In [36], the authors have presented a new SLMP localization technique with the prediction of mobility, for the large-

TABLE 2: Performance evaluation of underwater acoustic networks and underwater localization schemes.

Ref.	Energy consumption	Network lifetime	No. of nodes	Time synchronization	Packet exchange rate	Loca. accuracy	Comm. overhead	Delay	Error estimation	Link quality
[3]	X	✓	✓	—	✓	✓	X	✓	✓	✓
[18]	—	—	✓	X	✓	✓	—	—	✓	—
[21]	✓	X	X	X	X	✓	—	X	✓	X
[26]	X	—	✓	✓	✓	X	✓	✓	X	—
[41]	X	—	✓	—	✓	✓	—	✓	X	—
[42]	—	X	X	✓	X	✓	X	—	✓	—
[43]	X	—	✓	✓	✓	X	—	X	✓	—
[44]	—	—	X	✓	✓	✓	✓	—	✓	X
[46]	X	✓	✓	—	✓	✓	—	✓	✓	—
[47]	X	✓	✓	—	✓	✓	X	X	X	✓
[37]	X	✓	✓	✓	✓	✓	X	X	X	✓
[48]	X	—	✓	—	✓	✓	X	X	X	✓
[49]	X	—	✓	✓	✓	—	—	✓	—	X
[51]	X	X	✓	X	—	X	X	—	✓	—
[53]	X	✓	✓	X	✓	✓	X	X	✓	✓
[56]	X	—	✓	—	✓	✓	—	✓	✓	—
[57]	✓	—	✓	X	✓	X	X	✓	✓	—
[58]	X	—	—	—	X	X	X	—	✓	—
[59]	X	—	✓	X	✓	✓	X	X	✓	X
[61]	X	—	✓	X	✓	X	X	✓	✓	X
[62]	X	✓	✓	✓	—	✓	✓	—	—	—
[63]	X	—	✓	X	✓	✓	X	X	—	X
[65]	—	—	✓	X	X	X	✓	✓	✓	—
[67]	X	✓	✓	✓	✓	✓	✓	✓	✓	X
[68]	—	—	✓	—	✓	X	—	—	✓	✓
[36]	X	X	✓	X	✓	✓	X	X	✓	—
[73]	X	✓	✓	X	✓	✓	—	X	✓	X
[74]	—	—	✓	X	X	✓	X	X	✓	—
[75]	X	✓	✓	X	✓	X	✓	✓	✓	✓
[77]	X	✓	✓	X	✓	✓	X	X	✓	✓
[79]	X	—	—	✓	✓	✓	X	X	✓	—
[85]	X	—	✓	✓	✓	✓	—	—	✓	—
[89]	✓	—	✓	X	X	✓	✓	✓	✓	X
[91]	X	X	X	X	X	✓	X	—	X	X
[94]	—	—	✓	X	✓	✓	—	—	✓	—
[97]	✓	—	✓	—	✓	✓	X	—	✓	—

scale USNs. In this scheme, by taking benefits of the inherent temporal correlation of the mobility of objects in underwater, anchor sensor nodes conduct linear prediction. Every ordinary node guesses their position by using the spatial correlation of object mobility pattern in underwater and weighted-averaging its received motilities from the other sensor nodes. Simulation results of the new scheme show that SLMP can highly minimize the cost of communication while keeping constant relatively high accuracy and coverage in localization. The authors also estimated the impact of different design parameters, such as prediction step, confidence threshold, prediction window, and prediction error threshold, on the performance of localization.

A comparison of various localization techniques is studied above and some in the next coming section which is also shown in Table 2. Localization techniques are compared based on sensor node mobility, range estimation, time synchronization, localization accuracy, network lifetime, link quality, etc. The localized nodes must be time-synchronized if ToA is applied for the range estimation. Localization techniques such as silent positioning are useful in reducing the communication overheads because nodes only receive information and do not transmit any information for localization. As compared to the receiving side, transmission utilizes more energy. Recursive localization is more beneficial to increase coverage. Only for routing protocol, if the localization of

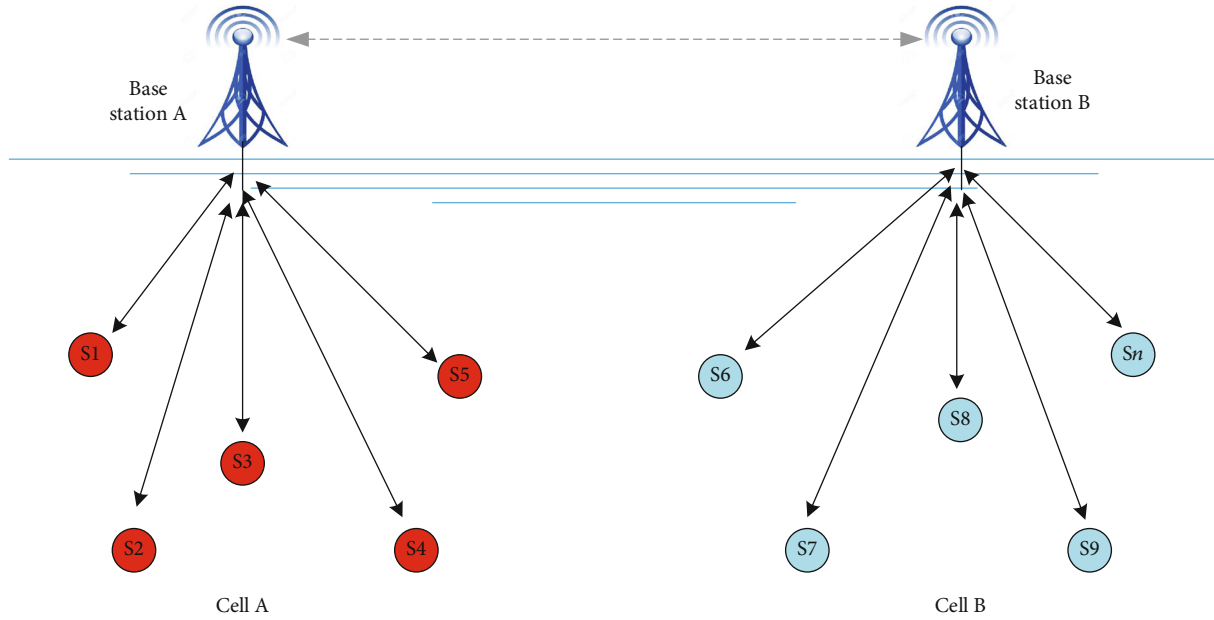


FIGURE 4: Centralized network topology.

sensor nodes is required, then any of the range-free techniques can be applied. Any localization technique can be applied according to the requirement of the application. Also, a performance-based comparison of LSL, PL, and DNR localization techniques is presented in [37]. However, these schemes encounter localization shortcomings. The aforementioned schemes provide a brief description of localization and still many important aspects need to be considered in underwater localization. Therefore, this review can provide a detail explanation of all localization techniques, the existing challenges which face underwater localization, and the future direction for the solution of these challenges.

5. Techniques Used for UASN Localizations

Briefly, localization of GPS-based algorithms has been proposed for terrestrial WSNs that, for reasons such as high-frequency GPS, cannot be applied directly to UASNs that attenuate underwater quickly and cannot reach the sensor nodes several meters below the water surface. Also, GPS-less systems of localization implement high overhead communication [38, 39]. For the above reasons, it is not possible to directly apply WSN localization to UASNs. In [40], the author's presented the adaptations of the "stochastic proximity embedding algorithm" and "multidimensional scaling algorithm" for UASN. These algorithms conduct concurrent localization of all target nodes compared to the straightforward localization algorithm based on ray tracing that conducts sequential localization of each target node. The proposed methods of localization take into account the bending of acoustic rays and thus, when deployed in real UWSN, give good accuracy. The algorithms have been adjusted to offer directly absolute locations. There are many localization techniques; some of them are categorized as centralized and distributed methods of localization. In centralized localization techniques, firstly, estimate the position of

every sensor node in a control center or sink and the sensor nodes do not know their location unless the sink or reference node explicitly sends this information to the node. In this technique, the sensor nodes may be localized at the end of the process such as in the postprocessing phase, or they may gather data periodically for the tracking of sensor nodes. The distributed localization technique allows each sensor node to do localization individually; they are free to do individually localization independently. Centralized and distributed localization techniques are divided into subcategories, i.e., estimation- and prediction-based localization. In the estimation-based localization, the latest available information is used to obtain the current location of the sensor node. For the prediction-based localization, the previous node location, distance information, and anchor location are used to predict the sensor node located at the next moment. Therefore, it is appropriate for mobile UWSN or a hybrid UWSN.

5.1. Centralized Localization (CL). In this technique, first, it calculates the position of each sensor node in the control center or sinks, and the sensor node initially does not know its location unless the sink sends this information explicitly. In this method, nodes may be located at the end of any operation, i.e., postprocessing phase or data may be collected sporadically for sensor node monitoring. In centralized algorithms in [41], in which a key organization (e.g., the control center) exists that gathers all the needed data or estimation (e.g., estimated distances between the nodes in communication ranges and calculates distances to the anchor sensor nodes) and centralizes the sites for the sensor nodes. After the central organization determines the location of the sensor nodes, it sends the location information back to the corresponding sensor nodes. Sensor nodes interact in a centralized algorithm through a base station that includes one cell as shown in Figure 4.

5.2. Estimation-Based Localization. Estimation-based localization techniques are further divided into subparts by the following:

- (1) *Hyperbola-Based Localization (HL)*. Using the localization method based on hyperbola, the location of a sound source, i.e., a target such as mammals, can be identified in the oceanographic scheme using hydrophones such as sensor nodes with known locations [42]. HL also adapts standard oceanographic sound source localization issues to standing 2D UASN localization. In HL, the sensor node sends wide-range signals to the anchor node about 1 km and a centralized sensor node estimates its location. Referring to [43], the authors present a new approach to a better localization accuracy for UASNs. This system uses the hyperbola-based strategy to detect event place and a normal distribution to estimate and standardize error modeling. This efficiency of the method demonstrates a separate enhancement over the estimation of the place of the frequently used minimum squares based on the circle. In terrestrial applications, a multi-iteration and least square measurement system are often implemented to find a decent estimate [44]. But this system is not useful in underwater applications due to its heavy communication costs. At the same moment, it was noted that distance measurement errors often follow a certain shape that can be implemented to further improve the precision of the localization. Authors evaluate and use distributions of measurement errors to improve the precision of localization
- (2) *Motion Aware Self-Localization (MASL)*. Due to the long delay in the propagation of signals in the underwater environment, it may take a longer time to collect the number of distance estimates which is required for localization, thus increasing the possibility of obsolete information. MASL's primary objective is to discover the faults in the estimates of distance and provide a precise scheme of localization. The underwater sensor node collects range estimates between the sensor nodes of the neighbors and itself in the MASL method. The distance estimation is performed through certain iterations performance. At each iteration, the algorithm polishes location distribution by distributing the field of an event into smaller grids operation and selecting the area in which nodes reside. In [45], the author models the ocean current as layers of equal density, variable velocity, and the nodes of the sensor move with those underwater currents
- (3) *3D Multipower Area Localization Scheme (3D-MALS)*. 3D-MALS varies from the MASL method, which combines the thinking of anchor nodes [46] with a variable rate of transmission energy and the thinking of anchor nodes with vertical mobility of buoys house mechanical device [47] that operates as an elevator for underwater transceivers called

Detachable Elevator Transceiver (DET). DET broadcasts its set of GPS-driven coordinates at different concentrations of energy and then goes down underwater. The unlocalized sensor nodes can retrieve the position of portable anchor nodes and their, respectively, smallest energy concentrations and then send them to the reference or sink node. The reference node can understand the position of each sensor node after gathering data

- (4) *Area-Based Localization Scheme (ALS)*. It is a type of scheme that provides an estimate of where the sensor node is in the area of the sensor instead of the precise set of coordinates. Anchor nodes in ALS divide the operating region by sending messages to nonoverlapping areas at different energy levels. ALS is appropriate for the setting where there is no need for accurate location data and when the anchor nodes can change their level of transmission power. The benefit of ALS is that the received signal strength (RSS) is jointly light, range-free, and no synchronization requirement. For applications demanding internet location estimation, ALS is not appropriate, so it is not appropriate for precise localization. In [37], ALS is an algorithm for USNs that is range-free, centralized, and coarse-grained. A sensor node underwater maintains a list of anchor nodes and associated energy concentrations. This data is sent to the reference or sink by the sensor node and the sink discovers the region in which the sensor nodes reside. ALS offers a coarse-grained localization evaluation and it is a centralized localization. Therefore, it is not suitable for large-scale USNs and applications that require accurate location estimation. After offering all the regions (one for each anchor node) in which it resides, a primary server offers the sensor node position assessment [48]. On the other hand, USP is a 3D localization algorithm with internal position graininess compared to ALS (i.e., it measures the position of a node within a coordinate system as protecting a location within a subarea). In [49], the authors suggest that only a supper sensor node transmits information from its neighboring sensor nodes and is then shared with nearby sensor nodes. Using this protocol, the packet collision in the network is obviated during node discovery. Also, only seed nodes can make additional results; the remaining nodes in the network do not include power consumption to transmit text messages to their other neighbor nodes. Farthest/Farthest algorithm, Farthest/Nearest algorithm, Nearest/Farthest algorithm, and Nearest/Nearest algorithm are the algorithms used to select additional seed nodes [50]

5.3. Prediction-Based Localizations

- (1) *Collaborative Localization (CL)*. A Collaborative Localization (CL) scheme [51] consideration of portable UASN applications is where underwater sensor nodes are accountable for gathering ocean depth

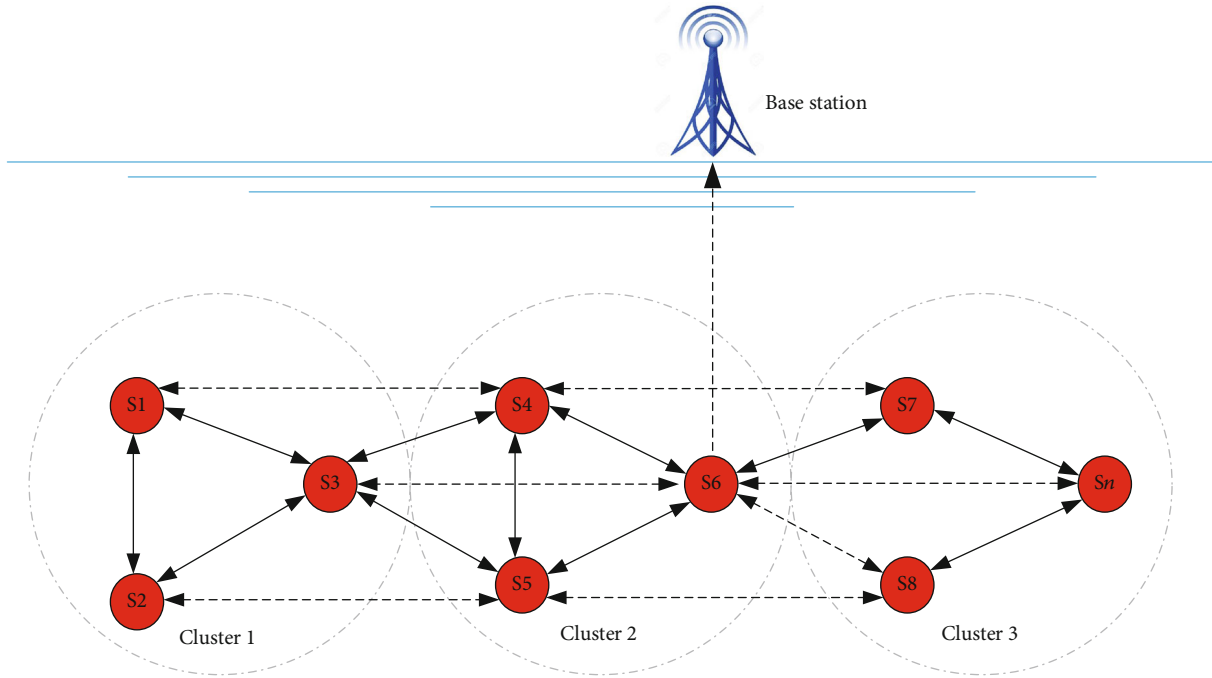


FIGURE 5: Distributed network topology.

information and are accountable for transferring it to the water surface. This architecture uses profilers and supporters of two kinds of underwater sensor nodes. These two kinds of sensor nodes come down underwater, but profilers come down ahead of them, i.e., deeper than other nodes. The distance between profilers and followers is periodically evaluated using the ToA to place the profilers to followers. In particular, the CL algorithm weighed time synchronization algorithm with elevated transmitting delay and a multipath acoustic propagation channel for UASN. By using the new time synchronization protocol, the target position is evaluated using maximum likelihood (MLL) techniques based on the distance of arrival (DoA), since the statistical model between the real and measuring location is based on the marine channel signal envelope. The suggested algorithm also follows the distributed-centralized computing operation that minimizes the energy transmitting node in USNs

- (2) *Distributed Localization*. The distribution localization method allows each sensor node to locate separately or nodes are free to locate such as neighborhood distance, anchor position, and connectivity data and then send all these data separately to the reference or super node. On the other hand, instead of being placed in one central entity, the function of location finding is distributed to the sensors themselves in the distributed localization algorithm. In a distributed network, sensor nodes communicate through peer-to-peer (P2P) as shown in Figure 5.

Distributed positioning algorithms usually assume that anchor sensor nodes are randomly distributed throughout

the sensor network, and the percentage of anchor nodes in the network is also high (5%-20%). Deploying anchor nodes in terrestrial sensor networks is not a challenge because a GPS-equipped node can act as an anchor node [52]. However, in the case of an underwater field, the network establishes the backbone of the randomly distributed anchor such as ABC nodes; the exact location of which is known before is not a trivial issue

5.4. Estimation-Based Localizations

- (1) *AUV-Aided Localization (AAL)*. An AAL-based approach is presented in [53] for a hybrid 3D UASN with stationary underwater sensor nodes and AUV traveling in the UASN sector. Using the dead-reckoning method, the AUV can get its position underwater. Dead reckoning with the costly inertial piloting machinery is feasible and the position has been periodically calibrated. The AUV goes to the water surface for this purpose at certain periods to achieve GPS coordination from a satellite. A wake-up message can be broadcasted from a separate point on its moving path during the AUV operation cycle. It occurs when AUV receives this signal from the underwater sensor node, it begins the localization action by transmitting a request signal to the AUV, and AUV responds with a reply signal. The pair of requests and response packets provide a two-way algorithm and the response packet includes the AUV coordinates so that the underwater node uses the lateration process to measure its self-location after the exchange message from three different noncoplanar AUV positions (see Figure 6).

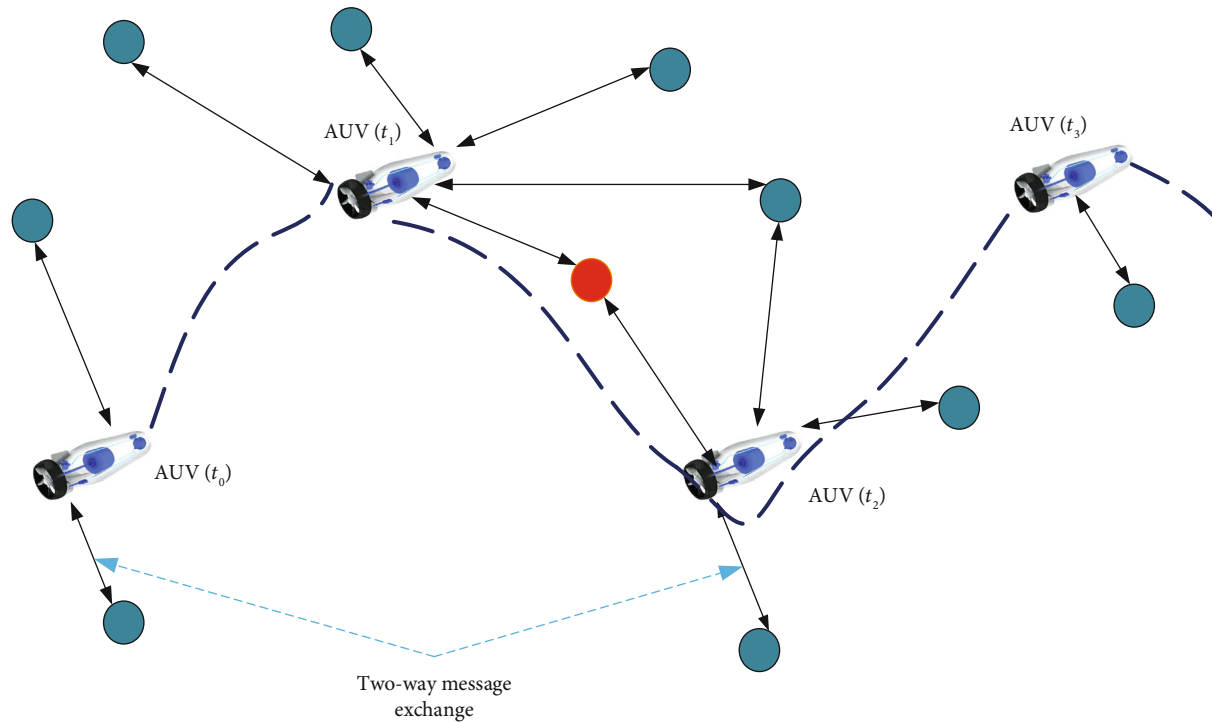


FIGURE 6: AUV cycle of operation with two-way message exchange.

AAL utilizes a two-way display to alleviate the need for synchronization, but on the other side, a sensor node can invest in a silent algorithm more energy than it does and also boosts the protocol's overhead communication. AAL's precision is also influenced by the AUV's localization calibration frequency. An assessment of an AUV's single beacon localization problem modeled as a double integrator [54], where its input is the acceleration in an inertial reference frame and its output is its range to a static beacon. The nonlinear map between range and position enables the range-based observability problem to be considered nonlinear. Two complementary problems are discussed here in the observability evaluation: firstly, the local weak observability of the nonlinear system and secondly, the worldwide observability of a linear time-varying system representation obtained by a worldwide technique of increase

AUVs emit an omnidirectional beacon [55]. When AUV crosses the sensor node at t_1 , this node receives a signal that can be used for the distance calculation d_1 between the AUV and the sensor node. Similarly, the distance d_2 can be calculated using the ToA technique as shown in Figure 7. To get the sensor node's coordinate, it requires the AUV's coordinates at two distinct time instants. The location of the node is chosen based on the easy triangulation operation. Also, AUV routing is very complex to guarantee that two necessary beacon messages can be acquired from AUV for each node. Differences in time indicate to some extent the distance. The method is based primarily on the time

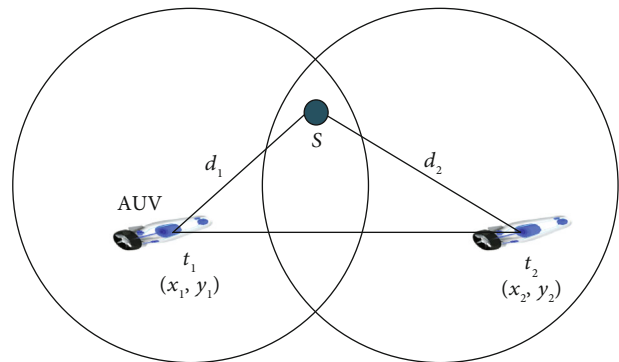


FIGURE 7: Omnidirectional AUV-aided localization.

difference [56]. At distinct locations, AUV broadcasts its coordinates. When receiving messages from more than three noncollinear AUV locations, the underwater nodes estimate their place laterally. This technique has a large delay in localization due to the slow velocity of AUV, which is why it is more useful for stationary USNs than dynamic USNs.

- (2) *Silent Localization (SL)*. There are three kinds of messages in AUV-assisted localization systems: wake-up, demand, and reaction messages. The process of positioning consists of three steps [57]. The AUV sends a wake-up signal when it joins the sensing operating region. All sensor nodes will send a request signal or packet after getting the wake-up signal

The AUV then responds with a response packet that contains the coordinates of AUV. For this stage, each

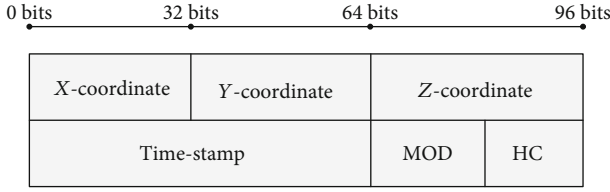


FIGURE 8: Localization packet format for proxy localization.

detector node shall communicate with the AUV at least once. Therefore, it is familiar to consume extra energy for localization. Due to the energy consumption of communication between the sensor nodes and the AUV, a better alternative is that during the localization era, only beacons are received by the sensor nodes without interacting with others. This sort of strategy is called a technique of “silent localization.” Beacons are interchanged between the sensor nodes and the AUV in the past methods. Lastly, silent localization can considerably decrease underwater localization power consumption.

- (3) *Dive and Rise Localization (DNRL)*. Refer to [58], to better define DNRL. It is a distributed, estimation-based localization protocol that applies mobile anchor using the localization of underwater sensor nodes, and these anchor nodes are named as beacons called “Dive’N’Rise (DNR).” By using the same hydraulic laws as the profiling floats laws and regulations, DNR can descend and ascend. When DNR reaches the water’s surface, it utilizes GPS receivers and reaches its GPS coordinates while floating on the water’s surface. After that dive again, they broadcast their coordinates at several periods until a precalibrated underwater depth. Mobile anchors climb up to the water surface in the first round of localization to obtain the updated coordinates from GPS. They descend and dive or ascend periodically on the second-round journey and so on until the end of the UASN phase. Underwater sensor nodes listen to time-stamped DNR texts and use a ToA method to evaluate distances to DNR beacons using one-way ranges. The range estimates and the coordinates of the anchor node are used in lateration. One advantage of DNRL is the silence that results in low overhead communication and very high energy efficiency. DNR has a wide coverage and gives an accurate estimate as the mobile anchors dive into the vicinity of the underwater nodes and periodically update their position when they reach the surface of the water. On the other hand, for high localization effectiveness, DNRL needed a big quantity of DNR beacons, while DNR beacons are expected to be more expensive than other underwater sensor nodes due to their movement ability
- (4) *Proxy Localization (PL)*. PL utilizes the DNRL method to locate the top of the network location. The DNR beacons sink to half of the 3D USN depth. Localized nodes then become proxies of location for

those nodes that float at greater concentrations. Location proxies advertise self-coordinates for further localization in proxy place. Nonlocalized underwater nodes can later use and locate themselves with the proxy coordinates. A nonlocalized underwater sensor node picks the trusted proxies between nodes using the hop count metric. Hop count is the distance from a proxy node to a beacon. Error accumulates in iterative methods of the localization at the proxy nodes remote from the beacons. Therefore, proxy nodes with the lowest hop range can be selected to enhance the accuracy of lateration equations as shown in Figure 8

- (5) *Localization Using Directional Beacons (LDB)*. LDB is suggested for a 3D UASN hybrid in which stationary underwater sensor nodes are located by AUV like to AAL [59]. When AUV reaches the water’s surface, it gets its coordinates from the GPS, dives again to a certain depth, and performs dead-reckoning for underwater self-localization. LDB differs from AAL during the localization operation in a way that the AUV travels above the operation area as shown in Figures 9 and 10. It utilizes a directional acoustic transceiver to transmit its position and the transceiver angle. The sensor node uses angle data to map the AUV coordinates with itself to the same horizontal plane. After two or more beacons nodes are obtained, the nodes can assess the location information. The sensor nodes listening to the beacon nodes and the beam form distinct circles h . The center of the circle is (x, y, h) . Thus, the circle radius can be expressed as follows:

$$r = \tan \frac{\alpha}{2} \times \Delta h, \quad (5)$$

where α is the angle of conic beacon and $\Delta h = |h_a - h|$. The rough position by using the receiving beacons (x, y, h) can be estimated [60].

On the other side, LDB is a range-free, silent localization method that is more energy-effective than AAL’s method. LDB has one disadvantage that the AUV is restricted to traveling above the UASN area, which may be impossible in a real situation. Furthermore, owing to hitting with each other, the frequency of the AUV messages affects the precision of the localization process

- (6) *Multistage Localization (MSL)*. To the best of our understanding, the authors suggest the MSL system that defines the DNRL-related by adding coverage and delay an additional localization stage and using effectively located underwater nodes as anchor nodes. An unlocalized node utilizes the coordinates and range estimation from three noncoplanar sensor nodes that can be DNR beacons or a localized sensor node of the underwater sensor. Due to the iterative localization method, MSL has the disadvantage of

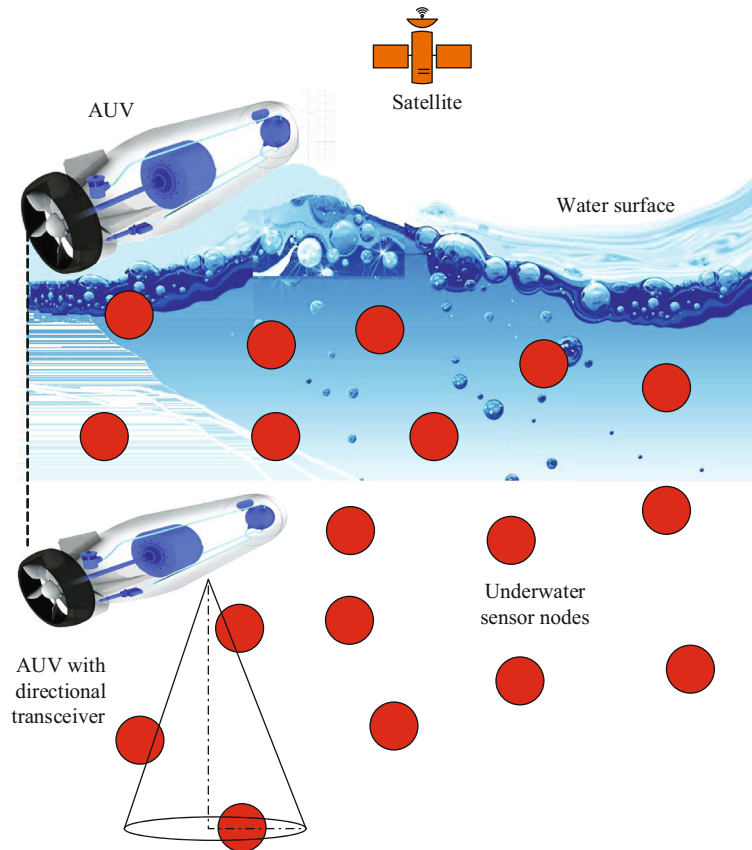


FIGURE 9: AUV with directional beam in the LDB scheme.

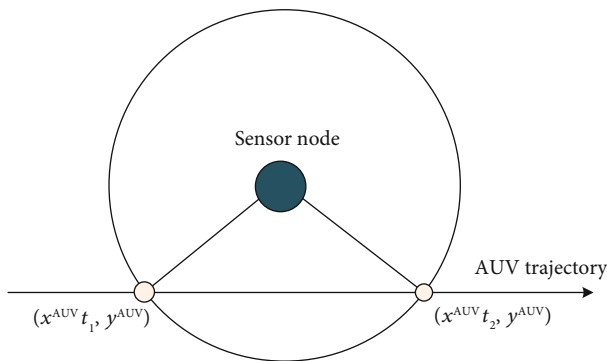


FIGURE 10: Sensor's localization in LDB.

its high overhead communication. For this purpose, therefore, MSL is less energy-efficient than DNRL. Furthermore, localized underwater nodes in MSL provide their estimated locations that already include failures in the estimate. Error accumulates at nodes using coordinates of localized underwater nodes instead of coordinates of anchor nodes. Because of its one-way ToA algorithm, comparable to the DNRL algorithm, MSL also required time synchronization

- (7) *Underwater Positioning System (UPS)*. UPS is a system used for monitoring and piloting underwater vehicles or divers through measurements of acoustic range and/or direction, and subsequent triangulation

tion of position. UPS is frequently used underwater, including oil and gas exploration, sea science, rescue activities, marine, law enforcement, and military purposes. The authors suggest UPS, an extension of the terrestrial WSN localization system introduced in [61]. UPS is a localization system based on TDoA for standing UASNs. It utilizes four anchors that transfer beacon messages sequentially. One anchor node works as a master anchor and initializes the procedure of localization. Assume the master anchor is selected as the “A” anchor (see Figure 11). This signal is heard by anchor “B” and sensor node “S” when the beacon signal is sent. Anchor “B” reacts to anchor “A” by recording the time difference between anchor “A” beacon arrival and the beacon signal transmission time. The anchors “C” and “D” repeat the same successive cycle after the “B” anchor. Node “S” hears these beacons of anchor and calculates the TDoA of beacons. Then, by multiplying them with sound velocity, it transforms TDoA values to range distinctions. Node S is presumed to understand the locations of the anchors and measure self-location using anchor position and trilateration equations range distinctions. Since UPS utilizes TDoA, synchronization is not necessary. The writers also suggest the UPS, i.e., a silent acoustic positioning system for the underwater vehicles/sensors, which depends on the

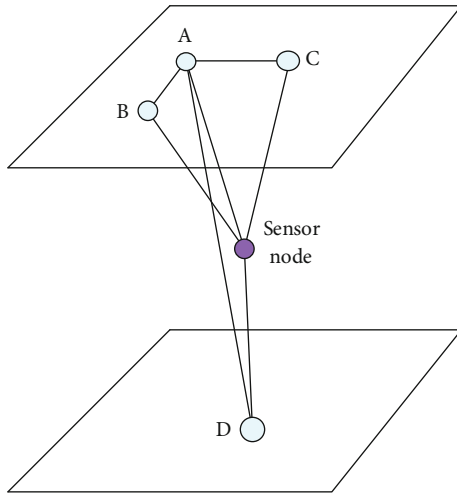


FIGURE 11: Underwater positioning system (UPS) using four anchors.

ToA of RF signals for location estimation from three anchor nodes. UPS comprises essentially two steps: in the first step, from four anchor nodes, they can detect variations in signal arrival times. These time distinctions are converted from the underwater vehicle/sensor to the anchor nodes into range distinctions. In the second step, the transformation of these distance estimates into their coordinates takes place through trilateration. The authors suggested that UPS silent placement should be further emphasized. First, because sensors/vehicles do not transmit any beacons for positioning purposes, it can considerably retain bandwidth and therefore modify network throughput. Second, UPS also applies four or more anchor nodes to an asymmetric UASNs where the underwater vehicles or sensor transmission could not reach. Third, silent positioning offers powerful privacy of location that can assist safeguard sensors/vehicles from detection in critical circumstances

- (8) *Wide Coverage Positioning (WPS)*. The UPS algorithm may not uniquely locate all sensor nodes in the four anchor nodes operating region [62]. It indicates that the sensor nodes near the anchor nodes need five anchors to fix the issue. In the event of WPS, four anchors are used whenever distinctive location can be achieved utilizing four anchors called UPS (4); otherwise, WPS will use five anchors (UPS (5)). UPS (4) and UPS (5) are used together to solve the overhead and price of communication for the sensor nodes with four anchors that can already be located. These nodes consume the same number of energy as the initial system of localization
- (9) *Underwater Sensor Positioning (USP)*. Using USP, for underwater localization, underwater nodes are fictitious to equip with the help of pressure sensor nodes by which nodes find their depth position. The depth data is used by an underwater node to map the accessible anchors on a horizontal plane

on which it rests. While mapping from 3D to 2D, some of the anchor nodes maybe reside in overlapping locations. In these situations, an underwater node picks out another set of the anchor's sensor node. Localized underwater nodes transmit their location data at each iteration of USP and burn their position estimates based on getting messages from the nodes of neighbors. The unlocalized nodes attempt to constitute localization using only two anchors nodes; the process is called as bilateration. If the two anchors do not compute a new location, the node will wait until it hears from other neighbors' nodes they are already localized. After a slumber period that is preconfigured timing, the same localization operation is reinitiated. In [63], authors present a positioning system in underwater sensor networks. For this, the writers implemented a weighted Gerchberg-Saxton algorithm to address the multipath acoustic propagation problem of various feasible distance measurements between two nodes. A standard positioning technique finds the range in between two sensor nodes which are based on either on initial arrival or the stronger way, but neither may agree to the immediate acoustic route in underwater. In WGSA, based on the ML rules, it can be used for identification of direct path from the overall existing multipaths by connecting each path with a weighting component; it can be understood in a certain way roughly as the chances of that path existence the immediate path

In the WGSA algorithm, the weighting component and the sensor node location are updated periodically or based on iteration, with each iteration computationally easy. USP [64] is based on sensor network technology, which uses many conventional hydrophone stations and GPS sensor nodes above the water surface. Referring to [65], a new underwater acoustic positioning system uses new terminologies. For the range calculation unit, the distance can be calculated alternately based on the time difference by using the connection between propagation noise loss and propagation distance. It is a very simple procedure for processing, and it can use to measure a long-distance winder medium. For an underwater robot, a system of acoustic positioning underwater is shown in Figure 12.

In [66], the geometric configuration of a surface sensor network will maximize the variety of information associated with the target positioning algorithm underwater in a well-defined sense. Because of the white Gaussian noise, the range estimate is not precise and its discrepancy depends on distance.

The Fisher Information Matrix (FIM) and its determinant maximization are used to evaluate the constellation of sensor nodes providing the target's most precise location. Another approach is to locating and mapping Underwater Robotic Fish (URF),

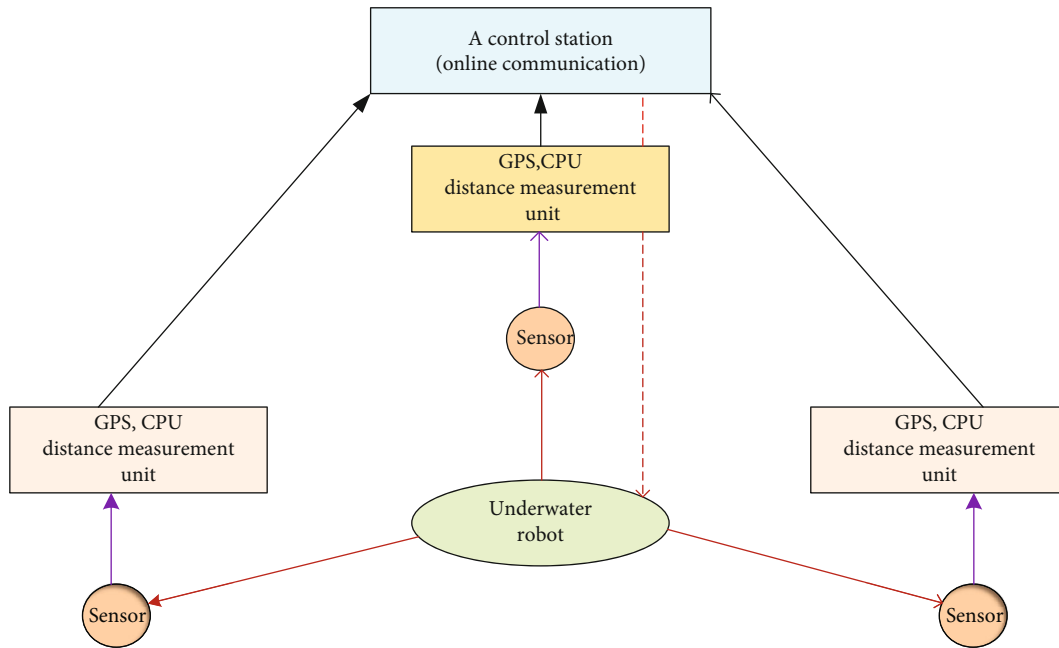


FIGURE 12: Underwater robot-based sensor positioning system.

which is based on both the Particle Filter (PF) system for cooperative localization and the Occupancy Grid Mapping Algorithm (OGMA). The suggested CLPF is more advantageous to use the probabilistic algorithm that they do not have previous data or information about the URF model is needed to accurately attain a 3D localization. If the number of mobile beacon nodes for some traditional localization algorithms is less than four, which is the minimum number, it can achieve good accuracy in the case. To build the environment map, the localization result of CLPF is fed into OGMA. Moreover, even under a normal degree of connectivity, USP has reduced localization achievement than the other surveyed localization methods

- (10) *Anchor-Free Localization (AFL) Scheme.* Conventionally, the existing localization algorithm mostly presumes that the network has a multitude of anchor nodes [67], for the assistant of node positioning. Mostly, it makes the use of AUV or sometimes a sensor node with a particular device, an anchor node, and AFLA. AFLA is especially intended for underwater networks with active restrictions. In the case of AFLA, they do not need anchor node information and use the data of its neighbor's sensor nodes. In [68], the author's present another algorithm for the difficulties in localization that license for node unrelated discovery on the Line-of-Sight (LoS) and any rigid reference sensor nodes. They create a surface-based reflection anchor-free localization (SBRAL) method in which all nodes use homomorphic deconvolution to establish a reflected communication connection from the water surface. A GPS-free protocol [69] can discover nodes and relative

location of nodes. The procedure of node discovery starts with first or an initial seed node with a known position or location. The first seed node can determine the relative positions of neighboring nodes without using inner information and is similar to the first node, other nodes in the network. Self-initialization includes certain distant nodes becoming seed nodes for further cycles of discovery and so on. Node is originated by seed node S_1 , then S_1 broadcast the message among its neighbors and receive response from different nodes, and then select a second node S_2 . S_2 revise the same procedure, broadcast, and receive, then S_3 , and so on. Finally, the sensor nodes in the intersection region of these three seed nodes can determine their position using the trilateration algorithm as shown in Figure 13. Also, owing to the maximum delay in propagation in the underwater medium, the node discovery process may take a long time owing to AFL based on communion range estimates among its neighboring sensor nodes. And the approach to the target station is being viewed as a survivor through the RSSI calibration and RDD without a premeasurement. This algorithm's weakness is fixed by using a moving distance for the PLE assessment instead of the known distance. By using the remaining counter that has a direction of movement until it exceeds, it is an indication to change direction

5.5. Prediction-Based Scheme

5.5.1. Scalable Localization with Mobility Prediction (SLMP). SLMP is a method that uses surface buoys, anchor nodes, and common nodes [36]. By using the prior coordinates and their mobility pattern, the anchor node measures its position. As

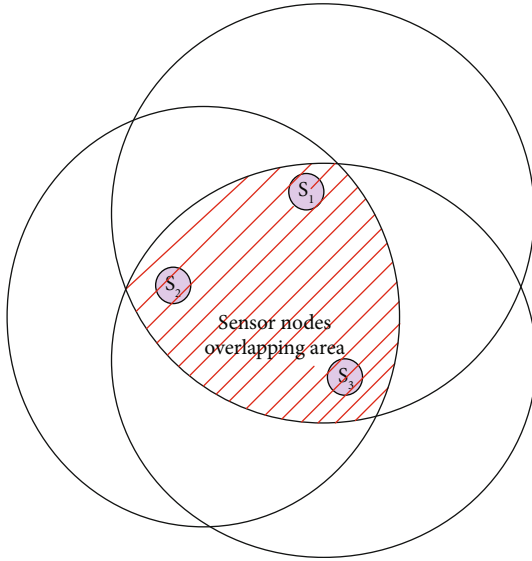


FIGURE 13: AFL using three seed nodes.

the mobility pattern may cease to be used in time, the anchor node periodically checks the pattern's validity. Updates anchor trigger when the model is no longer valid. GPS coordinates are received by the ground buoys and sent to anchor nodes. After predicting its position, an anchor node uses coordinates of surface buoys and lateration measurements of distance to buoys and estimates their position. If the Euclidean distinction is less than a limit between the expected and estimated position, the anchor node will consider its mobility model valid, depending on the mobility pattern, overhead communication, and energy consumption in SLMP. SLMP uses a temporally and spatially connected model of mobility representing the tidal current in shallow waters. Because of this correlated movement, SLMP needed fewer updates, resulting in low overhead interaction and power consumption. Anchor nodes periodically predict their position and through distance measurements check the accuracy of their predictions to surface buoys. They update their mobility pattern if the prediction is incorrect and send a signal to the ordinary sensor nodes. With their mobility model, which is updated when anchor nodes announce an update alert, ordinary sensors predict their location.

The algorithms are further classified into range-based and range-free [70].

6. Range-Based Algorithm

Accurate estimation of distance or angle measurement is made in the range-based algorithm, and TDoA, ToA, and AoA are the algorithms used for this purpose. Due to certain constraints like its time-varying characteristics, which are rarely used in UASNs, RSSI is not too convenient. TDoA employs arrival time difference and is the time difference between distinct transmission mediums or beacons from distinct reference nodes used to assess the distance between two objects. Similarly, ToA is the time of arrival using for distance estimation. In the suggested range-based algorithms [71], the most frequently used technique for UASNs is the ToA algo-

algorithm, and it is favored in UASNs as compared to terrestrial. It is several times smaller than the radio signal in the atmosphere owing to the sound velocity in water. ToA is mostly implemented to UASNs, although synchronization among nodes was needed by ToA. A hybrid bearing and range-based UWSN has been studied in [72]. The authors explore the impact of comparative sensor-target geometry on the underwater target location's prospective results. The optimality criterion function is built as the Fisher Information Matrix (FIM) determinant, and the mean square error (MSE) is also provided with a comparable assessment. The MSE is minimized only if, under the assumption of a set distance between the detectors to the underwater goal, the determinant of the FIM is maximized. The authors suggest a localization method called a Two-Phase Time Synchronization-Free Localization Algorithm (TP-TSFLA) in [73]. TP-TSFLA comprises of two algorithms, the algorithm of range-based assessment and the algorithm of range-free. The writers discuss a time synchronization-free localization system in the first algorithm that is based on the method of Particle Swarm Optimization (PSO) to achieve unknown node coordinates. In the second algorithm, authors present a Circle-Based Range-Free Localization Algorithm (CRFLA) to locate the unlocated nodes that cannot acquire position information through the first phase. For the second phase, finding the location is the conduct of those sensor nodes situated in the first phase such as helping the new anchor nodes. Below is a comprehensive TDoA, ToA, AoA, and RSSI description.

6.1. Time Difference of Arrival (TDoA). Localization is one of the main issues in a network of wireless sensors. The TDoA is a commonly used method for localizing underwater. By using the TDoA method, a goal with anchor nodes can be asynchronous [74]. An asynchronous ToA-based localization method is used [75–77], in which the transmission source time is unknown and ToA measurements have a favorable prejudice due to the synchronization mistake which can lead to a big localization mistake. One method is to use TDoA-based measurement to fix this issue, which does not rely on a transmitter source's transmission time. They also use the method of SDP to turn the nonconvex MLE issue into a convex issue. Since GPS signals are extremely attenuating underwater, it is necessary to develop a precise range-based algorithm for locating underwater. Authors define a sequential method for time synchronization and localization in the acoustic channel [78]. Authors consider it a realistic situation in which nodes are not time-synchronized and underwater sound speed is also unknown, validating the issue of localization as a series of two linear estimation issues. The velocity of propagation that changes with depth, temperature, salinity, etc., anchor nodes and unlocalized (UL) nodes cannot be regarded as time-synchronized, and the nodes of the water current are constantly moving or their self-motion. The authors define a fresh sequential algorithm in an underwater setting for joint time synchronization and location. This associated method is based on exchanging information between the anchor and UN nodes, using the directional navigation algorithm used in nodes to achieve precise short-term

estimates of movement and using continuous nodes. This method achieves a precise localization environment is utilizing only two anchor sensor nodes and exceeds the benchmark systems when node synchronization and propagation speed data are unknown.

6.2. Time of Arrival (ToA). In ToA-based systems, the target must be symmetric with anchor sensor nodes. The author's proposed a new model [79] called ToA-Based Tracked Synchronization (ToA-TS) expands GPS as localization to outline where beacon signals do not coincide and monitor the submersible while synchronizing time. And the beacon that transmits a signal will include the beacon's location data gathered from GPS, as well as the time stamp that represents the time it was sent based on worldwide time. On the receiver hand, the message's receiving time is saved according to the submersible's local clock. In [80], the investigator introduces a mixed localization algorithm for Time-of-Flight (ToF) and Direction-of-Arrival (DoA) which is desirable in the setting of shallow underwater control applications as well as harbor monitoring operations. Localization of both ToF and DoA can be measured using a single-way range operation. Then, we need to combine ToF and DoA to reduce the number of the reference node. ToF measurements are performed by calculating the transmission propagation time between the moored reference antenna at the bottom of the tank and an antenna array. The DoA measurement is performed by evaluating the signal touching DoA angle on the antenna array. For real-time positioning in [81], a cooperative low overhead monitoring method for portable underwater networks measures vehicle location in real-time circumstances. Where nodes follow more predictable paths, the efficiency of localization can be improved by strategically positioning beacons most importantly, so in this scenario, all cars are likely to hear a beacon periodically. A joint localization and time synchronization solution considers the underwater environment's stratification impact; thus, compensating for the prejudice in the distance calculation induced assuming sound waves travel underwater in straight lines. The precision of both is greatly enhanced to combine time synchronization and localization [82]. The issue of locating an underwater sensor node in [83, 84] is investigated by authors based on message broadcasting from various ground nodes. With the ToA readings from a multicarrier modem based on SDP, each sensor node can locate itself to the receiver nodes on the grounds of travel time differences between various sensor nodes.

6.3. Angle of Arrival (AoA). AoA is a distributed localization and orientation algorithm, which assumes that all unknown sensor nodes can detect incident signal angles from nearby sensor nodes [85, 86]. In this technique of localization, orientation and designing are several hops away from the beacon data. Under the noisy angle estimation assumption, this algorithm is intended. An evident DoA is initialized as the azimuth direction of peak power in the case of a low-resolution transducer. A tiny array is used as an antenna and the phase derivative along the array axis is used as a measure of the obvious AoA's sine. Perhaps the obvious DoA lies

outside the precise range of arrivals. The reason can be understood from a situation between two array components with a null attenuation. The AoA capability offers nearby nodes about the node's axis for each node bearing [87]. Radial is an angle from which an object can be seen from another point or a reverse bearing soon. In cases where nodes transmit their bearings concerning beacon nodes, AoA-based systems are accountable. In [88], A scheme used to collect coincident time and AoA information at some GHz is defined. Also, the algorithm for data processing is described and its outcomes are analyzed from information collected in two distinct structures. A model is suggested based on the measurement consequence used by Saleh and Valenzuela (1987) in the clustered double Poisson ToA model. In the time-angle indoor multipath data, an accurate clustering shape was determined. The information maintains the temporal clustering and the angle clustering shape has also been found. Each cluster's mean angles were determined to be split evenly over all angles.

6.4. Received Signal Strength Indicator (RSSI). There are many methods for measuring signal strength with RSSI such as distance from the nodes and the received signals. The signal power obtained mostly depends on the radio wave propagation path loss impact. If there is an obstacle between the sources of transmitter and receiver, the signal power can fall considerably on the respective obstructed connection, which is degrading the range estimate for precision [89, 90]. The author has suggested an RSS-based localization algorithm based on Maximum Likelihood Estimation (MLE) for obstructed fields with unknown Path Loss Exponent (PLE). An RSS-based localization was implemented in [91] for UWSNs using acoustic signals. They proposed a novel SDP estimator, including an RSS-based technique and a frequency-dependent differential process, called the FDRSS-based approach, based on the UWA transmission loss (TL) model; these two techniques provide important localization effectiveness. For an underwater range estimation based on RSS, a fresh implementation of the Lambert W function is suggested. It demonstrates that the derived mathematical equation can calculate precise distance using four iterations in [92] using the Lambert W function. Authors predict that more UWSN applications, particularly sensor networks, will be found in the Lambert W function. The author provided an RSS-based UASN localization algorithm with stratification compensation (NRA-WSE) in [93]. In NRAWSE, the Urlick propagation model brought the RSS-based localization to quality, and the stratification impact is modeled by the use of the ray tracing algorithm, further adopting the Newton-Raphson algorithm for the source localization solution. One of the fundamental problems in UWSNs is to determine the location of the detectors mostly achieved by evaluating the distance between anchor nodes and unknown nodes. Ranging algorithms are generally performed by either assessing the ToA or RSS signal. Previous studies traded underwater with the assumption of straight-line wave propagation with the location of sensors. However, the truth is that, due to the inhomogeneity of the underwater framework, acoustic waves move through a

curved manner. The writers used an analytical relationship [94, 95] that describes the loss in transmission of acoustic waves in the inhomogeneous landscape and then on a relationship basis. A unique algorithm is suggested to estimate the variety between two sensor nodes and show that the underwater source isotropically radiates acoustic noise and uses the RSS, which is drawn from the UWSN's sensors to correctly measure the source node location. Authors describe another sensor model relationship between range, RSS, and the 3D Extended Kalman Filter (EKF) in [96]. RF sensor is based on the underwater medium linearity of the RSSI value. Based on the respective sensor model, the vehicle measures the loudness of the signal and measures the distance to the beacon.

7. Range-Free Algorithm

To use range-free localization algorithms, we do not need to use a variety of bearing information; it only provides a coarse estimation of the node of the sensor position that is distinct from the range-based algorithm. A hybrid localization algorithm with multihop mobile underwater acoustic networks has been suggested by the author in [97] to enhance the effectiveness of the localization scheme in a mobile underwater medium. The sensor nodes in the network are split into multistage nodes for this algorithm and each stage has a distinct localization operation. Both range-based algorithms and range-free algorithms are used to enhance localization precision and decrease communication costs. Moreover, this algorithm does not involve any previous understanding of the velocity of motion that is readily used in an underwater medium. Also, the range-free algorithm is categorized into the hop count-based, area-based algorithm, and centroid algorithms.

7.1. Hop Count-Based Algorithms. The anchor sensor nodes are placed in the hop count-based algorithm along with the boundaries or corners of a square grid. Three algorithms are DV-Hope, solid positioning algorithm, and DHL. The DV-Hope utilizes an average estimation of the spectrum of hope and the counted number of hops to estimate the distance to the anchor node. Robust positioning algorithm is used to raise DV-Hop by inserting an extra refinement step, while DHL may use density consciousness to dynamically rather than statically estimate distance.

For actual deployments where sensor node distribution is more likely in some areas, it is uneven and sparse, such as DHL has been recommended to improve the accuracy of position estimation when the distribution of nodes in the network is not uniform [52]. This program needs taking into account the density of the neighborhood of the node calculates the average hop distance, as well as the wrong facts distance estimates tend to accumulate with increasing path length.

7.2. Area-Based Algorithm. Area-Based Localization Scheme (ALS) and approximate point in a triangle (APIT) are the two area-based algorithms. ALS is a centralized range-free system whose main benefits are the resistance and simplicity

in underwater to the variable sound speed. They can measure the location of a sensor node within a specific operating area and the sensor node clock must be synchronized in time. It presents the most recent algorithm based on ALS. For instance, 3D multipower area localization scheme (3D-MALS) has the function of extending 2D-ALS to 3D, whereas APIT requires a heterogeneous network. Anchors are fitted with high-power transmitters and can accurately acquire location data using GPS coordinates. In [98], the author's used a new technique which is based on Mel Frequency Cepstral Coefficients (MFCCs). The underwater acoustic method is generally nonlinear and very hard to evaluate, so a correct nonlinear algorithm is required. Thus, MFCC is applied to underwater radiated noise extraction characteristics. MFCC is, therefore, an efficient recognition and extraction algorithm.

7.3. Centroid Algorithm. The centroid algorithm is a localization algorithm based on proximity and coarse-grained range-free. The disadvantage of centroid localization algorithm is due to the high localization error because of the centroid formula, where (X_{en}, Y_{en}) is the estimated location of the receiver.

$$X_{en}, Y_{en} = \left(\frac{X_1 + X_2 + X_3 + \dots + X_n}{n}, \frac{Y_1 + Y_2 + Y_3 + \dots + Y_n}{n} \right). \quad (6)$$

For the 3D network application, the centroid algorithm which focuses on node self-localization may not be suitable. A distributed joint establishment control of generic multi-agent robots [99] is capable of underwater medium applications such as multiautonomous surface vehicles. The ASV agent's goal is to keep some institutions in a predefined geometric shape, particularly the formation of symmetric structures. Furthermore, the centroid of this to-be-sustained establishment is to come after a denominated leader agent whose dynamics appear like that of its other followers. A fresh 3D underwater localization algorithm utilizes three floating buoys on the ground called anchor nodes that are fixed with GPS, RF, and acoustic transceivers. A high number of nodes underwater sensors are installed at distinct depths. These can be anchored to the bottom of the ocean and fitted on the surface of the water with floating buoys. These sensor nodes thus have restricted capacity for movement and are referred to as semistationary nodes.

8. Performance Evaluation of Underwater Localization Schemes

In previous sections, we discussed comprehensively the underwater localization schemes and underwater acoustic networks. The underwater localization schemes are analyzed and compared with each other. This section contains the performance evaluation of the abovementioned underwater localization schemes concerning various aspects of localization and underwater communication. The performance evaluation is presented in Table 3.

TABLE 3: Analysis of UASNs and underwater localization algorithms.

Localization algorithms	Selection methodology	Advantages	Drawbacks/issues
CL [41]	Use a control sink.	Locate nodes at both condition: postprocessing or at the end.	Required centralized center.
HL [42]	Apply hydrophones/TDoA.	Adopt standard oceanographic localization issues.	Range is limited.
MAS [45]	Range estimates.	Provide precise localization.	No error estimation is performed.
3D-MASL [46]	Use DET (broadcasting).	Limited energy consumption.	Transmission rate is variable.
ALS [46]	Central sink/RSS.	Reduce energy consumption.	Unable to estimate the exact location.
CL [51]	Automatic localization.	Reduce localization errors.	Valid only for limited nodes.
AAL [53]	ToA/AUV.	Time-synchronized.	Invest more energy.
SL [57]	TDoA.	Required no time synchronization.	Channel modeling error is not estimated.
DNR [58]	GPS/acoustic.	Reduce communication cost.	Do not consider the sensor mobility.
LDB [59]	AUV/3D deployment.	Localization error estimation.	Unable for 3D-free drifting UASN.
UPS/TPS [61]	TDoA/extension of TWSN.	Use for oil, gas, and sea exploration.	Applicable only for outdoor WSN/not for ToA.
WPS [62]	Based on the premise of synchronized clock.	Low energy consumption and low localization latency.	Work only in a finite region.
USP [63]	Use hydrophone stations and GPS nodes.	Work in both 2D and 3D environments.	Nodes reside in the overlapping area while mapping from 2D to 3D.
AFLA [67]	AUV/nodes with a particular device.	No need of anchor nodes.	Only depend on the neighbor nodes, no communication with anchors.
SBRAL [68]	Surface water communication links.	No need for LoS/ToA.	Link quality is not convenient.
SLMP [36]	Surface buoys and anchor nodes.	Reduce communication cost.	Not suitable for dynamic environment.
ToA [70]	Acoustic/targets must be synchronized.	Most frequently used for UASN.	Time synchronization is required.
TDoA [70]	Known transmission time.	Do not depend on the transmission time of source.	High cost and energy consumption.
AoA [70]	Based on the arrival angles.	All unknown nodes can detect incident signal angles.	Ultrasound receiver increases the cost.
RSSI [70]	Depend on the strength of received signal and path loss impact.	Applicable in asynchronous scenarios.	Loss caused by multipath fading.

9. Challenges and Open Issues

UWSNs offer a range of applications from civil, military, and many others. During the localization process, the detected data can only be interpreted usefully when responding to the location of the sensor node, which makes localization a key problem. Thus, GPS receivers are frequently used for obtaining this in terrestrial WSNs; it is infeasible in UWSNs as less propagation of GPS signals in an underwater environment. The most secure method of communication for underwater is acoustic wave communication. Underwater acoustic channels, however, are faces with low high bit error, bandwidth, and high delay in propagation due to severe physical layer circumstances. Observing the current undersea acts, they are often based on complicated suppositions such as time synchronization, as they have exploited the ToA technique for the most part. When AUV reaches the water surface, it gets its coordinates from the GPS; it dives again to a certain depth and performs dead-reckoning for undersea self-localization. The difference between LDB and AAL is that the AUV is traveling above the operating region during the localization procedure and utilizes a directional acoustic transceiver to transmit its position and the angle of the trans-

ceiver beam. Synchronization might be a large challenge in such an atmosphere. The challenges of UWSN are divided into two categories: first, the underwater environment, such as the deployment of reference nodes in the deep sea, node mobility, internode time synchronization, and signal reflection owing to barriers and reflective surfaces. The second is the underwater acoustic channel such as long delay in propagation, multipath fading and shadowing, sound speed variation, low bit rate, heavily unreliable and asymmetric SNR, and asymmetric energy consumption. Thus, by increasing energy consumption resultantly decreases network lifetime and efficiency. Here, we presented some basic challenges and open issues that need to be solved in the recent future.

9.1. Time Synchronization. As discussed in Section 5, time synchronization is the main aspect of underwater localization. The surface sensor nodes are time-synchronized by using GPS or DNR, while the underwater sensor nodes cannot be time-synchronized, and the clocks of underwater nodes are subject to skew and offsets [60].

9.2. Reliability. Reliability is a key point in ensuring reliability in all forms, such as hop-by-hop, data, and end-to-

end reliability. Successfully forwarding and transferring data between participating sensor nodes in the UASN is an important aspect of reliability. Reliability guarantees successful delivery of packets between sensor nodes participating in collaborative processes [100]. The review of this study found that reliability is the most important aspect, but unfortunately, most of the current studies have not considered. Therefore, it is very important to propose a cooperation algorithm that considers this reliability.

9.3. Node Mobility. While it is reasonable to assume that nodes in terrestrial networks remain static, underwater nodes will inevitably drift due to underwater currents, winds, shipping activity, etc. Nodes may drift differently as the oceanic current is spatially dependent. While reference nodes attached to surface buoys can be precisely located through GPS updates, it is difficult to maintain submerged underwater nodes at precise locations. This may affect localization accuracy.

9.4. Efficiency. Efficiency is also a basic aspect in a communication network to provide an efficient cooperative mechanism and to facilitate communication among different nodes. Based on our review of the current algorithms, it has been found that no method takes into account this aspect [100, 101]. Collaborative controlling activities require an efficient method for successful data forwarding and delivery in underwater localization. It is also required to include efficiency in cooperative game techniques to use resources that ensure efficient delivery of information, if not, then the cost of such information delivery will increase, i.e., delays and throughput.

9.5. Sound Speed Variation. Most of the range-based localization techniques assume constant speed underwater sound, and it is depending on the water pressure, salinity, and temperature. Without measuring the sound speed, the accuracy of distance measurements based on ToA approaches may be degraded [60]. For a fair performance comparison of all techniques, they should be evaluated using a common and accurate sound speed scheme.

9.6. Security and Privacy. Most of the researchers do not consider these two points when designing positioning algorithms; however, there is no doubt that they play a key role in underwater localization. Security attacks for underwater localization and countermeasures, as well as the issue of privacy in underwater localization and countermeasures, are discussed in [102]. The sensor node must display certain information to be localized, which can lead to privacy holes. Location privacy is discussed in both the location-related information collection step and the estimation step. These attacks include DoS, range-based, no range estimation attacks, noncooperation, and false advertising information.

10. Conclusion

This paper presents a review of UWSNs, underwater localization, localization techniques, and the existing challenges in the underwater environment. The paper mainly focused on

the approaches recently used in underwater localization. Localization for UWSN is an important problem that attracts considerable interest from scientists working on localization underwater. In this paper, the unique characteristics of UWSN and underwater localization are explained in detail. Furthermore, the paper presented the localization basics, localization architecture, and the techniques used for underwater localization. A variety of underwater localization techniques are discussed and compared with each other based on their application and efficiency as shown in Table 2. Also, a range-based and range-free localization algorithm is discussed which included TDoA, ToA, AoA, and RSSI. Finally, the paper presented the existing challenges and issues in underwater localization and underwater acoustic communication. For short, it is not feasible to say that any particular method of localization is the best for all situations because each one has certain strengths and weaknesses and constancy for a particular situation. The ultimate goal of this review is to encourage and promote new scientists in the region by offering a basis on the so far suggested underwater localization. The field of USNs and localization is growing quickly, and yet many difficulties need to be investigated in the future.

Conflicts of Interest

The authors declare that they have no conflicts of interest.

Acknowledgments

This research was supported by the National Natural Science Foundation of China under Grant 61801166 and supported in part by the Key Research and Development Program of Jiangsu under Grants BE2017071 and BE2017647. This was also supported by the Fundamental Research Funds for the Central Universities under Grant 2019B22214 and in part by the Basic Science Research Program through the National Research Foundation of Korea (NRF) funded by the Ministry of Education under Grant NRF-2018R1D1A1B07043331.

References

- [1] H.-P. Tan, R. Diamant, W. K. G. Seah, and M. Waldmeyer, "A survey of techniques and challenges in underwater localization," *Ocean Engineering*, vol. 38, no. 14-15, pp. 1663–1676, 2011.
- [2] N. Yashwanth and B. R. Sujatha, "Wireless sensor node localization in underwater environment," in *2016 International Conference on Electrical, Electronics, Communication, Computer and Optimization Techniques (ICECCOT)*, Mysuru, India, December 2016.
- [3] M. Isik and O. Akan, "A three dimensional localization algorithm for underwater acoustic sensor networks," *IEEE Transactions on Wireless Communications*, vol. 8, no. 9, pp. 4457–4463, 2009.
- [4] D. Park, J. Jung, K. Kwak, W. K. Chung, and J. Kim, "3D underwater localization using EM waves attenuation for UUV docking," in *2017 IEEE Underwater Technology (UT)*, Busan, South Korea, 2017.

- [5] M. Raja, "Application of cognitive radio and interference cancellation in the L-band based on future air-to-ground communication systems," *Digital Communications and Networks*, vol. 5, no. 2, pp. 111–120, 2019.
- [6] M. M. K. Inamullah, I. Khan, and S. K. Haider, "Compensation of magnetic sensor with electric compass," in *2017 7th IEEE International Symposium on Microwave, Antenna, Propagation, and EMC Technologies (MAPE)*, Xi'an, China, October 2017.
- [7] D. Park, K. Kwak, J. Kim, and W. K. Chung, "3D underwater localization scheme using EM wave attenuation with a depth sensor," in *2016 IEEE International Conference on Robotics and Automation (ICRA)*, Stockholm, Sweden, May 2016.
- [8] C. Kim, S. Lee, and K. Kim, "3D underwater localization with hybrid ranging method for near-sea marine monitoring," in *2011 IFIP 9th International Conference on Embedded and Ubiquitous Computing*, Melbourne, VIC, Australia, October 2011.
- [9] M. Erol-Kantarci, H. T. Mouftah, and S. Oktug, "A survey of architectures and localization techniques for underwater acoustic sensor networks," *IEEE Communications Surveys & Tutorials*, vol. 13, no. 3, pp. 487–502, 2011.
- [10] S. Kaivonen and E. C.-H. Ngai, "Real-time air pollution monitoring with sensors on city bus," *Digital Communications and Networks*, 2019.
- [11] J. Heidemann, W. Ye, J. Wills, A. Syed, and Y. Li, "Research challenges and applications for underwater sensor networking," in *IEEE Wireless Communications and Networking Conference, 2006. WCNC 2006*, Las Vegas, NV, USA, 2006.
- [12] M. Goswami and H. M. Kwon, "Submillimeter wave communication versus millimeter wave communication," *Digital Communications and Networks*, 2019.
- [13] I. Ullah, Y. Liu, X. Su, and P. Kim, "Efficient and accurate target localization in underwater environment," *IEEE Access*, vol. 7, pp. 101415–101426, 2019.
- [14] D. Wang, L. Yang, and X. Cheng, "Underwater localization and tracking based on semi-definite programming," in *2013 IEEE International Conference on Signal Processing, Communication and Computing (ICSPCC 2013)*, KunMing, China, 2013.
- [15] H. Yu and W. Li-Hua, "Underwater localization iterative algorithm based on geomagnetic anomaly inversion," in *2012 International Conference on Industrial Control and Electronics Engineering*, Xi'an, China, 2012.
- [16] M. Erol, L. F. M. Vieira, A. Caruso, F. Paparella, M. Gerla, and S. Oktug, "Multi stage underwater sensor localization using mobile beacons," in *2008 Second International Conference on Sensor Technologies and Applications (sensorcomm 2008)*, Cap Esterel, France, 2008.
- [17] Y. Y. Al-Aboosi and A. Z. Sha'ameri, "Improved underwater signal detection using efficient time-frequency de-noising technique and pre-whitening filter," *Applied Acoustics*, vol. 123, pp. 93–106, 2017.
- [18] P. Carroll, K. Domrese, H. Zhou, S. Zhou, and P. Willett, "Localization of mobile nodes in an underwater distributed antenna system," in *Proceedings of the International Conference on Underwater Networks %Systems - WUWNET '14*, Rome, Italy, 2014.
- [19] M. M. K. Inam Ullah, S. H. E. N. G. Gao Ming, and Z. Khan, "A survey on underwater localization, localization techniques and its algorithms," in *Proceedings of the 3rd Annual International Conference on Electronics, Electrical Engineering and Information Science (EEEIS 2017)*, 2017.
- [20] T. Rossby, D. Dorson, and J. Fontaine, "The RAFOS system," *Journal of Atmospheric and Oceanic Technology*, vol. 3, no. 4, pp. 672–679, 1986.
- [21] A. Turetta, G. Casalino, E. Simetti, A. Sperinde, and S. Torelli, "Analysis of the accuracy of a LBL-based underwater localization procedure," in *2014 Oceans - St. John's*, St. John's, NL, Canada, 2014.
- [22] M. Jouhari, K. Ibrahimi, H. Tembine, and J. Ben-Othman, "Underwater wireless sensor networks: a survey on enabling technologies, localization protocols, and internet of underwater things," *IEEE Access*, vol. 7, pp. 96879–96899, 2019.
- [23] Y. Tanaka, Y. Nishida, J. Ahn, and K. Ishii, "Underwater vehicle localization considering the effects of its oscillation," in *2019 IEEE Underwater Technology (UT)*, Kaohsiung, Taiwan, Taiwan, 2019.
- [24] X.-y. Sun, L. Nan-song, and X. Liu, "Three-dimensional passive localization method for underwater target using regular triangular array," in *2019 13th Symposium on Piezoelectricity, Acoustic Waves and Device Applications (SPAWDA)*, Harbin, China, 2019.
- [25] J. Yan, Z. Xu, Y. Wan, C. Chen, and X. Luo, "Consensus estimation-based target localization in underwater acoustic sensor networks," *International Journal of Robust and Non-linear Control*, vol. 27, no. 9, pp. 1607–1627, 2017.
- [26] H. Yang and B. Sikdar, "A mobility based architecture for underwater acoustic sensor networks," in *IEEE GLOBECOM 2008 - 2008 IEEE Global Telecommunications Conference*, New Orleans, LO, USA, 2008.
- [27] A. Wang, J. Shen, C. Wang, H. Yang, and D. Liu, "Anonymous data collection scheme for cloud-aided mobile edge networks," *Digital Communications and Networks*, 2019.
- [28] N. Cochard, J. L. Lacoume, P. Arzelies, and Y. Gabillet, "Underwater acoustic noise measurement in test tanks," *IEEE Journal of Oceanic Engineering*, vol. 25, no. 4, pp. 516–522, 2000.
- [29] D. Pompili, T. Melodia, and I. F. Akyildiz, "Three-dimensional and two-dimensional deployment analysis for underwater acoustic sensor networks," *Ad Hoc Networks*, vol. 7, no. 4, pp. 778–790, 2009.
- [30] W. Lin, D. Li, Y. Tan, J. Chen, and T. Sun, "Architecture of underwater acoustic sensor networks: a survey," in *2008 First International Conference on Intelligent Networks and Intelligent Systems*, Wuhan, China, 2008.
- [31] K. M. Awan, P. A. Shah, K. Iqbal, S. Gillani, W. Ahmad, and Y. Nam, "Underwater wireless sensor networks: a review of recent issues and challenges," *Wireless Communications and Mobile Computing*, vol. 2019, Article ID 6470359, 20 pages, 2019.
- [32] N. Saeed, A. Celik, T. Y. Al-Naffouri, and M.-S. Alouini, "Underwater optical wireless communications, networking, and localization: a survey," *Ad Hoc Networks*, vol. 94, p. 101935, 2019.
- [33] J. H. Cui, J. Kong, M. Gerla, and S. Zhou, "Challenges: building scalable and distributed underwater wireless sensor networks (UWSNs) for aquatic applications," *Channels*, vol. 45, no. 4, pp. 22–35, 2005.
- [34] C. Lv, S. Wang, M. Tan, and L. Chen, "UA-MAC: an underwater acoustic channel access method for dense mobile

- underwater sensor networks,” *International Journal of Distributed Sensor Networks*, vol. 10, no. 2, 2014.
- [35] K. Chen, Y. Zhou, and J. He, “A localization scheme for underwater wireless sensor networks,” *International Journal of Advanced Science and Technology*, vol. 4, 2009.
 - [36] Z. Zhou, Z. Peng, J.-H. Cui, Z. Shi, and A. Bagtzoglou, “Scalable localization with mobility prediction for underwater sensor networks,” *IEEE Transactions on Mobile Computing*, vol. 10, no. 3, pp. 335–348, 2011.
 - [37] M. Erol-Kantarci, S. Oktug, L. Vieira, and M. Gerla, “Performance evaluation of distributed localization techniques for mobile underwater acoustic sensor networks,” *Ad Hoc Networks*, vol. 9, no. 1, pp. 61–72, 2011.
 - [38] S. Capkun, M. Hamdi, and J.-P. Hubaux, “GPS-free positioning in mobile ad hoc networks,” *Cluster Computing*, vol. 5, no. 2, pp. 157–167, 2002.
 - [39] A. Caruso, S. Chessa, S. De, and A. Urpi, “GPS free coordinate assignment and routing in wireless sensor networks,” in *Proceedings IEEE 24th Annual Joint Conference of the IEEE Computer and Communications Societies*, Miami, FL, USA, 2005.
 - [40] P. M. Ameer and L. Jacob, “Underwater localization using stochastic proximity embedding and multi-dimensional scaling,” *Wireless Networks*, vol. 19, no. 7, pp. 1679–1690, 2013.
 - [41] Y. Zhou, K. Chen, J. He, J. Chen, and A. Liang, “A hierarchical localization scheme for large scale underwater wireless sensor networks,” in *2009 11th IEEE International Conference on High Performance Computing and Communications*, Seoul, South Korea, 2009.
 - [42] V. M. Janik, S. M. Parijs, and P. M. Thompson, “A two-dimensional acoustic localization system for marine mammals,” *Marine Mammal Science*, vol. 16, no. 2, pp. 437–447, 2000.
 - [43] T. Bian, R. Venkatesan, and C. Li, “Design and evaluation of a new localization scheme for underwater acoustic sensor networks,” in *GLOBECOM 2009 - 2009 IEEE Global Telecommunications Conference*, Honolulu, HI, USA, 2009.
 - [44] T. Bian, R. Venkatesan, and C. Li, “An improved localization method using error probability distribution for underwater sensor networks,” in *2010 IEEE International Conference on Communications*, Cape Town, South Africa, 2010.
 - [45] D. Mirza and C. Schurgers, “Motion-aware self-localization for underwater networks,” in *Proceedings of the third ACM international workshop on Wireless network testbeds, experimental evaluation and characterization - WuWNet '08*, New York, NY, USA, 2008.
 - [46] V. Chandrasekhar and W. Seah, “An area localization scheme for underwater sensor networks,” in *OCEANS 2006 - Asia Pacific*, Singapore, 2006.
 - [47] Y. Zhou, B. J. Gu, K. Chen, J. B. Chen, and H. B. Guan, “An range-free localization scheme for large scale underwater wireless sensor networks,” *Journal of Shanghai Jiaotong University*, vol. 14, no. 5, pp. 562–568, 2009.
 - [48] W. Cheng, A. Y. Teymorian, L. Ma, X. Cheng, X. Lu, and Z. Lu, “Underwater localization in sparse 3D acoustic sensor networks,” in *2008 Proceedings IEEE INFOCOM - The 27th Conference on Computer Communications*, Phoenix, AZ, USA, 2008.
 - [49] A. K. Othman, A. E. Adams, and C. C. Tsimenidis, “Node discovery protocol and localization for distributed underwater acoustic networks,” in *Advanced Int'l Conference on Telecommunications and Int'l Conference on Internet and Web Applications and Services (AICT-ICIW'06)*, Guadelope, French Caribbean, French Caribbean, 2006.
 - [50] A.-K. Othman, “GPS-less localization protocol for underwater acoustic networks,” in *2008 5th IFIP International Conference on Wireless and Optical Communications Networks (WOCN '08)*, Surabaya, Indonesia, 2008.
 - [51] D. Mirza and C. Schurgers, “Collaborative localization for fleets of underwater drifters,” in *OCEANS 2007*, Vancouver, BC, Canada, 2007.
 - [52] V. Chandrasekhar, W. K. Seah, Y. S. Choo, and H. V. Ee, “Localization in underwater sensor networks: survey and challenges,” in *Proceedings of the 1st ACM international workshop on Underwater networks*, pp. 33–40, Los Angeles, CA, USA, September 2006.
 - [53] M. Erol, L. F. M. Vieira, and M. Gerla, “AUV-aided localization for underwater sensor networks,” in *International Conference on Wireless Algorithms, Systems and Applications (WASA 2007)*, Chicago, IL, USA, 2007.
 - [54] D. D. Palma, F. Arrichiello, G. Parlange, and G. Indiveri, “Underwater localization using single beacon measurements: observability analysis for a double integrator system,” *Ocean Engineering*, vol. 142, pp. 650–665, 2017.
 - [55] Z. Peng, J.-H. Cui, B. Wang, K. Ball, and L. Freitag, “An underwater network testbed: design, implementation and measurement,” in *Proceedings of the second workshop on Underwater networks - WuWNet '07*, Montreal, Quebec, Canada, 2007.
 - [56] H. Luo, Y. Zhao, Z. Guo, S. Liu, P. Chen, and L. M. Ni, “UDB: using directional beacons for localization in underwater sensor networks,” in *2008 14th IEEE International Conference on Parallel and Distributed Systems*, Melbourne, VIC, Australia, 2008.
 - [57] X. Cheng, H. Shu, Q. Liang, and D. H.-C. Du, “Silent positioning in underwater acoustic sensor networks,” *IEEE Transactions on Vehicular Technology*, vol. 57, no. 3, pp. 1756–1766, 2008.
 - [58] M. Erol, L. F. M. Vieira, and M. Gerla, “Localization with Dive'N'Rise (DNR) beacons for underwater acoustic sensor networks,” in *Proceedings of the second workshop on Underwater networks - WuWNet '07*, New York, NY, USA, 2007.
 - [59] H. Luo, Z. Guo, W. Dong, F. Hong, and Y. Zhao, “LDB: localization with directional beacons for sparse 3D underwater acoustic sensor networks,” *Journal of Networks*, vol. 5, no. 1, 2010.
 - [60] J. Luo, L. Fan, S. Wu, and X. Yan, “Research on localization algorithms based on acoustic communication for underwater sensor networks,” *Sensors*, vol. 18, no. 2, p. 67, 2018.
 - [61] X. Cheng, A. Thaeler, G. Xue, and D. Chen, “TPS: a time-based positioning scheme for outdoor wireless sensor networks,” in *IEEE INFOCOM 2004*, Hong Kong, China, 2004.
 - [62] H.-P. Tan, A. F. Gabor, Z. A. Eu, and W. K. G. Seah, “A wide coverage positioning system (WPS) for underwater localization,” in *2010 IEEE International Conference on Communications*, Cape Town, South Africa, 2010.
 - [63] X. Tan and J. Li, “Cooperative positioning in underwater sensor networks,” *IEEE Transactions on Signal Processing*, vol. 58, no. 11, pp. 5860–5871, 2010.
 - [64] B. Fu, F. Zhang, M. Ito, Y. Watanabe, and T. Aoki, “Development of a new underwater positioning system based on sensor network,” *Artificial Life and Robotics*, vol. 13, no. 1, pp. 45–49, 2008.

- [65] I. X. Gao, F. Zhang, and M. Ito, "Underwater acoustic positioning system based on propagation loss and sensor network," in *2012 Oceans – Yeosu*, Yeosu, South Korea, 2012.
- [66] D. Moreno, A. M. Pascoal, A. Alcocer, and J. Aranda, "Optimal sensor placement for underwater target positioning with noisy range measurements," *IFAC Proceedings Volumes*, vol. 43, no. 20, pp. 85–90, 2010.
- [67] Y. Guo and Y. Liu, "Localization for anchor-free underwater sensor networks," *Computers & Electrical Engineering*, vol. 39, no. 6, pp. 1812–1821, 2013.
- [68] L. Emokpae and M. Younis, "Surface based anchor-free localization algorithm for underwater sensor networks," in *2011 IEEE International Conference on Communications (ICC)*, Kyoto, Japan, 2011.
- [69] K. Ishii and N. Sato, "GPS-free host approaching in mobile ad-hoc networks," in *2013 Seventh International Conference on Innovative Mobile and Internet Services in Ubiquitous Computing*, Taichung, Taiwan, 2013.
- [70] Q. Fengzhong, W. Shiyuan, W. Zhihui, and L. Zubin, "A survey of ranging algorithms and localization schemes in underwater acoustic sensor network," *China Communications*, vol. 13, no. 3, pp. 66–81, 2016.
- [71] Y. Guo, X. Kang, Q. Han, and J. Wang, "A localization algorithm for underwater wireless sensor networks based on ranging correction and inertial coordination," *KSII Transactions on Internet and Information Systems*, vol. 13, 2019.
- [72] M. Zhou, Z. Zhong, and X. Fang, "Sensor-target geometry for hybrid bearing/range underwater localization," *IFAC Proceedings Volumes*, vol. 46, no. 20, pp. 724–729, 2013.
- [73] J. Luo and L. Fan, "A two-phase time synchronization-free localization algorithm for underwater sensor networks," *Sensors*, vol. 17, no. 4, p. 726, 2017.
- [74] S. Poursheikhali and H. Zamiri-Jafarian, "TDOA based target localization in inhomogenous underwater wireless sensor network," in *2015 5th International Conference on Computer and Knowledge Engineering (ICCKE)*, Mashhad, Iran, 2015.
- [75] R. M. Vaghefi and R. M. Buehrer, "Asynchronous time-of-arrival-based source localization," in *2013 IEEE International Conference on Acoustics, Speech and Signal Processing*, Vancouver, BC, Canada, 2013.
- [76] Y. Zou and Q. Wan, "Asynchronous time-of-arrival-based source localization with sensor position uncertainties," *IEEE Communications Letters*, vol. 20, no. 9, pp. 1860–1863, 2016.
- [77] I. Ullah, J. Chen, X. Su, C. Esposito, and C. Choi, "Localization and detection of targets in underwater wireless sensor using distance and angle based algorithms," *IEEE Access*, vol. 7, pp. 45693–45704, 2019.
- [78] R. Diamant and L. Lampe, "Underwater localization with time synchronization and propagation speed uncertainties," *IEEE Transactions on Mobile Computing*, vol. 12, no. 7, pp. 1257–1269, 2013.
- [79] J. Yi, D. Mirza, R. Kastner, C. Schurgers, P. Roberts, and J. Jaffe, "ToA-TS: time of arrival based joint time synchronization and tracking for mobile underwater systems," *Ad Hoc Networks*, vol. 34, pp. 211–223, 2015.
- [80] W. A. P. van Kleunen, K. C. H. Blom, N. Meratnia, A. B. J. Kokkeler, P. J. M. Havinga, and G. J. M. Smit, "Underwater localization by combining time-of-flight and direction-of-arrival," in *OCEANS 2014 – TAIPEI*, Taipei, Taiwan, 2014.
- [81] D. Mirza, P. Naughton, C. Schurgers, and R. Kastner, "Real-time collaborative tracking for underwater networked systems," *Ad Hoc Networks*, vol. 34, pp. 196–210, 2015.
- [82] J. Liu, Z. Wang, J. H. Cui, S. Zhou, and B. Yang, "A joint time synchronization and localization design for mobile underwater sensor networks," *IEEE Transactions on Mobile Computing*, vol. 15, no. 3, pp. 530–543, 2016.
- [83] P. Carroll, S. Zhou, H. Zhou, J.-H. Cui, and P. Willett, "Underwater localization based on multicarrier waveforms," in *OCEANS 2010 MTS/IEEE SEATTLE*, Seattle, WA, USA, 2010.
- [84] P. Carroll, S. Zhou, H. Zhou, X. Xu, J. H. Cui, and P. Willett, "Underwater localization and tracking of physical systems," *Journal of Electrical and Computer Engineering*, vol. 2012, Article ID 683919, 11 pages, 2012.
- [85] P. Rong and M. L. Sichitiu, "Angle of arrival localization for wireless sensor networks," in *2006 3rd Annual IEEE Communications Society on Sensor and Ad Hoc Communications and Networks*, Reston, VA, USA, 2006.
- [86] J. B. Andersen and K. I. Pedersen, "Angle-of-arrival statistics for low resolution antennas," *IEEE Transactions on Antennas and Propagation*, vol. 50, no. 3, pp. 391–395, 2002.
- [87] A. Mesmoudi, M. Feham, and N. Labraoui, "Wireless sensor networks localization algorithms: a comprehensive survey," *International journal of Computer Networks & Communications*, vol. 5, no. 6, pp. 45–64, 2013.
- [88] Q. H. Spencer, B. D. Jeffs, M. A. Jensen, and A. L. Swindlehurst, "Modeling the statistical time and angle of arrival characteristics of an indoor multipath channel," *IEEE Journal on Selected Areas in Communications*, vol. 18, no. 3, pp. 347–360, 2000.
- [89] K. Tong, X. Wang, A. Khabbazbasmenj, and A. Dounavis, "RSS-based localization in obstructed environment with unknown path loss exponent," in *2014 IEEE 80th Vehicular Technology Conference (VTC2014-Fall)*, Vancouver, BC, Canada, 2014.
- [90] T. L. N. Nguyen and Y. Shin, "An efficient RSS localization for underwater wireless sensor networks," *Sensors*, vol. 19, no. 14, p. 3105, 2019.
- [91] T. Xu, Y. Hu, B. Zhang, and G. Leus, "RSS-based sensor localization in underwater acoustic sensor networks," in *2016 IEEE International Conference on Acoustics, Speech and Signal Processing (ICASSP)*, Shanghai, China, 2016.
- [92] M. Hosseini, H. Chizari, C. K. Soon, and R. Budiarto, "RSS-based distance measurement in underwater acoustic sensor networks: an application of the Lambert W function," in *2010 4th International Conference on Signal Processing and Communication Systems*, Gold Coast, QLD, Australia, 2010.
- [93] B. Zhang, H. Wang, T. Xu, L. Zheng, and Q. Yang, "Received signal strength-based underwater acoustic localization considering stratification effect," in *OCEANS 2016 – Shanghai*, Shanghai, China, 2016.
- [94] S. Poursheikhali and H. Zamiri-Jafarian, "Ranging in underwater wireless sensor network: received signal strength approach," in *2016 IEEE Wireless Communications and Networking Conference*, Doha, Qatar, 2016.
- [95] Y.-s. Yan, H.-y. Wang, X.-h. Shen, F.-z. Yang, and Z. Chen, "Efficient convex optimization method for underwater passive source localization based on RSS with WSN," in *2012 IEEE International Conference on Signal Processing, Communication and Computing (ICSPCC 2012)*, Hong Kong, China, 2012.

- [96] D. Park, J. Kim, and W. K. Chung, "Simulated 3D underwater localization based on RF sensor model using EKF," in *2011 8th International Conference on Ubiquitous Robots and Ambient Intelligence (URAI)*, Incheon, South Korea, 2011.
- [97] J. Gao, X. Shen, and H. Wang, "A hybrid localization algorithm for multi-hop mobile underwater acoustic networks," *Journal of Marine Science and Technology*, vol. 22, no. 3, pp. 494–500, 2017.
- [98] W. Wang, S. Li, J. Yang, Z. Liu, and W. Zhou, "Feature extraction of underwater target in auditory sensation area based on MFCC," in *2016 IEEE/OES China Ocean Acoustics (COA)*, Harbin, China, 2016.
- [99] T. S. Tiang and M. N. Mahyuddin, "Cooperative formation control algorithm of a generic multi-agent system applicable for multiautonomous surface vehicles," in *2016 IEEE International Conference on Underwater System Technology: Theory and Applications (USYS)*, Penang, Malaysia, 2016.
- [100] D. Muhammed, M. Anisi, M. Zareei, C. Vargas-Rosales, and A. Khan, "Game theory-based cooperation for underwater acoustic sensor networks: taxonomy, review, research challenges and directions," *Sensors*, vol. 18, no. 2, p. 425, 2018.
- [101] S. Ashraf, M. Gao, Z. Chen, S. K. Haider, and Z. Raza, "Efficient node monitoring mechanism in WSN using contikimac protocol," *International Journal of Advanced Computer Science and Applications*, vol. 8, no. 11, pp. 429–437, 2017.
- [102] H. Li, Y. He, X. Cheng, H. Zhu, and L. Sun, "Security and privacy in localization for underwater sensor networks," *IEEE Communications Magazine*, vol. 53, no. 11, pp. 56–62, 2015.

Research Article

Online Measuring and Size Sorting for Perillae Based on Machine Vision

Bo Zhao,¹ Ye Wang,¹ Jun Fu ,^{1,2} Rongqiang Zhao ,² Yashuo Li,¹ Xin Dong,¹ Chengxu Lv,¹ and Hanlu Jiang¹

¹Chinese Academy of Agricultural Mechanization Sciences, Beijing 100083, China

²College of Biological and Agricultural Engineering, Jilin University, Changchun 130022, China

Correspondence should be addressed to Jun Fu; fu_jun@jlu.edu.cn

Received 18 September 2019; Accepted 31 October 2019; Published 13 January 2020

Guest Editor: Yuan Li

Copyright © 2020 Bo Zhao et al. This is an open access article distributed under the Creative Commons Attribution License, which permits unrestricted use, distribution, and reproduction in any medium, provided the original work is properly cited.

Perillae has attracted an increasing interest of study due to its wide usage for medicine and food. Estimating quality and maturity of a perillae requires the information with respect to its size. At present, measuring and sorting the size of perillae mainly depend on manual work, which is limited by low efficiency and unsatisfied accuracy. To address this issue, in this study, we develop an approach based on the machine vision (MV) technique for online measuring and size sorting. The geometrical model and the corresponding mathematical model are built for perillae and imaging, respectively. Based on the built models, the measuring and size sorting method is proposed, including image binarization, key point determination, information matching, and parameter estimation. Experimental results demonstrate that the average time consumption for a captured image, the average measuring error, the variance of measuring error, and the overall sorting accuracy are 204.175 ms, 1.48 mm, 0.07 mm, and 93%, respectively, implying the feasibility and satisfied accuracy of the proposed approach.

1. Introduction

Perillae is widely distributed throughout Asia, and it has attracted an increasing interest in the field of medicine and pharmacy. Perillae has been applied for bacteriostatic, detoxifying, antitussive, and phlegm for thousands of years in traditional Chinese medicine. Recently, more attentions have been paid to the study with respect to perillae, including the perillae herba ethanolic [1], the luteolin [2], and the rosmarinic acid [3]. Besides, perillae is also a popular food in countries such as China, Japan, and Korea. The size of perillae indicates its quality and maturity that closely relates to its medical and edible value. Hence, it is of great significance to measure and sort the size of perillae in advance. At present, measuring and sorting the size of perillae mainly depend on manual work, which is of low efficiency and unsatisfied accuracy. Therefore, it is valuable to develop an approach for accurate online measurement and sort of perillae.

Machine vision (MV) is the technique to provide imaging-based automatic inspection [4–6], and it has been widely used in the fields of industry, such as object detection and robot guidance [7, 8]. For the applications in agriculture, previous work has explored into various crops [9, 10]. In [11], a compact machine vision system based on hyperspectral imaging and machine learning is presented to detect aflatoxin in chili pepper. In [12], a hierarchical grading method is applied for real-time defect detection and size sorting of potatoes. In [13], a study is conducted to predict ripening quality in mangoes using RGB images, for which the hierarchical clustering method is employed to classify the ripening period into five stages based on quality parameters. In [14], the authors combine the MV and the support vector machine to develop an intelligent system for sorting of peeled pistachio kernels and shells. In [15], Sabliov et al. develop an MV-based method to measure volume and surface area of ellipsoidal agricultural products by regarding the objects as

the sum of superimposed elementary frustums of right circular cones. In [16], Yao et al. develop real-time detection instrumentation for aflatoxin-contaminated corn using a narrow-band fluorescence index. In [17], Pedreschi et al. present an inexpensive computer vision system for measuring the color of a highly heterogeneous food material such as potato chips. In [18], Huang et al. propose an approach for identification of defect pleurotus geesteranus based on computer vision. In [19], Sun et al. develop a machine vision system and the dynamic weighing system for the measurement of egg external physical characteristic and weight, such that the nondestructive method for online estimation of egg freshness is achieved. Additionally, a set of studies have been conducted on measurement, cabbage [20], flower mushroom [21], cherry [22], litchi [23], and other agricultural products [24–29].

However, the automatic online detection of perillae has not been explored till now. The geometry model and the corresponding mathematical model of perillae used for automatic detection have not been built yet. The size sorting of perillae still requires manual work. To address this issue, in this study, we develop a novel approach for online measuring and size sorting of perillae. A charge-coupled device (CCD) camera is employed to acquire the images of perillae in the lighting box, and the MV method is proposed for image processing. The contributions of this study can be summarized as follows.

- (1) We build the general geometry model of perillae and the corresponding mathematical model for image processing
- (2) We propose the MV-based method for accurate online measuring and size sorting of perillae under the proposed models
- (3) We develop the practical system for our theoretical method, the feasibility and accuracy of which are verified by the experimental results

The remainder of this paper is organized as follows. Section 2 introduces the proposed geometry model and mathematical model. Section 3 provides the MV-based online measuring method. Section 4 presents the experimental results and analysis. Section 5 concludes this paper.

2. Geometry and Mathematical Models

2.1. Geometry Model. Figure 1 shows a typical perillae for medical and food usage. The notation L_u is used to denote the length of a perillae, i.e., the maximum size of perillae leaf. We mainly consider the length between P_A and P_B as it is the useful part of perillae, regardless of the medical or food usage. The length between P_B and P_C , i.e., the length of perillae, is not taken into the measurement.

Figure 2 presents the sorting principle for the size of perillae. In this study, the sizes are divided into four grades according to L_u . As shown in Figure 2, the first grade is expressed as “Spec M” with the size of $7 \text{ cm} \leq L_u < 8.5 \text{ cm}$, denoting the smallest perillae. The second grade, “Spec

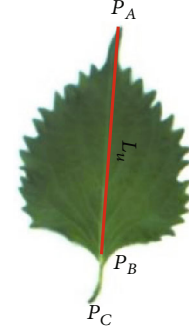


FIGURE 1: Geometry model of perillae where P_A , P_B , and P_C represent the apex of perillae, the separation point of leaf and petiole, and the endpoint of petiole, respectively.

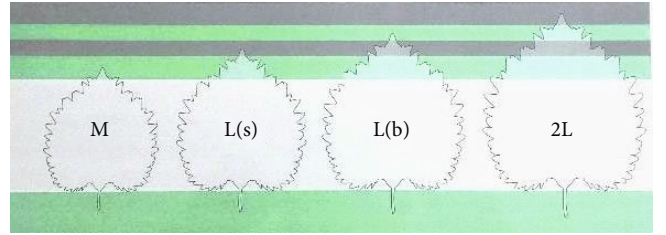


FIGURE 2: Classification of perillae sizes.

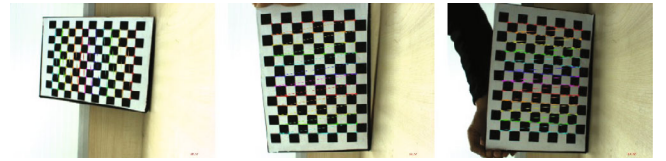


FIGURE 3: Classification of perillae sizes.

L(s),” and the third grade, “Spec L(b),” are determined by $8.5 \text{ cm} \leq L_u < 9.5 \text{ cm}$ and $9.5 \text{ cm} \leq L_u < 10.5 \text{ cm}$, respectively. The fourth grade, expressed as “Spec 2M,” is used to represent the largest size, given by $10.5 \text{ cm} \leq L_u < 12 \text{ cm}$.

2.2. Mathematical Model. Next, we provide the mathematical model for imaging of perillae. The camera used in this study was calibrated before it is employed for imaging. As shown in Figure 3, we captured 20 chessboard images with different poses and then utilized the calibration tool in the OpenCV to calibrate the camera.

Let u , v , and w denote the horizontal coordinate, the vertical coordinate, and the position perpendicular to the chessboard in the camera coordinate, respectively, and let x , y , and z denote the corresponding coordinates in the world coordinate. The calibration results demonstrate the distortion error, and the reprojection error can be ignored. Assume $M(x, y, z)$ is a pixel in the world coordinate system, and this pixel is then projected into the camera coordinate system, expressed



FIGURE 4: Image binarization.

as $m(u, v)$. Let \mathbf{G} be the intrinsic matrix of the used camera. Based on the used calibration tool, the transformation between the world coordinate system and the camera coordinate system can be expressed as

$$\begin{bmatrix} u \\ v \\ w \end{bmatrix} = \mathbf{G} \begin{bmatrix} x \\ y \\ z \end{bmatrix}. \quad (1)$$

The matrix \mathbf{G} is obtained through the calibration, and the result is

$$\mathbf{G} = \begin{bmatrix} \frac{1}{\alpha_x} & 0 & \frac{1}{\beta_x} \\ 0 & \frac{1}{\alpha_y} & \frac{1}{\beta_y} \\ 0 & 0 & 1 \end{bmatrix} = \begin{bmatrix} \frac{1}{1345.538} & 0 & \frac{1}{606.253} \\ 0 & \frac{1}{1345.538} & \frac{1}{470.283} \\ 0 & 0 & 1 \end{bmatrix}. \quad (2)$$

By combining the geometrical model and (2), we can rewrite the size of perillae as follows:

$$\begin{aligned} L_u &= \sqrt{(p_{A,x} - p_{B,x})^2 + (p_{A,y} - p_{B,y})^2} \\ &= \sqrt{\left(\frac{q_{A,x} - q_{B,x}}{\alpha_x}\right)^2 + \left(\frac{q_{A,y} - q_{B,y}}{\alpha_y}\right)^2}, \end{aligned} \quad (3)$$

where $p_{A,x}$, $p_{A,y}$, $p_{B,x}$, and $p_{B,y}$ are the coordinates of points P_A and P_B in the world coordinate system and $q_{A,x}$, $q_{A,y}$, $q_{B,x}$, and $q_{B,y}$ are the coordinates of points P_A and P_B in the image coordinate system. Obviously, the required size can be calculated out directly if parameter z and the coordinates of P_A and P_B are known. Hence, we introduce the proposed method to determine this information in the next section.

3. Method for Measuring Perillae

In this section, we provide the proposed method for measuring and size sorting of perillae based on the MV and the proposed models. The method is composed of the following steps, binarizing the original image, determining the positions of P_A and P_B , matching information, and estimating parameter z .

3.1. Image Binarization. Figure 4(a) presents the original image of perillae. The image should be binarized before it is used for measuring. The binarization principle is given by

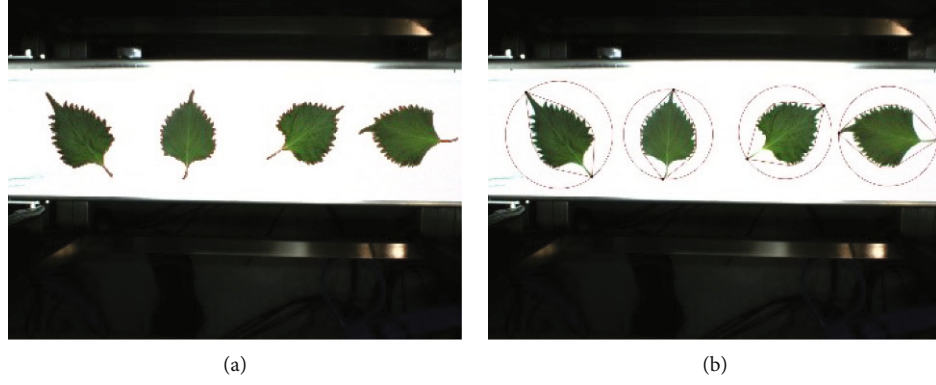
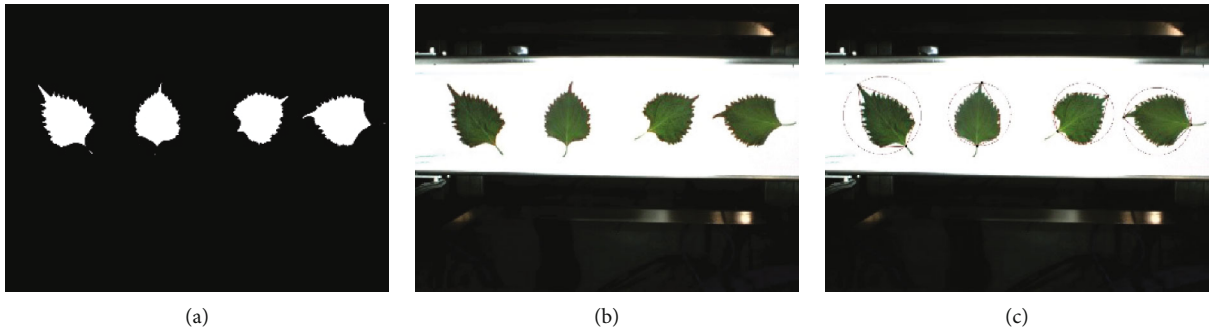
$$j(x, y) = \begin{cases} 255, & 380 \leq y \leq 690, h_b < 180, h_r < 220, \\ 0, & \text{otherwise,} \end{cases} \quad (4)$$

where $j(x, y)$ is the value of the pixel (x, y) in the binarized image. The depth of the image is 8 bits, and therefore, the value of white pixels is set to 255. As indicated in (4), a pixel is determined to be white as long as $380 \leq y \leq 690$, $h_b < 180$, and $h_r < 220$, where h_b and h_r are the values of the pixel in the blue channel and the red channel, respectively. The first condition, $380 \leq y \leq 690$, ensures that the background is set to be black, and only the area containing perillae is considered. The second and the third conditions are utilized to determine whether a pixel belongs to the area of perillae. The binarized image is shown as Figure 4(b).

3.2. Search for P_A . We first derive the contour from the binarized image. The strategy is to set the thresholds for the largest and the smallest areas of the perillae. Thus, the areas that satisfy the constraint of thresholds are selected, and their contours are regarded as the contours of perillae. This process can be expressed as

$$cjr_i = \begin{cases} 1, & 6000 < A_i < 30000, \\ 0, & \text{otherwise,} \\ 1 \leq i \leq N \end{cases} \quad (5)$$

where N denotes the total number of contours in the binarized image, A_i denotes the area of the i^{th} contours, and cjr_i

FIGURE 5: Determination of P_A .FIGURE 6: Determination of P_B .

is the judging result. Then, the minimum enclosing circle and the convex hull of each perillae can be obtained. These perillae are labelled as 1, 2, 3, and 4 from left to right based on the following judgement:

$$pjr_j = \begin{cases} 1, & 1 \leq c_{j,x} \leq 320, \\ 2, & 321 \leq c_{j,x} \leq 640, \\ 3, & 641 \leq c_{j,x} \leq 960, \\ 4, & 961 \leq c_{j,x} \leq 1280, \\ 1 \leq j \leq \text{Num1}, \end{cases} \quad (6)$$

where pjr_j is the judgement for each position of perillae, $c_{j,x}$ denotes the horizontal coordinate of the center of the j^{th} enclosing circle, and “Num1” denotes the amount of perillae in the captured image. The results are displayed in Figure 5(b) and are saved as “Pos1.”

Finally, we utilize the following strategy to find the endpoints of the l^{th} contours, written as $p_{11,l}$ and $p_{12,l}$:

$$p_{11,l} = \arg \min_{cp_{l,k}} \text{abs} \left(\sqrt{(cp_{l,k,x} - cc_{l,x})^2 + (cp_{l,k,y} - cc_{l,y})^2} - r_l \right), \quad (7)$$

$$1 \leq l \leq \text{Num1}, 1 \leq k \leq m_l,$$

$$p_{12,l} = \arg \min_{cp_{l,k}} \sqrt{(cp_{l,k,x} - p_{11,l,x})^2 + (cp_{l,k,y} - p_{11,l,y})^2}, \quad (8)$$

$$1 \leq l \leq \text{Num1}, 1 \leq k \leq m_l - 1,$$

where $cp_{l,k}$ denotes the k^{th} pixel in the l^{th} convex hull, $cp_{l,k,x}$ and $cp_{l,k,y}$ are the coordinates of $cp_{l,k}$, $cc_{l,x}$ and $cc_{l,y}$ are the coordinates of the center of the l^{th} enclosing circle, r_l represents the radius of the l^{th} enclosing circle, and m_l is the amount of pixels of the l^{th} convex hull. In fact, $p_{11,l}$ can be regarded as the point furthest away from the center of the enclosing circle, and $p_{12,l}$ is the point furthest away from $p_{11,l}$. These two points are generally P_A and P_C . The data of “Num1,” “Pos1,” p_{11} , and p_{12} are saved as “Info1.”

3.3. Search for P_B . To acquire the position of P_B , we conduct one close operation, four erode operations, and four dilate operations in the OpenCV for the binarized image, successively. The results are presented in Figure 6(a). Then, we derive the treated contours using the strategy given by (7) and (8). The results are shown in Figure 6(b) and are saved as “Pos2.” Finally, the minimum enclosing circle and the convex hull of the derived contours are obtained, shown as Figure 6(c). Similar to the procedure to search for P_A and P_C , two endpoints, p_{21} and p_{22} , are selected as the alternative

points of P_B . The other one is defined as P_D . The data of “Pos2,” p_{21} , and p_{22} are saved into “Info2.”

3.4. Information Matching. Next, we should recognize P_A and P_B from p_{11}, p_{12}, p_{21} , and p_{22} . For this purpose, we first compute the Euclidean distance from p_{21} to p_{11} , p_{21} to p_{12} , p_{22} to p_{11} , and p_{22} to p_{12} , respectively. Then, we compare the four distances and find out the two points that lead to the largest distance. Assuming the two points are p_{12} and p_{22} , we can draw the conclusion that P_C is p_{12} , as p_{12} is the alternative point of P_A and P_C , and the distance from P_C to P_D is always larger than that of P_A to P_B . Repeat the procedure for all “Num1” contours of perillae, such that the position of P_A and P_B of each perillae can be obtained. We summarize all four possibilities in Table 1.

3.5. Scale Factor Estimation and Size Computation. As indicated in (8), parameter z is the factor controlling the scale of imaging. Hence, we utilize the following scale method to estimate z . As shown in Figure 7, the original plane is $z = c_2$. We use A_2B_2 to represent the manual measurement and use A_0B_0 to represent the corresponding measurement in the camera coordinate system. Then, we manually set z to c_1 to acquire the measurement A_1B_1 by using (8). Based on these measurements, we have

$$\frac{A_0B_0}{A_1B_1} = \frac{f}{c_1}, \quad (9)$$

$$\frac{A_0B_0}{A_2B_2} = \frac{f}{c_2}. \quad (10)$$

Therefore, z can be calculated by

$$z = c_2 = \frac{A_2B_2}{A_1B_1} \cdot f. \quad (11)$$

To eliminate the measurement error, we repeat the above process for 20 times, and the average value is used for the experiments, computed by

$$z = c_2 = \frac{\sum_{i=1}^{20} c_{2i}}{20}, \quad (12)$$

where c_{2i} denotes the calculated value in the i^{th} trial.

The proposed approach is summarized in Figure 8.

4. Experimental Results

Our experimental system is shown in Figure 9, composed of a lighting box and a personal computer (PC). The lighting box contains four light-emitting diode (LED) light located as a ring on the top of the box and a CCD camera in the center of the box. The experimental setup is described as follows. Before conducting the experiments, we manually set $c_1 = 50$ cm and obtain $z = 68.765$ cm by using the strategy introduced in Subsection 3.5. This value of z is used for all experiments in this study. First, we randomly chose 100 perillae

TABLE 1: Information matching, P_A and P_B to p_{11}, p_{12}, p_{21} , and p_{22} .

Points leading to the largest distance	P_A	P_B
p_{11} and p_{21}	p_{12}	p_{22}
p_{11} and p_{22}	p_{12}	p_{21}
p_{12} and p_{21}	p_{11}	p_{22}
p_{12} and p_{22}	p_{11}	p_{21}

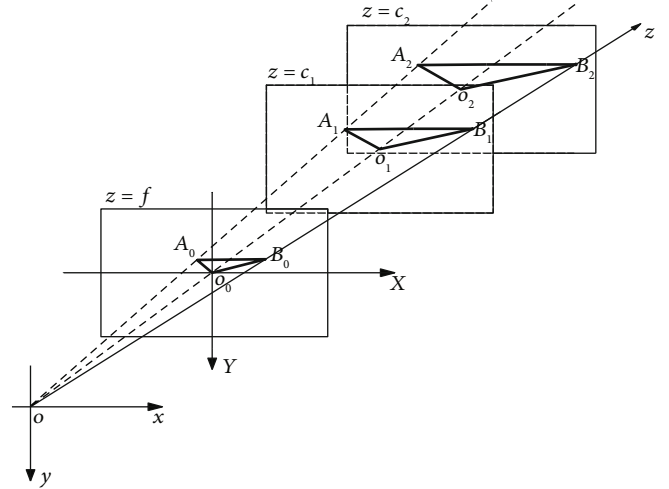


FIGURE 7: Pinhole imaging model.

and manually measured their sizes. Then, we used the developed system to measure these perillae.

The results by both manual measurement and automatic online measurement are presented in Figure 10. We computed the measurement error for each perillae, and the results are provided in Figure 11. Obviously, the results obtained by online measurement are close to those obtained by manual measurement. As provided in Table 2, among the 100 perillae, the maximum measuring error (MAME) is 3.66 mm, while the minimum measuring error (MIME) is 0.02 mm. Most of the errors are lower than 3 mm. The overall average measuring error (OAME) and the variance of measuring error (VME) are 1.47 mm and 0.07 mm, respectively.

5. Conclusions

We developed an MV-based approach for automatic measuring and size sorting of perillae. We first built the geometric model for perillae and the mathematical model for imaging. Based on the models, the measuring and size sorting method was proposed, including image binarization, key point determination, information matching, and parameter estimation. We employed the CCD camera for imaging and the OpenCV tools for image processing. Experimental results have verified the feasibility of our system and its high accuracy of measuring and size sorting. By using 100 perillae for experiments, the MAME and the MIME are 3.66 mm and 0.02 mm, respectively. Most of the errors are lower than 3 mm. The OAME

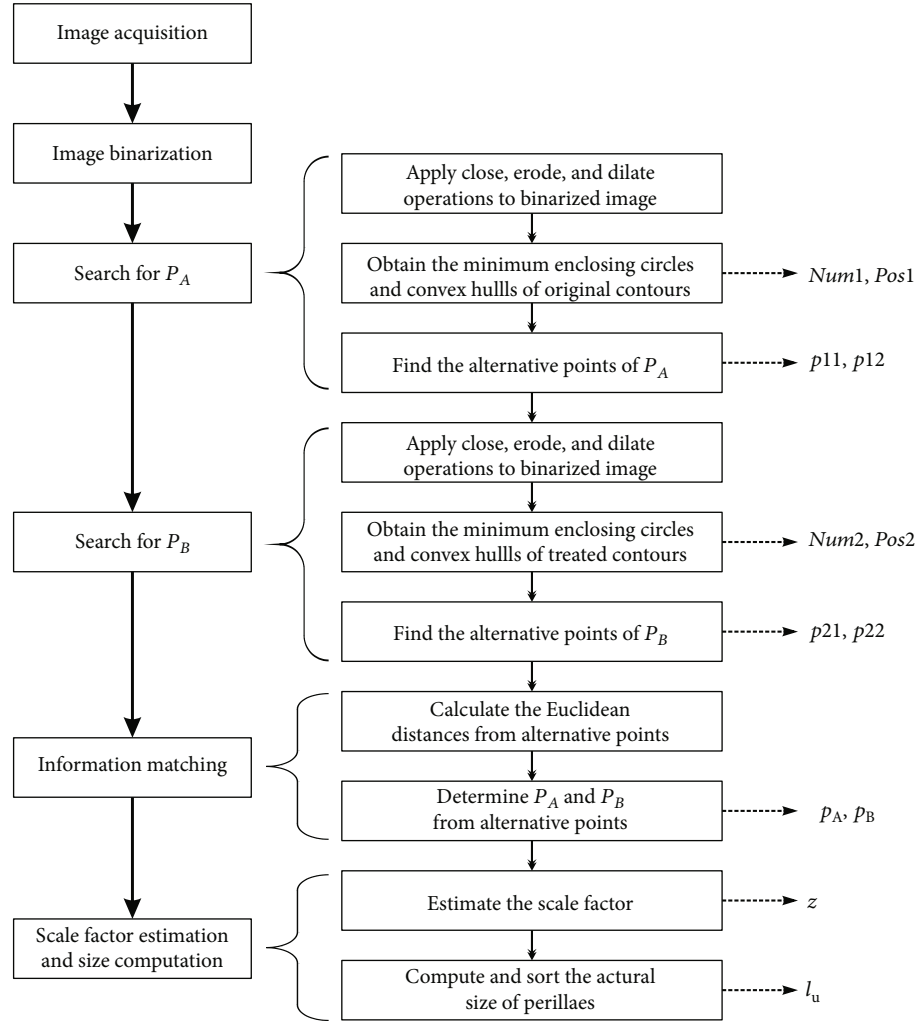


FIGURE 8: Outline of the proposed approach.

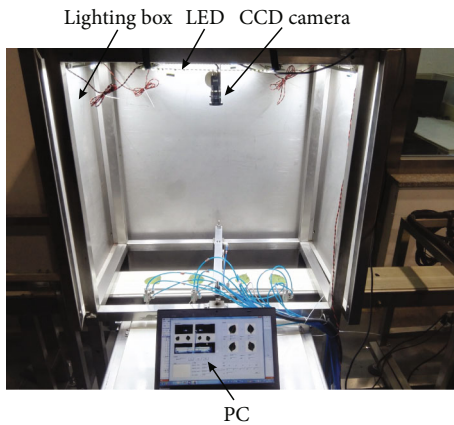


FIGURE 9: Experimental system.

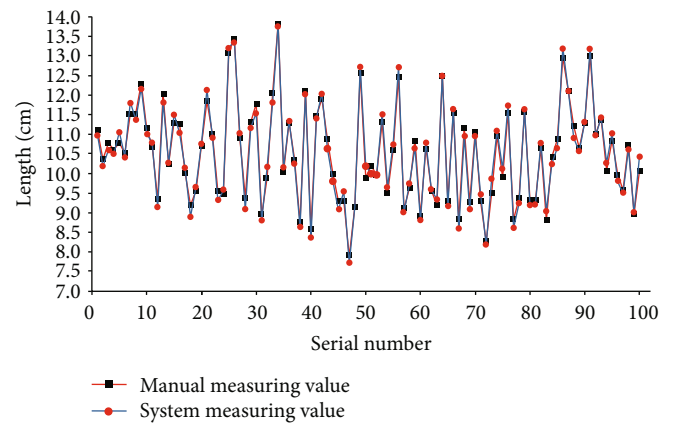


FIGURE 10: Measuring result.

and the VME are 1.47 mm and 0.07 mm, respectively. Further study could address on the following issues. First, miniaturization for the developed system requires future work to

make the proposed approach more particle. Second, utilizing the RGB image or hyperspectral image to detect the maturity of perillae is also valuable for further study.

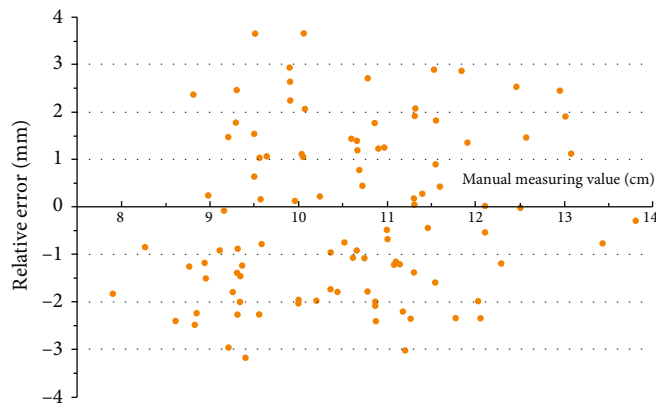


FIGURE 11: Measuring error for each perillae.

TABLE 2: Overall measuring and sorting results.

	ATCCI (ms)	MAME (mm)	MIME (mm)	OAME (mm)	VME (mm)	OSA (%)
Results	204.175	3.66	0.02	1.47	0.07	93

Data Availability

The data used to support the findings of this study are available from the corresponding author upon request.

Conflicts of Interest

The authors claim no conflicts of interest.

Acknowledgments

This work was supported by the National Key Research and Development Project under Grant 2017YFD0401305.

References

- [1] J. Yang, J. Yoo, E. Lee et al., "Anti-inflammatory effects of Perillae Herba ethanolic extract against TNF- α /IFN- γ -stimulated human keratinocyte HaCaT cells," *Journal of Ethnopharmacology*, vol. 211, pp. 217–223, 2018.
- [2] X. Kong, G. Huo, S. Liu, F. Li, W. Chen, and D. Jiang, "Luteolin suppresses inflammation through inhibiting cAMP-phosphodiesterases activity and expression of adhesion molecules in microvascular endothelial cells," *Inflammopharmacology*, vol. 27, no. 4, pp. 773–780, 2019.
- [3] N. Ito, T. Yabe, Y. Gamo et al., "Rosmarinic acid from perillae herba produces an antidepressant-like effect in mice through cell proliferation in the hippocampus," *Biological and Pharmaceutical Bulletin*, vol. 31, no. 7, pp. 1376–1380, 2008.
- [4] V. G. Narendra and K. S. Hareesh, "Quality inspection and grading of agricultural and food products by computer vision - a review," *International Journal of Computer Applications*, vol. 2, no. 1, pp. 43–65, 2010.
- [5] B. Zhang, W. Huang, J. Li et al., "Principles, developments and applications of computer vision for external quality inspection of fruits and vegetables: a review," *Food Research International*, vol. 62, no. 62, pp. 326–343, 2014.
- [6] Y. Chen, K. Chao, and M. S. Kim, "Machine vision technology for agricultural applications," *Computers and Electronics in Agriculture*, vol. 36, no. 2-3, pp. 173–191, 2002.
- [7] T. Brosnan and D. Sun, "Inspection and grading of agricultural and food products by computer vision systems—a review," *Computers and Electronics in Agriculture*, vol. 36, no. 2-3, pp. 193–213, 2002.
- [8] H. S. El-Mesery, H. Mao, and A. E. F. Abomohra, "Applications of non-destructive technologies for agricultural and food products quality inspection," *Sensors*, vol. 19, no. 4, p. 846, 2019.
- [9] Y. Ying, X. Rao, Y. Zhao, and J. YiYuan, "Application of machine vision technique to automatic quality identification of agricultural products (I)," *Transactions of the Chinese Society of Agricultural Engineering*, vol. 16, no. 3, pp. 103–108, 2000.
- [10] N. Zhao, P. Zhao, and Y. Gao, "Study on application of machine vision technology to modern agricultural in China," *Journal of Tianjin Agricultural University*, vol. 22, pp. 55–58, 2015.
- [11] M. Atas, Y. Yardimci, and A. Temizel, "A new approach to aflatoxin detection in chili pepper by machine vision," *Computers and Electronics in Agriculture*, vol. 87, pp. 129–141, 2012.
- [12] N. Razmjooy, B. S. Mousavi, and F. Soleymani, "A real-time mathematical computer method for potato inspection using machine vision," *Computers & Mathematics with Applications*, vol. 63, no. 1, pp. 268–279, 2012.
- [13] V. N. Eyarkai, K. Thangave, S. Shahir, and V. Thirupathi, "Comparison of various RGB image features for nondestructive prediction of ripening quality of "alphonso" mangoes for easy adoptability in machine vision applications: a multivariate approach," *Journal of Food Quality*, vol. 39, no. 6, 825 pages, 2016.
- [14] H. Nouri-Ahmadabadi, M. Omid, S. S. Mohtasebi, and M. Soltani Firouz, "Design, development and evaluation of an online grading system for peeled pistachios equipped with machine vision technology and support vector machine," *Information Processing in Agriculture*, vol. 4, no. 4, pp. 333–341, 2017.
- [15] C. M. Sabliov, D. Boldor, K. M. Keener, and B. E. Farkas, "Image processing method to determine surface area and volume of axi-symmetric agricultural products," *International Journal of Food Properties*, vol. 5, no. 3, pp. 641–653, 2002.
- [16] H. Yao, Z. Hruska, R. Kincaid et al., "Development of narrow-band fluorescence index for the detection of aflatoxin contaminated corn," in *Conference on the Sensing for Agriculture and Food Quality and Safety III*, vol. 8027, Orlando, Florida, United States, APRIL 2011.
- [17] F. Pedreschi, J. Leon, D. Mery, and P. Moyano, "Development of a computer vision system to measure the color of potato chips," *Food Research International*, vol. 39, no. 10, pp. 1092–1098, 2006.
- [18] X. Huang, S. Jiang, Q. Chen, and Z. Jiewen, "Identification of defect pleurotus geesteranus based on computer vision," *Transactions of the Chinese Society of Agricultural Engineering*, vol. 26, no. 10, pp. 350–354, 2010.
- [19] L. Sun, L. Yuan, J. Cai, H. Lin, and J. W. Zhao, "Egg freshness on-line estimation using machine vision and dynamic weighing," *Food Analytical Methods*, vol. 8, no. 4, pp. 922–928, 2015.

- [20] H. Li, H. Sun, and M. Li, "Identification of cabbage ball shape based on machine vision," *Transactions of the Chinese Society for Agricultural Machinery*, vol. s1, pp. 141–146, 2015.
- [21] H. Chen, Q. Xia, T. Zuo, T. HeQun, and B. YinBing, "Determination of shiitake mushroom grading based on machine vision," *Nongye Jixie Xuebao*, vol. 45, no. 1, pp. 281–287, 2014.
- [22] W. Hui, L. Yuchun, K. Feng, W. Qi, Z. Bo, and Z. Qin, "Size detection for cherry fruit based on machine vision," *Transactions of the Chinese Society for Agricultural Machinery*, vol. 43, no. s1, pp. 246–249, 2012.
- [23] J. Xiong, X. Zou, N. Liu, P. HongXing, L. JinHong, and L. GuiChao, "Fruit quality detection based on machine vision technology when picking litchi," *Nongye Jixie Xuebao*, vol. 45, no. 7, pp. 54–60, 2014.
- [24] F. Zhang, S. Li, and Z. Liu, "Screening method of abnormal corn ears based on machine vision," *Transactions of the Chinese Society for Agricultural Machinery*, vol. 46, pp. 45–49, 2015.
- [25] Z. Ping, Z. ChunJiang, W. JiHua, Z. Wen'gang, S. ZhongFu, and W. YouXian, "Egg geometry calculations based on machine vision," *Nongye Jixie Xuebao*, vol. 41, pp. 168–171, 2010.
- [26] H. Wang, J. Xiong, Z. Li, J. Deng, and X. Zou, "Potato grading method of weight and shape based on imaging characteristic parameters in machine vision," *Transactions of the Chinese Society of Agricultural Engineering*, vol. 32, no. 8, pp. 272–277, 2016.
- [27] W. Wei, Y. Xing, Y. Li, Y. Peng, and W. Zhang, "Online detection and classification system of external quality of leaf for dining hall and family," *Transactions of the Chinese Society of Agricultural Engineering*, vol. 34, no. 5, pp. 264–273, 2018.
- [28] L. Li, Y. Peng, and Y. Li, "Design and experiment on grading system for online non-destructive detection of internal and external quality of apple," *Transactions of the Chinese Society of Agricultural Engineering*, vol. 34, no. 9, pp. 267–273, 2018.
- [29] G. Wang, L. Sun, X. Li, M. Zhang, Q. Lyu, and J. Cai, "Design of postharvest in-field grading system for navel orange based on machined vision," *Journal of Jiangsu University*, vol. 38, no. 6, pp. 672–676, 2017.

Research Article

Accurate Variable Control System for Boom Sprayer Based on Auxiliary Antidrift System

Jun Fu ^{1,2}, Chao Chen,^{1,2} Rongqiang Zhao ^{1,2} and Luquan Ren^{1,2}

¹Key Laboratory of Bionic Engineering, Ministry of Education, Jilin University, Changchun, China

²College of Biological and Agricultural Engineering, Jilin University, Changchun 130022, China

Correspondence should be addressed to Rongqiang Zhao; sharmmi@126.com

Received 5 November 2019; Accepted 18 December 2019; Published 11 January 2020

Guest Editor: Yuan Li

Copyright © 2020 Jun Fu et al. This is an open access article distributed under the Creative Commons Attribution License, which permits unrestricted use, distribution, and reproduction in any medium, provided the original work is properly cited.

Control accuracy significantly affects the performances of boom sprayer. In this study, we develop a precise autocontrol technology based on the vehicle speed feedback. We utilize the auxiliary antidrift system of wind-curtain type air flow and the variable spraying control system for adaptive fertilizing and online measuring of working conditions. Experimental results demonstrate that the variable spraying control system could keep the speed error less than 3%. The air flow significantly improves the penetration of spraying, decreases the fog drip, and increases the pesticide utility. Benefitting from the auxiliary air flow, the average utility of pesticide is improved from 26.76% to 37.98%. Additionally, the speed feedback control reduces the consumption of pesticide by more than 12%.

1. Introduction

As an important technology for agriculture, spraying has attracted increasing attention over the world [1–4]. Boom sprayers can be employed for pesticide to reduce the threat of diseases, insect pests, and weeds of crops. Till now, a set of studies have been carried out to improve the performance of spraying, including reduction of pesticide consumption, decreasing the size of fog drip, and increasing the penetration [5–7]. In general, precise plant protection machineries are driven by electromechanical hydraulic systems and they are controlled through photoelectric systems. As the development of the remote sensing (RS), the geography information systems (GIS), and the global positioning systems (GPS), which are always referred to as the 3S technology, the air flow antidrift technologies have been widely used on the boom sprayer for higher control accuracy. Specifically, a set of parameters are collected online to achieve intelligent control of spraying, for instance, pressure and flow of pesticide [8–14]. In [8], a variable spraying control system is proposed to recognize weed from pea seedling images such that the intelligent weeding is realized. In [9],

the authors develop a suspended air-assisted system to improve the performance of boom sprayer. In [11], a variable spraying system is proposed by using multiple combined nozzles for spraying. In addition, the geographic information technology and higher pressure electrostatic spraying technology are also applied for intelligent spraying. For the control theory, various methods have been proposed to improve the accuracy [15, 16], the speed [17, 18], and the robustness [19, 20].

However, the study of boom sprayer still faces considerable challenges. First, the accuracy of control system is not satisfied. Second, the reduction of pesticide requires further improvement. To address these problems, in this study, we develop a novel variable control system boom sprayer based on the wind-curtain air flow and online inspection of working condition. We realize the online supervision of key parameters of a spraying system, including the spraying pipeline pressure, the flow of pesticide, the residue of pesticide in tank, and the traveling speed. The key parameters of work quality, such as the working conditions of boom, are also considered. Benefitting from the wind-curtain air flow antidrift technology, the penetration of spraying is improved,

and the drifting of fog drip is increased. Hence, the pesticide consumption is significantly reduced.

The remainder of this paper is organized as follows: Section 2 describes the outline of the developed variable control system. Section 3 introduces the proposed control method. Section 4 provides the developed hardware and software. Section 5 presents the experimental results and analysis. Section 6 draws the conclusion.

2. Outline of the Developed Variable Control System

In this section, we first describe the used variable boom sprayer in this study. Next, we briefly introduce the outline of the developed system.

2.1. Used Variable Boom Sprayer. The used variable boom sprayer in this study is introduced as follows: The least power is 45 kW. The rated capacity of pesticide tank is 3000 L. The spraying amplitude is 24 m. The wheel track is 1800 mm to 2200 mm that is adjustable. The ground clearance of nozzle is 0.5 m to 2.0 m. The rated spraying pressure is 0.3 MPa to 0.5 MPa. The adjusted range of the amount of pesticide application is 150 hm² to 750 L/hm². The control accuracy of pesticide application is $\pm 5\%$. The work speed is 6 km/h to 10 km/h. The productivity is set to be larger than 12 hm²/h. The overall size of the used mechanism is 5800 mm \times 3750 mm \times 3600 mm. As shown in Figure 1, the variable control system is composed of the wind curtain air flow antidrift system and the variable spraying control system.

2.2. Outline of the Developed System. By online monitoring of the working conditions, the variable spraying control system is able to adaptively adjust the amount of sprayed pesticide based on the traveling speed of the sprayer. For the proposed control method, the setting value of the amount of used pesticide for a unit area is first input into the control system. Then the control system carries out the monitored travelling speed to compute the current amount of pesticide for a unit area. Next, we compare the measured value with the setting value. If the difference between the compared values exceeds the threshold, the control system will wake the actuator to automatically adjust the spraying pressure. Based on this feedback, the actual amount of pesticide used for a unit area, i.e., the pesticide flow, can be close to the expected value. Therefore, the precise spraying is achieved.

With the on-board advanced reduced instruction set computing machine (ARM) controller, the work speed, pipeline flow, and pressure can be acquired by sensors through the controller area network bus (CAN BUS). The data input by users are combined to compute the required variables which are sent to the drive circuit. As a result, the speed regulation of the DC motor of the electrical ball valve is realized. The outline of the developed system is presented in Figure 2.



FIGURE 1: The used variable boom sprayer.

3. Proposed Control Method

The outline of the proposed control method is shown in Figure 3. The system input parameters are the machine forward speed value, and the output result is the flow value.

Assume that the entire farmland is divided into a set of areas, and the pesticide consumption per hectare R (L/hm²) is given by

$$R = 60000 \frac{\int Q dt}{S}, \quad (1)$$

where Q denotes the instantaneous flow of nozzle (L/min) and S denotes the actual spraying area (m²) that is given by

$$S = D \int v dt, \quad (2)$$

where D and v represent the width of the actual spraying area (m) and the work speed (m/s), respectively. Combining (1) and (2), we have

$$R = \frac{60000}{D} \int \frac{Q}{v} dt. \quad (3)$$

Therefore, we can estimate R in advance empirically. If D is given, the nozzle flow Q is regarded to be proportional to the instantaneous work speed v at a certain moment. To ensure the variable R reaches the expected value, Q and v should be kept proportional during the spraying.

For better atomization, we control the regular atomization cone to be 110° by using the dual sector nozzle. The nozzle interval is equivalent to be or more than 50 cm based on the requirement of the nozzle. The height of boom is generally 50 cm higher than the top of the crop. Combining the above analysis, the width of the actual spraying area D (m) can be expressed as

$$D = (m - 1)L + 2h \tan \alpha, \quad (4)$$

where m denotes the quantity of nozzles, L denotes the distance of adjacent nozzles, h represents the ground clearance of nozzle, and α is the spraying angle of nozzle. For

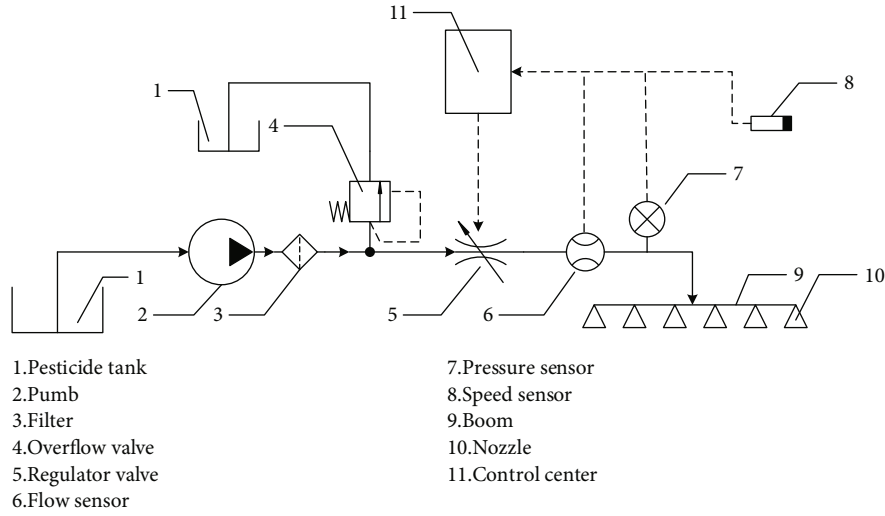


FIGURE 2: Outline of the developed system.

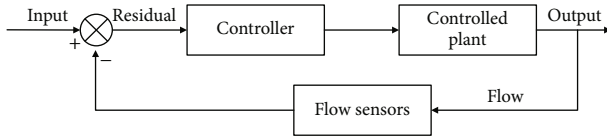


FIGURE 3: Outline of the closed loop.

the proposed closed-loop control method, when the current flow is close to the target flow, the controller employs the pulse width modulation method to reduce the speed of the ball valve motor. The purpose is to reduce the overshoot caused by the delay and reduce the adjustment time, which is equivalent to reducing the delay characteristics of the ball valve.

We use the PWM mode for motor control that is introduced as follows: The ARM controller first calculates the current feedback value according to the sensor acquisition information and then makes a judgment based on the feedback value. Finally, the controller sends a corresponding function code FC (function code). The function code is used to control the polarity, on-off, and size of the ball valve input voltage, thereby changing the DC motor motion state and finally changing the ball valve opening degree. The FC can be expressed as

$$FC = \begin{cases} 1, & C_1 < \frac{|Q_b - Q_a|}{|Q_a|}, \\ 0, & C_0 < \frac{|Q_b - Q_a|}{|Q_a|} < C_1, \\ -1, & 0 < \frac{|Q_b - Q_a|}{|Q_a|} < C_0, \end{cases} \quad (5)$$

where Q_a and Q_b denoted the theoretical value and the measured value of Q , respectively, C_0 is the maximum allowable error of the system, and C_1 is obtained through the experiments. For convenience of description, C_1 is hereinafter

regarded as a critical value, C . If $FC = 1$, set the full speed mode such that the ball valve motor rotates at full speed. If $FC = 0$, set the PWM mode such that the ball valve motor speed is reduced. The ARM calculates the duty cycle in real time according to the designed method. If $FC = -1$, The regulating valve does not move such that the flux is fixed.

The online flow is essential to the variable spraying. Specifically, it relates to the flow in the unit area and the accumulative flow. Therefore, it is necessary to control the speed of the regulator valve motor. In other words, when the motor is closed to the expected angle, the PWM works to slow down the speed. For the close loop control, the controller uses the pulse width modulation to decrease the rpm of the ball valve motor when the current flow is close to the expected value. It is aimed at reducing the overmodulation due to the delaying. The less modulation duration means the less delaying of the ball valve. The motor rpm downward curve is given by the antitrigonometric function, expressed as

$$f(x) = \frac{1}{2 \tan^{-1} 10} [\tan^{-1}(10 - 20x) + \tan^{-1} 10]. \quad (6)$$

We discretize the curve to obtain the duty ratio that is used to regulate the motor speed. As presented in Figure 4, it can be noted that the rpm drops rapidly as the percentage of time increases. We then calculate the residual between the integration of the discretized curve and that of the original curve, expressed as

$$\frac{\int_0^1 v_{\text{red}}(t) dt}{\int_0^1 v_{\text{blue}}(t) dt} = 0.9996. \quad (7)$$

Therefore, the error of the discretizing operation is only 0.04%, which can be ignored in practical. The duty ratio from the output of the drive circuit is directly selected from the discretized curve.

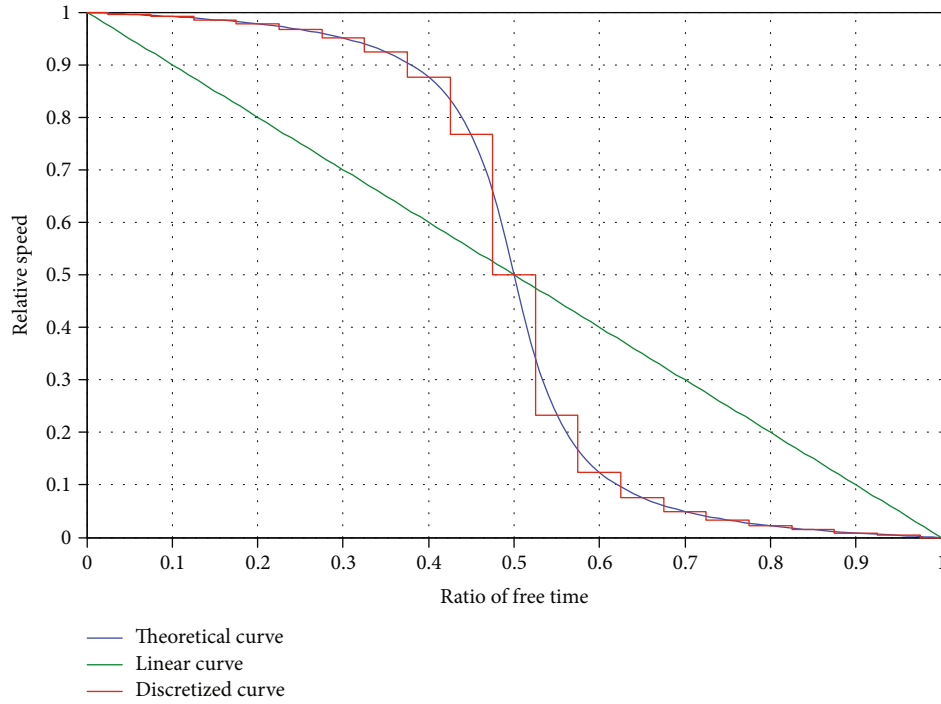


FIGURE 4: Speed reduction curves.

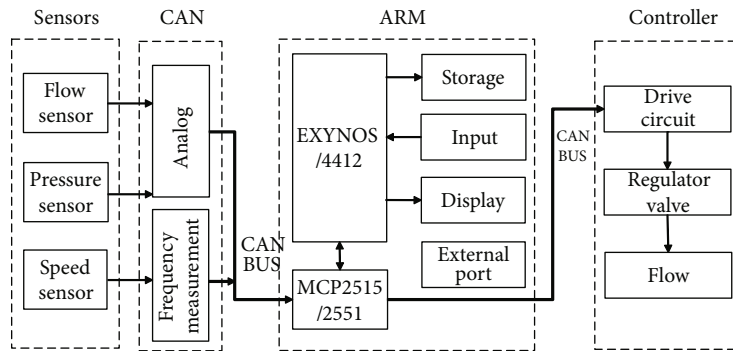


FIGURE 5: Speed reduction curves.

4. Hardware and Software of the Developed System

In this section, we introduce the hardware and software of the developed system, respectively.

4.1. Hardware. Our hardware system is mainly composed of the on-board ARM controller, the CAN collection module, the wheel rpm detection module, the real-time flow detection module, the pressure detection module, the flow regulator, the power supply, etc. As shown in Figure 5, the central processing unit is Samsung Exynos 4412 ARM. The base is mounted with the CAN receiving and sending ports, input and output ports of touchscreen, the peripheral collecting device, the changeover circuit, the drive module, the electrical ball valve, etc. Consisting of PIC18F2580 microcontroller and VNH3SP30 chips, the drive circuit is

used to drive the regulator valve motor and to control the rpm and direction of the motor.

The Exynos 4412 chip has low power consumption. The Cortex-A9 Quad Core chips have enriched sources, including the 1.4 GHz main frequency, 64-digit/128-digit bus, and 2GB of memory. There are ten functional modules, summarized as follows:

- (1) Storage and document modules
- (2) Multicore computer unit
- (3) Multimedia unit
- (4) BUS
- (5) Communication port
- (6) Management of power supply modules

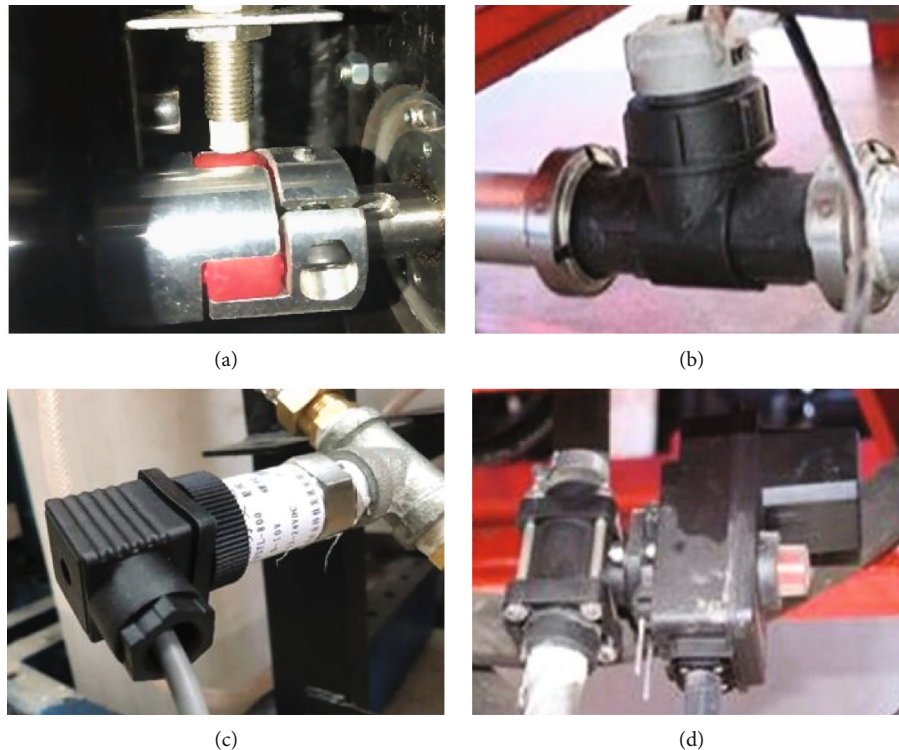


FIGURE 6: Sensors and controllers: (a) speed sensor, (b) flow sensor, (c) pressure sensor, and (d) flow valve.

- (7) System unit
- (8) Safety module
- (9) Audio module
- (10) GPS/GLONASS subsystem

Each detection system and regulation unit are integrated on the development board as a node that is connected to the BUS with the CAN controller and receiver. The CAN network sends the parameters in terms of the online wheel speed, the flow, and the pressure. The speed detection sensor utilizes the hall element to obtain the pulse frequency to calculate the work speed. The real-time flow monitor is in fact the turbine flow sensor. When the tested fluid flows through the sensor vanes, the vanes begin to rotate, periodically changing the reluctance of the pipeline. The pressure monitor uses the diffusion-silicon pressure transmitter to measure the pipeline pressure ranging from 0 to 1 MPa, with the power supply voltage at 12~36 VDC, the precision at $\pm 0.50\%$, and the two-wire output voltage signal from 0 to 5 V. The output signal is connected through the port to the CAN analog collection module. The real-time flow is controlled with a flow control valve. In addition, the flow regulator is composed of the electric regulator valve, the drive circuit, and the power supply. The electric regulator valve controls the fluid flowing from the valve body. The drive circuit of the regulator valve is employed to drive the DC motor of the regulator valve and to control the speed and directions of the DC motor. The power supply is 12 VDC. The installations are shown in Figure 6.

4.2. Software. The host computer is developed by using the Qt SDK. As shown in Figure 7, the working conditions of the sprayer are displayed in the left side of the window, including the pipeline pressure, the forward-movement speed, and the current amount of pesticide consumption. In the middle of the window, the flow-time curve created by the “Qt Widgets for Technical Applications” (QWT) is provided. The current time and the input of the sprayer parameters are presented in the right side of the window from top to bottom, respectively. The internally calculated parameters are dependent on the quantity of nozzles, the height of boom, and the nozzle interval. The functional buttons are provided in the bottom of the window, including “+,” “-,” “Auto,” “Manual,” and “Start/Stop,” which can be used to online adjust the parameters for better working conditions.

The host and slave computers communicated the network via the CAN BUS. As there is no CAN BUS port on the PC, the CAN is first converted to USB, and then the PC is connected with the CAN BUS network of the slave computer. The network communication between host and slave computers is realized by using the Secure SHell FileSystem (SSHFS).

5. Experimental Results

In this section, we present the experimental results and analysis. First, we conduct the experiments to verify the developed variable control method based on different working speeds. Second, we verify the reduction of pesticide consumption.

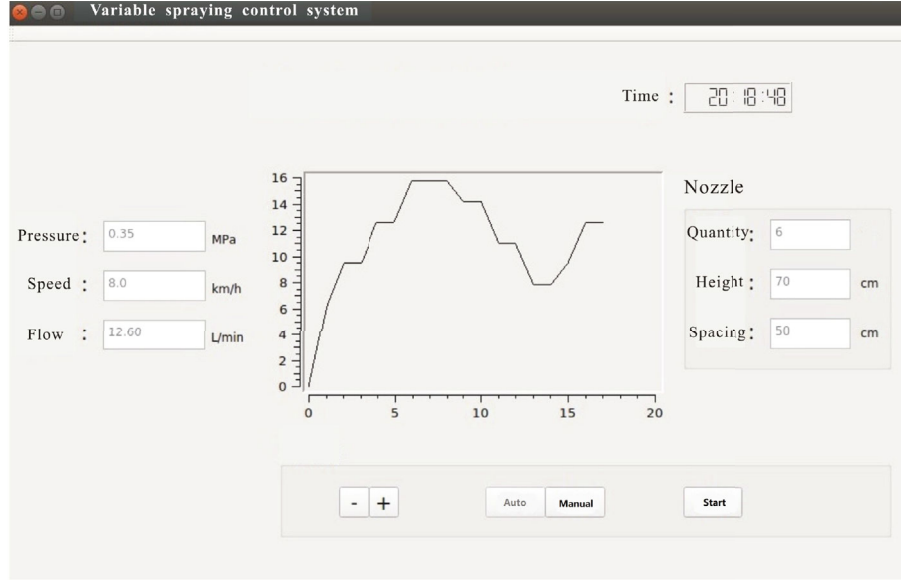


FIGURE 7: Software of the developed system.

TABLE 1: Comparison between the actual speed and the speed of control system.

Actual speed (km/h)	Speed of control system (km/h)	Relative error (%)
4.55	4.42	2.9
6.64	6.79	2.3
7.21	7.36	2.1
8.56	8.32	2.3
10.85	10.96	1.0
19.54	19.85	1.6

First, we considered the accuracy of the speed control. We conducted the experiments in the farming field and the grazing field from a national agricultural hi-tech demonstration zone. We set different working speeds during the experiments. For each value of speed, the actual speed and the speed of the control system were recorded. We then calculated the relative tolerance between them. The results are presented in Table 1. The results demonstrate that for different speeds the relative tolerances based on all set values are less than 3%. Thus, the accuracy of the monitoring system is satisfied.

Next, we focused on the accuracy of spraying. Similarly, we selected different working speeds and set different expected consumptions of pesticide per area. For each set of parameters, we recorded the theoretical amount of spraying and the actual amount of spraying and calculated the spraying error. The results are provided in Tables 2 and 3. It can be noted that, benefitting from the proposed approach, the spraying pressure can be tuned automatically, such that the spraying error is controlled less than 5%, regardless of the parameter settings. The results indicate that the accuracy of working speed control and the spraying pressure control could meet the requirements of agriculture production. The

results presented in Table 3 demonstrate the speed feedback control reduces the pesticide consumption by 12.7% to 15.2% for different experimental settings.

Finally, we performed the experiments to verify the reduction of pesticide consumption by using the proposed control system. This part of experiments was conducted in the corn field in Shaanxi farming and grazing farm. The line spacing is 70 cm and the corn spacing is 20 cm. The leaf area index (LAI) is 1.78. The environment for the experiments is described as follows: The wind speed is 2~2.5 m/s. The temperature is 30°C. The used pesticide is the rhodamine B (fluorescent tracer) with the concentration of 0.1%. Two conditions are considered for the variable boom sprayer, working with and without the auxiliary air flow, which are shown in Figures 8 and 9, respectively. For the variable boom sprayer, the spraying pressure is 0.4 MPa. The working speed is set to 6.7 km/h, and the air flow speed is 15 m/s.

To evaluate the efficiency of the spraying of the pesticide, we defined the “pesticide utility,” denoted by P , as follows,

$$P = \frac{A_1}{A_2}, \quad (8)$$

where A_1 represents the amount of pesticide deposited on the crop and A_2 denotes the amount of consumed pesticide from the sprayer. The results are presented in Table 4.

From the results, we can note that the proposed system significantly increases the pesticide utility. It is mainly because the wind-curtain air flow makes the pesticide more penetrative and reduces the drifting of drips. With the auxiliary air flow, the average utility of pesticide for different experimental settings is 37.98%. On the other hand, the results based on the system without the auxiliary air flow are only 26.76%. Therefore, we believe the proposed variable boom sprayer is able to reduce the consumption of spraying

TABLE 2: Results on the accuracy of spraying.

Nozzle model	Set value of pesticide consumption (L/hm ²)	Working speed (km/h)	Theoretical amount of spraying (L/min)	Actual amount of spraying (L/min)	Measured pressure (MPa)	Relative spraying error (%)
ST110-2 (yellow)	174	6.79	23.63	22.45	0.31	5.0
		7.46	26.0	24.65	0.35	5.2
	290	6.79	39.38	40.75	0.78	3.47
		7.46	43.27	43.75	0.95	1.1
ST110-4 (red)	400	6.79	54.32	54.54	0.52	0.4
		7.46	59.68	60.01	0.63	0.6
	550	3.39	37.29	37.68	0.35	1.1
		4.07	44.72	45.33	0.55	1.3
ST110-6 (grey)	673	3.39	45.63	43.65	0.37	4.3
		4.07	54.78	52.85	0.51	3.5
	750	3.39	50.85	50.75	0.48	0.2
		4.07	61.05	61.65	0.67	1.0

TABLE 3: Results on pesticide consumption with the speed feedback.

Nozzle model	Working speed (km/h)	Pesticide consumption (L/hm ²)		Pesticide reduction (%)
		The vehicle speed feedback	/	
ST110-2 (yellow)	6	281	322	12.7
	7	287	338	15.1
ST110-4 (red)	6	548	635	13.7
	4	543	641	15.2
ST110-6 (grey)	3	744	855	13.0
	4	743	860	13.6



FIGURE 8: Experiment with auxiliary airflow.



FIGURE 9: Experiment without auxiliary airflow.

TABLE 4: Results on pesticide utilization in maize fields.

Nozzle model	VMD Dv50 (μm)	Pesticide consumption (L/hm ²)	Pesticide utility (%)	
			With auxiliary air flow	Without auxiliary air flow
ST110-02	234.2	163	35.51	19.34
ST110-04	289.6	274	36.36	26.06
ST110-05	337.7	355	38.13	28.46
ST110-06	369.8	372	41.93	33.20
Average value	/	/	37.98	26.76

pesticide and reduce the environmental pollution by increasing its pesticide utility.

6. Conclusions

In this paper, we propose a novel boom sprayer based on the auxiliary antidrift system of wind-curtain type air flow. The developed variable spraying control system achieves adaptive

fertilizing and online measurement of working conditions. By using the developed variable spraying control system, the speed error can be controlled within 3%. The air flow significantly improves the penetration of spraying, decreases the fog drip, and increases the pesticide utility. Benefitting from the auxiliary air flow, the average utility of pesticide is improved from 26.76% to 37.98%. Additionally, the speed feedback control reduces the consumption of pesticide by more than 12%.

Data Availability

The data used to support the findings of this study are available from the corresponding author upon request.

Conflicts of Interest

The authors claim no conflicts of interest.

Acknowledgments

This work was supported by the Scientific and Technological Developing Scheme of Jilin Province under Grant 20190701055GH.

References

- [1] P. C. H. Miller and M. C. B. Ellis, "Effects of formulation on spray nozzle performance for applications from ground-based boom sprayers," *Crop Protection*, vol. 19, no. 8-10, pp. 609–615, 2000.
- [2] B. J. Qiu, R. Yan, J. Ma, X. Guan, and M. Ou, "Research progress analysis of variable rate sprayer technology," *Transactions of the Chinese Society for Agricultural Machinery*, vol. 46, no. 3, pp. 59–72, 2015.
- [3] M. T. Batte and M. R. Ehsani, "The economics of precision guidance with auto-boom control for farmer-owned agricultural sprayers," *Computers and Electronics in Agriculture*, vol. 53, no. 1, pp. 28–44, 2006.
- [4] A. Bayat and M. Itmec, "The current state of sprayer manufacturers in Turkey and some strategies for the future," *Scientific Papers-series A-agronomy*, vol. 61, no. 2, pp. 105–108, 2018.
- [5] Z. DongYan, Y. B. Lan, C. LiPing, W. Xiu, and L. Dong, "Status and future trends of agricultural aerial spraying technology in China," *Transactions of the Chinese Society for Agricultural Machinery*, vol. 45, no. 10, pp. 53–59, 2014.
- [6] D. Nuyttens, M. De Schampheleire, K. Baetens, and B. Sonck, "The influence of operator-controlled variables on spray drift from field crop sprayers," *Transactions of the ASABE*, vol. 50, no. 4, pp. 1129–1140, 2007.
- [7] T. Esau, Q. Zaman, D. Groulx et al., "Economic analysis for smart sprayer application in wild blueberry fields," *Precision Agriculture*, vol. 17, no. 6, pp. 753–765, 2016.
- [8] Z. XiaoLong, X. ZhengChun, Z. NianSheng, and C. ChengMao, "Weed recognition from pea seedling images and variable spraying control system," *Transactions of the Chinese Society for Agricultural Machinery*, vol. 43, no. 11, pp. 220–225, 2012.
- [9] Z. Haiyan, W. Jia, Y. Suzhen, J. Zhenhua, and W. Jinjiang, "Development of 3WQX-1300 type suspended air-assisted boom sprayer," *Agricultural Engineering*, vol. 4, pp. 67–70, 2011.
- [10] M. Yasin, "Air assisted sleeve boom sprayer," *Ama-agricultural Mechanization in Asia Africa and Latin America*, vol. 43, no. 1, pp. 61–66, 2012.
- [11] X. Yanlei, B. Jialin, F. Daping, and Z. Chiyang, "Design and experiment of variable spraying system based on multiple combined nozzles," *Transactions of the Chinese Society of Agricultural Engineering*, vol. 32, no. 17, pp. 47–54, 2016.
- [12] H. C. Foster, B. P. Sperry, D. B. Reynolds, G. R. Kruger, and S. Claussen, "Reducing herbicide particle drift: effect of hooded sprayer and spray quality," *Weed Technology*, vol. 32, no. 6, pp. 714–721, 2018.
- [13] X. Liu, X. Zhang, F. Liu, and M. Weiwe, "Multi-objective dynamic design optimization for air duct of air-assisted boom sprayer based on RVM," *Transactions of the Chinese Society for Agricultural Machinery*, vol. 41, no. 6, pp. 75–80, 2010.
- [14] M. E. Teske and H. W. Thistle, "Technical note: a comparison of single spray path ground boom sprayer deposition patterns," *Transactions of the ASABE*, vol. 54, no. 5, pp. 1569–1571, 2011.
- [15] B. Zhang, J. Wu, L. Wang, Z. Yu, and P. Fu, "A method to realize accurate dynamic feedforward control of a spray-painting robot for airplane wings," *IEEE-ASME Transactions on Mechatronics*, vol. 23, no. 3, pp. 1182–1192, 2018.
- [16] W. Huang, Y. Zhang, X. Zhang, and G. Sun, "Accurate torque control of interior permanent magnet synchronous machine," *IEEE Transactions on Energy Conversion*, vol. 29, no. 1, pp. 29–37, 2014.
- [17] H. Lens, J. Adamy, and D. Domont-Yankulova, "A fast nonlinear control method for linear systems with input saturation," *Automatica*, vol. 47, no. 4, pp. 857–860, 2011.
- [18] M. Van, M. Mavrovouniotis, and S. S. Ge, "An adaptive backstepping nonsingular fast terminal sliding mode control for robust fault tolerant control of robot manipulators," *IEEE Transactions on Systems, Man, and Cybernetics: Systems*, vol. 49, no. 7, pp. 1448–1458, 2019.
- [19] B. Zhu, J. Zhang, M. Suo, L. Chen, Y. Zhang, and S. Li, "Robust stability analysis and controller synthesis for uncertain impulsive positive systems under L1-gain performance," *ISA Transactions*, vol. 93C, pp. 55–69, 2019.
- [20] V. Fakhari, A. Ohadi, and H. A. Talebi, "A robust adaptive control scheme for an active mount using a dynamic engine model," *Journal of Vibration and Control*, vol. 21, no. 11, pp. 2223–2245, 2013.

Research Article

Variation in Morphological and Physiological Characteristics of Wild *Elymus nutans* Ecotypes from Different Altitudes in the Northeastern Tibetan Plateau

Juan Qi¹,^{ID} Wenhui Liu,² Ting Jiao,¹ and Ann Hamblin³

¹Key Laboratory of Grassland Ecosystem of Ministry of Education, College of Grassland Science, Gansu Agricultural University, Lanzhou, 730070 Gansu, China

²Key Laboratory of Superior Forage Germplasm in the Qinghai-Tibetan Plateau, Qinghai Academy of Animal Science and Veterinary Medicine, Xining, 810016 Qinghai, China

³School of Agriculture and Environment, The University of Western Australia, Perth WA 6009, Australia

Correspondence should be addressed to Juan Qi; qijuan0622@163.com

Received 26 September 2019; Revised 27 November 2019; Accepted 13 December 2019; Published 11 January 2020

Guest Editor: Yuan Li

Copyright © 2020 Juan Qi et al. This is an open access article distributed under the Creative Commons Attribution License, which permits unrestricted use, distribution, and reproduction in any medium, provided the original work is properly cited.

The availability of suitable native plant species for local animal husbandry development and ecological restoration is limited on the Qinghai-Tibetan Plateau. Therefore, comparisons of the ecological adaptability of native species to alternative habitats and their introduction into new habitats are of high importance. This study is aimed at identifying the alteration in morphological and physiological characteristics by measuring photosynthetic physiology, nutrient content, and growth associated with adaptation of plants to conditions at different altitudes 2450, 2950, 3100, and 3300 m above sea level (a. s. l.) on the plateau. Seeds of the dominant grass, *Elymus nutans*, were collected from locations at these altitudes and grown at a test location of 2950 m a. s. l. Results indicated that altitude had no significant effect on plant height and root depth. However, the leaf area and total root surface area of plants derived from 2950 and 3300 m a. s. l. showed a parabolic response, being greater than those of plants derived from the lowest (2450 m) and highest (3300 m a. s. l.). Total (root plus shoot) dry matter reduced progressively from 2450 to 3300 m a. s. l., while root:shoot ratio increased progressively with altitude. Seed yield of plants originating from the test altitude (2950 m a. s. l.) was significantly higher than at any other altitude, being 20% lower at 2450 m, and 38% and 58% less in populations originating from the higher altitudes (3100 and 3300 m a. s. l.). There was also a parabolic decline in response of *Elymus nutans* germplasm from 3100, 3300, and 2450 m, compared with plants from 2950 m a. s. l., to photosynthetic rate, total N, soluble sugar, and starch contents. Germplasm from 2450 m a. s. l. had significantly lower shoot and higher root carbon content, lower shoot nitrogen, and lower root carbon-to-nitrogen ratio compared with plants derived from the other three altitudes. It is suggested that the stable, genetically determined morphological and physiological features of ecotypes showed parabolic responses which means these ecotypes have become adapted to local habitats, whereas parameters such as dry matter, total root:shoot ratio, photosynthetic rate, and intercellular CO₂ concentration of plants reflected phenotypic linear response to current abiotic conditions. It is postulated that introduced ecotypes from 2450, 3100, and 3300 m could adapt to the environment at 2950 m a. s. l. gradually. We conclude that the increased thermal regime experienced by plants introduced from high altitude to low altitude may facilitate the increased growth of *Elymus nutans* subtypes. It is important to preserve local strains of native species, or ecotypes, for reintroduction into degraded environments and to maintain the greatest ecosystem stability in the northeastern Tibetan Plateau.

1. Introduction

Plants have the ability to alter their morphological and physiological traits in response to environmental variations

[1, 2] and adjust the expression of these traits to accommodate their adaptability across multiple environments [3]. Altitude can significantly influence plant growth, structure, function, and metabolism [4, 5]. The morphological and

physiological characteristics of alpine species reflect their environmental adaption under certain altitudinal gradients [6]. As a consequence, modern plant ecologists have paid much attention to these plant characteristics in different biological and ecological zones to better understand their adaptive mechanisms [7, 8].

Alpine plants exhibit specific morphological, physiological, and biochemical responses to an increasing altitude, such as size and increases in the leaf thickness [9–11]. Decreases in plant growth and a higher proportion of plant biomass in the roots usually result in a higher leaf N content and lower C:N ratio, which lead to a higher photosynthetic capacity in alpine plants [12]. Moreover, the relationship between plant functional traits and environmental factors has been recently gaining increasing attention. Plant species may have an optimum altitude for production of biomass and net photosynthetic rate; their enzymatic activities can increase or decrease upon deviation from this optimum altitude [13–15]. Grasses exposed to high altitudinal areas with extreme climatic factors (cold, frost, drought, salinity, low oxygen, high wind velocity, intense UV radiation, and geographical differentiation) provide opportunities to study such adaptive mechanisms [16, 17]. However, the adaptation mechanism in response to altitude variation and climate change is largely unknown [18].

Elymus nutans is a native perennial grass and plays an important ecological role in maintaining regional species diversity and ecosystem stability. It grows extensively across the Qinghai-Tibetan Plateau and Xinjiang of Northwestern China where it is well adapted to a range of environments and is extensively grazed by livestock [19, 20]. It is also one of the important pasture species sown to increase livestock production and groundcover by perennial species. However, research on the species is not equal to the scale of its resource utilization in China. Most reports [21–24] have focused on the biology, genetic diversity, nutrition value, and yield of the species, but there has been little information on the morphological and physiological characteristics of *E. nutans* and the species' local adaptation to variations in altitude [25, 26]. An understanding of these characteristics, particularly of the plant morphological attributes and variations in photosynthesis, is essential to help identify the mechanism of plant adaptability to local-scale environments. Our basic question was whether the physiological and ecological traits of plants of the same species grown in different habitats differed in their responses when grown in alternative environments and how they adapted to their new environment. We hypothesized that there was a set of significant differences in plant morphological, physiological, and biochemical responses of *E. nutans* to increasing altitude that could be taken as a surrogate for differences in thermal regime, solar radiation, and precipitation. Basing on previous work, we attempted to answer the following questions:

- (1) How do the plant functional traits, photosynthesis, and dry matter respond to altitudinal variation

- (2) What are the differences in physiological plasticity of the different physiological parameters of *E. nutans* in the alpine area

We selected changes in shoot and root length, leaf area and root area, dry matter and seed yield, soluble matter concentration, the ratio of carbon and nitrogen, and photosynthetic parameters to elucidate the ecophysiological processes. Because these processes may enable this plant to adapt to varying environments, we could use them to evaluate the potential of this species expanding into higher altitudes. It is expected that findings from this study will help to identify traits for plant breeding strains of *E. nutans* that may be increasingly adapted to climatically changing habitats and for the development of the management strategies to rehabilitate degraded pastures both for pastoral grazing production and environmental sustainability.

2. Materials and Methods

2.1. Experimental Material. Healthy *E. nutans* seeds were obtained from wild plants growing in Tianzhu county of Eastern Qilian Mountains (102°23'–102°78' E, 37°11'–37°18' N), Qilian Mountains, China, which lies in the northeast margin of the Tibetan Plateau, a key site to understanding the species' adaptation in the northeastern of Tibetan Plateau. At least 15 plants of *Elymus nutans* per site were cut from four sites (Dachaigou, Jinqianghe, Honggeda, Daiqian) selected randomly from habitats at 2450, 2950, 3100, and 3300 m a. s. l., in an area of 100–1000 m² that was ecologically homogeneous for the target ecotypes (see Figure 1).

The vegetation type in the sampling areas was composed of alpine meadow grasses and forbs. The soils on which each ecotype grew were of the same soil taxonomic category being shallow, postglacial subalpine meadow soils of high organic matter content. Livestock grazing is the only land use. *Elymus nutans* is the dominant species in this area and occurs naturally and abundantly at altitudes between 2000 and 5000 m a. s. l. in the Qinghai-Tibetan Plateau. After collection, the samples were bulked, dried to 30°C, and seeds threshed out. Seeds were stored at a constant 4°C temperature at the Seed Centre of the College of Grassland Science, Gansu Agricultural University, Lanzhou, China.

2.2. Site, Climate, and Design. Seeds of the 4 ecotypes were sown at the Tianzhu Alpine Grassland Experimental Station of Gansu Agricultural University at an altitude of 2950 m a. s. l., the northeastern margin of the Qinghai-Tibetan Plateau, China. The climate is alpine, cold, and semiarid, with thin air and low temperature, and strong solar radiation, where there is no frost-free season, only cold and cool seasons. The annual average temperature is 0.1°C, with the highest average temperature in July (mean 12.7°C) and the lowest in January (mean -18.3°C). The average annual precipitation is 328.7 mm, concentrated from June to September. The 4 ecotypes were sown as a randomized complete block design with 3 replicates and the plot size was 2 m × 5 m = 10 m² with a 1 m gap between plots. Each plot has row spacing of 40 cm. Sowing depth was 3–4 cm and sowing rate was 22.5 kg/ha.

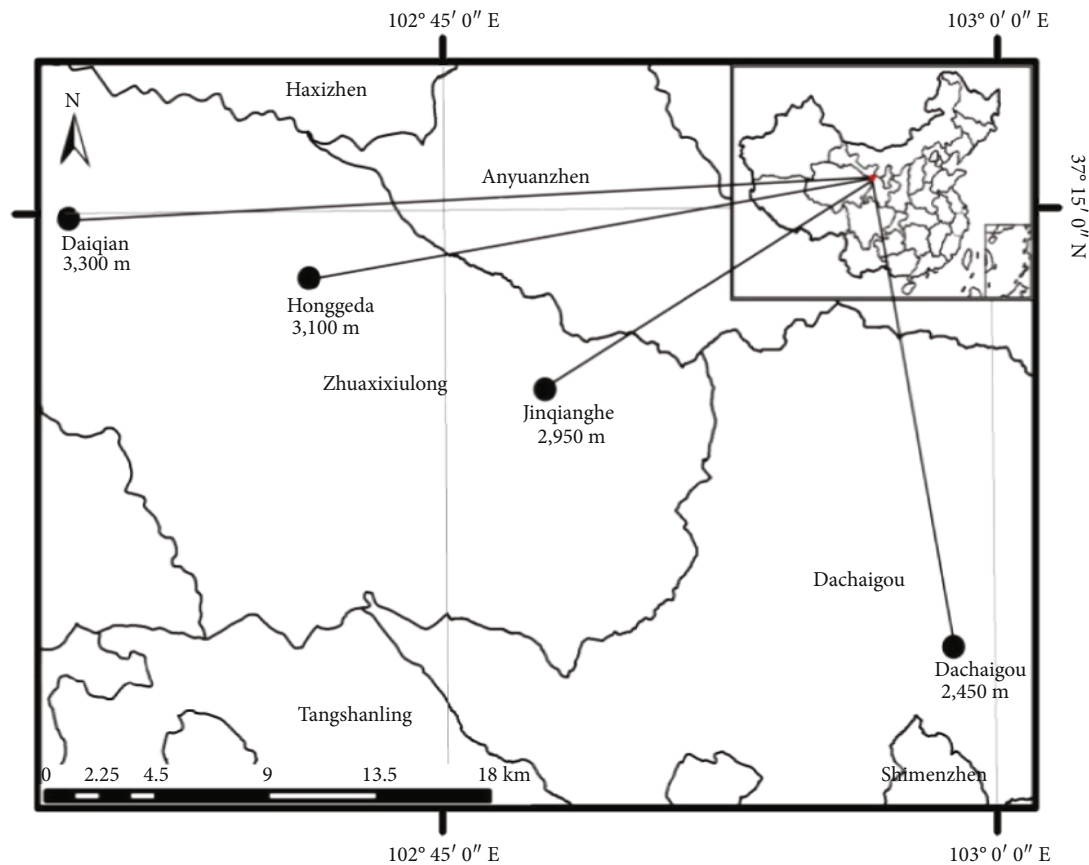


FIGURE 1: Sampling sites (dark spots) for *Elmus nutans* along eastern boundary Qilian Mountains in the Qinghai-Tibet Plateau.

The soil was a shallow, postglacial, subalpine scrub grassland soil with a higher organic matter content (9.45%) in the 0~20 cm soil layer.

2.3. Measurements

2.3.1. Plant Height and Root Depth, Root Surface Area, and Volume. Establishment and vegetative growth of *E. nutans* is slow at altitudes above 2000 m a. s. l., and plants only reach flowering and maturity by the second year. The first year's shoots die back and the growing points lie below the soil surface during the first winter, to reemerge in the second spring [27]. Therefore, all the data presented are from the second year of planting.

Selected measurements were made at different development stages. The plant morphological parameters (shoot height, root length, surface area, and volume) were measured during the period of rapid shoot extension in the second year (the end of July), flag leaf area was measured at full emergence of the flag leaf before flowering (the early of August), and the physiological parameters (soluble sugars, starch, total carbon and nitrogen, and gas exchange properties) and total aboveground (shoot) and belowground (root) dry matter were measured at flowering (August 10th).

Plant height was measured by recording the height of 20 randomly selected plants of *E. nutans* within a plot before each harvest with a 2 m ruler from the soil surface to the

highest point of the plant and averaged to give the mean for each treatment plot. Sections of rows 33 cm long were then randomly selected, whole plants were dug out, and root depth was measured. Whole plants were stored in the self-sealing, labeled bags and refrigerated. Cleaned roots were put into the root plate submerging the root system, and root surface areas and root volume were measured using Photo Scanner and the data analyzed by Root Analysis software.

2.3.2. Leaf Areas. The areas of 10 flag leaves from randomly selected plants taken when flag leaves had fully emerged, and at flowering were determined using an AM-300 Area Meter (Analytical Development Company, Herts, UK).

2.3.3. Herbage Yield. Individual treatment plots were harvested for herbage yield at fully flowering period, with subsamples then taken from each plot, freshly weighed and oven dried at 65°C for 48 hours before being ground.

2.3.4. Seed Yield. Seed yield was made at 80% seed maturity (seeds drop easily) in mid-September. Seed collection was carried out from randomly selected plots of each ecotype, and the seed yield of each experimental plot (10 m²) was determined and converted into kg/ha.

2.3.5. Total Soluble Sugar. The physiological traits were all measured when plants were flowering. Soluble sugar was extracted from a 0.05 g sample with 1-4 ml 80% (v/v) aqueous

ethanol in a water bath at 80°C for 40 min. This sample was centrifuged for 30 minutes at 12000 r/min the supernatant collected, the residue reextracted with 80% (v/v) aqueous ethanol, and finally, the sample was centrifuged and merged with the supernatant. The extracted solution was diluted to 50 ml after extracting 2 times. 1 ml of the extract obtained was mixed with 5 ml of anthrone-sulphuric acid reagent. After cooling to room temperature, the absorbance was measured at 627 nm using a UV-2550 UV-visible spectrophotometer.

2.3.6. Starch Contents. The residue from the soluble sugars was boiled with 6 mol/l HCl in a water bath at 80°C for 5 min, the sample centrifuged for 10 minutes at 4000 r/min the supernatant collected, and the above step repeated twice. Absorbance was measured at 580 nm using a UV-2550 UV-visible spectrophotometer. Starch content was calculated by multiplying by the coefficient of hydrolysis (0.9).

2.3.7. Determination of Total Organic Carbon Content. The samples were air-dried and ground to pass a 0.25 mm mesh for total organic carbon content. Approximately 0.015–0.020 g of each leaf and root sample was put into clear flask, mixed with 10 ml of $K_2Cr_2O_7$, and then heated 5 min. The solution was cooled and then titrated with $FeSO_4$ [28].

2.3.8. Nitrogen Analysis. N was determined by a small-scale Kjeldahl digestion [29]. 0.5 g of ground herbage from each sample was added to a flask, with 10 ml of H_2SO_4 and 3 g of $CuSO_4 \cdot 5H_2O$ and K_2SO_4 ($CuSO_4 \cdot 5H_2O : K_2SO_4 = 1 : 10$), and shaken until thoroughly mixed, heated from a low to high flame until the solution became clear, topped up to 100 ml with ammonium-free distilled water, and 10 ml of the solution mixed with 4 ml 40% NaOH and distilled using a Kjeldahl apparatus for 4 min. NH_3 released through distillation was absorbed by 1% boric acid and then titrated against 0.02 mol l^{-1} HCl to determine the N content.

2.3.9. Gas Exchange. The Li-6400 portable photosynthetic analyzer (Li-COR, USA) was used to determine the daily change (8:30 am–17:30 pm) of photosynthetic parameters of *E. nutans* in an open gas analysis system. All measurements were carried out on healthy leaves in the field on sunny days at flowering period. Three leaves from each plot were randomly selected. The photosynthetic parameters included a net photosynthesis rate (P_n , $\text{mmol CO}_2 \text{ m}^{-2} \text{ s}^{-1}$), transpiration rate (Tr , $\text{mmol H}_2O \text{ m}^{-2} \text{ s}^{-1}$), stomatal conductance ($Cond$, $\text{mmol m}^{-2} \text{ s}^{-1}$), and intercellular CO_2 concentration (C_i , $\mu\text{mol CO}_2 \text{ mol air}^{-1}$). The parameters were calculated as the mean value for the day.

2.3.10. Statistical Analyses. Normality of distribution and homogeneity of variance were checked before any further statistical analysis. An investigation into normality of the data was carried out by performing the Kolmogorov-Smirnov test using SPSS 19 software. The data were normally distributed and better meet the assumptions of the statistical tests used. Analysis of variance and calculation of means were conducted using Excel and SPSS19 software. Morphological data and photosynthetic responses of plant were analyzed

using a one-way analysis of variance (ANOVA), and the mean values were compared using the least significant difference (LSD) at $P = 0.05$.

3. Results

3.1. Changes in the Plant Height and Root Depth of Four *E. nutans* Populations from Different Altitudes. The plants originating from different altitudes showed no statistically significant differences in height and root depth when grown at 2950 m a. s. l. (Figure 2), which indicated that the altitude variations had less effect on the growth of plant height and root depth in alpine zone.

3.2. Changes in Leaf and Root Surface Area. Leaf and root area responses varied significantly along the altitudinal gradient, increasing from 2450 to 2950 m and then decreasing from 2950 to 3300 m a. s. l. Both of leaf areas and root surface areas were significantly different and smaller in value for plants collected from both the highest and lowest altitudes compared with those from 2950 and 3100 m a. s. l. (Figure 3). The leaf area and root surface area showed a significant negative correlation with altitude, and the correlation coefficient was 0.9938 and 0.9393, respectively.

3.3. Changes in Total Root Length and Root Volume. Original altitude significantly influenced total root length and root volume but to different extents (Figure 4). There was no significant difference in total root length from 2450 to 2950 m but root length decreased as altitude increased from 2950 to 3300 m a. s. l. The root length from 3300 m was lower than that from 2450 m and 2950 m a. s. l. 41% and 46%, respectively. Root volume increased as altitude increased from 2450 m to 2950 m a. s. l. and then decreased. The root volume from 3300 m was lower than that from 2950 m a. s. l. 47%.

Figures 3 and 4 show that the smaller leaf areas and root characteristics of plants from the lowest altitude (2450 m a. s. l.) when grown at higher altitude, and the inability of the plants from higher altitude (3310 and 3330 m a. s. l.) to increase their leaf and root size when grown at a lower altitude, provide good evidence that local adaptation has occurred, inhibiting the plants from taking advantage of the conditions prevailing at 2950 m a. s. l.

3.4. Changes in Aboveground and Belowground Dry Matter and Seed Yield. The aboveground dry matter decreased with altitude increased while the belowground dry matter showed a reverse trend. Ecotypes from high altitude allocated significantly ($P < 0.05$) greater dry matter yield to roots than those adapted to low and mid altitudes. Aboveground dry matter yield allocation averaged 875 kg/ha at the lowest altitude, nearly twice the value of the plants from the highest altitude. It was observed that ecotypes from lower altitudes allocated more dry matter to the stems of plants than those from higher altitudes. Total dry matter (combined root and shoot dry matter) values for the four ecotypes showed that there was a reduction with each increase in original elevation (Table 1), while root:shoot ratios also increased, providing a clear indication that the total abiotic stress increased with altitude, as root:shoot ratio increases with nearly every

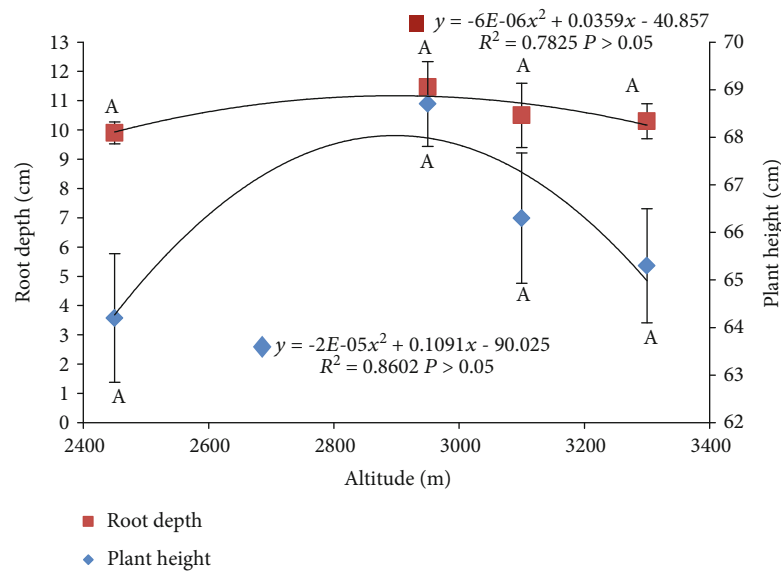


FIGURE 2: Plant and root depth of four *E. nutans* populations from different altitudes in the northeastern Tibetan Plateau, when grown at a single elevation of 2950 m a. s. l. Values are shown as the mean \pm SE of three replicated. Different letters indicate that the mean values are significantly different among the treatments ($P = 0.05$).

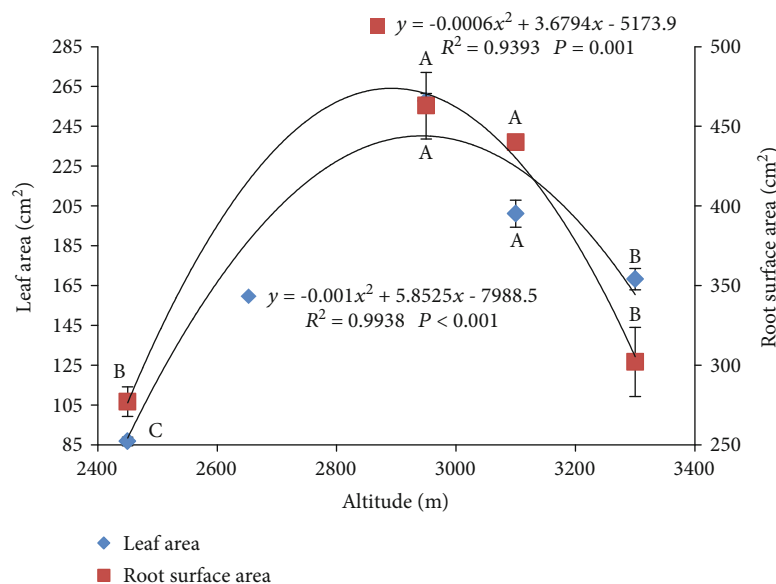


FIGURE 3: Changes in the plant and root area of four *E. nutans* populations from different altitudes in the northeastern Tibetan Plateau. Values are shown as the mean \pm SE of three replicated. Different letters indicate that the mean values are significantly different among the treatments ($P = 0.05$).

abiotic stress. The plants selected from, and grown at 2450 m a. s. l., were the largest in total weight, while the plants from the 2950 m a. s. l. were only slightly smaller, but they partitioned more of their assimilates into roots or seeds and less into dry matter. Plants from 3000 m a. s. l. were consistently smaller in every respect and were not able to take advantage of the milder conditions when grown at 2950 m a. s. l.

Seed yield of plants from 2450 to 2950 m a. s. l. increased 22.4 kg/ha and then decreased markedly and reached a minimum at the 3300 m (46.2 kg/ha), with the seed yields from

3100 and 3300 m a. s. l. being significantly lower than either of the lower altitudes. While seed production of the 2450 m a. s. l. ecotype was somewhat restricted by being grown at the higher elevation, the lack of capacity of the 3100 and 3300 m ecotypes to exploit the more favourable growing conditions at 2950 m a. s. l. again indicates that substantial local adaptation has taken place.

3.5. Soluble Sugar and Starch Content. Soluble sugar and starch content all showed significant differences in the leaves

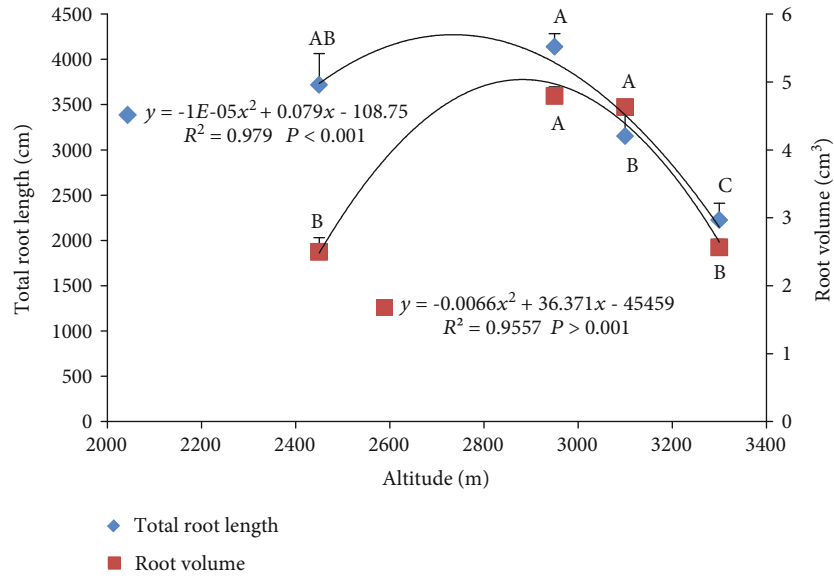


FIGURE 4: Changes in the total root length and root volume of four *E. nutans* populations from different altitudes in the northeastern Tibetan Plateau. Values are shown as the mean \pm SE of three replicated. Different letters indicate that the mean values are significantly different among the treatments ($P = 0.05$).

TABLE 1: Aboveground, belowground, and total dry matter with root:shoot ratios at flowering and seed yield at 80% maturity for four different populations of *E. nutans*.

Altitude (m)	Aboveground dry matter (kg hm ⁻²)	Belowground dry matter (kg hm ⁻²)	Root : shoot ratio	Total plant weight (kg hm ⁻²)	Seed yield (kg hm ⁻²)
2450	875 \pm 32.4 ^a	283.8 \pm 24.5 ^b	0.32 \pm 0.04 ^c	1159 \pm 8.9 ^a	85.6 \pm 3.07 ^b
2950	707 \pm 28.3 ^b	343.8 \pm 4.09 ^a	0.49 \pm 0.03 ^b	1051 \pm 24.3 ^b	108 \pm 2.71 ^a
3100	640 \pm 16.7 ^{bc}	347.3 \pm 14.2 ^a	0.55 \pm 0.03 ^{ab}	987 \pm 22.7 ^{bc}	67 \pm 3.18 ^c
3300	588 \pm 8.1 ^c	364.5 \pm 20.2 ^a	0.62 \pm 0.03 ^a	953 \pm 28.3 ^c	46.2 \pm 3.61 ^d

TABLE 2: Soluble sugar and starch content of seedlings along the altitude gradients.

Altitude (m)	Soluble sugar content (%)		Starch content (%)	
	Aboveground	Belowground	Aboveground	Belowground
2450	0.694 \pm 0.02 ^b	0.025 \pm 0.0 ^b	0.035 \pm 0.0 ^b	0.021 \pm 0.0 ^a
2950	0.918 \pm 0.01 ^a	0.043 \pm 0.0 ^{ab}	0.043 \pm 0.0 ^a	0.035 \pm 0.0 ^b
3100	0.889 \pm 0.01 ^a	0.053 \pm 0.0 ^a	0.034 \pm 0.0 ^b	0.033 \pm 0.0 ^b
3300	0.736 \pm 0.02 ^b	0.032 \pm 0.0 ^b	0.031 \pm 0.0 ^b	0.014 \pm 0.0 ^c

and roots of plants derived from different altitudes. The soluble sugars followed the similar parabolic curve to the root and shoot morphological traits increasing first with altitude from 2450 to 2950 m a. s. l. and then decreasing (Table 2). Soluble sugars of belowground roots reached the highest value at 3100 m a. s. l. The aboveground starch contents were only marginally different from plants originating from 2950 m a. s. l., but the belowground starch contents of plants from the highest and lowest altitudes were significantly less than those from the intermediate altitudes.

3.6. *Total C and Total N Concentration and the Ratios of C:N.* Table 3 shows that aboveground C contents were not significantly different except in plants derived from 2450 m, although plants from 3100 and 3300 m a. s. l. had numerically greater C contents. The root C was similarly higher in the plants from the lowest altitude. There were no significant differences in root C content among ecotypes from high altitudes. The plants derived from lowest altitude had a significantly lower aboveground nitrogen (N) content and higher belowground N content than the other ecotypes. The aboveground C:N increased as the altitude increased,

TABLE 3: Total C content, N content, and C:N of seedlings along the elevation gradients.

Altitude (m)	Carbon content (%)		Nitrogen content (%)		C:N	
	Aboveground	Belowground	Aboveground	Belowground	Aboveground	Belowground
2450	23.9 ± 1.4 ^b	48.57 ± 4.69 ^a	1.28 ± 0.01 ^b	2.23 ± 0.06 ^a	18.7 ± 1.2 ^{bc}	21.78 ± 1.5 ^a
2950	39.28 ± 3.6 ^a	33.06 ± 1.98 ^b	1.61 ± 0.05 ^a	2.11 ± 0.08 ^{ab}	24.4 ± 1.49 ^{bc}	15.67 ± 0.8 ^b
3100	49.5 ± 4.88 ^a	28.4 ± 3.14 ^b	1.65 ± 0.04 ^a	1.87 ± 0.07 ^b	30 ± 3.2 ^{ab}	15.2 ± 1.2 ^b
3300	47.9 ± 1.52 ^a	30.8 ± 2.45 ^b	1.55 ± 0.04 ^a	2.05 ± 0.10 ^{ab}	30.9 ± 0.4 ^a	15 ± 0.8 ^b

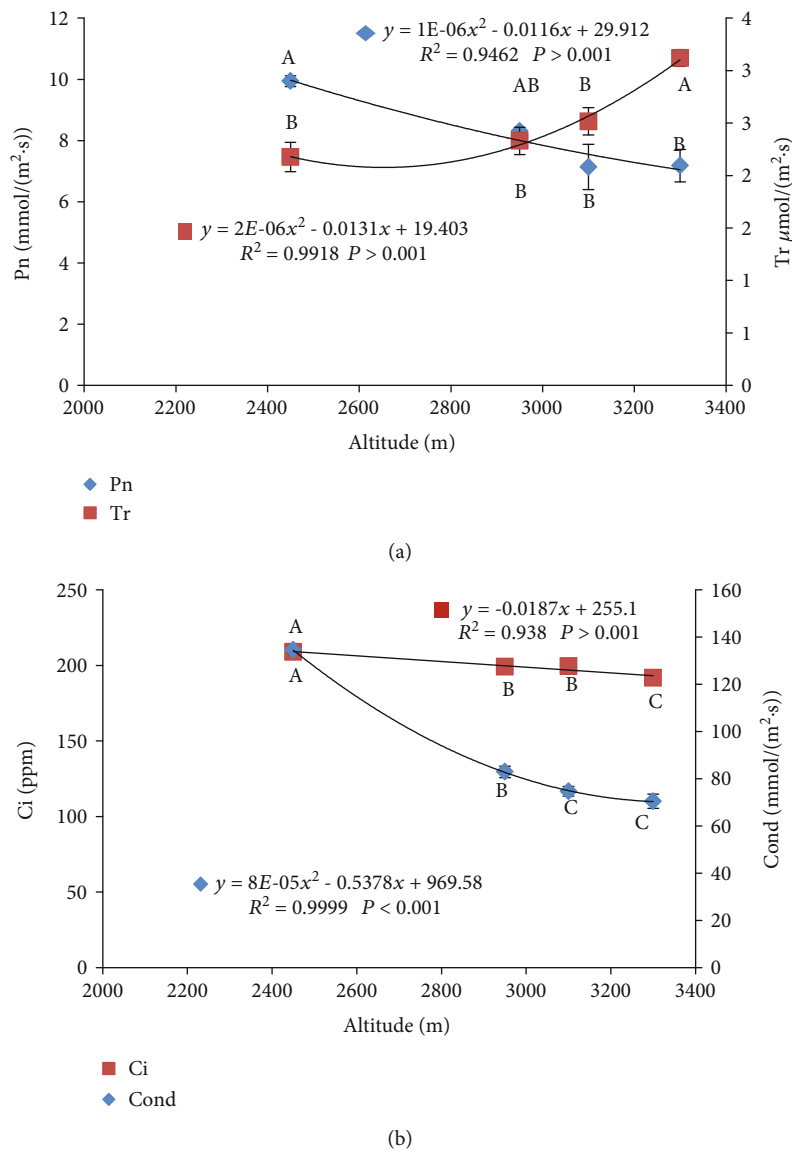


FIGURE 5: (a) Photosynthetic response (Pn—net photosynthetic rate) and transpiration (Tr). (b) Response of intercellular CO₂ concentration (Ci) and stomatal conductance (Cond) measured on four *E. nutans* populations from different altitudes. Values are shown as the mean ± SE of three replicated. Different letters indicate that the mean values are significantly different among the treatments ($P = 0.05$).

but the root C:N ratio was only significantly different in the 2450 m a. s. l. ecotype.

3.7. Photosynthetic Parameters of Leaves of Four *E. nutans* Populations from Different Altitudes.

Photosynthetic characteristics in leaves of the four ecotypes from different altitudes

were measured during the period of maximum growth (the end of July, second year). The results (Figure 5) are the means of data collected between 8:30 am–17:30 pm during 25 July. They showed the photosynthetic rate (Pn) and intercellular CO₂ concentration (Ci) responded in a similar manner to the shoot dry matter. Pn decreased as the altitude increased.

The Pn of plants from 3300 m was 28% lower than those from 2450 m a. s. l., but there was no significant difference among values of plants from 2950, 3100, and 3300 m a. s. l. However, Tr increased as the altitude from which the plants were derived increased. The Tr from 3300 m was 43% higher than that of 2450 m a. s. l. (Figure 5(a)). By calculating the water use efficiency ($WUE = Pn/Tr$), it was found the plant WUE gradually decreased from lower altitude to higher altitude. The Cond and Ci responses were highly correlated with the altitude of the original populations and decreased significantly as altitude increased (Figure 5(b)). The Ci and Cond from 3300 m were lower than that of from 2450 m a. s. l. 8% and 48%, respectively.

4. Discussion

4.1. Variation in Morphological Traits of *E. nutans* with Altitude Gradient Migration. Altitude is an important ecological factor that affects population differentiation and genetic variation. The high altitude especially in the alpine region has a pronounced influence on the plants. Plants have obvious adaptation strategies by modifying their morphological and physiological attributes [30]. The long-term effects of environment on plants can alter their morphology, physiological function, and ecology [31, 32]. Only those that adapt to their environment can survive well, while those that do not will gradually be eliminated from the local ecosystem. Therefore, morphological characterization of ecotypes provides useful information for evaluation of agronomic aptitude and development of new varieties [33].

In most alpine species, small stature is a genetic adaptation to low temperatures, and hence, they retain this feature when grown in a warm environment as low temperature affects the growth process and photosynthetic carbon gain [34]. In this experimental location, plant height, root depth, and root volume of *E. nutans* from different altitudes showed no significant change. These were the relatively conservative traits among the morphological traits measured along altitudinal gradients in an alpine region, similar to those described by Zhu's research [35]. However, ecotypes from 3300 m had larger leaf areas and root surface areas than those from 2450 m a. s. l. In the cold temperate zone, an increase in temperature reduces abiotic stress and improves the overall plant growth rate [36], especially affecting the photosynthetic and nutrient absorption processes. Our results are in line with other research findings for trees [37]. Furthermore, the plants derived from 2950 m a. s. l. and grown at the same altitude had the greatest morphological size in attributes such as plant height, root length, leaf area, total root length, and root volume. This indicated that local ecotypes performed better than the introduced plants from other altitudes because they were better adapted to local environmental conditions [38]. In addition, different ecotypes of the same species may adopt different survival strategies to adapt to the environmental stress [39]. For plants growing in the cold environments, for example, the leaf area and leaf size are normally small but the corresponding plant dry matter accumulation and net photosynthesis rate may be more profoundly affected [40]. The physiological measurements relating to photosyn-

thesis taken at the period of fastest daily growth (prior to flowering) showed that the plants derived from 2950 and 3100 m a. s. l. were growing faster, which supports this interpretation. The plants from the highest altitude (3300 m a. s. l.) were not able to adjust to the warmer growing conditions within a single generation, and the plants from the lowest altitude (2450 m a. s. l.) were probably restricted by the lower temperatures they encountered at 2950 m a. s. l. [41].

4.2. Effect of Altitude Migration on Material Accumulation and Distribution. Although the four ecotypes of the species *E. nutans* were generally similar in appearance and morphological characteristics, differences were observed in the dry matter characteristics, carbon, and nitrogen content. Plants from the lowest altitude maintained higher dry matter accumulation and seed yield than those adapted to 2950 m a. s. l. This is good evidence that there had been local adaptation to the conditions occurring at different altitudes [42]. We could expect that plants selected from the lowest altitude and grown at a higher altitude would not grow so fast because they were exposed to more cold, and that the plants from the higher altitudes grown at lower altitude would grow faster (and perhaps accumulate more belowground dry matter) and also through regulating physiological activity to adapt to the environment changes. When we compared (Table 1) the way the plants from different altitudes partitioned their assimilates, it was clear that the total amount of plant production (aboveground and belowground dry matter and seed yield) was significantly less in the plants from the higher altitudes, despite being grown at a more favourable (warmer) altitude, whereas the plants from the two lower altitudes had a similar total biomass but allocated their assimilates in different ways. The total amount of aboveground herbage was greatest in the plants from the lowest altitude (and probably if all ecotypes had been grown at 2450 m a. s. l., these plants would have been largest overall). The plants originating from the low altitude may have had some differences in morphological and physiological characteristics that could possibly have been due to the results of natural selection not just the altitude factor [43]. However, overall, each ecotype largely kept its original characteristic when being transplanted to another altitude [44]. As we found a linear decrease in seed set with altitudinal origin, it is likely that the higher growth rates of plants from lower altitudes would be maintained in other growing sites.

4.3. Effect of Altitude Migration on Physiological Characteristics. Nonstructural carbohydrate (NSC) which mainly refers to the sugar and starch has a great influence on plant growth and adaptability [45]. NSC is the product of photosynthesis. Therefore, factors affecting photosynthesis will also affect NSC of plants [46]. When photosynthesis changes, the NSC may change a variety of ways that can be induced directly or indirectly by various environmental factors [47, 48]. Previous studies have shown that photosynthetic capacity and plant N content may have a positive correlation while higher photosynthetic activity can increase CO_2 assimilation so that NSC is also enhanced [49, 50]. In our study, plants from the middle altitudes (2950 and

3100 m a. s. l.) had higher soluble sugars, and root starch contents, in the typical parabolic response form, whereas the carbon and nitrogen contents and C:N ratios were significantly different only in the plants derived from the lowest (2450 m a. s. l.) altitude suggesting they were partitioning their assimilates into structural components in different ways. The seedlings sourced from higher altitudes had better nitrogen utilization ability than those from lower altitudes. This suggests that ecotypes of *Elymus nutans* sourced from different altitudes may have beneficial attributes of adaptive value under the condition of future climate change.

We may postulate that plants from the lower elevations (below 3000 m a. s. l.) are therefore most suited to being sown in situations where the amount of grass for yak feed is of most importance, whereas ecotypes that have developed at higher specific altitudes are most suited for use in rehabilitation programs aimed at repairing degraded natural grasslands that have suffered from erosion or overgrazing.

5. Conclusions

We can conclude that local adaptation has occurred in *Elymus nutans* growing naturally at different altitudes: these adaptations include changes in the size of the plants, the ratio of roots to shoots, the ratio of C:N, the total herbage and seed produced over the growing season, and the extent of the genetic by environment interaction (responsiveness) when grown at intermediate elevations. We suggest that ecotypes from the lower altitudes will be most productive for increasing grazing by yaks below 3000 m a. s. l., but that locally adapted ecotypes should be used within their specific local habitats for ecological restoration of degraded grassland. Adaptation is the result of a long-term evolutionary process in concert with stress conditions. Further studies are needed to fully understand how altitude migration affects *Elymus nutans* growth on the Qinghai-Tibetan Plateau.

Data Availability

The data used to support the findings of this study are included within the article.

Conflicts of Interest

The authors declare there are no competing interests.

Acknowledgments

This work was supported by the National Natural Science Foundation of China (grant number 31660684), the Key Laboratory of Superior Forage Germplasm in the Qinghai-Tibetan Plateau (grant number 2020-ZJ-Y09), and the Earmarked Fund for China Agriculture Research System (grant number CARS-34). The authors are grateful to Changlin Xu for his help and valuable technical assistance and those students who were involved in part of the field and lab work.

References

- [1] S. E. Sultan, "Phenotypic plasticity and plant adaptation," *Acta Botanica Neerlandica*, vol. 44, no. 4, pp. 363–383, 1995.
- [2] P. Robakowski, P. Montpied, and E. Dreyer, "Plasticity of morphological and physiological traits in response to different levels of irradiance in seedlings of silver fir (*Abies alba* Mill.)," *Trees*, vol. 17, no. 5, pp. 431–441, 2003.
- [3] S. McIntyre, S. Lavorel, J. Landsberg, and T. D. A. Forbes, "Disturbance response in vegetation—towards a global perspective on functional traits," *Journal of Vegetation Science*, vol. 10, no. 5, pp. 621–630, 2009.
- [4] F. J. Berli, R. Alonso, R. Bressan-Smith, and R. Bottini, "UV-B impairs growth and gas exchange in grapevines grown in high altitude," *Physiologia Plantarum*, vol. 149, no. 1, pp. 127–140, 2013.
- [5] V. Dogra, P. S. Ahuja, and Y. Sreenivasulu, "Change in protein content during seed germination of a high altitude plant *Podophyllum hexandrum* Royle," *Journal of Proteomics*, vol. 78, no. 78, pp. 26–38, 2013.
- [6] L. Pellissier, A. Espíndola, J. N. Pradervand et al., "A probabilistic approach to niche-based community models for spatial forecasts of assemblage properties and their uncertainties," *Journal of Biogeography*, vol. 40, no. 10, pp. 1939–1946, 2013.
- [7] I. J. Wright, P. K. Groom, B. B. Lamont et al., "Short communication: leaf trait relationships in Australian plant species," *Functional Plant Biology*, vol. 31, no. 5, pp. 551–558, 2004.
- [8] J. S. He, Z. Wang, X. Wang et al., "A test of the generality of leaf trait relationships on the Tibetan Plateau," *New Phytologist*, vol. 170, no. 4, pp. 835–848, 2006.
- [9] A. D. Richardson, G. P. Berlyn, and T. G. Gregoire, "Spectral reflectance of *Picea rubens* (Pinaceae) and *Abies balsamea* (Pinaceae) needles along an elevational gradient, Mt. Moosilauke, New Hampshire, USA," *American Journal of Botany*, vol. 88, no. 4, pp. 667–676, 2001.
- [10] M. H. Li, J. Yang, and N. Kräuchi, "Growth responses of *Picea abies* and *Larix decidua* to elevation in subalpine areas of Tyrol, Austria," *Canadian Journal of Forest Research*, vol. 33, no. 4, pp. 653–662, 2003.
- [11] Q.-q. Guo, H. E. Li, and W. H. Zhang, "Variations in leaf functional traits and physiological characteristics of *Abies georgei* var. *smithii* along the altitude gradient in the Southeastern Tibetan Plateau," *Journal of Mountain Science*, vol. 13, no. 10, pp. 1818–1828, 2016.
- [12] C. C. Bresson, Y. Vitasse, A. Kremer, and S. Delzon, "To what extent is altitudinal variation of functional traits driven by genetic adaptation in European oak and beech?," *Tree Physiology*, vol. 31, no. 11, pp. 1164–1174, 2011.
- [13] Z. Q. Cai, D. Y. Jiao, S. X. Tang, X. S. Dao, Y. B. Lei, and C. T. Cai, "Leaf photosynthesis, growth, and seed chemicals of *Sacha Inchi* plants cultivated along an altitude gradient," *Crop Science*, vol. 52, no. 4, pp. 1859–1867, 2012.
- [14] J. A. Grytnes and O. R. Vetaas, "Species richness and altitude: a comparison between null models and interpolated plant species richness along the Himalayan altitudinal gradient, Nepal," *The American Naturalist*, vol. 159, no. 3, pp. 294–304, 2002.
- [15] S. K. Schmidt, S. C. Reed, D. R. Nemergut et al., "The earliest stages of ecosystem succession in high-elevation (5000 metres above sea level), recently deglaciated soils," *Proceedings of the*

- Royal Society B: Biological Sciences*, vol. 275, no. 1653, pp. 2793–2802, 2008.
- [16] S. Ahmed, M. Ahmad, B. L. Swami, and S. Ikram, “A review on plants extract mediated synthesis of silver nanoparticles for antimicrobial applications: a green expertise,” *Journal of Advanced Research*, vol. 7, no. 1, pp. 17–28, 2016.
 - [17] M. Hasanuzzaman, K. Nahar, M. Alam, R. Roychowdhury, and M. Fujita, “Physiological, biochemical, and molecular mechanisms of heat stress tolerance in plants,” *International Journal of Molecular Sciences*, vol. 14, no. 5, pp. 9643–9684, 2013.
 - [18] A. S. Jump and J. Penuelas, “Running to stand still: adaptation and the response of plants to rapid climate change,” *Ecology Letters*, vol. 8, no. 9, pp. 1010–1020, 2005.
 - [19] W. Xie, J. Zhang, X. Zhao, J. Zhang, and Y. Wang, “Siberian wild rye (*Elymus sibiricus* L.): Genetic diversity of germplasm determined using DNA fingerprinting and SCoT markers,” *Biochemical Systematics and Ecology*, vol. 60, no. 60, pp. 186–192, 2015.
 - [20] G. D. Zhou, Z. Y. Li, H. Y. Li, W. G. Shi, X. Y. Li, and L. Liu, “Research advances in germplasm resource of *Elymus sibiricus*,” *Pratacultural Science*, vol. 28, no. 11, pp. 2026–2031, 2009.
 - [21] X. Y. Gu, Z. H. Guo, X. Q. Zhang, Y. H. Zhou, S. Q. Bai, and C. B. Zhang, “Genetic diversity of *Elymus sibiricus* germplasm resources revealed by SRAP markers,” *Acta Prataculturæ Sinica*, vol. 23, no. 3, pp. 205–216, 2014.
 - [22] X. Ma, S. Chen, X. Zhang, S. Bai, and C. Zhang, “Assessment of worldwide genetic diversity of Siberian wild rye (*Elymus sibiricus* L.) germplasm based on gliadin analysis,” *Molecules*, vol. 17, no. 4, pp. 4424–4434, 2012.
 - [23] Y. Y. Zhao, D. J. Huang, Z. X. Mao, B. Nie, and H. Fu, “A study on forage nutritional quality of *Elymus nutans* from different populations in the Qinghai-Tibet Plateau,” *Acta Prataculturæ Sinica*, vol. 22, no. 1, pp. 38–45, 2013.
 - [24] J. H. Zheng, S. Y. Chen, Z. H. Chen, S. D. Li, and J. C. Zhong, “Assessment of genetic diversity of *Elymus nutans* in north-west plateau of Sichuan province using ISSR markers,” *Journal of Southwest University for Nationalities Natural Science Edition*, vol. 40, no. 3, pp. 330–335, 2014.
 - [25] B. X. Xiao, M. Y. Yang, Q. Chen et al., “Study on relation between leaf anatomic structure and drought resistance of five forages in the northwest alpine grassland region of Sichuan,” *Prataculture and Animal Husbandry*, vol. 209, no. 4, pp. 1–5, 2013.
 - [26] H. Q. Wang, *Study on the Morphological Anatomy of Elymus L. Plants*, [M.S. thesis], Chinese Academy of Agricultural Sciences Master Dissertation, Beijing, 2009.
 - [27] X. B. Yan, X. Wang, Y. X. Guo, and D. G. Zhang, “Biomass and feeding value dynamics of *Elymus nutans* pasture in cold alpine pastoral areas,” *Pratacultural Science*, vol. 20, no. 11, pp. 14–18, 2003.
 - [28] S. D. Bao, *Soil agrochemical analysis*, China Agricultural Press, Beijing, China, 2000.
 - [29] M. Korn, W. Dossantos, M. Korn, and S. Ferreira, “Optimisation of focused-microwave assisted digestion procedure for Kjeldahl nitrogen determination in bean samples by factorial design and Doehlert design,” *Talanta*, vol. 65, no. 3, pp. 710–715, 2005.
 - [30] D. L. Royer, P. Wilf, D. A. Janesko, E. A. Kowalski, and D. L. Dilcher, “Correlations of climate and plant ecology to leaf size and shape: potential proxies for the fossil record,” *American Journal of Botany*, vol. 92, no. 7, pp. 1141–1151, 2005.
 - [31] J. P. Gao, Y. H. Wang, and D. F. Chen, “Anatomical characteristics of leaf epidermis and vessel elements of *Schisandra sphenanthera* from different districts and their relationships to environmental factors,” *Acta Botanica Boreali-Occidentalia Sinica*, vol. 23, no. 5, pp. 715–723, 2003.
 - [32] W. D. Lu, P. B. Xu, and X. Pu, “Summary of the situation for applying genetic resources from *Elytrigia* in *Triticum aestivum* breeding,” *Acta Prataculturæ Sinica*, vol. 16, no. 6, p. 136, 2007.
 - [33] S. A. Rao, K. E. P. Rao, M. H. Mengesha, and V. G. Reddy, “Morphological diversity in sorghum germplasm from India,” *Genetic Resources and Crop Evolution*, vol. 43, no. 6, pp. 559–567, 1996.
 - [34] C. Körner, “Plant adaptation to cold climates,” *F1000 Research*, vol. 5, no. 5, 2016.
 - [35] W. H. Zhu, X. H. Zhang, and J. Z. Zhu, “Effect of different altitudes on the morphological traits of *Phleum pratense*,” *Pratacultural Science*, vol. 36, no. 3, pp. 754–762, 2019.
 - [36] L. Rustad, J. Campbell, G. Marion et al., “A meta-analysis of the response of soil respiration, net nitrogen mineralization, and aboveground plant growth to experimental ecosystem warming,” *Oecologia*, vol. 126, no. 4, pp. 543–562, 2001.
 - [37] L. Li, *Ecophysiological Variation in Two Elevation Gradient Sources of Larix rehtii and Picea asperata Seedlings across an Elevation Gradient*, [M.S. thesis], Shanxi Agricultural University, Shanxi, 2015.
 - [38] F. Montagnini, “Strategies for the recovery of degraded ecosystems: experiences from Latin America,” *Interciencia*, vol. 26, no. 10, pp. 498–503, 2001.
 - [39] J. Qi, W. X. Cao, and W. H. Yan, “Phenotypic diversity and environment relations of wild *Elymus* populations,” *Acta Botanica Boreali-Occidentalia Sinica*, vol. 33, no. 5, pp. 1027–1033, 2013.
 - [40] Y. H. Li, T. X. Luo, Q. Lu, X. Y. Tian, B. Wu, and H. H. Yang, “Comparisons of leaf traits among 17 major plant species in Shazhuyu sand control experimental station of Qinghai Province,” *Acta Ecologica Sinica*, vol. 25, no. 5, pp. 994–999, 2005.
 - [41] J.-d. He, J.-y. Xue, J. Gao, J.-n. Wang, and Y. Wu, “Adaptations of the floral characteristics and biomass allocation patterns of *Gentiana hexaphylla* to the altitudinal gradient of the eastern Qinghai-Tibet Plateau,” *Journal of Mountain Science*, vol. 14, no. 8, pp. 1563–1576, 2017.
 - [42] A. H. Halbritter, R. Billeter, P. J. Edwards, and J. M. Alexander, “Local adaptation at range edges: comparing elevation and latitudinal gradients,” *Journal of Evolutionary Biology*, vol. 28, no. 10, pp. 1849–1860, 2015.
 - [43] L. Gratani, “Plant phenotypic plasticity in response to environmental factors,” *Advances in Botany*, vol. 2014, Article ID 208747, 17 pages, 2014.
 - [44] Y. Hautier, P. A. Niklaus, and A. Hector, “Competition for light causes plant biodiversity loss after eutrophication,” *Science*, vol. 324, no. 5927, pp. 636–638, 2009.
 - [45] C. Körner, “Carbon limitation in trees,” *Journal of Ecology*, vol. 91, no. 1, pp. 4–17, 2003.
 - [46] P. Millard, M. Sommerkorn, and G. A. Grelet, “Environmental change and carbon limitation in trees: a biochemical, ecophysiological and ecosystem appraisal,” *New Phytologist*, vol. 175, no. 1, pp. 11–28, 2007.

- [47] M. C. Dietze, A. Sala, M. S. Carbone et al., "Nonstructural carbon in Woody plants," *Annual Review of Plant Biology*, vol. 65, no. 1, pp. 667–687, 2014.
- [48] J. Martínez-Vilalta, A. Sala, D. Asensio et al., "Dynamics of non-structural carbohydrates in terrestrial plants: a global synthesis," *Ecological Monographs*, vol. 86, no. 4, pp. 495–516, 2016.
- [49] S. -B. Zhang, H. Hu, K. Xu, and Z. . R. Li, "Photosynthetic performances of five *Cypripedium* species after transplanting," *Photosynthetica*, vol. 44, no. 3, pp. 425–432, 2006.
- [50] Y. Zheng, F. Li, L. Hao et al., "Elevated CO₂ concentration induces photosynthetic down-regulation with changes in leaf structure, non-structural carbohydrates and nitrogen content of soybean," *BMC Plant Biology*, vol. 19, no. 1, p. 255, 2019.